

https://dspace.org/

Trans-crustal and temporal perspectives of Palaeoproterozoic porphyry copper deposit formation (Haib deposit, Namibia)

Jogee, Bibi Ayesha

2023

University of the Witwatersrand, Johannesburg

https://hdl.handle.net/10539/42253

Jogee, Bibi Ayesha. (2024). Trans-crustal and temporal perspectives of Palaeoproterozoic porphyry copper deposit formation (Haib deposit, Namibia) [Master's dissertation, University of the Witwatersrand, Johannesburg]. WireDSpace.

Downloaded from a DSpace repository. https://dspace.org/

Trans-crustal and temporal perspectives of Palaeoproterozoic porphyry copper deposit formation (Haib deposit, Namibia).

Bibi Ayesha Jogee

1116755

A thesis submitted to the Faculty of Science, University of the Witwatersrand, in fulfilment of the requirements for the degree of Doctor of Philosophy



UNIVERSITY OF THE WITWATERSRAND, JOHANNESBURG

School of Geosciences
University of the Witwatersrand

September 2023

Johannesburg, South Africa

Declaration

I declare that this thesis is my own, unaided work. It is being submitted for the Degree of Doctor of Philosophy at the University of the Witwatersrand, Johannesburg. It has not been submitted before for any degree or examination to any other University.



Bibi Ayesha Jogee (signature of candidate)

15th day of September 2023 at the University of the Witwatersrand, Johannesburg, South Africa

بِسْمِ اللهِ الرَّحْمٰنِ الرَّحِيْمِ

***

We are our brother's keepers.

We are our sister's keepers.

~Trai Byers

Abstract

Porphyry copper deposits are the world's primary source of copper which is an essential critical metal in the green energy sector. These deposits are most often temporally found within the Phanerozoic Eon and occur principally at convergent plate boundaries. The Haib porphyry copper deposit is a rare example of a Palaeoproterozoic porphyry copper deposit. The Haib porphyry copper deposit is hosted by the rock types of the Richtersveld Subprovince. The Richtersveld Subprovince consists of an older volcano-sedimentary sequence, the Orange River Group (ORG), which was intruded by an extensive composite cogenetic suite of plutonic rocks, the Vioolsdrif Intrusive Suite (VIS). The Vioolsdrif Intrusive Suite is subdivided into several subunits, known as the Vuurdood Subsuite (mafic-ultramafic), Gaobis Diorite, Khoromus porphyry, Goodhouse Subsuite (Granodiorite) and the Ramansdrif Alkali Granite. These subsuites are variably composed of diorites, granodiorites, monzogranites, quartz-feldspar porphyry granodiorites and leucogranites as well as poorly-described clinopyroxenites and gabbros (named the Kokerboom Intrusion in this study). The age-range for the Richtersveld Subprovince is between approximately 1910 and 1865 Ma. The mineralization occurs as disseminations, blebs and veins in the feldspar porphyry andesites and quartz-feldspar porphyry granodiorites. The age of mineralization is bracketed at 1884 ± 2 Ma.

The Haib porphyry copper deposit is in close vicinity to clinopyroxene and amphibole-rich cumulates, which host novel sulphide mineralization, and present lines of evidence suggesting these are the deeper parts of the porphyry copper system. The mineralization is characterized into two main phases based on drill-core sample descriptions, petrographic observations, mineral liberation maps and isotopic analyses. Previous studies show that garnet and/or amphibole fractionation is related to the petrogenesis of porphyry copper deposits. The Haib porphyry copper deposit shows evidence for amphibole fractionation as opposed to garnet fractionation, which is supported by petrological and geochemical observations in this study. The Haib porphyry copper deposit also has limited ranges in $\delta^{65}Cu$ and $\delta^{56}Fe$ signatures supporting exposure at deeper crustal levels of an arc system.

Typical cumulates from deep crustal arc sections (arclogites) are coarse-grained, show cumulate textures and are composed of garnet-clinopyroxene-amphibole-iron-titanium oxides and in some cases plagioclase. The mafic-ultramafic cumulates such as the clinopyroxenites observed in the Kokerboom Intrusion, in close proximity to the Haib porphyry copper deposit, are coarse-grained, are composed of clinopyroxene-amphibole-iron-titanium oxides and consist of non-cotectic proportion of mineral phases. They also comprise a high modal abundance of pyroxene (>70 %) and show distinct cumulate textures. This study has demonstrated that the clinopyroxene and amphibole-rich cumulates which belong to the ultramafic end member of the Kokerboom Intrusion form part of the Vuurdood Subsuite. This conclusion was made through the analysis of lithological characteristics, mineral and alteration assemblages, major and trace element geochemistry and U-Pb age data.

Various lines of evidence from this study indicate that the Haib porphyry copper deposit represents the deeper levels of the porphyry system. These lines of evidence include the lack of shallow alteration assemblages (propylitic and argillic alteration), the presence of early dark micaceous veins, the coarse-grained nature of the Vioolsdrif Intrusive Suite (clinopyroxenites, granodiorites, diorites, gabbros), which is indicative of slow cooling at mid-crustal batholith depths, and the presence of clinopyroxene and amphibole rich cumulates of the Kokerboom Intrusion. The clinopyroxenites are mafic, dense, and usually occur at mid- to lower-crustal levels. Geothermobarometry conducted on rocks of the Vioolsdrif Intrusive Suite yield an

approximate depth of crystallization between ~4-12 km which forms part of the mid-crustal levels of an arc system.

Porphyry copper deposits are related to various phases of mineralization and alteration. Drill-core sample descriptions, petrographic observations, and mineral liberation maps indicate that the mineralization is characterized by disseminated, massive and vein-type sulphides (pyrite and chalcopyrite). Isotopically, the mineralization is characterized by two phases: disseminated-massive (heavier isotopic signature of 0.06 ± 0.07 to 0.21 ± 0.07 ‰ and 0.02 ± 0.07 to 0.06 ± 0.07 ‰ for δ^{65}Cu and δ^{56}Fe respectively) and vein-type (lighter isotopic signature of -0.08 ± 0.07 to 0.11 ± 0.07 ‰ and 0.11 ± 0.07 to -0.01 ± 0.07 ‰ for δ^{65}Cu and δ^{56}Fe respectively). Field and petrographic observations indicate that potassic and phyllic alteration are the dominant alteration phases in the Haib deposit area.

Petrographic observations (amphibole-rich mineral assemblages), trace element analyses (listric-shaped REE element analyses and elevated Yb and Y concentrations) and depleted δ^{56}Fe signatures in this study indicate that amphibole fractionation plays an important role in the formation of some porphyry copper deposits. Amphibole fractionation has the potential to form low δ^{56}Fe signature cumulates that are linked with an enriched δ^{56}Fe signature in the residual magma. This is observed by the low δ^{56}Fe isotopic signature of the more mafic components of Vioolsdrif Intrusive Suite (Vuurdood Subsuite) and the elevated δ^{56}Fe isotopic signature of the residual magma, which formed parts of the more intermediate to felsic components of the Vioolsdrif Intrusive Suite and Orange River Group.

The Palaeoproterozoic Haib deposit is similar to Phanerozoic porphyry deposits based on the overlap of the δ^{65}Cu and δ^{56}Fe isotopic signatures of the chalcopyrite grains, the direct comparison of the δ^{56}Fe signatures of the host granodiorite porphyry in the Duolong deposit and Haib deposit and the magmatic assemblage oxybarometers i.e. amphibole + magnetite + quartz + rutile + sphene in the host granodiorite porphyry which is indicative of elevated oxygen fugacity and corroborates with the enriched δ^{56}Fe signature of the host granodiorite porphyry. The δ^{65}Cu signatures for the Haib deposit are between -0.14 ‰ and 0.46 ‰ whereas, the δ^{65}Cu signatures for Phanerozoic deposits are between -1.8 ‰ and 1.2 ‰. The δ^{56}Fe signatures for the Haib deposit are between -0.11 ‰ and 0.29 ‰ whereas, the δ^{56}Fe signatures for Phanerozoic deposits are between -0.6 ‰ and 0.6 ‰. The limited ranges in the δ^{65}Cu and δ^{56}Fe signatures of the Haib porphyry copper deposit relative to Phanerozoic porphyry deposits is also indicative of deeper levels of the porphyry system. Therefore, the Palaeoproterozoic Haib deposit is different compared to Phanerozoic deposits based on the deposit exposure at deep levels of the porphyry system (~12 km) as indicated by the limited ranges in the δ^{65}Cu and δ^{56}Fe signatures. The shallower levels of the Haib porphyry copper deposit, where more extensive, secondary isotopic fractionation is more likely to have occurred, appears to have been eroded away. Thus, copper and iron isotopes can be used as a tool to identify the crustal level of porphyry copper deposits.

Dedication

For my parents

Acknowledgements

There are many individuals that have provided invaluable support throughout this PhD journey. Firstly, thank you to my supervisors, Grant Bybee and Laurence Robb, for the guidance, insightful input and motivation throughout the years. To Deep-South Resources, I would like to extend my gratitude for the field access and assistance. To Caiphus Majola, Sam Tshabalala and Louis Mudalahothe, thank you for the logistical and sample preparation assistance. To Marlin Patchappa, Nonkuselo Madlakana, Robert Bolhar and Ryan Mathur your assistance with analytical lab work and raw data processing is much appreciated. To Luca Caricchi, thank you for the assistance with the machine learning geothermobarometry.

To the staff of the School of Geosciences, thank you all for the knowledge shared and the much-needed advice given at various stages during this journey. To Paul Nex and Glen Nwaila, you both inspire me and ignited my passion for economic geology, thank you. To all my colleagues and friends, thank you for all the support. To my parents, thank you for the support and sacrifices made. I love you both very much.

I would like to acknowledge the funding support of the National Research Fund, the GSSA REI Fund and Deep-South Resources.

A special thank you is dedicated to my office colleagues/friends/brothers, Musa Buthelezi and Omphulusa Mulanduli. Thank you both for being the greatest support system. Both of you inspire me and your support and encouragement assisted me to reach the final stages of this journey. I have learnt so much from both of you and I am truly grateful for this.

To my significant other, Sikelela Gomo, thank you for your continuous love, care, inspiration, encouragement and support. The final product of this PhD would not have been possible without you. I learn from you each and every day. You are a blessing to my life. I sincerely appreciate you very much for being my light.

Finally, to the Almighty who continues to bless and guide me, I am humbly grateful. By your great will, all this was possible. Ameen.

Table of Contents

Declaration i

Abstract iii

Dedication v

Acknowledgements vi

List of Figures x

List of Tables xvi

1. Introduction 1

1.1. Scope of this study 5

1.2. Hypotheses 5

1.3. Objectives and approach implemented to address the aims 6

1.4. Structure of the thesis 7

2. Geological setting 8

2.1. The Richtersveld Subprovince 8

2.1.1. Lithostratigraphy 12

2.2. The tectonic setting of the Haib porphyry copper deposit 18

2.3. Regional structural geology 19

2.4. The Haib porphyry copper deposit 21

2.5. Controls on mineralization 22

2.6. The Mercaderes Rio-Mayo lower crustal cumulates, Columbia 23

2.7. Porphyry copper deposit formation 25

2.8. Cu and Fe isotopes theory 27

3. Analytical methods 29

3.1. Whole rock geochemistry 29

3.1.1. XRF analytical procedure for major elements 29

3.1.2. ICP-MS analytical procedures for trace elements 29

3.2. U-Pb zircon geochronology 31

3.3. Cu-Fe isotopic analyses 33

3.3.1. Digestion and ion exchange chromatography 33

3.3.2. MC-ICP-MS measurements 33

3.4. Geothermobarometry 34

4. Assessing the geological relationships between the mafic-ultramafic intrusion in the Haib area and the Vuurdood Subsuite, Richtersveld Subprovince 35

4.1. Introduction 35

4.2. Results 37

4.2.1. The Kokerboom Intrusion in the Haib area 37

4.2.2. Major and trace element geochemistry 42
4.2.3. Machine learning geothermobarometry 46
4.2.4. Geochronology of the Kokerboom Intrusion 47
4.3. Discussion 49
4.3.1. The mafic-ultramafic intrusion in the Haib area and the Vuurdood Subsuite 49
4.3.2. Evidence for deeper levels of the porphyry system 51
4.4. Conclusion 52
5. Cu and Fe isotope contrasts between the Palaeoproterozoic Haib porphyry copper deposit and representative Phanerozoic porphyry copper deposits 54
5.1. Introduction 54
5.2.1. Feldspar porphyry andesites 56
5.2.2. Quartz-feldspar porphyry granodiorites 57
5.2.3. Clinopyroxenites 58
5.2.4. Characterization of mineralization 59
5.2.5. Ore assemblages and textural analysis 60
5.2.6. In-situ and whole rock copper and iron isotope analyses 65
5.3. Discussion 68
5.3.1. Magmatic-hydrothermal nature for the Haib deposit sulphides 68
5.3.2. Controls on the ore-forming fluids linked to the progressive precipitation of various sulphide textures 68
5.3.3. Types of fluid related to hydrothermal alteration and mineralization 69
5.3.4. Controls on the isotopic fractionation between the ore-forming fluids and the host magmas 69
5.3.5. Comparisons between the Palaeoproterozoic Haib deposit and Phanerozoic porphyry copper deposits 70
5.3.6. δ^{65}Cu and δ^{56}Fe isotopic evidence that Haib formed in the deeper levels of the porphyry system 71
5.3.7. Application of δ^{65}Cu and δ^{56}Fe isotopes to infer crustal depth of the porphyry system 72
5.4. Conclusion 73
6. A trans-crustal perspective on porphyry copper deposit formation using Fe isotopes 74
6.1. Introduction 74
6.2. Results 76
6.2.1. Petrography 76
6.2.2. Major element analyses 85
6.2.3. Trace element analyses 89
6.2.4. δ^{56}Fe isotope analyses 94

6.3. Discussion 99

6.3.1. Kokerboom Intrusion represents cumulate material of the RMA 99

6.3.2. Rayleigh fractionation modelling of Yb 100

6.3.3. An amphibole fractionation control for the Orange River Group, Vioolsdrif Intrsuive Suite and Kokerboom Intrusion 101

6.3.4. A garnet fractionation control for the Mercaderes-Rio Mayo lower crustal cumulates 101

6.3.5. An amphibole vs. garnet fractionation control constrained using various trace element concentrations and ratios 102

6.3.6. δ^{56}Fe isotopic fractionation of the Orange River Group, Vioolsdrif Intrusive Suite and Kokerboom Intrusion 102

6.3.7. Rayleigh fractionation modelling of the δ^{56}Fe composition for the Kokerboom Intrusion 103

6.3.8. A garnet vs. an amphibole fractionation control on the δ^{56}Fe signature in arc magmas 104

6.4. Conclusion 107

7. Discussion and conclusions 108

7.1. Discussion for various aspects of the proposed hypotheses in this study 109

7.1.1. Cumulates 109

7.1.2. Depth perspective 109

7.1.3. Mineralization 110

7.1.4. Trans-crustal perspective: comparing Palaeoproterozoic Haib and Phanerozoic porphyry deposits 111

7.1.5. Temporal perspective 111

7.2. Integrated conclusions 114

7.3. Future recommendations 115

References 116

Appendices 132

List of Figures

Figure 1.1: The location of the Haib porphyry copper-molybdenum deposit, approximately 5 km from the Haib-Orange River confluence in the lower part of the Orange River, along the border between South Africa and Namibia. Modified from Minnitt (1979, 1986) ……3

Figure 1.2: The occurrence of porphyry copper deposits through geological time. Porphyry copper deposits are predominantly Phanerozoic in age. The Haib copper-molybdenum deposit is one of the few occurrences of porphyry copper mineralization in the Precambrian (Lee and Tang, 2020) ……...……...….4

Figure 2.1: The tectonostratigraphic location of the Richtersveld Subprovince between the Bushmanland Subprovince and Kakamas Domain in the Namaqua sector of the Mesoproterozoic Namaqua-Natal Province, modified from Petterson (2008) and Macey et al. (2017) ……9

Figure 2.2: Regional tectonostratigraphy of the western Namaqua sector illustrating the full extent of the Pella and Vioolsdrif Domains respectively (after of Macey et al. (2015), Gresse et al. (2016) and Thomas et al. (2016), including components of Blignault et al. (1983), Hartnady et al. (1985), Thomas et al. (1994), Colliston and Schoch (1996), Moen and Toogood (2007) and Miller (2008) and 1:250,000 geological map data supplied by the GSN and CGS)……10

Figure 2.3: The Haib porphyry copper-molybdenum deposit, indicated by the red star, is located in the Vioolsdrif Domain of the Richtersveld Subprovince (Vermond, 2019) …….11

Figure 2.4: The lithostratigraphy of the Haib area in the Richtersveld Subprovince. The Haib area is composed of the Haib Subgroup of the Orange River Group, further divided into the basal Tsams Formation and overlying Nous Formation, and the Vioolsdrif Intrusive Suite (after Minnitt, 1979; Blignault, 1974, 1977; Reid, 1977; Blignault et al., 1983; Macey et al., 2015; Shifotoka et al., 2016) ……...……...13

Figure 2.5: The volcanic lithologies of the Orange River Group in the Haib area. a) Aphyric rhyolites that are distinctly bedded. b) Phyric rhyolites with distinct flow banding. c-d) Feldspar porphyry andesites composed of distinct feldspar phenocrysts altered to epidote and chlorite. e) Sheared feldspar porphyry andesite. f-g) Mafic tuff with evidence of grain sorting and fiamme textures……14

Figure 2.6: The plutonic lithologies of the felsic Vioolsdrif Intrusive Suite in the Haib area: a) Distinct speckled and equigranular diorites. b) Granodiorite with mafic enclaves. c-d) Monzogranites with distinct K-feldspar phenocrysts. e-f) Altered quartz-feldspar porphyry granodiorites with distinct evidence of potassic and sericitic alteration as well as bleb-like sulphides. g-i) Leucogranite dykes and veins that pervasively intrudes all the other plutonic rocks in the region……15

Figure 2.7: The distribution of the four distinct volcanic zones and the location of the Mercaderes as indicated by the red star (modified after Harmon et al., 1984) …….24

Figure 2.8: A trans-crustal section of a mature continental arc (Lee and Tang, 2020). Garnet fractionation in the lower crust results in Fe depletion and oxidation of the residual magma. The Fe depletion causes sulphide segregation which in turn, isolates the Cu into the lower crustal cumulates. The oxidation caused by garnet fractionation results in the conversion of sulphide to sulphate in the differentiated felsic magmas that eventually reach the upper crust near the brittle-ductile transition zone (BDT). This releases Cu from the sulphides into solution and enhances the capacity of magmatic fluids to scavenge and transport Cu from Cu poor magmas to top of the pluton (cupola), resulting in the immobilization and concentration of Cu, forming a Cu-enriched cupola (Lee and Tang, 2020) …….26

Figure 3.1: Comparison of the BCR-2 and BHVO-2 standards from this study and the reference values from the USGS (2001). Most of the data agree within 5% (shaded band) except for P_2O_5…….30

Figure 3.2: Comparison of the BCR-2 and BHVO-2 standards from this study and the reference values from the USGS (2001). Some of the data agree within 5 % (shaded band) uncertainty. However, elements such as Cr, Cs and Ta fall out of this reproducibility range and have been assigned an uncertainty of 10 %.....30

Figure 3.3: Concordia ages of measured reference standard ages compared with the accepted ages for the Plesovice and Temora 2 standards……32

Figure 4.1: Simplified geological map of the Richtersveld Magmatic Arc in the Vioolsdrif-Haib area showing the distribution of the Orange River Group, Vioolsdrif Intrusive Suite and the main localities of the Vuurdood Subsuite (Minnaar and Reid, 2021). Inset shows the position of map with reference to the Namaqua-Natal tectonic province and the Kaapvaal Craton…….…….….35

Figure 4.2: Geological map of the Haib porphyry copper-molybdenum deposit with sample locations from this study. Map modified from Minnitt (1979) and Meng et al. (2021) ……36

Figure 4.3: The plutonic lithologies of the Viooldrif Intrusive Suite in the Haib area: a) Coarse-grained clinopyroxenite hand samples. b) Gabbros with evidence of grain-size variations on the outcrop scale. Certain sections of the outcrop are darker depicting a coarser grain size. c) Distinct speckled and equigranular gabbros…….38

Figure 4.4: The contacts of the main gabbroic body with the surrounding granodiorite. a) A distinct sharp contact. b) NW-SE trending sheared contact. c) Diffuse/assimilated contact with mingling textures…….…….38

Figure 4.5: Photomicrographs of the gabbro (a), and clinopyroxenite (b) of the mafic-ultramafic intrusion. a) The primary stubby prisms of clinopyroxene are altered to hornblende, chlorite and epidote whereas the plagioclase is pervasively altered to sericite and epidote and displays a myrmerkitic texture. b) Fibrous-granular actinolite is evident. Primary clinopyroxene is altered to actinolite with minor chlorite and epidote. Opaque material is prevalent (inset i). Chalcopyrite is being replaced by covellite…….…….….40

Figure 4.6: Mineral liberation maps of representative thin sections for the gabbros (a), and clinopyroxenites (b). There is a decrease in modal plagioclase from the gabbros to the clinopyroxenites. From the mineral liberation maps the non-cotectic proportions of dominant mineral phases are clear……..…….……..…41

Figure 4.7: The SiO_2, Al_2O_3, Fe_2O_3, CaO, TiO_2, Na_2O and K_2O vs. Mg# diagrams show a general decrease in these oxide compositions from the primitive to more evolved mafic units of the mafic-ultramafic intrusion and Vuurdood Subsuite…….43

Figure 4.8: The AFM diagram illustrating the various lithologies of the Vioolsdrif Intrusive Suite (VIS) shows that the felsic units of the RMA plots in the calc-alkaline field of the diagram whereas, the mafic units of the RMA plots in the tholeiitic field of the diagram. The quartz-feldspar granodiorites of the Khoromus porphyry of the VIS are the host rocks of the Haib deposit. The AFM diagram illustrating the various rock types constituting the Vuurdood Subsuite shows that the peridotites and pyroxenites from literature plots distinctly in the tholeiitic field whereas, the gabbros from literature plots in both the calc-alkaline and tholeiitic fields. The clinopyroxenites the mafic-ultramafic intrusion plots in the tholeiitic field whereas, the gabbros plots in both the calc-alkaline and tholeiitic fields. The Vuurdood Subsuite and mafic-ultramafic intrusion plots in the same area of the AFM diagram as continental and island arc cumulates from studies conducted by Chin et al. (2018) …….44

Figure 4.9: a) Chondrite-normalized REE patterns for the various rock types constituting the mafic-ultramafic intrusion shows a relatively flat REE pattern for the clinopyroxenites whereas, the gabbros have a slightly elevated slope and minor Eu anomalies. The chondrite normalizing values of Anders and Grevesse (1988) were used. b) MORB-normalized multi-element patterns for the various rock types constituting the mafic-ultramafic intrusion and the average Vuurdood Subsuite. The mafic-ultramafic intrusion has strong negative Nb and Hf-Zr anomalies. The MORB-normalized multi-element patterns for the mafic-ultramafic intrusion and average Vuurdood Subsuite overlap. The mantle normalizing values of White (2005) were used…….45

Figure 4.10: P-T graph showing the results from the machine learning geothermobarometry conducted on pyroxenes and hornblende grains from the Vuurdood Subsuite pyroxenites. Pressure and temperature ranges from ~1.5-7 kbar and ~800-900 °C respectively……46

Figure 4.11: U-Pb geochronological results. a) 38 analyses on zircons from sample AJ-21-04 provide a concordia age of 1875 ± 9 Ma. b) 33 analyses on zircons from sample AJ-21-23 yielded a concordia age of 1857 ± 9 Ma. c) 38 analyses on zircons from sample AJ-21-34 yielded a concordia age of 1896 ± 9 Ma. d) 37 analyses on zircons from sample AJ-21-28 provided a weighted mean age of 1889 ± 22 Ma. e) 36 analyses conducted on sample AJ-21-29 yielded a weighted mean age of 1862 ± 18 Ma. A full compilation of CL and BSE images can be found in Appendix J…..48

Figure 4.12: Age range diagram for the Orange River Group (ORG), Kokerboom Intrusion (KI) and Vioolsdrif Intrusive Suite (VIS). The data for the ORG and VIS from literature is from Meng et al. (2020) ……50

Figure 5.1: Plane (left) and cross-polarized (right) photomicrographs of the feldspar porphyry andesites. Plagioclase and mafic phenocrysts are observed. The plagioclase phenocrysts are altered to sericite and the mafic phenocrysts are strained…….56

Figure 5.2: Plane (left) and cross-polarized (right) photomicrographs of the quartz feldspar porphyry granodiorites. Plagioclase phenocrysts are highly altered to sericite. Quartz and calcite veins are apparent with the latter truncating and cross-cutting the former……57

Figure 5.3: Plane (left) and cross-polarized (right) photomicrographs of the clinopyroxenites. Fibrous-granular actinolite is visible. Primary clinopyroxene is altered to actinolite with minor chlorite, and epidote. Massive opaque material is prevalent as well which consists of chalcopyrite rimmed by covellite.……58

Figure 5.4: Mineralization in the feldspar porphyry andesites and quartz-feldspar porphyry granodiorites. a) Disseminated chalcopyrite and pyrite in quartz-feldspar porphyry granodiorite. b) Massive chalcopyrite and pyrite in feldspar porphyry andesite. c) Vein-controlled mineralization (chalcopyrite and pyrite) in close relation to biotite and quartz rich shear fractures……...59

Figure 5.5: Reflected light photomicrographs of the mineralization. The mineralization (pyrite and chalcopyrite) occurs either disseminated (a), bleb-like (b) vein-type (c) or massive (d and e) 60

Figure 5.6: TIMA analyses were conducted to produce mineral liberation maps of the disseminated sulphides in the quartz-feldspar porphyry granodiorite. The disseminated mineralization occurs as euhedral-subhedral pyrite and subhedral-anhedral chalcopyrite that are either associated with each other, where pyrite is incorporated within chalcopyrite, or occurs as isolated/dispersed grains……...61

Figure 5.7: TIMA analyses were conducted to produce mineral liberation maps of the vein-type sulphides in the quartz-feldspar porphyry granodiorite. The vein type sulphides occur as subhedral-euhedral pyrite incorporated within massive chalcopyrite in close relation to quartz-biotite veins…….…….62

Figure 5.8: TIMA analyses were conducted to produce mineral liberation maps of the massive sulphides in the quartz-feldspar porphyry granodiorite. The massive sulphides occur as subhedral-euhedral pyrite incorporated within massive chalcopyrite. The chalcopyrite clearly postdates the pyrite here…….…….63

Figure 5.9: TIMA analyses were conducted to produce mineral liberation maps of the massive sulphides in the clinopyroxenite. The sulphides in the clinopyroxenite occur as coarse bleb-like aggregates of chalcopyrite replaced by chalcocite-covellite…….64

Figure 5.10: Typical δ^{65}Cu and δ^{56}Fe signatures for the various occurrences of chalcopyrite i.e. disseminated, massive and vein-type…….65

Figure 5.11: δ^{65}Cu variations on chalcopyrite for the Paleoproterozoic Haib porphyry deposit and Phanerozoic porphyry deposits: Northparkes (Li et al., 2010) and Pebble (Gregory and Mathur, 2017). The data for I-type granites are from Li et al. (2009) ……66

Figure 5.12: δ^{56}Fe variations on chalcopyrite for the Paleoproterozoic Haib porphyry deposit and Phanerozoic porphyry deposits such as Duolong (Li et al., 2018), Tongshankou (He et al., 2020), Taiyangshan (Zhang et al., 2021). The average mantle value is after Johnson et al. (2020) ……...……...……67

Figure 5.13: Diagram illustrating the greater range in $\delta^{65}Cu$ and $\delta^{56}Fe$ signatures in shallow Phanerozoic porphyry deposits compared to the deeper Palaeoproterozoic Haib porphyry deposit. Hydrothermal fluids cause greater isotopic fractionation at shallow levels……73

Figure 6.1: Streckeisen classification diagrams for the Kokerboom Intrusion and Rio-Mayo lower crustal cumulates. The Kokerboom Intrusion ranges in composition from gabbros to clinopyroxenites whereas, the Rio-Mayo lower crustal cumulates is composed of a variety of pyroxenites……...77

Figure 6.2: A representative photomicrograph of the Kokerboom Intrusion cumulates illustrating cumulus subhedral to euhedral clinopyroxene and intercumulus hornblende and plagioclase. Inset i shows subhedral to euhedral hornblende with inclusions of magnetite and quartz……....78

Figure 6.3: Plane (left) and cross-polarized (right) photomicrographs of the garnet clinopyroxenite. The intercumulus subhedral to euhedral garnet is highly fractured, zoned and consists of clinopyroxene and apatite inclusions. The cumulus to intercumulus subhedral clinopyroxene consists of garnet, biotite, spinel and apatite inclusions…….79

Figure 6.4: Plane (left) and cross-polarized (right) photomicrographs of the garnet-rich hornblende pyroxenite. The cumulus to intercumulus subhedral to euhedral garnet occurs with hornblende and has inclusions of magnetite, apatite and quartz. Kelyphitic rims are distinct……..…80

Figure 6.5: Plane (left) and cross-polarized (right) photomicrographs of the garnet-rich hornblende olivine pyroxenite. The intercumulus subhedral to euhedral garnet has minor reaction rims. Cumulus subhedral hornblende is found with garnet and pyroxene…….81

Figure 6.6: Plane (left) and cross-polarized (right) photomicrographs of the garnet-rich plagioclase bearing olivine hornblende pyroxenite. A distinct feature is the cumulus to intercumulus subhedral to euhedral garnet with inclusions of clinopyroxene, apatite, magnetite and quartz…….82

Figure 6.7: Plane (left) and cross-polarized (right) photomicrographs of the tonalite gneiss. The intercumulus subhedral to euhedral plagioclase is zoned and exhibits a distinct undulose extinction in certain areas. Intercumulus subhedral to euhedral garnet has inclusions of magnetite and quartz……83

Figure 6.8: Plane (left) and cross-polarized (right) photomicrographs of the quartz-rich granitoid gneiss. Intercumulus subhedral to euhedral garnet has inclusions of quartz, spinel, plagioclase and magnetite. Plagioclase is subhedral and exhibits an undulose extinction……84

Figure 6.9: The Harker variation diagrams show that from the Orange River Group and Vioolsdrif Intrusive Suite to theVuurdood Subsuite, the Al_2O_3, TiO_2, MgO, Fe_2O_3, CaO and MnO compositions gradually decreases with increasing SiO_2 from mafic to felsic compositions whereas, the Na_2O and K_2O compositions show a gradual increase with increasing SiO_2. Data from literature includes results from Macey et al. (2017) …….86

Figure 6.10: The AFM plots of the Orange River Group, Vioolsdrif Intrusive Suite, Vuurdood Subsuite and Rio-Mayo lower crustal cumulates show that the Orange River Group and Vioolsdrif Intrusive Suite plot in the calc-alkaline field whereas, the Vuurdood Subsuite and Rio-Mayo lower crustal cumulates plot both in the calc-alkaline and tholeiitic fields of the

AFM plot. The Andes arc magmas both “normal” and “thick” crust as well as the igneous plutonic rocks are plotted for comparative purposes…….……..….87

Figure 6.11: The Harker variation diagrams for the Rio-Mayo lower crustal cumulates. The Al_2O_3, TiO_2, MgO, Fe_2O_3, CaO and MnO compositions gradually decreases with increasing SiO_2 from mafic to felsic compositions whereas, the Na_2O and K_2O compositions show a gradual increase with increasing SiO_2. The Andes arc magmas both “normal” and “thick” crust as well as the igneous plutonic rocks in the Northern Andes are plotted for comparison purposes……88

Figure 6.12: The REE patterns for the Orange River Group, Vioolsdrif Intrusive Suite, Kokerboom Intrusion and Rio-Mayo lower crustal cumulates. The REE patterns for the Orange River Group and Vioolsdrif Intrusive Suite show distinct listric shaped patterns whereas, the REE for the Kokerboom Intrusion has a lower overall concentration and flatter slope compared to the Orange River Group and Vioolsdrif Intrusive Suite……90

Figure 6.13: Several trace element (concentrations and ratios) diagrams and in some cases major element vs. trace elements (concentrations and ratios) diagrams illustrating various trends for the Orange River Group, Vioolsdrif Intrusive Suite and Kokerboom Intrusion. An important trend is observed in the MgO vs. La/Yb plot, there is an increase in La/Yb with decreasing MgO from the Kokerboom Intrusion to the Orange River Group and Vioolsdrif Intrusive Suite. The line in the MgO vs. La/Yb plot represents the typical amphibole fractionation trend. Other important trends observed are depicted in the SiO_2 vs. Yb and Y plots as positive linear correlations are shown. As the SiO_2 concentration increases, the Yb and Y concentrations decrease……92

Figure 6.14: Several trace element (concentrations and ratios) diagrams and some cases major element diagrams vs. trace elements (concentrations and ratios) illustrating various trends for the Rio-Mayo lower crustal cumulates. Again, the Andes arc magmas both “normal” and “thick” crust as well as the igneous plutonic rocks in the Northern Andes are plotted for comparison purposes. The MgO vs. La/Yb plot for the Andes arc magmas (traversing normal and thickened arc crust) and lower crustal cumulates show a distinct increase in La/Yb from the Rio-Mayo lower crustal cumulates to the Tongde dikes followed by the Andes arc magmas. The line in the MgO vs. La/Yb plot represents the typical garnet fractionation trend. The other plots illustrate various trends as well. A noteworthy observation is the elevated Yb and Y concentrations for the Rio-Mayo lower crustal cumulates with concentrations ranging between 0.5-6 ppm and 5-60 ppm respectively. The Tongde dikes are emplaced into the Proterozoic rocks of the Yangtze Block located in South China……93

Figure 6.15: The $\delta^{56}Fe$ isotope diagram shows that the Kokerboom Intrusion have a lower $\delta^{56}Fe$ signature relative to the Vioolsdrif Intrusive Suite which is followed by the Orange River Group. The $\delta^{56}Fe$ isotope diagram shows that the Rio-Mayo lower crustal cumulates overlap with the Kokerboom Intrusion, Vioolsdrif Intrusive Suite and Orange River Group. The $\delta^{56}Fe$ signature of mineral separates including garnet, pyroxene, amphibole and magnetite is plotted for comparison (Liang et al., 2022) ……95

Figure 6.16: Box plot of the $\delta^{56}Fe$ isotope signatures for the Rio-Mayo lower crustal cumulates, Orange River Group, Vioolsdrif Intrusive Suite and Kokerboom Intrusion……96

Figure 6.17: Rayleigh fractionation modelling of bulk rock trace element Yb in the Rio-Mayo lower crustal cumulates and Kokerboom Intrusion……100

Figure 6.18: Rayleigh fractionation modelling showing the $\delta^{56}Fe$ compositions of the residual melt from the Kokerboom Intrusion cumulates……104

Figure 6.19: During intra-crustal differentiation both garnet and amphibole has a strong control on the $\delta^{56}Fe$ signature. Intra-crustal differentiation results in mid- to deep- crustal cumulates with depleted $\delta^{56}Fe$ signatures and residual host porphyry magmas with enriched $\delta^{56}Fe$ signatures……106

List of Tables

Table 2.1: Various subdivisions of the Vioolsdrif Intrusive Suite in the Vioolsdrif and Pella Domains (Macey et al. 2017) ...……16

Table 2.2: Summary of published age-data for the Vioolsdrif Domain of the Richtersveld Magmatic Arc……...17

Table 2.3: The five deformation events in the western sector of the Namaqua-Natal Province (Macey et al., 2017) ……20

Table 3.1: An external standard, the USGS rock standard BVHO-2, was measured and values are within recommended values from publications……..……34

Table 4.1: Average pressure and temperature estimates for the Vuurdood Subsuite pyroxenites, Arizona arclogites and Tongling cumulates……46

Table 6.1: Geochemical and isotope data obtained in this study for the Orange River Group (ORG), Vioolsdrif Intrusive Suite (VIS) and Kokerboom Intrusion (KI)……...97

Table 6.2: Geochemical and isotope data obtained in this study for the Rio-Mayo lower crustal cumulates…….……...98

1. Introduction

Porphyry copper deposits are hosted by high-level, arc-related, granitoid intrusions and are associated with structurally-controlled veins, fractures, stockworks and breccias arising from the exsolution of hydrothermal fluids (Richards, 2005; Sinclair, 2007; John et al., 2010). These high-temperature, metal-rich fluids are exsolved from an underlying magma chamber at approximately 5-15 km depth and migrate into the surrounding country rock and upward to the cupola zone where the Cu-rich metals are precipitated (Hedenquist and Lowenstern, 1994; Sillitoe, 2010 and Richards, 2011, 2013). The copper mineralization is evenly distributed in large volumes of rock, forming high tonnage and low- to moderate-grade ores (Sinclair, 2007; John et al., 2010). Copper is an essential critical metal in the development and implementation of green energy solutions (Elshkaki et al, 2016; World Bank, 2021). Porphyry copper deposits are the world's most important source of this critical metal and account for more than 60 percent of the annual world production (John et al., 2010).

Porphyry copper magmatic systems are hosted by km-scale magmatic intrusions of felsic to intermediate compositions and porphyritic textures, in which cm-scale euhedral feldspar phenocrysts occur in a fine-grained groundmass (Richards, 2005; Sillitoe, 2010). The copper ore is restricted to cupolas situated at the top of these porphyritic bodies (Sillitoe, 2010). Globally, porphyry copper deposits are mainly formed adjacent to convergent plate margins and are almost exclusively found within evolving magmatic arcs associated with calc-alkaline or I-type magmas (Robb, 2021; John et al., 2010; Sillitoe, 2010; Lee and Tang, 2020). The formation of porphyry copper deposits involves a wide range of processes, but there are two main mechanisms proposed for their formation, namely, source driven and intra-crustal differentiation processes. Source driven processes are associated with Cu enrichment in parental magmas from the lower crust, lithospheric mantle, mantle wedge or subducting slab. In contrast, differentiation processes do not require parental magmas to be Cu-rich and involve the concentration of Cu from mid-crustal to shallow level plutons (Richards, 2005; Lee and Tang, 2020). Arc magmas are Cu-depleted (Chin et al., 2018; Chen et al., 2020 Lee et al., 2020) thus an unresolved paradox exists with regard to the missing Cu-reservoir. Evidence of residual magmatic sulphides in cumulates is significant and accounts for this missing Cu-reservoir (Chen et al., 2020). The Cu from sulphides in lower crustal cumulates is released in aqueous solutions to the top of the pluton (cupola zone), where the Cu is immobilized and concentrated (Lee and Tang, 2020). Therefore, studying deep crustal cumulates provides insight with regard to understanding magmatic differentiation in the lower crust and its effect on metallogenesis in porphyry copper deposit systems.

The Palaeoproterozoic Richtersveld Subprovince of the Namaqua-Natal Province is composed of weakly deformed calc-alkaline rocks of the Vioolsdrif Domain, and moderate- to highly-deformed rocks near the margins of the Subprovince in the Pella Domain (Reid et al., 1987; Cornell et al., 2006; Macey et al., 2017). The Haib porphyry copper-molybdenum deposit, situated in the Richtersveld Subprovince, is geographically located approximately 5 km from the Haib-Orange River confluence in the lower part of the Orange River, in Southern Namibia at the Orange River border with South Africa (Figure 1.1; Minnitt, 1979; Minnitt, 1986; Barr and Reid, 1992; Colliston and Schoch, 2000). The porphyry copper-molybdenum deposit is characterized by disseminated, vein- and shear-zone-localized copper mineralization (Minnitt, 1979; Barr and Reid, 1992). The mineralization occurs in a distinct NW-SE trending zone of low-grade mineralization (Minnitt, 1986, Walker and Richards, 2018; Vermond, 2019).

The Haib prospect was discovered by European prospectors in the 18th Century, but it did not receive much consideration until 1972, when Rio Tinto Zinc (RTZ) conducted a comprehensive and systematic investigation of the deposit (Barr & Reid, 1992). A total of 120 holes were drilled during this investigation and the prospect was classified as a porphyry copper-molybdenum deposit (Minnitt, 1986; Walker and Richards, 2018). The plummet of Cu prices in 1974, as well as the scarcity of high-grade zones, led to RTZ's abandonment of the project in 1976 (Walker and Richards, 2018; Vermond, 2019). Subsequently, several junior mining companies were part of several drilling campaigns until 2003, when Deep-South Resources acquired the mineral rights of the area, which they currently still hold (Walker and Richards, 2018; Vermond, 2019). Teck Resources conducted further drilling programs on both Haib and its surrounding areas from 2008-2015, under an agreement with Deep-South Resources. A total of 32 holes were drilled and a mineral resource estimate was produced (Walker and Richards, 2018; Vermond, 2019). Deep-South Resources are currently conducting metallurgical test work and further drilling, ultimately aiming to complete a pre-feasibility study in the near future (Walker and Richards, 2018; Vermond, 2019).

Three aspects make the copper mineralization in the Richtersveld Subprovince of particular interest for understanding porphyry copper deposit metallogenesis globally, and form the focus of this work:

1. It is one of two known occurrences of this specific style of mineralization in southern Africa (Minnitt, 1979).
2. The close proximity to a suite of mafic-ultramafic intrusions that hold promise for future critical metal exploration.
3. Porphyry copper deposits are predominantly Phanerozoic in age and are therefore rare in the Precambrian (Figure 1.2; Sillitoe, 2010; Richards and Mumin, 2013). The Haib copper-molybdenum deposit is one of the few occurrences of porphyry copper mineralization in the Precambrian.

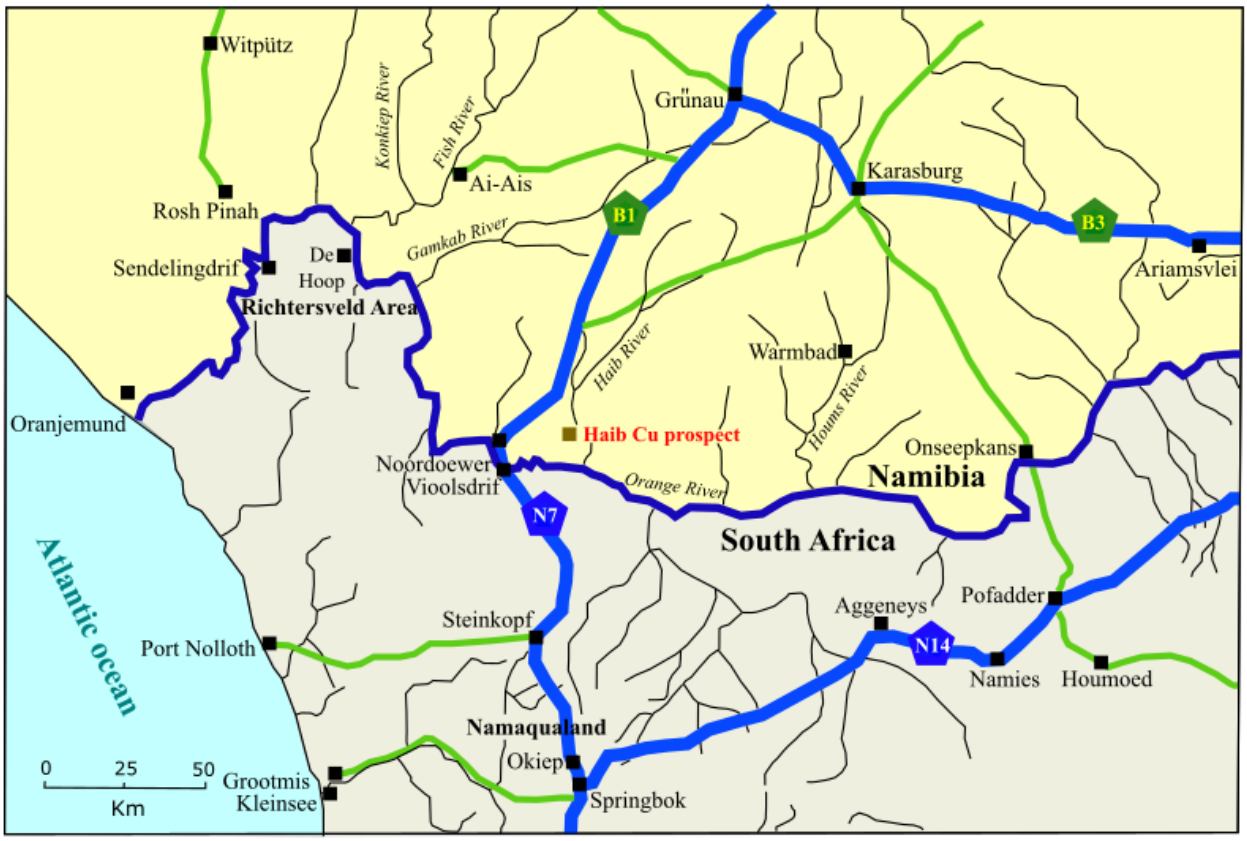

Figure 1.1: *The location of the Haib porphyry copper-molybdenum deposit, approximately 5 km from the Haib-Orange River confluence in the lower part of the Orange River, along the border between South Africa and Namibia. Modified from Minnitt (1979, 1986).*

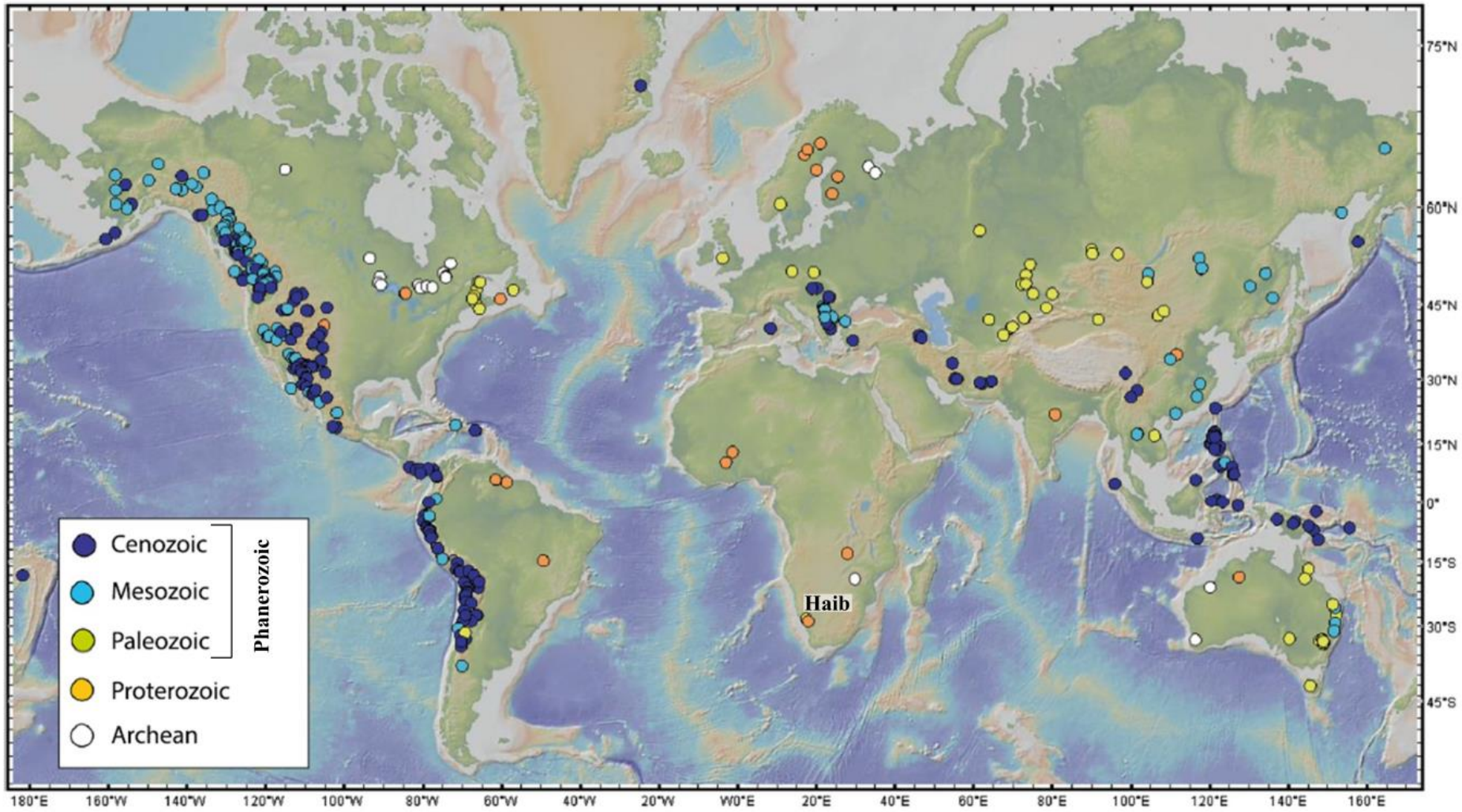

Figure 1.2: *The occurrence of porphyry copper deposits through geological time. Porphyry copper deposits are predominantly Phanerozoic in age. The Haib copper-molybdenum deposit is one of the few occurrences of porphyry copper mineralization in the Precambrian (Lee and Tang, 2020).*

1.1. Scope of this study

The main goals in mineral deposit research are to identify the source of the metals and the processes involved in metallogenesis (Li et al., 2010). Geochemists have applied various isotopic tools including light stable isotopes and radiogenic isotopes to establish the metal source and unravel the processes involved in the formation of ore deposits, however, light stable and radiogenic isotopes provide indirect constraints on the sources of metals and ore-forming processes (Li et al., 2010 and He at al., 2020). In porphyry systems, the application of non-traditional stable isotopes (Cu and Fe) is limited (Cooke et al., 2014), yet these non-traditional isotope systems have the ability to provide direct evidence for understanding the source of the metals and the mineralization processes involved in porphyry formation (Markl et al., 2006; Hannah et al., 2007; Li et al., 2010a; Wang et al., 2011; Gagnevin et al., 2012; Mathur et al., 2012; Duan et al., 2015; Knipping et al., 2015; Bilenker et al., 2016; Childress et al., 2016; Yao et al., 2016; Gregory and Mathur, 2017; Gao et al., 2018; He et al., 2020).

The focus of this study is addressed by the following aims:

1. assess the links between the Haib porphyry copper deposit and mafic-ultramafic rocks regionally and ascertain depth of emplacement and implications for future exploration.

2. understand the spatial and temporal variations of predominantly Phanerozoic porphyry Cu deposits around the world and assess if, and in what ways, the Proterozoic Haib porphyry copper deposit is unique or different from a petrological and geochemical perspective.

3. evaluate whether the Haib porphyry copper deposit and associated cumulate and host magmatic rocks show geochemical signatures associated with intra-crustal differentiation processes such as amphibole or garnet fractionation. Conduct non-traditional stable isotopes analyses and make a comparison with the Mercaderes-Rio Mayo lower crustal xenoliths, situated in the Northern Andean arc, in order to constrain differentiation processes associated with various levels of an arc system.

1.2. Hypotheses

The following hypotheses are presented as a way to test the aims and objectives of this project:

Cumulates	1) The mafic units in close vicinity to the Haib porphyry copper deposit represent mid-crustal cumulate material.
Depth perspective	2) The Haib porphyry copper deposit presents evidence relating to mid-deep crustal levels as it is documented in literature that there is a lack of shallow alteration assemblages.
Mineralization	3) The mineralization is primary (hypogene) and was subsequently remobilized forming secondary mineralization assemblages (supergene).
Trans-crustal Perspective	4) The Haib porphyry copper deposit was formed in a continental arc setting associated with the fractionation of garnet in deep crustal cumulates during the Precambrian.
Temporal perspective	5) Porphyry copper formation in the Proterozoic was similar to the Phanerozoic.

1.3. Objectives and approach implemented to address the aims

To address the aims of the project, a multi-disciplinary approach was adopted with the application of several analytical methods:

1) Determine the field relationships between the volcanic and plutonic units of the Haib porphyry copper deposit and similarities between the mafic-ultramafic units of the Haib porphyry copper deposit and Vuurdood Subsuite of the Richtersveld Magmatic Arc (RMA).
    - Tested through conducting field observations of lithologies in and around the vicinity of the Haib porphyry copper deposit.

2) Describe the mineral and textural relationships of host rock types and the textural relationships of mineralization and alteration assemblages.
    - Tested through conducting petrographic observations of thin sections of the volcanic and plutonic rocks of the Haib porphyry copper deposit, TESCAN Integrated Mineral Analyzer (TIMA) imagery of the mafic-ultramafic units and TESCAN Integrated Mineral Analyzer (TIMA) imagery of ore blocks of the volcanic and plutonic rocks of the Haib porphyry copper deposit that host sulphides.

3) Determine the absolute age of the mafic-ultramafic units of the Vuurdood Subsuite in the Haib area and compare these data with felsic units of the Haib and the rest of the Richtersveld Arc to deduce the timing of intrusive events.
    - Tested through conducting cathodoluminescence (CL) image-guided U-Pb zircon geochronology on the mafic-ultramafic units.

4) Evaluate existing geochemical and new isotopic data from the Orange River Group and the Vioolsdrif Intrusive Suite, in particular exploring linkages between the mafic Vuurdood Subsuite and mineralization in the region.
    - Tested through conducting whole rock major and trace element geochemistry to evaluate calc-alkaline signatures, magmatic nature, petrogenetic and fractionation trends of the Haib porphyry copper deposit samples and by conducting non-traditional stable isotope (Cu and Fe isotopes) geochemistry to understand the source of the sulphides, trans-crustal and magmatic differentiation processes, variations in fO_2 and temporal variations of porphyry copper deposit formation.

1.4. Structure of the thesis

This thesis is divided into seven chapters, with Chapters 4, 5 and 6 intended for publication as research articles in various journals and are in various stages of the publication process.

Chapter 1 outlines an overview and scope of the study. The chapter includes the main aims of the study and the associated objectives, hypotheses and methods implemented to address the aims of the study.

Chapter 2 focuses on the literature background for the study including a detailed geological background on the Haib porphyry copper deposit and the proposed formation mechanisms for porphyry copper deposits globally.

Chapter 3 focuses on the analytical methods employed in the study which include whole-rock chemical analyses (major and trace elements), U-Pb zircon geochronology and Cu-Fe isotopic analyses on both in-situ sulphide mineral separates and whole rock powders and the machine learning geothermobarometry conducted on pyroxenes from the Vuurdood Subsuite.

Chapter 4 focuses on assessing the petrogenetic links between the mafic-ultramafic intrusion (that hosts copper mineralization) in the Haib area and the Vuurdood Subsuite. The petrogenetic links are assessed using petrology, major and trace element geochemistry and U-Pb geochronology. The chapter has been submitted for publication to the South African Journal of Geology. The authors for this particular manuscript are: Jogee B.A.; Bybee G.M.; Robb L.J.; Reid, D.L.; Minnaar, H.; Caricchi, L and Bolhar, R.

Chapter 5 evaluates the Cu and Fe isotope variations between the Palaeoproterozoic Haib porphyry copper deposit and representative Phanerozoic porphyry copper deposits. The methods conducted include the descriptive analyses of drill-core samples, petrographic observations, automated mineralogy and textural analyses and Cu and Fe isotope analyses (both in-situ on sulphides and whole rock (host quartz-feldspar porphyry granodiorite and clinopyroxnite)) from the Haib porphyry copper deposit. The Cu and Fe isotope analyses are compared with existing Cu and Fe isotope data from Phanerozoic porphyry copper deposits in order to evaluate the geochemical and metallogenic variations of porphyry copper deposits from a temporal perspective.

Chapter 6 addresses the trans-crustal perspective on porphyry copper deposit formation using Fe isotopes. The chapter investigates the petrography, trace element analyses and whole rock iron isotope signature ($\delta^{56}Fe$) of the Haib porphyry copper deposit and the Rio-Mayo lower crustal cumulates in order to understand intra-crustal differentiation processes related to amphibole or garnet fractionation. The mafic-ultramafic intrusion in close proximity to the Haib porphyry copper deposit is associated with clinopyroxene- and amphibole-rich cumulates whereas, the Rio-Mayo lower crustal cumulates are associated with garnet-rich cumulates.

Chapters 5 and 6 are in preparation for submission to international journals for publication.

Chapter 7 is an integrated discussion and conclusion of the findings and interpretations of Chapters 4,5 and 6. Various rationale for the temporal perspective of porphyry copper deposits are argued. It is proposed that cooling of the ambient mantle temperature through geological time from the Precambrian to the Phanerozoic allowed for stable subduction and increased the rate of the formation of porphyry copper deposits on a global scale. Several recommendations for future research are given at the end of Chapter 7.

2. Geological setting

2.1. The Richtersveld Subprovince

The Mesoproterozoic (~1.1 Ga) Namaqua-Natal Province (NMP) is a major orogenic belt that extends from Lüderitz on the west coast of Namibia to the eastern (KwaZulu-Natal) coast of South Africa. It comprises igneous and metamorphic rocks that formed or experienced metamorphism during the Namaqua Orogeny (Cornell et al., 2006; Macey et al., 2017; van Niekerk et al., 2022). The Namaqua "Sector" of the Namaqua-Natal Province consists of five tectono-stratigraphic terranes, namely (from west to east): the Richtersveld and Bushmanland Subprovinces, and the Kakamas, Areachap and Kaaien Domains (Cornell et al. and Macey et al., 2017). The westernmost Richtersveld Subprovince is composed of the oldest (Paleoproterozoic) supracrustal rocks in the NMP. It is tectonically bounded by the Bushmanland Subprovince and Kakamas Domain by thrusts or subvertical shear zones (Figure 2.1; Cornell et al., 2006; Macey et al., 2017). In the west, SE-directed thrust and transpressive shear zones transported part of the Neoproterozoic Gariep Group over the Richtersveld Subprovince during the "Pan-African" orogeny (Cornell et al., 2006; Macey et al., 2017). The Subprovince covers an area of approximately 29 000 km^2 and forms an approximately 200-km-wide, wedge-shaped crustal block composed of calc-alkaline volcanic and plutonic rocks (including the poorly-studied mafic-ultramafic intrusions of the Vuurdood Subsuite) that were formed in an island-arc setting (Reid et al., 1987; Reid, 1997; Cornell et al., 2006; Macey et al., 2017). According to Joubert (1986) and Macey et al. (2017), the Richtersveld Subprovince is composed of two recognizable tectono-metamorphic domains: (i) a western section, known as the Vioolsdrif Domain, composed of Paleoproterozoic rocks that underwent greenschist facies metamorphism and were not pervasively reworked by the Mesoproterozoic Namaqua Orogeny, and (ii) an eastern section, known as the Pella Domain, composed of Paleoproterozoic rocks that were pervasively affected by the Mesoproterozoic Namaqua Orogeny (Figure 2.2). The Haib porphyry copper-molybdenum deposit is situated in the former and is host to disseminated, vein- and shear-zone-localized copper mineralization (Figure 2.3; Minnitt, 1979; Minnitt, 1986; Barr and Reid, 1992; Colliston and Schoch, 2000; Walker and Richards, 2018; Vermond, 2019). The shear-zone-localized mineralization is in close relation to early dark micaceous veins (Meng et al., 2021). There is a lack of evidence of argillic and propylitic alteration assemblages, but potassic and chlorite-sericite alteration is dominant (Minnitt, 1979; Minnitt, 1986; Vermond, 2019; Meng et al., 2021).

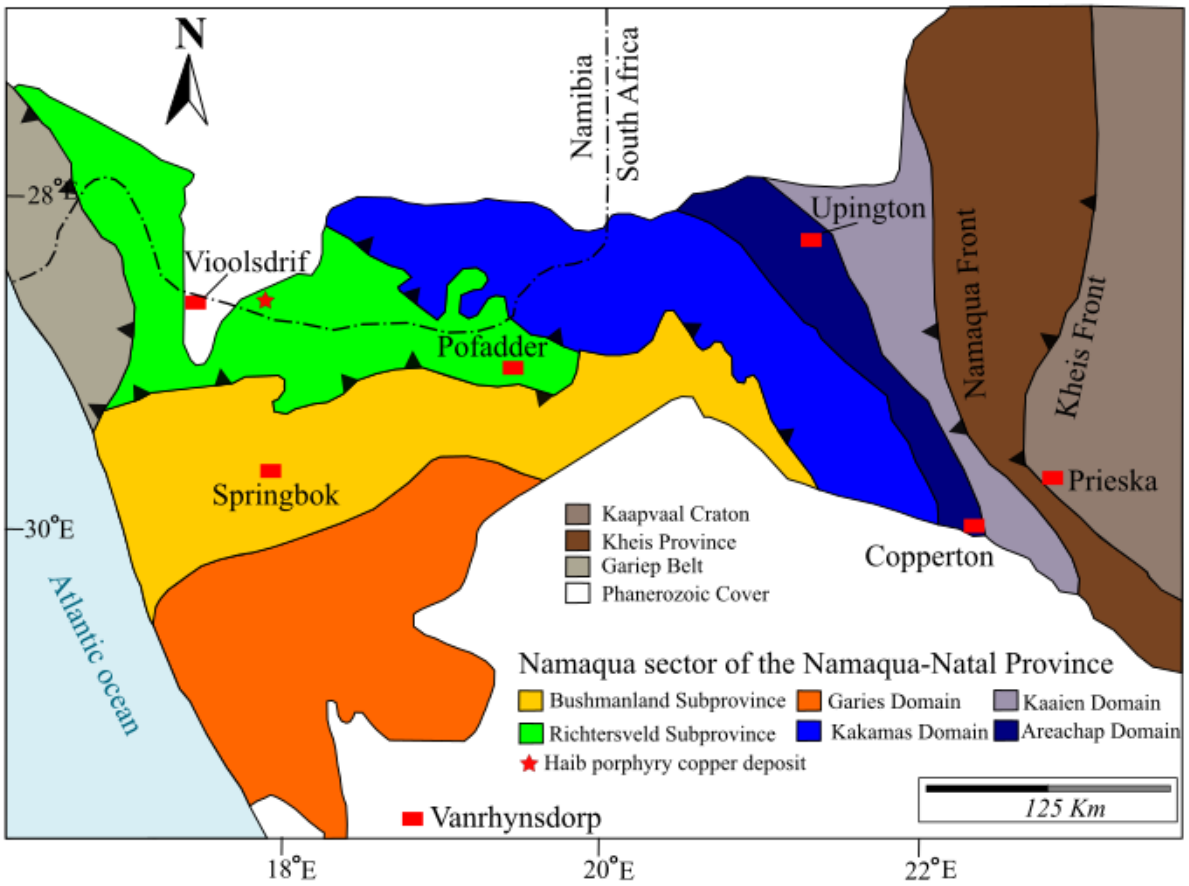

Figure 2.1: *The tectonostratigraphic location of the Richtersveld Subprovince between the Bushmanland Subprovince and Kakamas Domain in the Namaqua sector of the Mesoproterozoic Namaqua-Natal Province, modified from Petterson (2008) and Macey et al. (2017).*

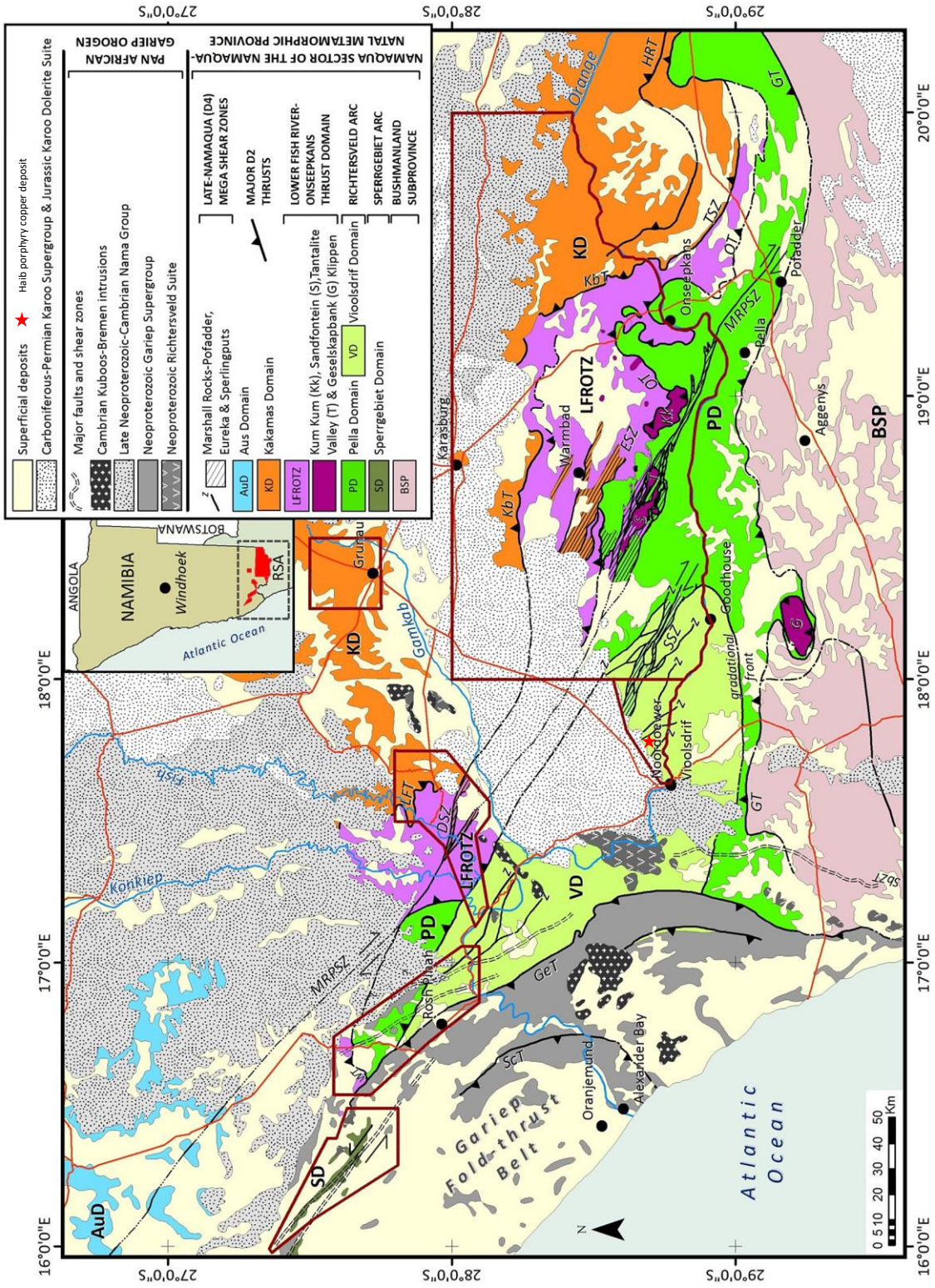

Figure 2.2: *Regional tectonostratigraphy of the western Namaqua sector illustrating the full extent of the Pella and Vioolsdrif Domains respectively (Taken from Macey et al., 2017; includes components of Macey et al. (2015), Gresse et al. (2016) and Thomas et al. (2016), Blignault et al. (1983), Hartnady et al. (1985), Thomas et al. (1994), Colliston and Schoch (1996), Moen and Toogood (2007) and Miller (2008) and 1:250,000 geological map data supplied by the GSN and CGS).*

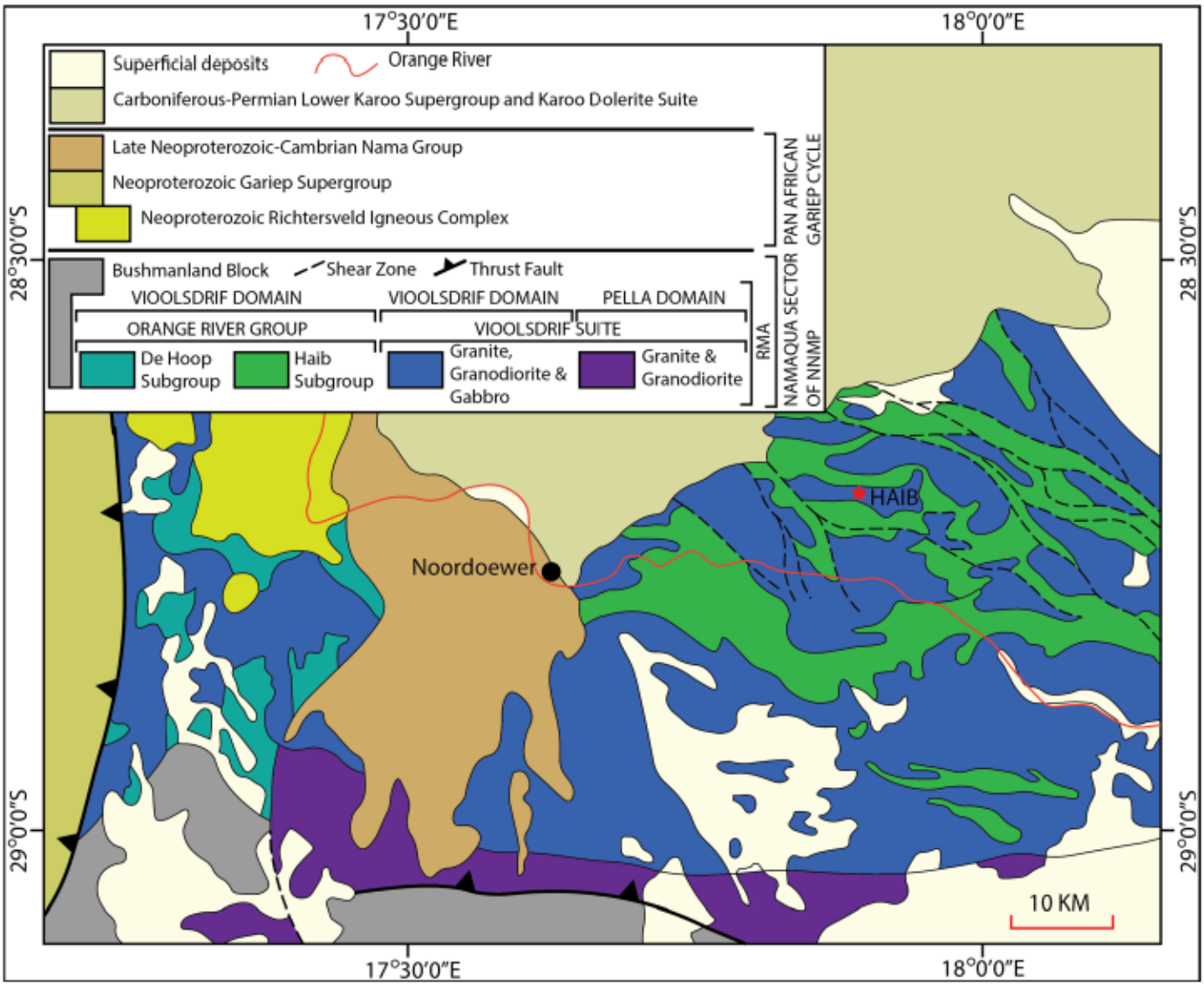

Figure 2.3: The *Haib porphyry copper-molybdenum deposit, indicated by the red star, is located in the Vioolsdrif Domain of the Richtersveld Subprovince (Vermond, 2019).*

2.1.1. Lithostratigraphy

The Richtersveld Subprovince consists of an older volcano-sedimentary sequence, the Orange River Group (ORG), which was intruded by an extensive composite cogenetic suite of plutonic rocks, the Vioolsdrif Intrusive Suite (VIS) (Minnitt, 1979, 1986). The age-range for the Richtersveld Subprovince is between approximately 1910 and 1865 Ma (Meng et al., 2021). The ORG is composed of subaerial volcanic rocks ranging in composition from basaltic andesite to rhyolite, cogenetic pyroclastics including ignimbrite and welded lapilli tuff (Figure 2.4; Reid 1977; Reid, 1979a, 1979b, Minnitt, 1986; Reid et al., 1987; Cornell et al., 2006; Macey et al., 2017; Meng et al., 2021). The VIS is composed of mafic-ultramafic intrusions, diorite, tonalite, granodiorite, monzogranite, quartz-feldspar porphyry (QFP) granodiorite and leucogranite (Figure 2.4; Reid 1977; Reid, 1979a, 1979b, Minnitt, 1986; Reid et al., 1987; Cornell et al., 2006; Macey et al., 2017; Meng et al., 2021). The ORG has been subdivided into two subgroups, the De Hoop and the Haib Subgroups, within which several formations are recognized (Reid, 1979a; Cornell et al., 2006; Minnaar, 2012; Macey at al., 2017). In the Haib area, the Haib Subgroup of the ORG has been further subdivided into the basal volcanic Tsams Formation and the overlying volcanic Nous Formation (Blignault, 1977; Minnitt, 1986). However, the Tsams Formation are the only volcanic rocks preserved in the vicinity of the Haib copper prospect (Minnitt, 1986).

Within this lithologic framework, the Haib porphyry copper deposit is hosted by the coeval and comagmatic Orange River Group and Vioolsdrif Intrusive Suite (Minnitt, 1979, 1986). The volcanic rocks, part of the Tsams Formation of the ORG, are bimodal, interlayered and are composed of aphyric rhyolites, phyric rhyolites, feldspar porphyry andesites and mafic tuffs. The plutonic rocks, represented by a composite plutonic mass part of the VIS, intrude the volcanic rocks of the Tsams Formation. The VIS is subdivided into several subunits, known as the Vuurdood Subsuite (mafic-ultramafic), Gaobis Diorite, Khoromus porphyry, Goodhouse Subsuite (Granodiorite) and the Ramansdrif Alkali Granite. These subsuites are variably composed of diorites, granodiorites, monzogranites, quartz-feldspar porphyry granodiorites and leucogranites as well as poorly-described clinopyroxenites and gabbros, which are the subject of this work (Minnitt, 1979 and Minnitt, 1986). The leucogranites are the last intrusive phase which pervasively intrudes all the other plutonic rocks in the region (Minnitt, 1979, 1986). Generally, the contacts between the various volcanic and plutonic units are either sharp, gradational, mingled or sheared (Minnitt, 1979, 1986). The granodiorites are the most extensive and abundant rock type in the region, whereas the clinopyroxenites, gabbros, diorites and leucogranites are volumetrically minor (Minnitt, 1979, 1986). The volcanic rocks are preserved in approximately sub-parallel linear belts which are separated by the composite intrusive rocks of the VIS (Minnitt, 1979 and Minnitt, 1986). Various detailed subdivisions of the calc-alkaline magma series of mafic to felsic rocks have been proposed by various authors (Table 2.1): McMillian (1968), Beukes (1973), Strydom et al. (1987), Cilliers (1989), Colliston (1990), Moen and Toogood (2007), Minnaar (2012) and Macey et al. (2017).

The Vuurdood Subsuite consists of lithologically composite intrusions, predominantly composed of meta-gabbroic rocks with ~25 % peridotites and pyroxenites. The intrusions vary in size and shape, ranging from about 100 m to about 2 km across and have been named as discrete complexes such as the Swartkop, Subruins, Nougaseb Complexes (Minnaar, 2011; Reid and Minnaar, 2021). These intrusions either occur as metre-scale xenoliths in granite, 100-m-scale fragments, and roof pendants, or as 1-2 km scale complexes showing internal differentiation. The intrusions are metamorphosed to amphibolite grade. The peridotites have been serpentinised with variable amounts of secondary amphibole and chlorite present. The

gabbros and pyroxenites have been altered to coarse-grained amphibolites, the primary magmatic pyroxene-plagioclase assemblage has been replaced by actinolite-hornblende, with secondary albitic plagioclase, epidote, chlorite and quartz (Reid, 1987; Minnaar, 2011; Reid and Minnaar, 2021). In the Haib area, apparently similar rocks are located east of the Haib copper prospect and constitute several distinct gabbroic intrusions (Figure 4.1 and 4.2). The gabbroic intrusions in the Haib area have never been directly shown to be part of the Vioolsdrif Intrusive Suite and have an intriguingly close proximity to the Haib porphyry copper deposit. The main gabbroic intrusion in the Haib area is predominantly composed of gabbros and is pervasively intruded by leucogranite dykes/veins.

There is no published age data for the Vuurdood Subsuite but other rocks from the Vioolsdrif Domain of the Richtersveld Magmatic Arc have been dated. The previous radiometric ages for the Vioolsdrif Domain of the Richtersveld Magmatic Arc have been presented by Reid (1987), Grumbley (2015), Macey et al. (2017) and Meng et al. (2021) (refer to Table 2.2). Meng et al. (2021) conducted high precision U-Pb geochronology on zircon and rutile from the intermediate-felsic rocks of the VIS and results show that the Richtersveld Magmatic Arc intruded between 1881-1886 Ma (Meng et al., 2021). No published age data exist for the mafic-ultramafic rocks of Vuurdood Subsuite in the Vioolsdrif Domain, in either South Africa or Namibia, however we have produced the first U-Pb zircon age data for this unit in this work.

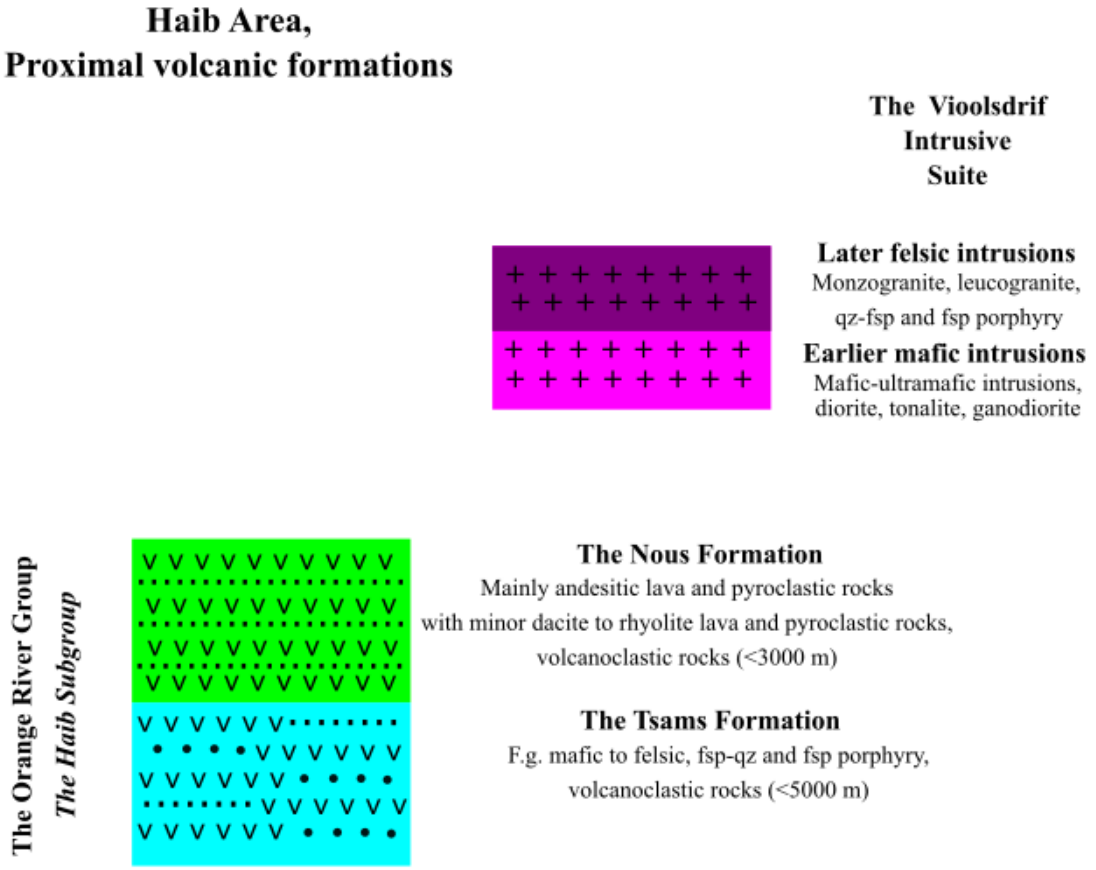

***Figure 2.4**: The lithostratigraphy of the Haib area in the Richtersveld Subprovince. The Haib area is composed of the Haib Subgroup of the Orange River Group, further divided into the basal Tsams Formation and overlying Nous Formation, and the Vioolsdrif Intrusive Suite (after Minnitt, 1979; Blignault, 1974, 1977; Reid, 1977; Blignault et al., 1983; Macey et al., 2015; Shifotoka et al., 2016).*

Orange River Group (ORG)

The aphyric rhyolites of the ORG are fine-grained (~0.1 mm), beige to grey and bedded (with dark and light layers) and mainly composed of quartz, orthoclase, and biotite (Figure 2.5a; Minnitt, 1979). Phyric rhyolites are also fine-grained (~1 mm), brown-red with distinct flow banding (alternating light and dark bands) and are composed of ~2 mm quartz, orthoclase and microcline phenocrysts (~1 mm), set in a medium-grained quartzo-feldspathic groundmass (Figure 2.5b; Minnitt, 1979). Feldspar porphyry andesites are fine-grained, dark grey and contain~2 mm feldspar phenocrysts that have been altered to sericite, epidote and chlorite (Figure 2.5c-d; Minnitt, 1979). They are locally sheared (D_4 shears), indicative of strain partitioning (Figure 2.5e). The mafic tuffs are medium-grained, dark grey-green, interbedded (felsic and mafic bands) and show evidence of grain sorting of pyroclastic grains and fiamme textures (Figure 2.5f-g; Minnitt, 1979).

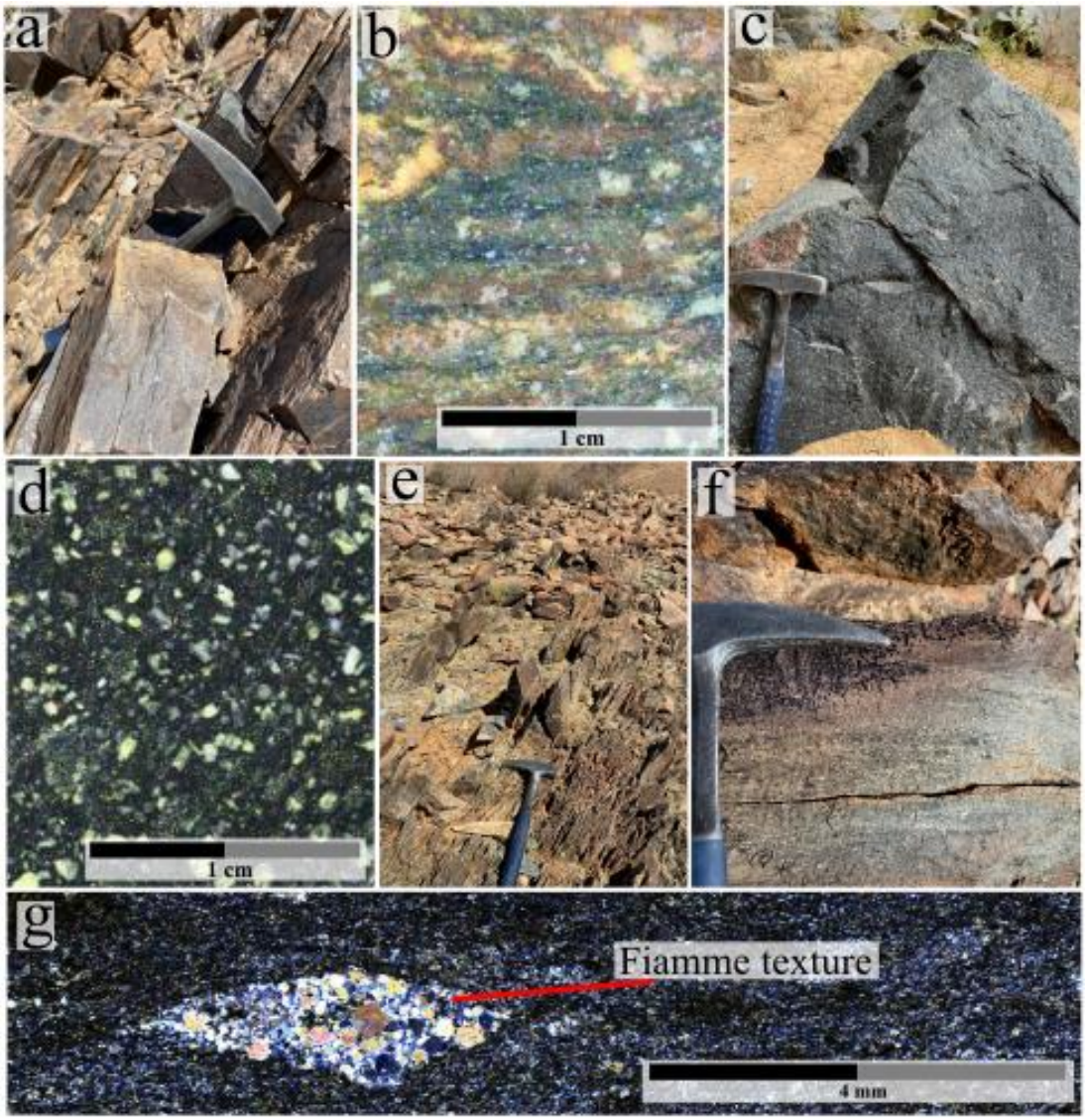

Figure 2.5: *The volcanic lithologies of the Orange River Group in the Haib area. a) Aphyric rhyolites that are distinctly bedded. b) Phyric rhyolites with distinct flow banding. c-d) Feldspar porphyry andesites composed of distinct feldspar phenocrysts altered to epidote and chlorite. e) Sheared feldspar porphyry andesite. f-g) Mafic tuff with evidence of grain sorting and fiamme textures.*

Vioolsdrif Intrusive Suite (VIS)

The diorites are coarse-grained (0.5 - 2 mm), dark grey, with a distinct speckled appearance, equigranular and are composed of plagioclase (80%), biotite (10%), quartz (5%) and K-feldspar (5%) (Figure 2.6a; Minnitt, 1979). The granodiorites are medium- to coarse-grained (~3 mm), light grey, equigranular and are composed of plagioclase (40%), K-feldspar (30%), quartz (20%), hornblende (5%) and biotite (5%) (Figure 2.6b; Minnitt, 1979). The monzogranites are medium- to coarse-grained (1-2 mm), grey-pink, porphyritic with ~ 1 mm - 20 mm K-feldspar phenocrysts and are composed of K-feldspar (40%), plagioclase (35%), quartz (20%) and biotite (5%) (Figure 2.6c-d; Minnitt, 1979). The matrix of the quartz-feldspar porphyry granodiorites is medium-grained (~2.5 mm), light pink-green depending on alteration and have ~5 mm quartz and feldspar phenocrysts (Figure 2.6e; Minnitt, 1979). Disseminated, massive and vein-type sulphides are evident in the quartz-feldspar porphyry granodiorites (Figure 2.6e; inset f; Minnitt, 1979). The sulphides present are pyrite, chalcopyrite, bornite, chalcocite and molybdenite. The leucogranites are fine- to medium-grained (~0.5 - 1 mm), pink, equigranular and are composed of quartz (60%), K-feldspar (25%), plagioclase (10%), and biotite (5%) (Figure 2.6g-h; inset i; Minnitt, 1979). There are two generations of leucogranites: an earlier coarser-grained phase and a later finer-grained phase usually as dykes.

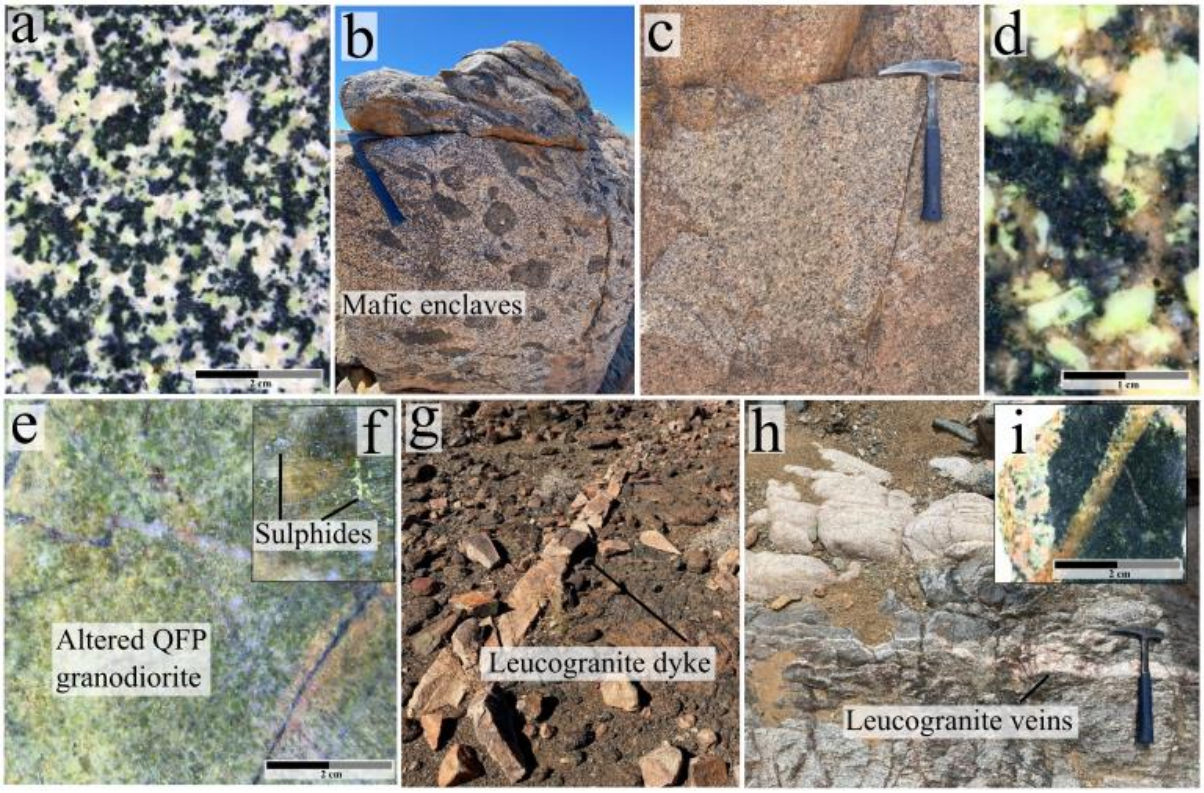

Figure 2.6: *The plutonic lithologies of the felsic Vioolsdrif Intrusive Suite in the Haib area: a) Distinct speckled and equigranular diorites. b) Granodiorite with mafic enclaves. c-d) Monzogranites with distinct K-feldspar phenocrysts. e-f) Altered quartz-feldspar porphyry granodiorites with distinct evidence of potassic and sericitic alteration as well as bleb-like sulphides. g-i) Leucogranite dykes and veins that pervasively intrudes all the other plutonic rocks in the region.*

Table 2.1: *Various subdivisions of the Vioolsdrif Intrusive Suite in the Vioolsdrif and Pella Domains (Macey et al. 2017).*

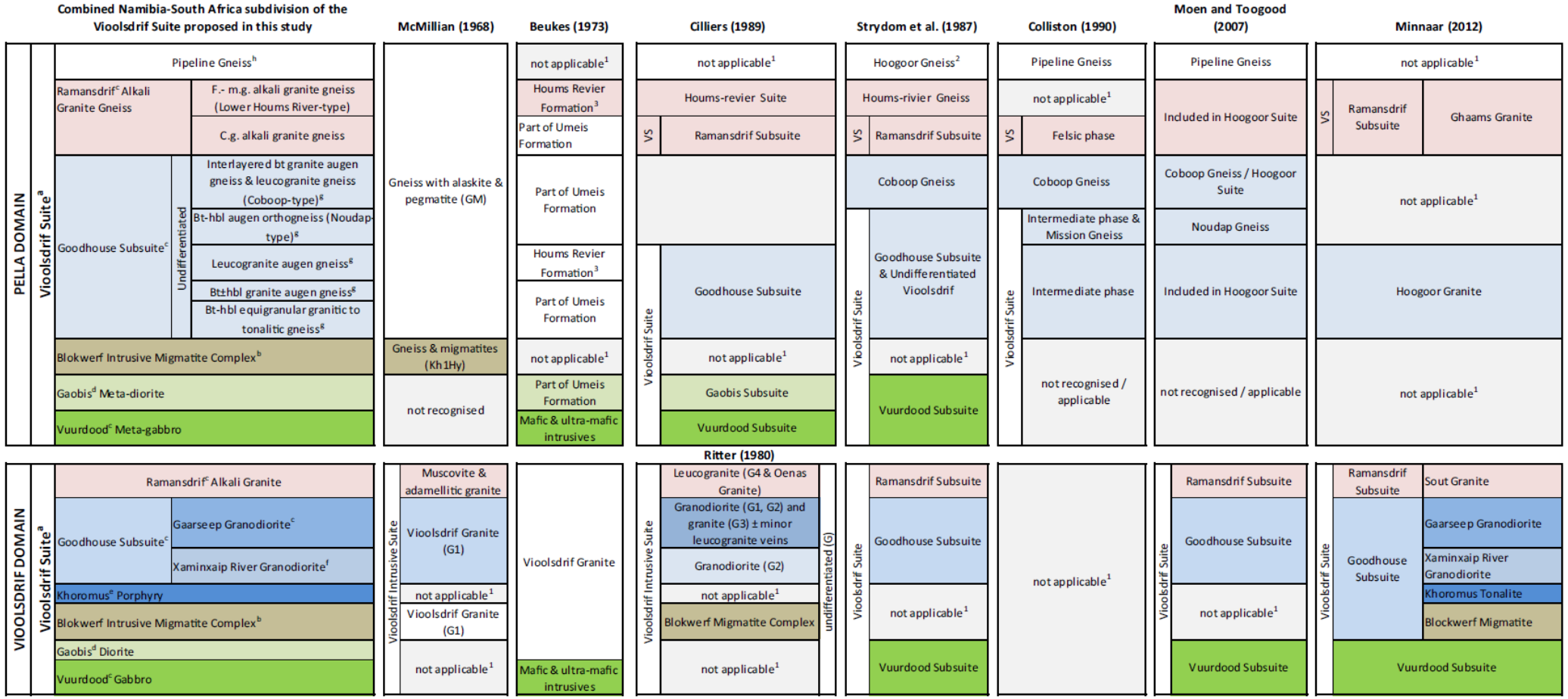

Table 2.2: *Summary of published age-data for the Vioolsdrif Domain of the Richtersveld Magmatic Arc.*

	Orange River Group		**Vioolsdrif Intrusive Suite**					
Reference	**Rhyolites**	**Andesites**	**Mafic-ultramafic intrusions**	**Diorites**	**Granodiorites**	**Monzogranites**	**Quartz-feldspar porphyry granodiorites**	**Leucogranites**
Reid, 1987	1970 ±70 – 2020 ± 70 Ma (Rb-Sr method)		1900 ± 130 Ma (Rb-Sr method)	1975 ± 55 Ma (Rb-Sr method)	1925 ± 45 Ma (Rb-Sr method)	1800 ± 40 Ma (Rb-Sr method)	1800-1900 Ma (Rb-Sr method)	1730-1835 Ma (Rb-Sr method)
Grumbley, 2015	-	1874 ± 8.5 Ma (Pb-Pb method)	-	-	-	-	1856.8 ± 9.5 Ma (Pb-Pb method)	-
Macey et al., 2017	1884 ± 4 Ma (LA U-Pb method)	1902 ± 7 Ma (LA U-Pb method)	-	-	1879 ± 7 Ma (LA U-Pb method) 1885 ±7 Ma (LA U-Pb method) 1896 ± 12 Ma (LA U-Pb method)	1893 ± 5 Ma (LA U-Pb method)	1893 ± 10 Ma (LA U-Pb method)	1844 ± 26 Ma (U-Pb method)
Meng et al., 2021	1892 ± 6 Ma (LA U-Pb method)	1892 ± 9 Ma (LA U-Pb method) 1912 ± 10 Ma (LA U-Pb method)	-	1875 ± 10 Ma (LA U-Pb method)	1887 ± 7 Ma (LA U-Pb method)	1886 ± 1.6 Ma (LA U-Pb method)	1885.47 ± 0.93 Ma (TIMS U-Pb) 1892 ± 14 Ma (LA U-Pb method)	1881 ± 0.71 Ma (TIMS U-Pb)

2.2. The tectonic setting of the Haib porphyry copper deposit

Various authors have debated whether the Haib porphyry copper deposit formed in an island arc setting or a continental arc setting (Van Zyl, 1981; Reid, 1977; Reid et al., 1987; Minnaar, 2012). The calc-alkaline signature of the Orange River Group and the Vioolsdrif Intrusive Suite is characteristic of an arc complex (Reid et al., 1987). It was initially concluded by Reid (1977) that the chemistry of the Orange River Group and the Vioolsdrif Intrusive Suite indicate similarities with Cenozoic-age igneous rocks that formed in island arc settings and active continental margins. However, later it was established that the intimate association between the Orange River Group and the Vioolsdrif Intrusive Suite, its high-K nature, the formation of copper porphyries and minor evidence of an underlying Archean crust, all suggest a mature island arc environment for the Richtersveld Subprovince (Reid et al., 1987). Further evidence for a mature island arc setting is the island-arc geochemical signatures and the Hf and O isotopes signatures which indicate little or no older continental crust involvement (Macey et al., 2017 and Meng et al., 2021). Initial isotope ratios (Sr, Pb, Nd) in the Richtersveld Subprovince indicate juvenile crust generation in a mature arc setting during the early Proterozoic (Reid et al., 1987). The magmas from an undifferentiated mantle source underwent enrichment (slightly high μ and ε_{Sr}) associated with metasomatism in the mantle wedge above the subduction zone (Reid, 1997). This was associated with the introduction of small amounts of radiogenic Pb and Sr which is a process observed in modern arcs (Reid, 1997). In addition, rare earth element signatures shown by the andesites and the corresponding plutonic equivalents adhere with the idea that the lavas and the plutonic equivalents were derived from arc-type basaltic magmas setting associated with fractional crystallisation (Reid, 1997). The dacites and lavas (and their plutonic equivalents) can to some extent be related to fractional crystallisation but, according to Reid (1997) partial melting of juvenile crust can also be achieved to produce signatures observed. Thus, the products from these igneous processes may be regarded as young crust formation in a mature arc environment (Reid, 1997).

The geochemistry of modern continental margin arc settings is characterized by high La/Yb ratios which indicate a thick crust (Minnaar, 2012). However, there is minor evidence of an underlying Archean crust except in the Blockwerf migmatite which is characterized by high La/Yb ratios (Reid et al., 1987; Minnaar, 2012). The Orange River Group show no evidence of crustal contamination by pre-existing crust and the Vioolsdrif Intrusive Suite have low La/Yb ratios indicating that the Haib area cannot be compared to modern continental margin arc settings (Minnaar, 2012). The lack of evidence of a pre-existing crust may be explained by two factors: (1) the crust was thin, suggesting that only a minor volume of the crust was recycled and (2) the pre-existing crust was a primary crust which was not subjected to recycling events thus its radiogenic isotope ratios were not altered significantly (Minnaar, 2012). The age of this pre-existing crust could have been 2.7 Ga as indicated by a single inherited zircon age (Nordin, 2009; Minnaar, 2012). In addition, Macey et al. (2017) states that the detrital zircons in the Bankwesser Migmatite have Archaean ages and possibly represent a fragment of Archaean Kaapvaal craton basement that was entrained into the Richtersveld Subprovince prior to the Orange River Orogeny. Sm-Nd modal ages of ~ 2.4 Ga indicate that there is older continental crust involvement (Macey et al., 2017). 2.02 Ga inherited zircons indicate specifically some sourcing from the Spierregebiet Arc (Macey et al., 2017).

2.3. Regional structural geology

According to Macey et al. (2017), the western section of the Namaqua-Natal Province has been subjected to five main deformation events (Table 2.3): the Orange River Orogeny (D_1), the Namaqua Orogeny (D_{2-4}) and the Pan-African Gariep Orogeny (D_5).

The Paleoproterozoic Orange River orogeny (~1900 Ma) led to deformation of the Orange River Group with evidence of large-scale, open to isoclinal, upright to recumbent F_1 folds of the S_0 bedding (Blignault, 1977; Macey et al., 2017). The folding resulted in the development of an axial planar S_1 foliation and a L_1 stretching lineation (Macey et al., 2017). Various authors have debated whether the D_1 event predates or coincides with the intrusion of the Vioolsdrif Intrusive Suite (Blignault, 1977; Ritter, 1980) however, field relationships by Blignault (1977) and Macey et al. (2017) have confirmed that the D_1 event is constrained by the extrusion of the Orange River Group and the intrusion of the early, more mafic granitoids of the Vioolsdrif Intrusive Suite. The D_1 event is related to greenschist facies metamorphism in both the Pella and Vioolsdrif Domains (Colliston and Schoch, 2000; Macey at al., 2017). The Pella Domain is overprinted by the Namaqua Orogeny (Macey et al., 2017).

The ~1.2-1.0 Ga Mesoproterozoic Namaqua orogeny (Joubert, 1986) led to the formation of various thrust- and shear zone-bound tectonic domains as strain was accommodated heterogeneously. Within the Richtersveld Subprovince, strain was partitioned into the highly deformed Pella Domain. The Pella Domain was subject to intense ductile deformation and medium-grade metamorphism, with at least three deformational episodes (D_2-D_4) recognized (Macey et al., 2017). The D_2 event (1200-1100) involved the formation of an intense regional penetrative S_2 gneissosity, isoclinal folds and L_2 stretching lineations that plunge NE (Macey at al., 2017). The D_3 event involved km- to 10-km-scale F_3 folding of the D_2 fabrics and thrusts, forming upright, NE-plunging folds (Macey et al., 2017). The D_4 event (~1000-960 Ma) was associated with discrete dextral transcrustal shear zones, distinguished by subvertical mylonitic, phyllonitic and cataclastic foliations, and subhorizontal lineations on one major shear zone, and near down-dip lineations on others (Macey et al., 2017). The D_4 dextral shear zones cross-cut both the Pella and Vioolsdrif Domains (refer to Macey et al., 2017). The D_{2-4} event is associated with amphibolite/granulite to greenschist facies conditions (Macey at al., 2017; refer to Table 2.3). The D_2 and D_3 events are not present in the Haib area and D_4 structures are present in the northern (major Poffadder shear zone) and southern sections of the Haib porphyry copper deposit.

The Neoproterozoic Pan African Orogeny resulted in the SE-directed thrusting of the Gariep Belt onto the Richtersveld Subprovince causing penetrative refoliation of the Richtersveld Subprovince in the thrust footwall with preferential partitioning of strain into the Orange River Group (Macey et al., 2017). This D_5 event is associated with lower amphibolite to greenschist facies conditions (Macey at al., 2017). Discrete north and south oriented faults and shears are present in the Haib area and relate to D_5.

Table 2.3: *The five deformation events in the western sector of the Namaqua-Natal Province (Macey et al., 2017).*

Deformation event	Associated structures	Metamorphism	Age	Orogenic event
D_5	SE- directed thrusting of the Gariep over the NMP associated with shear zones in the FW and faulting in the hinterland	Lower amphibolite to greenschist	~ 540-500 Ma	Gariep Pan African
D_4	Dextral transcurrent shear zones	Amphibolite to greenschist	~1000-960 Ma	Namaqua
D_3	Regional scale folds	Amphibolite	Ages poorly constrained	Namaqua
D_2	Polyphase SW-directed thrusting and associated ductile fabrics	Amphibolite/Granulite	~1200-1100 Ma	Namaqua
D_1	Folds, localized weak fabrics	Greenschist	~1900 Ma	Orange River

2.4. The Haib porphyry copper deposit

The Haib porphyry copper deposit occurs as an east-west trending elongated stock that is 11 by 3 km and is tilted between 15°–30° to the north (Minnitt, 1979 and Vermond, 2019). The stock is widest in the vicinity of the main mineralized area of the deposit and progressively narrows and wedges out approximately 3 km west of the ore zone (Minnitt, 1979). Within the Haib porphyry stock, is an approximate NW-SE trending, curvilinear zone, between 300 and 500 m wide and 2 km long of enriched mineralization composed of chalcopyrite, pyrite and molybdenite (Minnitt, 1979). The immediate host rocks include feldspar porphyry andesites and quartz-feldspar porphyry granodiorites which intrude the adjacent andesites and granodiorites (Minnitt, 1979). The feldspar porphyry andesites are fine- to medium-grained, dark grey and consist of ~2 mm feldspar phenocrysts that have been altered to sericite, epidote and chlorite (Minnitt, 1979). The quartz-feldspar porphyry granodiorites are medium-grained (~2.5 mm), light pink-green depending on alteration, porphyritic and composed of ~5 mm quartz and feldspar phenocrysts (Minnitt, 1979). The various vein types include early dark micaceous veins (EDM veins), sinuous chalcopyrite-rich A veins, molybdenite-rich B veins, pyrite-rich D veins and later tourmaline-rich veins (Vermond, 2019). The A, B and D vein types are rare and the EDM veins reflect the relatively deep levels of exposure of the Haib porphyry copper system (Vermond, 2019). The sulphide mineralization dominantly includes pyrite, chalcopyrite, and molybdenite, in decreasing order of abundance (Minnitt, 1979). The mineralization occurs as disseminations, blebs and veins in the feldspar porphyry andesites and quartz-feldspar porphyry granodiorites (Minnitt, 1979). The alteration phases include potassic, phyllic, argillic and propylitic alteration. Potassic and phyllic alteration are the dominant alteration phases (Minnitt, 1979). The mineralization is mainly related to the potassic and phyllic alteration phases. Stable isotopes and fluid inclusion analyses indicate that there are two fluid types: an early high-salinity high-temperature fluid that is trapped in primary inclusions and a late-stage lower-temperature fluid that is trapped as secondary inclusions in healed fractures (Barr and Reid, 1992). The mineralization occurred post-D1 but prior to D_4 (Vermond, 1979). D_1 structures are found in the earlier phases of the VIS such as the diorites but not in the intermediate phases such as the quartz-feldspar porphyry granodiorites (Vermond, 1979). D_4 structures crosscut the main mineralized zone. Age dating conducted by Meng et al. (2021), has bracketed the mineralization at 1884 ± 2 Ma. This was based on the age range between the quartz-feldspar porphyry granodiorite and the leucogranite and coincides with the LA-ICPMS upper intercept U-Pb age of 1891 ± 3 Ma which was established for the hydrothermal rutile associated with chalcopyrite mineralization in the Haib area.

2.5. Controls on mineralization

There are three contrasting views with regard to the controls on mineralization in the region:

1) The mineralization in the Haib porphyry stock was structurally-controlled and related to N-S and E-W fault zones (Minnitt, 1979; 1986),
2) The mineralization was lithologically-controlled and related to hydrothermal brecciation (Walker and Richard, 2018),
3) In contrast, Vermond (2019) proposed two episodes of mineralization; the first episode was associated with lithologically-controlled mineralization related to igneous brecciation, while the second episode was structurally controlled and related to E-W extensional faults and massive quartz veining.

According to Minnitt (1979,1986), east-west trending fracture zones along the northern and southern flanks of the Haib indicate that the quartz-feldspar porphyry stock intruded the floor of an east-west trending graben, that was approximately 5-km-wide and 20-km-long. Sericite alteration is restricted to the flanks of the stock and the graben faults, suggesting that the faults flanking the stock served as conduits for hydrothermal fluids (Minnitt, 1979; Minnitt, 1986). The zone of high-grade mineralization is parallel to regionally developed fractures that are orientated NW-SE and NE-SW (Minnitt, 1979; Minnitt, 1986). This set of fractures probably formed prior to or concurrent with the mineralization and served as conduits along which the hydrothermal fluids migrated (Minnitt, 1979; Minnitt, 1986). The majority of the alteration within the Haib porphyry body is confined to areas centred around veins (Minnitt; 1979; Minnitt, 1986). The earlier potassic alteration is extensive whereas, the latter chlorite-sericite and quartz-sericite ± pyrite is mainly fracture-controlled and is only prevalent where vein alteration envelopes merge or overlap (Minnitt, 1979; Minnitt, 1986).

Minnitt (1986) acknowledged that mineralization is hosted within the igneous breccia, but did not realize that the emplacement of the igneous breccia was linked to the bulk mineralization episode (Vermond, 2019). Minnitt (1979, 1986) did not establish that the N-S and E-W fault zones post-date the emplacement of the igneous breccia, thus producing a separate mineralizing episode (Vermond, 2019). Teck Resources favors a model associated with lithological-controlled mineralization related to igneous brecciation (referred to as the hydrothermal breccia in Teck's study), without considering a subsequent episode of structurally-controlled mineralization (Vermond, 2019). However, Vermond's model incorporates both a lithologically-controlled mineralization episode and a subsequent structurally-controlled mineralization episode. During the lithologically-controlled mineralization episode, the igneous breccia served as the main host for the high-grade mineralization, and during the structurally-controlled mineralization episode, the E-W and N-S normal faults, associated with sericite and silicic alteration, were related to mineralized quartz veins and local zones of high-grade mineralization.

2.6. The Mercaderes Rio-Mayo lower crustal cumulates, Columbia

Porphyry copper deposits are located along convergent plate margins and are therefore found within arc settings. Trans-crustal magmatic differentiation processes from the lower to upper crust in arc settings have implications for porphyry copper formation. A well-known convergent plate boundary where the generation of arc magmas is extensive is the Andean continental margin volcanic arc. The Andes have been extensively used to understand crustal growth processes and therefore provide a unique insight into crustal petrogenesis. However, arc magmas differentiate substantially as they reach shallow crustal levels and undergo subsequent assimilation, obscuring our understanding of primary magma generation, mineralization and ultimately deeper processes in the lower crust. Lower crustal cumulates/xenoliths brought up by volcanic host rocks provide an opportunity to understand lower crustal processes. The composition of the lower crust in the Andes provides an ideal-case study to understand lower crustal processes. The Mercaderes-Rio Mayo lower crustal cumulates in the Andes formed during magmatism related to the subduction of the Nazca plate beneath the South American plate (Weber, 1998, 2002). The Andes has been separated into four distinct volcanic belts based on their geochemical characteristics (Figure 2.7). These volcanic belts include the Austral Volcanic Zone (AVZ), the Southern Volcanic Zone (SVZ), the Central Volcanic Zone (CVZ) and the Northern Volcanic Zone (NVZ) (Figure 2.7; Weber, 1998, 2002). The Mercaderes-Rio Mayo crustal cumulates are located in the Granatifera Tuff, situated in the Northern Volcanic Zone (Figure 2.7; Weber, 1998, 2002). The Mercaderes area in SW Colombia is characterized by late Cenozoic volcanic activity and comprises volcanic and volcano-sedimentaryrocks (Weber, 1998, 2002). The Granatifera Tuff is located in the southeastern section of Mercaderes and occurs as a minor partially eroded tuff cone/tuff ring containing lower crustal xenolith material (Weber, 1988, 2002).

The Phanerozoic lower crustal cumulates are lithologically distinct and diverse, characterized by a heterogenous assemblage of predominantly mafic-intermediate rocks including garnet clinopyroxenite, garnet-rich hornblende pyroxenite, garnet-rich olivine hornblende pyroxenite, garnet-rich olivine hornblende gabbro, tonalite gneiss and quartz-rich granitoid gneiss. The lower crust is composed of both hydrated (hornblende and biotite-bearing) and dehydrated (clinopyroxene and garnet-bearing) rocks (Weber, 1998; Rodriguez-Vargas, 2005). These rocks represent the transition from amphibolite to granulite facies recording a prograde metamorphism path (Weber, 1998; Rodriguez-Vargas et al., 2005). The transition from amphibolite to granulite facies involves dehydration and possible melting of hydrated assemblages (amphibole and biotite) to form anhydrous assemblages (clinopyroxene and garnet) caused by an increase in temperature and pressure (Weber, 1998; Rodriguez-Vargas et al., 2005). Mafic rocks predominate but felsic lower crustal rocks are present. The proportion of amphibole in the lower crustal rocks indicate a distinctly hydrous lower crust in the Northern Andes (Weber, 1998; Rodriguez-Vargas et al., 2005). Both deep and shallow crustal material is observed in the Granatifera Tuff (Weber, 1998). The dehydration of the lower crust possibly produced melt that differentiated forming felsic magmas leaving behind a dense, mafic assemblage (Weber, 1998). The temperatures and pressures calculated for the Mercaderes-Rio Mayo lower crustal cumulates are ~730-830 °C (hydrated assemblages), ~950-1050 °C (dry assemblages) and ~9-14 kbar (Weber, 1998). Our understanding of primary magma generation and metallogenesis of ore deposits is obfuscated by shallower processes in the crust. Thus, by studying the Mercaderes-Rio Mayo lower crustal cumulates, we see through shallow crustal processes that influences arc magma composition and differentiation (Chin et al., 2018). Conducting iron isotopic analyses on the Rio-Mayo lower crustal cumulates will assist in

understanding intra-crustal differentiation processes associated with garnet fractionation as the Rio-Mayo lower crustal cumulates represent the lower levels of a Phanerozoic arc system.



Figure 2.7: *The distribution of the four distinct volcanic zones and the location of the Mercaderes as indicated by the red star (modified after Harmon et al., 1984).*

2.7. Porphyry copper deposit formation

There are two main competing hypotheses for the origin of porphyry copper deposits which include either source-driven or intra-crustal differentiation processes (Lee and Tang, 2020). Source-driven processes are associated with Cu enrichment in parental magmas from the lower crust, lithospheric mantle, mantle wedge or subducting slab (Lee and Tang, 2020). The proposed mechanisms which result in Cu-rich magmas include partial melting of subducted oceanic crust (Thiéblemont et al., 1997; Sajona and Maury, 1998; Oyarzun et al., 2001; Mungall, 2002; Sun et al., 2010; Sun et al., 2011), metasomatism of the continental lithospheric mantle (Richards, 2009; Rielli et al., 2018) or modification of the mantle wedge by fluids (Hattori and Keith, 2001; Richards, 2009; Lee et al., 2012). In these cases, the effects of intra-crustal differentiation processes and shallow crustal level processes are subordinate (Lee et al., 2012; Lee and Tang, 2000). In contrast, differentiation-driven processes do not require Cu-rich parental magmas but involve the removal of Cu from mid-crustal to shallow level plutons (Lee and Tang, 2020). This process is proceeded by the trapping and concentration of the mobilized Cu into a localized reservoir (Lee and Tang, 2020). According to Lee and Tang (2020), deep source regions or the parental magmas from which porphyry copper deposits derive have no unique characteristics. Therefore, some source-driven processes are not related to the formation of porphyry copper deposits and are therefore implausible.

According to Lee and Tang (2020), porphyry copper deposits are mainly found within thick continental arcs, as opposed to island arcs. Thick continental arc magmas become progressively Cu-depleted and undergo early Fe depletion. According to Chin et al. (2018) and Lee et al. (2006, 2007), deep crustal cumulates have sufficient Fe to cause iron depletion. Cumulates in continental arcs are characterized by garnet pyroxenites (arclogites) which have a high modal abundance of garnet (>50%) and are enriched in Fe (Lee and Tang, 2020). Arclogite cumulates from Arizona and California have elevated Cu contents (hosted in magmatic sulphides) which explains the Cu-depleted nature of continental arc magmas (Lee and Tang, 2020). Further geochemical evidence for intra-crustal differentiation is presented by the high Nb/Ta ratios of arclogites that are required to accommodate the low Nb/Ta signatures of continental arc magmas (Tang et al., 2019). Thick crust and high pressures are needed for the generation of garnet-bearing cumulates, the extraction of which results in the oxidation of the residual magma (Lee and Tang, 2020).

Thus, porphyry copper deposits are typically formed in thick continental arc (> 45 km) settings associated with intra-crustal differentiation processes which involve the fractionation of garnet, depletion of total Fe in the magma and enrichment of ferric iron causing oxidation of the magma (Figure 2.8; Lee and Tang, 2020). The Fe depletion promotes sulphide segregation and extraction which, in turn, isolates the Cu into lower crustal cumulates (Lee and Tang, 2020). The oxidation caused by garnet fractionation results in the conversion of sulphide to sulphate into differentiated felsic magmas that eventually reach the upper crust near the brittle-ductile transition zone (Figure 2.8; Lee and Tang, 2020). This releases Cu from the sulphides into aqueous solutions and enhances the capacity of magmatic fluids to scavenge and transport Cu to the top of the pluton (cupola), resulting in the immobilization and concentration of Cu (Figure 2.8; Lee and Tang, 2020).

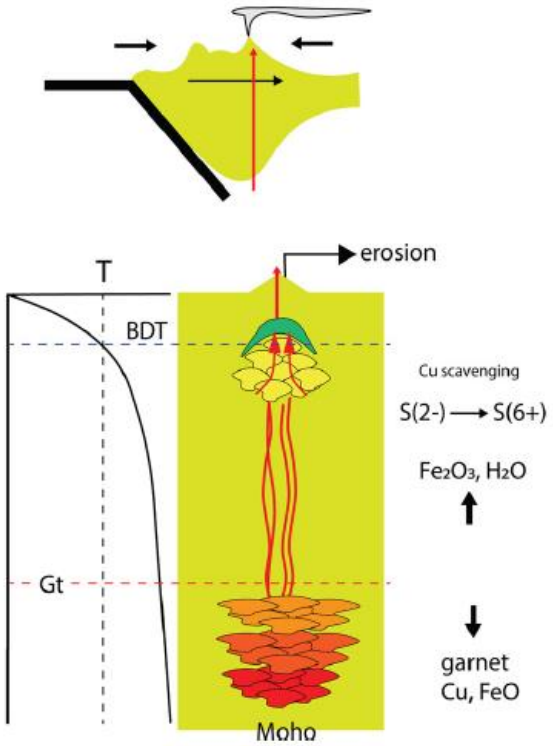

Figure 2.8: *A trans-crustal section of a mature continental arc (Lee and Tang, 2020). Garnet fractionation in the lower crust results in Fe depletion and oxidation of the residual magma. The Fe depletion causes sulphide segregation which in turn, isolates the Cu into the lower crustal cumulates. The oxidation caused by garnet fractionation results in the conversion of sulphide to sulphate in the differentiated felsic magmas that eventually reach the upper crust near the brittle-ductile transition zone (BDT). This releases Cu from the sulphides into solution and enhances the capacity of magmatic fluids to scavenge and transport Cu from Cu poor magmas to top of the pluton (cupola), resulting in the immobilization and concentration of Cu, forming a Cu-enriched cupola (Lee and Tang, 2020).*

2.8. Cu and Fe isotopes theory

Stable isotope studies have become an advanced method for understanding mineralization processes. There has been a remarkable renaissance in stable isotope geochemistry in the last two decades (Johnson et al., 2020). The application of non-traditional stable isotopes in various deposits including porphyry deposits is limited (Cooke et al., 2014). Research that has been conducted focusses on mineral deposits in both hypogene and supergene environments (Cooke et al., 2014). Studies have identified zoning patterns that are a reflection of temperature, redox conditions and fractional crystallization. Results from existing studies show that limited isotopic variation is related to hypogene environments as a result of the small equilibrium isotope fractionation and limited variation in the redox state for Cu and Fe. In contrast, supergene environments have a greater variability at lower temperatures as the changes in the oxidation state can induce larger fractionations (Cooke et al., 2014). There are various types of fractionation that can account for variations in isotopic compositions in rocks and minerals (Dauphas et al., 2017; Johnson et al., 2020). The two main mechanisms of fractionation are categorized into kinetic and equilibrium processes (Dauphas et al., 2017; Johnson et al., 2020).

The first category consists of several kinetic processes which include diffusion, thermal diffusion, condensation, evaporation, as well as several other kinetic processes (Dauphas et al., 2017). Diffusion and thermal diffusion are based on the ability of light isotopes to move more easily compared to heavy isotopes (Dauphas et al., 2017). Thermal diffusion processes are related to the light isotopes moving towards the higher temperature regions of a system and the heavy isotopes moving towards the colder regions of a system (Lundstrom, 2009; Zambardi et al., 2014). Richter et al. (2009a and b), Huang et al. (2010) and Zambardi et al. (2014) suggested that the iron isotopic variations in several magmatic suites may be related to thermal fractionation. The heavy iron isotopes tend to concentrate towards the colder regions of a magmatic suite during differentiation. Condensation processes are not well-constrained and therefore cannot be properly quantified. Evaporation processes can be calculated and modelled (Dauphas et al., 2017). High-temperature evaporation processes are uncommon and include evaporation from solar nebulae and planetary collisions (Dauphas et al., 2017). Isotopic fractionation that is related to chemical reaction kinetics is one of the most poorly understood isotopic phenomena. As a result, most work has focused on redox reactions under experimental conditions (Dauphas et al., 2017). Kinetic isotope fractionation processes are complex making them difficult to characterize and quantify. Kinetic isotope fractionation processes most likely include a combination of processes.

Equilibrium isotopic fractionation processes in mineral-mineral, mineral-melt, fluid-fluid and fluid-mineral pairs can be constrained (Dauphas et al., 2017). An equilibrium reaction involves the exchange between two phases until thermodynamic equilibrium is reached. In these processes, isotopic fractionation is related to the bond strength, coordination and redox state. In equilibrium isotopic fractionation closed and open systems exist (Dauphas et al., 2017). Studies conducted on natural isotopic fractionation between minerals and melt show that experimental work has been undertaken at high temperature and pressure conditions for the fractionation in different systems (Dauphas et al., 2017). Mineral-mineral and mineral-melt fractionation are controlled by the coordination and valence of the minerals concerned and associated redox reactions. There is also a difference in bond energies between different phases, with the heavier isotopes preferring the higher energy bond and the lighter isotopes preferring the lower energy bond (Li et al., 2010).

For both equilibrium and kinetic fractionation processes, equilibrium between reduced and oxidized ions in solution play a significant role, in addition, temperature plays a dominant role and can result in significant change in fractionation. Previous studies on porphyry copper systems have shown that there are various suggested mechanisms for high temperature fractionation of stable isotopes such as copper and iron. These mechanisms mainly include variations in the hydrothermal oxidation state as the system evolves with time, this has been demonstrated for low temperature weathering environments (e.g., Ehrlich et al., 2004; Mathur et al., 2005, 2010, 2012; Pekala et al., 2011; Zhu et al., 2002) and the fractionation of copper and iron between the fluids and minerals during precipitation of sulphides and mineral phases (Li et al., 2010; Maher and Larson, 2007). Cu solubility in silicate melts significantly increases with increasing oxygen fugacity and the isotopically heavy copper tends to concentrate in Cu^{2+} -bearing sites. As a result, when oxidized melt intersects with copper bearing sulphides, the copper in the sulphides can be potentially oxidized to Cu^{2+} and is incorporated into the oxidized liquids which leaves the residual sulphides relatively depleted in the heavy isotope (Zhang et al., 2021). Exsolved fluids are enriched in light Fe isotopic compositions as the Fe^{2+} species in fluids preferentially incorporate the lighter isotope (Simon et al., 2004; Heimann et al., 2008; Hill et al., 2010; Saunier et al., 2011; Wang et al., 2011, 2015; Telus et al., 2012). Iron isotopes have also been used to identify fractional crystallization processes (He et al., 2020). Inter-mineral iron isotope fractionation is a result of the smaller Fe^{3+} that prefers the low coordination which is associated with stiffer bonds compared to Fe^{2+} and therefore the Fe^{3+} sites enrich heavy Fe isotopes (Du et al., 2022). Fe^{3+} rich minerals are expected to concentrate the heavy Fe isotopes. As a result, fractional crystallization of Fe^{2+} rich minerals form cumulate material with a depleted Fe isotope signature and a residual melt with an enriched Fe isotope signature.

3. Analytical methods

Several analytical procedures were employed in this study including whole-rock chemical analyses (major and trace elements), U-Pb zircon geochronology, Cu-Fe isotopic analyses on both in-situ sulphide mineral separates and whole rock powders and machine learning geothermobarometry on the Vuurdood Subsuite.

3.1. Whole rock geochemistry

30 samples were prepared for whole rock geochemistry and analyses were conducted at the Earth Lab (University of the Witwatersrand). The samples were first crushed into coarse aggregates using a carbide-steel jaw crusher. The coarse aggregates were then milled using a carbide-steel swing mill. Major elements were analysed through X-Ray Fluoresence (XRF) using an Axios Max Panalytical instrument and trace elements were analysed by inductively coupled plasma mass spectrometry (ICP-MS) using a Thermo Scientific iCAP RQ ICP-MS instrument.

3.1.1. XRF analytical procedure for major elements

Analyses were completed on fused disks using the Norrish Fusion (Norrish and Hutton, 1969) technique and in-house correction procedures. Milled samples were ignited for 40 minutes at 1000 °C and loss of ignition (LOI) was calculated. Samples (0.34 g) were then mixed with Johnson Matthey Spectrolflux 105 (2.0 g) and fired once again at 100 °C for 40 minutes and then poured and pressed into a fused disk. Calibration standards used were primary International Reference Materials USGS series (USA) and NIM series (South Africa) and were made up using synthetic oxide mixtures and international standard rocks as well as in-house controls. Precision is taken as 1% for elements in abundance of greater than 5% by weight, and 5% for elements in abundance less than 5% (Figure 3.1). Standard calibrations used include BCR2 and BHVO2 standards.

3.1.2. ICP-MS analytical procedures for trace elements

Samples were prepared for trace element analysis using a standard microwave digestion method. Firstly, 50 mg of sample was weighed and added to a Teflon tube to which 6 mL of 2:1 HF: HNO_3 was added. The Teflon tubes were then sealed and heated to 180 °C for 40 minutes in a CEM Mars 206 microwave and left to cool for 30 minutes to room temperature. The samples were transferred to small 15 mL Savillex beakers and the teflon tubes were rinsed with 10% HNO_3. Samples were then put on a hot plate (70 °C) for 24 hours and left to dry. Once dry, 2 mL of pure HNO_3 was added to the sample. The mixture was capped and left to digest at 70 °C for 24 hours. Thereafter, the sample was left to dry down at 70 °C. Once dry, another 2 mL of pure HNO_3 was added. The sample was left to dry down again at 70 °C. Finally, 3 mL of HNO_3 was added and the mixture was capped until analysis. Two main reference standards (BCR-2 and BHVO-2) were included in the analyses were within 10% relative error, for all elements, in agreement with accepted values (Figure 3.2).

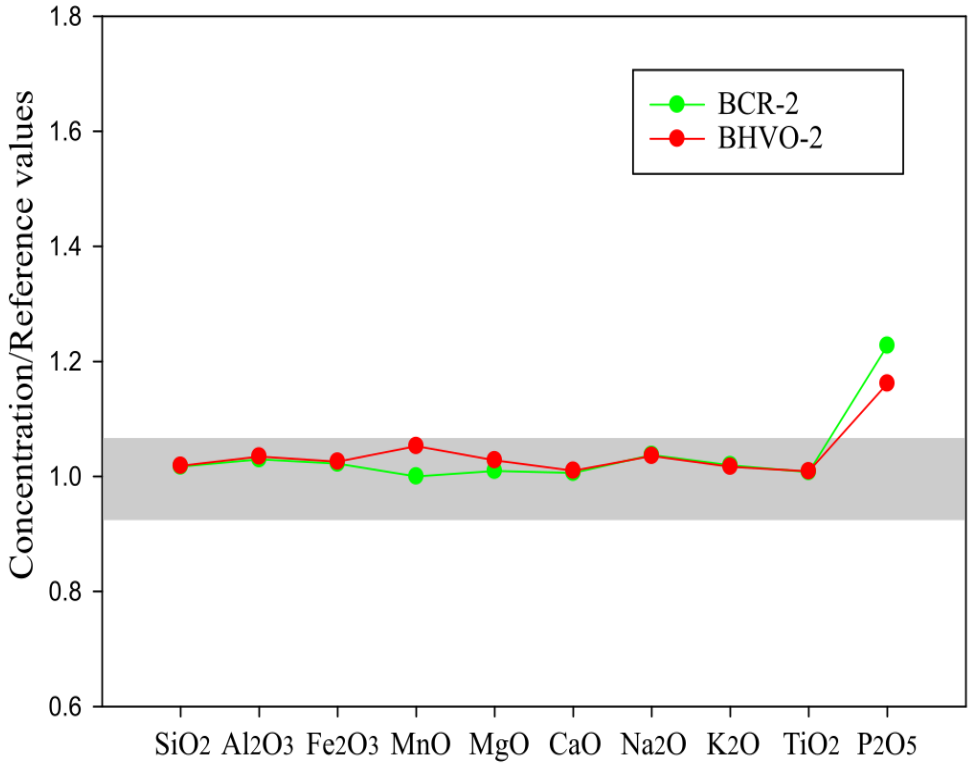

Figure 3.1: *Comparison of the BCR-2 and BHVO-2 standards from this study and the reference values from the USGS (2001). Most of the data agree within 5% (shaded band) except for* P_2O_5.

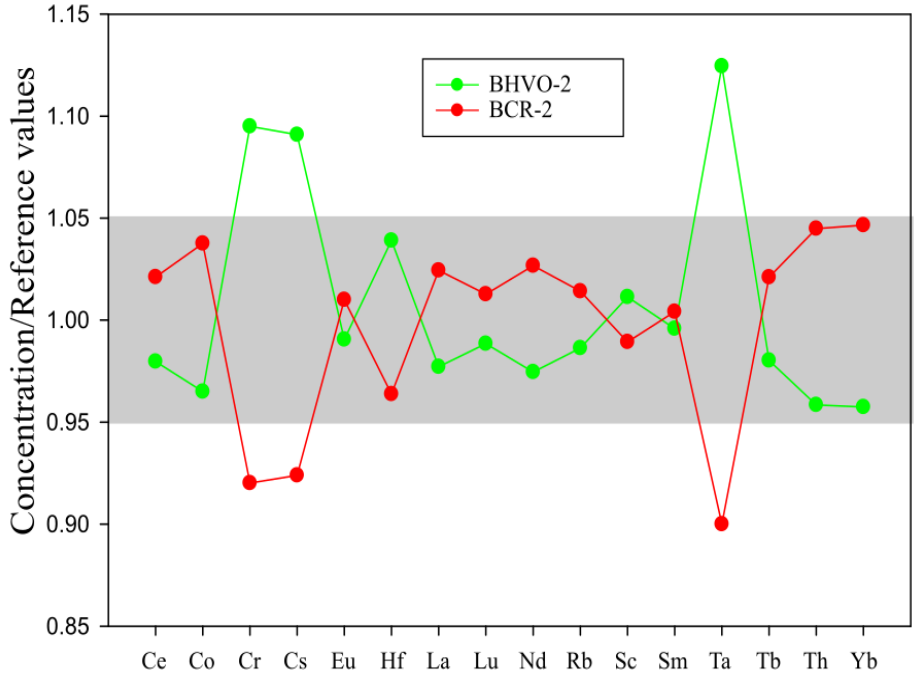

Figure 3.2: *Comparison of the BCR-2 and BHVO-2 standards from this study and the reference values from the USGS (2001). Some of the data agree within 5 % (shaded band) uncertainty. However, elements such as Cr, Cs and Ta fall out of this reproducibility range and have been assigned an uncertainty of 10 %.*

3.2. U-Pb zircon geochronology

5 samples were prepared for U-Pb zircon geochronology and include representative samples of clinopyroxenite and gabbro from the Kokerboom Intrusion as well as diorite and granodiorite from the Vioolsdrif Intrusive Suite. The zircons were separated through traditional Wilfley table, heavy liquid and Frantz magnetic separation at the University of the Witwatersrand. The zircons were then picked using a binocular microscope and were mounted in epoxy resin and polished to expose the interior of the grains. Thereafter, backscattered electron (BSE) and cathodoluminescence (CL) imaging were conducted on zircon grains in order to select laser ablation spot areas (Appendix J) using an accelerating voltage of 25 kV and beam intensity of 17.68 nA respectively on a VEGA3 SEM instrument, coupled with the VEGA3 X64 TESCAN TIMA 2.4.1. software in the Wits Automated Mineralogy Laboratory.

The U-Th-Pb measurements were conducted in the Earth Lab at the University of the Witwatersrand, employing an Australian Scientific Instruments (ASI) Resolution 193 nm ArF excimer system coupled to a Thermo Scientific Fisher magnetic sector field, single collector ICPMS (Element XR). The data were acquired by single spot analysis (30 µm), using a fluence of 2.5 $J.cm^{-2}$ and a laser repetition rate of 8 Hz. The total signal acquisition time was 50 seconds, comprising 10 seconds of pre- and post-ablation (gas blank) and 30 seconds of ablation measurements. Laser sampling took place in a SE155 dual-volume ablation cell (Laurin Technic, Canberra, Australia) using a mixed He-Ar atmosphere and a small volume of N_2 to enhance signal stability and sensitivity. Analyses of the primary calibration standard were obtained at the beginning and end of a sequence, and approximately ten analyses of unknowns were followed by analyses of one primary calibration standard and two to three secondary standards for quality control purposes.

The data reduction was conducted using the Iolite and VizualAge data reduction scheme (Petrus and Kamber, 2012). Graphic presentation and calculation of concordia and weighted mean $^{207}Pb/^{206}Pb$ zircon ages was conducted using the software ISOPLOT-R (Vermeesch, 2018). Uncertainties on individual isotope ratios are 2 SE (standard error, absolute). Concordia ages ($^{206}Pb/^{238}U$-$^{207}Pb/^{235}U$) for certified reference zircons agree with accepted reference values: Plesovice: 337 ± 1.00 Ma (MSWD of equivalence = 10, n = 10; accepted value: 337.13 ± 0.37 Ma (Slama et al., 2008)) and Temora 2: 416 ± 10 Ma (MSWD of equivalence = 2.5, n = 3; accepted value: 416.17 ± 0.24 Ma (Black et al., 2004)). Data processing in ISOPLOT-R ensured that a discordance of greater than 10 and anomalously negative discordance were removed from the plots produced in the software.

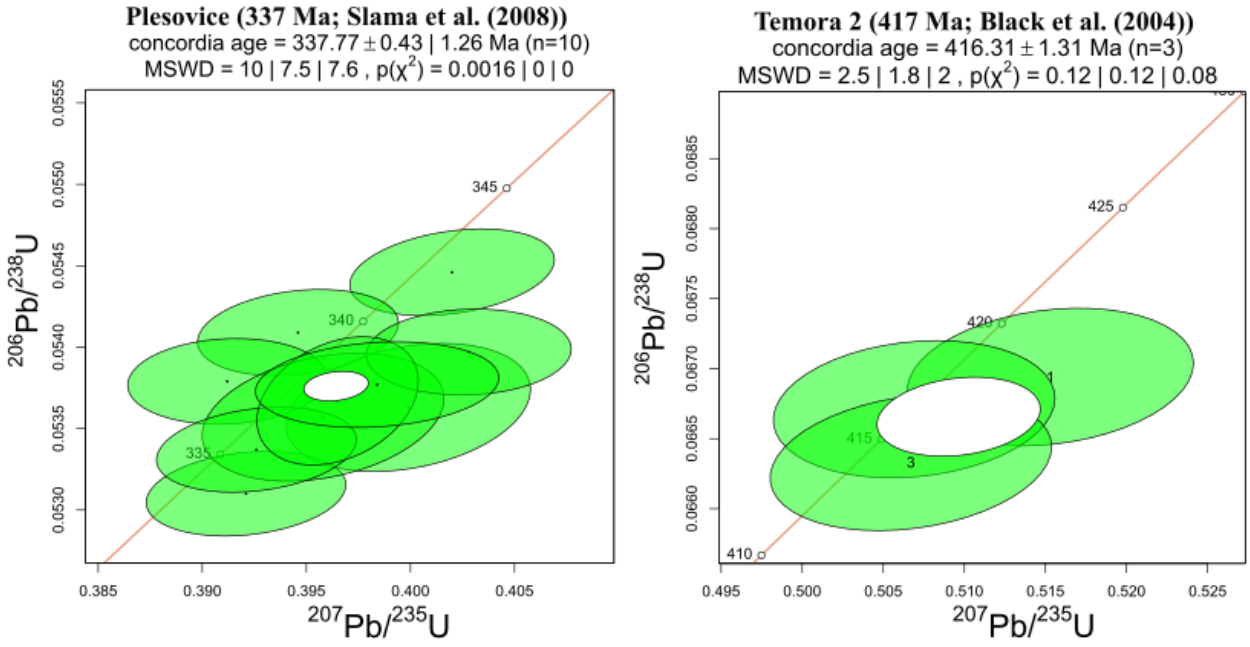

Figure 3.3: *Concordia ages of measured reference standard ages compared with the accepted ages for the Plesovice and Temora 2 standards.*

3.3. Cu-Fe isotopic analyses

24 whole rock samples and 7 in-situ sulphide grains were prepared for copper and iron isotopic analyses. The samples underwent chemical dissolution, ion exchange chromatography and were measured using a multi-collector inductively coupled plasma mass spectrometry (MC-ICP-MS).

3.3.1. Digestion and ion exchange chromatography

For the whole rock samples, approximately 50 mg of rock powder was dissolved in 4 ml of heated ultra-pure aquaregia at 80 °C overnight. The solutions were then dried and the salts were further dissolved in 4 ml of heated ultra-pure 16 molar HF and 8 molar nitric acid. These solutions were dried and prepared for column chromatography as described below.

For the in-situ samples, sulphide grains were handpicked from disseminated and vein type variations. A microdrill was used and the sulphide powders were carefully collected after drilling. The micro-drilled sulphide powders were between 7 and 26 mg. They were dissolved in 4 ml of heated ultra-pure aquaregia at 80 °C overnight. To confirm mineralogy, before drying, a 0.2 ml aliquot was removed and diluted to determine the Cu/Fe ratio on an Agilent 5900 Inductively Coupled Plasma Optical Emission spectroscopy (ICP OES) at Juniata College. Samples possessed Cu/Fe ratios between 0.91 to 1 indicating are chalcopyrite.

The dried rock powder and mineral separates were processed with the ion exchange protocol initially developed by Marechal et al. (1999) and slightly modified in Mathur et al. (2005). In brief, approximately 1.8 ml of wet BioRad Mp-1 HCl form, 200-400 grain size resin was loaded into a 10ml BioRad chromatography column. The resin was rinsed with 10 ml of MQ water (18 Ω water), 10 ml 2% nitric acid, 5 ml of 6 molar HCl. The sample was loaded with 2 ml of 6 molar HCl and cations were further eluted with 5 ml of 6 molar HCl. Copper was collected in the subsequent 27 ml of 6 molar HCl, and iron was collected in 10 ml of 2 molar HCl. The procedure was repeated to further clean solutions.

3.3.2. MC-ICP-MS measurements

The dried salts were solubilized in 2% nitric for analysis on the Neptune Plus (double-focusing multicollector ICPMS) at Rutgers University. The copper isotopes were measured in wet plasma and in low resolution mode as described (Mathur et al., 2009). Samples at 150 ppb generated ^{63}Cu = 5V and mass bias was corrected using standard (NIST 976) sample bracketing. All copper isotope values are reported in the traditional per mil format. As an internal check the 1838 USA was measured throughout the sessions and produced overlapping $\delta^{65}Cu$ = -0.01 ± 0.08 ‰, n = 9 to reported values (Mathur et al., 2009b). As an external standard, the USGS rock standard BVHO-2 was measured ($\delta^{65}Cu$ = 0.10 ± 0.07 ‰, n = 2) and overlaps with reported values of Sossi et al. (2015) (Table 3.1). Since the most analyzed material was the 1838 standard, its error is considered the maximum error.

The iron isotopes were measured in a similar manner to that of Yesavage et al. (2012). Iron was measured in a wet plasma with the instrument in high resolution mode. Samples at 1.5 ppm Fe generated ^{56}Fe = 12V for analysis on the left side of the argide interference and mass bias was corrected using standard (IRMM 014) -sample bracketing. All reported iron isotope values displayed mass dependence and are reported in the traditional per mil format. As an internal check SRM-3126a was measured throughout the sessions and produced overlapping

δ^{56}Fe = 0.31 ± 0.07 ‰, n = 9 to reported values. As an external standard, the USGS rock standard BVHO-2 was measured (δ^{56}Fe = 0.05 ± 0.05 ‰, n = 2) and overlaps with reported values of Sossi et al. (2015) (Table 3.1). Since the most analyzed material was the SRM standard, its error is considered the maximum error.

The measured values are within error of the accepted value for both δ^{65}Cu and δ^{56}Fe. The measured value for δ^{65}Cu is between 0 and 0.1 ‰ and the accepted value for δ^{65}Cu is between 0.04 and 0.14 ‰. The measured value for δ^{56}Fe is between 0.03 and 0.17 ‰ and the accepted value for δ^{56}Fe is between 0.10 and 0.12 ‰.

Table 3.1: *An external standard, the USGS rock standard BVHO-2, was measured and values are within recommended values from publications.*

Standard	δ^{65}Cu (‰) (n=2)	Error (±)	δ^{56}Fe (‰) (n=2)	Error (±)
BHVO-2 measured	0.05	0.05	0.10	0.07
BHVO-2 accepted	0.09	0.05	0.11	0.01

3.4. Geothermobarometry

The data used for the algorithm was obtained from D. Reid's 1977 thesis that had data on pyroxenes from the Vuurdood Subsuite. These samples were chosen as the pyroxenes are unaltered. Samples from the Haib could not be analyzed as the pyroxenes have been subjected to alteration associated with porphyry copper deposits.

The geothermobarometry algorithm is extensively explained in Jorgenson et al. (2022) and Higgins et al. (2022). All algorithms are available on github: https://github.com/corinjorgenson/RandomForest-cpx-thermobarometer and in the open access publication Higgins et al. (2022): https://link.springer.com/article/10.1007/s00410-021-01874-6 and therefore we think it is beyond the scope of our contribution to explain this approach in more detail again.

As demonstrated in Higgins et al. (2022) the machine learning algorithm used to estimate pressure and temperature of clinopyroxene and amphibole crystallization, compares natural sample analyses with all experiments present in a global database finding the closest match (see Figure 9 of Higgins et al., 2022). The regression performed by the random forest algorithm, allows more precise estimates with respect to the simple comparison of the chemistry of natural and experimentally produced minerals. The methodology was applied to existing EPMA data on pyroxenes and amphiboles that formed part of D. Reid's (1977) PhD thesis. EPMA analyses from this study were conducted on amphiboles from the gabbro from the Kokerboom Intrusion, however, due to alteration of amphiboles, meaningful results from these phases could not be reported.

4. Assessing the geological relationships between the mafic-ultramafic intrusion in the Haib area and the Vuurdood Subsuite, Richtersveld Subprovince

4.1. Introduction

Palaeoproterozoic igneous rocks form a large magmatic arc complex known as the Richtersveld Magmatic Arc (RMA), which is well-exposed in the lower Orange River region of South Africa and Namibia (Macey et al., 2017). Recent studies have provided evidence for its formation during the period 1910 - 1865 Ma, with subsequent incorporation into a Mesoproterozoic continental assembly, now preserved in the Namaqua-Natal tectonic province (Macey et al., 2017 and references therein). The RMA consists of a volcanic succession (the Orange River Group) intruded by a mainly granitic batholith (the Vioolsdrif Suite), with compositions ranging from ultramafic to felsic (Figure 4.1). Epiclastic sedimentary lithologies occur locally, interpreted as reworked lavas and welded tuffs, erosion and re-deposition of exhumed granitic members of the batholith, and also as extraneous transported material tectonically juxtaposed during Meso- and Neoproterozoic orogenesis. The Vioolsdrif Intrusive Suite of the RMA hosts the Haib porphyry copper deposit (Figure 4.2). This deposit is unique as it may be the only known occurrence of this specific style of mineralization in southern Africa and one of the few occurrences globally of Precambrian porphyry copper mineralization (Meng et al., 2021).

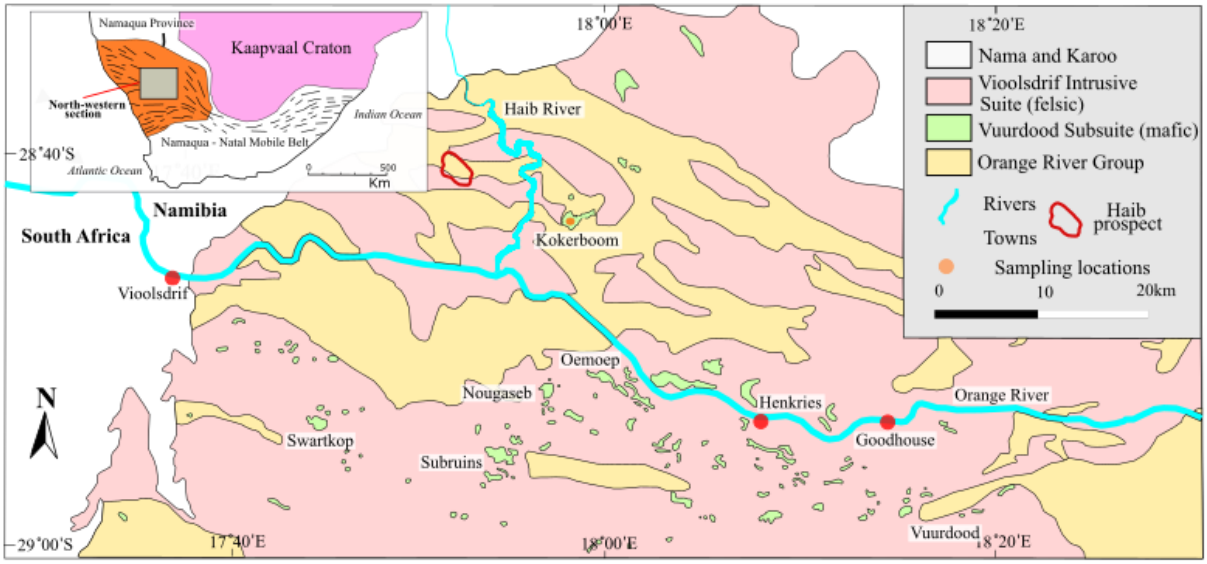

Figure 4.1: *Simplified geological map of the Richtersveld Magmatic Arc in the Vioolsdrif-Haib area showing the distribution of the Orange River Group, Vioolsdrif Intrusive Suite and the main localities of the Vuurdood Subsuite (Minnaar and Reid, 2021). Inset shows the position of map with reference to the Namaqua-Natal tectonic province and the Kaapvaal Craton.*

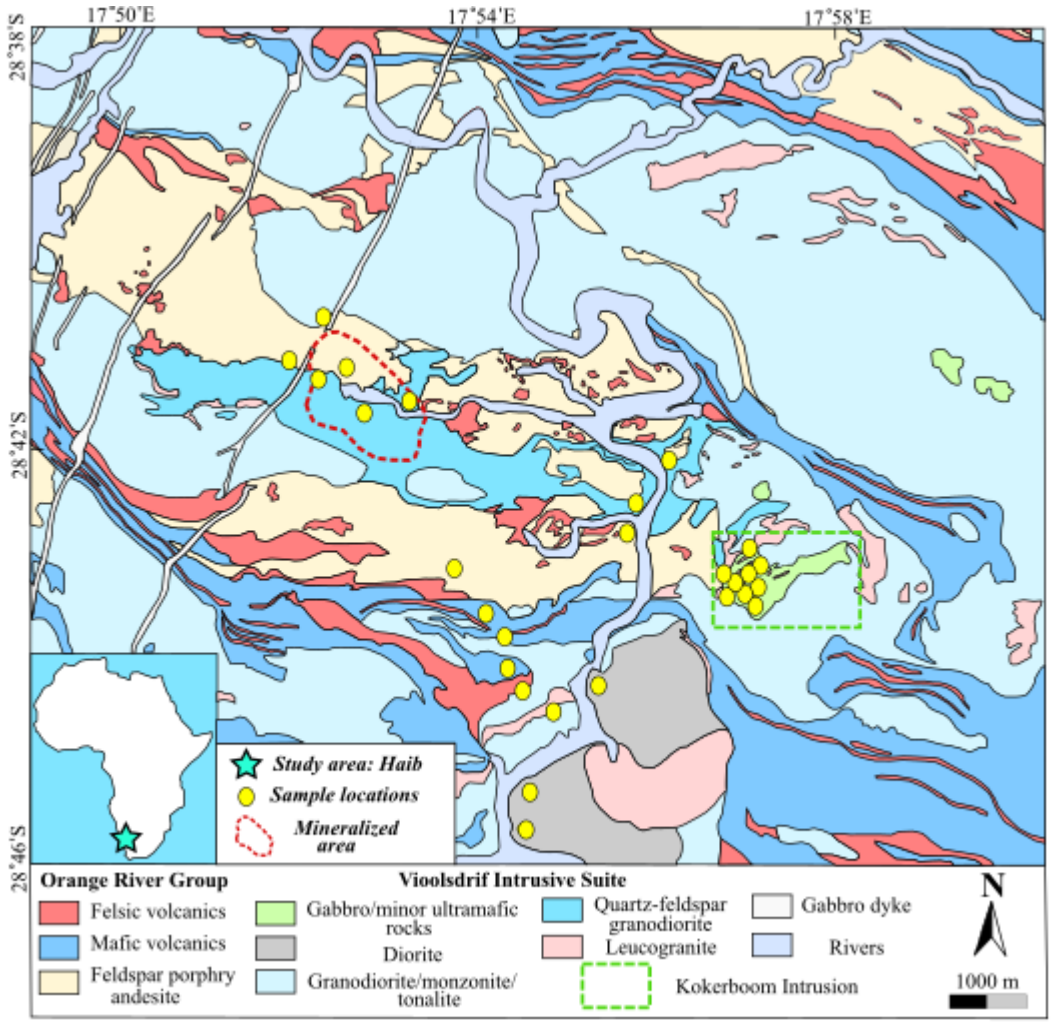

Figure 4.2: *Geological map of the Haib porphyry copper-molybdenum deposit with sample locations from this study. Map modified from Minnitt (1979) and Meng et al. (2021).*

The current study focuses on mafic-ultramafic intrusions that occur throughout the batholith, as numerous, relatively small intrusions (Figure 4.1; 4.2). Many of them appear to have been emplaced before, and subsequently disrupted by, later granitic intrusions of the Vioolsdrif Intrusive Suite (Reid and Minnaar, 2021). They have been assigned to a separate lithostratigraphic unit known as the Vuurdood Subsuite of the Vioolsdrif Intrusive Suite (Minnaar, 2012). Much of our knowledge of these early mafic-ultramafic components of the batholith has been confined to localities in the Vioolsdrif area of South Africa, but several intrusions have now been identified in the vicinity of the Haib copper deposit in Namibia. This thesis assesses the petrogenetic links (if any) between the mafic-ultramafic intrusions that may possibly be linked to mineralization of the Haib deposit and the known intrusions of the Vuurdood Subsuite, using petrography, major and trace element geochemistry, as well as U-Pb ages determined for these units. Typically, arc magmas that form part of porphyry copper deposits are relatively copper depleted and thus a crucial question arises as to where the missing copper resides (Cline and Bodnar, 1992; Chelle-Michou et al., 2017; Zhang and Audetat, 2017; Chen et al., 2020; Du and Audetat, 2020). Given that continental arc magmas are relatively depleted in copper and Precambrian porphyry copper deposits are rare, the presence and nature of these, possibly Cu-enriched, mafic-ultramafic intrusions may provide insights into the metallogenesis of porphyry copper deposits globally.

4.2. Results

The results presented in this study include field descriptions of the mafic-ultramafic intrusion in the Haib area, with a focus on the petrography, TIMA analysis, major and trace element geochemistry, U-Pb age dating and geothermobarometry on pyroxenes and amphiboles from pyroxenites of the Vuurdood Subsuite. This study documents the first detailed analyses of the mafic-ultramafic intrusion in the Haib area, which is then compared with existing data of the Vuurdood Subsuite from the literature.

4.2.1. The Kokerboom Intrusion in the Haib area

The rocks show a range of mineralogical types including gabbros (95 %) and clinopyroxenites (5 %). Clinopyroxenites are coarse-grained (~ 4 mm), dark grey-green, massive, composed of clinopyroxene altered to fibrous-granular actinolite and contain disseminated and massive sulphides (chalcopyrite) (Figure 4.3a). Gabbros are coarse-grained (3 mm), grey with a distinct speckled appearance, equigranular and are composed of pyroxene and plagioclase (Figure 4.3b and c). There are minor sulphides present in the gabbros.



Figure 4.3: *The plutonic lithologies of the Vioolsdrif Intrusive Suite in the Haib area: a) Coarse-grained clinopyroxenite hand samples. b) Gabbros with evidence of grain-size variations on the outcrop scale. Certain sections of the outcrop are darker depicting a coarser grain size. c) Distinct speckled and equigranular gabbros.*

There are several intrusions located east of the Haib River (Figure 4.1, 4.2). The largest is ~ 2 km in diameter, predominantly gabbroic in composition, with grain-size and modal variations on the outcrop scale. (Figure 4.3b). The contacts with the surrounding granodiorite are sharp, sheared or show signs of assimilation of the gabbro into the granodiorite (Figure 4.4a-c). The Kokerboom Intrusion is composed of clinopyroxenites and gabbros. The intrusion is pervasively intruded by leucogranitic dykes/veins. From field evidence, there are clear mingling textures at the contacts between the surrounding granodiorite and the gabbroic intrusion (Figure 4.4c).

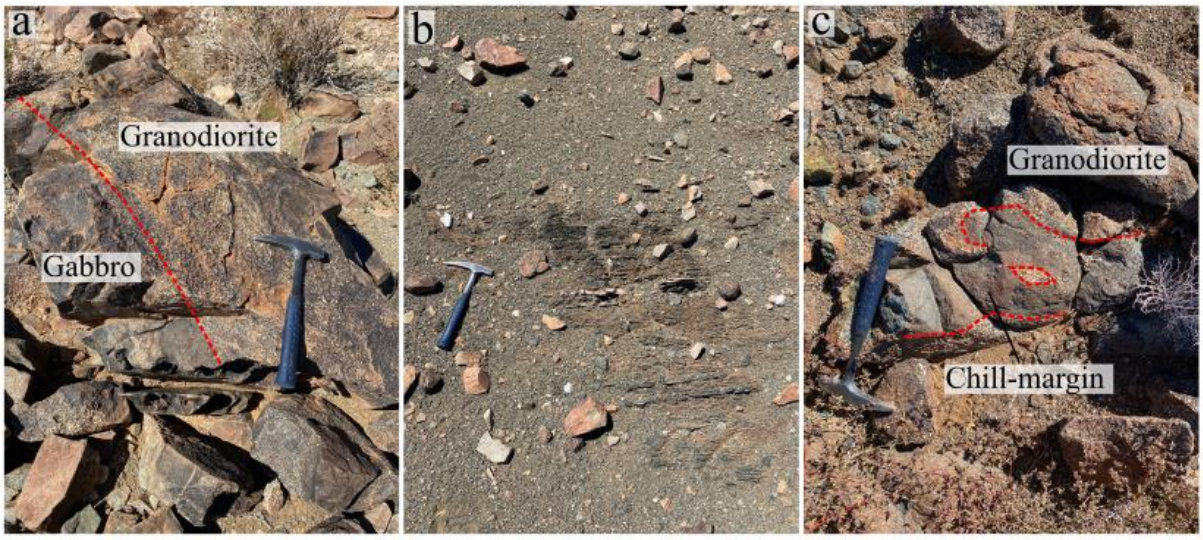

Figure 4.4: *The contacts of the main gabbroic body with the surrounding granodiorite. a) A distinct sharp contact. b) NW-SE trending sheared contact. c) Diffuse/assimilated contact with mingling textures.*

Alteration is pervasive throughout the lithologies of the mafic-ultramafic intrusion and thus classification is based on the preserved primary mineral phases as opposed to the altered mineral assemblages.

Gabbro

The gabbro is medium- to coarse-grained (~3 mm), equigranular and composed of plagioclase (60 %), clinopyroxene (20 %), hornblende-actinolite (10 %), quartz (7 %), apatite (2 %), rutile, sphene and magnetite (1 %) (Figure 4.5a; 4.6a). Cumulus clinopyroxene is replaced by hornblende-actinolite-chlorite-epidote pseudomorphs. There are also primary stubby prisms of hornblende/actinolite that are altered to chlorite and epidote, whereas plagioclase is pervasively altered to sericite and epidote and displays a myrmerkitic texture (Figure 4.5a). Intercumulus, primary hornblende contains inclusions of magnetite, rutile and quartz. Hornblende/actinolite exhibits exsolution lamellae or simple twinning. Quartz is anhedral and displays a distinct undulose extinction. Magnetite occurs as distinct bleb-like and disseminated grains.

Clinopyroxenite

The clinopyroxenite is coarse-grained (~4 mm), massive and composed predominantly of cumulus clinopyroxene (95 %), altered to fibrous-granular actinolite with minor chlorite-epidote-hornblende (3 %), rutile, sphene and sulphides (2 %) (Figure 4.5b; 4.6b). The actinolite has a fibrolite texture and shows exsolution lamellae and simple twinning. The actinolite is altered to chlorite and epidote. Magnetite is disseminated throughout and is in close relation to rutile, sphene, chlorite and actinolite. The sulphides in the clinopyroxenite occur as coarse (~2 mm) bleb-like aggregates of chalcopyrite rimmed by chalcocite-covellite assemblages, which are subsequently rimmed by hematite-magnetite-ilmenite assemblages (Figure 4.5b-inset i).

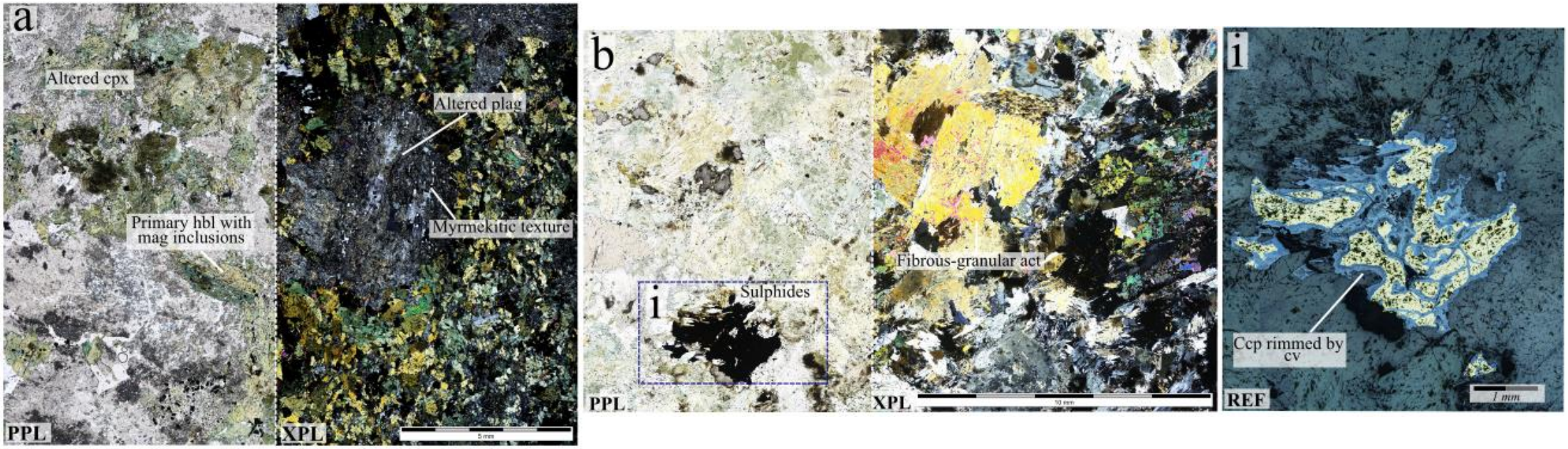

Figure 4.5: *Photomicrographs of the gabbro (a), and clinopyroxenite (b) from the mafic-ultramafic intrusion. a) The primary stubby prisms of clinopyroxene are altered to hornblende, chlorite and epidote whereas the plagioclase is pervasively altered to sericite and epidote and displays a myrmerkitic texture. b) Fibrous-granular actinolite is evident. Primary clinopyroxene is altered to actinolite with minor chlorite and epidote. Opaque material is prevalent (inset i). Chalcopyrite is being replaced by covellite.*

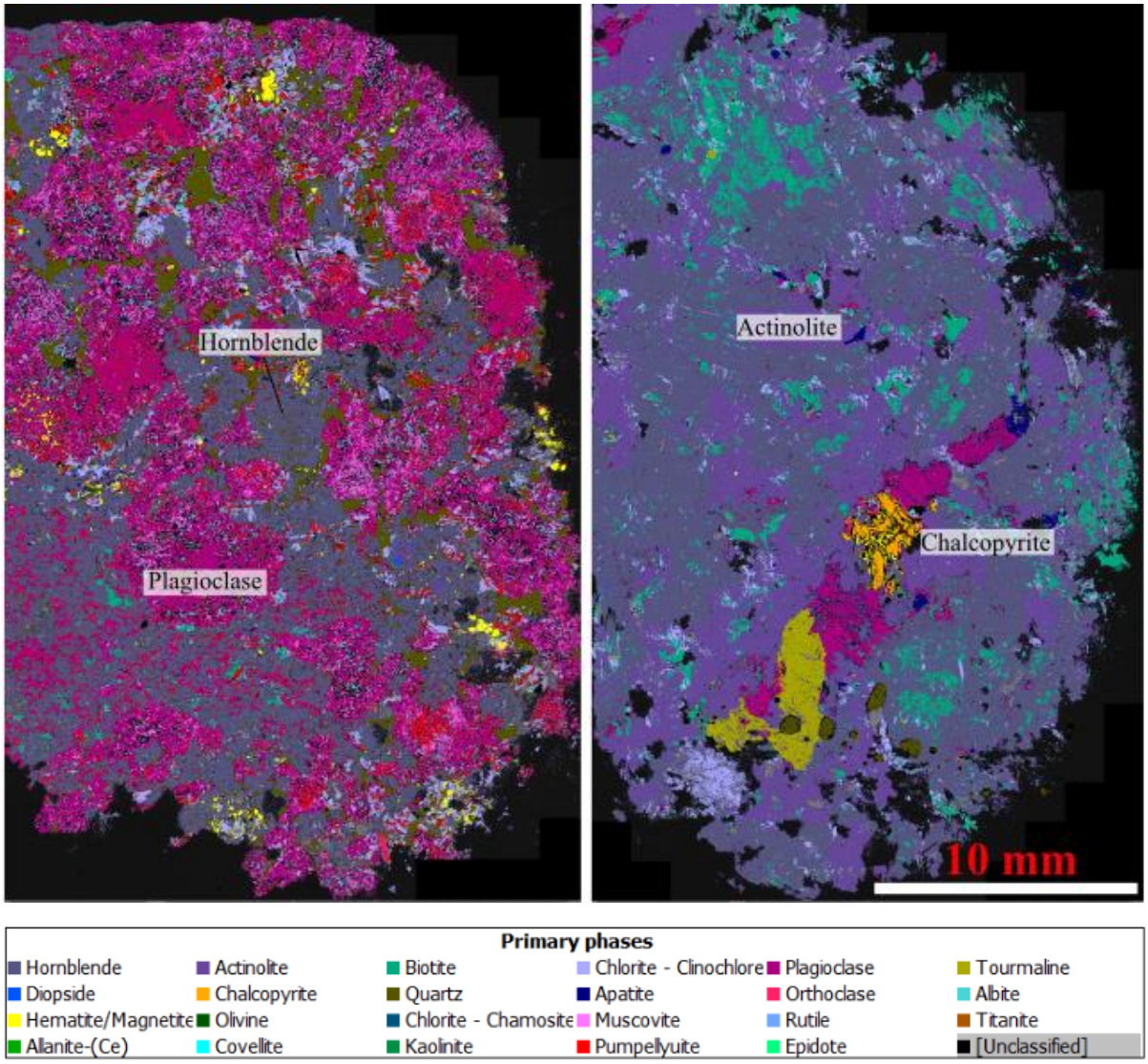

Figure 4.6: *Mineral liberation maps of representative thin sections for the gabbros (a), and clinopyroxenites (b). There is a decrease in modal plagioclase from the gabbros to the clinopyroxenites. From the mineral liberation maps the non-cotectic proportions of dominant mineral phases are clear.*

All the new data for the mafic-ultramafic intrusion (in Namibia) will be supplemented and compared with literature data (Reid, 1977 and Reid and Minnaar, 2021) for Vuurdood Subsuite, which is the mafic component of VIS in South Africa.

4.2.2. Major and trace element geochemistry

The SiO_2, Al_2O_3, Fe_2O_3, CaO, TiO_2, Na_2O and K_2O vs. Mg# diagrams show a general decrease in concentration from the primitive to more evolved lithologies of the mafic-ultramafic intrusion and Vuurdood Subsuite (Figure 4.7). For the mafic-ultramafic intrusion, the clinopyroxenite has the lowest concentrations of Al_2O_3, CaO, TiO_2, Na_2O and K_2O and the highest Mg#, whereas Al_2O_3, CaO, TiO_2, Na_2O and K_2O concentrations for the gabbro is higher, showing overall lower Mg# compositions. For the Vuurdood Subsuite from literature, the peridotite has the lowest TiO_2, Al_2O_3 and CaO concentrations and the highest Mg# whereas, the TiO_2, Al_2O_3 and CaO concentrations for the pyroxenite and gabbro from literature shows a broad range in concentration and is not linear (Figure 4.7). The AFM diagram shows a distinct array or continuum of compositions from the mafic-ultramafic to felsic plutonic units of the RMA (Figure 4.8). The felsic plutonic units of the RMA plots in the calc-alkaline field of the diagram whereas, the mafic units' plots both in both the calc-alkaline and tholeiitic fields of the diagram (Figure 4.8). The quartz-feldspar porphyry granodiorites of the Khoromus porphyry of the VIS are the host rocks of the Haib deposit. The section of the AFM diagram illustrating the various rock types constituting the mafic-ultramafic intrusion shows that the clinopyroxenite from the mafic-ultramafic intrusion plots in the tholeiitic field, whereas the gabbro plots in both the calc-alkaline and tholeiitic fields (Figure 4.8). The AFM diagram also illustrates the various rock types constituting the Vuurdood Subsuite for comparison and shows that the peridotite and pyroxenite from literature plot distinctly in the tholeiitic field, whereas the gabbro from literature plots in both the calc-alkaline and tholeiitic fields (Figure 4.8). In addition, the AFM diagrams shows that the mafic-ultramafic intrusion and the Vuurdood Subsuite overlap with average compositions of deep crustal cumulates from continental and island arc environments (Chin et al., 2018). The more evolved composition from the mafic-ultramafic intrusion and Vuurdood Subsuite trend towards the calc-alkaline array of the felsic and intermediate components of the Vioolsdrif Intrusive Suite.

Chondrite-normalized REE patterns for the various rock types constituting the mafic-ultramafic intrusion form relatively flat REE patterns, with lower abundances for the clinopyroxenite, whereas the gabbro has slightly elevated concentrations and minor negative Eu anomalies (Figure 4.9a). MORB-normalized, multi-element variation patterns for the various rocks constituting the mafic-ultramafic intrusion show a distinct decoupling between the LILE and HFSE (Figure 4.9b). The LILE are elevated and have higher concentrations, whereas, the HFSE show lower concentrations. The mafic-ultramafic intrusion has strong negative Nb and Hf-Zr anomalies. A distinct variation is observed between the clinopyroxenite and gabbro of the mafic-ultramafic intrusion including: a systematic increase in LILE, Nb-Ta and Hf-Zr and a decrease in Ti. The average MORB-normalized multi-element variation patterns for the mafic-ultramafic intrusion overlap with the Vuurdood Subsuite, with similar Nb anomalies (Figure 4.9b).

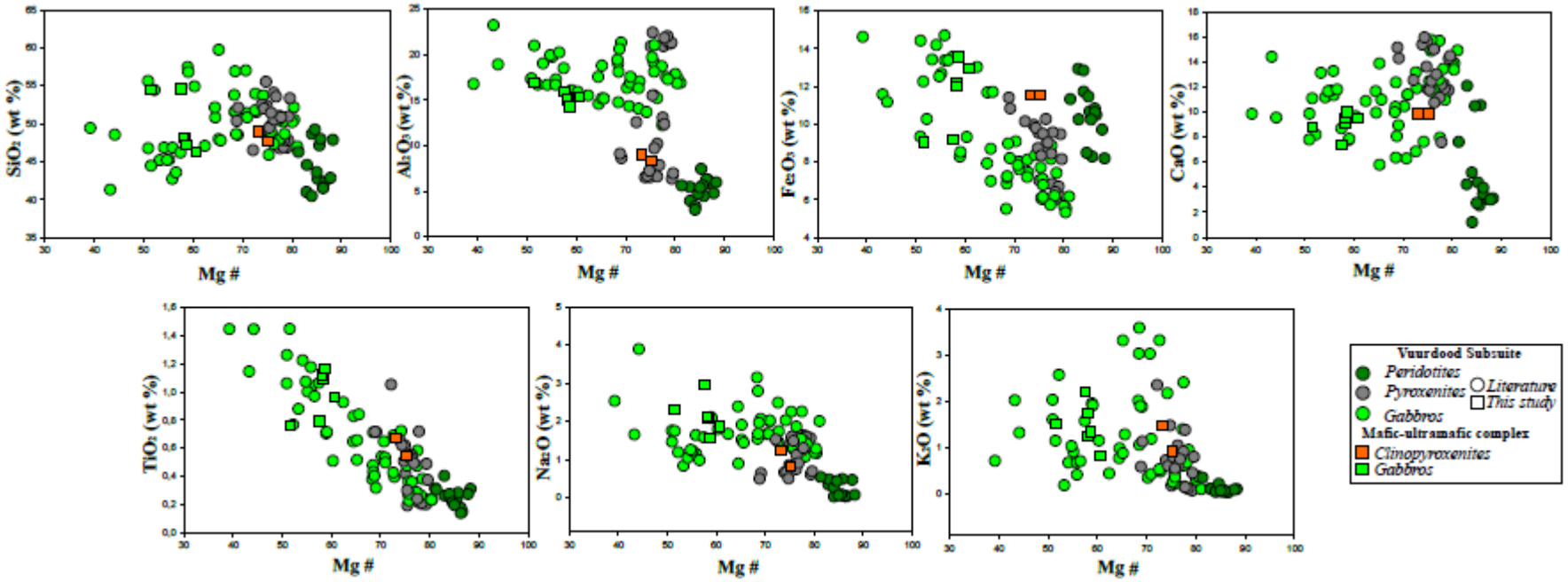

Figure 4.7: *The SiO_2, Al_2O_3, Fe_2O_3, CaO, TiO_2, Na_2O and K_2O vs. Mg# diagrams show a general decrease in these oxide compositions from the primitive to more evolved mafic units of the mafic-ultramafic intrusion and Vuurdood Subsuite.*

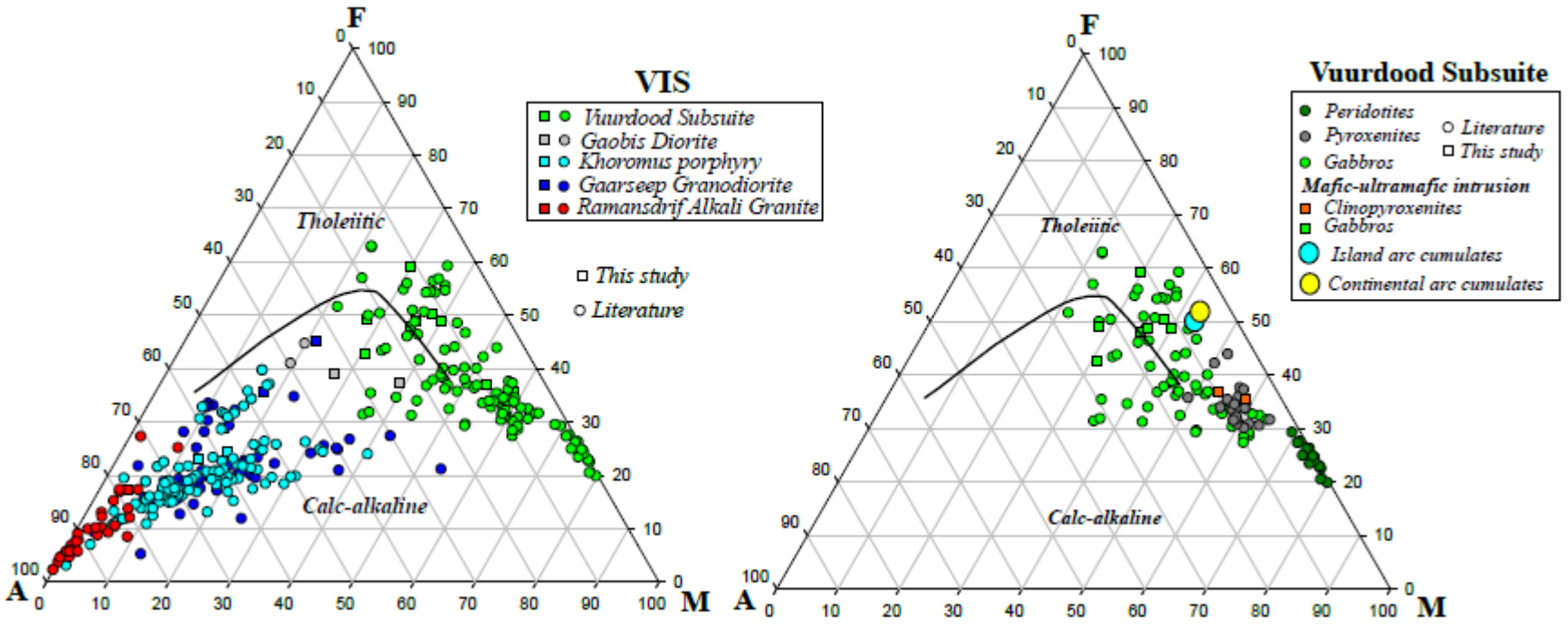

Figure 4.8: *The AFM diagram illustrating the various lithologies of the Vioolsdrif Intrusive Suite (VIS) shows that the felsic units of the RMA plots in the calc-alkaline field of the diagram whereas, the mafic units of the RMA plots in the tholeiitic field of the diagram. The quartz-feldspar porphyry granodiorites of the Khoromus porphyry of the VIS are the host rocks of the Haib deposit. The AFM diagram illustrating the various rock types constituting the Vuurdood Subsuite shows that the peridotites and pyroxenites from literature plots distinctly in the tholeiitic field whereas, the gabbros from literature plots in both the calc-alkaline and tholeiitic fields. The clinopyroxenites the mafic-ultramafic intrusion plots in the tholeiitic field whereas, the gabbros plots in both the calc-alkaline and tholeiitic fields. The Vuurdood Subsuite and mafic-ultramafic intrusion plots in the same area of the AFM diagram as continental and island arc cumulates from studies conducted by Chin et al. (2018).*

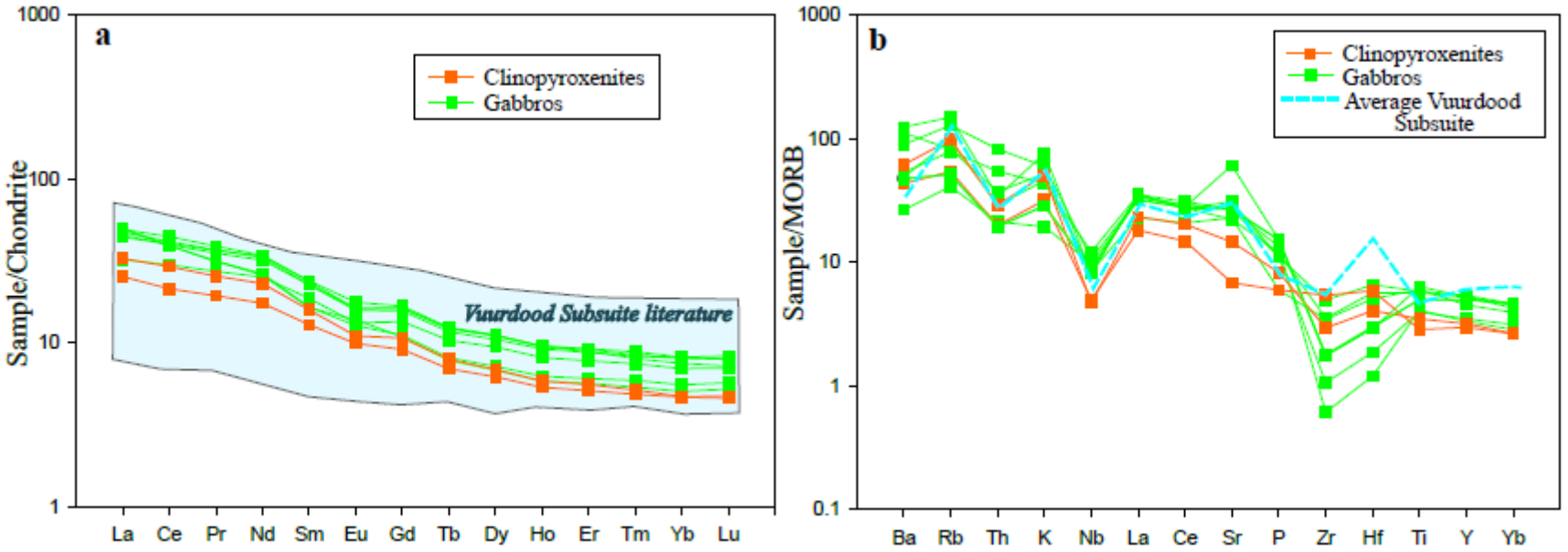

Figure 4.9: *a) Chondrite-normalized REE patterns for the various rock types constituting the mafic-ultramafic intrusion shows a relatively flat REE pattern for the clinopyroxenites whereas, the gabbros have a slightly elevated slope and minor Eu anomalies. The chondrite normalizing values of Anders and Grevesse (1988) were used. b) MORB-normalized multi-element patterns for the various rock types constituting the mafic-ultramafic intrusion and the average Vuurdood Subsuite. The mafic-ultramafic intrusion has strong negative Nb and Hf-Zr anomalies. The MORB-normalized multi-element patterns for the mafic-ultramafic intrusion and average Vuurdood Subsuite overlap. The mantle normalizing values of White (2005) were used.*

4.2.3. Machine learning geothermobarometry

Machine learning geothermobarometry (refer to Jorgenson et al., 2022 and Higgins et al., 2022) conducted on pyroxenes and amphiboles from the Vuurdood Subsuite pyroxenites yield average pressure and temperature estimates of 4 kbar and 870 °C respectively with pressure and temperature ranges from ~1.5-7 kbar and ~800-900 °C (Figure 4.10). Table 1 shows the average P-T estimates for the Vuurdood Subsuite and for the Arizona arclogites and Tongling cumulates from literature for comparison purposes. The Arizona arclogites represents lower crustal material from a Phanerozoic arc and the Tongling cumulates represents rare cumulate material linked to a Phanerozoic porphyry deposit.

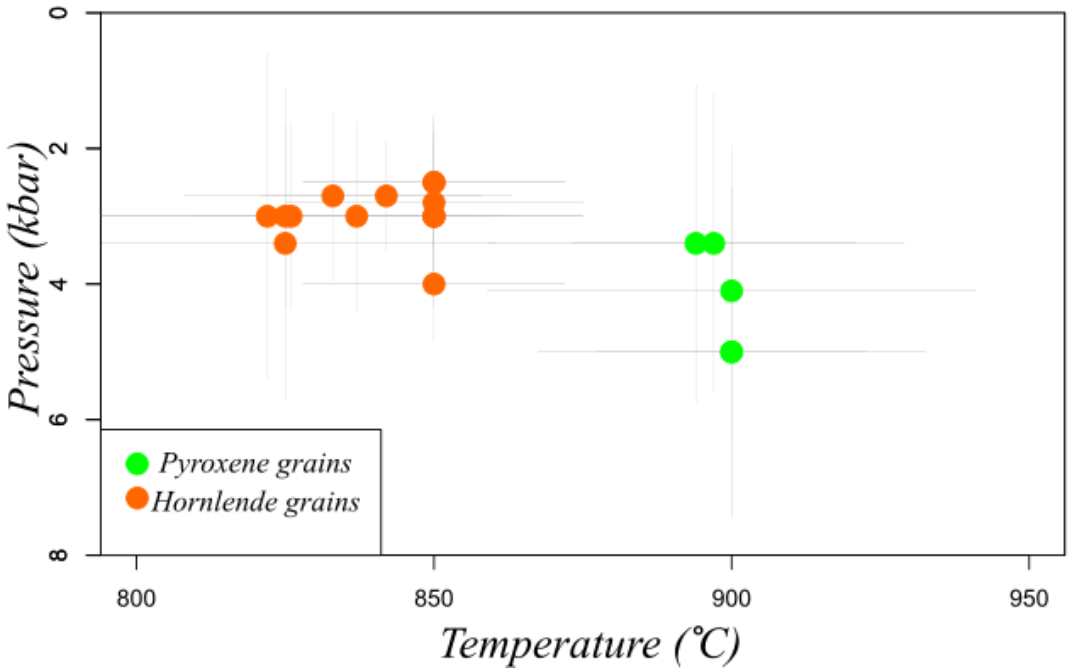

Figure 4.10: *P-T graph showing the results from the machine learning geothermobarometry conducted on pyroxenes and hornblende grains from the Vuurdood Subsuite pyroxenites. Pressure and temperature ranges from ~1.5-7 kbar and ~800-900 °C respectively.*

Table 4.1: *Average pressure and temperature estimates for the Vuurdood Subsuite pyroxenites, Arizona arclogites and Tongling cumulates.*

Cumulates	Pressure	Temperature
Vuurdood Subsuite pyroxenites	4 kbar	870 °C
Arizona arclogites	25 kbar	725 °C
Tongling cumulates	4.7 kbar	980 °C

4.2.4. Geochronology of the Kokerboom Intrusion

Zircons (~70 – 100 µm in size) separated from gabbro, clinopyroxenite, diorite and granodiorite are euhedral to subhedral, generally stubby to elongate in morphology, show no distinct core and rim domains based on cathodoluminescence (CL) imaging and contain inclusions of apatite. Sample AJ-21-04 (gabbro) yields a weighted mean $^{207}Pb/^{206}Pb$ zircon age of 1877 ± 20 Ma (n = 38, MSWD = 0.025). The calculated concordia age for the sample is 1875 ± 9 Ma (n = 38, MSWD = 0.064; Figure 4.11). Sample AJ-21-23 (gabbro) yields a weighted mean $^{207}Pb/^{206}Pb$ zircon age of 1858 ± 20 Ma (n = 33, MSWD = 0.055). The calculated concordia age for the sample is 1857 ± 9 Ma (n = 33, MSWD = 0.0046; Figure 4.11). Sample AJ-21-34 (diorite) yields a weighted mean $^{207}Pb/^{206}Pb$ zircon age of 1896 ± 20 Ma (n = 38, MSWD = 0.13). The calculated concordia age for the sample is 1896 ± 9 Ma (n = 38, MSWD = 0.22; Figure 4.11). The concordia ages are interpreted as crystallization ages for samples AJ-21-04, AJ-21-23, AJ-21-34 due to the smaller errors obtained for these ages. Sample AJ-21-28 (granodiorite in contact with the main gabbroic intrusion) yields a weighted mean $^{207}Pb/^{206}Pb$ zircon age (with a 10 % discordance cut-off) of 1889 ± 22 Ma (n = 37, MSWD = 0.72; Figure 4.11). The calculated concordia age for the sample is 1808 ± 9 Ma (n = 37, MSWD = 160). Sample AJ-21-29 (clinopyroxenite) yields a weighted mean $^{207}Pb/^{206}Pb$ zircon age of 1862 ± 18 Ma (n = 36, MSWD = 0.36; Figure 4.11). The calculated concordia age for the sample is 1843 ± 9 Ma (n = 36, MSWD = 7.4). The weighted mean ages are interpreted as the crystallization age for samples AJ-21-28 and AJ-21-29 as the concordia ages yield high MSWDs. A full compilation of CL and BSE images can be found in Appendix J.

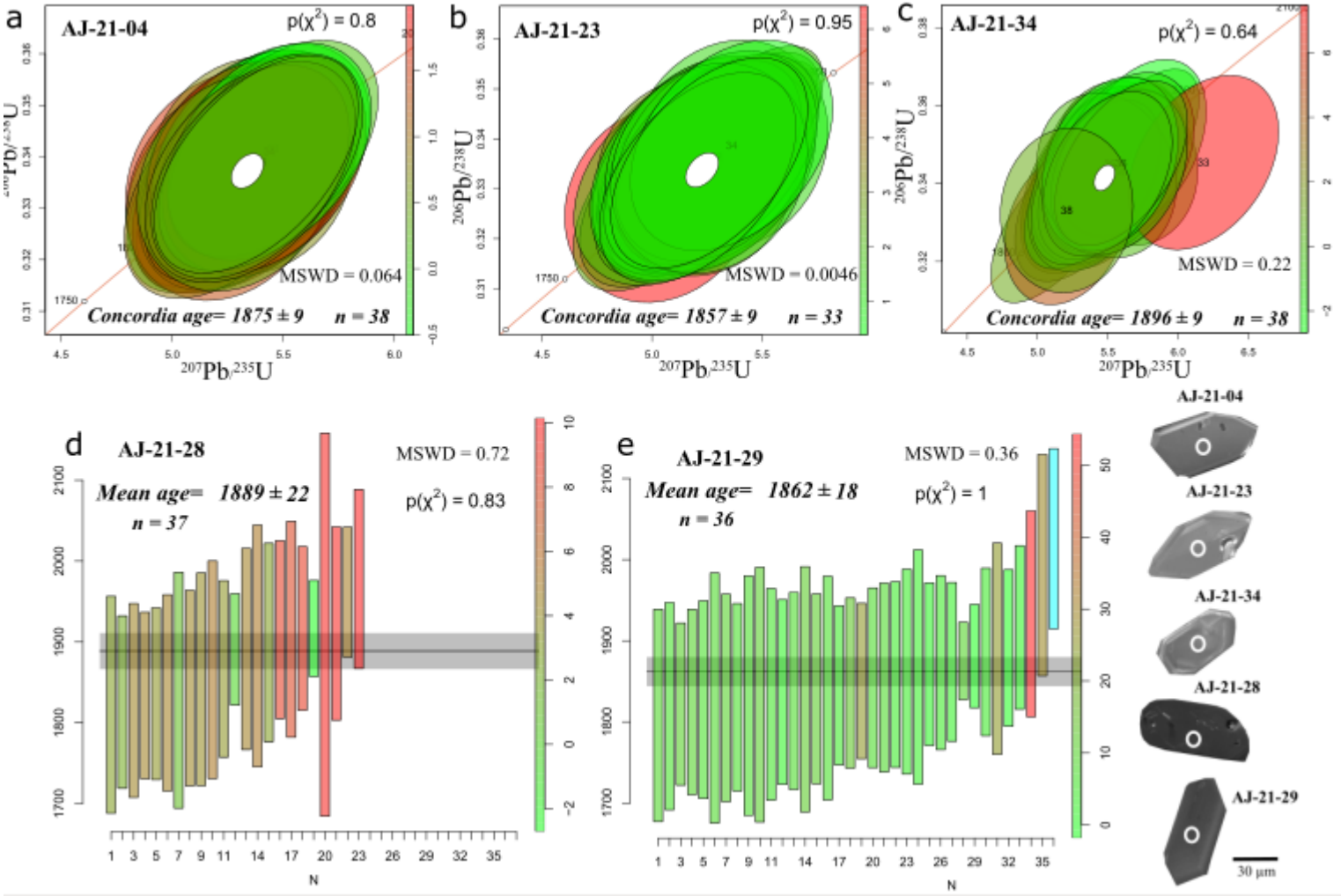

Figure 4.11: *U-Pb geochronological results. a) 38 analyses on zircons from sample AJ-21-04 provide a concordia age of 1875 ± 9 Ma. b) 33 analyses on zircons from sample AJ-21-23 yielded a concordia age of 1857 ± 9 Ma. c) 38 analyses on zircons from sample AJ-21-34 yielded a concordia age of 1896 ± 9 Ma. d) 37 analyses on zircons from sample AJ-21-28 provided a weighted mean age of 1889 ± 22 Ma. e) 36 analyses conducted on sample AJ-21-29 yielded a weighted mean age of 1862 ± 18 Ma. A full compilation of CL and BSE images can be found in Appendix J.*

4.3. Discussion

Previous work has shown that there is a distinct petrological and geochemical link between the Orange River Group, Vioolsdrif Intrusive Suite and Vuurdood Subsuite (Reid, 1977; Minnitt, 1979 and Macey et al., 2017). Reid (1977), Minnitt (1979) and Macey et al (2017) stated that the Orange River Group and Vioolsdrif Intrusive Suite are comagmatic. Reid (1997) proposed that the Vuurdood Subsuite either represents primitive cumulate material of the Vioolsdrif Intrusive Suite or could have a different petrogenetic evolution relative to the other units of the Vioolsdrif Intrusive Suite. Studies conducted by Reid (1977), Minnaar (2011), and Reid and Minnaar (2021) focused on the Vuurdood Subsuite in the Vioolsdrif area of South Africa. This study focuses on the poorly described mafic-ultramafic intrusion which occurs in the Haib region, Namibia. The mafic-ultramafic intrusion is compared to the Vuurdood Subsuite from a geochronological, petrological and geochemical perspective. Thereafter, we present evidence illustrating that the Haib deposit and the associated mafic-ultramafic intrusion represent the deeper parts of a porphyry system in a convergent margin environment.

4.3.1. The mafic-ultramafic intrusion in the Haib area and the Vuurdood Subsuite

This study reports the first U-Pb zircon ages from the mafic-ultramafic intrusion in Namibia and represent the most recent age determinations on the Richtersveld Magmatic Arc. The U-Pb ages for the gabbro samples within the mafic-ultramafic intrusion is 1875 ± 9 Ma and 1857 ± 9 Ma (Figure 4.12), while the age for the clinopyroxenite sample is 1862 ± 18 Ma. A granodiorite in contact with the main gabbroic intrusion returns an age of 1889 ± 22 Ma. The ages for both broadly overlap with one another. This granodiorite has been previously mapped as part of the central granodiorite of the Haib area. Age data of the northern granodiorite yields an age of 1887 ± 7 Ma suggesting that there is more than one intrusive phase of the granodiorites in the Haib region. Given the various ages for the Kokerboom Intrusion rocks and the granodiorites, it is probable that there were multiple phases of intrusions for the VIS, indicating coeval emplacement of intrusive phases. Macey et al. (2017) supports a cyclic model with multiple pulses of mafic to felsic volcanism and plutonism. Age data supports this cyclic model of multiple pulses rather than a single differentiation of the Vuurdood Subsuite, to the Goodhouse Subsuite and Ramansdrif Alkali Granite. These new ages for the mafic-ultramafic intrusion in the Haib area, overlap with previous age data for the VIS (Table 2.2; Reid, 1987; Grumbley, 2015; Macey et al., 2017 and Meng et al., 2021) and support the notion that both of these units are a coeval members of the VIS. These ages overlap with recent high precision ages for the intermediate to felsic rocks of the Haib porphyry deposit reported by Meng et al. (2021) which range between 1920 and 1880 Ma. In addition, our ages from the mafic-ultramafic intrusion, overlap with unpublished ages from outcrops of the Vuurdood Subsuite in South Africa (Reid and Minnaar, 2021).

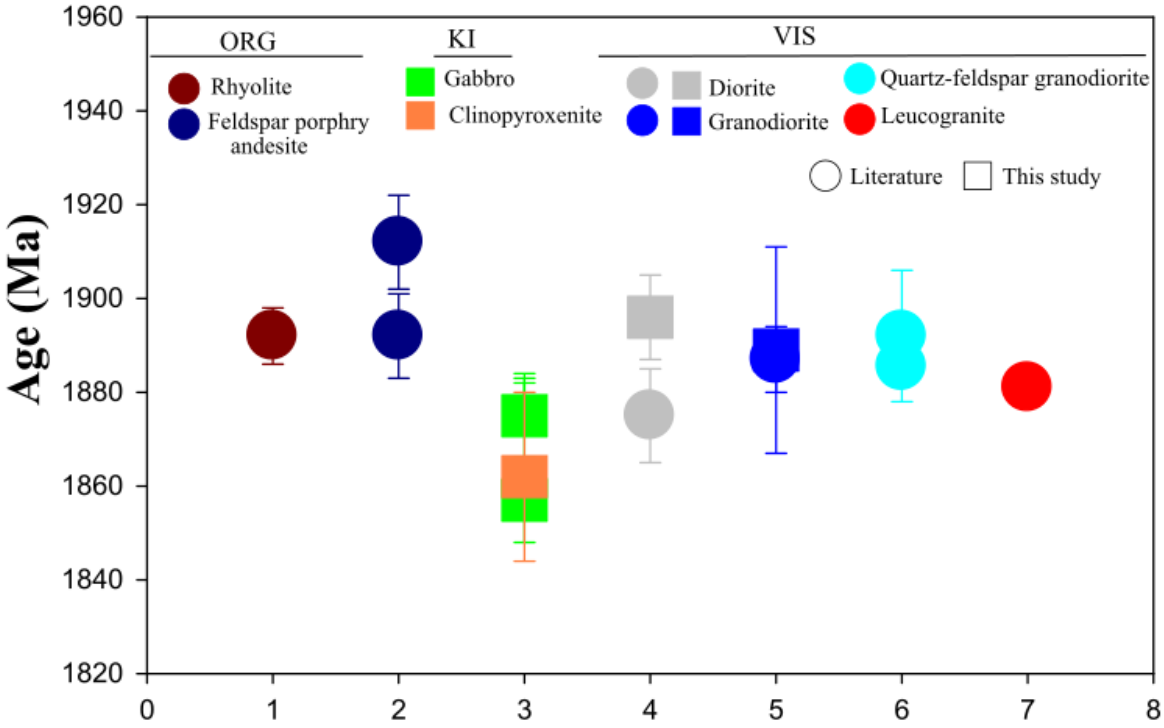

Figure 4.12: *Age range diagram for the Orange River Group (ORG), Kokerboom Intrusion (KI) and Vioolsdrif Intrusive Suite (VIS). The data for the ORG and VIS from literature is from Meng et al. (2020).*

In comparison to the mafic-ultramafic intrusions of the Vuurdood Subsuite in the northern Cape, the mafic-ultramafic intrusion near Haib is predominantly composed of clinopyroxenite and gabbro, but lacks the peridotitic end member. The alteration assemblages of hornblende-actinolite-chlorite-epidote pseudomorphs after clinopyroxene observed in the mafic-ultramafic intrusion are similar to the alteration assemblages observed in the mafic-ultramafic intrusion of the Vuurdood Subsuite. The mafic-ultramafic intrusion shows typical, coarse-grained cumulate textures and is defined by non-cotectic proportions of mineral phases.

As typical cumulates, the major element geochemistry of the mafic-ultramafic intrusion is controlled by the proportion of accumulating phases. This is clearly seen in Figure 4.7 with covariation of Mg# with Al_2O_3, CaO, TiO_2, Na_2O and K_2O, indicative of fractional crystallization of plagioclase, Fe-Ti oxides, pyroxene and hornblende. Similar trends have been noted in the differentiation sequence of the Vuurdood Subsuite in South Africa, suggesting that the mafic-ultramafic intrusion in the Haib area and the Vuurdood Subsuite form part of the same differentiated suite (Reid, 1987 and Macey et al., 2017).

The comagmatic nature of these magmatic units is also corroborated through analysis of typical AFM diagrams (Figure 4.8), where broad overlap between the Vuurdood Subsuite and the mafic-ultramafic intrusion is observed. The average composition of mafic cumulates sampled from the Vuurdood Subsuite and mafic-ultramafic intrusion, correspond closely with the average composition of deep- to mid-crustal island and continental arc cumulates (Chin et al., 2018). Moreover, the most Mg-enriched components of the Vuurdood Subsuite overlap with the most primitive deep crustal cumulates (Figure 4.8). Together, these mafic and ultramafic cumulates form the earliest stages of a differentiation sequence forming a calc-alkaline trend with the more felsic volcanic and plutonic members of the VIS.

The relatively flat REE patterns of the mafic-ultramafic intrusion are indicative of minimal fractional crystallization of pyroxenes and amphiboles. The minor negative Eu anomalies in the REE patterns of the gabbro is indicative of plagioclase fractionation. Overall, the REE patterns of the mafic-ultramafic intrusion correlate and overlap geochemically with the REE pattern of the Vuurdood Subsuite from literature. The distinct negative anomalies of Nb, Hf and Zr illustrated by the MORB-normalized multi-element variation patterns are an indication of subduction magmatism, as Nb negative anomalies are a characteristic feature of modern volcanic arcs (Gill, 2010; Condie, 2005b; Castillo, 2006; Sillitoe, 2010). An important interpretation from the MORB-normalized multi-element variation patterns is the overlap of the mafic-ultramafic intrusion with the average Vuurdood Subsuite. Together with our new U-Pb age data and machine learning geothermobarometry, we show not only that the mafic-ultramafic intrusion is a coeval and comagmatic component of the Vuurdood Subsuite, but that these magmatic entities represent mid- to upper- crustal material (~12 km depth) formed during construction of the calc-alkaline Richtersveld Magmatic Arc. As a result of the cogenetic relationship between the poorly described mafic-ultramafic intrusion in the Haib area and the Vuurdood Subsuite, and following the practice of naming discrete ultramafic intrusions of the Vuurdood Subsuite, the mafic-ultramafic intrusion in the Haib area is named the Kokerboom Intrusion in this study.

4.3.2. Evidence for deeper levels of the porphyry system

The Kokerboom Intrusion is intimately associated with the petrogenesis of the Haib porphyry deposit, not only because of their grouping within the VIS, but because of the temporal and geochemical relationship (Figure 4.8). The Kokerboom Intrusion is also in close vicinity (approximately 5 km) to the Haib porphyry deposit. The age of the Kokerboom Intrusion and the Haib porphyry mineralization broadly coincides.

Several lines of evidence indicate that the Haib deposit and the associated Kokerboom Intrusion preserve the deeper levels of a porphyry system. These include:

- The presence of early dark micaceous veins (the first phase of veins observed in the quartz-feldspar porphyry granodiorites) that are composed of quartz and coarse mica (Runyon et al., 2017, 2019). Early dark micaceous veins are located at deep levels (paleodepths of ~4–12 km) which is indicative of the root zones of porphyry systems (Runyon et al., 2017, 2019). The mica present in the early dark micaceous hosted in the quartz-feldspar granodiorites are composed of biotite.
- Lack of evidence of shallow alteration assemblages such as propylitic and argillic alteration (Minnitt, 1979, 1986; Meng et al., 2021).
- Coarse-grained nature of the Vioolsdrif Intrusive Suite (clinopyroxenites, granodiorites, diorites, gabbros), indicative of slow cooling at mid-crustal batholith depths (Vermond, 2019).
- The presence of geochemically primitive mafic units such as the gabbros and clinopyroxenites. The clinopyroxenites are mafic, dense, and usually occur at mid to lower crustal levels.
- Mineralization linked with shear fractures which is indicative of deformation within the ductile regime (5-15 km depth) (Davis et al., 2012).

- Finally, geothermobarometry performed in this study on clinopyroxenes in clinopyroxenites from the Vuurdood Subsuite yield average pressure and temperature estimates of 4 kbar and 870 °C respectively.

Despite evidence for the Haib being at deeper levels of the porphyry system, hypabyssal volcanics are present in the Haib area. These volcanics in the vicinity of the Haib porphyry copper deposit have an approximate thickness of 5-8 km (Minnitt, 1979). The emplacement depth for the Haib porphyry copper deposit is estimated to have been in the order of 5-8 km. The 5-8 km thickness correlates with emplacement at mid-crustal levels. This evidence corroborates with evidence presented for deeper crustal levels of the porphyry system.

These lines of evidence also agree with and refine previously estimated emplacement pressures of 2-3 kbar for the Vioolsdrif Intrusive Suite (Minnitt, 1979 and Meng et al., 2021), which according to Minnitt (1979) and Meng et al. (2021) are comparable to deeper sections of Phanerozoic porphyry deposits (such as San-Manuel-Kalamazoo Ore body, Arizona (Lowell and Guilbert, 1970); Fortuna pluton, Chile (Sillitoe, 1973); Los Loros, Chile, Appalachian porphyry systems (Hollister et al., 1974); Cornelia Pluton, Arizona (Wadsworth, 1968), Little Mine Area, Arizona (Durning and Davis, 1978), Laramide porphyry system, Arizona (Seerdoff et al, 2008; Runyon et al., 2017) and Yerington batholith, Nevada (Seerdoff et al, 2008; Runyon et al., 2017). Our refined pressures of 4 kbar for the mafic-ultramafic cumulates of the Vuurdood Subsuite correspond to a crustal depth of ~12 km. These pressures and depths are comparable to the crustal depths of other cumulates formed in porphyry systems and arc environments, such as the Tongling cumulates (~14.1 km) however, the pressures and temperatures are not comparable to the Arizonan arclogites (20-70 km crustal depth) as the Arizonan arclogites occur at much deeper crustal depths. The Tongling cumulates represent rare mid-crustal cumulate material linked to a Phanerozoic porphyry copper deposit (Du and Audetat; 2020), while the Arizonan arclogites represent lower crustal cumulate material (Lee and Tang, 2020).

The Kokerboom Intrusion and the Haib porphyry deposit therefore provide a unique insight into the development of the mid-crustal root zones of a Palaeoproterozoic porphyry deposit.

4.4. Conclusion

The purpose of this work was to establish whether or not there is a link between the mafic-ultramafic intrusion in the Haib area and the Vuurdood Subsuite. It is shown from petrological, geochemical and geochronological observations that the Kokerboom Intrusion (the name given to the mafic-ultramafic intrusion in this study) is a continuation of the Vuurdood Subsuite into Namibia. These similarities include lithological variation within the intrusion, the mineral and alteration assemblages, major and trace element geochemistry and U-Pb age data. The overlap of the major element compositions shown by the AFM diagram for the Kokerboom Intrusion and Vuurdood Subsuite with the lower crustal cumulates in both island and continental arc settings is significant and provides further evidence of the convergent arc tectonic setting for these Richtersveld lithologies, from a cumulate perspective. The sulphides present in the clinopyroxenite are significant and contributes to work done by Wilkinson (2013), Du and Audetat (2020) and Chen et al. (2020) which state that early sulphide saturation is not detrimental to porphyry copper metallogenesis. Magmatic sulphides are observed in the lower arc sections of the Talkeetna gabbros, Khohistan cumulates, Arizona garnet pyroxenite cumulates, as well as in the amphibole-rich cumulate xenoliths and amphibole megacrysts of the Late Jurassic to Early Cretaceous (~147–136 Ma) Tongling porphyry deposit (Deng et al.,

2007; Wu et al., 2010; Audetat and Simon, 2012; Lee et al., 2012; Hou et al., 2017; Jenner, 2017; Chang and Audetat, 2018; Chen et al., 2020). The amphibole-rich cumulate xenoliths and amphibole megacrysts of the Late Jurassic to Early Cretaceous Tongling deposit are linked to porphyry copper formation. Based on observations from Phanerozoic porphyry copper deposits that are related with cumulate material at mid- to lower crustal levels, such as the above mentioned, especially the Tongling deposit, it can be inferred that the Kokerboom Intrusion serves as a cumulate-type source for the Haib deposit. A link between the Kokerboom Intrusion and the Haib porphyry copper deposit can further be made through the age of the Kokerboom Intrusion and the Haib mineralization, which broadly coincides. Future recommendations include conducting copper and iron isotope analyses on the Haib deposit which will shed light on our global understanding of the metallogenesis of porphyry copper deposits from both a temporal and trans-crustal perspective as the Haib deposit is Palaeoproterozoic in age relative to the dominance of Phanerozoic porphyry deposits and the Haib deposit represents deeper levels of the porphyry system in contrast to shallower level younger Phanerozoic porphyry deposits.

5. Cu and Fe isotope contrasts between the Palaeoproterozoic Haib porphyry copper deposit and representative Phanerozoic porphyry copper deposits

5.1. Introduction

An important goal in mineral deposit research is to identify the source of the metals and the processes involved in metallogenesis (Li et al., 2010). According to Anbar and Rouxel (2007), "metal isotopes received little attention because conventional wisdom argued they were too heavy to fractionate. As is often the case, this conventional wisdom was distilled from more complex reality". Recent advances in analytical methods and experimental developments have stimulated a renaissance in non-traditional stable isotopes (Shanks, 2014). Emerging studies show that non-traditional stable isotope systems serve as a powerful tool in ore deposit investigation (e.g., Bilenker et al., 2016; Childress et al., 2016; Duan et al., 2015; Gagnevin et al., 2012; Gao et al., 2018; Gregory and Mathur, 2017; Hannah et al., 2007; Knipping et al., 2015; Li et al., 2010a; Markl et al., 2006; Mathur et al., 2012; Wang et al., 2011; Yao et al., 2016). In porphyry systems, the application of non-traditional stable isotope systems, such Cu and Fe, to ore genesis has been limited (Cooke et al., 2014), yet these non-traditional isotope systems have the ability to provide direct evidence to understanding the source of the metals and the mineralization processes (Markle et al., 2006; Hannah et al., 2007; Li et al., 2010a; Wang et al., 2011; Gagnevin et al., 2012; Mathur et al., 2012; Duan et al., 2015; Knipping et al., 2015; Bilenker et al., 2016; Childress et al., 2016; Yao et al., 2016; Gregory and Mathur, 2017; Gao et al., 2018; He et al., 2020).

Copper isotopes have been used for ore characterization for several years (Maréchal et al., 1999; Graham et al., 2004; Mathur and Fantle, 2015; Moynier et al., 2017 and Le Bras et al., 2020). Copper isotope fractionation is caused by variations in oxygen fugacity, copper source, and fractionation of copper between vapour and brine, as well as between minerals and fluids during the precipitation of sulphides (Gregory and Mathur, 2009). Many of these processes are also influenced by variations in temperature and pH (Gregory and Mathur, 2009). The differences in copper isotope compositions between magmatic and high-temperature hydrothermal ore deposits allow the differentiation of hypogene ($\delta^{65}Cu = 0.0 \pm 1‰$) from supergene and secondary ($\delta^{65}Cu$ = -3 to more than +6‰) processes (Mathur and Fantle, 2015; Baggio et al., 2018; Larson et al., 2003; Markl et al., 2006a; Ikehata et al., 2011; Zhao et al., 2019).

Iron isotopes have also been used to identify mineralization processes (He et al., 2020). Iron isotope fractionation is caused by magmatic processes, partial melting, fractional crystallization as well as chemical and thermal diffusion between the mineral and fluid phases (He et al., 2020; Zhang et al., 2021). Iron isotopes are useful in determining ore-forming processes by enabling the discrimination between magmatic crystallization and hydrothermal precipitation (Graham et al., 2004; Wawryk and Foden, 2015; He et al., 2020). Redox-driven iron isotope fractionation can assist in determining the redox conditions related to porphyry copper deposit formation (He et al., 2020). Various rocks have distinct $\delta^{56}Fe$ signatures and therefore it is possible to determine the source composition and subsequent mixing processes (Williams and Bizimis, 2014; Nebel et al., 2019). The typical $\delta^{56}Fe$ value for the mantle is 0 ± 0.2 ‰.

Porphyry copper deposits are predominantly Phanerozoic in age. The Haib copper-molybdenum deposit is one of the few occurrences of porphyry copper mineralization in the Precambrian of Africa. Our knowledge of the characteristic differences of mineralization during the Precambrian and the Phanerozoic is limited. By applying in-situ and whole-rock Cu and Fe isotope analyses, together with an understanding of the petrography and mineralization style in the Haib porphyry copper deposit, we aim to better understand the metallogenic processes influencing the formation of this deposit and other Precambrian porphyry Cu deposits. These isotopic systems may also prove useful as vectors to identify the crustal level of porphyry systems in arc settings.

5.2. Results

The results in this chapter include petrographic observations conducted on the host porphyry lithologies (feldspar porphyry andesites and quartz-feldspar porphyry granodiorites) and the clinopyroxenites from the Kokerboom Intrusion (mafic-ultramafic intrusion in close proximity to and association with the Haib porphyry copper deposit) (refer to Chapter 4), ore-petrography and mineral liberation analyses on the various sulphide textures and in-situ and whole-rock Cu and Fe isotope analyses on the various sulphide textures (chalcopyrite), the host porphyry granodiorite and the clinopyroxenites from the Kokerboom Intrusion.

5.2.1. Feldspar porphyry andesites

The feldspar porphyry andesites are composed of plagioclase, quartz and mafic phenocrysts (~2 mm), which are strongly altered to sericite, chlorite and epidote, set in a fine-grained biotite-sericite-chlorite-epidote-rich, quartzo-feldspathic groundmass (Figure 5.1). The plagioclase phenocrysts are highly altered to sericite and show evidence of zoning. The quartz phenocrysts exhibit distinct undulose extinction and the mafic phenocrysts are altered to chlorite-epidote-rich aggregates and stringers, which are aligned in certain areas. Magnetite occurs as inclusions in the chlorite. Both quartz- and calcite-rich veins cross-cut phenocrysts, whereas quartz veins are cross-cut by calcite veins. Minor disseminated sulphides are also observed and are composed of bleb-like chalcopyrite with inclusions of subhedral pyrite. These disseminated sulphides are in close relation with primary quartz, plagioclase and secondary epidote. Rutile is also present and is in close relation with quartz and magnetite.

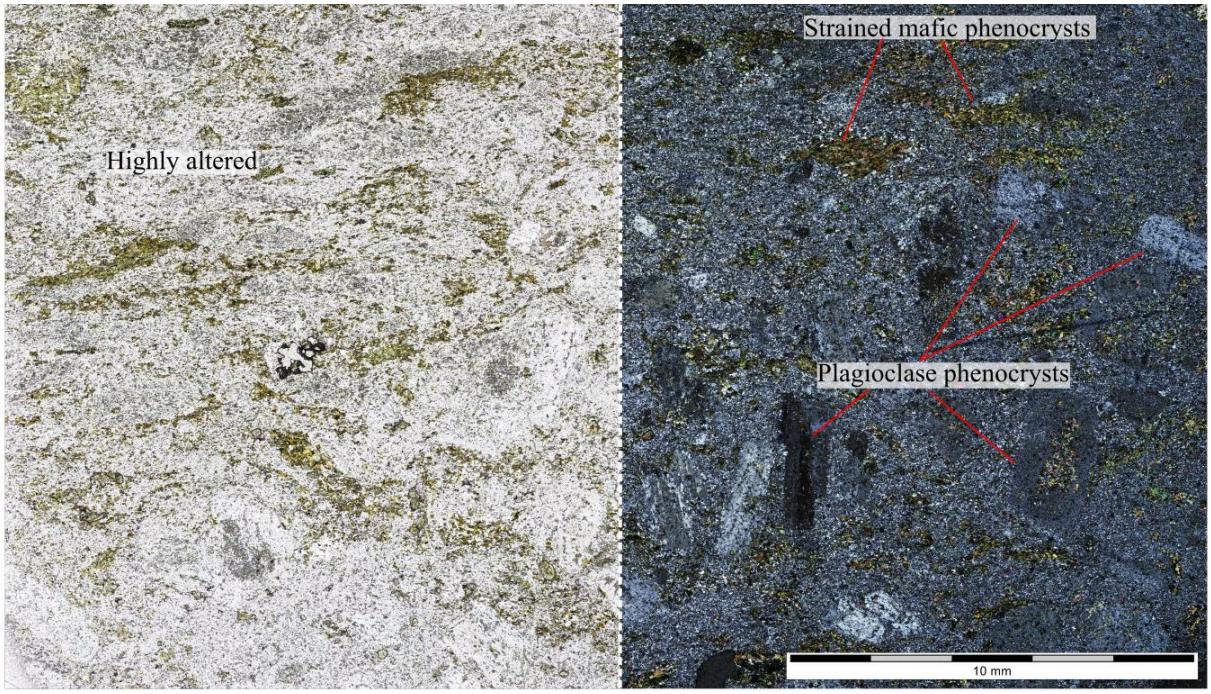

Figure 5.1: *Plane (left) and cross-polarized (right) photomicrographs of the feldspar porphyry andesites. Plagioclase and mafic phenocrysts are observed. The plagioclase phenocrysts are altered to sericite and the mafic phenocrysts are strained.*

5.2.2. Quartz-feldspar porphyry granodiorites

The quartz-feldspar porphyry granodiorites are medium-coarse grained (~2.5 mm), porphyritic, altered and are composed of plagioclase, orthoclase, quartz, calcite, hornblende, chlorite and rutile (Figure 5.3). The subhedral-euhedral plagioclase phenocrysts (~3 mm) are highly altered to sericite and epidote and the hornblende phenocrysts (~1 mm) are altered to coarse aggregates of chlorite and epidote. Magnetite (1 mm) occurs as inclusions within hornblende and is also strongly related with rutile, sphene and quartz. Subhedral-anhedral quartz is recrystallized and displays undulose extinction. Bluish opalescent quartz phenocrysts are also clear. The groundmass is medium-grained and composed of granular sericite-chlorite-epidote-quartz and feldspar. Mineralization is typically found within the quartz-feldspar porphyry granodiorites and consists of disseminated, bleb-like, vein-type or massive pyrite and chalcopyrite. Quartz and calcite veins are apparent with the latter truncating and cross-cutting the former.

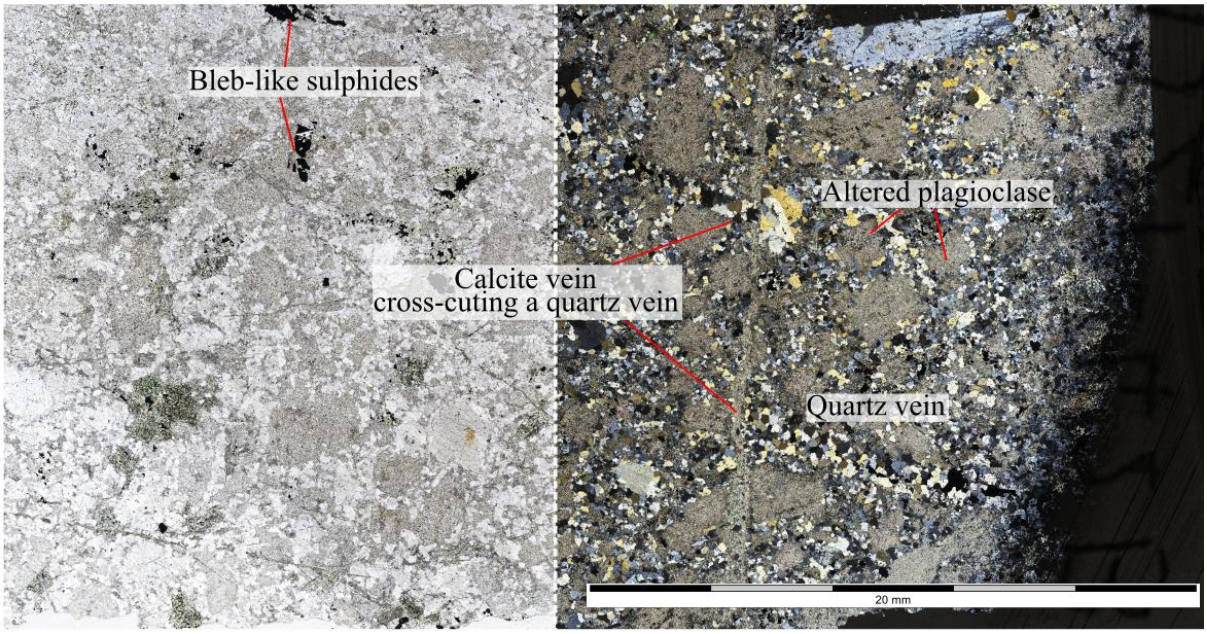

Figure 5.2: *Plane (left) and cross-polarized (right) photomicrographs of the quartz feldspar porphyry granodiorites. Plagioclase phenocrysts are highly altered to sericite. Quartz and calcite veins are apparent with the latter truncating and cross-cutting the former.*

5.2.3. Clinopyroxenites

The clinopyroxenites are coarse (~4 mm), massive and composed predominantly of clinopyroxene altered to fibrous-granular actinolite with minor chlorite, epidote, hornblende, rutile and sphene (Figure 5.3). The actinolite has a fibrolite texture and shows exsolution lamellae and simple twinning. The actinolite is altered to chlorite and epidote. Magnetite is disseminated throughout and is in close relation to rutile, sphene, chlorite and actinolite. The sulphides in the clinopyroxenite occur as coarse (~2 mm) bleb-like aggregates of chalcopyrite rimmed by chalcocite-covellite assemblages, which are subsequently rimmed by hematite-magnetite-ilmenite assemblages.

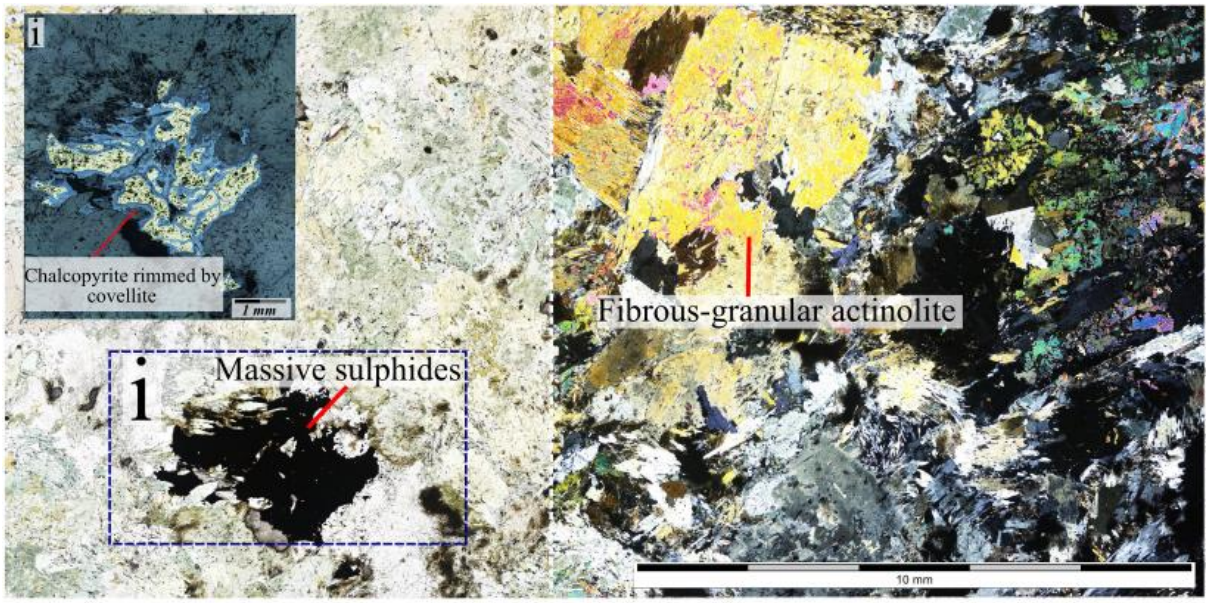

Figure 5.3: *Plane (left) and cross-polarized (right) photomicrographs of the clinopyroxenites. Fibrous-granular actinolite is visible. Primary clinopyroxene is altered to actinolite with minor chlorite, and epidote. Massive opaque material is prevalent as well which consists of chalcopyrite rimmed by covellite.*

5.2.4. Characterization of mineralization

The Cu-Mo sulphide mineralization in the Haib porphyry copper deposit is hosted within the chlorite-sericite altered and sheared quartz-feldspar porphyry granodiorites and feldspar porphyry andesites. Minor mineralization is found within the clinopyroxenite cumulates. Shear fractures observed in drill-core host biotite and quartz-rich veins, which are sub-horizontal and cross-cut and off-set later quartz veins. Time constraints did not permit observation of these shear structures in the field, but they were observed in borehole core. The mineralization is mainly chalcopyrite, pyrite, minor bornite, chalcocite and molybdenite. It is either disseminated throughout the host, massive or vein-hosted related to the shear fractures (Figure 5.4a-c). Potassic alteration is distinctly associated with molybdenite, whilst chlorite-sericite alteration is associated with chalcopyrite and pyrite. The calcite and ankerite carbonate veins occur and cross-cut each other. Sulphides are present in the clinopyroxenites of the Kokerboom Intrusion (refer to Chapter 4).

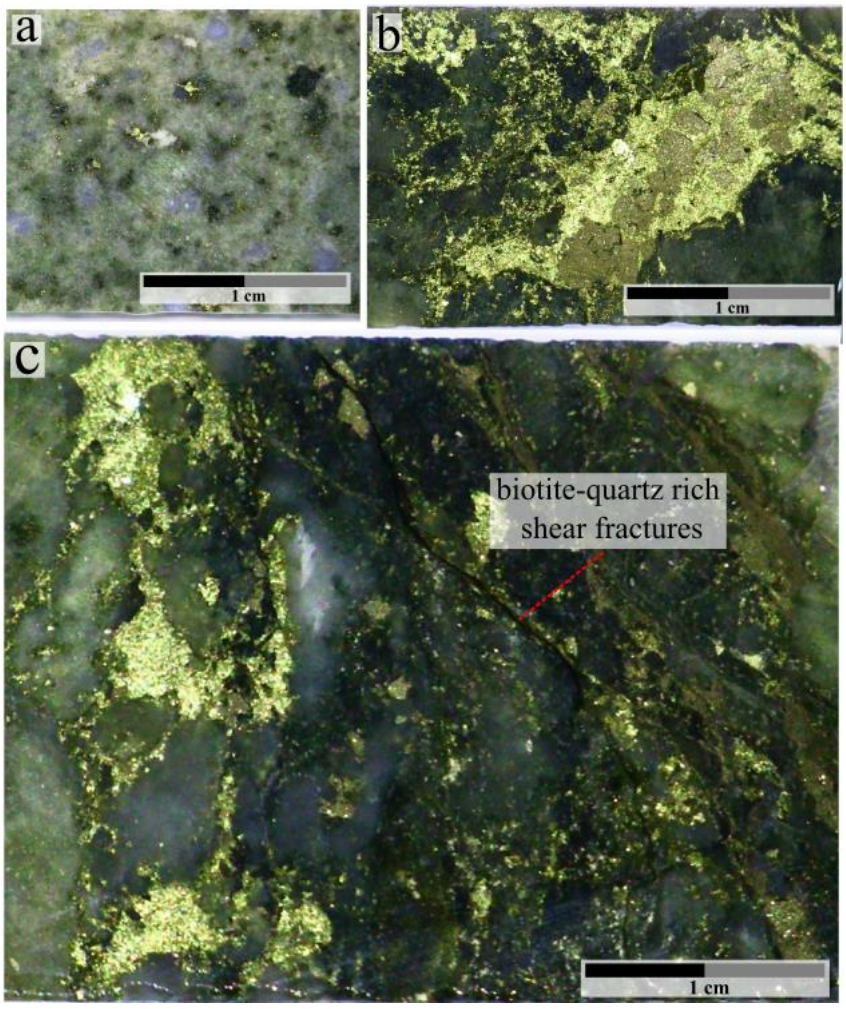

Figure 5.4: *Mineralization in the feldspar porphyry andesites and quartz-feldspar porphyry granodiorites. a) Disseminated chalcopyrite and pyrite in quartz-feldspar porphyry granodiorite. b) Massive chalcopyrite and pyrite in feldspar porphyry andesite. c) Vein-controlled mineralization (chalcopyrite and pyrite) in close relation to biotite and quartz rich shear fractures.*

5.2.5. Ore assemblages and textural analysis

The mineralization (pyrite and chalcopyrite) occurs either in disseminated, bleb, vein or massive form and occurs in close relation to biotite, muscovite and quartz mineral assemblages (Figure 5.5a-e; Figure 5.6-5.9). The disseminated mineralization occurs as ~0.5 mm euhedral-subhedral pyrite and subhedral-anhedral chalcopyrite that are either associated with each other, where pyrite is incorporated within chalcopyrite, or occur as isolated, dispersed grains (Figure 5.5a; Figure 5.6). Coarse (2-3 mm) bleb-like aggregates of pyrite are more common relative to chalcopyrite, the former occurring as inclusions in the latter (Figure 5.6b). The vein-type sulphides occur as subhedral-euhedral pyrite (~0.1-0.25 mm) incorporated within massive chalcopyrite. The vein-type sulphides are found within quartz-biotite veins (Figure 5.5c; Figure 5.7). The massive sulphides occur as subhedral-euhedral pyrite (~5-8 mm) incorporated within massive chalcopyrite (Figure 5.5d; Figure 5.8). In Figure 5.5d, it is clear that pyrite is being replaced by chalcopyrite, therefore the former formed first. The sulphides in the clinopyroxenite occur as coarse (~2 mm) bleb-like aggregates of chalcopyrite rimmed by chalcocite-covellite and hematite-magnetite-ilmenite so the original hypogene sulphide assemblage has been oxidized. (Figure 5.5e; Figure 5.9). The covellite occurs as feathery vein-type material cross-cutting the chalcopyrite. In addition, 0.5 mm subhedral hematite intergrown with ilmenite is observed. Disseminated magnetite (~0.1 mm) occurs in the quartz-feldspar porphyry granodiorites and the clinopyroxenites.

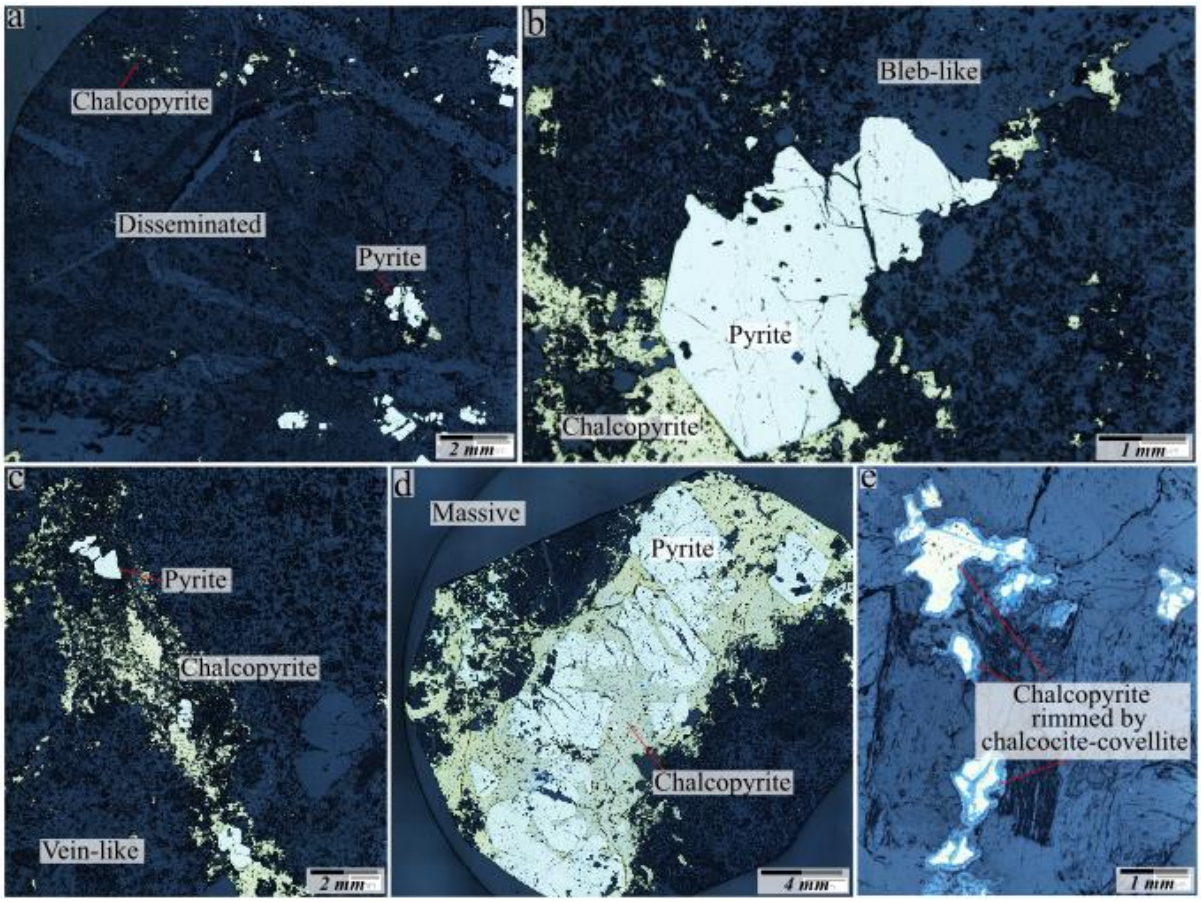

Figure 5.5: *Reflected light photomicrographs of the mineralization. The mineralization (pyrite and chalcopyrite) occurs either disseminated (a), bleb-like (b) vein-type (c) or massive (d and e).*

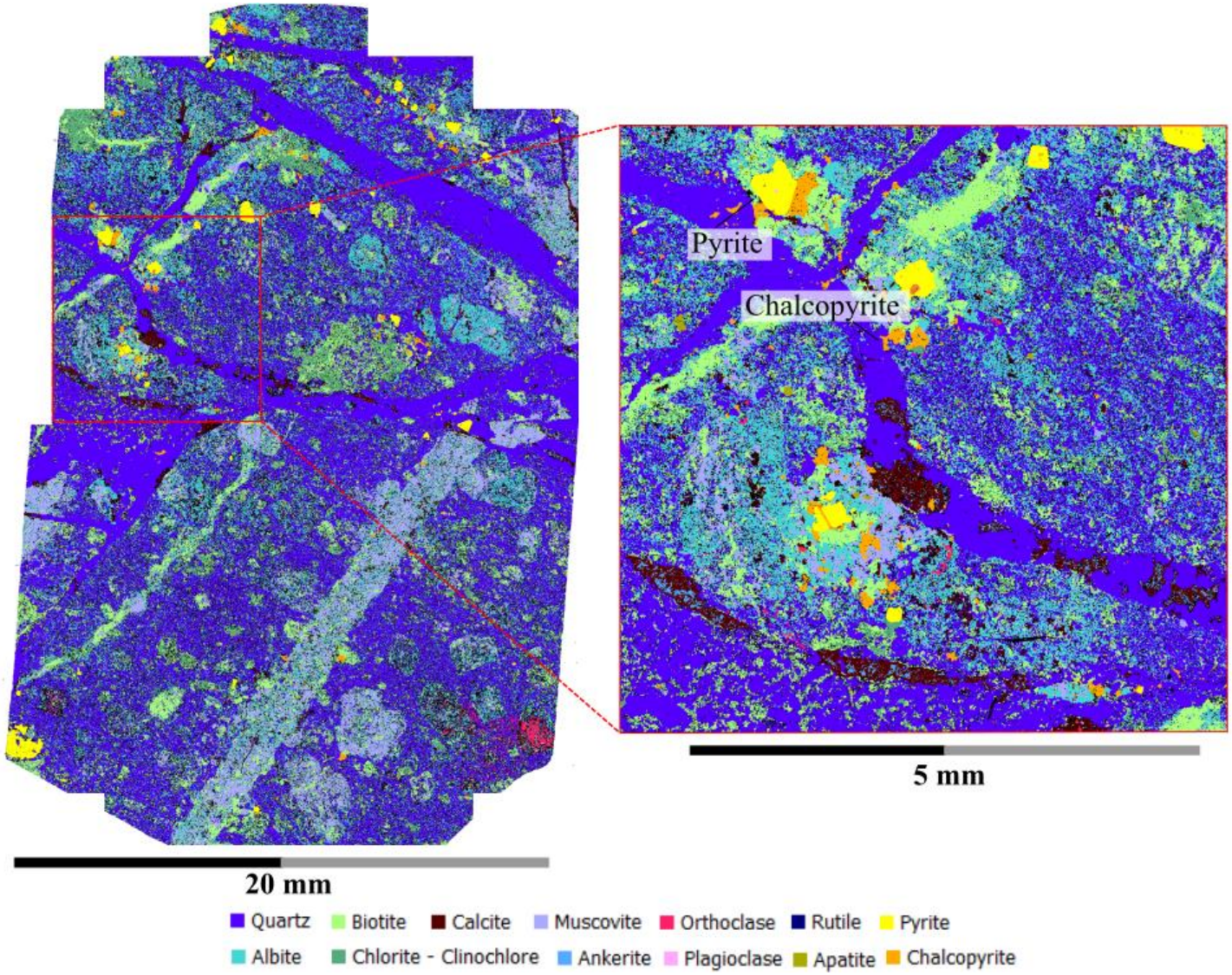

Figure 5.6: *TIMA analyses were conducted to produce mineral liberation maps of the disseminated sulphides in the quartz-feldspar porphyry granodiorite. The disseminated mineralization occurs as euhedral-subhedral pyrite and subhedral-anhedral chalcopyrite that are either associated with each other, where pyrite is incorporated within chalcopyrite, or occurs as isolated/dispersed grains.*

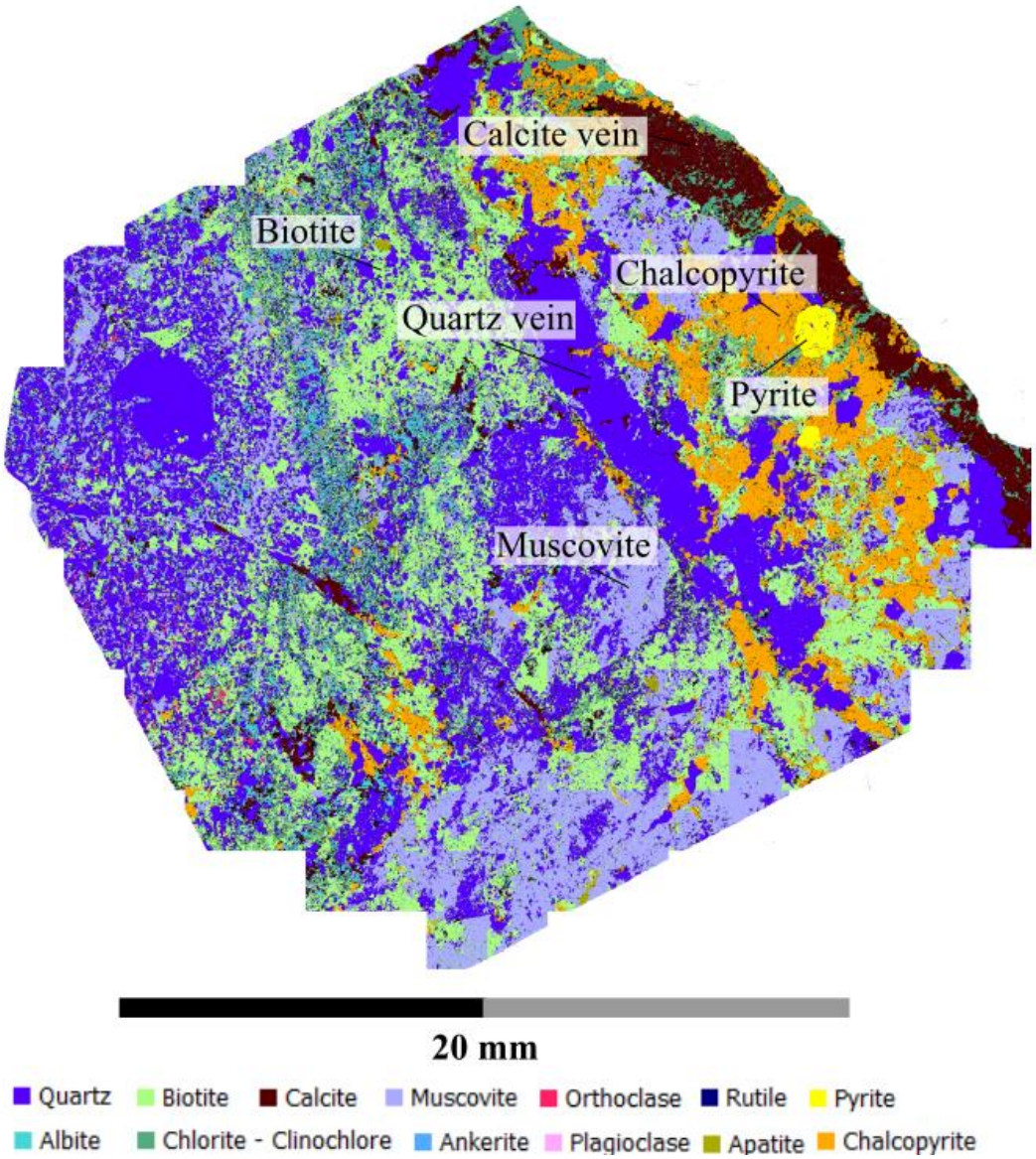

Figure 5.7: *TIMA analyses were conducted to produce mineral liberation maps of the vein-type sulphides in the quartz-feldspar porphyry granodiorite. The vein type sulphides occur as subhedral-euhedral pyrite incorporated within massive chalcopyrite in close relation to quartz-biotite veins.*

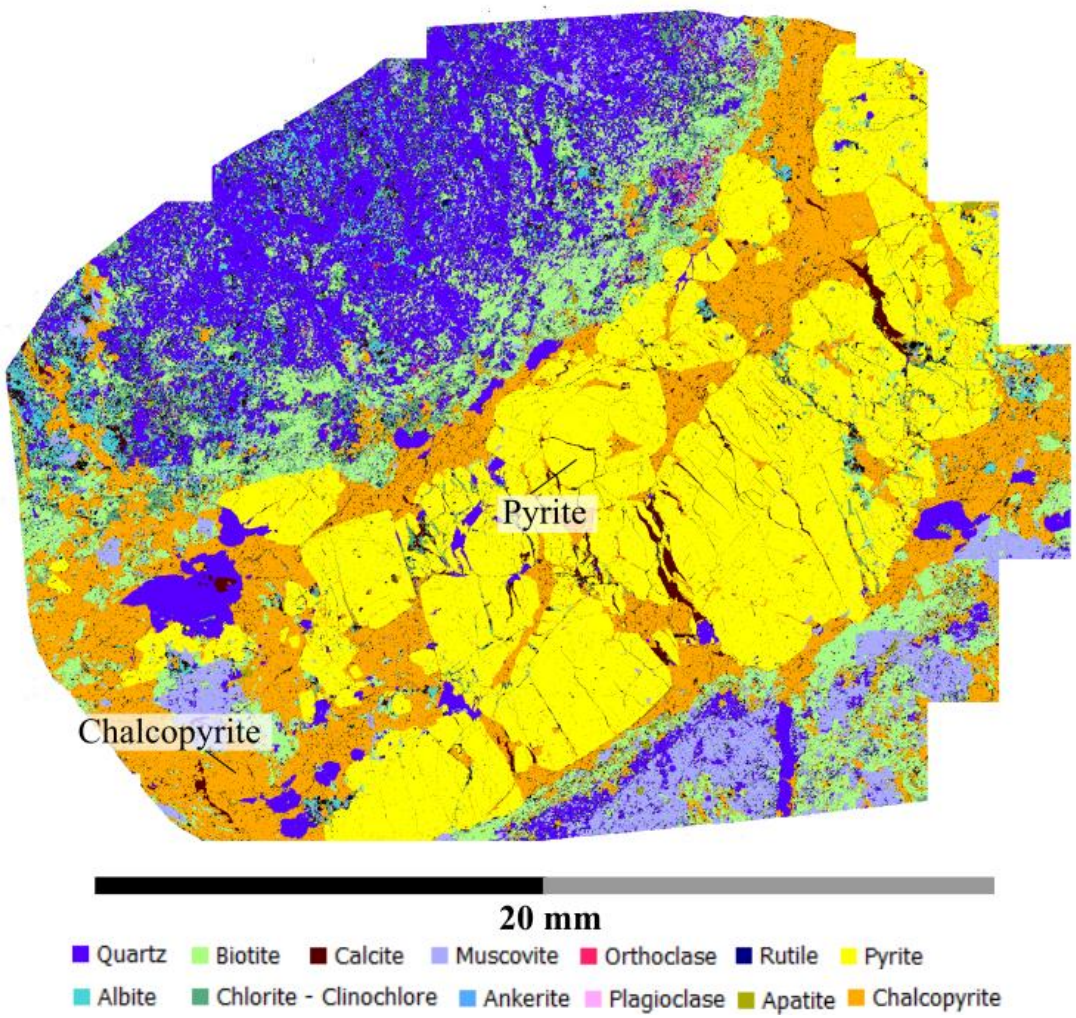

Figure 5.8: *TIMA analyses were conducted to produce mineral liberation maps of the massive sulphides in the quartz-feldspar porphyry granodiorite. The massive sulphides occur as subhedral-euhedral pyrite incorporated within massive chalcopyrite. The chalcopyrite clearly postdates the pyrite here.*

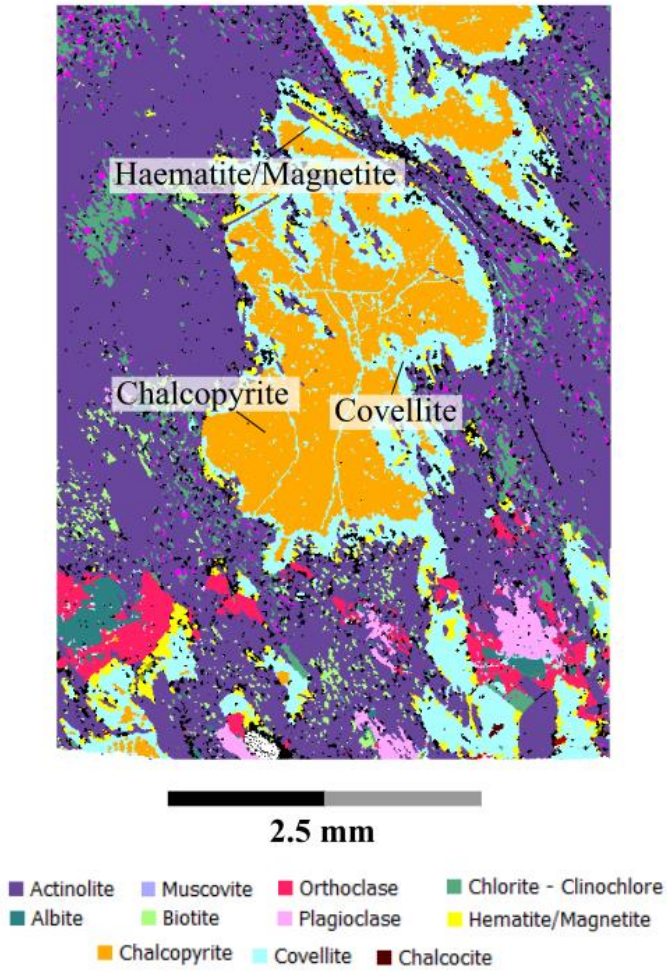

Figure 5.9: *TIMA analyses were conducted to produce mineral liberation maps of the massive sulphides in the clinopyroxenite. The sulphides in the clinopyroxenite occur as coarse bleb-like aggregates of chalcopyrite replaced by chalcocite-covellite.*

5.2.6. In-situ and whole rock copper and iron isotope analyses

The various occurrences of chalcopyrite, which include disseminated, massive and vein-type forms, show distinct $\delta^{65}Cu$ and $\delta^{56}Fe$ signatures (Figures 5.10, 5.11 and 5.12). The $\delta^{65}Cu$ values for the disseminated chalcopyrite grains range from 0.06 ± 0.07 to 0.21 ± 0.07 ‰, and $\delta^{56}Fe$ values range from 0.02 ± 0.07 to 0.06 ± 0.07 ‰. The $\delta^{65}Cu$ value for the massive chalcopyrite grain is 0.06 ± 0.07 ‰ and the $\delta^{56}Fe$ value is 0.03 ± 0.07 ‰. The $\delta^{65}Cu$ values for the vein-type chalcopyrite grains range from -0.08 ± 0.07 to 0.11 ± 0.07 ‰, whereas $\delta^{56}Fe$ values range from -0.11 ± 0.07 to -0.01 ± 0.07 ‰. The whole rock $\delta^{65}Cu$ and $\delta^{56}Fe$ values for three unaltered host granodiorite porphyry samples range from 0.16 ± 0.07 to 0.46 ± 0.07 ‰ and 0.24 ± 0.07 to 0.29 ± 0.07 ‰ respectively. The whole rock $\delta^{56}Fe$ value for the clinopyroxenite sample is -0.07 ± 0.07 ‰. The $\delta^{65}Cu$ and $\delta^{56}Fe$ measured values for the disseminated and massive textural types broadly overlap with the $\delta^{65}Cu$ and $\delta^{56}Fe$ measured values for the vein-type textural type. The disseminated and massive textural types have an enriched $\delta^{65}Cu$ and $\delta^{56}Fe$ value relative to the vein-type textural type which extend to depleted $\delta^{65}Cu$ and $\delta^{56}Fe$ values.

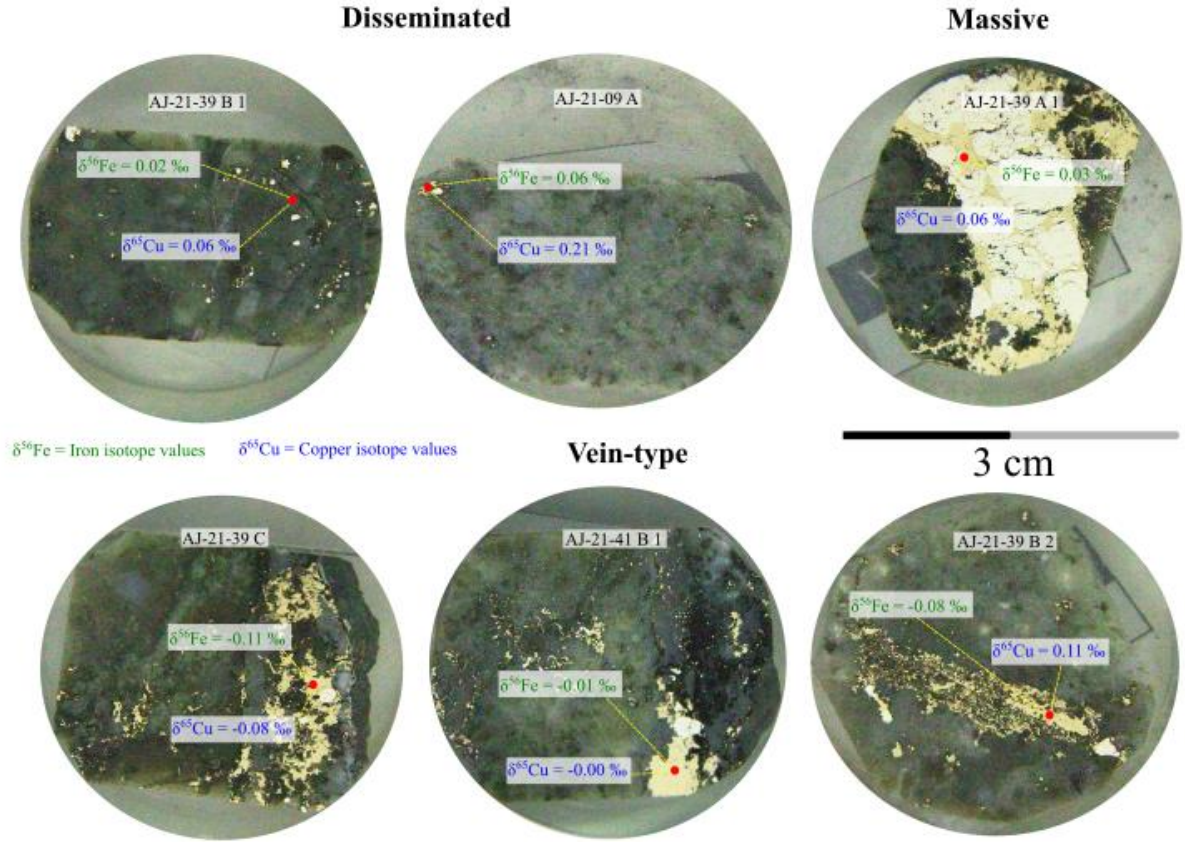

Figure 5.10: *Typical $\delta^{65}Cu$ and $\delta^{56}Fe$ signatures for the various occurrences of chalcopyrite i.e. disseminated, massive and vein-type.*

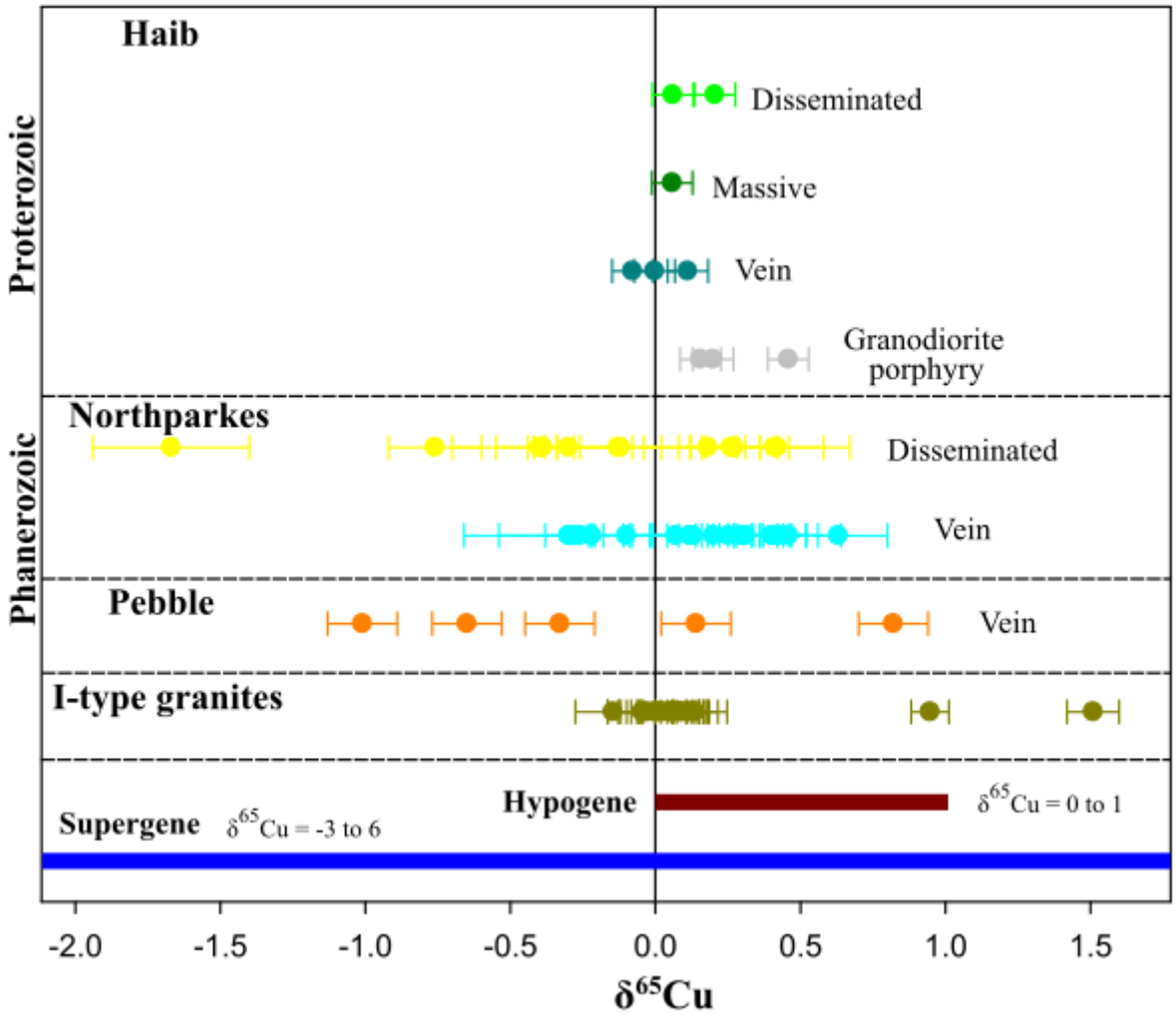

Figure 5.11: *δ^{65}Cu variations on chalcopyrite for the Paleoproterozoic Haib porphyry deposit and Phanerozoic porphyry deposits: Northparkes (Li et al., 2010) and Pebble (Gregory and Mathur, 2017). The data for I-type granites are from Li et al. (2009). The boundaries in the figure between the Paleoproterozoic Haib deposit and the representative Phanerozoic deposits are indicated by the dotted lines.*

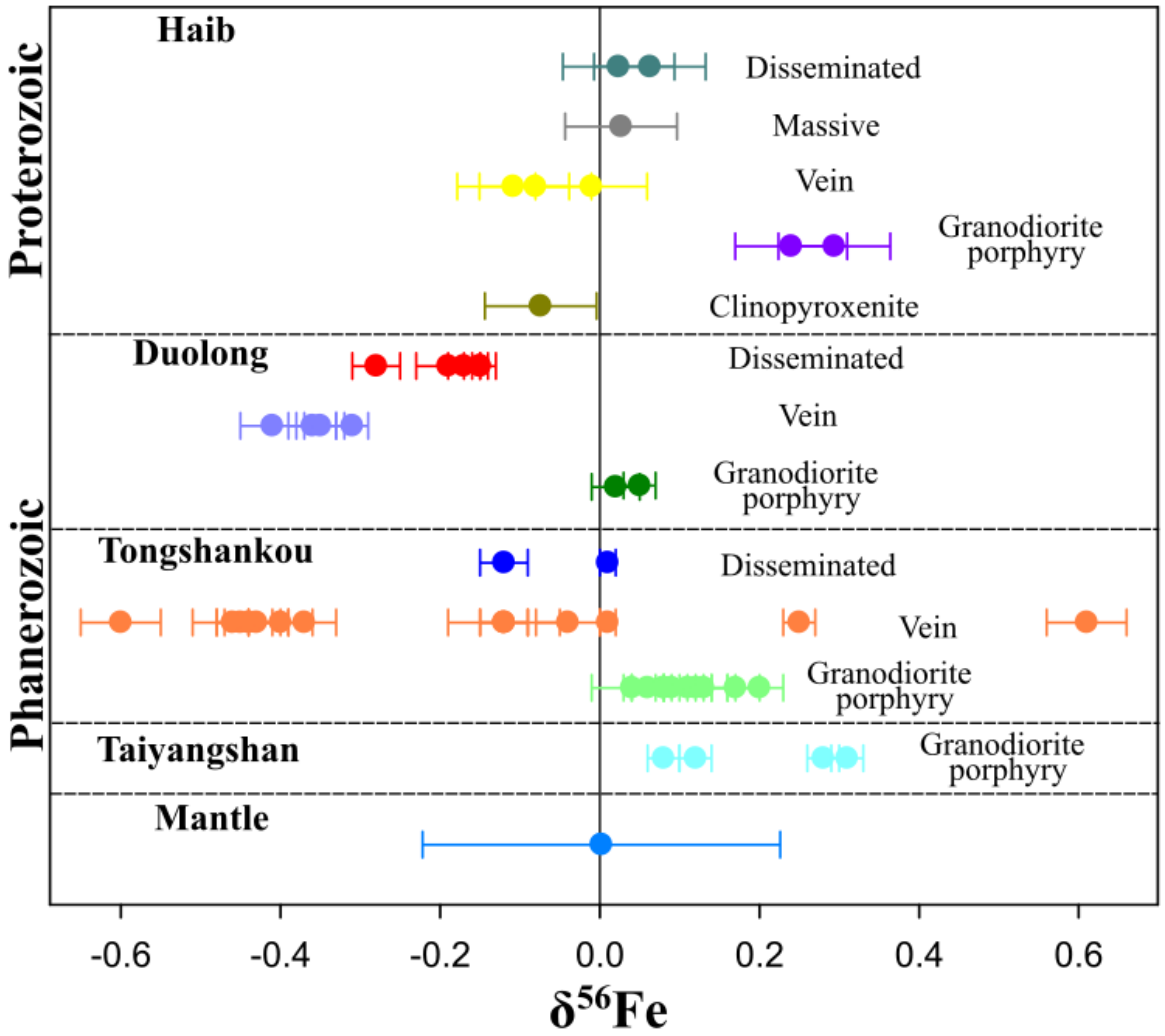

Figure 5.12: *δ^{56}Fe variations on chalcopyrite for the Paleoproterozoic Haib porphyry deposit and Phanerozoic porphyry deposits such as Duolong (Li et al., 2018), Tongshankou (He et al., 2020), Taiyangshan (Zhang et al., 2021). The average mantle value is after Johnson et al. (2020). The boundaries in the figure between the Paleoproterozoic Haib deposit and the representative Phanerozoic deposits are indicated by the dotted lines.*

5.3. Discussion

The focus of this discussion is to understand the temporal variations of porphyry copper deposits through evaluating Cu and Fe isotopic contrasts between the Palaeoproterozoic Haib porphyry copper deposit and representative Phanerozoic porphyry copper deposits. In order to discern this, the discussion is divided into various sections which include: the nature of the sulphides, fractionation controls on the ore-forming fluids forming the various sulphide textures (disseminated, massive and vein-type), the types of fluid related with hydrothermal alteration and mineralization, the controls on the isotopic fractionation between the ore-forming fluids and the host magmas, comparisons between the Palaeoproterzoic Haib deposit and Phanerozoic deposits, δ^{65}Cu and δ^{56}Fe isotopic evidence for deeper levels of the porphyry system and the application of δ^{65}Cu and δ^{56}Fe isotopes to infer crustal depth of the porphyry system.

5.3.1. Magmatic-hydrothermal nature for the Haib deposit sulphides

The δ^{65}Cu signature of the disseminated sulphides in the Haib deposit overlap with the host granodiorite porphyry, indicating the magmatic nature of the disseminated sulphides. The δ^{65}Cu isotopic signatures of the chalcopyrite grains overlap with magmatic-hydrothermal or hypogene sulphides (-1 to 1 ‰), although it is plausible that the Haib porphyry copper deposit does host mineralization linked to supergene processes as suggested by the copper staining observed in the field. Further analyses on minerals such as chalcocite, digenite and covellite will provide additional insights.

5.3.2. Controls on the ore-forming fluids linked to the progressive precipitation of various sulphide textures

One key aspect in forming porphyry copper deposits is the exsolution of ore-forming fluids from the magma (Li et al., 2018). The isotopic composition of the exsolved fluids is controlled by temperature, fractionation between fluid and melt, sulphide precipitation, fluid salinity (which influences the amount of Cl^- accessible for complexation) and redox conditions (Li et al., 2010 and Li et al., 2018). According to Li et al. (2010), temperature is the dominant control on Cu solubility in hydrothermal fluids. Herzarkhani et al. (1999) generated a Rayleigh fractionation model of the isotopic composition of Cu that was precipitated from a saturated hydrothermal fluid. Results from Herzarkhani et al. (1999) showed that the isotopic signature of the sulphides become lighter as temperature of the hydrothermal fluid decreases - the evolved fluid constantly incorporates the lighter isotopic signature - therefore, the sulphides that progressively precipitate from the fluid have a lighter isotopic signature. A temperature change is observed in porphyry copper deposits and is recorded in the alteration assemblages which include higher temperature potassic alteration and lower temperature phyllic and propylitic alterations (Li et al., 2010). Copper-bearing fluids precipitate copper in response to this temperature change (Li et al., 2010). Therefore, understanding the fluid temperature, hydrothermal histories, and sulphide precipitation is key to interpreting isotopic variations (Li et al., 2010; Gregory and Mathur, 2017; Li et al., 2018).

The heavier isotopic composition of the disseminated and massive sulphides in the host lithologies of the Haib deposit compared to the vein-type sulphides in the host lithologies of the Haib deposit is indicative of progressive precipitation of various sulphides as the ore-forming fluids evolved, cooled, and fractionated isotopes. The precipitation of the disseminated and massive chalcopyrite from the higher temperature fluids causes the evolved fluid to get progressively lighter in δ^{65}Cu and δ^{56}Fe values (Li et al., 2020). This results in a lighter δ^{65}Cu

and $\delta^{56}Fe$ signature for the vein-type sulphides and a heavier $\delta^{65}Cu$ and $\delta^{56}Fe$ signature for the disseminated and massive sulphides. The change in the $\delta^{65}Cu$ and $\delta^{56}Fe$ values for the disseminated, massive and vein-type sulphides is a result of progressive mineral crystallization and temperatures changes related to different equilibrium rates between minerals and fluids.

5.3.3. Types of fluid related to hydrothermal alteration and mineralization

Studies conducted by Barr and Reid (1992) found that there are two types of fluids that relate to hydrothermal alteration and mineralization at Haib. The two types of fluids include a high-salinity, high-temperature fluid and a low-salinity, lower-temperature fluid. It is plausible that the disseminated and massive sulphides are related with the high-salinity, high-temperature fluid and that the vein-type sulphides are related with the low-salinity, lower-temperature fluid. Studies conducted by Minnitt (1986) show that there are two phases of alteration and mineralization. Results from this study suggest this and imply that the mineralization can be texturally and isotopically characterized into two phases: disseminated and massive texture (heavier isotopic signature of 0.06 to 0.21 ‰ and 0.02 to 0.06 ‰ for $\delta^{65}Cu$ and $\delta^{56}Fe$ respectively) and vein-type (lighter isotopic signature of -0.08 to 0.11 ‰ and 0.11 to -0.01 ‰ for $\delta^{65}Cu$ and $\delta^{56}Fe$ respectively). This suggest that the high-saline, high-temperature fluids are related to the precipitation of disseminated and massive chalcopyrite and produce enrichment of the heavy isotope, whereas, low-saline, lower-temperature fluids are related with the precipitation of vein-type chalcopyrite and the enrichment of the light isotope.

5.3.4. Controls on the isotopic fractionation between the ore-forming fluids and the host magmas

Notably, all textural types of sulphide, which precipitated from the ore-forming fluids, have measurably lighter $\delta^{56}Fe$ values than the host granodiorite porphyry (-0.11 ‰ to 0.06 ‰ c.f. 0.27 ‰; Figure 5.12). This finding corroborates with studies conducted on the Duolong deposit by Li et al. (2020), which established that exsolved fluids have a lighter Fe isotope signature than the parental magmas. Exsolved fluids are enriched in light Fe isotopic compositions as the Fe^{2+} species in fluids preferentially incorporate the lighter isotope (Simon et al., 2004; Heimann et al., 2008; Hill et al., 2010; Saunier et al., 2011; Wang et al., 2011, 2015; Telus et al., 2012). Experimental and theoretical studies show that fluid phases that carry dissolved iron in the form of Fe^{2+}-chloride complexes are enriched in light Fe isotopes relative to the magma with Fe^{3+}-bearing minerals such as hematite, magnetite, and amphibole. (Polyakov and Mineev, 2000; Saunier et al., 2011; Sossi and O'Neill, 2017). According to Woodland and Koch (2003), during processes such as melt extraction and fractional crystallization, Fe^{3+} behaves more incompatibly relative to Fe^{2+}. As a result, isotopically heavy Fe is predicted to be concentrated in Fe^{3+}-bearing sites that occur in magnetite and silicate melt structures relative to Fe^{2+}-bearing sites that occur in olivine, pyroxene, crystalline sulphide and sulphide melt structures (Polyakov and Mineev, 2000; Shahar et al., 2008; Schuessler et al., 2009; Macris et al., 2015; Young et al., 2015; Sossi et al., 2016).

5.3.5. Comparisons between the Palaeoproterozoic Haib deposit and Phanerozoic porphyry copper deposits

In comparison to Phanerozoic deposits, the $\delta^{65}Cu$ and $\delta^{56}Fe$ signatures of Haib chalcopyrite overlap with deposits such as Northparkes, Pebble, Duolong, Tongshankou and Taiyanshan (Figures 5.11, 12; Li et al., 2010; Gregory and Mathur, 2017; Li et al., 2018; He et al., 2020; Zhang et al., 2021). The Northparkes and Haib deposits have similar ranges in $\delta^{65}Cu$ signatures. The Duolong and Haib deposits show several similarities as the $\delta^{56}Fe$ signatures of the disseminated chalcopyrite grains are isotopically heavier than the vein-type chalcopyrite grains.

The $\delta^{56}Fe$ signatures of the host granodiorite porphyry in the Haib deposits overlap with the host granodiorite porphyry in the Tongshankou and Taiyanshan deposits. The $\delta^{56}Fe$ signatures of the disseminated sulphides and the clinopyroxenite overlap with the average mantle $\delta^{56}Fe$ signature suggesting a mantle origin for the sulphides (Le Bras et al., 2020). The $\delta^{56}Fe$ signature of the clinopyroxenite supports the hypothesis that the clinopyroxenite represent primitive cumulate material (refer to chapter 4). The host granodiorite porphyry has an enriched $\delta^{56}Fe$ signature relative to the average mantle value which indicate processes such as magmatic differentiation caused isotopic fractionation. Differentiation processes such as fractional crystallization of pyroxene sequestrated the lighter isotope causing the residual silicate bearing magma to be enriched in Fe^{3+} incorporating the heavier isotope. This caused the isotopic signature of the silicate-bearing host granodiorite porphyry to have a heavier $\delta^{56}Fe$ relative to mantle values whereas, the clinopyroxenite reflects mantle values as the Fe^{2+} bearing sites in clinopyroxene incorporated the lighter isotope.

An important petrographic observation is the assemblage of amphibole + magnetite + quartz + rutile + sphene in the quartz-felspar granodiorite which suggests elevated oxygen fugacity. I-type granites have higher oxygen fugacity than S-type granites (Foden et al., 2015), from geochemical results (moderate Al_2O_3 and high Na_2O concentrations) and mineral assemblages composed of amphibole and pyroxene, the Haib magmas are typical I-type. Observations from a recent study conducted on the Haib support elevated oxygen fugacity, which found sphene + magnetite + quartz assemblages in the diorite (Meng et al., 2021). In addition, Meng et al. (2021) used 3 independent oxybarometers on the Haib showing that the ore-forming magmas were relatively oxidized (1–2 log units above the fayalite-magnetite-quartz redox buffer). The elevated oxygen fugacity in the Precambrian related to the formation of porphyry copper deposits is due to the subduction of sulfate during intervals associated with locally high magmatic sulfur contents.

Globally, there are examples of Phanerozoic deposits which have mineral assemblages that reflect oxidized magmas in host rocks. Mineralized granodiorites in the Cretaceous Pebble porphyry deposit in Alaska contain abundant sphene and amphibole, which have been interpreted as reflecting more oxidized and hydrous conditions compared to pre-mineralized intrusions (Olson et al., 2017). Amphibole-sphene-magnetite-quartz assemblages in the Cenozoic Grasberg host intrusive rocks indicate that the Grasberg ore-forming magmas were oxidized, with fO_2 > FMQ +3 (Sulaksono et al., 2021).

Arc-related, calc-alkaline magmas linked with porphyry copper formation are moderately oxidized (at ΔFMQ +1 to +3) and hydrous (Audetat and Simon, 2012; Sun et al., 2015; Richards, 2015) and this is seen in the Vioolsdrif Intrusive Suite due to the amphibole + magnetite + quartz + rutile + sphene assemblages. The similarities of mineral assemblages

between the Paleoproterozoic Haib and Phanerozoic Pebble and Grasberg porphyry deposits supports high oxygen fugacity for the Haib porphyry copper deposit.

5.3.6. δ^{65}Cu and δ^{56}Fe isotopic evidence that Haib formed in the deeper levels of the porphyry system

The smaller range in the δ^{65}Cu and δ^{56}Fe signatures for the Haib porphyry deposit relative to the δ^{65}Cu and δ^{56}Fe signatures for Phanerozoic porphyry deposits (Figure 5.11 and 5.12) may be a reflection of the deeper crustal levels at which the Palaeoproterozoic Haib porphyry deposit is preserved. The lack of fractionated δ^{65}Cu signatures may indicate that there was barely transport of copper as a volatile phase in the lower part of the porphyry system. As mentioned before, the Haib copper-molybdenum deposit is one of the few occurrences of porphyry copper mineralization in the Precambrian. The temporal distribution of porphyry copper deposits through geological time is largely controlled by exhumation: burial, uplift, and erosion (Kesler and Wilkinson, 2006). The scarcity of Precambrian deposits is attributed to this process causing deep erosion of Precambrian mobile belts (Gaal and Isohanni, 1979; Kesler and Wilkinson, 2006). The shallower crustal levels of the porphyry systems, where hydrothermal fluids have undergone more isotopic fractionation have been eroded away (Figure 5.13). The deeper crustal levels of the porphyry system, which is less influenced by shallow hydrothermal processes, and by extensive heavy, stable isotope fractionation (Figure 5.13) is exposed in the Haib porphyry copper deposit. The deposit therefore may represent the deeper crustal levels of the porphyry system. This notion is supported by corroboratory evidence including:

- The presence of early dark micaceous veins (the first phase of veins observed in the quartz-feldspar porphyry granodiorites) that are composed of quartz and coarse mica (Runyon et al., 2017, 2019). Early dark micaceous veins are located at deep levels (paleodepths of ~4–12 km) which is indicative of the root zones of porphyry systems (Runyon et al., 2017, 2019). The mica present in the early dark micaceous hosted in the quartz-feldspar granodiorites are composed of biotite.
- Machine learning geothermobarometry on pyroxenes from the Vuurdood Subsuite pyroxenite which yield average pressure and temperature estimates of 4 kbar and 870 °C respectively (see Chapter 4).
- Lack of evidence of shallow alteration assemblages such as propylitic and argillic alteration (Minnitt, 1979; Minnitt, 1986; Meng et al., 2021).
- Coarse-grained nature of the Vioolsdrif Intrusive Suite (clinopyroxenites, granodiorites, diorites, gabbros) which is indicative of slow cooling at mid-crustal batholith depths (Vermond, 2019).
- The presence of geochemically primitive mafic units such as the gabbros and clinopyroxenites. The clinopyroxenites are mafic, dense, and usually occur at mid to lower crustal levels.
- Mineralization linked with shear fractures which is indicative of deformation within the ductile regime (5-15 km depth) (Davis et al., 2012)).

5.3.7. Application of $\delta^{65}Cu$ and $\delta^{56}Fe$ isotopes to infer crustal depth of the porphyry system

Previous studies indicate that there are distinct Cu isotopic signatures for high temperature hypogene enrichment, and leach cap minerals (Mathur et al., 2009). Chalcopyrite analysed from high temperature primary mineralization yield $\delta^{65}Cu$ isotopic signatures clustered between 1‰ to -1‰ whereas, secondary copper minerals formed from low temperature hydrothermal processes yield $\delta^{65}Cu$ isotopic signatures from -3 to more than +6‰ (Figure 5.11; Mathur et al., 2009). The $\delta^{65}Cu$ signatures for the Haib deposit are between -0.14 ‰ and 0.46 ‰ whereas, the $\delta^{65}Cu$ signatures for Phanerozoic deposits are between -1.8 ‰ and 1.2 ‰. The $\delta^{56}Fe$ signatures for the Haib deposit are between -0.11 ‰ and 0.29 ‰ whereas, the $\delta^{56}Fe$ signatures for Phanerozoic deposits are between -0.6 ‰ and 0.6 ‰. This study reveals that the range in $\delta^{65}Cu$ and $\delta^{56}Fe$ signatures for the Haib deposit representing the deeper parts of the porphyry system is limited compared to Phanerozoic deposits representing the shallower parts of the porphyry system.

Precambrian deposits have overall lower copper grades and tonnages compared to Phanerozoic deposits (Gaal and Isohanni, 1979; Nironen and Csongradi, 1984). According to Nironen and Csongradi (1984), there is uncertainty pertaining to the reason for this. Possibilities include that our understanding of such deposits is limited and thus, we still need to learn how to search for porphyry ore deposits in the Precambrian (Gaal and Isohanni, 1979). Greater ranges in $\delta^{65}Cu$ and $\delta^{56}Fe$ signatures are related with higher grades and tonnages which is seen in Phanerozoic deposits. The shallower levels of the porphyry system have been subjected to hydrothermal fluids and supergene processes which upgrades the copper mineralization. This is seen in Phanerozoic deposits as argillic and propylitic alteration present in these deposits correspond with higher grade copper oxides.

Measurements from this research indicate that the Haib porphyry copper deposit has a limited range in $\delta^{65}Cu$ and $\delta^{56}Fe$ signatures corroborating with the fact that Precambrian deposits have lower grades and tonnages. The shallower levels of the Haib deposit, where more extensive, secondary isotopic fractionation is more likely to have occurred, appears to have been eroded away. Thus, copper and iron isotopes can be used to identify the crustal depth of a porphyry copper system. Copper and iron isotopes may provide insight on the enrichment of copper and provide a better understanding on the grade and the overall resource quality of the deposit.

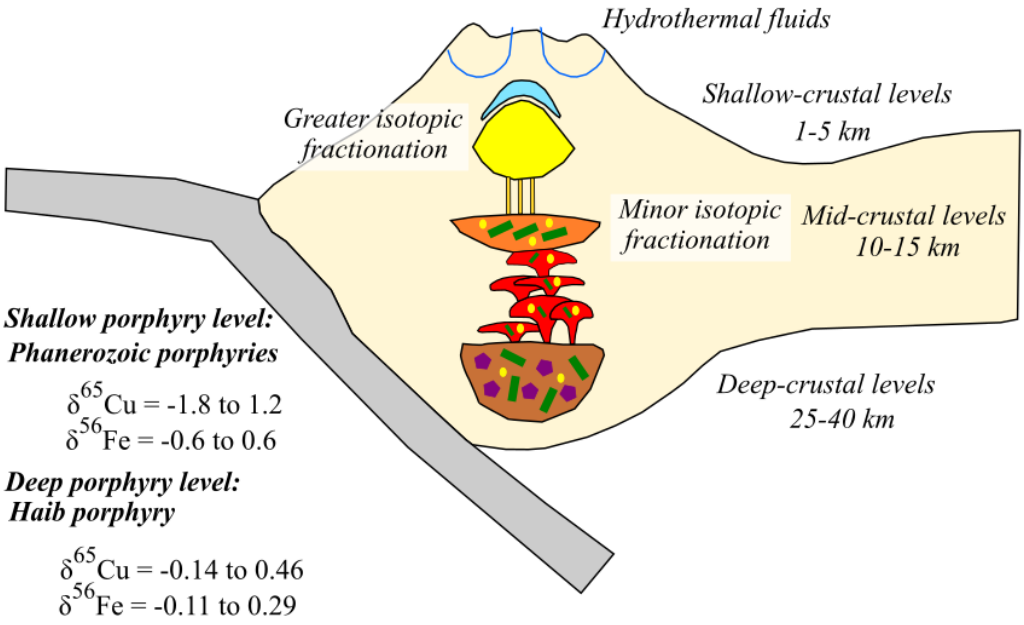

Figure 5.13: *Diagram illustrating the greater range in $\delta^{65}Cu$ and $\delta^{56}Fe$ signatures in shallow Phanerozoic porphyry deposits compared to the deeper Palaeoproterozoic Haib porphyry deposit. Hydrothermal fluids cause greater isotopic fractionation at shallow levels.*

5.4. Conclusion

The mineralization in the Palaeoproterozoic (1.88 Ga) Haib deposit is characterized texturally and isotopically by two ore-forming phases: 1. Disseminated-massive mineralization characterized by heavier isotopic signature of $\delta^{65}Cu$ and $\delta^{56}Fe$ and 2. vein-type mineralization with lighter isotopic signature of $\delta^{65}Cu$ and $\delta^{56}Fe$. The results indicate that the ore-forming fluid evolved and progressively precipitated various generations of sulphide with fractionated $\delta^{65}Cu$ and $\delta^{56}Fe$ isotope signatures due to sequential mineral crystallization and temperatures changes related to different equilibrium rates between minerals and fluids. The overlap of the $\delta^{56}Fe$ signature of the disseminated sulphides with the $\delta^{56}Fe$ signature of the mantle indicates a mantle source for the copper. Fractional crystallization of pyroxene (forming the clinopyroxenite cumulates) sequestrated the lighter isotope causing the residual silicate bearing magma (host granodiorite porphyry) to be enriched in the heavier isotope. The Palaeoproterozoic Haib deposit is similar to Phanerozoic porphyry deposits based on various lines of evidence which include (1) the overlap of the $\delta^{65}Cu$ and $\delta^{56}Fe$ signatures for the chalcopyrite grains in the deposits, (2) the direct comparison of the $\delta^{56}Fe$ signatures for the host granodiorite porphyry in the Duolong deposit and Haib deposit and (3) the magmatic assemblage oxybarometers i.e. amphibole + magnetite + quartz + rutile + sphene in the host granodiorite porphyry which is indicative of elevated oxygen fugacity and corroborates with the heavy $\delta^{56}Fe$ signature of the host granodiorite porphyry. The limited range in the $\delta^{65}Cu$ and $\delta^{56}Fe$ signatures of the Palaeoproterozoic Haib deposit relative to Phanerozoic deposits is suggestive of deeper levels of the porphyry system i.e. the shallower levels where isotopic fractionation occurred has been eroded away. Cu and Fe isotopes can be used as a tool to identify the crustal level of the porphyry system.

6. A trans-crustal perspective on porphyry copper deposit formation using Fe isotopes

6.1. Introduction

In several geological terrains, porphyry copper systems are investigated exclusively from the top down (Seedorff et al., 2008). This means our understanding of primary magma generation and metallogenesis of ore deposits can be obfuscated by shallower processes in the crust. This can be mitigated by studying lower crustal cumulates and 'seeing through' shallow crustal processes such as crustal contamination (Chin et al., 2018). Lower crustal cumulates serve as a record of the deeper roots of the crust and a correlative view of the chemical composition of the arc crust (Cooper and Inglis, 2022). The composition of the lower crust located in the Andes provides an ideal-case study to understand lower crustal processes. The Phanerozoic Mercaderes-Rio Mayo lower crustal cumulates, located in the Northern Andes, are hosted by magmatism related to the subduction of the Nazca plate beneath the South American plate (Weber, 1998, 2002). Through conducting analysis on the Mercaderes-Rio Mayo lower crustal xenoliths, which are located in the Northern Andes, we see through shallow crustal processes that influences arc magma composition (Chin et al., 2018).

Lee and Tang (2020) proposed that porphyry copper deposits are formed in thick continental arc settings (> 45 km) related with intra-crustal differentiation processes which involve the fractionation of garnet resulting in the depletion of ferrous iron in the magma and enrichment of ferric iron causing oxidation of the magma (Lee and Tang, 2020). Studies conducted by Li et al. (2021) using Fe isotopes found that garnet fractionation in the lower crust contributes to the increased oxygen fugacity prevalent in arc settings. Our understanding of the systematics in which garnet fractionation results in a heavy iron isotope signature in arc settings remains limited (Liang et al., 2022). This study focuses on evaluating the iron isotope signature of the Haib porphyry copper deposit located in southern Namibia and the Rio-Mayo lower crustal cumulates situated in the Northern Andes in order to constrain the effect of amphibole and garnet on magmatic differentiation processes in the various crustal levels on an arc system.

The Haib porphyry copper deposit is composed of coeval and comagmatic volcanic and plutonic rocks of the calc-alkaline Richtersveld Subprovince. The volcanic rocks, part of the Tsams Formation of the Orange River Group, are bimodal, interlayered and composed of aphyric rhyolite, phyric rhyolite, feldspar porphyry andesite and mafic tuff (Minnitt, 1979). The plutonic rocks, represented by a composite pluton termed the Vioolsdrif Intrusive Suite, intrudes the volcanic rocks of the Tsams Formation, and is composed of clinopyroxenite, gabbro, diorite, granodiorite, monzogranite, quartz-feldspar porphyry granodiorite and leucogranite (Minnitt, 1979). According to Minnitt (1979) and Meng et al. (2021), the Haib porphyry copper deposit represents the lower levels of a porphyry system (approximately 10-15 km). The solidus temperatures calculated for crystallization of the diorite using titanium-in-zircon thermometer is 768 ± 23 °C (Meng et al., 2021). For the purposes of this study the clinopyroxenite and gabbro form part of the Kokerboom Intrusion (Refer to Chapter 4). As indicated in chapter 4, the Kokerboom Intrusion forms part of the ultramafic component of the Vioolsdrif Intrusive Suite, the Vuurdood Subsuite.

The Rio-Mayo lower crustal cumulates have been selected for this study as the lower crustal cumulates represents one of the few cumulate localities that occur within the typical arc environment. The Rio-Mayo lower crustal cumulates are lithologically distinct and diverse,

characterized by a heterogenous assemblage of predominantly mafic-intermediate rocks including garnet clinopyroxenite, garnet-rich hornblende pyroxenite, garnet-rich olivine hornblende pyroxenite, garnet-rich olivine hornblende gabbro, tonalite gneiss and quart-rich granitoid gneiss. The solidus temperatures and pressures calculated for the Mercaderes-Rio Mayo lower crustal xenoliths are ~730-830 °C (hydrated assemblages), ~950-1050 °C (dry assemblages) and ~9-14 kbar (Weber, 1998).

This chapter investigates the whole rock iron isotope signature ($\delta^{56}Fe$) of the gabbros and clinopyroxenites from the Kokerboom Intrusion which is an intrusion within the Vuurdood Subsuite of the Vioolsdrif Intrusive Suite, the andesites and rhyolites from the Orange River Group, the diorites, granodiorites, monzogranites and leucogranites from the Vioolsdrif Intrusive Suite and the Rio-Mayo lower crustal cumulates in order to understand intra-crustal differentiation processes linked with garnet or amphibole fractionation. A portion of the Kokerboom Intrusion contains clinopyroxene- and amphibole-rich cumulates whereas, the Rio-Mayo lower crustal cumulates contains garnet-rich cumulates. The Kokerboom Intrusion potentially forms part of a mid-crustal Proterozoic porphyry copper deposit whereas, the Rio-Mayo lower crustal cumulates forms part of the deeper crustal levels of the Phanerozoic arc. Therefore, the Kokerboom Intrusion and Rio-Mayo lower crustal cumulates serve as parallels to compare the effect and significance of garnet and amphibole fraction in the lower and mid-crustal levels of an arc system. 10 representative samples were selected from the 21 samples of the Rio-Mayo lower crustal cumulates for the Fe isotope analyses.

The Rayleigh fractionation modelling conducted and presented in this chapter was constrained using the formula below:

$CL = Co*F^{(D-1)}$

Where;

CL= the concentration in the liquid

Co = the total concentration

F = the liquid remaining

D = the distribution co-efficient/fractionation factor

The bulk rock distribution co-efficient was calculated based on partition co-efficient data and the modal proportions for various minerals that comprise the cumulates (the Rio-mayo lower crustal cumulates and the Kokerboom Intrusion). The data of the partition co-efficients for the trace element modelling were obtained from Rollison (1993) and the proportion of mineral phases were based on petrographic observations. The inter-mineral fractionation factor that was used for the iron isotope modelling includes amphibole and magnetite pairs. These inter-mineral Fe isotopic fractionations were obtained from He et al. (2020). The parent rock magma trace element and Fe isotope compositions were obtained from the results of this study. The parent rock magma trace element and Fe isotope compositions are consistent with high temperature processes.

6.2. Results

The results presented in this chapter include petrographic observations for the Kokerboom Intrusion and Rio-Mayo lower crustal cumulates, whole rock geochemistry (major and trace elements analyses) and whole rock $\delta^{56}Fe$ isotope analyses for the Orange River Group, Vioolsdrif Intrusive Suite, Kokerboom Intrusion and Rio-Mayo lower crustal cumulates. These results, particularly the trace element and whole rock $\delta^{56}Fe$ isotope analyses are used to understand intra-crustal differentiation processes linked with garnet or amphibole fractionation. Rayleigh fractionation modelling was conducted on the bulk rock Yb values for Kokerboom Intrusion and Rio-Mayo lower crustal cumulates in order to understand the effect of amphibole and garnet fractionation (see discussion section 6.3.2.). Rayleigh fractionation modelling of the $\delta^{56}Fe$ composition for the Kokerboom Intrusion clinopyroxenite cumulates was conducted to show that the residual melt/fractionation of iron remaining in the melt evolves to heavier or elevated $\delta^{56}Fe$ compositions (see discussion section 6.3.7.).

6.2.1. Petrography

Petrographic observations were conducted to deduce the mineral and textural relationships of cumulate samples from the Kokerboom Intrusion and Rio-Mayo lower crustal cumulates. The Kokerboom Intrusion cumulates are composed of clinopyroxene, plagioclase, hornblende, quartz, apatite, rutile and magnetite whereas, the Rio-Mayo lower crustal cumulates are composed of garnet, plagioclase, clinopyroxene, orthopyroxene, hornblende, olivine, quartz, biotite, sphene and magnetite (Figure 6.1a and 1b). The rock types comprising the Kokerboom Intrusion vary in composition from gabbros to clinopyroxenites whereas, the rock types comprising the Rio-Mayo lower crustal cumulates are composed of pyroxenites (Figure 6.2).

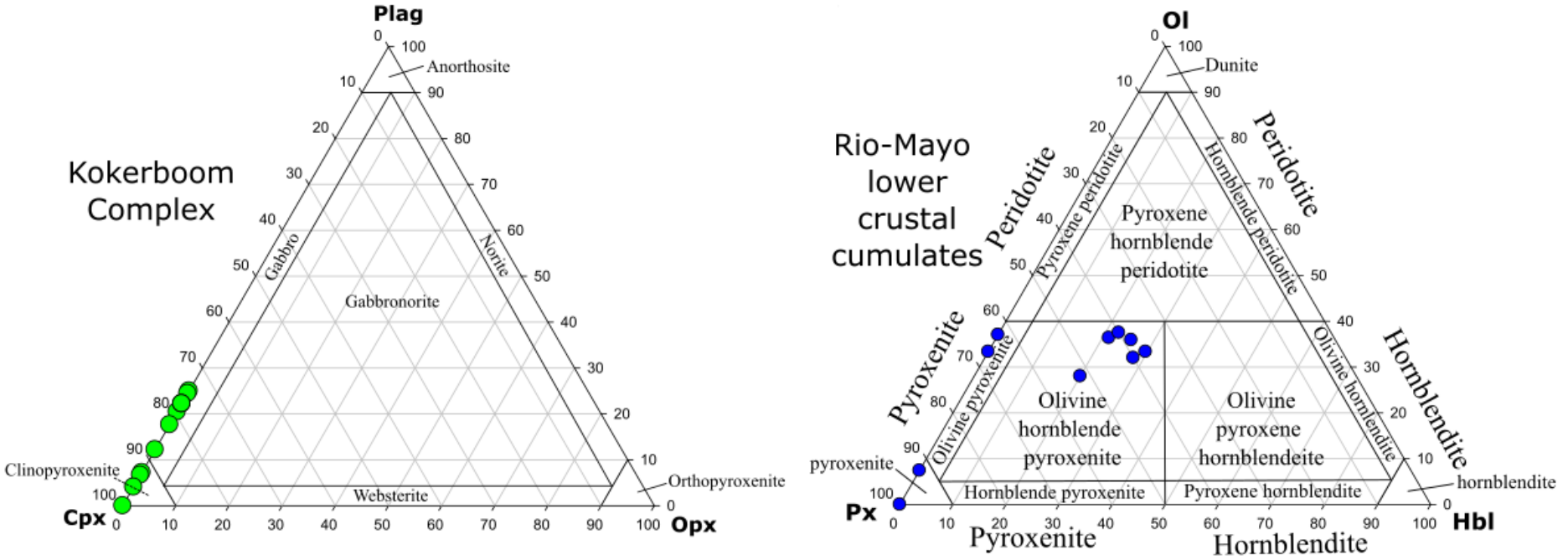

Figure 6.1: *Streckeisen classification diagrams for the Kokerboom Intrusion and Rio-Mayo lower crustal cumulates. The Kokerboom Intrusion ranges in composition from gabbros to clinopyroxenites whereas, the Rio-Mayo lower crustal cumulates is composed of a variety of pyroxenites.*

The Kokerboom Intrusion

A detailed petrographic and textural analyses of the Kokerboom Intrusion samples can be found in Chapter 4 and Appendix C. The general petrography for the Kokerboom Intrusion shows that the coarse grained (5 mm) cumulus clinopyroxene is altered to actinolite and hornblende, whereas plagioclase is interstitial and is altered to sericite and epidote (Figure 6.2). There is also intercumulus primary hornblende present which is altered to chlorite and epidote. Clinopyroxene and hornblende also have inclusions of magnetite, quartz, apatite and rutile (Figure 6.2). Clinopyroxene, hornblende and actinolite exhibit exsolution lamellae and simple twinning. Quartz is a minor component and occurs as anhdedral grains with distinct undulose extinction. Disseminated magnetite is also found close to chlorite and epidote mineral assemblages. Disseminated chalcopyrite is prevalent as well. As established in chapter 4, the Kokerboom Intrusion represents mid-crustal cumulate material (~12 km depth) that hosts significant sulphides (chalcopyrite).

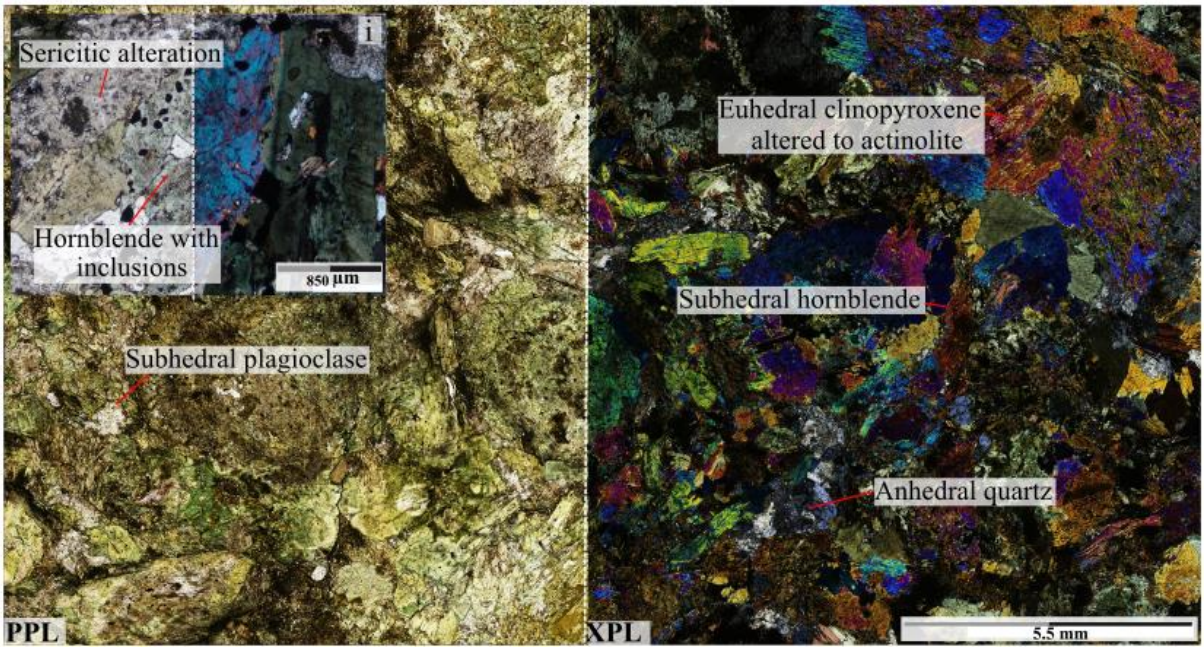

Figure 6.2: *A representative photomicrograph of the Kokerboom Intrusion cumulates illustrating cumulus subhedral to euhedral clinopyroxene and intercumulus hornblende and plagioclase. Inset i shows subhedral to euhedral hornblende with inclusions of magnetite and quartz.*

The Rio-Mayo lower crustal cumulates

Garnet clinopyroxenite

The garnet clinopyroxenite is medium-coarse grained (1-5 mm), heteradcumulate and is composed of garnet (45%), clinopyroxene (25%), biotite (20%), spinel (4%), apatite (4%), and opaques: rutile and magnetite (2%) (Figure 6.3). The intercumulus subhedral to euhedral garnet is highly fractured, zoned and consist of clinopyroxene and apatite inclusions. The cumulus to intercumulus subhedral clinopyroxene contains garnet, biotite, spinel and apatite inclusions. Kelyphitic reaction rims are present along both garnet and clinopyroxene grain boundaries. Spinel has a distinct massive texture occurring interstitially between various mineral phases. Apatite is subhedral, elongate and occurs as inclusions within various mineral phases including garnet and clinopyroxene. Disseminated magnetite and rutile occur as inclusions in garnet, clinopyroxene and biotite.

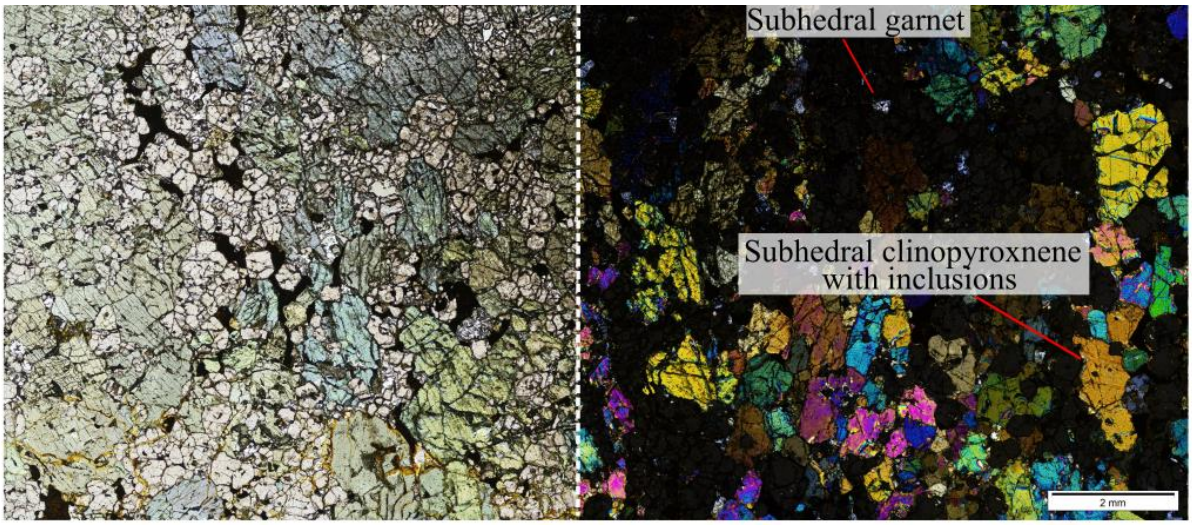

Figure 6.3: *Plane (left) and cross-polarized (right) photomicrographs of the garnet clinopyroxenite. The intercumulus subhedral to euhedral garnet is highly fractured, zoned and consists of clinopyroxene and apatite inclusions. The cumulus to intercumulus subhedral clinopyroxene consists of garnet, biotite, spinel and apatite inclusions.*

Garnet-rich hornblende pyroxenite

The garnet-rich hornblende pyroxenite is medium-coarse (~2.5 mm), orthocumulate and is composed of garnet (~42%), clinopyroxene (~17%), hornblende (~12%), orthopyroxene (~8%), plagioclase (~5%), quartz (~5%), apatite (~3%), spinel (~3%), sphene (~3%) and magnetite (~2%) (Figure 6.4). The cumulus to intercumulus subhedral to euhedral garnet occurs with hornblende and has inclusions of magnetite, apatite and quartz. Intercumulus subhedral clinopyroxene is fractured and is found close to orthopyroxene. Subhedral hornblende has inclusions of quartz, apatite and opaques. Both garnet and hornblende have reaction rims around grain boundaries which are composed of spinel. Spinel is in close relation to various mafic phases whereas sphene occurs with clinopyroxene.

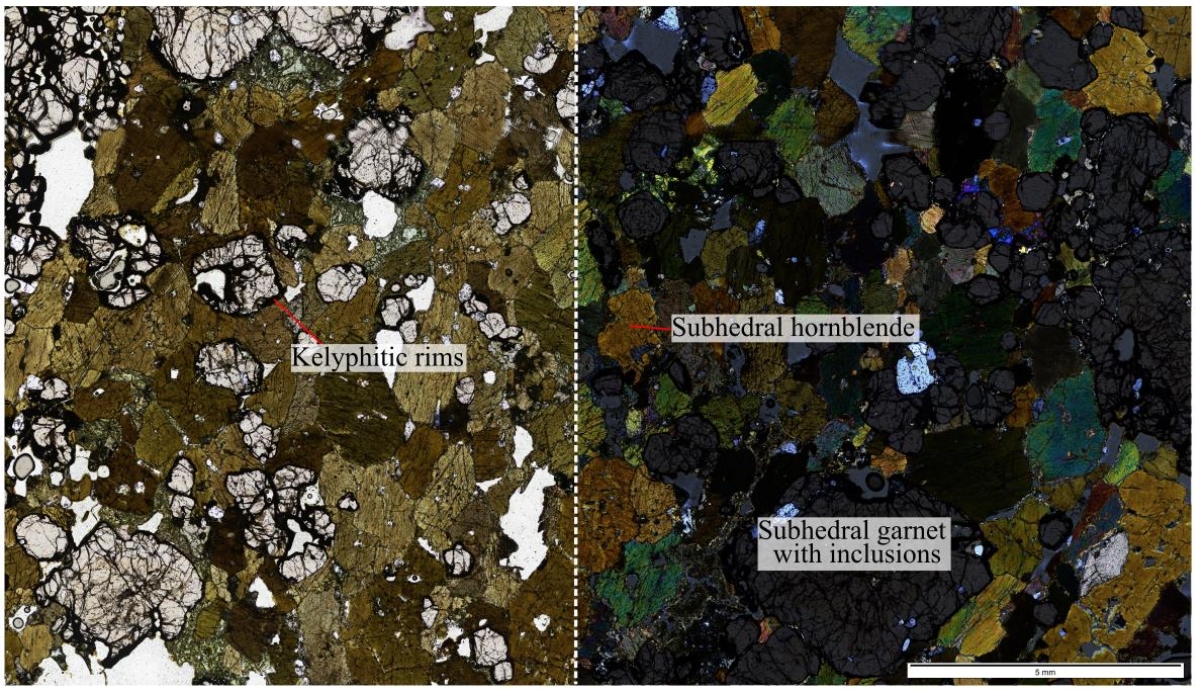

Figure 6.4: *Plane (left) and cross-polarized (right) photomicrographs of the garnet-rich hornblende pyroxenite. The cumulus to intercumulus subhedral to euhedral garnet occurs with hornblende and has inclusions of magnetite, apatite and quartz. Kelyphitic rims are distinct.*

Garnet-rich olivine hornblende pyroxenite

The garnet-rich olivine hornblende pyroxenite is medium-coarse grained (~2.5 mm) hereradcumulate and is composed of garnet (54%), clinopyroxene (14%), orthopyroxene (12%), hornblende (10%), olivine (7%), biotite (2%) and magnetite (1%) (Figure 6.5). The intercumulus subhedral to euhedral garnet has minor reaction rims composed of spinel and pyroxene. Cumulus subhedral clinopyroxene occurs with orthopyroxene and exhibits exsolution lamellae. Cumulus subhedral hornblende is found with garnet and pyroxene mineral assemblages. Cumulus subhedral olivine occurs with clinopyroxene, is highly fractured and altered to serpentine. Subhedral biotite has inclusions of magnetite.

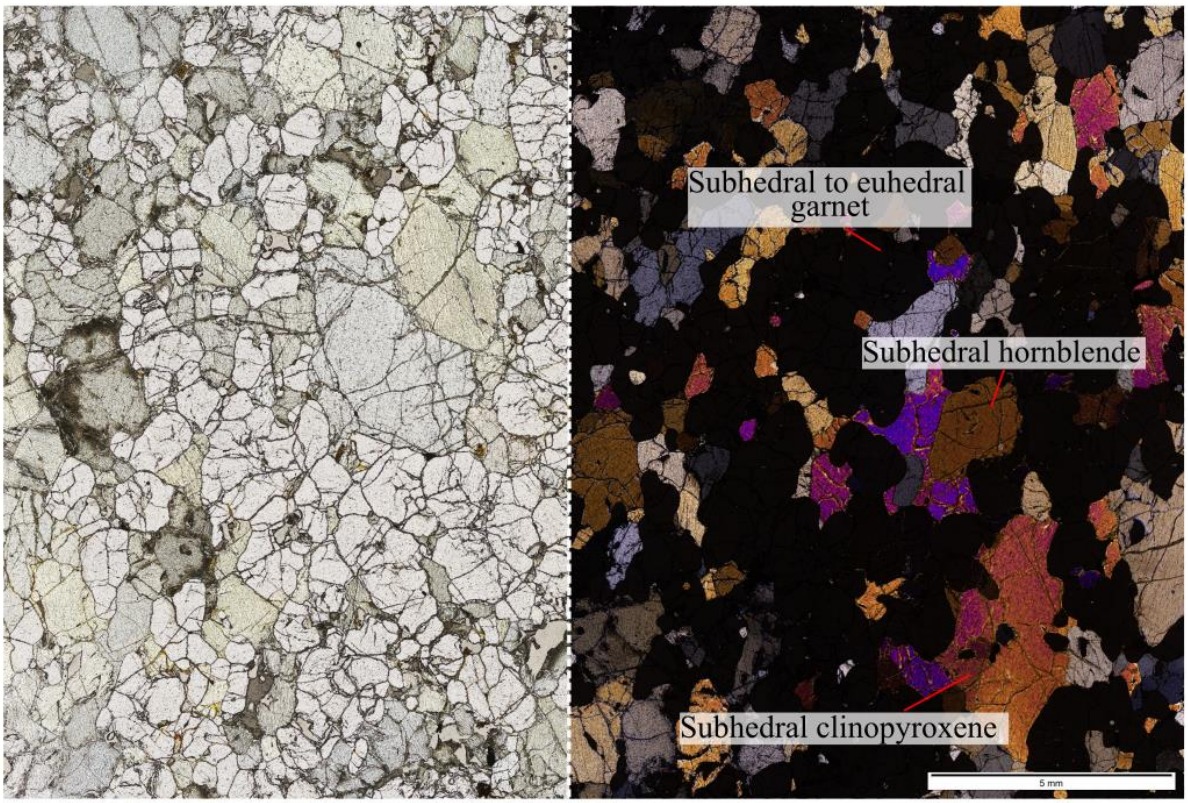

Figure 6.5: *Plane (left) and cross-polarized (right) photomicrographs of the garnet-rich hornblende olivine pyroxenite. The intercumulus subhedral to euhedral garnet has minor reaction rims. Cumulus subhedral hornblende is found with garnet and pyroxene.*

Garnet-rich olivine hornblende gabbro

The garnet-rich plagioclase bearing olivine hornblende pyroxenite is medium-coarse (~3 mm), orthocumulate and is composed of garnet (35%), plagioclase (15%), clinopyroxene (14%), orthopyroxene (8%), hornblende (8%), olivine (8%), quartz (5%), biotite (2%), sphene (2%), apatite (2%) and magnetite (1%) (Figure 6.6). The cumulus to intercumulus subhedral to euhedral garnet is fractured, exhibits corona textures and consists of clinopyroxene, apatite, magnetite and quartz inclusions. In certain areas the garnet is embayed and xenomorphic. The cumulus to intercumulus subhedral clinopyroxene exhibits exsolution lamellae and is replaced by secondary hornblende. Primary hornblende is subhedral to euhedral with quartz and apatite inclusions. Cumulus subhedral to anhedral olivine generally occurs with clinopyroxene and orthopyroxene. Euhedral quartz has a distinct undulose extinction. Subhedral biotite has inclusions of magnetite forming a poikilitic texture.

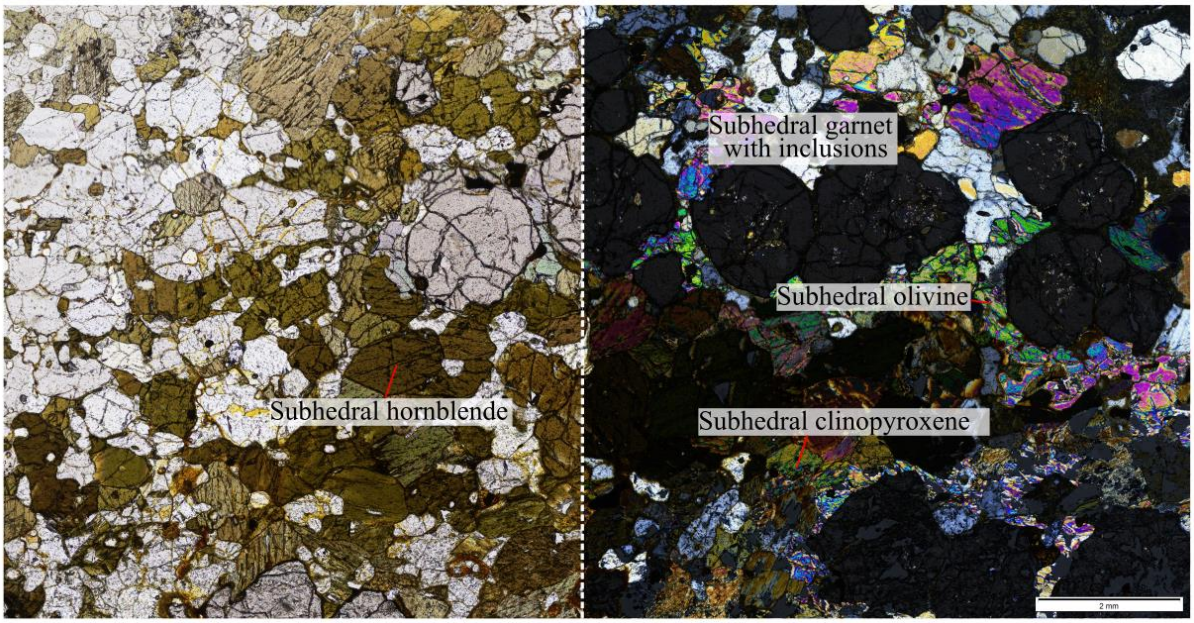

Figure 6.6: *Plane (left) and cross-polarized (right) photomicrographs of the garnet-rich plagioclase bearing olivine hornblende pyroxenite. A distinct feature is the cumulus to intercumulus subhedral to euhedral garnet with inclusions of clinopyroxene, apatite, magnetite and quartz.*

Tonalite gneiss

The tonalite gneiss is medium-coarse (~2 mm), mesocumulate and is composed of plagioclase (27%), quartz (22%), clinopyroxene (15%), orthopyroxene (10%), hornblende (8%), garnet (7%), biotite (4%), chlorite (2%), spinel (2%), apatite (2%) and magnetite (1%) (Figure 6.7). The intercumulus subhedral to euhedral plagioclase is zoned, altered to epidote, and exhibits a distinct undulose extinction. Intercumulus subhedral clinopyroxene is in close relation with orthopyroxene, has exsolution lamellae and is altered to hornblende. Intercumulus subhedral to euhedral garnet has inclusions of magnetite and quartz. Subhedral to anhedral biotite is altered to chlorite and contains opaque material.

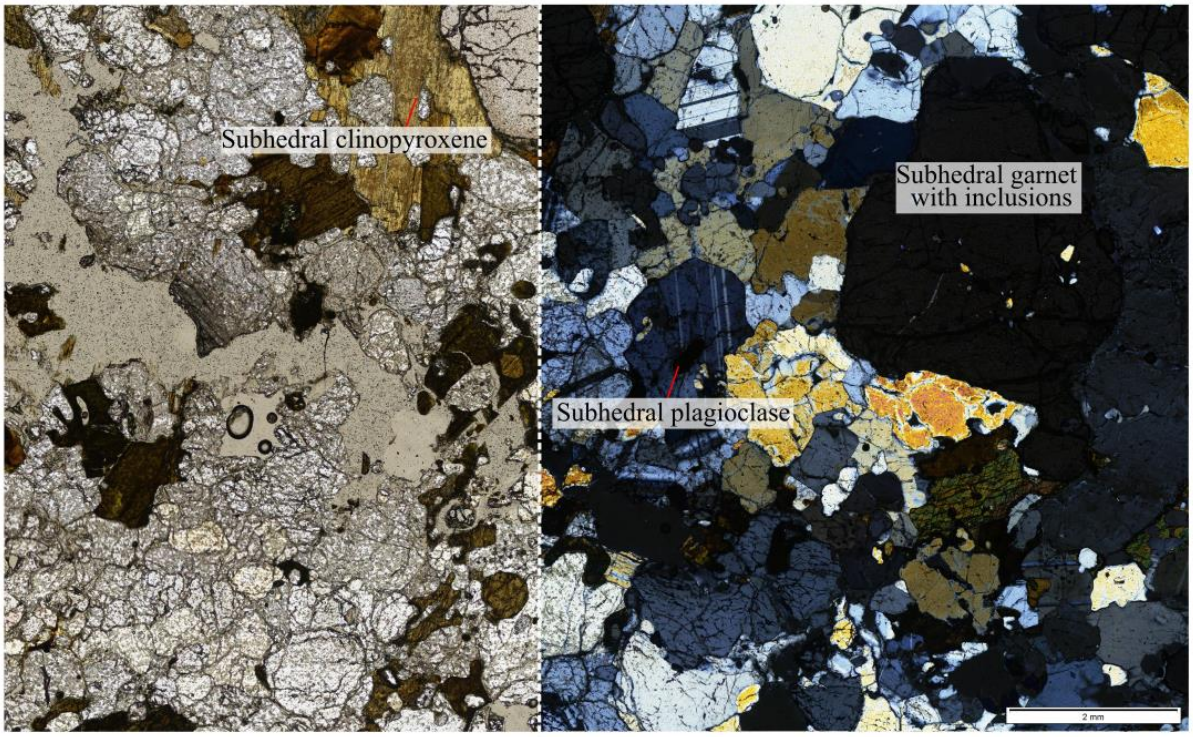

Figure 6.7: *Plane (left) and cross-polarized (right) photomicrographs of the tonalite gneiss. The intercumulus subhedral to euhedral plagioclase is zoned and exhibits a distinct undulose extinction in certain areas. Intercumulus subhedral to euhedral garnet has inclusions of magnetite and quartz.*

Quartz-rich granitoid gneiss

The quartz-rich granitoid gneiss is medium-coarse (~3 mm), orthocumulus and is composed of quartz (40%), garnet (25%), plagioclase (15%), clinopyroxene (8%), orthoclase (5%), scapolite (4%), apatite (2%) and opaques: magnetite (1%) (Figure 6.8). The cumulus anhedral quartz is irregular and displays a distinct undulose extinction. Intercumulus subhedral to euhedral garnet has inclusions of quartz, spinel, plagioclase and magnetite. Plagioclase is subhedral and exhibits an undulose extinction. Intercumulus subhedral scapolite occurs with apatite whereas, spinel is anhedral and occurs as inclusions in various mafic phases.

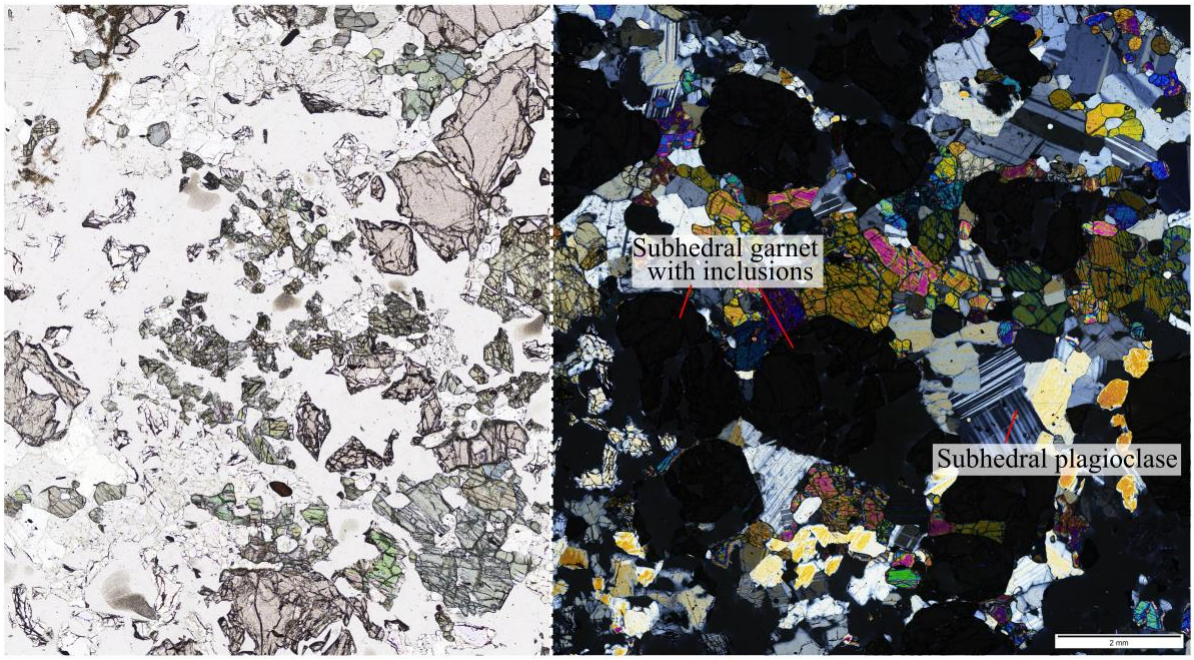

Figure 6.8: *Plane (left) and cross-polarized (right) photomicrographs of the quartz-rich granitoid gneiss. Intercumulus subhedral to euhedral garnet has inclusions of quartz, spinel, plagioclase and magnetite. Plagioclase is subhedral and exhibits an undulose extinction.*

6.2.2. Major element analyses

The Harker variation diagrams illustrate that there is a consistent trend from the Orange River Group and Vioolsdrif Intrusive Suite to the Vuurdood Subsuite. For the data presented here, the Orange River Group consists of rhyolites and andesites, the Vioolsdrif Intrusive Suite consists of diorites, granodiorites, monzogranites and leucogranites and the mafic-ultramafic units are grouped into the Vuurdood Subsuite which forms part of the Vioolsdrif Intrusive Suite. From variation diagrams it is clear that the Al_2O_3, TiO_2, MgO, Fe_2O_3, CaO and MnO compositions gradually decrease with increasing SiO_2 from mafic to felsic compositions whereas, the Na_2O and K_2O compositions show a gradual increase with increasing SiO_2. (Figure 6.9). However, a few analyses of the Vuurdood Subsuite have lower concentrations of Al_2O_3 (0.25-10 wt %) and TiO_2 (0-1.5 wt %) compositions. The SiO_2 compositions for the Orange River Group and Vioolsdrif Intrusive Suite ranges from 50-60 wt % whereas, the SiO_2 compositions for the Vuurdood Subsuite ranges from 30-60 wt %. The Al_2O_3, TiO_2, MgO, Fe_2O_3, CaO and MnO compositions for the Orange River Group and Vioolsdrif Intrusive Suite decreases from 60-30 wt %, 1-0 wt %, 10-0 wt %, 8-0 wt %, 10-0 wt %, 0.2-0 wt % respectively with increasing SiO_2 whereas, Na_2O and K_2O compositions for the Orange River Group and Vioolsdrif Intrusive Suite increases from 0-8 wt % and 1-3 wt % respectively with increasing SiO_2. The Al_2O_3, TiO_2, MgO, Fe_2O_3, CaO and MnO compositions for Vuurdood Subsuite decreases from 25-0 wt %, 1.5-0 wt %, 40-0 wt %, 16-4 wt %, 16-0 wt %, 0.05-0.25 wt % respectively with increasing SiO_2 whereas, the Na_2O and K_2O compositions for the Orange River Group and Vioolsdrif Intrusive Suite increases from 0-4 wt % and 0-4 wt % respectively with increasing SiO_2. The AFM plot of the Orange River Group, Vioolsdrif Intrusive Suite, and Vuurdood Subsuite show that the Orange River Group and Vioolsdrif Intrusive Suite plot in the calc-alkaline field whereas, the Vuurdood Subsuite plot both in the calc-alkaline and tholeiitic fields of the AFM plot (Figure 6.10). From the AFM plot the alkali's, iron oxide and magnesium oxide composition ranges from 0-80, 0-50 and 0-60 respectively for the Orange River Group and Vioolsdrif Intrusive Suite. The alkali's, iron oxide and magnesium oxide composition ranges from 0-35, 20-65 and 20-80 respectively for the Vuurdood Subsuite.

The Harker variation diagrams illustrate that there is a consistent trend from the mafic to felsic compositions of the Rio-Mayo lower crustal cumulates. The variation diagrams show that the Al_2O_3, TiO_2, MgO, Fe_2O_3, CaO and MnO compositions gradually decreases with increasing SiO_2 from mafic to felsic compositions whereas, the Na_2O and K_2O compositions show a gradual increase with increasing SiO_2. (Figure 6.11). The SiO_2 compositions for the Rio-Mayo lower crustal cumulates ranges from 40-65 wt %. The Al_2O_3, TiO_2, MgO, Fe_2O_3, CaO and MnO compositions for the Rio-Mayo lower crustal cumulates decreases from 20-2 wt %, 2.5-0 wt %, 25-5 wt %, 20-4 wt %, 16-5 wt %, 0.4-0.1 wt % respectively with increasing SiO_2 whereas, the Na_2O and K_2O compositions for the Rio-Mayo lower crustal cumulates increases from 0-6 wt % and 0-1 wt % respectively with increasing SiO_2. The AFM plot shows that the Rio-Mayo lower crustal cumulates plots in both the calc-alkaline and tholeiitic fields (Figure 6.10). The alkali's, iron oxide and magnesium oxide composition ranges from 0-50, 20-70 and 18-73 respectively for the Rio-Mayo lower crustal cumulates. The Andes arc magmas both "normal" and "thick" crust as well as the igneous plutonic rocks are plotted for comparison purposes.

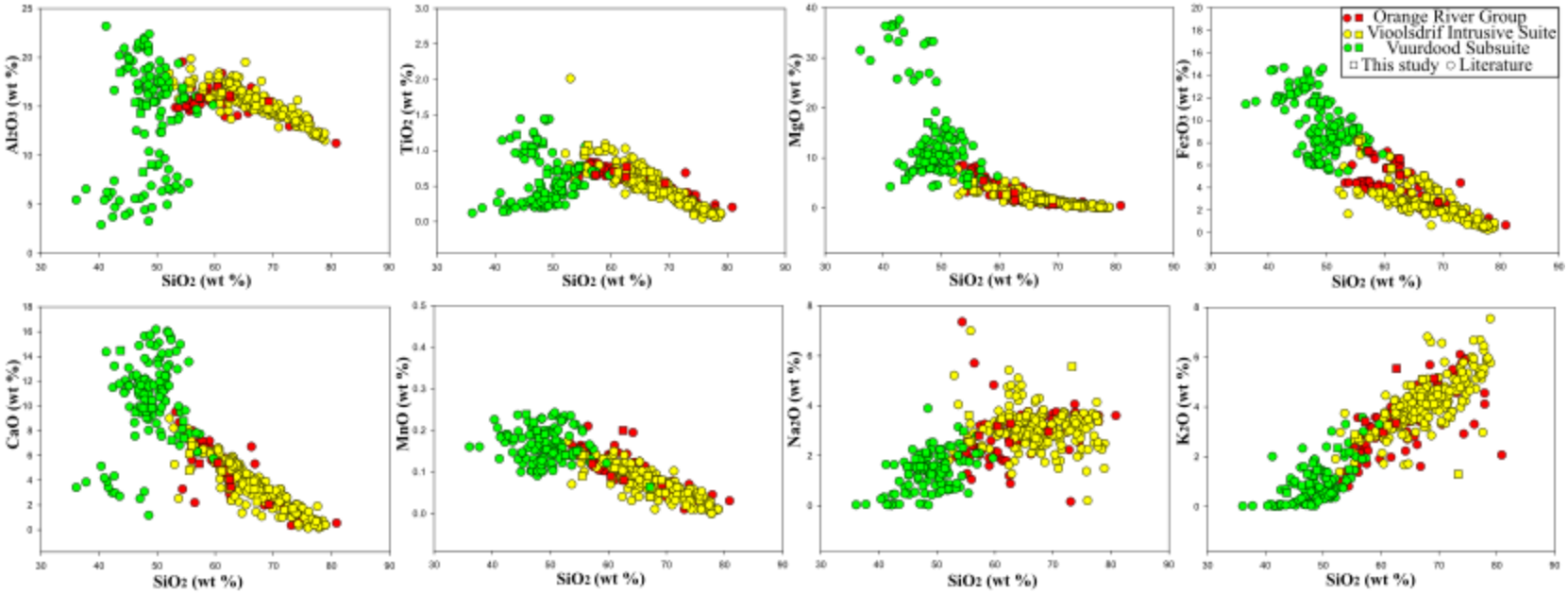

Figure 6.9: *The Harker variation diagrams show that from the Orange River Group and Vioolsdrif Intrusive Suite to the Vuurdood Subsuite, the Al_2O_3, TiO_2, MgO, Fe_2O_3, CaO and MnO compositions gradually decreases with increasing SiO_2 from mafic to felsic compositions whereas, the Na_2O and K_2O compositions show a gradual increase with increasing SiO_2. Data from literature includes results from Macey et al. (2017).*

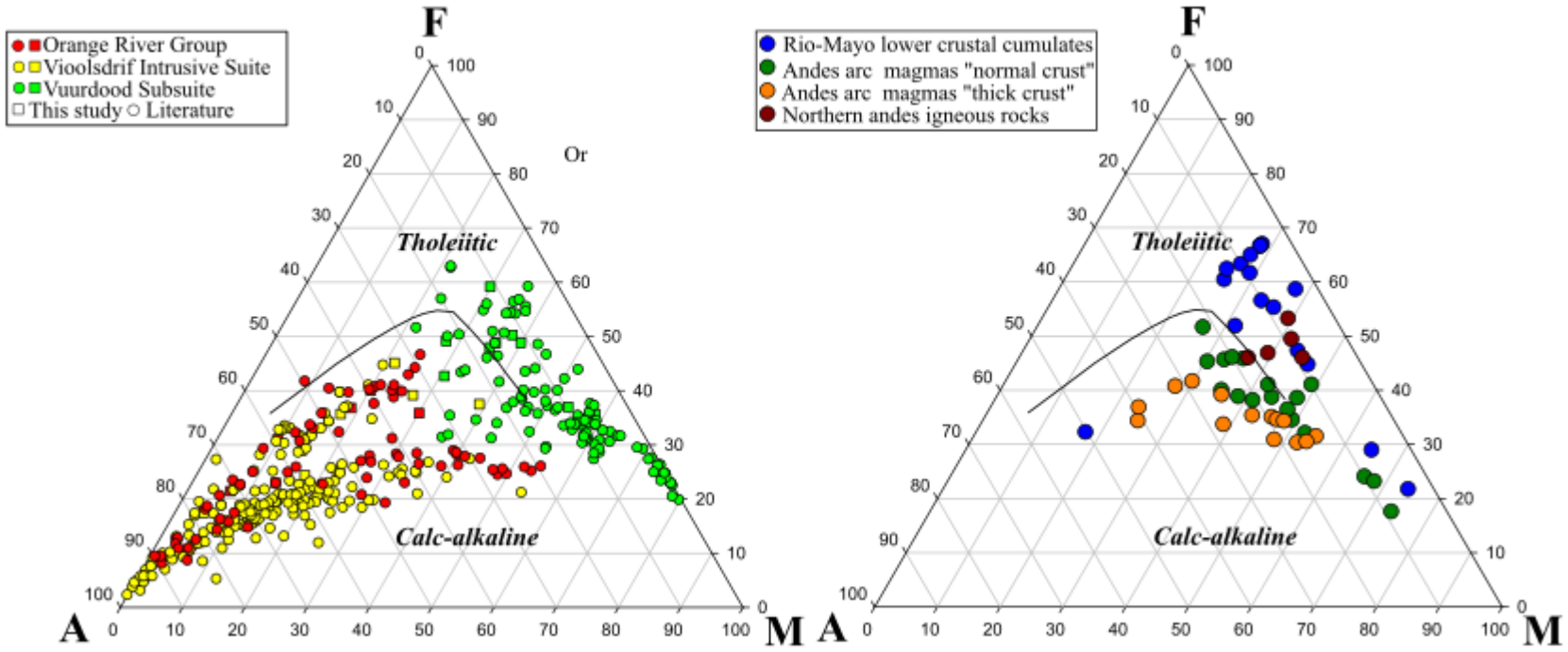

Figure 6.10: *The AFM plots of the Orange River Group, Vioolsdrif Intrusive Suite, Vuurdood Subsuite and Rio-Mayo lower crustal cumulates show that the Orange River Group and Vioolsdrif Intrusive Suite plot in the calc-alkaline field whereas, the Vuurdood Subsuite and Rio-Mayo lower crustal cumulates plot both in the calc-alkaline and tholeiitic fields of the AFM plot. The Andes arc magmas both "normal" and "thick" crust as well as the igneous plutonic rocks are plotted for comparative purposes.*

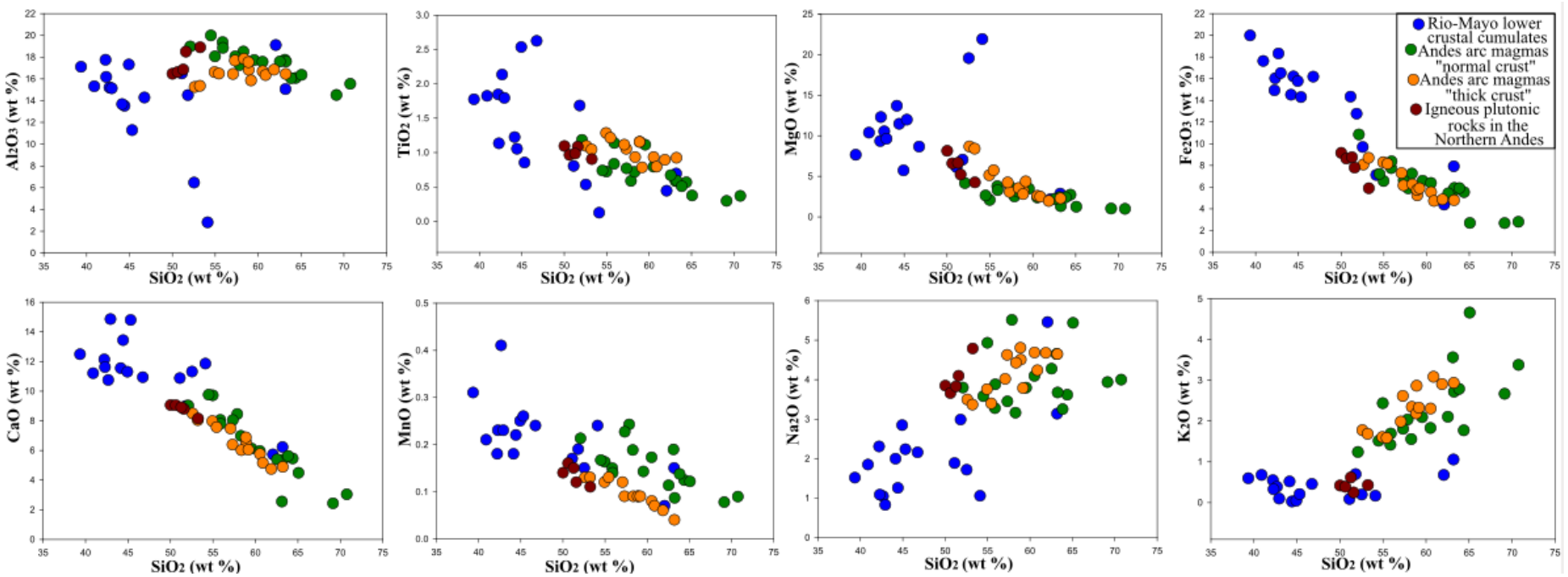

Figure 6.11: *The Harker variation diagrams for the Rio-Mayo lower crustal cumulates. The Al_2O_3, TiO_2, MgO, Fe_2O_3, CaO and MnO compositions gradually decreases with increasing SiO_2 from mafic to felsic compositions whereas, the Na_2O and K_2O compositions show a gradual increase with increasing SiO_2. The Andes arc magmas both "normal" and "thick" crust as well as the igneous plutonic rocks in the Northern Andes are plotted for comparison purposes.*

6.2.3. Trace element analyses

REE plots were made to constrain the effect of amphibole and garnet fractionation. Variation diagrams for the various trace elements were developed to further constrain and understand garnet and amphibole fractionation. Elements such as Y and Yb were specifically selected due to the affinity these elements have for amphibole and more specifically garnet.

The chondrite normalized REE patterns of the Haib porphyry copper deposit show distinct listric shaped REE patterns (Figure 6.12). The REE patterns for the Orange River Group and Vioolsdrif Intrusive Suite are enriched in LREE relative to the HREE with negative Eu anomalies present (Figure 6.12). The Kokerboom Intrusion has a lower overall concentration of REE and flatter slope compared to the Orange River Group and Vioolsdrif Intrusive Suite. The La_N/Lu_N, La_N/Sm_N, Gd_N/Lu_N ratios for the Orange River Group ranges from 8-15, 3.2-3.8 and 1.7-2.4. The La_N/Lu_N, La_N/Sm_N, Gd_N/Lu_N ratios for the Vioolsdrif Intrusive Suite ranges from 10-12, 3-5 and 1.5-2. The La_N/Lu_N, La_N/Sm_N, Gd_N/Lu_N ratios for the Kokerboom Intrusion ranges from 5.5-6, 1.9-2 and 1.95-1.98. The Eu/Eu^* anomalies for the Orange River Group, Vioolsdrif Intrusive Suite and Kokerboom Intrusion ranges from 0.7-0.8, 0.5-0.9 and 0.8-0.9 respectively.

The Rio-Mayo lower crustal cumulates show relatively flat REE patterns (Figure 6.12). The REE patterns for the Rio-Mayo lower crustal cumulates are slightly enriched in HREE relative to LREE with negative Eu and Ce anomalies present (Figure 6.12). The La_N/Lu_N, La_N/Sm_N, Gd_N/Lu_N ratios for the Rio-Mayo lower crustal cumulates ranges from 0.4-14, 0.4-3 and 1-2 respectively. The Eu/Eu^* and Ce/Ce^* anomalies range from 0.61-1 and 0.5-1.

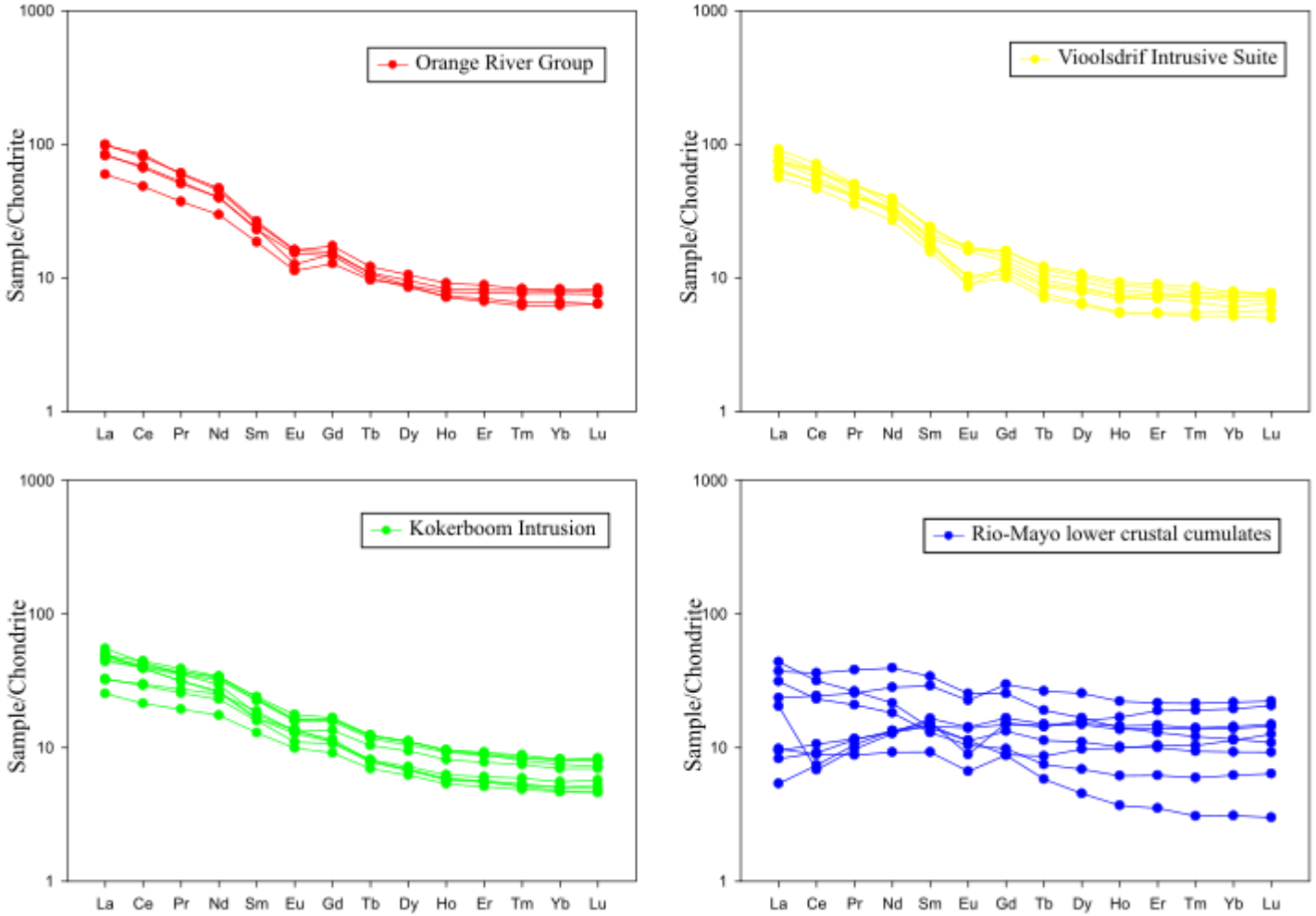

Figure 6.12: *The REE patterns for the Orange River Group, Vioolsdrif Intrusive Suite, Kokerboom Intrusion and Rio-Mayo lower crustal cumulates. The REE patterns for the Orange River Group and Vioolsdrif Intrusive Suite show distinct listric shaped patterns whereas, the REE for the Kokerboom Intrusion has a lower overall concentration and flatter slope compared to the Orange River Group and Vioolsdrif Intrusive Suite.*

The MgO vs. La/Yb plot for the Haib porphyry deposit show a distinct increase in La/Yb with decreasing MgO from the Kokerboom Intrusion to the Orange River Group and Vioolsdrif Intrusive Suite (Figure 6.13). The approximate La/Yb ratio for the Kokerboom Intrusion is between 5 and 20 whereas, the La/Yb ratio for the Orange River Group and Vioolsdrif Intrusive Suite is between 10 and 30. The MgO concentration ranges between 4-18 wt % and 0-6 wt % for the Kokerboom Intrusion and for both the Orange River Group and Vioolsdrif Intrusive Suite respectively (Figure 6.13). The Yb vs. La/Yb plot does not show a consistent trend. The Yb concentration (ppm) ranges between 1-2 ppm for the Kokerboom Intrusion and between 0.5-3 for the Orange River Group and Vioolsdrif Intrusive Suite (Figure 6.13). The SiO_2 vs. La/Yb plot shows an increase in La/Yb with increasing SiO_2. The SiO_2 concentration ranges from 40-60 wt % for the Kokerboom Intrusion and 55-60 wt % for the Orange River Group and Vioolsdrif Intrusive Suite respectively (Figure 6.13). Again, the approximate La/Yb ratio for the Kokerboom Intrusion is between 5 and 20 whereas, the La/Yb ratio for the Orange River Group and Vioolsdrif Intrusive Suite is between 10 and 30 (Figure 6.13). The SiO_2 vs. Sr/Y plot shows a decrease in Sr/Y with increasing SiO_2. The Sr/Y ratio for the Kokerboom Intrusion ranges from 55-40 whereas, the La/Yb ratio for the Orange River Group and Vioolsdrif Intrusive Suite ranges from 55-80 wt %. The Y vs. Sr/Y plot does not show a consistent trend (Figure 6.13). The SiO_2 vs. Yb, Sr and Y plots show positive linear correlations. As the SiO_2 concentration increases, the Yb, Sr and Y concentrations decrease (Figure 6.13).

The MgO vs. La/Yb plot for the Andes arc magmas (traversing normal and thickened arc crust) and lower crustal cumulates show a distinct increase in La/Yb from the Rio-Mayo lower crustal cumulates to the Tongde dikes followed by the Andes arc magmas (Figure 6.14). The data for the Tongde dikes and Andes arc magmas are from literature and were plotted for comparison purposes in order to illustrate the garnet fractionation trend in thickened arc settings. The Tongde dikes are emplaced into the Proterozoic rocks of the Yangtze Block located in South China (Li et al., 2021). The approximate La/Yb ratio for the Rio-Mayo lower crustal cumulates is between 0 and 30 whereas, the La/Yb ratio for the Tongde dikes is between 0 and 30. The approximate La/Yb ratio for the Andes arc magmas is between 10 and 70. The magmas traversing normal arc crust is between 10 and 20 whereas, the magmas traversing thickened arc crust is between 15 and 70. The MgO concentration ranges between 0-20 wt %, 2-13 wt %, 0-5 wt % and 0-10 wt % for the Rio-Mayo lower crustal cumulates, Tongde dikes, magmas traversing normal arc crust and magmas traversing thickened arc crust respectively (Figure 6.14). The Yb vs. La/Yb plot shows that there is a decrease from the Tongde dikes to the Rio-Mayo lower crustal cumulates (Figure 6.14). As the Yb concentration increases, the La/Yb ratio decreases. The Yb concentration for the Rio-Mayo lower crustal cumulates ranges from 1-5 ppm (Figure 6.14). The SiO_2 vs. La/Yb and SiO_2 vs. Sr/Y plots show no distinct trends. The SiO_2 wt % for the Rio-Mayo lower crustal cumulates ranges from 40-65 wt % (Figure 6.14). The Y vs. Sr/Y plot shows a distinct trend from the Rio-Mayo lower crustal cumulates to the Tongde dikes and Andes arc magmas traversing thickened arc crust (Figure 6.14). As the Y concentration increases, the Sr/Y ratio decreases (Figure 6.14). The Y concentration and Sr/Y ratio ranges between 10-50 ppm and 0-160 respectively for the Rio-Mayo lower crustal cumulates. The SiO_2 vs. Yb, Sr and Y plots shows no consistent trends. However, the Yb and Y concentrations for the Rio-Mayo lower crustal cumulates are relatively high ranging between 0.5-6 ppm and 5-60 ppm respectively (Figure 6.14).

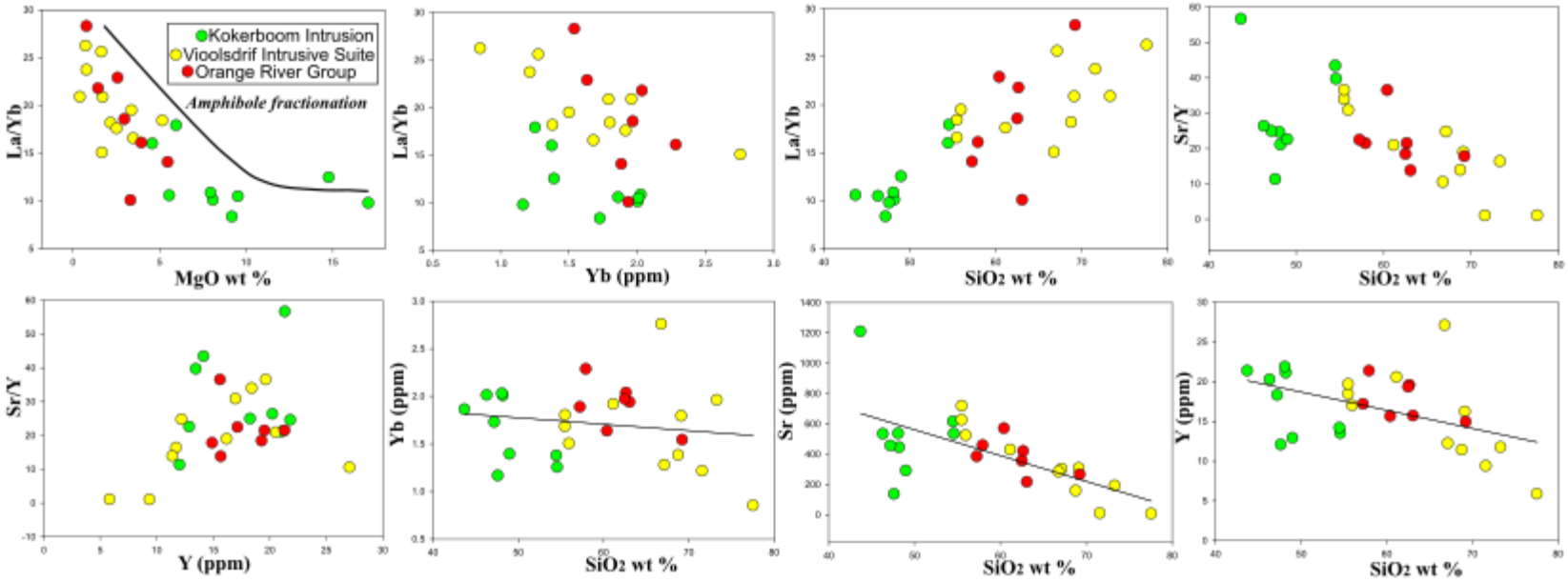

Figure 6.13: *Several trace element (concentrations and ratios) diagrams and in some cases major element vs. trace elements (concentrations and ratios) diagrams illustrating various trends for the Orange River Group, Vioolsdrif Intrusive Suite and Kokerboom Intrusion. An important trend is observed in the MgO vs. La/Yb plot, there is an increase in La/Yb with decreasing MgO from the Kokerboom Intrusion to the Orange River Group and Vioolsdrif Intrusive Suite. The line in the MgO vs. La/Yb plot represents the typical amphibole fractionation trend. Other important trends observed are depicted in the SiO_2 vs. Yb and Y plots as positive linear correlations are shown. As the SiO_2 concentration increases, the Yb and Y concentrations decrease.*

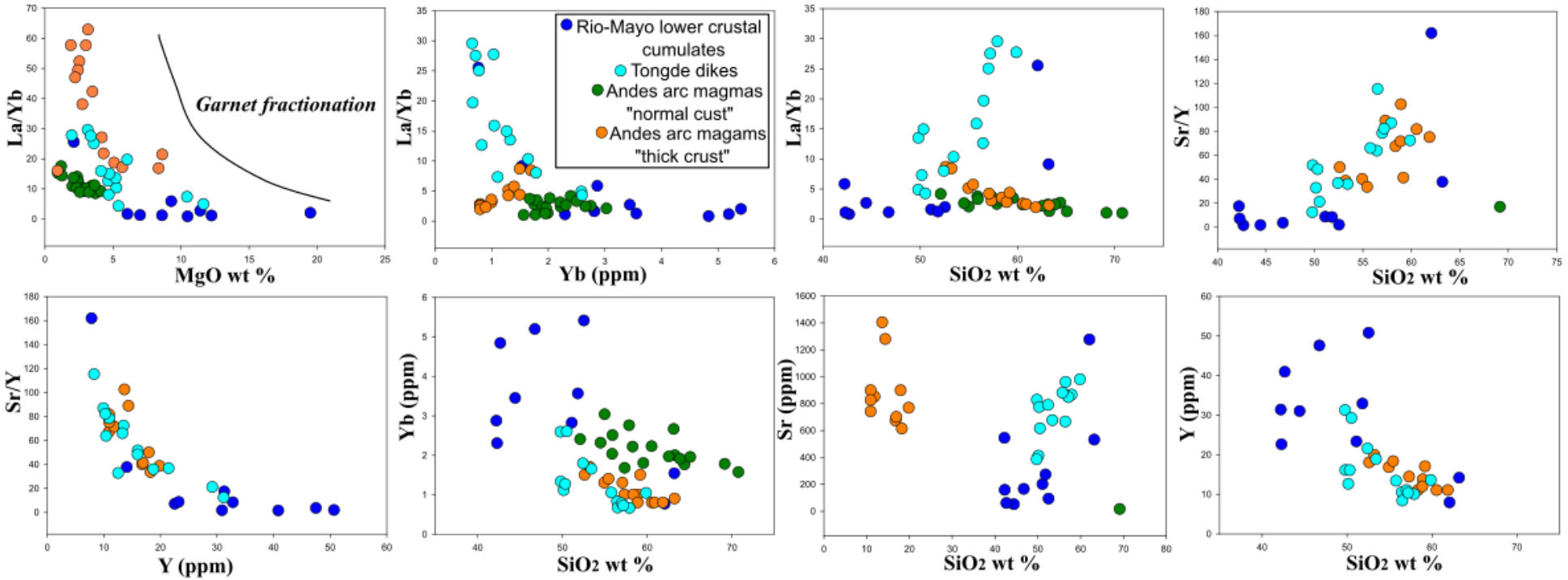

Figure 6.14: *Several trace element (concentrations and ratios) diagrams and some cases major element diagrams vs. trace elements (concentrations and ratios) illustrating various trends for the Rio-Mayo lower crustal cumulates. Again, the Andes arc magmas both "normal" and "thick" crust as well as the igneous plutonic rocks in the Northern Andes are plotted for comparison purposes. The MgO vs. La/Yb plot for the Andes arc magmas (traversing normal and thickened arc crust) and lower crustal cumulates show a distinct increase in La/Yb from the Rio-Mayo lower crustal cumulates to the Tongde dikes followed by the Andes arc magmas. The line in the MgO vs. La/Yb plot represents the typical garnet fractionation trend. The other plots illustrate various trends as well. A noteworthy observation is the elevated Yb and Y concentrations for the Rio-Mayo lower crustal cumulates with concentrations ranging between 0.5-6 ppm and 5-60 ppm respectively. The Tongde dikes are emplaced into the Proterozoic rocks of the Yangtze Block located in South China. The Tongde dikes are basaltic to andesitic in composition and consist of calc-alkaline rocks that are related to the fractional crystallization of garnet-bearing assemblages in the lower crust under high pressures.*

6.2.4. δ^{56}Fe isotope analyses

The δ^{56}Fe isotope diagram shows that the Kokerboom Intrusion has a lower δ^{56}Fe signature relative to the δ^{56}Fe isotope for the Vioolsdrif Intrusive Suite which is followed by the δ^{56}Fe isotope for the Orange River Group (Figure 6.15 and 6.16). The average δ^{56}Fe signature for the Kokerboom Intrusion is 0.03 ± 0.07 ‰ (n=3) whereas the average δ^{56}Fe signature for the Vioolsdrif Intrusive Suite is 0.20 ± 0.07 ‰ (n=5). The average δ^{56}Fe signature for the Orange River Group is 0.30 ± 0.07 ‰ (n=5). The Rio-Mayo lower crustal cumulates have an average δ^{56}Fe signature of 0.17 ± 0.07 ‰ (n=10) and the overall range overlaps with the Kokerboom Intrusion, Orange River Group and Vioolsdrif Intrusive Suite (Figure 6.15 and 6.16). The ranges in the δ^{56}Fe isotope data for the Orange River Group, Vioolsdrif Intrusive Suite, Kokerboom Intrusion and Rio-Mayo lower crustal cumulates are 0.25-0.34 ± 0.07 ‰, 0.09-0.29 ± 0.07 ‰, -0.07-0.15 ± 0.07 ‰ and -0.01-0.24 ± 0.07 ‰ respectively.

From the statistical analyses conducted (refer to Appendix L), it is clear that the Kokerboom Intrusion has a lower δ^{56}Fe average (mean) compared to the Orange River Group and Vioolsdrif Intrusive Suite (refer to Appendix L). This pattern observed is also applicable to the lower (25 %), middle (50 %), and upper (75 %) quartiles for the Kokerboom Intrusion, Orange River Group and Vioolsdrif Intrusive Suite. Refer to figure 6.16 for the box plot representation of the statistical analyses.

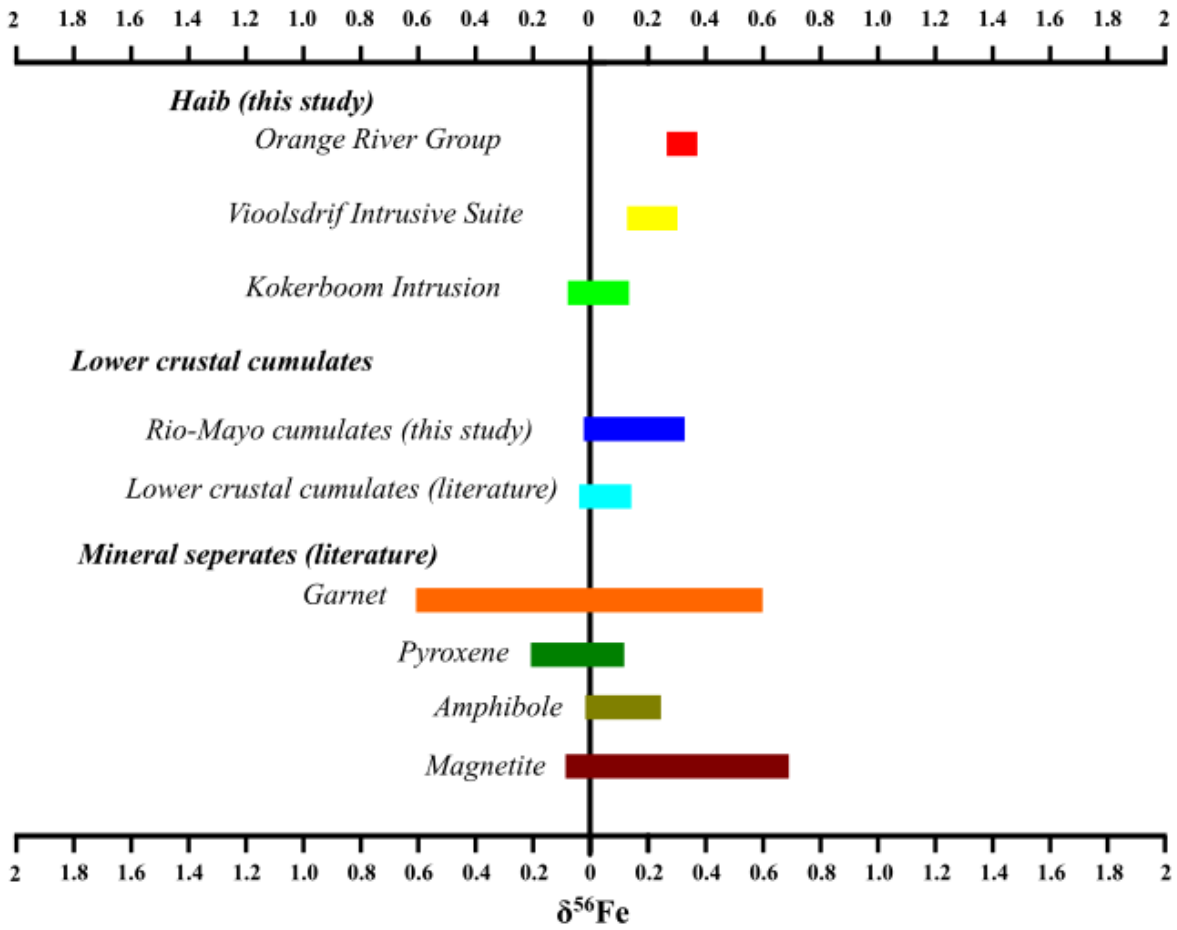

Figure 6.15: *The $\delta^{56}Fe$ isotope diagram shows that the Kokerboom Intrusion have a lower $\delta^{56}Fe$ signature relative to the Vioolsdrif Intrusive Suite which is followed by the Orange River Group. The $\delta^{56}Fe$ isotope diagram shows that the Rio-Mayo lower crustal cumulates overlap with the Kokerboom Intrusion, Vioolsdrif Intrusive Suite and Orange River Group. The $\delta^{56}Fe$ signature of mineral separates including garnet, pyroxene, amphibole and magnetite is plotted for comparison (Liang et al., 2022).*

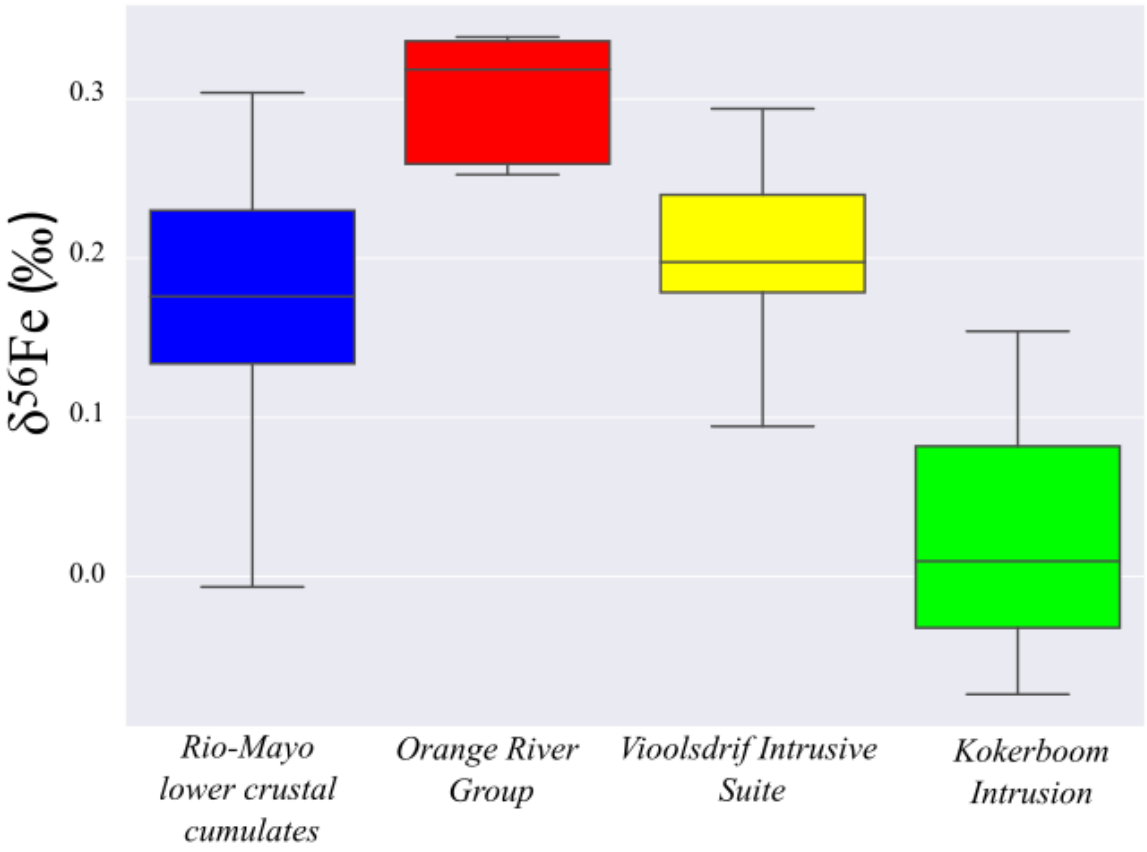

Figure 6.16: *Box plot of the $\delta^{56}Fe$ isotope signatures for the Rio-Mayo lower crustal cumulates, Orange River Group, Vioolsdrif Intrusive Suite and Kokerboom Intrusion.*

Table 6.1: *Geochemical and isotope data obtained in this study for the Orange River Group (ORG), Vioolsdrif Intrusive Suite (VIS) and Kokerboom Intrusion (KI).*

Sample material	ORG	ORG	ORG	ORG	ORG	VIS	VIS	VIS	VIS	VIS	KI	KI	KI
Sample #	AJ 13	AJ 14	AJ 15	AJ 17	AJ 38	AJ 2	AJ 18	AJ 28	AJ 36	AJ 37	AJ 30	AJ 4	AJ 23
$^{56}\delta$Fe (‰)	0.3190	0.2593	0.3365	0.3390	0.2526	0.0944	0.1786	0.2399	0.1976	0.2939	-00740	0.0097	0.1541
SD	0.07	0.07	0.07	0.07	0.07	0.07	0.07	0.07	0.07	0.07	0.07	0.07	0.07
SiO_2	60.43	62.67	57.26	69.25	62.52	73.32	66.79	61.16	55.97	69.14	47.63	46.32	48.11
TiO_2	0.71	0.77	0.66	0.54	0.63	0.22	0.71	0.69	1.08	0.41	0.55	0.96	1.12
Al_2O_3	17.04	15.92	15.92	15.52	16.14	14.88	14.62	16.45	17.35	14.77	8.29	15.39	15.04
Cr_2O_3	0.01	0.01	0.03	0	0.02	0.01	0.01	0.01	0.02	0.01	0.18	0.07	0.03
Fe_2O3	5.69	5.14	7.26	2.7	6.56	1.71	5.02	5.72	8.33	3.78	11.57	12.98	12.02
MnO	0.09	0.08	0.12	0.07	0.2	0.02	0.09	0.11	0.14	0.08	0.2	0.24	0.18
MgO	2.59	1.46	5.48	0.79	2.98	0.41	1.68	2.53	3.39	1.72	17.07	9.54	7.96
CaO	5.4	3.5	5.35	2.04	4.05	1.71	3.25	4.74	6.74	3.33	9.83	9.48	9.52
Na_2O	3.2	3.28	2.81	2.97	2.52	5.57	2.81	3.49	2.59	2.53	0.81	1.87	2.14
K_2O	3	5.54	3.41	5.14	3.34	1.3	4.42	3.25	2.73	4.11	0.92	0.83	1.25
P_2O_5	0.27	0.41	0.18	0.02	0.17	0.07	0.22	0.22	0.4	0.12	0.13	0.33	0.24
NiO	0	0	0.01	0	0	0	0	0	0.01	0	0.06	0.02	0.01
LOI	1.43	1.29	1.36	1.11	1.23	0.97	1.08	1.45	1.48	1	2.8	2.23	1.7
Total	99.87	100.06	90.84	100.15	100.36	100.19	100.7	99.83	100.22	101	100.04	100.25	99.32
La	37.397	44.335	26.5	43.573	36.528	40.909	41.508	33.695	29.254	37.366	23.495	21.063	21.983
Ce	75.405	91.096	54.855	95.385	77.779	80.685	90.16	72.593	58.113	73.042	47.816	47.341	50.607
Pr	8.434	10.139	6.205	9.948	8.715	8.41	10.096	8.286	6.705	7.421	5.629	6.17	6.501
Nd	33.15	38.706	24.552	37.242	32.872	28.966	38.555	32.566	26.723	26.301	22.947	27.601	28.374
Sm	5.929	6.837	4.774	6.557	6.017	4.953	7.106	6.237	5.059	4.611	4.765	5.844	6.102
Eu	1.488	1.568	1.099	1.562	1.225	0.827	1.453	1.571	1.544	0.997	1.268	1.54	1.575
Gd	4.825	5.702	4.21	5.139	4.993	4.099	6.157	5.225	4.417	3.807	4.213	5.188	5.358
Tb	0.603	0.729	0.58	0.643	0.658	0.542	0.86	0.73	0.582	0.521	0.598	0.705	0.739
Dy	3.347	4.147	3.464	3.448	3.756	3.224	5.138	4.214	3.356	3.085	3.514	4.137	4.364
Ho	0.645	0.809	0.695	0.636	0.735	0.65	1.034	0.825	0.652	0.615	0.699	0.818	0.851
Er	1.755	2.21	1.941	1.67	2.036	1.878	2.901	2.255	1.75	1.781	1.908	2.192	2.308
Tm	0.246	0.312	0.287	0.233	0.306	0.289	0.44	0.323	0.248	0.276	0.282	0.314	0.334
Yb	1.635	2.037	1.886	1.541	1.97	1.96	2.758	1.917	1.502	1.792	1.758	2.012	2.028
Lu	0.233	0.286	0.276	0.234	0.305	0.282	0.408	0.279	0.239	0.279	0.267	0.292	0.306

Table 6.2: *Geochemical and isotope data obtained in this study for the Rio-Mayo lower crustal cumulates.*

Sample material	Rio-Mayo lower crustal cumulate	Rio-Mayo lower crustal cumulate	Rio-Mayo lower crustal cumulate	Rio-Mayo lower crustal cumulate	Rio-Mayo lower crustal cumulate	Rio-Mayo lower crustal cumulate	Rio-Mayo lower crustal cumulate	Rio-Mayo lower crustal cumulate	Rio-Mayo lower crustal cumulate	Rio-Mayo lower crustal cumulate
Sample #	CA 14	CA 15	CA 16	CA 17	CA 18	CA 24	CA 25	CA 26	CA 27	CA 28
$^{56}\delta$Fe (‰)	0.2308	-0.0065	0.1124	0.12795	0.2433	0.3040	0.1610	0.1911	0.1515	0.2278
SD	0.07	0.07	0.07	0.07	0.07	0.07	0.07	0.07	0.07	0.07
SiO_2	42.24	44.46	42.71	42.32	63.23	62.1	52.57	46.78	51.14	51.85
TiO_2	1.84	1.05	2.13	1.13	0.69	0.44	0.53	2.62	0.8	1.68
Al_2O_3	17.72	13.5	15.18	16.15	15.03	19.08	6.44	14.26	16.47	14.48
Cr_2O_3	0	0.04	0	0	0.01	0.01	0	0	0.01	0.03
Fe_2O_3	13.41	14.56	16.46	14.4	7.1	3.92	8.7	14.54	12.88	11.47
MnO	0.18	0.22	0.41	0.23	0.15	0.07	0.15	0.24	0.17	0.19
MgO	9.3	11.43	10.5	12.26	2.82	2.14	19.52	8.62	6.08	7.01
CaO	12.12	13.42	10.73	11.6	6.21	5.71	11.3	10.92	10.86	8.98
Na_2O	2.3	1.25	1.04	1.08	3.13	5.45	1.71	2.15	1.88	2.98
K_2O	0.54	0.02	0.38	0.32	1.05	0.67	0.19	0.45	0.08	0.69
P_2O_5	0.68	0.05	0.24	0.06	0.43	0.19	0.08	0.22	0.13	0.16
NiO	0	0.01	0	0	0	0	0.01	0	0	0.01
LOI	0.004	0.33	0.367	0.501	0.49	0.5	0.1	0.271	-0.13	0.75
Total	100.34	100.32	99.78	100.05	100.34	100.29	101.29	101.09	100.37	100.26
La	16.642	9.116	3.687	2.397	13.981	19.567	10.529	5.679	4.378	4.231
Ce	41.131	7.739	10.4	8.4	26.294	35.969	27.747	16.7	10.114	12.07
Pr	6.377	1.63	1.917	1.753	3.489	4.414	4.266	2.772	1.468	1.944
Nd	32.714	10.548	11.056	11.059	15.073	17.827	23.409	15.368	7.645	10.742
Sm	8.812	4.269	4.012	3.796	3.347	3.62	7.503	5.316	2.389	3.75
Eu	2.469	1.386	0.864	1.096	1.014	1.104	2.196	1.877	0.647	1.364
Gd	8.386	5.496	5.065	4.382	3.235	2.889	9.82	7.029	2.915	4.916
Tb	1.146	0.906	0.866	0.683	0.451	0.35	1.597	1.222	0.521	0.873
Dy	6.588	5.873	6.281	4.347	2.714	1.787	10.058	8.543	3.841	6.027
Ho	1.251	1.217	1.498	0.903	0.547	0.328	1.976	1.871	0.882	1.291
Er	3.26	3.5	4.741	2.502	1.555	0.883	5.415	5.34	2.615	3.695
Tm	0.458	0.519	0.721	0.355	0.225	0.116	0.811	0.77	0.392	0.532
Yb	2.871	3.446	4.839	2.301	1.539	0.768	5.41	5.194	2.82	3.561
Lu	0.399	0.53	0.757	0.339	0.234	0.11	0.819	0.791	0.464	0.549

6.3. Discussion

Previous studies conducted by Lee and Tang (2020), Li et al (2021) and Liang et al (2022) proposed that garnet fractionation in the lower crust causes depletion of ferrous iron in the magma resulting in an enriched iron isotope signature and contributes to increased oxygen fugacity prevalent in arc settings. According to Liang et al (2022), our understanding of the systematics in which garnet fractionation results in a heavy iron isotope signature in arc settings remains limited. According to Park et al (2021), porphyry copper deposits show evidence for the fractionation of amphibole in the mid-lower crust compared to the fractionation of garnet.

This discussion focuses on constraining controls for amphibole and garnet fractionation for the Kokerboom Intrusion and the Rio-Mayo lower crustal cumulates using the geochemical (major and trace elements) and isotopic data presented in the results section. The whole rock iron isotope signature ($\delta^{56}Fe$) of the Kokerboom Intrusion, Orange River Group, the Vioolsdrif Intrusive Suite and the Rio-Mayo lower crustal cumulates is evaluated in order to understand intra-crustal differentiation processes linked to garnet or amphibole fractionation.

6.3.1. Kokerboom Intrusion represents cumulate material of the RMA

Parts of the Kokerboom Intrusion such as the clinopyroxenites consist of mafic minerals and show typical, coarse-grained cumulate textures where the non-cotectic proportion of mafic minerals are present. From work conducted by Weber (1998), the Rio-Mayo lower crustal cumulates have been constrained as cumulate material based on the coarse-grained nature, mineral assemblages, modal abundances, and cumulate textures. Therefore, the Rio-Mayo lower crustal cumulates and the most mafic components of the Kokerboom Intrusion such as the clinopyroxnites can be classified as typical cumulate material. This is based on the mineral and textural characteristics of the rocks comprising the rocks of the Rio-Mayo lower crustal cumulates and parts of the Kokerboom Intrusion.

6.3.2. Rayleigh fractionation modelling of Yb

Rayleigh fractionation modelling of bulk rock Yb values was applied to the Kokerboom Intrusion and Rio-Mayo lower crustal cumulates (Figure 6.17). The dominant minerals composing the Kokerboom Intrusion and Rio-Mayo lower crustal cumulates were used to calculate the bulk rock distribution co-efficient used for the modelling. Results show that the Yb value in the melt decreases as various minerals comprising the Rio-Mayo lower crustal cumulates fractionate. From petrographic observations the dominant minerals comprising the Rio-Mayo lower crustal cumulates include garnet, clinopyroxene, orthopyroxene, amphibole, olivine and plagioclase. In contrast, the Yb value in the melt increases as various minerals constituting the Kokerboom Intrusion fractionate. From petrographic observations the dominate minerals comprising the Kokerboom Intrusion include clinopyroxene, amphibole and plagioclase.

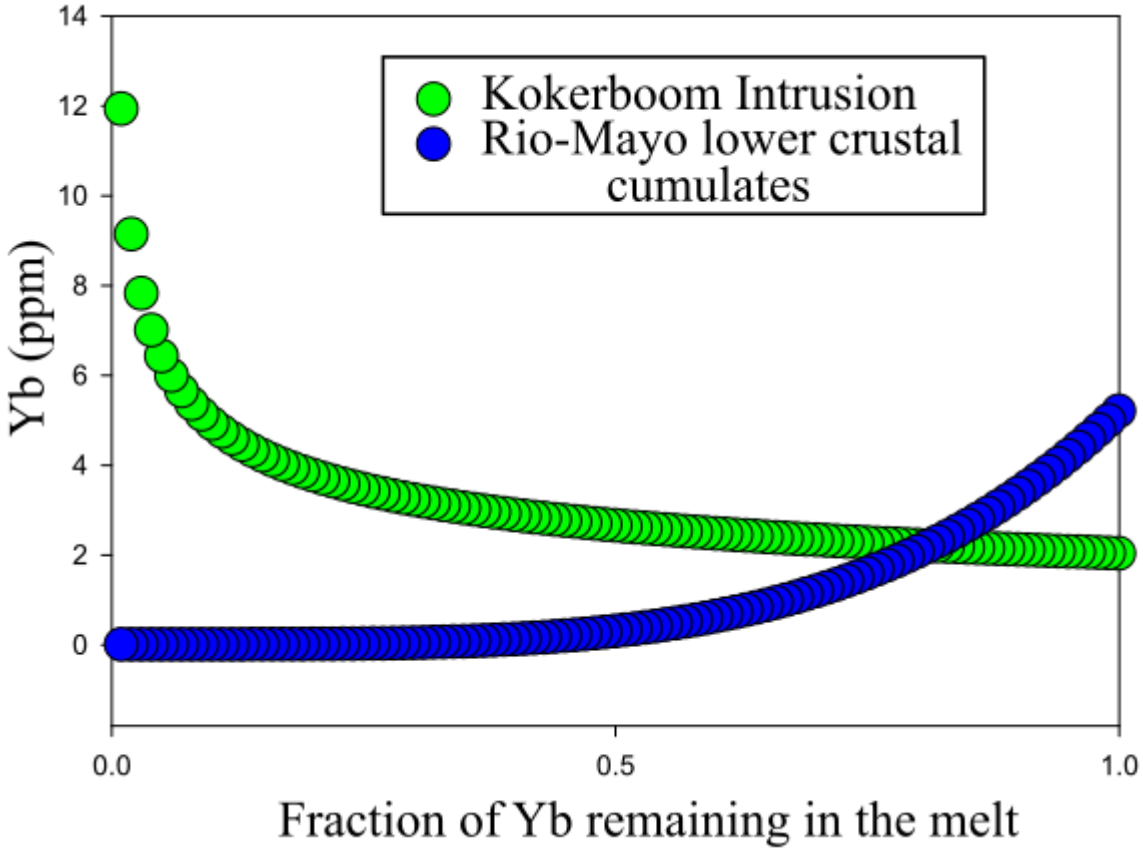

Figure 6.17: *Rayleigh fractionation modelling of bulk rock trace element Yb in the Rio-Mayo lower crustal cumulates and Kokerboom Intrusion.*

6.3.3. An amphibole fractionation control for the Orange River Group, Vioolsdrif Intrsuive Suite and Kokerboom Intrusion

The chondrite-normalized REE patterns for the Orange River Group and Vioolsdrif Intrusive Suite show a listric-shaped REE signature with fractionation of the MREE. The listric-shaped REE signature with fractionation of MREE is controlled mainly by amphibole and to some extent, by clinopyroxene (Frey et al., 1978; Hanson, 1980; Lopez, 1982; Lang and Titley, 1998; Richards, 2001; Rollison, 1993; Richards, 2011; Carrasquero, 2018; Meng et al., 2021). In fact, amphibole preferentially accommodates HREE and MREE (Y,Yb) relative to LREE (La) (Richards, 2011). The chondrite-normalized REE patterns for the Kokerboom Intrusion are less enriched in LREE, flatter and have negligible Eu anomalies indicating a strong amphibole fractionation control on the REE signature. Petrographic observations support an amphibole fractionation control.

6.3.4. A garnet fractionation control for the Mercaderes-Rio Mayo lower crustal cumulates

The chondrite-normalized REE patterns for the Mercaderes-Rio Mayo lower crustal cumulates are relatively flat indicating minimal fractionation (Figure 6.12). The HREE enrichment relative to LREE is indicative of a dominant garnet fractionation control (Chin et al., 2014b). The Ce anomaly observed is indicative of increased oxygen fugacity as Ce anomalies are controlled by oxygen fugacity (Dill, 2017). Under oxidizing conditions, Ce^{3+} state is transformed into Ce^{4+} thus, minerals that accept exclusively trivalent REE over tetravalent REE show a Ce-depletion resulting in a negative Ce anomaly (Dill, 2017). Cumulates in arc environments are relatively enriched in HREE due to their affinity for garnet and this is observed in the Sierra Nevada and Arizona lower crustal cumulates due to the presence of garnet in the residue (Ducea et al., 2020). Petrographic observations support a garnet fractionation control as mineral assemblages consist of garnet, plagioclase, clinopyroxene, orthopyroxene, hornblende, olivine, quartz, biotite, sphene and magnetite. Further evidence for a garnet fractionation control is the Yb Rayleigh fractionation on the bulk rock Yb value in the Rio-Mayo lower crustal cumulates. Modelling shows that Yb content in the melt decreases as minerals forming the Rio-Mayo lower crustal cumulates crystallize. These minerals include garnet which is a dominant phase in the cumulates. Ytterbium has a strong affinity and compatibility for garnet and therefore, as fractionation of garnet occurs, Yb is incorporated within garnet resulting in a decrease of the Yb value within the residual melt.

6.3.5. An amphibole vs. garnet fractionation control constrained using various trace element concentrations and ratios

Listric-shaped REE trends are related to the fractionation of the MREE (Y, Yb) relative to the LREE (La) and is attributed to the fractionation of amphibole. Amphibole preferentially partitions Yb relative to La. REE trends that show an enrichment of the HREE relative to the LREE is related to the fractionation of garnet. HREE have an affinity for garnet relative to the LREE. Yb is one of the HREE that has a strong affinity for garnet relative to amphibole.

The REE patterns for the Haib porphyry copper deposit is listric-shaped REE signature with fractionation of the MREE relative to LREE and the REE patterns for the Rio-Mayo lower crustal cumulates show an enrichment of HREE relative to LREE (Figures 6.12). The variations in the normalized La/Yb ratio for the Orange River Group, Vioolsdrif Intrusive Suite and Kokerboom is between 4 and 30 and a progression is observed from the Kokerboom Intrusion followed by the Orange River Group and Vioolsdrif Intrusive Suite (Figure 6.13). The normalized La/Yb ratios for the Orange River Group and Vioolsdrif Intrusive Suite are similar and therefore overlaps (Figure 6.13). The Kokerboom Intrusion has the lower normalized La/Yb ratio followed by the Orange River Group and Vioolsdrif Intrusive Suite. The SiO_2 vs. Yb, Sr and Y plots show positive linear correlations. As the SiO_2 concentration increases, the Yb and Y concentrations decrease (Figure 6.13). The normalized La/Yb ratio for the Rio-Mayo lower crustal cumulates have lower La/Yb ratios (0 to 30) and the residual magmas (Andes arc magmas) have higher normalized La/Yb ratios (as high as 70) (Figure 6.14). The SiO_2 vs. Yb and Y plots for the Rio-Mayo lower crustal cumulates show elevated concentrations in Yb (0.5-6 ppm) and Y (5-60 ppm) (Figure 6.14).

The REE patterns and trace element ratios and concentrations for the Haib porphyry copper deposit and the Rio-Mayo lower crustal cumulates are related to the fractionation of amphibole and the fractionation of garnet. The normalized La/Yb ratios and SiO_2 vs. Yb and Y plots corroborate with chondrite-normalized REE patterns for the Haib porphyry copper deposit and Rio-Mayo lower crustal cumulates in terms of amphibole fractionation for the Haib porphyry copper deposit and garnet fractionation for the Rio-Mayo lower crustal cumulates. The La and Yb concentrations further support a garnet fractionation control for the Rio-Mayo crustal cumulates as the Rio-Mayo lower crustal cumulates have lower La concentrations and higher Yb concentrations compared to the Kokerboom Intrusion, Orange River Group and Vioolsdrif Intrusive Suite. Rayleigh fractionation modelling does not support a garnet fractionation control for the Kokerboom Intrusion cumulates as the Yb value in the melt increases as various minerals constituting the Kokerboom Intrusion fractionate.

6.3.6. δ^{56}Fe isotopic fractionation of the Orange River Group, Vioolsdrif Intrusive Suite and Kokerboom Intrusion

During magmatic differentiation, cumulate minerals preferentially incorporate ^{54}Fe relative to ^{56}Fe driving the evolved magmas towards enriched δ^{56}Fe signatures (Dauphas et al., 2009). The δ^{56}Fe signature for the Vioolsdrif Intrusive Suite is lower (0.20 ± 0.07 ‰) compared to the δ^{56}Fe signature for the Orange River Group (0.30 ± 0.07 ‰) and, the Kokerboom Intrusion has the lowest δ^{56}Fe signature (0.03 ± 0.07 ‰). This systematic variation is clearly observed in Figure 6.16. The gradual increase in the δ^{56}Fe signature from the Kokerboom Intrusion to the Vioolsdrif Intrusive Suite and Orange River Group is related to the progressive isotopic fractionation of the δ^{56}Fe isotope signature through magmatic differentiation of amphibole and

pyroxene. Part of the Kokerboom Intrusion represents early fractionated cumulate material (refer to chapter 4) and therefore, has depleted $\delta^{56}Fe$ signatures. The residual magma underwent further fractionation forming the Vioolsdrif Intrusive Suite and the Orange River Group with intermediate and enriched $\delta^{56}Fe$ signatures. The intermediate isotopic signature for the Vioolsdrif Intrusive Suite compared to the slightly more elevated signature for the Orange River, may be explained by temperature processes, as igneous intrusions cool much slower at higher pressures compared to volcanic lavas which cool rapidly at lower pressures. It is possible that greater isotopic fractionation occurs at shallow crustal levels where lavas are emplaced relative to igneous intrusions which crystallize at depth. In addition, shallow crustal levels are more likely subjective to greater hydrothermal alteration. According to Minnitt (1979), the Orange River Group is representative of the evolved melt phases whereas, the Vioolsdrif Intrusive Suite is representative of the evolved cumulate phases. Therefore, the magma that formed the Haib fractionated the plutonic phases of the Vioolsdrif Intrusive Suite at depth with intermediate $\delta^{56}Fe$ signatures and extruded the extrusive equivalent forming the volcanic phases of the Orange River Group with enriched $\delta^{56}Fe$ signatures.

6.3.7. Rayleigh fractionation modelling of the $\delta^{56}Fe$ composition for the Kokerboom Intrusion

Rayleigh fractionation modelling of the $\delta^{56}Fe$ composition for part of the Kokerboom Intrusion was conducted in order to understand how the $\delta^{56}Fe$ composition changes as the residual melt evolves. The results from the modelling show that the fraction of iron remaining in the melt progressively evolves to enriched $\delta^{56}Fe$ compositions that coincide with the average $\delta^{56}Fe$ compositions for the Orange River Group and Vioolsdrif Intrusive Suite (refer to Appendix L) (Figure 6.18). The average $\delta^{56}Fe$ compositions for the Orange River Group and Vioolsdrif Intrusive Suite are 0.3012 ‰ and 0.2009 ‰ respectively. The Rayleigh fractionation modelling suggests that the fractionation of amphibole cumulates that formed part of the Kokerboom Intrusion caused the residual melt to evolve to progressively enriched iron isotope signatures. This residual melt that progressively evolved formed the Orange River Group and Vioolsdrif Intrusive Suite.

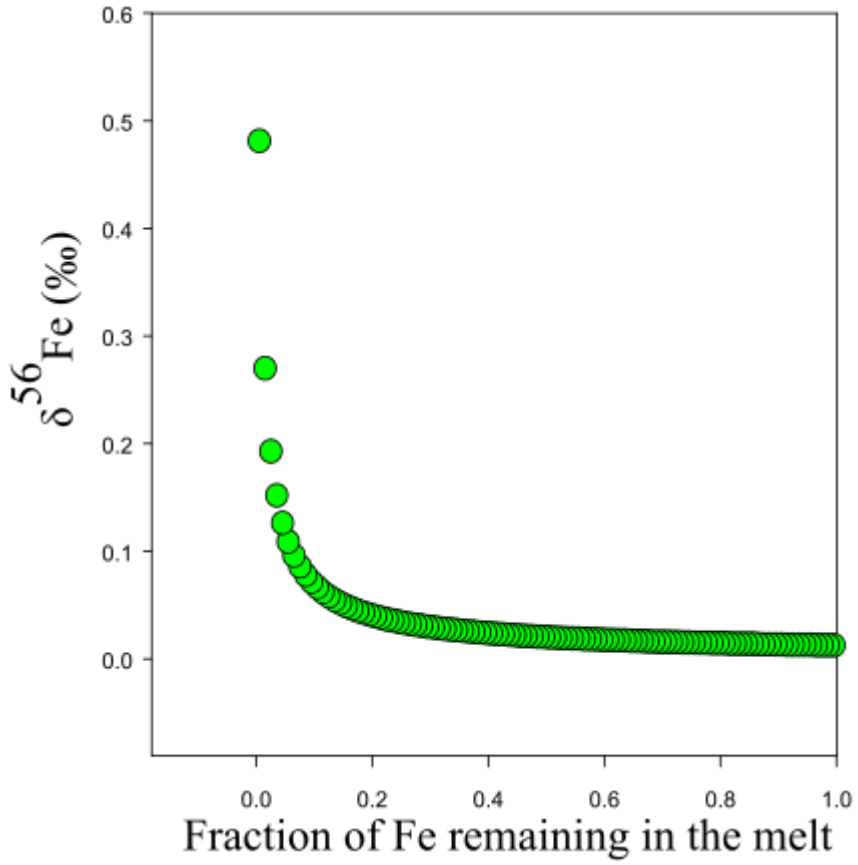

Figure 6.18: *Rayleigh fractionation modelling showing the δ^{56}Fe compositions of the residual melt from the Kokerboom Intrusion cumulates.*

6.3.8. A garnet vs. an amphibole fractionation control on the δ^{56}Fe signature in arc magmas

Cumulus minerals normally have depleted δ^{56}Fe signatures compared to the melts from which they were derived (Dauphus et al., 2009). Some studies show that ferrous iron has a strong affinity for garnet relative to ferric iron and therefore, garnet fractionation should result in a heavier iron isotope signature in the residual melt and form cumulates with lighter δ^{56}Fe compositions (Lee and Tang, 2020; Barber et al., 2021; Li et al., 2021; Du et al., 2022). In contrast, experimental modelling conducted by Holycross and Cottrell (2023), shows that the compatibilities between ferrous and ferric iron in garnet are of similar magnitude. The δ^{56}Fe signature for the Rio-Mayo lower crustal cumulates (-0.01 ± 0.07 ‰ to 0.24 ± 0.07 ‰) overlap with the Kokerboom Intrusion (-0.07 ± 0.07 ‰ to 0.15 ± 0.07 ‰), Orange River Group (0.25 ± 0.07 ‰ to 0.34 ± 0.07 ‰) and Vioolsdrif Intrusive Suite (0.09 ± 0.07 to 0.29 ± 0.07 ‰). In addition, the δ^{56}Fe data for the Tongde dikes, composed of garnet rich cumulates, have signatures that overlap with the δ^{56}Fe signatures for the Kokerboom Intrusion. The overlap of garnet rich cumulates, such as the Rio-Mayo lower crustal cumulates and the Tongde dikes, with the Kokerboom Intrusion, Orange River Group and Vioolsdrif Intrusive Suite is unexpected as some studies have shown that garnet rich cumulate is related to depleted iron isotope signatures and an enriched iron isotope signature of the residual melt causing oxidation of the melt. However, recent studies by Holycross and Cottrell (2023) suggest that the compatibility of ferrous and ferric in garnet is not related to the oxidation of the residual melt. The overlap of the Rio-Mayo lower crustal cumulates with the Haib magmas may indicate that

additional minerals other than garnet influences the δ^{56} Fe signature and oxidation state of arc magmas.

A study conducted by Liang et al. (2022) shows the δ^{56} Fe signature of mineral separates including garnet, pyroxene, amphibole and magnetite (Figure 6.15). From the data, it is observed that garnet has a wide range in δ^{56} Fe compositions. Pyroxene and amphibole separates have smaller ranges in δ^{56} Fe compositions that overlap with the Rio-Mayo lower crustal cumulates, Kokerboom Intrusion and to some extent with the Vioolsdrif Intrusive Suite. From detailed petrographic observations (see Appendix C), the Kokerboom Intrusion is dominated by pyroxene (~90 %) and amphibole (~15 %) fractionation whereas, the Rio-Mayo lower crustal cumulates is dominated by garnet (~43 %), pyroxene (21 %) and amphibole (10 %). It is possible that during intra-crustal differentiation both garnet and amphibole has a strong control on the δ^{56} Fe signature. As observed from petrographic observations, cumulate minerals such as pyroxene and amphibole form the clinopyroxenite cumulates of the Kokerboom Intrusion. These minerals have smaller ranges in δ^{56} Fe compositions from studies by Liang et al. (2022). Results from this study show that the cumulate part of the Kokerboom Intrusion, such as the clinopyroxenites, has lighter δ^{56}Fe signature isotope signatures than the residual melts. It is possible that the fractional crystallization of pyroxene and amphibole incorporated the lighter isotope causing the residual magma to have an enriched δ^{56}Fe signature.

Iron has two valence states in magmatic systems, namely Fe^{2+} and Fe^{3+}, and their relative proportions reflect the redox conditions of the melt and can, therefore, serve as a tool for determining oxygen fugacity (Li et al., 2021). Ferrous iron has a lower charge, higher co-ordination and longer bond length that leads to a lower force constant (reflection of the strength of the bond) (Sossi and O'Neill, 2017; Young et al., 2009), such that ferrous iron incorporates the lighter isotope. By contrast, ferric iron has a higher charge, lower co-ordination and shorter bond length that leads to a higher force constant and thus incorporates more of the heavier isotope (Li et al., 2021). Whilst oxygen fugacity does not have a direct influence on the iron isotope signature of the melt, it can be used to monitor the partitioning of heavy (Fe^{3+}) vs. light (Fe^{2+}) isotopes between minerals and melt during fractional crystallization (Li et al., 2021). According to Foden et al. (2018), Fe^{3+} is more incompatible than Fe^{2+} and this results in the melt becoming more oxidized relative to the residue. During magmatic differentiation, crystallization lowers the δ^{56}Fe value of the cumulate material, driving the evolved magmas towards more enriched δ^{56}Fe compositions (Duaphas et al., 2009). Therefore, fractional crystallization results in arc magmas becoming progressively oxidized. The host granodiorite porphyry has a heavier isotope signature relative to the clinopyroxenite, suggesting that clinopyroxenite cumulates became lighter in δ^{56}Fe compositions (-0.07 ± 0.07 ‰) which caused the residual host magmas to incorporate heavier δ^{56}Fe values (0.24 ± 0.07 to 0.29 ± 0.07 ‰). The incorporation of the heavier δ^{56}Fe values (0.24 ± 0.07 to 0.29 ± 0.07 ‰) by the host magmas is due to the nature of Fe^{3+} in the residual magmas.

According to He et al. (2020) and Du et al. (2020) amphibole has a higher Fe^{3+} content relative to garnet and is therefore slightly enriched in light Fe isotopes. Park et al. (2021) has suggested that garnet fractionation and auto-oxidation may be the reason for the Fe-depleted, oxidized nature of arc magmas in thick continental arc sections. This is supported by garnet-bearing cumulates in arc sections (Lee et al., 2020). However, from studies conducted on arc intrusive rocks linked to porphyry copper deposits found in thick crustal sections, REE patterns indicate an amphibole-dominant fractionation as opposed to a garnet-dominant fractionation (Park et al., 2021). Tang et al. (2019), has suggested that Fe^{2+} preferentially partitions into garnet leading to high oxygen fugacity in arc magmas, this claim has been disputed by Holycross and Cottrell (2023). Chiaradia (2015) and Park et al. (2021) both indicated that garnet cannot be a

prerequisite in porphyry copper deposits due to its reduced stability in the shallow crust where amphibole is the main fractionating mineral controlling the REE patterns. A recent publication by Tatnell et al. (2023), indicates that garnet fractionation is not observed in REE trends that are related to porphyry copper forming intrusions. The study by Tatnell et al. (2023) show that porphyry forming intrusions in areas such as the western Pacific and the Eocene porphyry intrusions located in northern Chile have REE patterns that is consistent with a "garnet-free, amphibole-dominated cumulate." This study confirms that amphibole plays a role in the formation of porphyry copper deposits based on petrographic observations, REE patterns, trace element concentrations and ratios and the depleted δ^{56}Fe signature for the Kokerboom Intrusion. Garnet is normally found in thick crustal sections whereas, amphibole is found in moderate to thick crustal sections (Lee et al., 2020; Park et al., 2021). Many porphyry copper deposits globally show evidence for amphibole fractionation as opposed to garnet fractionation (Park et al., 2021). Thus, porphyry copper deposits may form in crustal sections that are correlated with both garnet and amphibole fractionation in both continental and island arc settings (Figure 6.19).

The evidence presented suggests that the Haib porphyry copper deposit was either formed in a mature island arc setting or continental arc setting associated with amphibole fractionation in the mid-crust during the Palaeoproterozoic. The evidence for a mature island arc setting includes the limited inheritance of Hf and O isotopes in zircon that is indicative of little or no older continental crust involvement (Meng et al., 2021). The evidence for a continental arc setting includes inherited zircons which have Sm-Nd modal ages of ~ 2.4 Ga and indicates an older continental crust involvement (Macey et al., 2017).

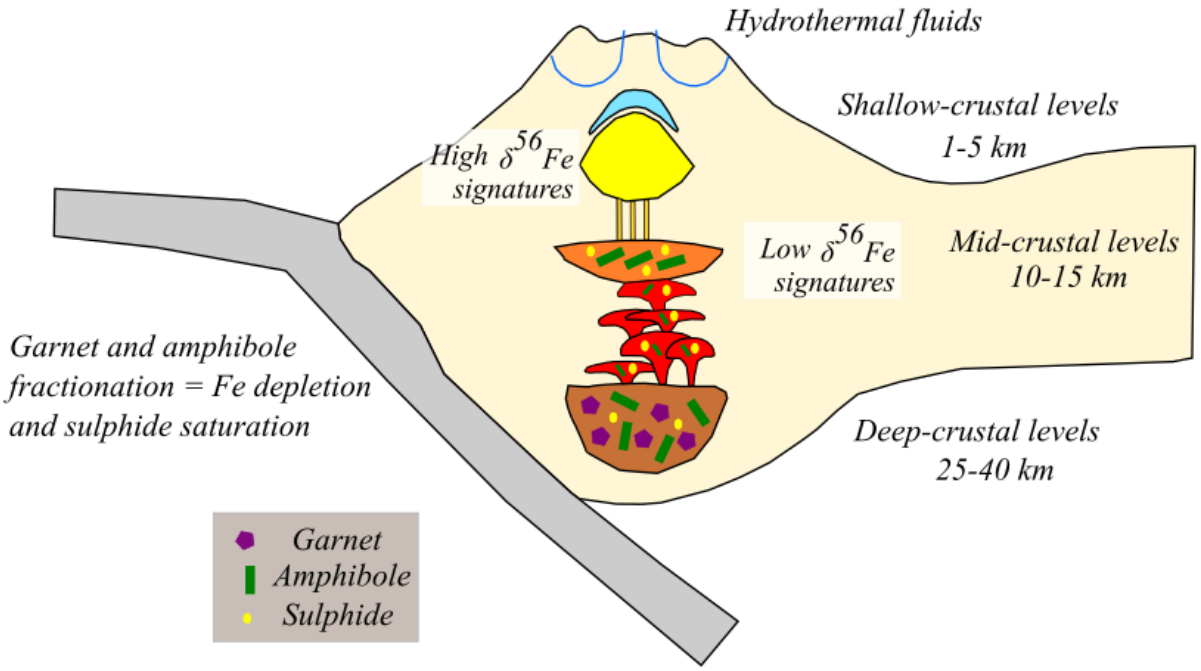

Figure 6.19: *During intra-crustal differentiation both garnet and amphibole has a strong control on the δ^{56}Fe signature. Intra-crustal differentiation results in mid- to deep- crustal cumulates with depleted δ^{56}Fe signatures and residual host porphyry magmas with enriched δ^{56}Fe signatures.*

6.4. Conclusion

Previous studies conducted by Lee and Tang (2020), Barber et al. (2021), Li et al. (2021), Du et al. (2022) and Liang et al. (2022) indicate that garnet fractionation results in the depletion of Fe in arc magmas and enrichment of ferric iron causing oxidation of the magma. However, the REE patterns for the Haib porphyry copper deposit indicate a strong amphibole control (amphibole fractional crystallization) which is demonstrated by the trace element concentrations and ratios for the Kokerboom Intrusion, Vioolsdrif Intrusive Suite and Orange River Group. The Kokerboom Intrusion represents cumulate material composed of pyroxene (~90 %) and amphibole (~15 %) and has a low $\delta^{56}Fe$ signature (average of 0.03 ± 0.07 ‰). The magmatic fractionation of amphibole which formed the Kokerboom Intrusion caused isotopic fractionation of the $\delta^{56}Fe$ signature. The residual magma underwent further fractionation forming the Vioolsdrif Intrusive Suite and the Orange River Group with enriched $\delta^{56}Fe$ signatures. Amphibole has a higher Fe^{3+} content compared to garnet and is thus slightly enriched in light Fe isotopes. Therefore, amphibole has the potential to form low $\delta^{56}Fe$ signature cumulates. From this study, it is apparent that amphibole fractionation has a control on the $\delta^{56}Fe$ signature and the oxidation state of arc magmas. This is observed by the low $\delta^{56}Fe$ signatures of the Kokerboom Intrusion and the elevated $\delta^{56}Fe$ signature of the residual magma which formed the Vioolsdrif Intrusive Suite and Orange River Group.

7. Discussion and conclusions

This chapter integrates the discussions and conclusions from chapters four to six and provides recommendations for future research. The focus of this current research was to evaluate the role of trans- or intra-crustal differentiation processes and the temporal variations in the formation of the Haib porphyry copper-molybdenum deposit through a comparison with typical Phanerozoic porphyry Cu deposits (Cu and Fe isotopes) and with the Mercaderes-Rio Mayo lower crustal xenoliths (Cu and Fe isotopes).

The following aims were the focus of this PhD thesis:

1) assess the links between the Haib porphyry copper deposit and mafic-ultramafic rocks regionally and ascertain depth of emplacement and implications for future exploration.

2) understand the spatial and temporal variations of predominantly Phanerozoic porphyry Cu deposits around the world and assess if, and in what ways, the Proterozoic Haib porphyry copper deposit is unique or different from a petrological and geochemical perspective.

3) evaluate whether the Haib porphyry copper deposit and associated cumulate and host magmatic rocks show geochemical signatures associated with intra-crustal differentiation processes such as amphibole or garnet fractionation. Conduct non-traditional stable isotopes analyses and comparison with the Mercaderes-Rio Mayo lower crustal xenoliths, situated in the Northern Andean arc, in order to constrain differentiation processes associated with various levels of an arc system.

The several hypotheses that were proposed to guide the aims of this research:

Cumulates	1) The mafic in close vicinity to the Haib porphyry copper deposit represent mid-crustal cumulate material.
Depth perspective	2) The Haib porphyry copper deposit presents evidence relating to mid-deep crustal levels as it is documented in literature that there is a lack of shallow alteration assemblages.
Mineralization	3) The mineralization is primary (hypogene) and was subsequently remobilized forming secondary mineralization assemblages (supergene).
Trans-crustal Perspective	4) The Haib porphyry copper deposit was formed in a continental arc setting associated with the fractionation of garnet in deep crustal cumulates during the Precambrian.
Temporal perspective	5) Porphyry copper formation in the Proterozoic was similar to the Phanerozoic.

7.1. Discussion for various aspects of the proposed hypotheses in this study

7.1.1. Cumulates

Typical cumulates from deep crustal arc sections (arclogites) are coarse-grained, show cumulate textures and are composed of garnet-clinopyroxene-amphibole-iron-titanium oxides and in some cases plagioclase (Lee and Anderson, 2015; Ducea et al., 2020). The mafic-ultramafic cumulates such as the clinopyroxenites observed in the Kokerboom Intrusion in close proximity to the Haib porphyry copper deposit are coarse-grained, are composed of clinopyroxene-amphibole-iron-titanium oxides and consist of non-cotectic proportion of mineral phases. They also comprise a high modal abundance of pyroxene (> 70 %) and show distinct cumulate textures (i.e. dominant cumulus phases are present with minor inter-cumulus phases- typical adcumulate texture observed) as well as atypical sulphide mineralization. The Kokerboom Intrusion correlates petrologically and geochemically with the Vuurdood Subsuite of the Vioolsdrif Intrusive Suite. Therefore, an inference can be made from the machine learning geothermobarometry on the pyroxenes yielding an approximate depth of 12 km. According to Minnaar (2012), the Vuurdood Subsuite is expected to be limited to the lower parts of the crust due to the high density of mafic magmas. Thus, from the aforementioned evidence, the mafic units associated with the Haib porphyry copper deposit represents mid-crustal cumulate material. An inference can also be made based on observations from Phanerozoic porphyry copper deposits that are related to lower crustal cumulate material such as the Tongling porphyry copper deposit. Previous work has shown that there is a distinct petrological and geochemical link between the Orange River Group, Vioolsdrif Intrusive Suite and Vuurdood Subsuite (Reid, 1977; Minnitt, 1979; Macey et al., 2017). This study shows that the Kokerboom Intrusion represents cumulate material compared to the Orange River Group and Vioolsdrif Intrusive Suite. This is discernable from petrographic observations, geochemical analyses (major and trace elements) and iron isotopic analyses.

7.1.2. Depth perspective

The Haib porphyry copper deposit represents deeper parts of the porphyry system (mid-crustal levels). Various lines of evidence suggest this and include the:

- Presence of early dark micaceous veins (the first phase of veins observed in the quartz-feldspar porphyry granodiorites) that are composed of quartz and coarse mica (Runyon et al., 2017, 2019). Early dark micaceous veins are located at deep levels (paleodepths of ~4–12 km) which is indicative of the root zones of porphyry systems (Runyon et al., 2017, 2019). The mica present in the early dark micaceous hosted in the quartz-feldspar granodiorites are composed of biotite.
- Geothermobarometry on pyroxenes from the Vuurdood Subsuite pyroxenite which yield average pressure and temperature estimates of 4 kbar and 870 °C respectively.
- Lack of evidence of shallow alteration assemblages such as propylitic and argillic alteration (Minnitt, 1979; Minnitt, 1986; Meng et al., 2021).
- Coarse-grained nature of the Vioolsdrif Intrusive Suite (clinopyroxenites, granodiorites, diorites, gabbros) which is indicative of slow cooling at mid-crustal batholith depths (Vermond, 2019).
- Presence of geochemically primitive mafic units such as the gabbros and clinopyroxenites. The clinopyroxenites are mafic, dense, and usually occur at mid to lower crustal levels.

- Mineralization associated with shear fractures which is indicative of shear zones. According to Davis et al. (2012) shear zones form in the ductile regime between 5-15 km.

Despite evidence for the Haib being at deeper levels of the porphyry system, hypabyssal volcanics are present in the Haib area. These volcanics in the vicinity of the Haib porphyry copper deposit, have an approximate thickness of 5-8 km (Minnitt, 1979). The emplacement depth of the Haib porphyry copper deposit is estimated to have been in the order of 5-8 km. The 5-8 km thickness correlates with emplacement at mid-crustal levels. This evidence corroborates with evidence presented for deeper crustal levels of the porphyry system.

The emplacement pressures for the Vioolsdrif Intrusive Suite are approximately 2-3 kbar (Minnitt, 1979, Meng et al., 2021) which according to Minnitt (1979) and Meng et al. (2021) is comparable to deeper sections of Phanerozoic porphyry deposits ((San-Manuel-Kalamazoo Ore body, Arizona (Lowell and Guilbert, 1970); Fortuna pluton, Chile (Sillitoe, 1973); Los Loros, Chile, Appalachian porphyry systems (Hollister, 1974); Cornelia Pluton, Arizona (Wadsworth, 1968), Little Mine Area, Arizona (Durning and Davis, 1978), Laramide porphyry system, Arizona (Seerdoff et al, 2008; Runyon et al., 2017) and Yerington batholith, Nevada (Seerdoff et al, 2008; Runyon et al., 2017)). 2-3 kbar is approximately 10 km depth corresponding to the middle continental crust which is approximately 10-15 km depth. Therefore, from these various lines of evidence the Haib porphyry copper deposit represents the root zones of the porphyry system. The geothermobarometry on pyroxenes and amphiboles from the Vuurdood Subsuite pyroxenites shows that the Haib porphyry copper deposit is located at approximately 12 km depth as approximate pressures of 4 kbar were attained. Conclusions made by Minnaar (2012), suggests that the Haib deposit represents the deeper parts of the Vioolsdrif Intrusive Suite batholith and is characteristic of intrusion at the root zone of the volcanic pile based on contact relationships between the Orange River Group and Vioolsdrif Intrusive Suite. Another important key result from this study that is evidence for and indicates that the Haib deposit represents deeper levels of the porphyry copper system is the limited ranges in the copper and iron isotopic signatures of the Haib relative to Phanerozoic porphyry copper deposits. The shallower levels where magmatic-hydrothermal alteration is most likely to have caused isotopic fractionation has been eroded away exposing the deeper levels of the porphyry copper system with depleted copper and iron isotopic signatures.

7.1.3. Mineralization

Porphyry copper deposits are related with various phases of mineralization and alteration. Lowell and Guilbert (1970) has shown that porphyry copper deposits are typically zoned on the deposit scale. The alteration zones on a deposit scale include various phases that reflect the cooling and acidification of hydrothermal fluids as they ascend towards the surface: an inner potassic zone, and outer propylitic zone with zones of phyllic, argillic and advanced argillic alteration (Sinclair, 2007). These first two phases of alteration (potassic and phyllic alteration) are associated with the precipitation of hypogene sulphide assemblages (Robb, 2020). Later supergene mineralization is associated with propylitic and argillic alteration (Robb, 2020). In the Haib field area, there is lack of shallow alteration assemblages with minor evidence of supergene mineralization. Argillic and propylitic alteration is not observed whereas, phyllic and potassic alteration is dominant. The deposit is overall low in grade and show minimum ranges in copper and iron isotopic signatures relative to Phanerozoic deposits. It is probable that supergene mineralization is eroded away due to the Precambrian nature of the deposit. Drill-core sample descriptions, petrographic observations, and TIMA analyses (mineral

liberation maps) indicate that the mineralization is characterized by disseminated, massive and vein-type sulphides (pyrite and chalcopyrite). Isotopically the mineralization is characterized by two phases: disseminated-massive (heavier isotopic signature of 0.06 ± 0.07 to 0.21 ± 0.07 ‰ and 0.02 ± 0.07 to 0.06 ± 0.07 ‰ for δ^{65}Cu and δ^{56}Fe respectively) and vein-type (lighter isotopic signature of -0.08 ± 0.07 to 0.11 ± 0.07 ‰ and 0.11 ± 0.07 to -0.01 ± 0.07 ‰ for δ^{65}Cu and δ^{56}Fe respectively).

7.1.4. Trans-crustal perspective: comparing Palaeoproterozoic Haib and Phanerozoic porphyry deposits

Studies conducted by Li et al. (2021), indicate that garnet fractionation results in the depletion of iron in arc magmas and enrichment of ferric iron causing oxidation of the residual magma. Petrographic and geochemical signatures of the Haib porphyry deposit show distinct evidence of amphibole fractionation and not garnet fractionation. Petrographic observations for the Kokerboom Intrusion indicate that clinopyroxene, amphibole, and plagioclase are the dominate minerals comprising the clinopyroxenite cumulates. Geochemical signatures that support a strong amphibole control which includes the listric-shaped REE patterns, trace element concentrations and ratios for the Kokerboom Intrusion, Vioolsdrif Intrusive Suite and Orange River Group. Rayleigh fractionation modelling for the Kokerboom cumulates show no evidence for a garnet control. Amphibole has a higher Fe^{3+} content than garnet and is thus slightly enriched in light Fe isotopes. Therefore, amphibole has the potential to form low δ^{56}Fe signature cumulates. From this study, it is observed that amphibole has a control on the δ^{56}Fe signature and the oxidation state of arc magmas. This is observed by the low δ^{56}Fe isotopic compositions of the Kokerboom Intrusion and the elevated δ^{56}Fe isotopic signature of the residual magma which formed the Vioolsdrif Intrusive Suite and Orange River Group. Thus, the lower parts (mid-crustal levels) of the Haib porphyry copper system are associated with pyroxene and amphibole rich cumulates with depleted δ^{56}Fe isotopic signatures whereas, the shallower crustal sections represented by the Vioolsdrif Intrusive Suite and Orange River Group is associated with enriched δ^{56}Fe isotopic signatures. Evidence suggests that the Haib porphyry copper deposit was formed in a mature island arc setting or continental arc setting associated with amphibole fractionation in the mid-crust during the Palaeoproterozoic. The evidence for a mature island arc setting includes the limited inheritance of Hf and O isotopes in zircon that is indicative of little or no older continental crust involvement (Meng et al., 2021). The evidence for a continental arc setting includes inherited zircons which have Sm-Nd modal ages of ~ 2.4 Ga and indicates an older continental crust involvement (Macey et al., 2017). Additional evidence for an older continental crust involvement includes the Bankwasser fragment which is located at the boundary between the Pella and Vioolsdrif Domains and possibly forms part of the Kaapvaal Craton (Macey et al., 2017).

7.1.5. Temporal perspective

The Palaeoproterozoic Haib deposit is similar to Phanerozoic porphyry deposits based on the overlap of the δ^{65}Cu and δ^{56}Fe isotopic signatures of the chalcopyrite grains, the direct comparison of the δ^{56}Fe signatures of the host granodiorite porphyry in the Duolong deposit and Haib deposit and the magmatic assemblage oxybarometers i.e. amphibole + magnetite + quartz + rutile + sphene in the host granodiorite porphyry which is indicative of elevated oxygen fugacity and corroborates with the enriched δ^{56}Fe signature of the host granodiorite porphyry. The limited range in the δ^{65}Cu and δ^{56}Fe signatures of the Palaeoproterozoic Haib deposit relative to Phanerozoic deposits suggests preservation of the Haib system at relatively

deep crustal levels. This is supported by the association with the Kokerboom Intrusion. The shallower levels of the Haib porphyry copper deposit, where more extensive, secondary isotopic fractionation is more likely to have occurred, appears to have been eroded away. Therefore, the Palaeoproterozoic Haib deposit is different compared to Phanerozoic deposits based on the deposit exposure at deep levels of the porphyry system (~12 km), the limited ranges in the $\delta^{65}Cu$ and $\delta^{56}Fe$ signatures, the association with mafic-ultramafic cumulates (Kokerboom Intrusion) that hosts unique sulphide mineralization (chalcopyrite) and lack of shallow alteration (propylitic and argillic).

According to Gaal and Isohanni (1979), Precambrian porphyry copper deposits are similar to Phanerozoic porphyry copper deposits however, there are certain variations which are noteworthy:

1. Precambrian host rocks have initial $^{87}Sr/^{86}Sr$ ratios that are < 0.705 which indicate that the magma was sourced from mantle material in an arc setting lacking substantial contamination or residence time from the lithospheric plate or crustal material (Sikka and Nehru, 1997). This is applicable to the Palaeoproterozoic Haib deposit as according to Reid et al. (1987) initial isotope ratios (Sr, Pb, Nd) in the Richtersveld Subprovince indicate juvenile crust generation in a mature arc setting during the early Proterozoic. The lack of crustal contamination is further supported by the limited inheritance of Hf and O isotopes in zircon.

2. Precambrian ore deposits have grades and tonnages that are considerably lower than Phanerozoic deposits (Gaal and Isohanni, 1979; Nironen and Csongradi, 1984). The limited ranges in the $\delta^{65}Cu$ and $\delta^{56}Fe$ signatures of the Haib porphyry copper deposit relative to Phanerozoic porphyry deposits support this as greater ranges in $\delta^{65}Cu$ and $\delta^{56}Fe$ signatures are associated with higher grades and tonnages which is seen in Phanerozoic deposits.

3. Hydrothermal alteration and distinct zonal patterns of sulphide minerals are rarely present (Nironen and Csongradi, 1984). The Haib porphyry copper deposit lacks shallow alteration assemblages (propylitic and argillic) and is dominantly associated with potassic and phyllic alteration.

Porphyry copper deposits occur throughout the geological record but are more abundant in younger terranes that have been subjected to the least erosion (Seedorff et al., 2005; Kesler and Wilkinson, 2005; William and Kesler, 2009). The longer-lived continental crust in the Precambrian has been subjected to exhumation and therefore near surface ores at mineralized destructive plate margins have been destroyed (Hawkesworth et al., 2020). Phanerozoic deposits are better preserved as they have not been subjected to intense and prolonged exhumation.

Richards and Mumin (2013) has indicated that the rarity of Precambrian porphyry copper deposits is difficult to be explained solely by erosion despite the lack of evidence of porphyry copper deposits found in abundance prior to the Phanerozoic. There are many Precambrian supracrustal sequences preserved globally, including arc sequences, however irrefutable porphyry-type deposits in these sequences are practically non-existent (Seedorff et al., 2005). Porphyry copper deposits can be correlated with various metallogenic epochs which reflect intervals of subduction (Wilkinson and Kesler, 2009). The greater probability of porphyry copper deposits in the Phanerozoic as opposed to the Precambrian is due to the amount of erosion experienced **and the possible non-formation of porphyry copper deposits prior to**

the onset of "modern" plate tectonics (Richards, 2021). It is also possible that during the Precambrian, tectonic processes were different to the Phanerozoic. The Earth as a planetary system has experienced significant changes since its formation (Palin et al., 2020). Some of these changes include the secular cooling of the mantle, changes in plate velocities, crustal thickness, subduction depth, magmatic regimes and metamorphic conditions which have directly affected tectonic processes and are manifested by temporal trends observed in the geological record (Palin et al., 2020; Neill et al., 2022). The occurrence of mineral deposits is not randomly distributed spatially and temporally (Robb and Hawkesworth (2020)). There are geological trends that correlates deposit types to crustal evolution and tectonic setting. According to Hawkesworth et al. (2020) ore deposits reflect local tectonic processes, and their distribution has been modified by subsequent geological events. There are various proposed estimates for the onset of modern plate tectonics (Hawkesworth et al., 2020; Neill et al., 2022). The unambiguous evidence to support this includes the occurrence of blueschists, low temperature eclogites, emergence of contemporaneous metamorphic asymmetry/paired metamorphism, calc-alkaline igneous rocks, structural style in orogenic belts, dyke swarms, large sedimentary basins and high-pressure metamorphism associated with crustal thickening and mountain building (Brown, 2014; Brown and Johnson, 2018; Brown et al., 2020; Hawkesworth et al., 2020; Neill et al., 2022). These lines of evidence are related to destructive plate margins at convergent orogenic belts.

Porphyry copper deposits occur at convergent margins and are found in shallow crustal rocks (1-5 km) above magmatic batholiths (5-10 km). Therefore, porphyry copper deposits are related with cooler shallow country rocks (Richards and Mumin, 2013). The lower geothermal gradient in the Phanerozoic facilitated the greater formation of porphyry copper deposits. It is possible that higher mantle temperatures limited or even prevented stable subduction (Brown et al., 2022). It has been debated and proposed that the Precambrian was most likely affiliated with a hotter mantle, higher heat flow, increased melting and lower viscosity (Brown, 2014; Brown and Johnson, 2018; Brown et al., 2020; Hawkesworth et al., 2020; Neill et al., 2022). All these parameters resulted in vigorous whole mantle convection producing thicker primary oceanic crust that underwent shallow subduction (Hawkesworth et al., 2020; Neill et al., 2022). The thicker oceanic crust was difficult to subduct as slab suction rates were lower in the Precambrian (Hawkesworth et al., 2020; Neill et al., 2022). Therefore, tectonic processes that took place were plume-lid tectonics and delamination (Brown, 2014; Brown and Johnson, 2018; Brown et al., 2020; Hawkesworth et al., 2020; Neill et al., 2022). It is proposed that the rate of crustal reworking and destruction was greater, and plate tectonic processes were faster (Brown, 2014; Brown and Johnson, 2018; Brown et al., 2020, Hawkesworth et al., 2020; Neill et al., 2022). This presumably led to a relatively small volume of crust preserved in the Precambrian. Numerical modelling of continental collision shows that as the geothermal gradient cooled there was a transition from shallow to deep slab break off (Brown et al., 2022). This was related with stronger crustal-mantle coupling that enabled subduction to deep mantle depths as the upper mantle temperature cooled (Brown et al., 2022).

The requirements to generate a porphyry copper deposit include i) the formation of calc-alkaline magmas with high oxidation states and high H_2O, O, Cl and sulphur contents, ii) the supply of this magma must have a sufficient volume and be localized to maintain an upper crustal magmatic system ($\geq$100 km^2) in order for Cu (and S) to be extracted by magmatic-hydrothermal fluids (Richards, 2005). The requirements imply that a long-lived magmatic system that is rooted in the supra-subduction zone mantle wedge associated with the formation of an extensive lower crustal melting and assimilation (MASH) zone is imperative (Richards, 2005). Thus, the formation of porphyry copper deposits is associated with long-lived trans-crustal magma chambers and MASH processes. These MASH processes include melting of

crustal rocks, assimilation of crustal rocks, storage into lower crustal dykes/sills complexes and homogenisation to form hybrid calc-alkaline magmas (Richards, 2005). A long-lived magma chamber is dependent on stable subduction therefore, as the ambient mantle temperature cooled and stabilized, the formation of porphyry copper deposits became more dominant. The few occurrences of porphyry copper deposits in the Precambrian can be explained by variations in geothermal gradients and source sulphur contents. These variations probably allowed for the formation of a long-lived magmatic crustal system that was also related with the formation of cratons such as the Kaapvaal, Pilbara and Slave cratons (Richards and Mumin, 2013).

7.2. Integrated conclusions

Porphyry copper deposits are important in the geological record as these deposits serve as the primary source of the world's copper. The Haib porphyry copper deposit is a unique porphyry copper deposit as the deposit is Palaeoproterozoic in age, is associated with clinopyroxene and amphibole rich cumulates which host novel sulphide mineralization, show lines of evidence related to the deeper parts of the porphyry copper system and has limited ranges in $\delta^{65}Cu$ and $\delta^{56}Fe$ signatures. Previous studies show that garnet and/or amphibole fractionation is associated with the petrogenesis of porphyry copper deposits. The Haib porphyry copper deposit is associated with amphibole fractionation as opposed to garnet fractionation which is supported by petrological and geochemical observations (trace element analyses) from this study. Previous work also indicate that garnet fractionation should result in a heavier iron isotope signature in the residual melts and form cumulates with lower $\delta^{56}Fe$ compositions. $\delta^{56}Fe$ analyses (depleted $\delta^{56}Fe$ signatures with an average of 0.03 ± 0.07 ‰) in this study indicate that amphibole fractionation plays an important role in the formation of porphyry copper deposits as amphibole fractionation has the potential to form low $\delta^{56}Fe$ signature cumulates associated with an enriched $\delta^{56}Fe$ signature in the residual magma. This is observed by the depleted $\delta^{56}Fe$ isotopic compositions of the Kokerboom Intrusion and the enriched $\delta^{56}Fe$ isotopic signature of the residual magma which formed the Vioolsdrif Intrusive Suite and Orange River Group. The deposit represents mid-crustal levels and therefore reflects the deeper parts of the porphyry system which is supported by the presence of early dark micaceous veins, the limited ranges in $\delta^{65}Cu$ and $\delta^{56}Fe$ signatures for the Haib sulphides relative to Phanerozoic deposits, the lack of shallow alteration (propylitic and argillic alteration) and by the geothermobarometry as results indicate an approximate pressure of 4 kbar correlating with a crustal depth of approximately 12 km. The probability of forming a porphyry copper deposit is estimated to be ~0.001% (Richard, 2021). Less than 1/10 of deposits are uplifted and exposed at shallow crustal levels to be economically mined (0.0001%) (Richards, 2021). Continued exhumation (uplift and erosion) in active continental margins remove these upper-crustal deposits from the geological record (Richards, 2021). This then reduces the probability of finding them in older arc systems making them almost non-existent in the Precambrian (Richards, 2021). In addition, it is probable that plate tectonic processes in the Precambrian was different from the Phanerozoic influencing the formation of porphyry copper deposits in the Precambrian. The copper and iron isotopic results from this study indicate that copper and iron isotopes can be used as a tool to identify the crustal depth of a porphyry system.

7.3. Future recommendations

1. **Zn isotope analyses** will be useful in determining crustal thickness as the amphiboles in the Haib samples from this study are highly altered to biotite and is therefore not a robust barometer. The results from the Zn isotopes can be compared to the machine learning geothermobaromtry conducted in this study.
2. **In-situ trace element analyses** on the sulphides (chalcopyrite and pyrite) will add to our understanding on the metallogenesis based on in-situ concentrations of various metals.
3. **Sulphur isotope analyses** will assist in better constraining mineralization and comparison with copper and iron isotopes will be useful and contribute to further understanding the metallogenesis based on variations in isotopic trends.
4. **Re-Os age dating** will be useful in determining the age of the various sulphide phases.
5. **Geochemical analyses on additional lower crustal cumulates** i.e. the Arizona arclogites will assist in better understanding metallogenesis in the deeper parts of the porphyry system.
6. **Detailed structural analyses in the field** will assist in better constraining the structural controls on mineralization.
7. **Copper and iron isotope analyses on additional Proterozoic porphyry copper deposits** such as the Samba deposit in the Zambian Copperbelt, the Malanjkhand deposit in the Singhbum Craton, India, the Gaoua deposits of Burkino Faso, the Yongkuanyu deposit in the South China Craton and the Aitik and Tallberg deposits in the Skellefte District of Sweden and compare data with the Haib deposit.
8. Porphyry copper deposits generally occur in linear belts. The Richtersveld Magmatic Arc is covered by a considerable portion of Phanerozoic cover. **Conducting geophysical methods including gravity, magnetics, electrical chargeability, resistivity and radiometrics** will be useful in determining whether there are additional porphyry copper deposits similar to Haib concealed beneath this Phanerozoic cover.
9. **Copper and iron isotope analyses on samples from the various alteration zones associated with mineralization** will assist in better constraining the spatial variations of copper and iron isotope systematics and will serve as a vector for targeting highly mineralized zones.
10. **Geochemical analyses (major and trace element analyses and Cu and Fe isotope analyses) on the mafic enclaves.** Previous studies on the Phanerozoic Dabu porphyry Cu-Mo deposit show that there is a link between mafic enclaves and porphyry copper metallogenesis. The analyses will assist in better constraining mineralization links, serve as a comparison with a Phanerozoic deposit and provide further understanding on the temporal variations of porphyry copper deposits through geological time.
11. **In-situ trace element analyses on zircon** to assess porphyry copper potential. Studies conducted by Lee et al. (2021) show that changes in zircon trace element composition from barren lithologies to mineralized lithologies coincides with copper mineralization.

References

Anbar, A.D. and Rouxel, O. (2007). Metal stable isotopes in paleoceanography. *Annual Review of Earth Planetary Science,* **35,** 717–746.

Audétat, A. and Simon, A.C. (2012). Magmatic controls on porphyry copper genesis. In: Hedenquist J.W., Harris M., Camus F. (eds) Geology and genesis of major copper deposits and districts of the world: a tribute to Richard H Sillitoe. *Society of Economic Geologists,* **16,** 553-572.

Baggio, S. B., Hartmann, L. A., Lazarov, M., Massonne, H.-J., Theye, T., Viefhaus, T. (2018). Origin of native copper in the Paraná volcanic province, Brazil, integrating Cu stable isotopes in a multi-analytical approach. *Mineralium Deposita,* **53,** 417-434.

Barber, N.D., Edmonds, M., Jenner, F., Audétat, A., Williams, H. (2021). Amphibole control on copper systematics in arcs: Insights from the analysis of global datasets, *Geochimica et Cosmochimica Acta,* **307,** 192-211.

Barr, J.M. and Reid, D.L. (1992). Hydrothermal alteration at the Haib porphyry copper deposit, Namibia: Stable isotope and fluid inclusion patterns. *Communications of the Geological Survey of Namibia, **8,*** 23-35.

Beukes, G.J., (1973). 'n Geologiese ondersoek van die gebied suid van Warmbad, Suidwes-Afrika, met spesiale verwysing na die metamorf-magmatiese assosiasies van die Voorkambriese gesteentes. D.Sc. Thesis, Univ. Orange Free State, Bloemfontein, 333p.

Bilenker L. D., Simon A. C., Reich M., Lundstrom C. C., Gajos N., Bindeman I., Barra F. and Munizaga R. (2016). Fe–O stable isotope pairs elucidate a high-temperature origin of Chilean iron oxide-apatite deposits. *Geochimica et Cosmochimica Acta*, **177,** 94-104.

Black, L.P., Kamo, S.L., Allen, C.M., Davis, D.W., Aleinikoff, J.N., Valley, J.W. and Foudoulis, C., (2004). Improved $^{206}Pb/^{238}U$ microprobe geochronology by the monitoring of a trace-element-related matrix effect; SHRIMP, ID–TIMS, ELA–ICP–MS and oxygen isotope documentation for a series of zircon standards. *Chemical Geology*, **205,** 115-140.

Blignault, H.J. (1977). Structural-metamorphic imprint on part of the Namaqua mobile belt in South West Africa. Bulletin, Precambrian Research Unit, University of Cape Town, **23,** 197.

Brown, M. (2014). The contribution of metamorphic petrology to understanding lithosphere evolution and geodynamics. *Geoscience Frontiers,* **5,** 553-569.

Brown, M. and Johnson, T. (2018). Secular change in metamorphism and the onset of global plate tectonics. *American Mineralogist,* **103,** 181-96.

Brown, M., Johnson, T. and Gardiner, N. J. (2020) Plate tectonics and the Archean Earth. *Annual Review of Earth and Planetary Science* **48**, 291-320.

Carrasquero, S.I., Rubinstein, N.A, Gómez, A.L.R.; Chiaradia, M.; Fontignie, D., Valencia, V.A., (2018). New insights into petrogenesis of Miocene magmatism associated with porphyry copper deposits of the Andean Pampean flat slab, Argentina. *Geoscience Frontiers*, **9,** 1565-1576.

Chang, J., and Audétat, A. (2018). Petrogenesis and metal content of hornblende-rich xenoliths from two Laramide-age magma systems in southwestern USA: Insights into the metal budget of arc magmas. *Journal of Petrology,* **59,** 1869-1898.

Chelle-Michou, C., Rottier, B., Caricchi, L. & Simpson, G. (2017) Tempo of magma degassing and the genesis of porphyry copper deposits. *Science Reports*, **7**, 40566.

Chen, K., Tang, M., Lee, C.T.A., Wang, Z., Zou, Z., Hu Z., Liu, Y. (2020). Sulfide-bearing cumulates in deep continental arcs: The missing copper reservoir. *Earth and Planetary Science Letters*, **531,** 115971.

Childress T. M., Simon A. C., Day W. C., Lundstrom C. C. and Bindeman I. N. (2016). Iron and oxygen isotope signatures of the Pea Ridge and Pilot Knob magnetite-apatite deposits, southeast Missouri, USA. *Economic Geology*, **111,** 2033-2044.

Chin, E.J., Lee, C.-T.A., Barnes, J., (2014). Thickening, refertilization, and the deep litho-sphere filter in continental arcs: constraints from major and trace elements and oxygen isotopes. *Earth and Planetary Science Letters,* **397,** 184-200.

Chin, E.J., Shimizu, K., Bybee, G.M., Erdman, M.E. (2018). On the development of the calc-alkaline and tholeiitic magma series: a deep crustal cumulate perspective. *Earth and Planetary Science Letters,* **482,** 277-287.

Cilliers, B., 1989. 'n Petrogenetiese studie van 'n gedeelte van die Namakwalandse Metamorfe Kompleks langs die Oranjerivier tussen die Ramansdrif- en Homriviere, Warmbad distrik, suidelike Suidwes-Afrika/Namibia M.Sc. Thesis (Unpubl.). Univ. Orange Free State. 227 pp.

Cline, J. S. & Bodnar, R. J. (1991). Can economic porphyry copper mineralization be generated by a typical calc-alkaline melt. *Journal for Geophysical Research Solid Earth,* **96**, 8113–8126.

Coetzee, C.B., (1941). The petrology of the Goodhouse-Pella area, Namaqualand, South Africa. *Transactions of the Geological Society of South Africa,* **44,** 167-206 / 28, 199-205.

Colliston, W.P. and Schoch, A.E. (2000). Mid-Proterozoic tectonic evolution along the Orange River on the border between South Africa and Namibia. *Communications of the Geological Survey of Namibia*, **12,** 57-66.

Cooke, D. R., Hollings, P., Wilkinson, J. J., & Tosdal, R. M. (2014). Geochemistry of porphyry deposits. *Treatise on geochemistry: Geochemistry of mineral deposits 2nd ed., Oxford: Elsevier.* **3,** 357-381 Oxford: Elsevier.

Cornell, D.H., Thomas, R.J., Moen, H.F.G., Reid, D.L., Moore, J.M., Gibson, R.L. (2006). The Namaqua-natal province. *In:* Johnson, M.R., Anhaeusser, C.R., Thomas, R.J. (Eds.*), The Geology of South Africa.* Geological Society of South Africa and Council for Geoscience, South Africa, 325-379.

Dauphas, N., Craddock, P.R., Asimow, P.D., Bennett, V.C., Nutman, A.P., Ohnenstetter, D. (2009). Iron isotopes may reveal the redox conditions of mantle melting from Archean to present. *Earth and Planetary Science Letters,* **288,** 255-267.

Dauphas, N., John, S. G., Rouxel, O., (2017). Iron isotope systematics In: Teng, F.-Z., Watkins, J. M., Dauphas, N. (eds) Non-Traditional Stable Isotopes. *Reviews in Mineralogy & Geochemistry,* **82,** 415-510.

Davis, G.H., Reynolds, S.J. and Kluth, C.F. (2012). Structural Geology of Rocks and Regions. *Wiley*, 3rd edition.

De Villiers, J. and Burger, A.J., (1967). Note on the minimum age of certain granites from the Richtersveld area. *Annual Geological Survey of South Africa,* **6,** 83-84.

Du, D.-H., Tang, M., Li, W., Kay, S.M., and Wang, X.-L., (2022). What drives Fe depletion in calc-alkaline magma differentiation: Insights from Fe isotopes: *Geology,* **50,** 10.

Duan J., Tang J., Li Y., Liu S. A., Wang Q., Yang C. and Wang Y. (2015) Copper isotopic signature of the Tiegelongnan high-sulfidation copper deposit, Tibet: implications for its origin and mineral exploration. *Mineralium Deposita*, **51,** 591-602.

Ducea, M.N., Bowman, E., Chapman, A.D., Balica, C. (2020). Arclogites and their role in continental evolution; Part 1: Background, locations, petrography, geochemistry, chronology and thermobarometry. *Earth-Science Reviews,* **214.**

Durning, W.P. and Davids, J.D. (1978). The root-zone characteristics of porphyry copper deposits. *Arizona Geological Digest,* **11,** 81-89.

Ehrlich S., Butler I., Halicz L., Rickard D., Oldroyd A. and Matthews A. (2004). Experimental study of the copper isotope fractionation between aqueous Cu(II) and covellite, CuS. *Chemical Geology,* **209(3–4),** 259-269.

Foden, J., Sossi, P. A., Nebel, O. (2018). Controls on the iron isotopic composition of global arc magmas. *Earth and Planetary Science Letters,* **494,** 190-201.

Frey, F. A., Haskin M. A., Poetz, J. and Haskin, L. A. (1968). Rare earth abundances in some basic rocks. *Journal of Geophysical Research,* **73,** 6085-6098.

Gaal, G. and Isohanni, M. (1979). Characteristics of Igneous Intrusions and Various Wall Rocks in some Precambrian Porphyry Copper-Molybdenum Deposits in Pohjanmaa, Finland. *Economic Geology*, **74,** 1198-1210.

Gagnevin D., Boyce A., Barrie C., Menuge J. and Blakeman R. (2012). Zn, Fe and S isotope fractionation in a large hydrothermal system. *Geochimica et Cosmochimica Acta,* **88,** 183-198.

Gagnevin, D., Boyce, A.J., Barrie, C.D., Menuge, J.F., Blakeman, R.J. (2012). Zn, Fe and S isotope fractionation in a large hydrothermal system. *Geochimica et Cosmochimica Acta*, **88,** 183-198.

Gao Z., Zhu X., Sun J., Luo Z., Bao C., Tang C. and Ma J. (2018). Spatial evolution of Zn-Fe-Pb isotopes of sphalerite within a single ore body: a case study from the Dongshengmiao ore deposit, Inner Mongolia, China. *Mineralium Deposita,* **53,** 55-65.

Gevers, T.W., (1941). Correlation of the pre-Cape formations in the western Cape Province: Discussion, Proc. *Geological Society of South Africa.*, **43,** 1xvii-1xxx.

Graham S., Pearson N., Jackson S., Griffin W. and O'Reilly S. Y. (2004). Tracing Cu and Fe from source to porphyry: in situ determination of Cu and Fe isotope ratios in sulfides from the Grasberg Cu–Au deposit. *Chemical Geology,* **207,** 147-169.

Gregory M. J. and Mathur R. (2017). Understanding copper isotope behavior in the high temperature magmatic-hydrothermal porphyry environment. *Geochemistry, Geophysics, Geosystems,* **18,** 4000-4015.

Gresse, P.G., Macey, P.H., Smith, H., Hartnady, M.I. and Frei, D., (2016). The Pre-Gariep geology east of Rosh Pinah, Karas Region, S. Namibia. Explanation to parts of 1:50 000 Geological Map Sheets 2716DA, 2716DB, 2716DC, 2716DD, 2717CC, 2816BB and 2817AA. *Geological Survey of Namibia,* Council for Geoscience S.A., Min. Mines and Energy, Namibia. 193 pp.

Grumbley, N. L. (2015). *The Geological Evolution of the Haib Cu-Mo Porphyry, Namibia.* MSc thesis, Trinity College Dublin.

Hannah J., Stein H., Wieser M., De Laeter J. and Varner M. (2007). Molybdenum isotope variations in molybdenite: vapor transport and Rayleigh fractionation of Mo. *Geology,* **35,** 703-706.

Hanson, G.A. (1980). Rare earth elements in petrogenetic studies of igneous systems. *Annual Review of Earth and Planetary Science,* **8,** 371-406.

Hao, H., Campbell, I.H., Park, J.-W., and Cooke, D.R. (2017). Platinum-group element geochemistry used to determine Cu and Au fertility in the Northparkes igneous suites, New South Wales, Australia. *Geochimica et Cosmochimica Acta,* **216,** 372-392.

Harmon, R. S., Barreiro, B. A., Moorbath, S., Hoefs, J., Francis, P. W., Thorpe, R. S., Deruelle, B., McHugh, J. and Viglino, J. A., (1984). Regional O -, Sr-, and Pb-isotope relationships in late Cenozoic calc-alkaline lavas of the Andean Cordillera. *Journal of the Geological Society, London,* **141,** 803-822.

Hartnady, C.J.H., Joubert, P., Stowe, C.W., (1985). Proterozoic crustal evolution in southwestern Africa. *Episodes,* **8,** 236-244.

Hattori, K.H., Keith, J.D. (2001). Contribution of mafic melt to porphyry copper mineralization: evidence from Mount Pinatubo, Philippines, and Bingham Canyon, Utah, USA. *Mineral Deposits,* **36,** 799-806.

Hawkesworth, C.J., Cawood, P.A. and Dhuime, B. (2020). The Evolution of the Continental Crust and the Onset of Plate Tectonics. *Frontiers in Earth Science.* **8,** 326.

He, Z., Zhang, X., Deng, X., Hu, H., Li, Y, Yu, H., Archer, C., Li, J., Huang, F. (2020). The behavior of Fe and S isotopes in porphyry copper systems: Constraints from the Tongshankou Cu-Mo deposit, Eastern China. *Geochemica et Cosmochimica Acta,* **270,** 61-83.

Hedenquist, J., Lowenstern, J. (1994). The role of magmas in the formation of hydrothermal ore deposits. *Nature,* **370**, 519-527.

Heimann, A., Beard, B. L. and Johnson, C. M. (2008). The role of volatile exsolution and sub-solidus fluid/rock interactions in producing high Fe-56/Fe-54 ratios in siliceous igneous rocks. *Geochimica et Cosmochimica Acta,* **72,** 4379-4396.

Herzarkhani A., Williams-Jones A. E. and Gammons C. H. (1999). Factors controlling copper solubility and chalcopyrite deposition in the Sungun porphyry copper deposit, Iran. *Mineralium Deposita,* **34(8),** 770-783.

Hill, P. S., Schauble, E. A. and Young, E. D. (2010) Effects of changing solution chemistry on Fe3+/Fe2+ isotope fractionation in aqueous Fe–Cl solutions. *Geochimica et Cosmochimica Acta,* **74,** 6669-6689.

Hollister, V.F., Potter, R.R. and Barker, A.C. (1974). Porphyry-type deposits of the Appalachian orogen. *Economic Geology,* **69,** 618-630.

Holwell, D.A., Fiorentini, M.L., Knott, T.R., McDonald, I., Blanks, D.E., McCuaig, T.C. and Gorczyk, W. (2022). Mobilisation of deep crustal sulfide melts as a first order control on upper lithospheric metallogeny. *Nature Communications,* **13,** 573.

Huang, F., Chakraborty, P., Lundstrom, C. C., Holmden, C., Glessner, J. J., Kieffer, S. W., Lesher, C. E. (2010). Isotope fractionation in silicate melts by thermal diffusion. *Nature,* **464,** 396-400.

Ikehata, K., Notsu, K., Hirata, T. (2011). Copper isotope characteristics of copper-rich minerals from Besshi-type volcanogenic massive sulfide deposits, Japan, determined using a femtosecond LA-MC-ICP-MS. *Economic Geology,* **106,** 307-316.

Jenner, F.E. (2017). Cumulate causes for the low contents of sulfide-loving elements in the continental crust. *Nature Geoscience,* **10,** 524-529.

John, D.A., Ayuso, R.A., Barton, M.D., Blakely, R.J., Bodnar, R.J., Dilles, J.H., Gray, Floyd, Graybeal, F.T., Mars, J.C., McPhee, D.K., Seal, R.R., Taylor, R.D., and Vikre, P.G. (2010). *Porphyry copper deposit model, chap. B of Mineral deposit models for resource assessment,* U.S. Geological Survey Scientific Investigations Report 2010–5070–B, 1-169.

Johnson, C. M., Beard, B. L., Weyer, S. (2020). Iron Geochemistry: An Isotopic Perspective. *Springer.*

Jorgenson, C., Higgins, O., Petrelli, M., Bégué, F., & Caricchi, L. (2022). A Machine Learning-Based Approach to Clinopyroxene Thermobarometry: Model Optimization and Distribution for Use in Earth Sciences. *Journal of Geophysical Research: Solid Earth, **127*****(4),** 1-21.

Joubert, P. (1986). Namaqualand - A model of Proterozoic accretion? *Transactions of the Geological Society of South Africa,* **89,** 79-96.

Kesler, S.E. and Wilkinson, B.H. (2006). The role of exhumation in the temporal distribution of ore deposits. *Economic Geology,* **101,** 919-922.

Knipping J. L., Bilenker L. D., Simon A. C., Reich M., Barra F., Deditius A. P., Lundstrom C., Bindeman I. and Munizaga R. (2015). Giant Kiruna-type deposits form by efficient flotation of magmatic magnetite suspensions. *Geology,* **43,** 591-594.

Lang, J.R., Titley, S.R. (1998). Isotopic and geochemical characteristics of Laramide magmatic systems in Arizona and implications for the genesis of porphyry copper deposits. *Economic Geology,* **93,** 138-170.

Larson, P. B., Maher, K., Ramos, F.C., Chang, Z., Gaspar, M., Meinert, L. D. (2003). Copper isotope ratios in magmatic and hydrothermal ore-forming environments. *Chemical Geology,* **201,** 337-350.

Le Bras, L. Y., Bolhar, R., Bybee, G. M., Nex, P. A. M., Guy, B. M., Moyana, T., Lourens, P. (2020). Platinum-Group and trace elements in Cu-sulphides from the Loolekop pipe, Phalaborwa: Implications for ore-forming processes. *Mineralium Deposita,* **56,** 161-177.

Lee, C.-T.A., and Tang, M. (2020) How to makes porphyry copper deposit. *Earth and Planetary Science Letters, **529,*** 1-11.

Lee, C.-T.A., Anderson, D., (2015). Continental crust formation at arcs, the arclogite "delamination" cycle, and one origin for fertile melting anomalies in the mantle. *Science Bulletin.*

Lee, C.-T.A., Cheng, X., Horodyskyj, U. (2006). The development and refinement of continental arcs by primary basaltic magmatism, garnet pyroxenite accumulation, basaltic recharge and delamination: insights from the Sierra Nevada, California. *Contributions to Mineralogy and Petrology,* **151,** 222-242.

Lee, C.-T.A., Luffi, P., Chin, E.J., Bouchet, R., Dasgupta, R., Morton, D.M., Le Roux, V., Yin, Q.-z., Jin, D. (2012). Copper systematics in arc magmas and implications for crust–mantle differentiation. *Science,* **336,** 64-68.

Lee, C.-T.A., Morton, D.M., Kistler, R.W., Baird, A.K. (2007). Petrology and tectonics of Phanerozoic continent formation: from island arcs to accretion and continental arc magmatism. *Earth and Planetary Science Letters,* **263,** 370-387.

Lee, C-T.A. and Anderson, D. (2015). Continental crust formation at arcs, the arclogite "delamination" cycle, and one origin for fertile melting anomalies in the mantle. *Science Bulletin.*

Lee, C-T.A., Luffi, P., Chin, E.J., Bouchet, R., Dasgupta, R., Morton, D.M., Le Roux, V., Xin, Q.-z., and Jin, D. (2012). Copper systematics in arc magmas and implications for crust-mantle differentiation. *Science,* **336,** 64-68.

Li J. W., Zhao X. F., Zhou M. F., Ma C. Q., de Souza Z. S. and Vasconcelos P. (2009). Late Mesozoic magmatism from the Daye region, eastern China: U-Pb ages, petrogenesis, and geodynamic implications. *Contributions to Mineralogy and Petrology,* **157,** 383-409.

Li J. X., Qin K. Z., Li G. M., Evans N. J., Huang F. and Zhao J. X. (2018). Iron isotope fractionation during magmatic-hydrothermal evolution: A case study from the Duolong porphyry Cu-Au deposit Tibet. *Geochimica et Cosmochimca Acta,* **238,** 1-15.

Li W. Q., Jackson S. E., Pearson N. J. and Graham S. (2010). Copper isotopic zonation in the Northparkes porphyry Cu–Au deposit, SE Australia. *Geochimica et Cosmochimca Acta,* **74,** 4078-4096.

Li, Q.-W., Nebel-Jacobsen, Y., Zhao, J.-H., Nebel, O., Richter, M., Cawood, P. A. and Wang, Q. (2021). An early garnet redox-filter as an additive oxidizer in lower continental arc crust traced through Fe isotopes. *Journal of Geophysical Research: Solid Earth*, **126,** 1-15.

Li, W. Q., Jackson, S. E., Pearson, N. J. and Graham, S. (2010a). Copper isotopic zonation in the Northparkes porphyry Cu–Au deposit, SE Australia. *Geochimica et Cosmochimica Acta,* **74,** 4078-4096.

Liang, W., Huang, J., Zhang, G., F., Huang. (2022). Iron isotopic fractionation during eclogite anatexis and adakitic melt evolution: insights into garnet effect on Fe isotopic variations in high-silica igneous rocks. *Contributions to Mineralogy and Petrology*, **177**, 33.

Lowell, J.D. and Guilbert, J.M. (1970). Lateral and Vertical Alteration-Mineralization Zoning in Porphyry Ore Deposits. *Economic Geology,* **65,** 373-408.

Lundstrom, C. (2009). Hypothesis for the origin of convergent margin granitoids and Earth's continental crust by thermal migration zone refining. *Geochimica et Cosmochimica Acta,* **73,** 5709-5729.

Macey, P.H., Minnaar, H., Miller, J.A., Lambert, C., Kisters, A.F.M., Diener, J., Thomas, R.J., Groenewald, C., Indongo, J., Angombe, M., Smith, H., Shifatoka, G., Le Roux, P., Frei D. (2015). The Precambrian geology of the Warmbad Region, southern Namibia. An interim explanation to 1:50 000 Geological Map Sheets of the 1:250 000 2818 Warmbad sheet. *Geological Survey of Namibia and Council for Geoscience of South Africa,* 720, Accompanied by twenty-four 1:50 000 geological maps.

Macey, P.H., Thomas, R.J., Minnaar, H.M., Gresse, P.G., Lambert, C.W., Groenewald, C.A., Miller, J.A., Indongo, J.I., Angombe, M., Shifotoka, G., Frei, D., Diener, J.F.A., Kisters, A.F.M., Dhansay, T., Smith, H., Doggart, S., le Roux, P., Hartnady, M.I., Tinguely, C. (2017). Origin and evolution of the ~1.9 Ga Richtersveld Magmatic Arc, SW Africa. *Precambrian Resources,* **292,** 417–451.

Macris, C. A., Manning, C. E. and Young, E. D. (2015) Crystal chemical constraints on inter-mineral Fe isotope fractionation and implications for Fe isotope disequilibrium in San Carlos mantle xenoliths. *Geochimica et Cosmochimica Acta,* **154,** 168-185.

Mahan, B., Mathur, R., Sanislav, I., Rea, P., and Dirks, P. (2023). Cu isotopes in groundwater for hydrogeochemical mineral exploration: A case study using the world-class Mount Isa Cu–Pb–Zn deposit (Australia), *Applied Geochemistry,* **148,** 1-9.

Maher K. C. and Larson P. B. (2007). Variation in copper isotope ratios and controls on fractionation in hypogene skarn mineralization at Coroccohuayco and Tintaya, Peru. *Economic Geology,* **102(2),** 225-237.

Maréchal, C., Télouk, P., Albarède, F. (1999). Precise analysis of copper and zinc isotopic compositions by plasma source mass spectrometry. *Chemical Geology,* **156,** 251-273.

Markl G., von Blanckenburg F. and Wagner T. (2006). Iron isotope fractionation during hydrothermal ore deposition and alteration. *Geochimica et Cosmochimica Acta,* **70,** 3011-3030.

Mathur R., Ruiz J., Casselman M. J., Megaw P. and van Egmond R. (2012). Use of Cu isotopes to distinguish primary and secondary Cu mineralization in the Can˜ariaco Norte porphyry copper deposit, Northern Peru. *Mineralium Deposita,* **47,** 755-762.

Mathur, R. and Fantle, M. S. (2015). Copper isotopic perspectives on supergene processes: implications for the global Cu cycle. *Elements,* **11,** 323-329.

Mathur, R., Jin, L., Prush, V., Paul, J., Ebersole, C., Fornadel, A., Williams, J.Z., and Brantley, S. (2012). Cu isotopes and concentrations during weathering of black shale of the Marcellus Formation, Huntingdon County, Pennsylvania (USA). *Chemical Geology,* **304-305,** 175-184.

Mathur, R., Ruiz, J., Casselman, M.J., Megaw, P. and van Egmond, R., (2012). Use of Cu isotopes to distinguish primary and secondary Cu mineralization in the Cañariaco Norte porphyry copper deposit, Northern Peru. *Mineralium Deposita,* **47(7),** 755-762.

Mathur, R., Ruiz, J., Titley, S., Liermann, L., Buss, H., Brantley, S. (2005). Cu isotopic fractionation in the supergene environment with and without bacteria. *Geochimica et Cosmochimica Acta,* **69,** 5233-5246.

Mathur, R., Titley, S., Barra, F., Brantley, S., Wilson, M., Phillips, A., Munizaga, F., Maksaev, V., Vervoort, J., and Hart, G., (2009). Exploration potential of Cu isotope fractionation in porphyry copper deposits. *Journal of Geochemical Exploration,* **2,** 1-6.

McMillan, M.D., (1968). The geology of the Witputs-Sendelingsdrif area. Bull. Precambrian Res. Unit, vol. 4. Univ. Cape Town. 177 pp.

Meng et al. (2021). Oxidized sulfur-rich arc magmas formed porphyry Cu deposits by 1.88 Ga. *Nature communications,* **12,** 2189.

Miller, R., McG. (2008). The geology of Namibia. Handbook, Geological Survey of Namibia, **3,** 5-15.

Minnaar, H. (2012). *Composition and evolution of the Proterozoic Vioolsdrif Batholith (including the Orange River Group), northern Cape Province, South Africa.* Ph.D. thesis. University of the Free State.

Minnitt, R.C.A. (1979). *The geological setting of porphyry-type copper mineralization in the Haib River area, South West Africa.* Ph.D. thesis, University of the Witwatersrand, Johannesburg.

Minnitt, R.C.A. (1986). Porphyry Copper-Molybdenum Mineralisation at Haib River, South West Africa/Namibia. *Mineral Deposits of Southern Africa,* **2**, 1567-1585.

Minnitt, R.C.A. (1986). Porphyry Copper-Molybdenum Mineralisation at Haib River, South West Africa/Namibia. *Mineral Deposits of Southern Africa,* **2**, 1567-1585.

Moynier, F., Vance, D., Fujii, T., Savage, P. S. (2017). The isotope geochemistry of zinc and copper. In: Teng, F.-Z., Watkins, J. M., Dauphas, N. (eds) Non-Traditional Stable Isotopes. *Reviews in Mineralogy & Geochemistry,* **82,** 543-600.

Müller, D., Franz, L., Herzig, P.M., Steve, H. (2001). Potassic igneous rocks from the vicinity of epithermal gold mineralization, Lihir Island, Papua New Guinea. *Lithos,* **57,** 163-186.

Mungall J. E. (2002). Roasting the mantle: slab melting and the genesis of major Au and Au-rich Cu deposits. *Geology,* **30,** 915-918.

Nebel, O., Sossi, P. A., Bénard, A., Arculus, R. J., Yaxley, G. M., Woodhead, J. D., Rhodri Davies, D., Ruttor, S. (2019). Reconciling petrological and isotopic mixing mechanisms in the Pitcairn mantle plume using stable Fe isotopes. *Earth and Planetary Science Letters,* **521,** 60-67.

Nironen, M. and Csongradi, J. (1984). Characteristics of Proterozoic porphyry-type Cu occurrence at Tienpää, Halsua, western Finland. *Bulletin of the Geological Society of America,* **56,** 89-97.

Norman, N. (2013). Geology off the beaten track exploring South Africa's hidden treasures. *Struik Nature,* South Africa 173.

Norrish, K., & Hutton, J. T. (1969). An accurate X-ray spectrographic method for the analysis of geologic samples. *Geochemica et Cosmochimica Acta,* **33,** 431-454.

O'Neill, C., Brown, M., Schaefer, B., Gazi, J.A. (2022). Earth's anomalous middle-age magmatism driven by plate slowdown. *Scientific Reports,* **12**, 10460.

Olson, Nansen H., Dilles, J.H., Kent, A.J.R. and Lang, J.R. (2017). Geochemistry of the Cretaceous Kaskanak Batholith and genesis of the Pebble porphyry Cu-Au-Mo deposit, Southwest Alaska. *American Mineralogist,* **102,** 1597-1621.

Oyarzun, R., Marquez, A., Lillo, J., Lopez, I., and Rivera, S. (2001). Giant versus small porphyry copper deposits of Cenozoic age in northern Chile: adakitic versus normal calc-alkaline magmatism. *Mineralium Deposita,* **36,** 794-798.

Palin, R.M., Santosh, M., Cao, W., Li, S., Hernández-Uribe, D. and Parsons, A. (2020). Secular change and the onset of plate tectonics on Earth. *Earth-Science Reviews,* **207,** 103172.

Park, J.W., Campbell, I.H., Chiaradia, M. Hao, H., Lee, C.-T.A. (2021) Crustal magmatic controls on the formation of porphyry copper deposits. *Nature Reviews Earth Environment*, **2**, 542-557.

Park, J.-W., Campbell, I.H., Kim, J., and Moon, J.-W. (2015). The role of late sulfide saturation in the formation of a Cu- and Au-rich magma: Insights from the platinum-group geochemistry of Niuatahi-Motutahi lavas, Tonga rear arc. *Journal of Petrology,* **56,** 59-81.

Park, J.-W., Campbell, I.H., Malaviarachchi, S.P.K., Cocker, H., Hao, H., and Kay, S.M. (2019). Chalcophile element fertility and the formation of porphyry Cu ± Au deposits. *Mineralium Deposita*, **54,** 657-670.

Petrus, J.A. and Kamber, B.S. (2012). VizualAge: A novel approach to laser ablation ICP-MS U-Pb geochronology data reduction. *Geostandards and Geoanalytical Research,* **36,** 247-270.

Petrus, J.A. and Kamber, B.S., (2012). VizualAge: A novel approach to laser ablation ICP-MS U-Pb geochronology data reduction. *Geostandards and Geoanalytical Research,* **36,** 247-270.

Petterson, A., Cornell, D. H., Yuhara, M. and Hirahara, Y. (2009). Sm-Nd data for granitoids across the Namaqua sector of the Namaqua-Natal Province, South Africa. *Geological Society, London, Special Publications,* **323,** 219-230.

Polyakov, V. B. and Mineev, S. D. (2000). The use of Mo¨ssbauer spectroscopy in stable isotope geochemistry. *Geochimica et Cosmochimica Acta,* **64,** 849-865.

Reid, D. L., Welke, H. J., Erlank, A. J. and Moyes, A. B. (1987). The Orange River Group, a Proterozoic volcanic belt in the western Namaqua Province, South Africa. In: *Geochemistry and mineralisation of Proterozoic volcanic suites* (Edited by Pharaoh, T. C., Beckinsale, R. D. and Rickard, D. T.) *Special Publication Geological Society* **33,** 327-346.

Reid, D.L. (1977). *Geochemistry of Precambrian igneous rocks in the lower Orange River region.* Bulletin, Ph.D. thesis, Precambrian Research Unit, University of Cape Town.

Reid, D.L. (1979). Petrogenesis of calc-alkaline metalavas in the mid-Proterozoic Haib Volcanic Subgroup, lower Orange River region. *Transactions of the Geological Society of South Africa,* **82,** 109-131.

Reid, D.L. (1979a). Age relationships within the mid-Proterozoic Vioolsdrif Batholith, lower Orange River region. *Transactions of the Geological Society of South Africa,* **82,** 305-311.

Reid, D.L. (1979a). Age relationships within the mid-Proterozoic Vioolsdrif Batholith, lower Orange River region. *Transactions of the Geological Society of South Africa,* **82,** 305-311.

Reid, D.L. (1979b). Total rock Rb-Sr and U-Th-Pb isotopic study of Precambrian metavolcanic rocks in the Lower Orange River region. *Earth and Planetary Science Letters,* **42,** 368-378.

Reid, D.L. (1997). Sm-Nd age and REE geochemistry of Proterozoic arc-related igneous rocks in the Richtersveld Subprovince, Namaqua Mobile Belt, Southern Africa. *Journal of African Earth Sciences, **24(4),** 621-633.*

Reid, D.L. and Minnaar, H. (2021). Lithostratigraphy of the Vuurdood Subsuite, an early mafic-ultramafic phase of the Palaeoproterozoic Vioolsdrif Intrusive Suite, Richtersveld Magmatic Arc, Northern Cape Province. *South African Journal of Geology,* **124 (3)**, 805-814.

Richard, J.P. (2015). The oxidation state, and sulfur and Cu contents of arc magmas: implications for metallogeny. *Lithos,* **233,** 27-45.

Richards J. P. (2011). High Sr/Y arc magmas and porphyry Cu ± Mo ± Au deposits: just add water. *Economic Geology.* **106,** 1075-1081.

Richards, J.P. (2005). Cumulative Factors in the Generation of Giant Calc-alkaline Porphyry Cu Deposits. *In:* Porter, *T.M.* (Eds.), *Super Porphyry Copper & Gold Deposits: A Global Perspective*, PGC Publishing, Adelaide, vol 1**,** 7-25.

Richards, J.P. (2009). Postsubduction porphyry Cu–Au and epithermal Au deposits: products of remelting of subduction-modified lithosphere. *Geology,* **37,** 247-250.

Richards, J.P., and Mumin, A.H. (2013). Magmatic-hydrothermal processes within an evolving Earth: Iron oxide-copper-gold and porphyry Cu ± Mo ± Au deposits. *Geology,* **41,** 767-770.

Richter, F. M., Dauphas, N., Teng, F.-Z. (2009a). Non-traditional fractionation of non-traditional isotopes: evaporation, chemical diffusion and Soret diffusion. *Chemical Geology,* **258,** 92-10.

Richter, F. M., Watson, E. B., Mendybaev, R., Dauphas, N., Georg, B., Watkins, J., Valley, J. (2009b). Isotopic fractionation of the major elements of molten basalt by chemical and thermal diffusion. *Geochimica et Cosmochimica Acta,* **73,** 4250-4263.

Rielli, A., Tomkins, A.G., Nebel, O., Raveggi, M., Jeon, H., Martin, L., Ávila, J.N. (2018). Sulfur isotope and PGE systematics of metasomatised mantle wedge. *Earth and Planetary Science Letters,* **497,** 181-192.

Ritter U. (1980). The Precambrian evolution of the eastern Richtersveld. Bulletin, *Precambrian Research Unit, University of Cape Town,* **26,** 276.

Robb, L. (2020). *Introduction to ore-forming processes.* Wiley-Blackwell.

Rodriguez-Vargas, A., Koester, E., Mallmann, G., Conceição, R. V., Kawashita, K., & Weber, M. B. I. (2005). Mantle diversity beneath the Colombian Andes, Northern Volcanic Zone: Constraints from Sr and Nd isotopes. *Lithos, **82*(3-4 SPEC. ISS.),** 471-484.

Rogers, A.W., (1916). The nature of the copper deposits of Little Namaqualand. Proceedings, *Geological Society of South Africa,* **19,** 21-35.

Rollinson, H.R. (1993). Using geochemical data Evaluation, presentation, interpretation. Longman Scientific and Technical, Wiley, New York, 352.

Runyon, S.E., Seedorff, E., Barton, M.D., Steele-MacInnis, M., Lecumberri-Sanchez, P. and Mazdab F.K. (2019). Coarse Muscovite Veins and Alteration in Porphyry Systems. *Ore Geology Reviews,* **113.** 1-32.

Runyon, S.E., Steele-MacInnis, M., Seedorff, E., Lecumberri-Sanchez, P. and Mazdab F.K. (2017). Coarse muscovite veins and alteration deep in the Yerington batholith, Nevada: insights into fluid exsolution in the roots of porphyry copper systems. *Mineralium Deposita,* **52,** 463-470.

Sajona, F.G., and Maury, R.C. (1998). Association of adakites with gold and copper mineralization in the Philippines Association d'adakites et de minéralisations Au-Cu aux Philippines. *Elsevier,* **326,** 27-34.

Saunier, G., Pokrovski, G. S. and Poitrasson, F. (2011) First experimental determination of iron isotope fractionation between hematite and aqueous solution at hydrothermal conditions. *Geochimica et Cosmochimica Acta,* **75,** 6629-6654.

Schoenberg, R., von Blanckenburg, F. (2006). Modes of planetary-scale Fe isotope fractionation. *Earth and Planetary Science Letters,* **252,** 342-359.

Schuessler, J. A., Schoenberg, R. and Sigmarsson, O. (2009). Iron and lithium isotope systematics of the Hekla volcano, Iceland – evidence for Fe isotope fractionation during magma differentiation. *Chemical Geology,* **258,** 78-91.

Seedorff, E., Barton, M.D., Stavast, J.A., Maher, D.J. (2008). Root Zones of Porphyry Systems: Extending the Porphyry Model to Depth. *Economic Geology,* **103 (5),** 939-956.

Seedorff, E., Einaudi, M.T., (2004). Henderson porphyry molybdenum system, Colorado: I. Sequence and abundance of hydrothermal mineral assemblages, flow paths of evolving fluids, and evolutionary style. *Economic Geology,* **99,** 3-37.

Shahar, A., Young, E. D. and Manning, C. E. (2008). Equilibrium high-temperature Fe isotope fractionation between fayalite and magnetite: an experimental calibration. *Earth and Planetary Science Letters,* **268,** 330-338.

Shifotoka, G., Indongo, J.I., Thomas, R.J., Macey, P.H. and Miller, J.A.M. (2016). 1:50000 geological map of the Haib region. Portions of map sheets 2817DA, DB, DC, DD. *Geological Survey of Namibia and Council for Geoscience, South Africa*

Sikka, D. and Nehru, C.E. (1997). Review of Precambrian porphyry Cu±Mo±Au deposits with special reference to Malanjkhand porphyry copper deposit, Madhya Pradesh, India. *Geological Society of India*, ***49*(3),** 239-288.

Sillitoe, R. H. (1973). The tops and bottoms of porphyry copper deposits. *Economic Geology*, **68 (6),** 799-815.

Sillitoe, R.H. (2010). Porphyry Copper systems. Society of Economic Geologists, Inc. *Economic Geology,* **105,** 3-41.

Simon, A. C., Pettke, T., Candela, P. A., Piccoli, P. M. and Heinrich, C. A. (2004). Magnetite solubility and iron transport in magmatic-hydrothermal environments. *Geochimica et Cosmochimica Acta,* **68,** 4905-4914.

Sinclair, W. (2007). Porphyry deposits. *In:* Mineral deposits of Canada: A synthesis of Major Deposit-Types, District Metallogeny, the Evolution of Geological Provinces and Exploration Methods. *In:* Geological Association of Canada, Mineral deposits division, Special Publication, vol 5, 223-243.

Skinner, B.J. (1997). Hydrothermal mineral deposits: What we do and don't know, *in* Barnes, H.L., ed., Geochemistry of hydrothermal ore deposits, 3rd edition: New York, *John Wiley and Sons*, 1-29.

Sláma, J. & Košler, J. (2008). Plešovice zircon-A new natural reference material for U-Pb and Hf isotopic microanalysis. *Chemical Geology,* **249**, 1-35.

Sossi P. A. and O'Neill H. S. C. (2017). The effect of bonding environment on iron isotope fractionation between minerals at high temperature. *Geochimica et Cosmochimica Acta,* **196,** 121-143.

Sossi, P. A., Halverson, G. P., Nebel, O., Eggins, S. M. (2015). Combined separation of Cu, Fe and Zn from rock matrices and improved analytical protocols for stable isotope determination. *Geostandards and Geoanalytical Research,* **39,** 129-149.

Sossi, P. A., Nebel, O. and Foden, J. (2016). Iron isotope systematics in planetary reservoirs. Earth Planet. Sci. Lett. 452, 295–308. Stern R. J. and Ito E. (1983). Trace-element and isotopic constraints on the source of magmas in the active Volcano and Mariana Island arcs, Western Pacific. *Journal of Volcanology and Geothermal Research,* **18,** 461-482.

Strydom, D., Colliston, W.P., Praekelt, H.E., Schoch, A.E., Van Aswegen, G., Pretorius, J.J., Beukes, G.J., De Villiers, B., Watkeys, M.K. and Botes, F.J., (1987). The tectonic units of parts of Namaqualand, Bushmanland and southern Namibia. Map (1:250 000), Bushmanland Research Project, Department of Geology, Univ. Orange Free State.

Sulaksono, A., Watanabe, Y., Arribas, A. Echigo, T., Al Furqan, R., and Leys., C.A (2021). Reduction of oxidized sulfur in the formation of the Grasberg porphyry copper-gold deposit, Papua, Indonesia. *Mineralium Deposita,* **56**, 1027-1042.

Sun, W., Huang, R., Li, H., Hu, Y., Zhang, C., Sun, S., Zhang, Li., Ding, X., Li, C., Zartman, R.E. and Ling, M. (2015). Porphyry deposits and oxidized magmas. *Ore Geology Reviews,* **65,** 97-131.

Sun, W., Ling, M., Yang, X., Fan, W., Ding, X., Liang, H. (2010). Ridge subduction and porphyry copper–gold mineralization: an overview. *Science China Earth Sciences,* **53,** 475-484.

Sun, W., Zhang, H., Ling, M.-X., Ding, X., Chung, S.-L., Zhou, J., Yang, X.-Y., Fan, W. (2011). The genetic association of adakites and Cu–Au ore deposits. *International Geology Review,* **53,** 691-703.

Tang, M., Lee, C.-T.A., Chen, K., Erdman, M., Costin, G., Jiang, H. (2019a). Nb/Ta systematics in arc magma differentiation and the role of arclogites in continent formation. *Nature Communications,* **10,** 235.

Telus, M., Dauphas, N., Moynier, F., Tissot, F. L. H., Teng, F. Z., Nabelek, P. I., Craddock, P. R. and Groat, L. A. (2012). Iron, zinc, magnesium and uranium isotopic fractionation during continental crust differentiation: the tale from migmatites, granitoids, and pegmatites. *Geochimica Cosmochimica Acta,* **97,** 247-265.

Tatnell, L., Anenburg, M., & Loucks, R. (2023). Porphyry copper deposit formation: Identifying garnet and amphibole fractionation with REE pattern curvature modeling. *Geophysical Research Letters,* **50,** e2023GL103525.

Thieblemont, D., Stein G., and Lescuyer, J.-L. (1997). Epithermal and porphyry deposits: The adakite connection. *Earth and Planetary Sciences*, **325,** 103-109.

Thomas, R.J., Agenbacht, A.L.D., Cornell, D.H., Moore, J.M., (1994). The Kibaran of Southern Africa: tectonic evolution and metallogeny. *Ore Geology Reviews,* **9,** 131-160.

Thomas, R.J., Macey, P.H., Dhansay, T., Spencer, C. and Lambert, C.W., (2016). The Precambrian Geology of the Aurus Mountains, Sperrgebiet, SW Namibia. Explanation to parts of 1:50 000 Geological Map Sheets 2716AC, 2716CA, 2716CC, 2716CD and 2715BD. Geol. Surv. Namibia – Council for Geoscience, S. Africa.

Van Nienerek, H.S., Elburg, M.A., Andersen, T. and Armstrong, R.A. (2022). Provenance of metasedimentary rocks of the Kheis Terrane and Kakamas Domain: support for accretionary tectonics during the development of the western Namaqua-Natal metamorphic province. *South African Journal of Geology,* **125 (1),** 61-78.

Van Zyl, C.Z. (1981). Structural and metamorphic evolution in the transitional zone between craton and mobile belt, Upington Geotraverse. *Department of Geology University of Cape Town, Cape Town,* 243.

Vermeesch, P. (2018). IsoplotR: a free and open toolbox for geochronology. *Geoscience Frontiers,* **9,** 1479-1493.

Vermond, D. (2019). *Identifying the controls on mineralisation and re-defining the evolution of the Haib porphyry Cu deposit.* M.Sc. thesis, Camborne School of Mines, University of Exeter.

Von Backström, J.W. and De Villiers, J., (1972). The geology along the Orange River Valley between Onseepkans and the Richtersveld. Expl. 2817D (Vioolsdrif), 2818C

(Goodhouse), 2818D (Dabenoris) and 2819C (Onseepkans), *Geological Survey of South Africa*, 101.

Wadsworth, W.B. (1968). The Cornelia pluton, Ajo, Arizona. *Economic geology*, **63,** 101-115.

Walker, P.W.A. & Richards, D.S. (2018). Independent Technical Review and Resource Estimate – The Haib Copper Porphyry Project, Namibia.

Wang Y., Zhu X. K., Mao J. W., Li Z. H. and Cheng Y. B. (2011). Iron isotope fractionation during skarn-type metallogeny: a case study of Xinqiao Cu–S–Fe–Au deposit in the Middle-Lower Yangtze valley. *Ore Geology Reviews*, 43, 194-202.

Ward, J.H.W., (1977). Geology of the area south of Vioolsdrif, Cape Province. Report to the Atomic Energy Board, Republic of South Africa, 52pp.

Wawryk C. M. and Foden J. D. (2015). Fe-isotope fractionation in magmatic-hydrothermal mineral deposits: a case study from the Renison Sn–W deposit, Tasmania. *Geochimica et Cosmochimica Acta,* **150,** 285-298.

Weber, M. I. (1998). *The Mercaderes-Rio Mayo xenoliths, Colombia: their bearing on mantle and crustal processes in the Northern Andes.* Ph.D. thesis.

Weber, M. I., Tarney, J., Kempton, P.D., Kent, R. W. (2002). Crustal make-up of the Northern Andes: Evidence based on deep crustal xenolith suites, Mercaderes, SW Colombia. *Tectonophysics*. **345(1),** 49-82.

Weyer, S., Ionov, D. A. (2007). Partial melting and melt percolation in the mantle: The message from Fe isotopes. *Earth and Planetary Science Letters,* **259,** 119-133.

Wilkinson, B.H. and Kesler, S.E. (2009). Quantitative Identification of Metallogenic Epochs and Provinces: Application to Phanerozoic Porphyry Copper Deposits. *Economic Geology*, **104 (5),** 607-622.

Wilkinson, J. (2013). Triggers for the formation of porphyry ore deposits in magmatic arcs. *Nature Geoscience,* **6,** 917-925.

Williams, H. M., Bizimis, M. (2014). Iron isotope tracing of mantle heterogeneity within the source regions of oceanic basalts. *Earth and Planetary Science Letters*, **404,** 396-407.

Williams, H., Peslier, A., McCammon, C., Halliday, A., Levasseur, S., Teutsch, N., Burg, J. (2005). Systematic iron isotope variations in mantle rocks and minerals: The effects of partial melting and oxygen fugacity. *Earth and Planetary Science Letters,* **235,** 435-452.

Woodland, A. B. and Koch, M. (2003). Variation in oxygen fugacity with depth in the upper mantle beneath the Kaapvaal craton, Southern Africa. *Earth and Planetary Science Letters,* **214,** 295-310.

Yao J., Mathur R., Sun W., Song W., Chen H., Mutti L., Xiang X. and Luo X. (2016). Fractionation of Cu and Mo isotopes caused by vapor-liquid partitioning, evidence from the Dahutang W-Cu-Mo ore field. *Geochemistry, Geophysics, Geosystems,* **17,** 1725-1739.

Yesavage T., Fantle M. S., Vervoort J., Mathur R., Jin L., Liermann L. J. and Brantley S. L. (2012). Fe cycling in the Shale Hills Critical Zone Observatory, Pennsylvania: An analysis of biogeochemical weathering and Fe isotope fractionation. *Geochimica et Cosmochimica Acta,* **99,** 18-38.

Young, E. D., Manning, C. E., Schauble, E. A., Shahar, A., Macris, C. A., Lazar, C. and Jordan, M. (2015). High-temperature equilibrium isotope fractionation of non-traditional stable isotopes: experiments, theory, and applications. *Chemical Geology,* **395,** 176-195.

Young, E. D., Tonui, E., Manning, C. E., Schauble, E., & Macris, C. A. (2009). Spinel-olivine magnesium isotope thermometry in the mantle and implications for the Mg isotopic composition of Earth. *Earth and Planetary Science Letters*, **288,** 524-533.

Zambardi, T., Lundstrom, C. C., Li, X., McCurry, M. (2014). Fe and Si isotope variations at Cedar Butte volcano; insight into magmatic differentiation. *Earth and Planetary Science Letters,* **405,** 169-179.

Zhang, D. & Audétat, A. (2017). What caused the formation of the giant Bingham Canyon porphyry Cu-Mo-Au deposit? Insights from melt inclusions and magmatic sulfides. *Economic Geology and the Bulletin of the Society of Economic Geologists,* **112**, 221–244.

Zhang, L., Qiu, K., Hou, Z., Pirajno, F., Shivute, E., and Cai. (2021). Fluid-rock reactions of the Triassic Taiyangshan porphyry Cu-Mo deposit (West Qinling, China) constrained by QEMSCAN and iron isotope. *Ore Geology Reviews,* **132,** 104068.

Zhao, Y., Xue, C., Liu, S.-A., Mathur, R., Zhao, X., Yang, Y., Dai, J., Man, R., Liu, X. (2019). Redox reactions control Cu and Fe isotope fractionation in a magmatic Ni–Cu mineralization system. *Geochimica et Cosmochimica Acta,* **249,** 42-58.

Appendices

Appendix A: Table of samples used in this study and corresponding methods conducted.

Sample #	Co-ordinates	Rock type	Thin sections	Ore blocks/ mounts	Mineral liberation	Major elements	Trace elements	CL-BSE images	U-Pb dating	Cu & Fe isotopes
AJ-21-01	28° 43' 09.1" S, 17° 56' 51.4" E	Gabbro	Yes	No	Yes	Yes	Yes	No	No	No
AJ-21-02	28° 43' 12.3" S, 17° 56' 48.0" E	Leucogranite	Yes	No	No	Yes	Yes	No	No	Yes
AJ-21-03	28° 43' 13.6" S, 17° 56' 46.0" E	Gabbro	Yes	No	Yes	Yes	Yes	No	No	No
AJ-21-04	28° 43' 14.1" S, 17° 56' 43.4" S	Gabbro with mafic enclaves	Yes	Yes	No	Yes	Yes	Yes	Yes	Yes
AJ-21-05	28° 41' 22.3" S, 17° 52' 20.3" E	Chlorite-sericite altered quartz-felspar porphyry granodiorite	Yes	No	No	Yes	Yes	No	No	No
AJ-21-06	28° 41' 19.6" S, 17° 52' 12.8" E	Chlorite-sericite altered quartz-felspar porphyry granodiorite with quartz-carbonate veins	Yes	No	No	Yes	Yes	No	No	No
AJ-21-07	28° 41' 24.8" S, 17° 52' 45.6" E	Porphyritic andesite with blocks of granodiorite	Yes	No	No	Yes	Yes	No	No	No
AJ-21-08	28° 41' 24.8" S, 17° 52' 45.6" E	Porphyritic andesite with blocks of granodiorite	Yes	No	No	Yes	Yes	No	No	No
AJ-21-09A	28° 41' 35.0" S, 17° 53' 09.4" E	Potassic altered quartz-feldspar porphyry granodiorite	Yes	Yes	No	Yes	Yes	No	No	Yes
AJ-21-09B	28° 41' 35.0" S, 17° 53' 09.4" E	Potassic altered quartz-feldspar porphyry granodiorite with disseminated mineralization (sulphides)	Yes	Yes	No	Yes	Yes	No	No	Yes
AJ-21-10	28° 42' 27.0" S, 17° 55' 55.8" E	Fine grained mafic material with mafic phenocrysts	Yes	No	No	Yes	Yes	No	No	No
AJ-21-11	28° 42' 49.5" S, 17° 55' 45.9" E	Porphyritic andesite	Yes	No	No	Yes	Yes	No	No	No
AJ-21-12	28° 43' 43.0" S, 17° 54' 23.5" E	Bedded tuff	Yes	No	No	No	No	No	No	No
AJ-21-13	28° 43' 34.1" S, 17° 54' 20.3" E	Sheared porphyritic andesite	Yes	No	No	Yes	Yes	No	No	Yes
AJ-21-14	28° 43' 50.7" S, 17° 54' 27.4" E	Rhyolite	Yes	No	No	Yes	Yes	No	No	Yes
AJ-21-15	28° 43' 50.9" S, 17° 54' 28.8" E	Mafic tuff	Yes	No	No	Yes	Yes	No	No	Yes
AJ-21-16	28° 43' 55.0" S, 17° 54' 26.6" E	Monzogranite	Yes	No	No	No	No	No	No	No

AJ-21-17	28° 44' 12.3" S, 17° 54' 29.2" E	Phenocrystic rhyolite	Yes	No	No	Yes	Yes	No	No	Yes
AJ-21-18	28° 44' 19.1" S, 17° 55' 39.0" E	Monzogranite	Yes	No	No	Yes	Yes	No	No	Yes
AJ-21-19	28° 44' 25.5" S, 17° 54' 48.7" E	Granodiorite	Yes	No	No	No	No	No	No	No
AJ-21-20	28° 44' 29.9" S, 17° 54' 50.9" E	Granodiorite	Yes	No	No	Yes	Yes	No	No	No
AJ-21-21	28° 43' 10.0" S, 17° 56' 44.6" E	Gabbroic mafic material (chill zone) partially digesting the granodiorite	Yes	No	Yes	Yes	Yes	No	No	No
AJ-21-22	28° 43' 07.7" S, 17° 56' 46.3" E	Gabbro with finer sections	Yes	No	Yes	No	No	No	No	No
AJ-21-23	28° 43' 00.5" S, 17° 56' 53.5" E	Gabbro	Yes	Yes	Yes	Yes	Yes	Yes	Yes	Yes
AJ-21-24	28° 42' 54.4" S, 17° 56' 56.4" E	Gabbro-assimilation/chill zone	Yes	No	Yes	No	No	No	No	No
AJ-21-25	28° 42' 53.1" S, 17° 56' 59.7" E	Gabbro-liquid mafic melt composition	Yes	No	Yes	Yes	Yes	No	No	No
AJ-21-26	28° 42' 59.5" S, 17° 57' 02.8" E	Gabbro	Yes	No	Yes	Yes	Yes	No	No	No
AJ-21-27	28° 43' 14.7" S, 17° 56' 45.2" E	Gabbro	Yes	No	Yes	No	No	No	No	No
AJ-21-28	28° 43' 12.7" S, 17° 56' 38.4" E	Granodiorite with mafic enclaves	Yes	Yes	Yes	Yes	Yes	Yes	Yes	Yes
AJ-21-29	Boulder	Pyroxenite	Yes	Yes	Yes	Yes	Yes	Yes	Yes	No
AJ-21-30	Boulder	Pyroxenite with distinct interstitial plagioclase	Yes	No	Yes	Yes	Yes	No	No	Yes
AJ-21-31	Boulder	Enclave in coarse lecucogranite crosscut by leucogranite vein	Yes	No	No	No	No	No	No	No
AJ-21-32	28° 44' 09.0" S, 17° 55' 18.3" E	Diorite with mafic enclaves	Yes	No	Yes	Yes	Yes	No	No	No
AJ-21-33	28° 45' 44.4" S, 17° 54' 27.9" E	Coarse grained mafic material	Yes	No	No	No	No	No	No	No
AJ-21-34	28° 45' 42.4" S, 17° 54' 24.7" E	Diorite	Yes	No	No	Yes	Yes	Yes	Yes	No
AJ-21-35	28° 45' 42.4" S, 17° 54' 24.7" E	Fine grained mafic material	Yes	No	No	No	No	No	No	No
AJ-21-36	28° 45' 03.0" S, 17° 54' 34.5" E	Diorite with mafic enclaves	Yes	No	Yes	Yes	Yes	No	No	Yes
AJ-21-37	28° 42' 21.2" S, 17° 55' 59.2" E	Quartz-feldspar porphyry granodiorite	Yes	No	No	Yes	Yes	No	No	Yes
AJ-21-38	28° 43' 06.7" S, 17° 55' 46.6" E	Porphyritic andesite	Yes	No	No	Yes	Yes	No	No	Yes

HM 01 (24.36-24.78 m)	28° 41' 34.5" S, 17° 53' 14.7" E	Quartz-feldspar porphyry granodiorite with vein-controlled mineralization	Yes	Yes	Yes	No	No	No	No	No
HM 01 (69.80-69.90 m)	28° 41' 34.5" S, 17° 53' 14.7" E	Quartz-feldspar porphyry granodiorite with disseminated mineralization	Yes	Yes	Yes	No	No	No	No	No
HM 06 (68.00-68.38 m)	28° 41' 20.1" S, 17° 52' 49.2" E	Quartz-feldspar porphyry granodiorite with vein-controlled sulphides	Yes	Yes	Yes	No	No	No	No	No
HM 06 (59.50-69.00 m)	28° 41' 20.1" S, 17° 52' 49.2" E	Quartz-feldspar porphyry granodiorite with massive sulphides	Yes	Yes	Yes	No	No	No	No	No

Appendix B: Google Earth image of the Kokerboom Intrusion and corresponding sample locations.

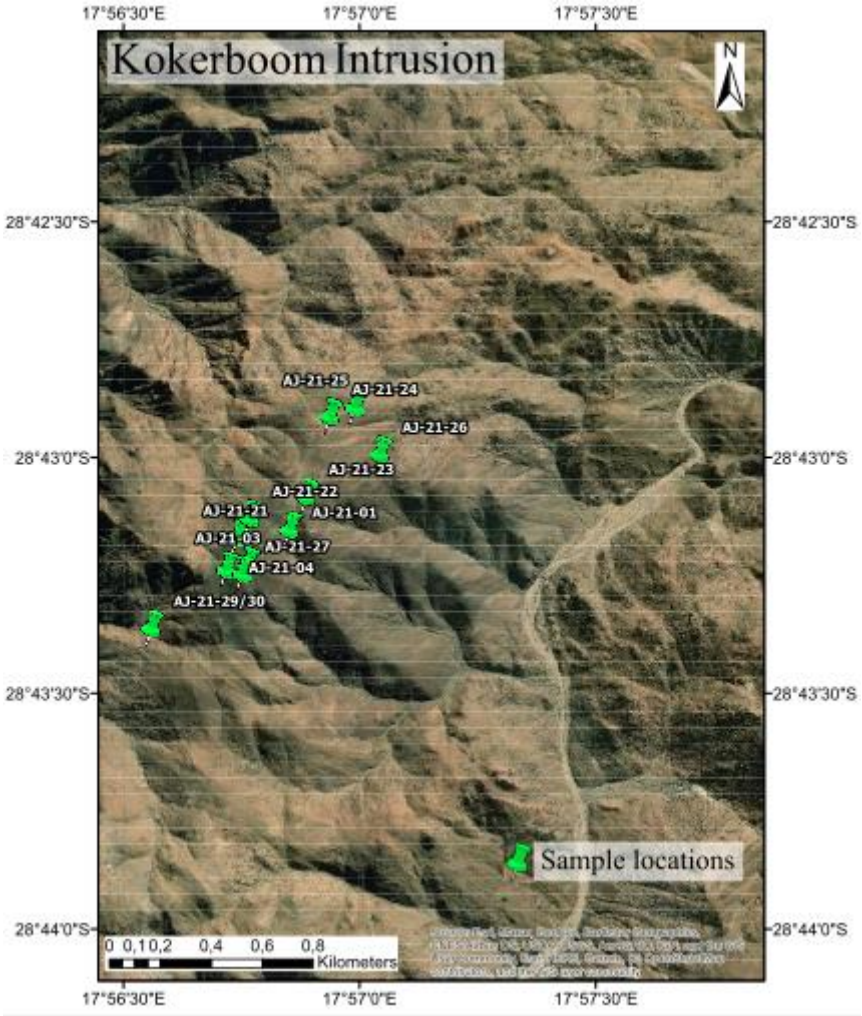

Appendix C: Detailed petrographic observations for the Kokerboom Intrusion.

Sample #	Lithology	Grain size	Minerals	General description
AJ-21-01	Gabbro	Coarse grained (3-5 mm)	Clinopyroxene (72 %), plagioclase (10 %), hornblende (10 %), quartz (5 %), apatite (2 %), rutile and magnetite/haematite (1 %).	Equigranular texture. Euhedral to subhedral clinopyroxene is altered to hornblende and actinolite and has distinct inclusions of magnetite/haematite and quartz. Euhedral primary hornblende is twinned and also has inclusions of magnetite/haematite and quartz. Subhedral plagioclase is highly altered to sericite and epidote and displays distinct myrmeritic textures. Quartz is anhedral, recrystallized and displays a distinct undulose extinction. ~0.1 mm quartz-calcite veins associated with rutile and iron oxide staining crosscuts mineral assemblages.
AJ-21-03	Gabbro	Fine grained (0.5 mm)	Clinopyroxene (90 %), plagioclase (7 %), quartz (2 %) and magnetite/haematite with ilmenite exsolution lamellae (1 %).	Equigranular to acicular texture. Hornblende-actinolite-chlorite-epidote pseudomorphs are evident and replace clinopyroxene. Clinopyroxene is distinctly associated with quartz and subhedral to needle-like magnetite/haematite with ilmenite exsolution lamellae. ~ 2.5 mm subhedral phenocrysts of plagioclase is altered to sericite and epidote.
AJ-21-04	Gabbro	Medium-coarse (~3 mm)	Plagioclase (60 %), clinopyroxene (20 %), hornblende-actinolite (10 %), quartz (7 %), apatite (2 %), rutile, sphene and magnetite (1 %).	Equigranular texture. Hornblende-actinolite-chlorite-epidote pseudomorphs are evident and replace clinopyroxene. The primary stubby prisms of hornblende/actinolite are altered to chlorite and epidote whereas, the plagioclase is pervasively altered to sericite and epidote and displays a myrmerkitic texture. The hornblende has inclusions of magnetite, rutile and quartz. Hornblende/actinolite either exhibits exsolution lamellae or simple twinning. Quartz is anhedral and displays a distinct undulose extinction. Magnetite occurs as distinct bleb-like and disseminated grains.

AJ-21-21	Gabbro/ granodiorite contact	Fine-coarse grained (0.5-5 mm)	Finer section: clinopyroxene (70 %), plagioclase (18 %), hornblende (5 %), quartz (5 %), apatite (2 %), rutile and magnetite/haematite (1 %). Coarser section: plagioclase (60 %), hornblende-biotite-chlorite (20 %) and quartz (20 %).	The sample represents a sharp contact between the gabbro and granodiorite. Equigranular texture. The gabbro is fine grained and not as altered compared to the other leucopyroxenites. Subhedral clinopyroxene is altered to hornblende and actinolite and has inclusions of magnetite/haematite and quartz. Subhedral plagioclase is altered to sericite and epidote but not to a very high degree. Anhedral, recrystallized quartz displays a distinct undulose extinction. Euhedral to subhedral hornblende is altered to chlorite and epidote in certain areas and has inclusions of quartz and haematite with exsolution lamellae of ilmenite. The granodiorite is coarse and displays a distinct equigranular texture. Euhedral to subhedral plagioclase is zoned, altered to sericite and epidote and displays a myrmerkitic texture. Anhedral quartz is recrystallized. Subhedral hornblende (with inclusions of quartz and magnetite) is altered to biotite which is subsequently altered to aggregates of chlorite with an undulose extinction. Disseminated (0.25 mm) of chalcopyrite rimmed by covellite is evident and is associated with plagioclase, epidote and chlorite.
AJ-21-22	Gabbro	Medium grained (1-2 mm)	Clinopyroxene (68 %), plagioclase (22 %), hornblende (8 %), quartz (5 %), apatite (2 %), rutile and magnetite (1 %).	Equigranular texture. Subhedral to anhedral clinopyroxene is altered to hornblende and actinolite. Clinopyroxene is also zoned. Abundant inclusions of opaque material (magnetite) are apparent in pristine euhedral hornblende which are altered to actinolite in certain sections. Quartz has a distinct vermicular texture and occurs as inclusions in hornblende as well. Variations in grain size is apparent throughout the thin section. Finer euhedral to subhedral tabular clinopyroxene is less altered compared to coarser sections. Subhedral plagioclase is highly altered to sericite and epidote. Magnetite and haematite are mainly associated with clinopyroxene. Anhedral quartz displays a distinct undulose extinction.

AJ-21-23	Gabbro	Medium-coarse grained (1-3 mm)	Clinopyroxene (70 %), plagioclase (20 %), hornblende (8 %), quartz (5 %), apatite (2 %), rutile and magnetite (1 %).	Equigranular texture. Clinopyroxene is completely altered to actinolite, whereas plagioclase is interstitial and is altered to sericite and epidote. Hornblende is altered to chlorite and epidote. Primary hornblende has inclusions of magnetite and quartz. The magnetite and quartz are strongly associated with rutile. Hornblende/actinolite either exhibit exsolution lamellae or simple twinning. Quartz is a minor component and occurs as anhdedral recrystallized grains with distinct undulose extinction. Disseminated magnetite is also associated with chlorite and epidote.
AJ-21-24	Gabbro/ granodiorite contact	Fine-coarse grained (0.25-5 mm)	Finer section: clinopyroxene (70 %), plagioclase (20 %), hornblende (5 %), quartz (5 %), rutile and magnetite/haematite (1 %). Coarser section: plagioclase (60 %), hornblende-biotite-chlorite (20 %), quartz (15 %) and orthoclase (5 %).	The sample represents a sharp contact between the gabbro and granodiorite. Equigranular texture. The gabbro is composed of euhedral to subhedral phenocrysts of clinopyroxene and hornblende. Both clinopyroxene and hornblende has distinct inclusions of quartz and magnetite/haematite and rutile. Hornblende is distinctly altered to aggregates of biotite and chlorite. The granodiorite is composed of subhedral plagioclase which is altered to sericite and epidote. In certain areas there are coarser sections with ~ 1 mm anhedral recrystallized quartz that display undulose extinction. ~ 0.5 mm euhedral to subhedral magnetite/haematite with ilmenite exsolution lamellae in the cores of the grains is also apparent. Subhedral plagioclase altered to sericite and epidote. The subhedral plagioclase also has vermicular quartz inclusions with clear undulose extinction. Subhedral is altered to aggregates of chlorite and epidote and are strongly associated with haematite with ilmenite exsolution lamellae in the core. Subhedral tabular orthoclase and biotite is also distinct and are altered to clay and chlorite respectively. Irregular quartz with undulose extinction is also apparent.
AJ-21-25	Gabbro	Fine-medium grained (1-3 mm)	Clinopyroxene (70 %), plagioclase (15 %), hornblende (10 %), quartz (4 %), rutile and magnetite (1 %).	Equigranular texture. Euhedral to subhedral tabular clinopyroxene show twinning and have inclusions of quartz and opaque material. Subhedral hornblende is altered to chlorite and epidote and have inclusions of quartz and opaque material. Subhedral interstitial plagioclase is zoned and highly altered to sericite, epidote and clay. Anhedral quartz is recrystallized and displays undulose extinction. Euhedral to subhedral and cubic shaped magnetite (0.1-0.5 mm) is also apparent throughout.
AJ-21-26	Gabbro	Coarse grained (~4 mm)	Clinopyroxene (70 %), plagioclase (20 %), hornblende (8 %), quartz (5 %), apatite (2 %), rutile and magnetite (1 %).	Equigranular texture. Subhedral zoned clinopyroxene is altered to hornblende and actinolite and has inclusions of quartz and magnetite. Subhedral primary hornblende is twinned, zoned and altered to chlorite and epidote. Subhedral plagioclase is highly altered to sericite and epidote and display myrmerkitic textures. Anhedral recrystallized quartz is also distinct. Magnetite is distinctly associated with the mafic minerals.

AJ-21-27	Gabbro	Medium-coarse grained (0.5-5 mm)	Finer section: clinopyroxene (70 %), hornblende (20 %), plagioclase (5 %), quartz (4 %), rutile and magnetite/haematite (1 %). Coarser section: clinopyroxene (60 %), plagioclase (20 %), hornblende (10), quartz (5 %) and rutile and magnetite/haematite (5 %).	Equigranular to massive texture and shows distinct grain size variations. Euhedral to subhedral clinopyroxene is altered to hornblende and actinolite. Fibrous actinolite displays undulose extinction, zoning and has exsolution lamellae. Subhedral plagioclase is altered to sericite and epidote. Primary euhedral pristine hornblende and tabular clinopyroxene show exsolution lamellae and twinning. Magnetite/haematite is distinctly associated with the mafic minerals.
AJ-21-29	Clinopyroxenite	Coarse grained (5-7 mm)	Clinopyroxene (94 %) altered to fibrous-granular actinolite, plagioclase (4 %), apatite (1 %) and magnetite (1 %).	Massive to granular texture. Predominantly composed of euhedral to subhedral, twinned clinopyroxene with inclusions of quartz, apatite and magnetite. The clinopyroxene is altered to hornblende, actinolite, chlorite and epidote. Actinolite is deformed and displays undulose extinction. Clinopyroxene has exsolution lamellae. Minor subhedral to anhedral plagioclase is altered to sericite and epidote. Generally, a brownish altered appearance and iron oxide staining is observed. Magnetite is strongly associated with clinopyroxene.
AJ-21-30	Clinopyroxenite	Coarse grained (4 mm)	Clinopyroxene (95 %) altered to fibrous-granular actinolite with minor chlorite, epidote, hornblende, rutile, sphene, opaques and sulphides (5 %).	Massive to granular texture. The actinolite has a fibrolite texture and shows exsolution lamellae and simple twinning. The actinolite is altered to chlorite and epidote. Magnetite is disseminated throughout and is strongly associated with rutile, sphene, chlorite and actinolite. The sulphides in the clinopyroxenite occur as coarse (~2 mm) bleb-like aggregates of chalcopyrite rimmed by chalcocite-covellite assemblages, which are subsequently rimmed by hematite-magnetite-ilmenite assemblages.

Appendix D: Full-scan photomicrographs and Mineral liberation analyses for the Kokerboom Intrusion.

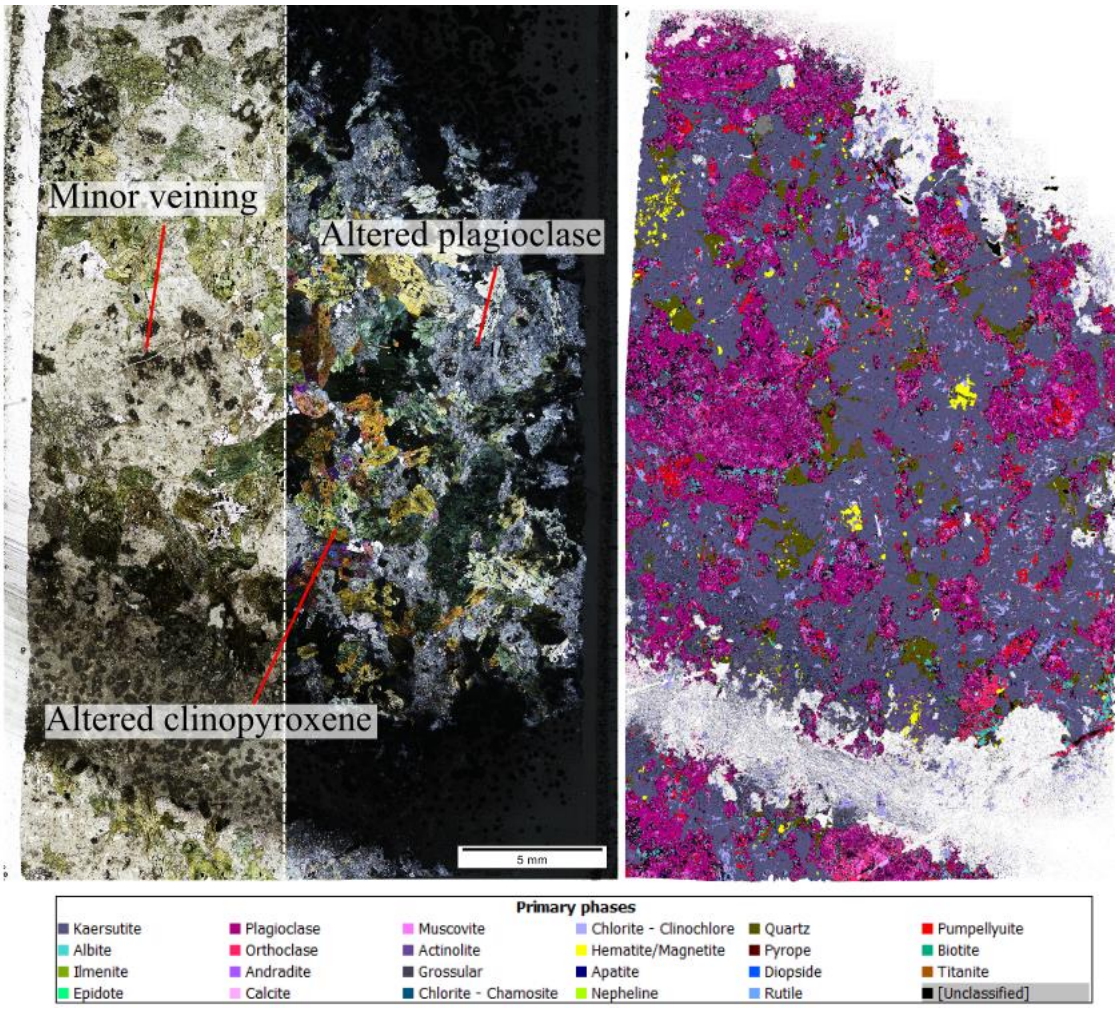

Figure 1: Plane (left) and cross-polarized (center) photomicrographs and mineral liberation map (right) of sample AJ-21-01.

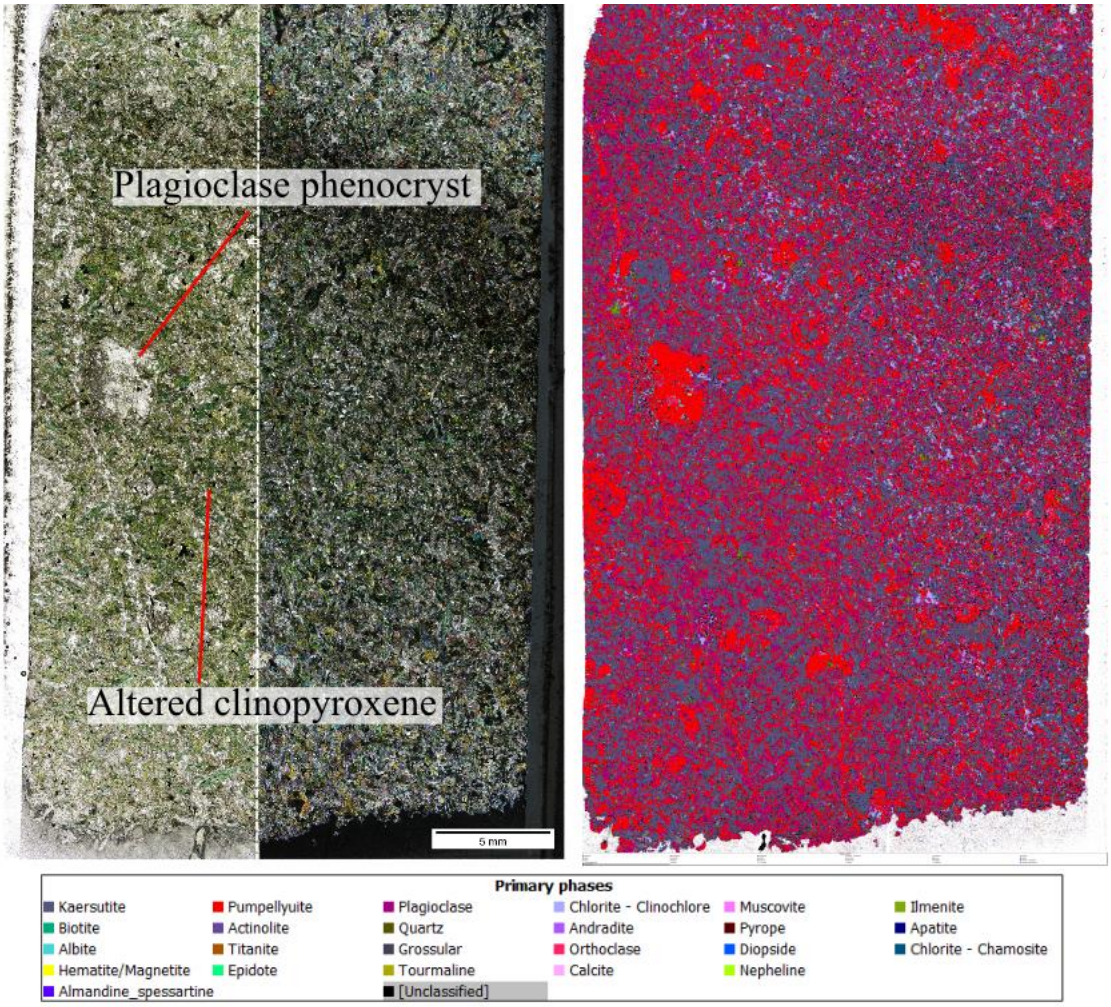

Figure 2: Plane (left) and cross-polarized (center) photomicrographs and mineral liberation map (right) of sample AJ-21-03.

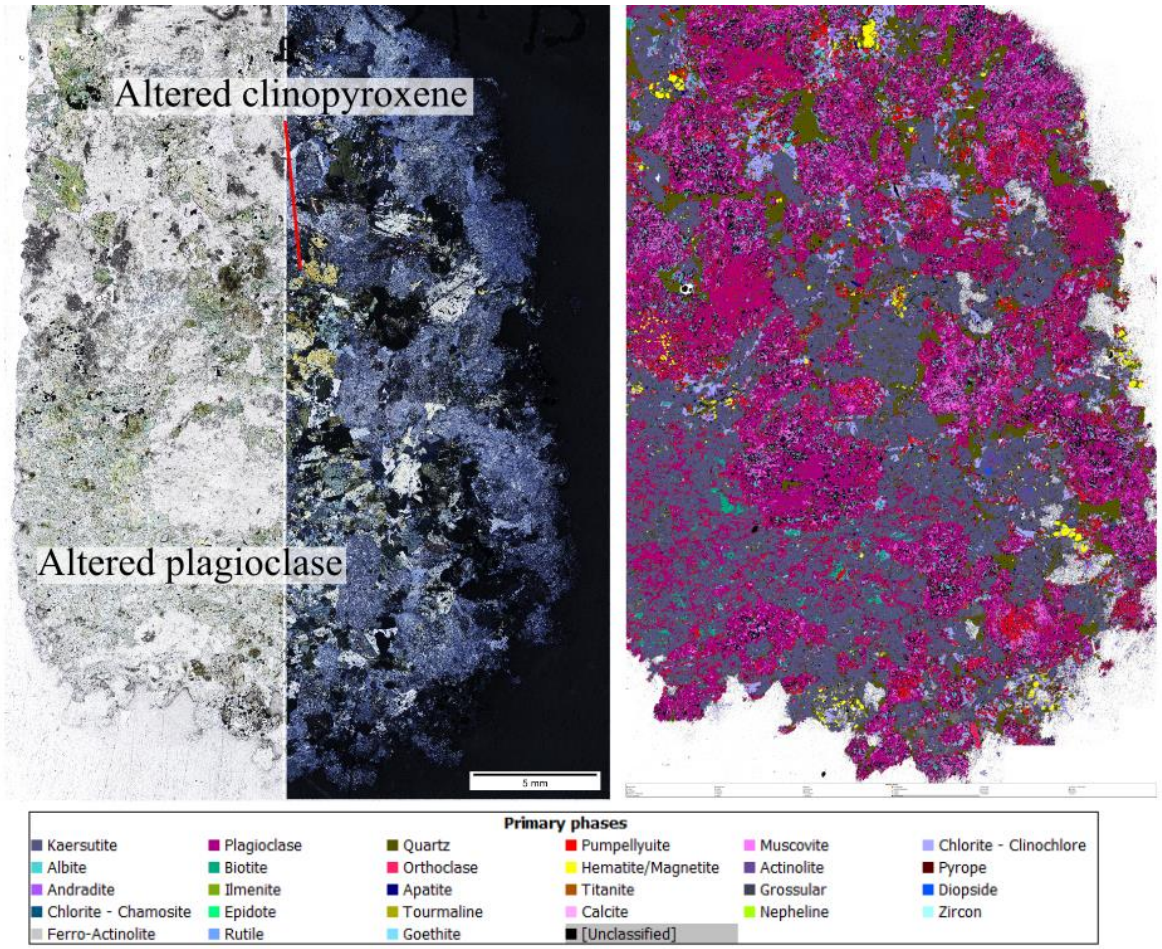

Figure 3: Plane (left) and cross-polarized (center) photomicrographs and mineral liberation map (right) of sample AJ-21-04.

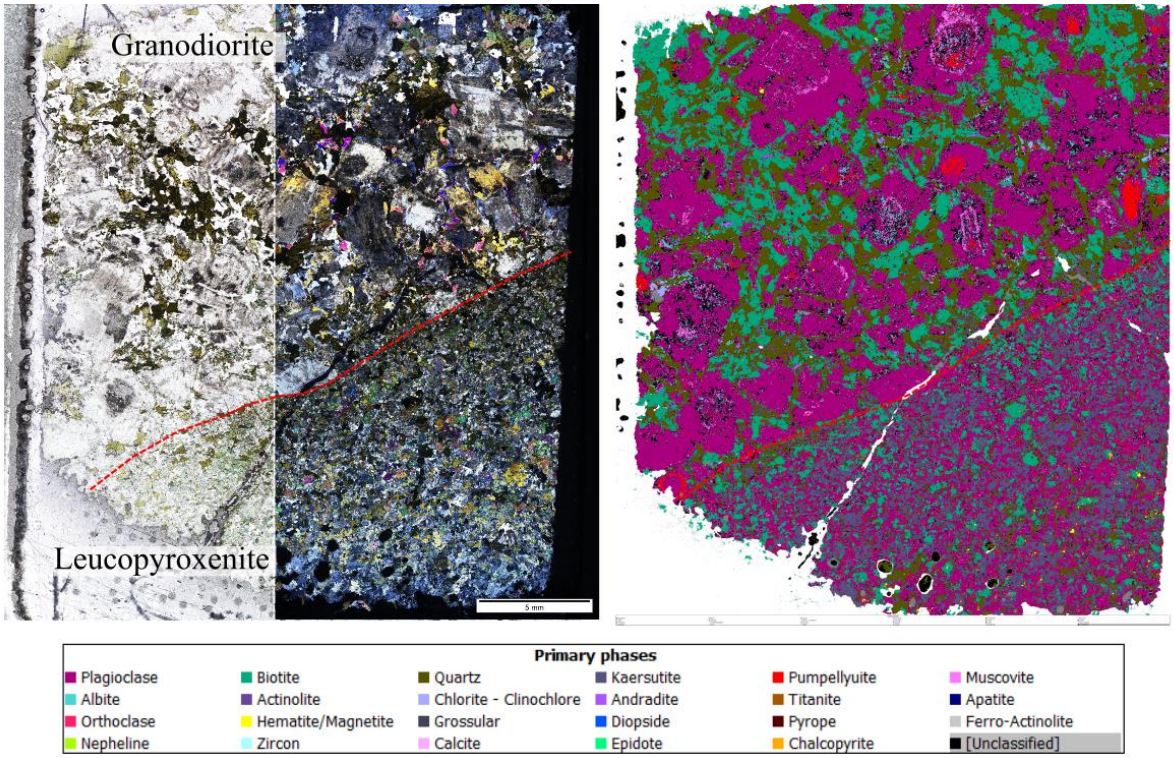

Figure 4: Plane (left) and cross-polarized (center) photomicrographs and mineral liberation map (right) of sample AJ-21-21.

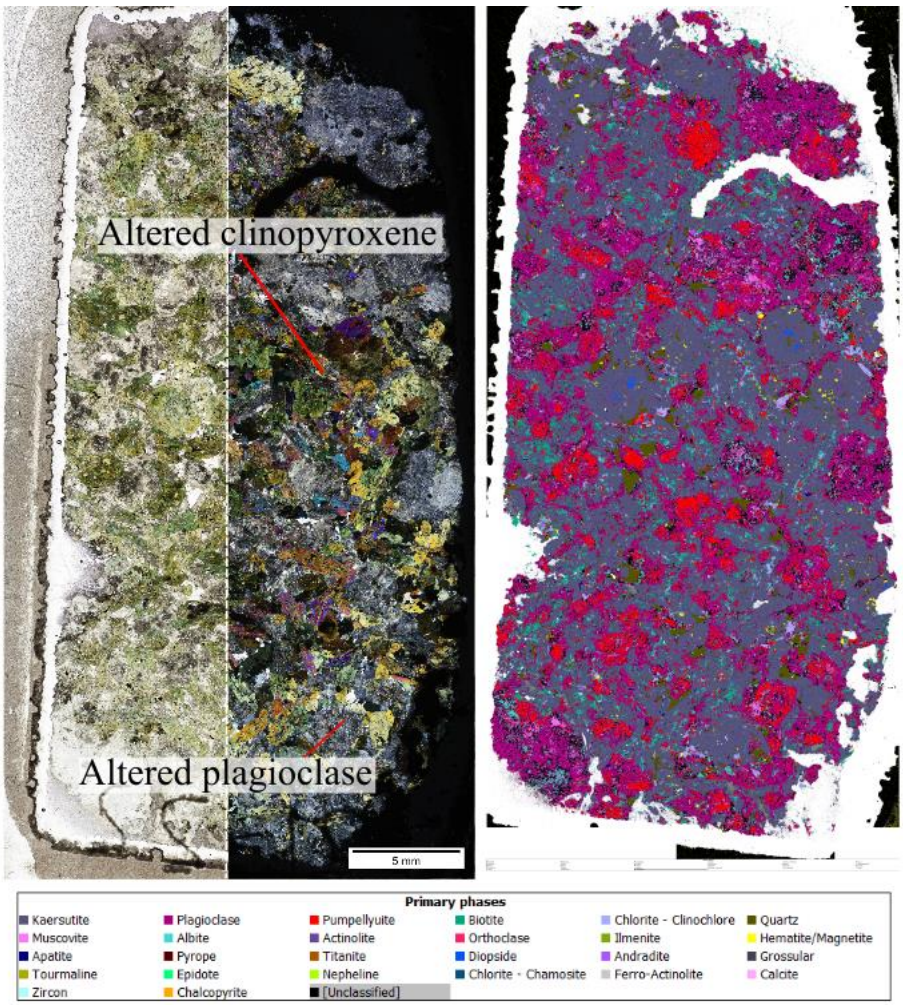

Figure 5: Plane (left) and cross-polarized (center) photomicrographs and mineral liberation map (right) of sample AJ-21-22.

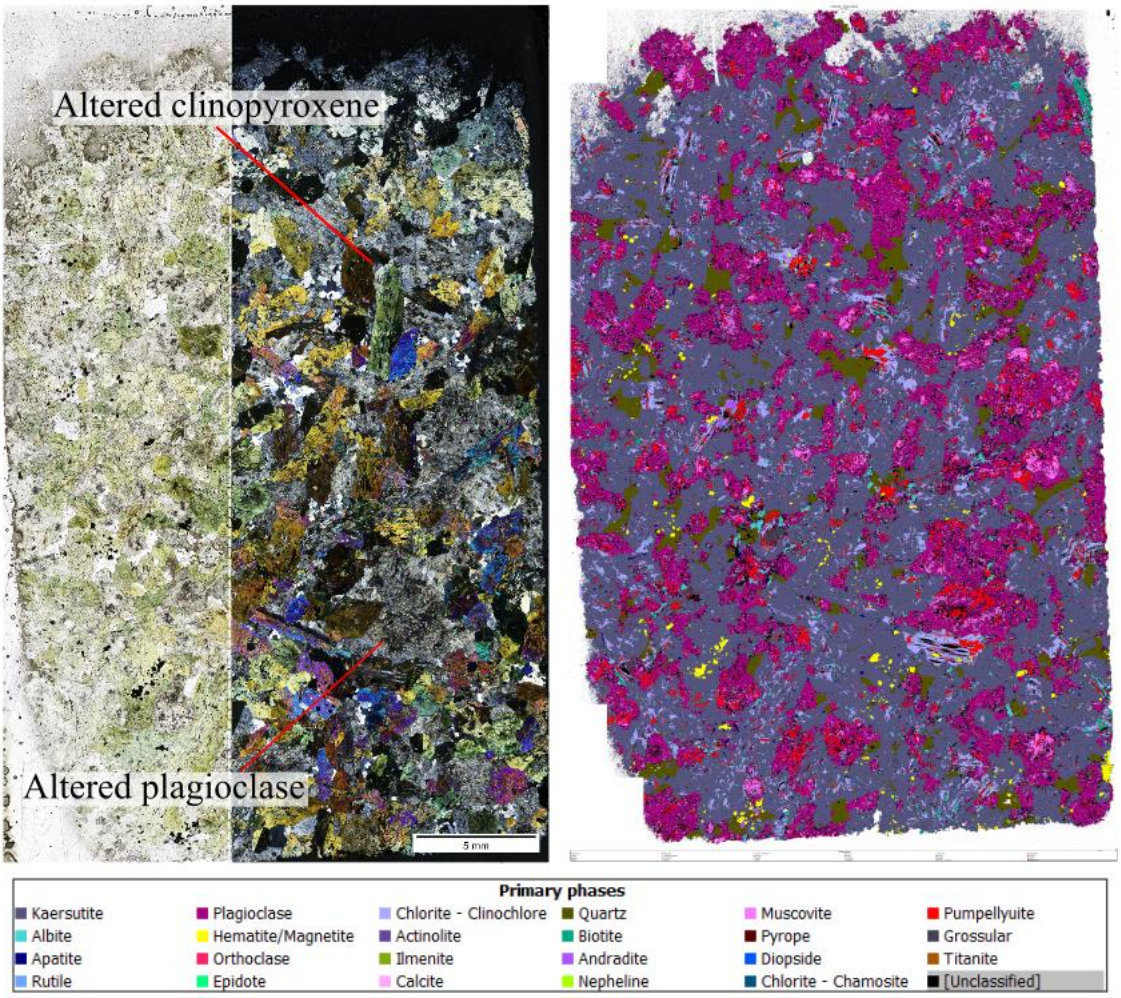

Figure 6: Plane (left) and cross-polarized (center) photomicrographs and mineral liberation map (right) of sample AJ-21-23.

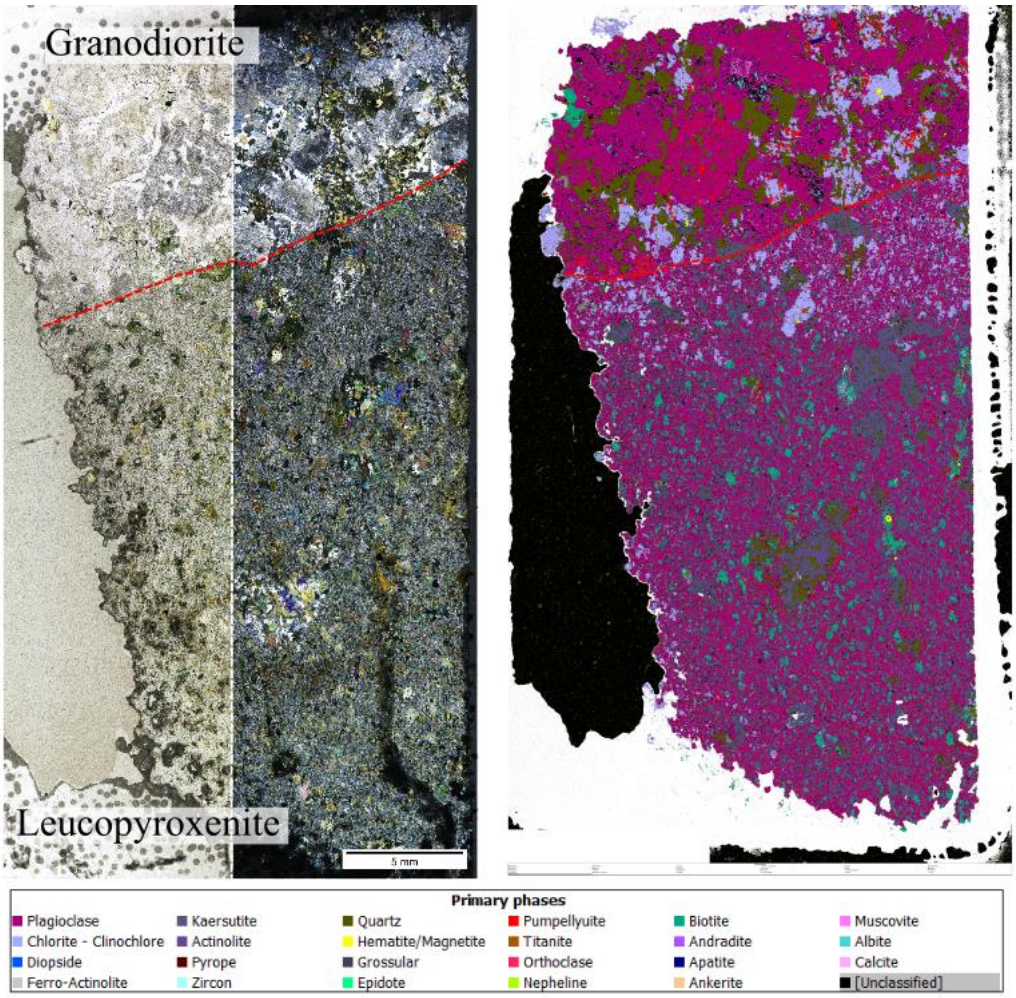

Figure 7: Plane (left) and cross-polarized (center) photomicrographs and mineral liberation map (right) of sample AJ-21-24.

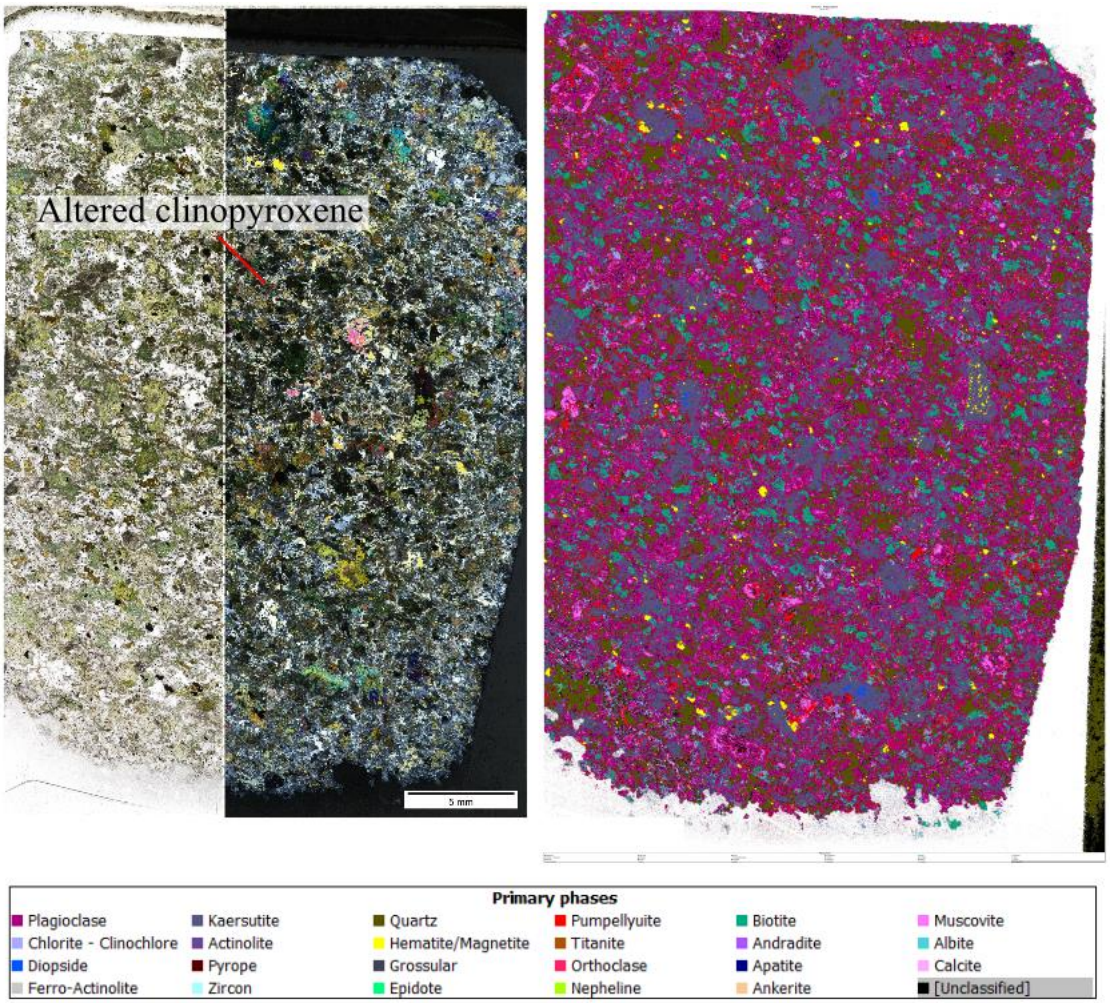

Figure 8: Plane (left) and cross-polarized (center) photomicrographs and mineral liberation map (right) of sample AJ-21-25.

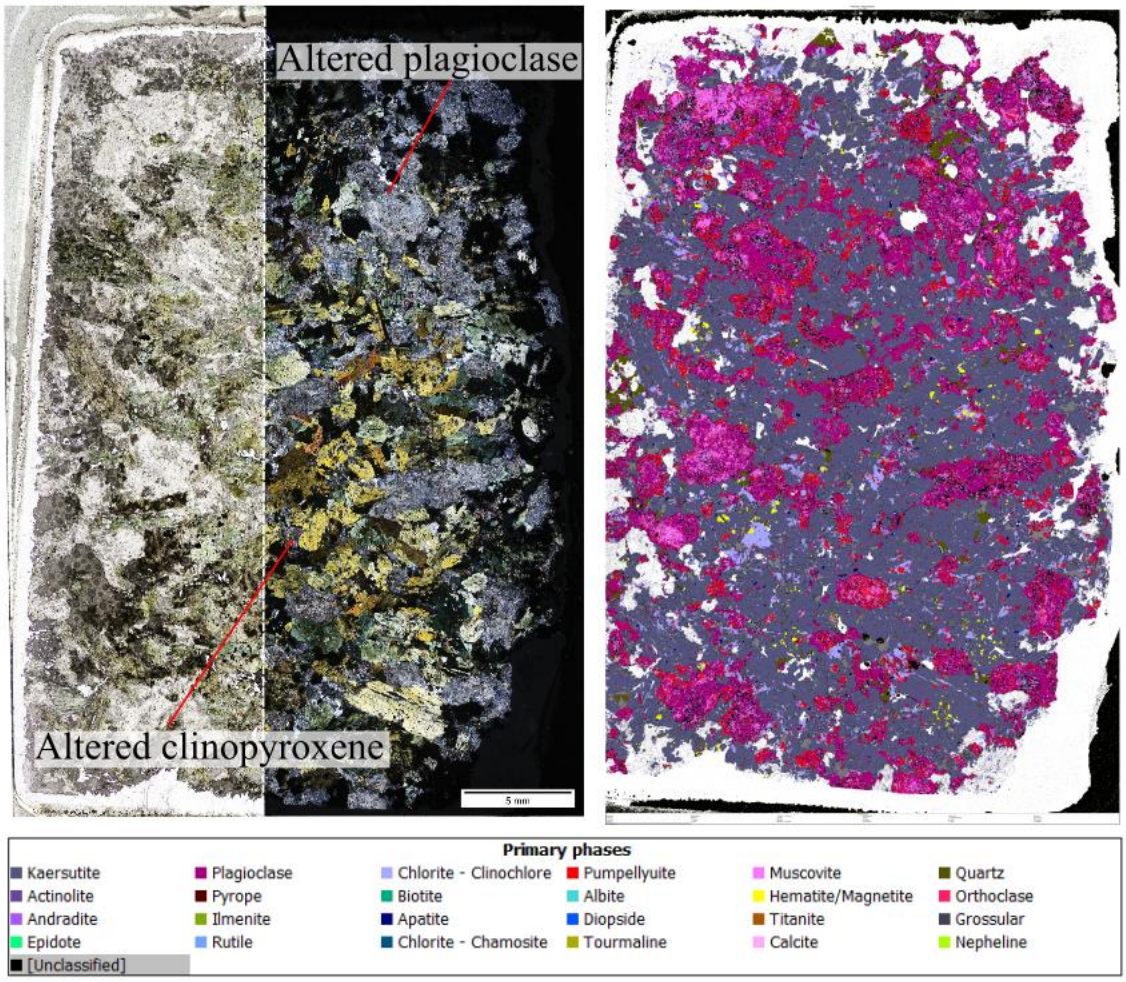

Figure 9: Plane (left) and cross-polarized (center) photomicrographs and mineral liberation map (right) of sample AJ-21-26.

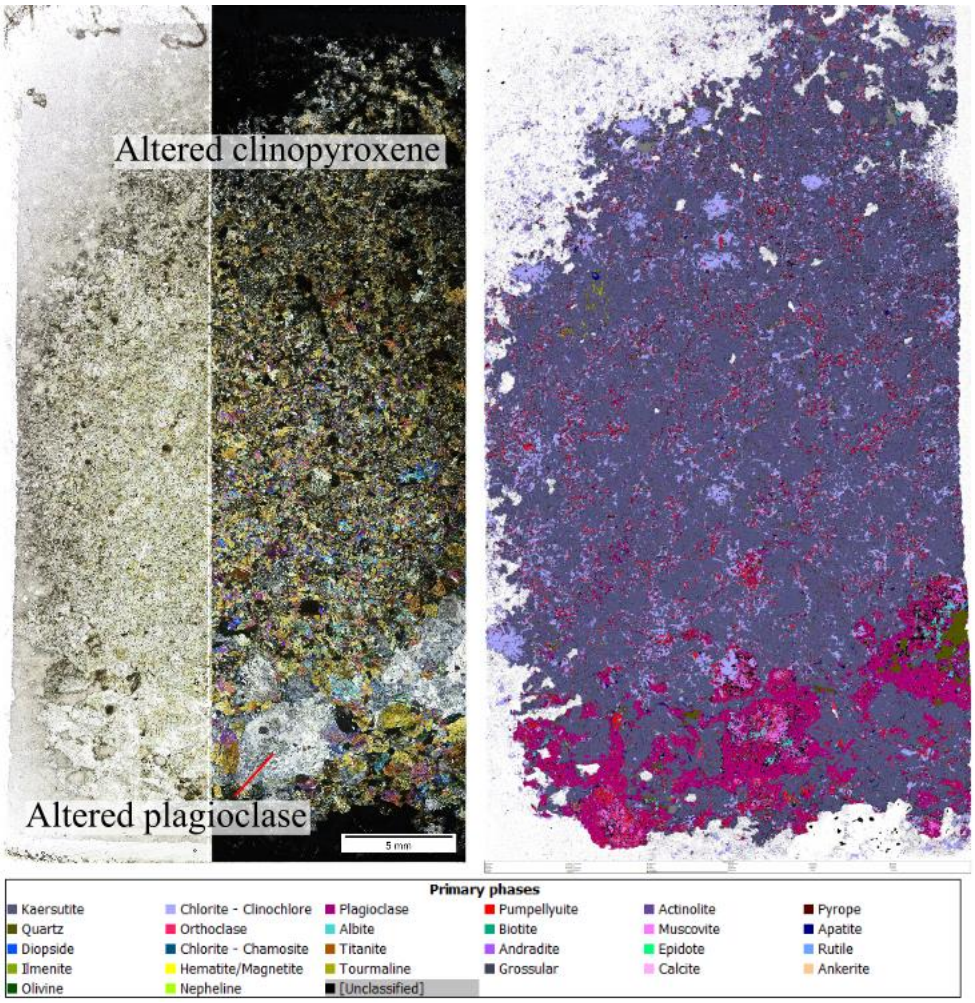

Figure 10: Plane (left) and cross-polarized (center) photomicrographs and mineral liberation map (right) of sample AJ-21-27.

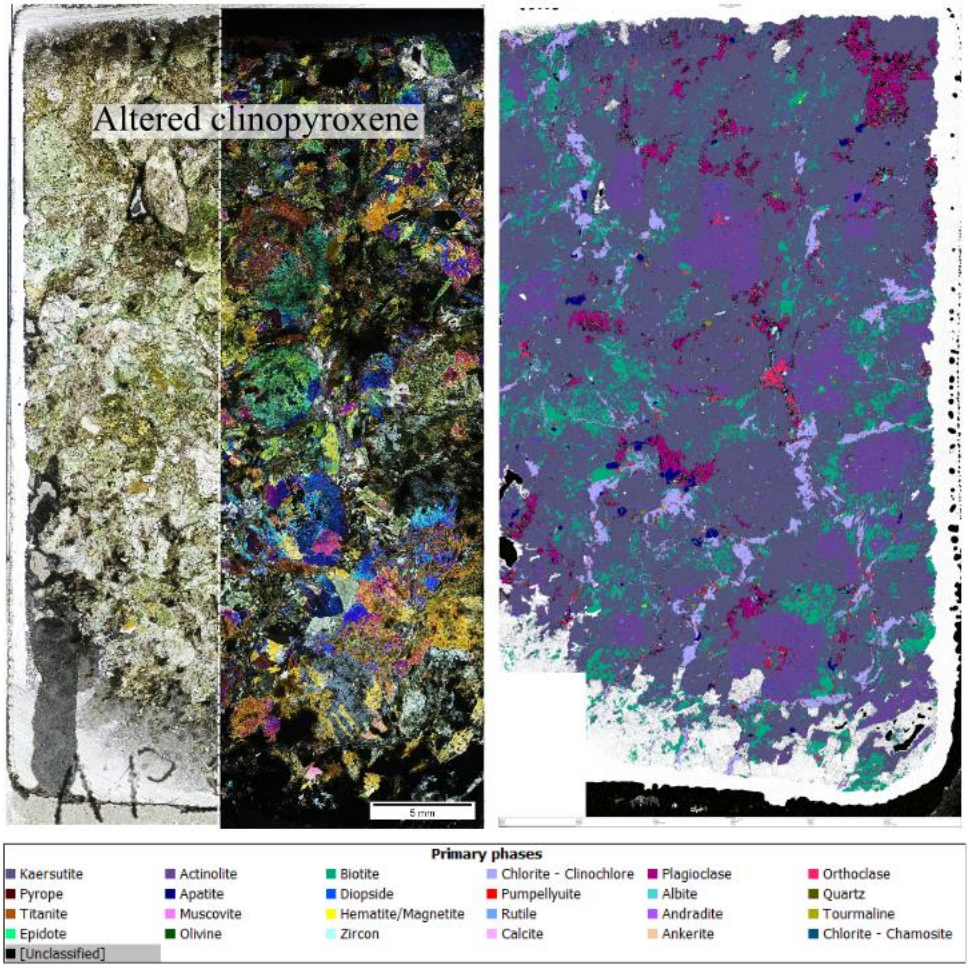

Figure 11: Plane (left) and cross-polarized (center) photomicrographs and mineral liberation map (right) of sample AJ-21-29.

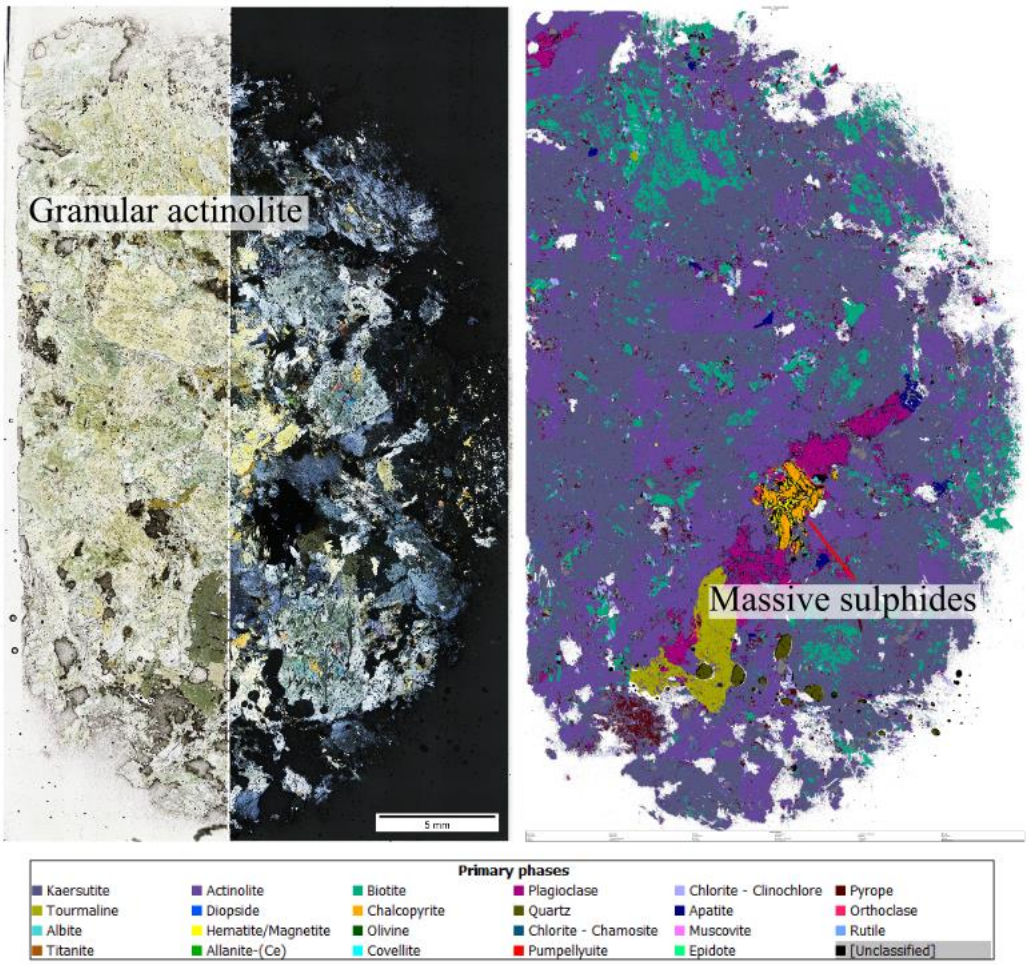

Figure 12: Plane (left) and cross-polarized (center) photomicrographs and mineral liberation map (right) of sample AJ-21-30.

Appendix E: General petrography for the Orange River Group and Vioolsdrif Intrusive Suite.

Petrography

Petrographic observations were conducted to deduce the mineral and textural relationships of samples from the Orange River Group, Vioolsdrif Intrusive Suite and Kokerboom Intrusion. The Orange River Group in the Haib area consist of aphyric rhyolite, phyric rhyolite, feldspar porphyry andesite and mafic tuff. The Vioolsdrif Intrusive Suite in the Haib area consist of diorite, granodiorite, monzogranite, quartz-feldspar porphyry granodiorite and leucogranite. Refer to chapter 4 for petrographic observations on the Kokerboom Intrusion and chapter 5 for petrographic observations on the feldspar porphyry andesite and quartz-feldspar porphyry granodiorite.

Aphyric rhyolite

The aphyric rhyolite is bedded (with felsic and mafic bands), fine-grained (~0.1 mm) and mainly composed of quartz, orthoclase, plagioclase, biotite, chlorite, muscovite, calcite, anhydrite, rutile, magnetite and ilmenite (Figure 1). The finer mafic bands are composed predominantly of biotite altered to chlorite with minor evidence of oxide staining, whereas the coarser felsic bands are composed of orthoclase, plagioclase, muscovite and ~0.5 mm phenocrysts of quartz. Orthoclase is either altered to calcite or clay whereas, plagioclase is altered to epidote and sericite. Disseminated subhedral-euhedral magnetite is evident throughout with ilmenite evident in the cores of the magnetite. Rutile is associated with quartz and magnetite. Carbonate veins composed of calcite occur parallel to bedding. Subhedral anhydrite is also evident in the felsic bands.

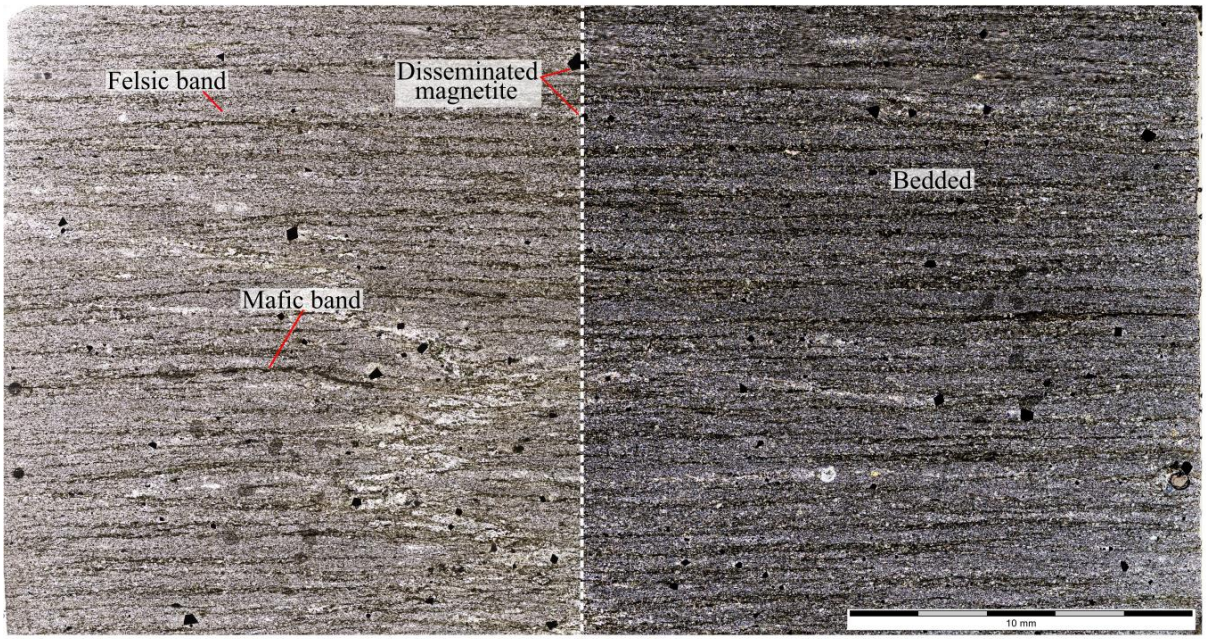

Figure 1: *Plane (left) and cross-polarized (right) photomicrographs of the aphyric rhyolite. Distinct mafic and felsic bands are evident. Disseminated magnetite occurs throughout the section.*

Phyric rhyolite

The phyric rhyolite shows distinct flow banding, eutaxitic textures, and is composed of quartz, orthoclase and microcline phenocrysts (~1 mm), set in a fine-grained quartzo-feldspathic groundmass (Figure 2). Grain size variations are evident as finer and coarser grained sections are observed and are composed of quartz, orthoclase and microcline. Finer grained mafic bands are also evident and are composed predominantly of chlorite, biotite, epidote and magnetite. The fine-grained quatzo-feldspathic groundmass is altered to sericite. Rutile is distinct throughout the phyric rhyolites and is associated with quartz and magnetite. Magnetite is strongly associated with chlorite and rutile and preferentially associated with the mafic sections.

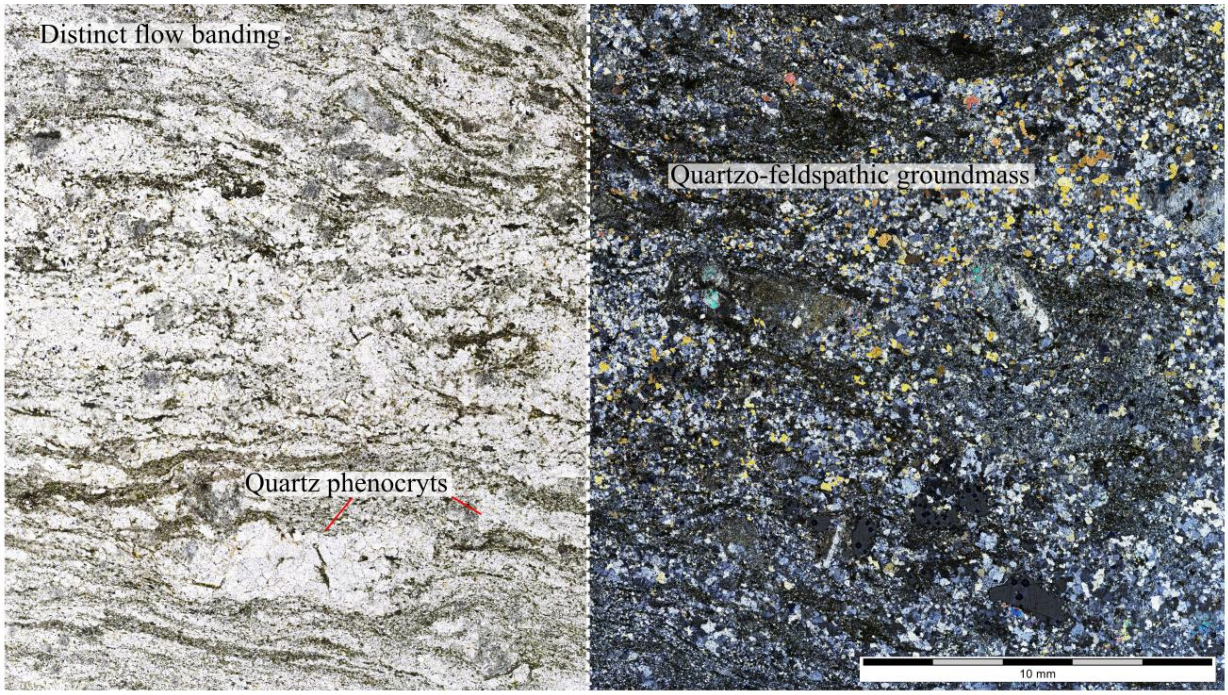

Figure 2: *Plane (left) and cross-polarized (right) photomicrographs of the phyric rhyolite. Distinct flow banding is evident. Phenocrysts are set in a fine-grained quartzo-feldspathic groundmass.*

Mafic tuff

The mafic tuff is clearly bedded (felsic and mafic bands), fine-grained and composed of quartz, chlorite, biotite, epidote and rutile-rich aggregates which form the mafic bands and quartz-feldspar-rich aggregates which form the felsic bands (Figure 3). The mafic bands are more dominant relative to the felsic bands. The chlorite in the mafic bands is associated with inclusions of magnetite. The felsic bands appear sheared. Lensoid-shaped quartz phenocrysts have a distinct undulose extinction and appear aligned. Fiamme textures are associated with recrystallized quartz. In some areas calcite overprints the fiamme textures. Fe-oxide rich veins cross-cut fiamme textures and bedding.

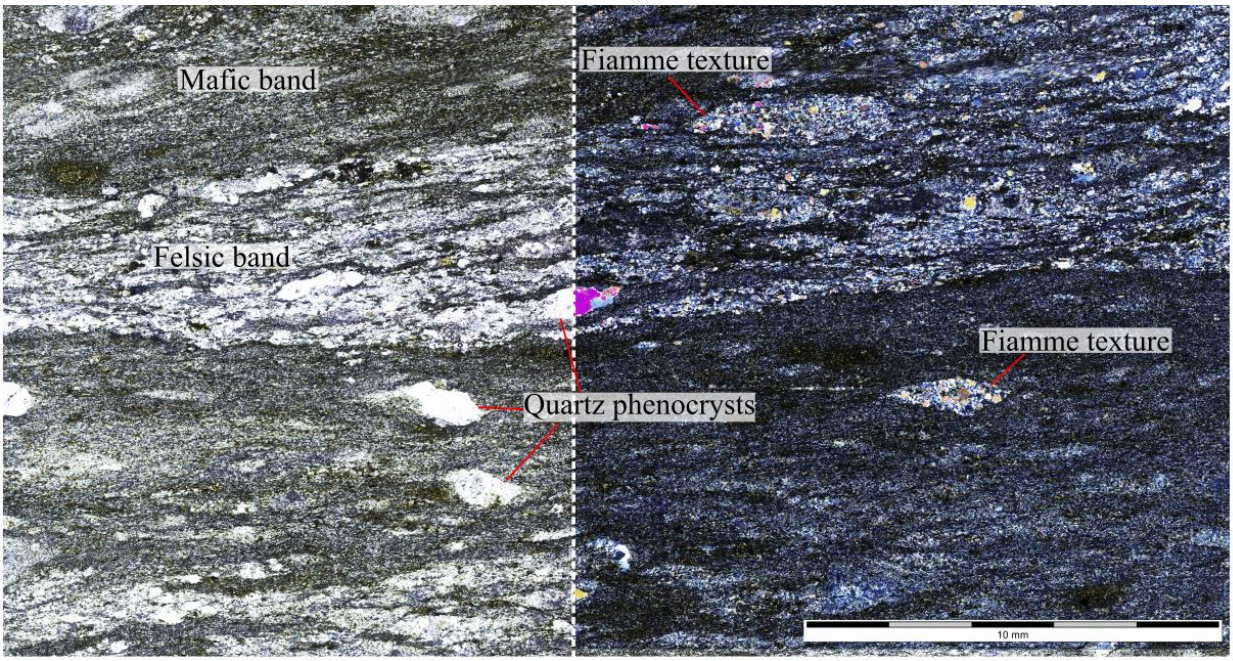

Figure 3: *Plane (left) and cross-polarized (right) photomicrographs of the mafic tuff. Mafic and felsic bands are prevalent. Lensoid-shaped quartz phenocrysts and fiamme textures are distinct as well.*

Diorite

The diorite is medium-grained (0.5 - 2 mm), equigranular and is composed of plagioclase, hornblende, quartz, alkali feldspar, biotite, chlorite, epidote, rutile and sphene (Figure 4). Subhedral plagioclase is zoned and altered to sericite and epidote. The hornblende occurs as stubby-lenticular laths and is altered to coarse aggregates of biotite, chlorite and epidote. Both the plagioclase and hornblende are subhedral-euhedral and occur in approximately equal proportions. The quartz is recrystallized and displays undulose extinction. The quartz and alkali feldspar constitute the interstitial phases. Magnetite occurs as inclusions within chlorite and is also closely associated with rutile. Magnetite occurs also occurs either as disseminated grains or coarse bleb-like aggregates.

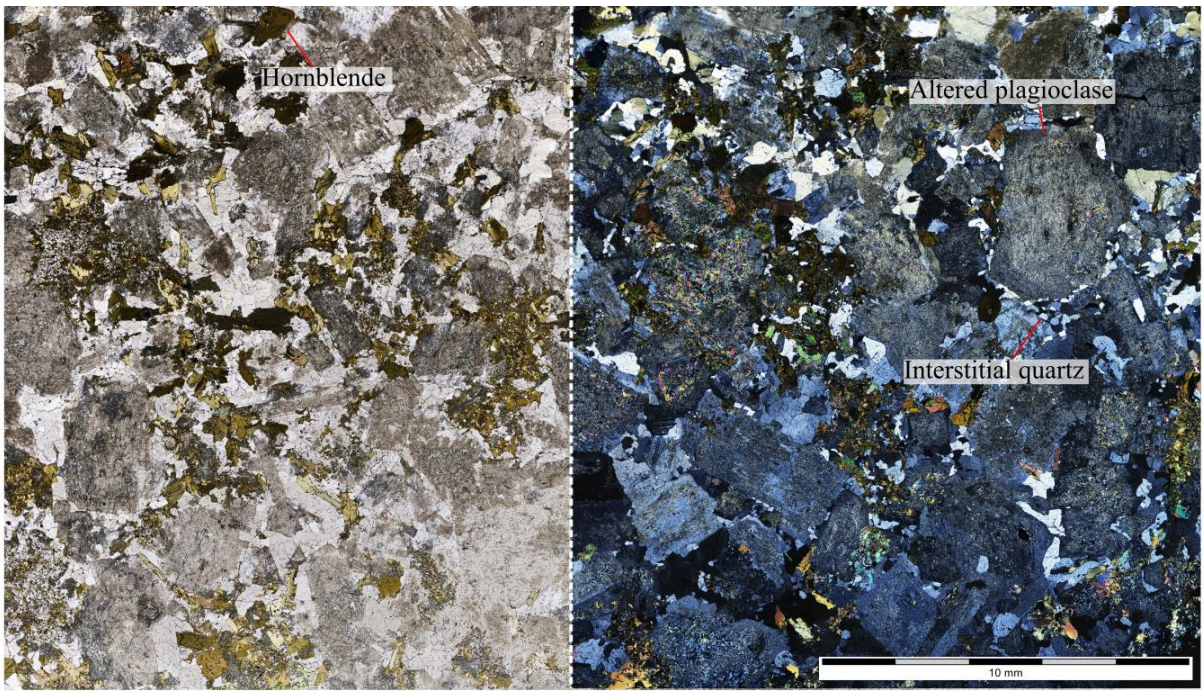

Figure 4: *Plane (left) and cross-polarized (right) photomicrographs of the diorite. Plagioclase is altered to sericite, hornblende is altered to coarse aggregates of biotite, chlorite and epidote. The quartz is recrystallized and displays undulose extinction.*

Granodiorite

The granodiorite is medium-coarse grained (~3 mm), equigranular and is composed of plagioclase, orthoclase, microcline, quartz, hornblende, biotite, chlorite, epidote, apatite, sphene and rutile (Figure 5). The subhedral to euhedral plagioclase is altered to sericite and epidote whereas, the subhedral orthoclase and microcline are altered to clay. The hornblende is altered to coarse biotite, chlorite and epidote aggregates. Primary biotite occurs as subhedral distinct brown flakes. The anhedral quartz is recrystallized, displays an undulose extinction and is associated with sphene and rutile. Apatite and quartz occur as inclusions in biotite and chlorite. Plagioclase and quartz also occur as phenocrysts in some sections of the thin sections. Plagioclase is zoned and altered to sericite and epidote whereas, quartz have a distinct undulose extinction. Disseminated pyrite and magnetite is evident, with magnetite included within hornblende.

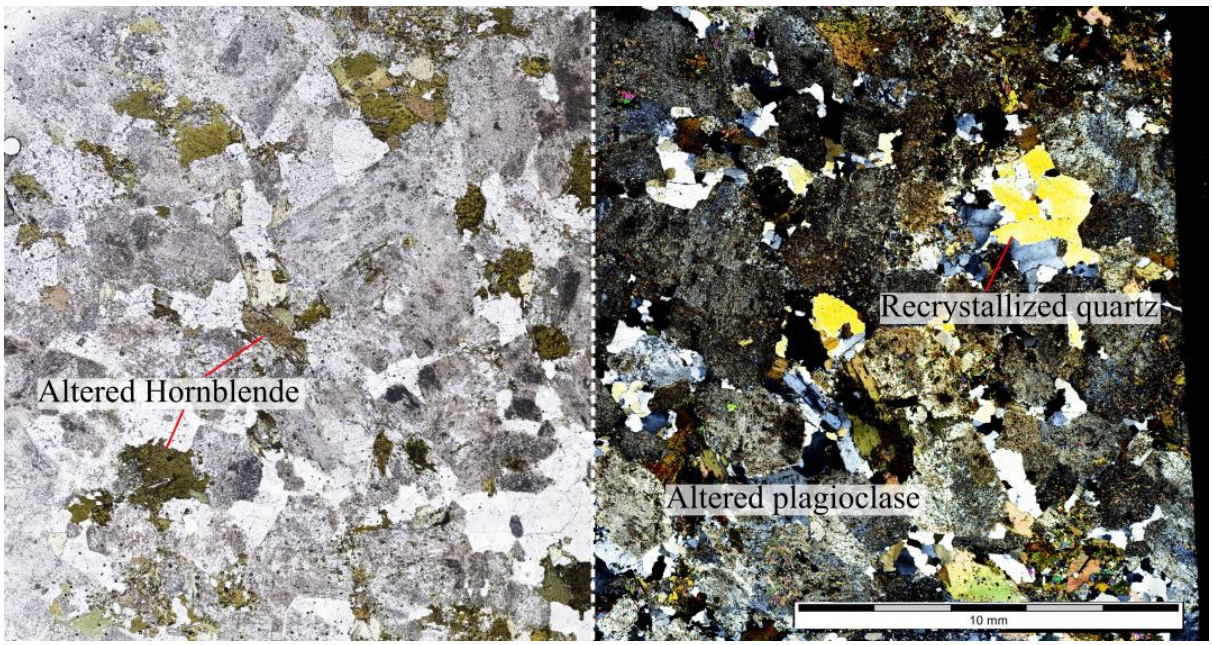

Figure 5: *Plane (left) and cross-polarized (right) photomicrographs of the granodiorite. The degree of alteration is evident in both plane and cross-polarized light. The feldspars, especially plagioclase, are highly altered. Quartz is distinctly recrystallized and exhibits an undulose extinction. Hornblende is altered to biotite, chlorite and epidote aggregates.*

Monzogranite

The monzogranite is medium-grained (~1 mm), porphyritic to equigranular and is composed of microcline, orthoclase, plagioclase, quartz, hornblende, biotite, chlorite, sphene and rutile (Figure 6). Subhedral to euhedral phenocrysts of microcline and orthoclase are altered to clay, plagioclase is altered to sericite and epidote, quartz has a distinct undulose extinction and hornblende is altered to aggregates of biotite, chlorite and epidote. Primary biotite occurs as subhedral distinct brown flakes and is altered to chlorite. Magnetite-haematite-ilmenite occur as inclusions in hornblende and are associated with sphene and rutile. The porphyritic adamellites are foliated with evidence of stretched phenocrysts of quartz, plagioclase, orthoclase, microcline and hornblende, set in a quartzo-feldspathic groundmass. Disseminated pyrite and chalcopyrite are associated with epidote.

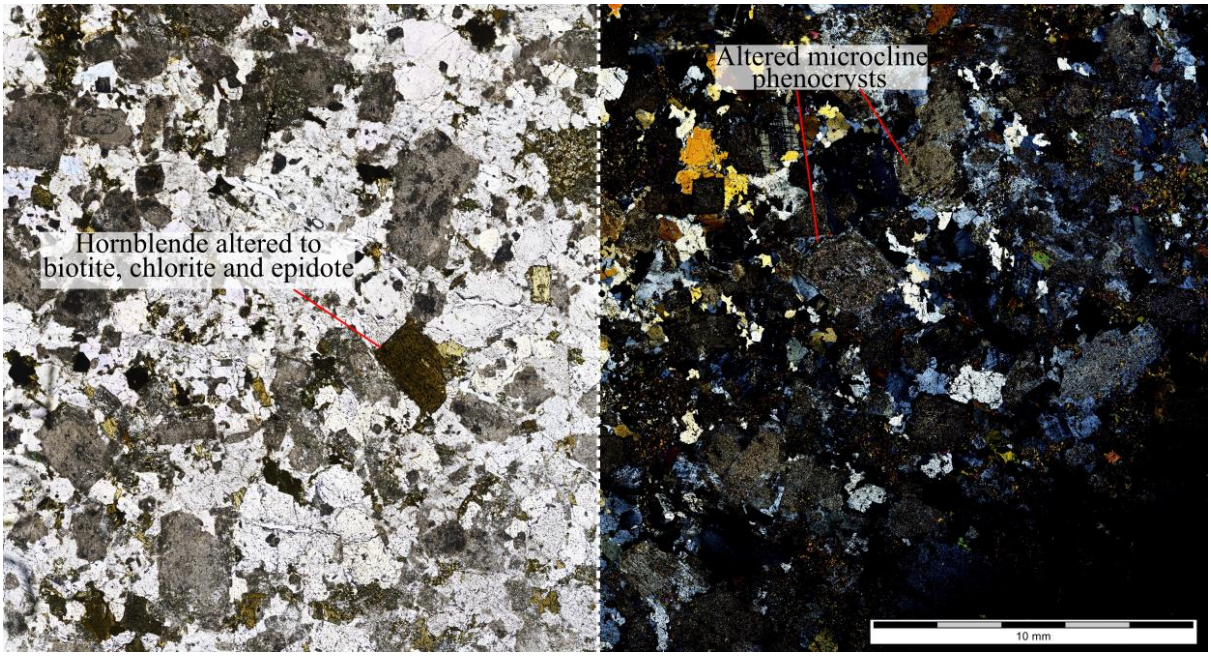

Figure 6: *Plane (left) and cross-polarized (right) photomicrographs of the adamellite. Microcline phenocrysts are distinctly altered to clay. Hornblende is altered to aggregates of biotite, chlorite and epidote.*

Leucogranite

The leucogranite is medium-fine grained (~0.5 - 1 mm), equigranular and composed of quartz, microcline, plagioclase, hornblende, biotite, chlorite, muscovite, calcite, rutile and sphene (Figure 7). The subhedral-euhedral plagioclase is altered to sericite and epidote. Orthoclase and microcline are altered to clay. The anhedral quartz is recrystallized and exhibits undulose extinction. The mafic minerals, which are subhedral, constitute twinned hornblende and lath-like biotite and chlorite, which are associated with magnetite, rutile and sphene. Calcite occurs as anhedral grains with inclusions of quartz. Quartz veins cross-cut through the mineral assemblages. Distinct perthite and anti-perthite textures are observed in plagioclase and orthoclase respectively. Haematite-ilmenite assemblages are disseminated and are closely associated with quartz, rutile and sphene.

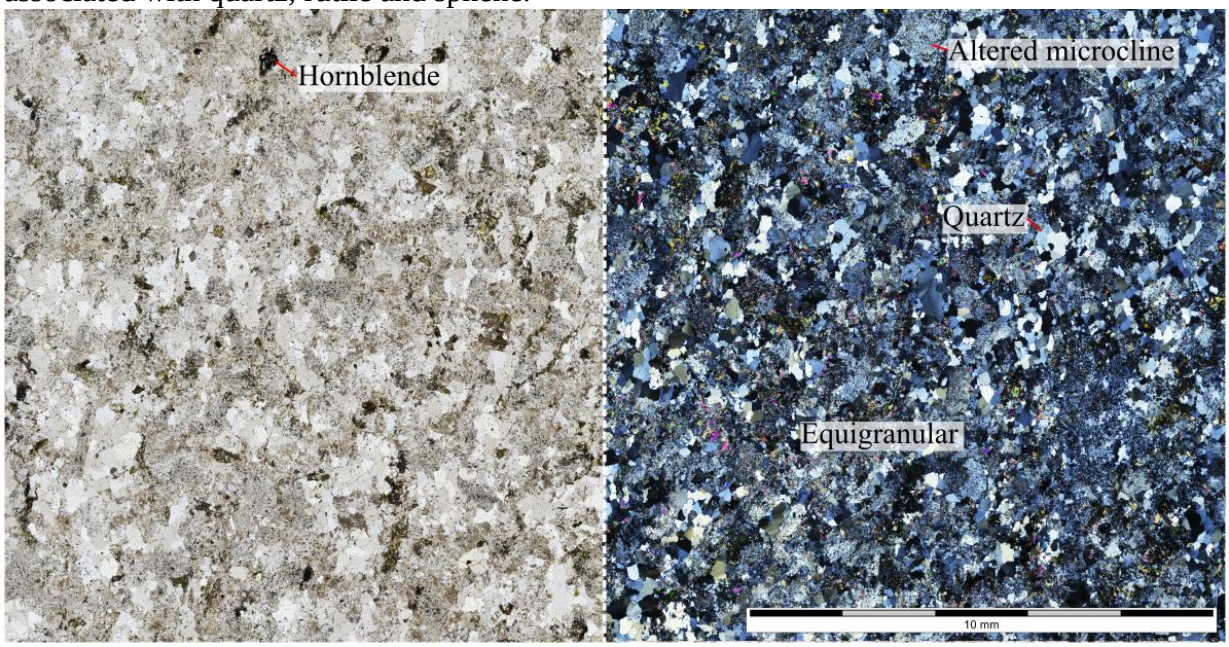

Figure 7: *Plane and cross-polarized photomicrographs of the leucogranite. The leucogranite have a distinct equigranular texture and are predominantly composed of quartz, microcline, orthoclase and biotite.*

Appendix F: Descriptions for the mafic enclaves.

Mafic enclaves are found in the granodiorites, adamellites, quartz-feldspar porphyry granodiorites, gabbros, diorites and leucogranites. There are three main types of mafic enclaves: clinopyroxenite, aphyric and phyric enclaves (Figure 1). The clinopyroxenite enclaves are coarse, dark grey with a distinct green tinge, massive and consists of disseminated chalcopyrite, the aphyric enclaves are fine, dark grey and equigranular and the phyric enclaves are medium, grey and are composed of ~0.5 cm plagioclase phenocrysts (Figure 1a and b). The clinopyroxenite enclaves are found in the leucopyroxenites, gabbros and diorites. The phyric and aphyric enclaves are found in the granodiorites, adamellites, diorites and leucogranites.

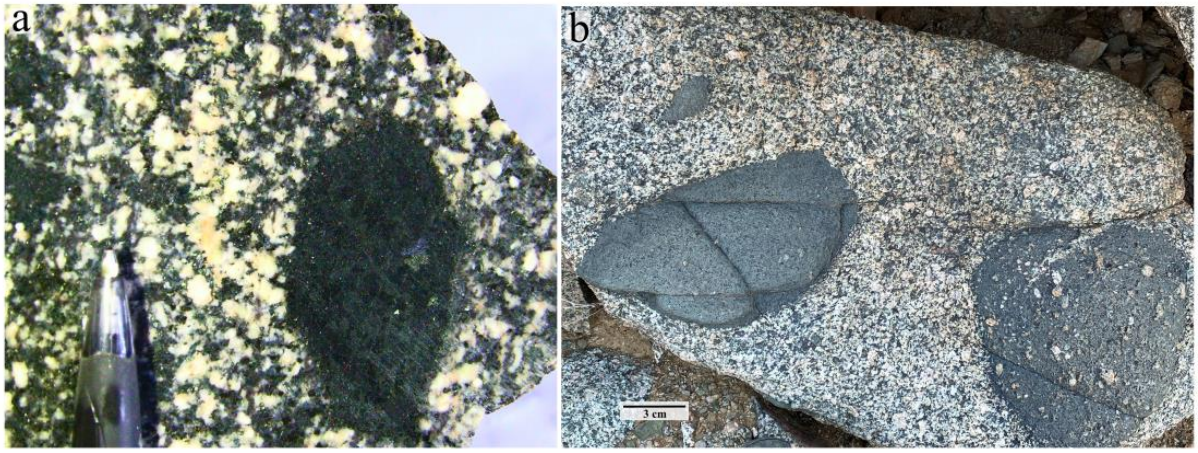

tinge, massive and consist of ~1 mm disseminated and massive chalcopyrite and molybdenite. b) Aphyric enclaves are fine, dark grey and equigranular while the phyric enclaves are medium, grey and are composed of ~0.5 cm plagioclase phenocrysts.

The clinopyroxenite enclaves are coarse (3-5 mm), massive to equigranular and is composed predominantly of clinopyroxene (95 %) altered to hornblende, quartz (4 %) and magnetite (1 %) (Figure 2a). The clinopyroxene and hornblende are both subhedral, twinned and composed of distinct inclusions of quartz and magnetite.

The aphyric enclaves are fine (0.5 mm), equigranular and is composed of clinopyroxene (55 %), plagioclase (35 %), quartz (8 %), rutile (1 %) and magnetite (1 %) (Figure 2b). Subhedral zoned clinopyroxene is altered to hornblende which is subsequently altered to aggregates of biotite and chlorite. Subhedral plagioclase is zoned and altered to sericite and epidote. Anhedral quartz is distinctly recrystallized and exhibits undulose extinction. Zoned rutile is closely associated with magnetite.

The phyric enclaves are fine-medium (0.5-1 mm), equigranular and is composed of clinopyroxene (50 %), plagioclase (31 %), quartz (8 %), biotite (5 %), chlorite (5 %), rutile and magnetite (1 %) (Figure 2c). Tabular to acicular biotite altered to chlorite is aligned in certain areas and in other areas clinopyroxene is altered to aggregates of hornblende, chlorite and biotite. ~1 mm subhedral plagioclase phenocryst is altered to epidote and have inclusions of chlorite. Anhedral quartz is distinctly recrystallized and exhibits undulose extinction. Magnetite is disseminated and is closely associated with altered aggregates of biotite and chlorite.

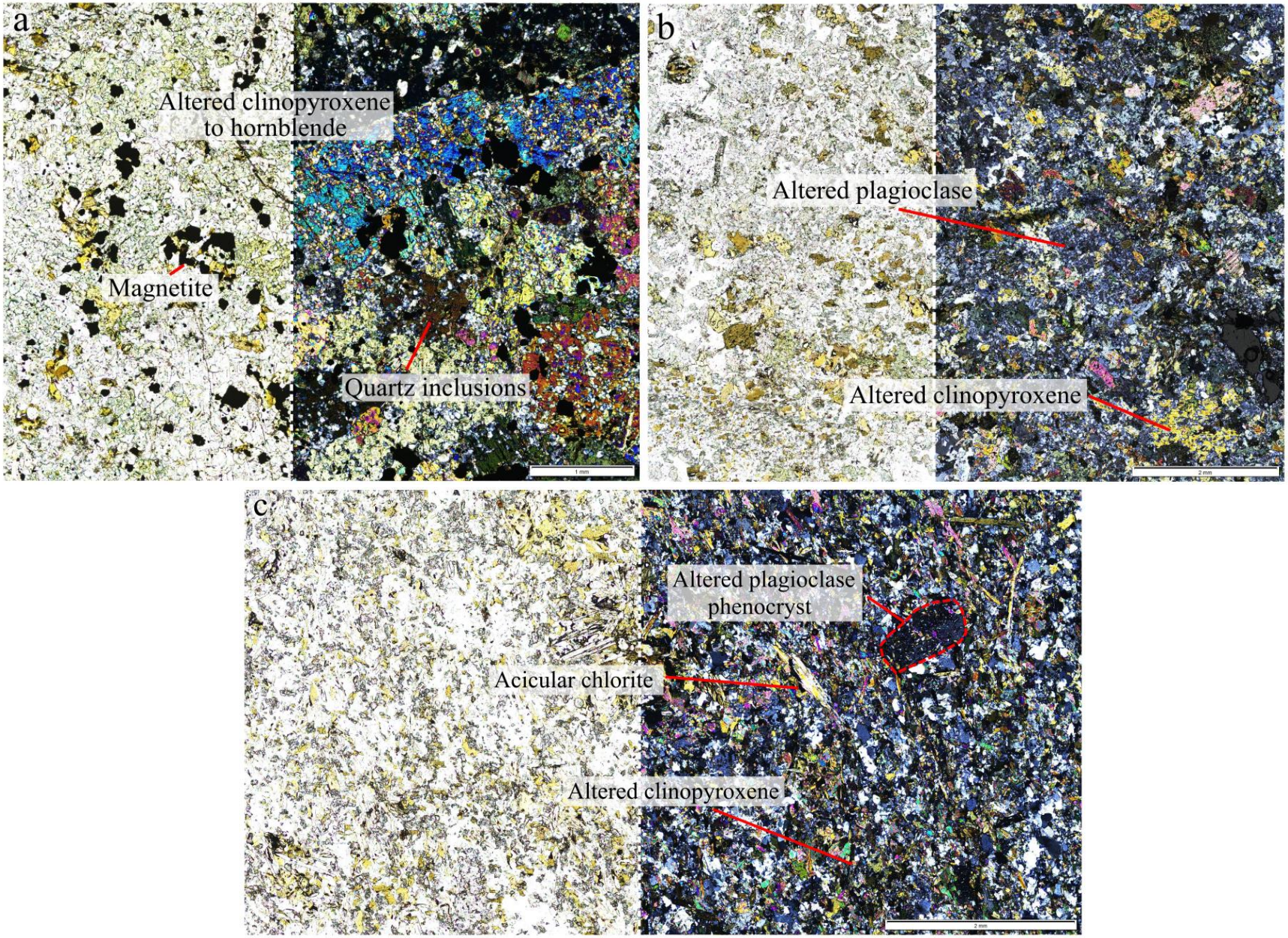

Figure 2: Plane and cross-polarized photomicrographs of the ultramafic (a), aphyric (b) and phyric enclaves (c).

Appendix G: Major element analyses for the Orange River Group, Vioolsdrif Intrusive Suite and Kokerboom Intrusion.

wt%	Rock type	SiO_2	Al_2O_3	Fe_2O_3	MnO	MgO	CaO	Na_2O	K_2O	TiO_2	P_2O_5	Cr_2O_3	NiO	LOI	Total
AJ 21-01	Gabbro	48.22	15.28	12.18	0.19	8.09	9.12	2.09	1.73	1.09	0.26	0.04	0.01	1.82	100.14
AJ 21-02	Gabbro	73.32	14.88	1.71	0.02	0.41	1.71	5.57	1.30	0.22	0.07	0.01	0.00	0.97	100.19
AJ 21-03	Gabbro	43.71	18.46	12.28	0.18	5.57	14.48	1.50	0.56	1.22	0.33	0.01	0.00	1.80	100.08
AJ 21-04	Gabbro	46.32	15.39	12.98	0.24	9.54	9.48	1.87	0.83	0.96	0.33	0.07	0.02	2.23	100.25
AJ 21-05	Quartz-feldspar porphyry granodiorite	71.59	15.73	1.85	0.01	0.79	0.26	0.06	5.06	0.46	0.15	0.01	0.00	2.97	98.94
AJ 21-06	Quartz-feldspar porphyry granodiorite	77.56	12.32	2.46	0.01	0.74	0.15	0.01	4.17	0.36	0.12	0.01	0.00	2.24	100.13
AJ 21-07	Andesite	63.09	15.17	6.76	0.08	3.33	2.61	1.79	3.46	0.63	0.16	0.01	0.01	2.83	99.93
AJ 21-08	Granodiorite	68.78	14.66	3.38	0.04	2.18	1.30	2.57	4.70	0.39	0.12	0.00	0.00	2.08	100.21
AJ 21-09	Quartz-feldspar Porphyry granodiorite	67.15	15.05	3.13	0.04	1.65	2.29	2.70	5.10	0.46	0.15	0.01	0.00	1.79	99.51
AJ 21-10	Cumulate material	52.52	13.58	8.70	0.14	10.41	7.21	2.37	2.35	0.75	0.27	0.12	0.03	1.30	99.73
AJ 21-11	Porphyritic andesite	57.95	17.82	7.47	0.14	3.96	4.20	3.51	2.89	0.75	0.20	0.01	0.01	0.97	99.88
AJ 21-13	Sheared porphyritic andesite	60.43	17.04	5.69	0.09	2.59	5.40	3.20	3.00	0.71	0.27	0.01	0.00	1.43	99.87
AJ 21-14	Rhyolite	62.67	15.92	5.14	0.08	1.46	3.50	3.28	5.54	0.77	0.41	0.01	0.00	1.29	100.06
AJ 21-15	Mafic tuff	57.26	15.92	7.26	0.12	5.48	5.35	2.81	3.41	0.66	0.18	0.03	0.01	1.36	99.84
AJ 21-17	Phenocrystic rhyolite	69.25	15.52	2.70	0.07	0.79	2.04	2.97	5.14	0.54	0.02	0.00	0.00	1.11	100.15

AJ 21-18	Monzogranite	66.79	14.62	5.02	0.09	1.68	3.25	2.81	4.42	0.71	0.22	0.01	0.00	1.08	100.70
AJ 21-20	Granodiorite	55.50	17.53	8.14	0.14	3.49	6.13	2.53	2.90	1.00	0.46	0.02	0.00	1.94	99.79
AJ 21-21	Gabbro	54.59	15.92	9.22	0.16	5.97	7.39	2.98	2.19	0.79	0.29	0.03	0.01	1.05	100.57
AJ 21-23	Gabbro	48.11	15.04	12.02	0.18	7.96	9.52	2.14	1.25	1.12	0.24	0.03	0.01	1.70	99.32
AJ 21-25	Gabbro	54.49	16.91	9.04	0.15	4.59	8.77	2.32	1.50	0.76	0.24	0.01	0.00	1.34	100.11
AJ 21-26	Gabbro	47.20	14.31	13.57	0.22	9.19	9.97	1.56	1.33	1.16	0.13	0.04	0.03	1.63	100.33
AJ 21-28A	Granodiorite	61.16	16.45	5.72	0.11	2.53	4.74	3.49	3.25	0.69	0.22	0.01	0.00	1.45	99.83
AJ 21-28B	Enclave	58.62	15.57	7.13	0.13	4.64	6.01	2.88	3.05	0.71	0.26	0.03	0.01	1.09	100.11
AJ 21-29	Pyroxenite	49.00	9.05	11.57	0.19	15.04	9.84	1.24	1.46	0.67	0.18	0.15	0.04	1.74	100.17
AJ 21-30	Pyroxenite	47.63	8.29	11.57	0.20	17.07	9.83	0.81	0.92	0.55	0.13	0.18	0.06	2.80	100.04
AJ 21-32B	Enclave	54.90	14.50	8.77	0.17	8.18	7.17	2.55	2.42	0.68	0.24	0.08	0.02	1.06	100.75
AJ 21-34A	Diorite	55.51	16.88	8.21	0.09	5.17	4.79	3.62	2.69	0.93	0.33	0.05	0.01	1.94	100.21
AJ 21-36	Diorite	55.97	17.35	8.33	0.14	3.39	6.74	2.59	2.73	1.08	0.40	0.02	0.01	1.48	100.22
AJ 21-37	Quartz-feldspar porphyry granodiorite	69.14	14.77	3.78	0.08	1.72	3.33	2.53	4.11	0.41	0.12	0.01	0.00	1.00	101.00
AJ 21-38	Porphyritic andesite	62.52	16.14	6.56	0.20	2.98	4.05	2.52	3.34	0.63	0.17	0.02	0.00	1.23	100.36
BCR2	Standard	54.74	13.74	1.4	11.31	0.2	3.66	7.21	3.19	1.81	2.28	0.36	0.01	0	99.91
BHVO 2	Standard	50.3	13.78	1.25	10.15	0.17	7.3	11.52	2.22	0.52	2.75	0.27	0.05	0.02	100.28

Appendix H: Trace element analyses for the Orange River Group, Vioolsdrif Intrusive Suite and Kokerboom Intrusion.

ppm	AJ-21-01	AJ-21-02	AJ-21-03	AJ-21-04	AJ-21-05	AJ-21-06	AJ-21-07	AJ-21-08	AJ-21-09	AJ-21-10	AJ-21-11	AJ-21-13	AJ-21-14	AJ-21-15	AJ-21-17	AJ-21-18
Li	17.44	5.68	11.44	26.71	5.21	11.78	35.08	24.733	31.517	40.94	34.45	20.76	10.55	28.38	8.76	20.53
P	1164.41	214.90	1508.68	1366.31	549.97	389.36	626.63	423.62	522.61	1029.39	694.94	1010.21	1523.49	661.30	45.32	878.44
Sc	35.10	3.48	36.89	30.33	9.05	6.65	17.14	7.79	8.63	21.23	20.38	11.75	9.91	21.58	7.60	12.72
Ti	5939.54	1004.74	6683.67	5080.84	2030.30	1584.97	3039.28	1825.08	2064.76	2756.75	3683.94	3367.27	3648.94	3237.19	2394.15	3714.32
V	334.56	23.55	392.58	296.48	79.89	74.82	142.50	82.16	91.99	206.74	197.87	142.62	189.24	161	35.56	84.26
Cr	192.04	2.00	5.30	404.68	29.39	7.58	48.22	9.96	11.13	722.10	59.91	40.21	1.30	172.65	1.87	17.76
Co	44.70	1.72	32.66	47.91	1.74	2.69	16.36	8.82	7.88	38.58	20.01	13.35	10.28	23.20	2.47	11.33
Ni	96.04	2.85	21.69	169.82	6.43	6.62	35.10	10.71	10.68	210.09	39.43	21.71	1.83	38.40	2.35	14.90
Cu	226.32	9.15	241.78	64.44	8790.81	234.02	1761.42	168.52	2219.36	38.38	44.40	57.57	41.55	2.76	2.89	68.20
Zn	118.38	18.96	78.80	141.29	20.11	25.50	76.36	40.69	30.05	80.64	116.65	67.16	62.46	72.64	39.77	66.48
Ga	18.50	15.79	23.30	19.00	16.63	12.80	14.77	15.13	16.30	14.54	19.54	18.40	16.67	16.63	18.66	19.33
Rb	76.86	62.58	24.62	30.86	227.89	219.61	191.86	205.26	230.52	71.90	178.78	145.10	169.27	113.14	157.02	190.67
Sr	443.97	191.72	1208.94	533.06	11.73	6.00	215.68	157.85	301.83	638.07	457.51	569.68	419.17	384.39	264.93	284.00
Y	21.09	17.08	21.35	20.26	9.37	5.85	15.69	11.40	12.21	12.14	21.35	15.62	19.55	17.17	14.92	27.08
Zr	37.11	60.82	18.40	18.70	57.44	48.01	108.64	48.87	44.71	45.01	135.90	123.59	140.44	61.22	190.42	56.12
Nb	6.98	12.56	6.37	5.70	8.82	7.42	10.34	9.35	7.82	1.13	11.15	9.04	13.67	8.60	13.31	13.21
Sn	1.93	6.07	1.14	1.11	4.06	3.05	5.04	2.77	3.04	1.19	4.17	2.34	3.77	2.47	3.40	3.69
Sb	0.89	0.51	1.34	0.67	1.17	3.28	1.46	1.23	1.80	0.84	0.72	3.13	2.38	2.47	0.92	0.64
Cs	1.43	1.63	0.84	0.88	14.00	7.47	12.56	5.53	8.53	12.03	27.32	8.41	3.39	5.21	3.97	5.38
Ba	554.80	510.44	164.65	292.54	272.60	290.91	676.95	743.68	947.48	875.80	605.73	928.56	1437.07	847.27	1668.03	1021.69
La	20.25	40.91	19.66	21.06	28.81	22.31	19.49	25.08	32.68	24.59	36.75	37.40	44.34	26.50	43.57	41.51
Ce	45.08	80.69	45.83	47.34	61.86	46.34	37.79	52.77	64.48	49.60	77.16	75.41	91.10	54.86	95.39	90.16
Pr	5.91	8.41	6.13	6.17	6.55	5.11	4.36	5.90	6.92	5.93	8.69	8.43	10.14	6.21	9.95	10.10
Nd	26.48	28.97	28.07	27.60	23.44	19.30	17.03	22.18	25.44	24.50	33.38	33.15	38.71	24.55	37.24	38.56
Sm	5.87	4.95	6.18	5.84	3.95	3.38	3.55	4.04	4.43	4.60	6.29	5.93	6.84	4.77	6.56	7.11

Eu	1.58	0.83	1.72	1.54	0.66	0.65	0.79	0.87	0.97	1.30	1.38	1.49	1.57	1.10	1.56	1.45
Gd	5.39	4.10	5.54	5.19	2.71	2.38	3.41	3.31	3.58	3.81	5.40	4.83	5.70	4.21	5.14	6.16
Tb	0.74	0.54	0.75	0.71	0.34	0.27	0.52	0.43	0.46	0.48	0.73	0.60	0.73	0.58	0.64	0.86
Dy	4.38	3.22	4.40	4.14	1.97	1.37	3.31	2.47	2.56	2.67	4.36	3.35	4.15	3.46	3.45	5.14
Ho	0.85	0.65	0.84	0.82	0.39	0.26	0.67	0.48	0.49	0.51	0.87	0.65	0.81	0.70	0.64	1.03
Er	2.29	1.88	2.23	2.19	1.20	0.75	1.93	1.38	1.35	1.39	2.43	1.76	2.21	1.94	1.67	2.90
Tm	0.32	0.29	0.30	0.31	0.18	0.12	0.29	0.21	0.19	0.20	0.35	0.25	0.31	0.29	0.23	0.44
Yb	2.01	1.96	1.86	2.01	1.22	0.85	1.94	1.38	1.28	1.26	2.29	1.64	2.04	1.89	1.54	2.76
Lu	0.29	0.28	0.27	0.29	0.18	0.13	0.28	0.21	0.18	0.18	0.33	0.23	0.29	0.28	0.23	0.41
Hf	1.61	2.35	0.82	0.85	2.18	1.82	3.38	1.85	1.69	1.37	3.95	3.14	3.58	1.80	5.29	2.02
Ta	0.41	1.38	0.30	0.28	0.84	0.71	0.97	0.72	0.66	0.10	1.01	0.65	1.01	0.66	0.84	1.03
W	0.62	1.21	0.60	4.22	22.43	4.34	6.21	2.76	3.60	0.37	0.49	0.75	1.05	0.74	0.32	0.65
Tl	0.64	0.30	0.18	0.25	2.43	2.62	2.32	2.33	2.25	0.85	2.75	1.92	0.93	0.99	1.46	1.56
Pb	7.36	14.23	11.60	7.97	3.21	11.79	17.67	12.62	13.59	13.72	28.20	24.62	37.73	25.90	29.08	23.15
Th	6.70	24.59	1.73	1.58	10.13	9.32	16.04	11.07	10.47	3.65	16.15	8.28	15.29	10.03	11.88	12.89
U	1.01	8.00	0.44	0.44	1.22	1.75	4.19	2.20	2.34	0.81	4.58	1.95	3.62	2.29	2.12	3.01

ppm	AJ-21-20	AJ-21-21	AJ-21-23	AJ-21-25	AJ-21-26	AJ-21-28A	AJ-21-28B	AJ-21-29	AJ-21-30	AJ-21-32B	AJ-21-34A	AJ-21-36	AJ-21-37	AJ-21-38	BCR2	BHVO2
Li	31.03	30.34	22.91	21.16	17.55	28.81	38.50	21.76	23.36	28.925	25.39	27.30	27.33	46.15	9.65	5.134
P	2009.97	1252.28	1085.12	1068.48	559.81	891.76	1109.68	759.84	596.21	998.58	1385.51	1793.01	458.63	644.27	1534.75	1206.69
Sc	20.30	27.22	34.55	25.09	38.68	13.975	18.01	37.55	34.94	26.86	19.64	22.20	10.98	17.62	31.66	31.35
Ti	5911.29	4566.54	6406.08	4439.55	6578.05	3806.77	3959.98	3309.14	2745.32	3728.23	4003.68	5868.78	2111.32	3378.60	12676.73	16036.53
V	174.93	228.06	321.71	239.40	375.89	105.10	177.14	187.17	173.34	165.89	159.67	171.90	86.45	134.22	417.02	326.66
Cr	79.60	166.49	251.33	37.50	245.10	56.14	159.00	918.64	1197.82	508.40	273.90	60.55	15.89	62.74	15.64	312.09
Co	21.51	30.62	45.05	28.75	50.52	14.80	24.21	62.74	67.73	34.68	24.98	21.25	10.15	20.49	37.15	45.36
Ni	30.96	38.39	99.24	22.51	117.45	24.44	62.66	330.83	466.63	175.42	102.34	29.09	12.29	35.85	12.06	118.27
Cu	119.32	43.75	208.76	46.72	253.26	58.87	5.71	66.00	26.68	12.02	4.92	109.79	21.42	80.50	18.80	146.72
Zn	95.42	92.42	107.29	91.00	111.39	76.54	102.16	101.70	113.96	98.33	63.20	144.30	67.29	243.67	143.13	109.98
Ga	21.35	18.55	20.00	19.61	18.40	20.05	20.23	12.01	10.79	17.37	20.69	20.74	16.40	19.69	22.03	21.66
Rb	127.08	89.10	47.25	49.38	58.29	150.96	169.59	58.79	32.57	96.75	138.51	126.76	190.59	184.84	49.69	9.96
Sr	625.21	534.38	535.97	614.87	455.46	429.33	549.40	290.45	135.80	408.08	717.58	523.49	306.79	354.73	319.21	384.16
Y	18.42	13.48	21.84	14.17	18.29	20.55	14.95	12.89	12.05	17.61	19.67	16.99	16.21	19.30	31.30	22.79
Zr	9.47	6.42	51.98	11.17	36.32	35.57	57.95	30.96	56.81	16.50	18.19	7.37	48.71	131.35	184.07	169.12
Nb	8.58	5.262	7.90	5.28	5.51	11.10	7.65	3.07	3.23	5.69	5.87	9.31	9.71	10.85	11.72	18.06
Sn	1.81	1.21	5.31	1.29	1.19	2.68	1.86	1.16	0.85	1.48	2.15	1.90	4.26	3.98	2.10	1.31
Sb	1.70	1.08	0.67	0.74	0.71	1.95	1.19	1.42	1.03	1.88	3.98	1.71	0.68	2.56	0.59	0.17
Cs	4.35	3.01	1.79	1.75	1.18	5.58	6.17	3.85	2.00	4.64	3.94	5.58	12.77	11.91	1.08	0.12
Ba	919.35	769.93	330.19	688.33	302.80	1045.79	708.15	380.61	267.79	711.08	842.54	712.50	783.38	493.82	629.80	131.04
La	27.82	22.43	21.98	22.00	14.41	33.70	31.76	14.59	11.32	23.50	33.15	29.25	37.37	36.53	25.10	15.24
Ce	59.47	44.69	50.61	44.61	34.04	72.59	66.77	33.23	24.31	47.82	70.30	58.11	73.04	77.78	51.57	36.25
Pr	6.90	5.24	6.50	5.28	4.57	8.29	7.56	4.27	3.24	5.63	8.10	6.71	7.42	8.72	6.37	4.95
Nd	27.71	21.53	28.37	21.89	20.90	32.57	29.76	19.05	14.48	22.95	32.22	26.72	26.30	32.87	27.72	23.39
Sm	5.39	4.24	6.10	4.28	4.84	6.24	5.30	4.11	3.34	4.77	6.01	5.06	4.61	6.02	6.33	5.78
Eu	1.68	1.34	1.58	1.24	1.29	1.57	1.39	1.07	0.97	1.27	1.65	1.54	1.00	1.23	1.93	1.98
Gd	4.76	3.61	5.36	3.68	4.45	5.23	4.20	3.53	3.02	4.21	5.24	4.42	3.81	4.99	6.52	5.88

Tb	0.64	0.47	0.74	0.49	0.63	0.73	0.53	0.48	0.42	0.60	0.70	0.58	0.52	0.66	0.97	0.84
Dy	3.72	2.69	4.36	2.83	3.72	4.21	2.94	2.72	2.45	3.51	4.01	3.36	3.09	3.76	6.03	4.88
Ho	0.72	0.52	0.85	0.56	0.72	0.83	0.57	0.52	0.48	0.70	0.78	0.65	0.62	0.74	1.22	0.80
Er	1.93	1.42	2.31	1.52	1.95	2.26	1.54	1.40	1.28	1.91	2.12	1.75	1.78	2.04	3.36	2.26
Tm	0.27	0.20	0.33	0.22	0.28	0.32	0.22	0.20	0.18	0.28	0.30	0.25	0.28	0.31	0.48	0.29
Yb	1.68	1.25	2.03	1.38	1.73	1.92	1.39	1.17	1.16	1.76	1.80	1.50	1.79	1.97	3.35	1.93
Lu	0.25	0.19	0.31	0.21	0.26	0.28	0.21	0.17	0.17	0.27	0.27	0.24	0.28	0.31	0.48	0.26
Hf	0.46	0.34	1.86	0.53	1.43	1.15	1.62	1.15	1.66	0.72	0.68	0.40	1.86	3.70	4.82	4.26
Ta	0.47	0.32	0.47	0.33	0.31	0.67	0.48	0.20	0.24	0.38	0.42	0.48	0.92	0.98	0.70	1.06
W	0.45	0.41	7.04	0.33	0.76	0.63	0.38	1.06	0.60	0.42	0.80	0.55	5.92	1.21	0.35	0.36
Tl	1.03	0.76	0.38	0.41	0.45	1.19	1.46	0.54	0.31	0.80	0.92	0.98	2.02	2.43	0.55	0.04
Pb	15.08	12.48	7.20	11.49	7.58	23.68	21.69	4.38	2.85	13.89	19.37	14.83	26.67	45.42	10.08	1.53
Th	5.32	2.77	4.44	3.04	2.35	9.22	5.58	2.37	1.62	4.41	7.98	5.54	17.33	15.49	5.75	1.13
U	1.27	0.66	0.95	0.70	0.64	2.77	3.30	0.49	0.55	0.97	1.70	1.22	4.24	4.52	1.75	0.43

Appendix I: U-Pb data for the Kokerboom Intrusion (Vuurdood Subsuite of the Vioolsdrif Intrusive Suite), the diorite and granodiorite from the Vioolsdrif Intrusive Suite.

Sample	$^{207}Pb/^{235}U$	Int 2SE	$^{206}Pb/^{238}U$	Int 2SE	rho	$^{207}Pb/^{206}Pb$	Int 2SE	rho	$^{207}Pb/^{235}U$ age Ma	Int 2SE	$^{206}Pb/^{238}U$ age Ma	Int 2SE	$^{207}Pb/^{206}Pb$ age Ma	Int 2SE	U/Th	Disc %
AJ-21-28-1	4.7	0.32	0.2852	0.014	0.16112	0.11568	0.00067	0.41659	1766.9	4.5	1617.3	5.4	1890	10	1.1066	14.428571
AJ-21-28-2	4.822	0.33	0.2927	0.015	0.50731	0.1153	0.00052	0.25895	1789.9	4.4	1655.1	6.5	1883.8	8.1	0.9452	12.140355
AJ-21-28-3	5.033	0.35	0.311	0.015	0.59283	0.11672	0.00074	-0.12128	1824.6	7	1745	12	1906	11	1.084	8.4470094
AJ-21-28-4	4.939	0.34	0.3013	0.015	0.53659	0.11551	0.00046	0.18121	1808.7	4.9	1697.8	5.3	1888	7.1	0.887	10.074153
AJ-21-28-5	4.938	0.34	0.2998	0.015	0.43785	0.116	0.00054	0.23243	1809.7	4.5	1690	6.4	1897.2	8.7	1.72	10.921358
AJ-21-28-6	4.724	0.33	0.2848	0.015	0.50854	0.11678	0.00061	0.19932	1771.8	5	1615.6	6.9	1906.8	9.5	0.992	15.271659
AJ-21-28-7	4.959	0.34	0.3005	0.015	0.39362	0.11615	0.00059	0.31421	1812.5	4.8	1693.8	5.4	1898	9	1.049	10.758693
AJ-21-28-8	4.906	0.33	0.2986	0.015	0.67992	0.11584	0.00055	-0.044294	1803.5	5	1684.4	6.5	1894.1	8.5	0.767	11.071221
AJ-21-28-10	4.978	0.34	0.3036	0.015	0.2597	0.11722	0.00052	0.31174	1815.5	3.8	1708.8	7.4	1913.8	7.9	0.798	10.711673
AJ-21-28-11	4.977	0.34	0.2992	0.015	0.2517	0.11711	0.00058	0.38142	1815.2	4	1687.5	5.2	1911.8	8.9	1.3185	11.732399
AJ-21-28-13	4.975	0.34	0.3239	0.016	0.24425	0.11446	0.00084	0.49119	1814.9	5.8	1808	10	1871	13	0.835	3.3671833
AJ-21-28-14	5.087	0.34	0.3145	0.015	0.18869	0.117	0.001	0.48144	1833.7	6.6	1763	12	1910	15	1.162	7.6963351
AJ-21-28-15	5.12	0.35	0.2925	0.014	0.29471	0.12466	0.00079	0.24762	1839.6	5.9	1654.1	6.4	2027	11	0.143	18.396645
AJ-21-28-16	4.935	0.34	0.3039	0.015	0.404	0.11544	0.00063	0.26961	1807.9	4.7	1710.4	6.9	1885.7	9.8	1.131	9.2962825
AJ-21-28-17	5.632	0.36	0.348	0.017	0.86086	0.11521	0.00064	0.56851	1920.5	7.1	1925	13	1882.5	9.9	1.412	-2.2576361
AJ-21-28-18	4.956	0.34	0.3026	0.015	0.55218	0.11606	0.00046	0.19036	1811.6	4.1	1703.9	6.1	1896.7	7.2	2.804	10.165023

AJ-21-28-19	5.454	0.35	0.3419	0.017	0.80306	0.11561	0.0008	0.12256	1893	12	1895	21	1892	12	0.923	-0.1585624
AJ-21-28-20	5.63	0.36	0.3167	0.015	0.4988	0.1262	0.0023	-0.18799	1921	21	1776	11	2047	34	0.474	13.238886
AJ-21-28-21	5.121	0.4	0.3062	0.016	0.14768	0.11951	0.00062	0.44452	1839.8	4.9	1721.9	7	1948.2	9.3	1.1414	11.615851
AJ-21-28-22	4.968	0.34	0.3072	0.015	0.49533	0.11526	0.00059	0.23058	1813.6	4.6	1727.2	7.6	1883.7	9.2	0.7259	8.308117
AJ-21-28-23	5.496	0.36	0.3312	0.016	0.72632	0.1187	0.00077	0.1329	1899.7	6.9	1844	12	1938	12	1.1009	4.8503612
AJ-21-28-24	4.948	0.34	0.30258	0.015	0.33736	0.1166	0.00053	0.39817	1810.8	3.8	1704	4.8	1904.1	8.1	1.1678	10.508902
AJ-21-28-25	5.056	0.34	0.3235	0.015	0.22241	0.1151	0.00065	0.26343	1828.6	6.1	1807	10	1882.9	9.8	1.309	4.031016
AJ-21-28-26	5.294	0.42	0.3161	0.016	0.62152	0.12	0.0013	-0.35479	1867	12	1770.7	7.3	1954	18	1.4196	9.3807574
AJ-21-28-27	5.262	0.35	0.3283	0.016	0.33035	0.11559	0.00074	0.99917	1862.2	7.1	1829.8	8.8	1888	12	1.457	3.0826271
AJ-21-28-28	5.014	0.34	0.324	0.015	0.52634	0.11501	0.00083	0.087497	1822.6	7.6	1809	16	1879	13	1.684	3.7253858
AJ-21-28-29	5.155	0.34	0.3275	0.016	0.47826	0.1158	0.0012	0.17046	1844.7	9.3	1826	19	1890	19	1.06	3.3862434
AJ-21-28-30	5.067	0.35	0.3221	0.016	0.24506	0.11626	0.00094	0.47373	1830.5	5.4	1800	15	1899	15	1.12	5.2132701
AJ-21-28-31	5.205	0.35	0.3262	0.016	0.32617	0.1168	0.00082	0.29701	1853.1	6.2	1822	13	1910	12	0.8767	4.6073298
AJ-21-28-32	5.187	3.5	0.3164	0.035	0.10427	0.1193	0.0011	0.2205	1849.8	9.1	1772.2	9.9	1945	17	0.9515	8.8843188
AJ-21-28-33	5.08	0.35	0.327	0.016	0.398	0.11654	0.00082	0.23099	1832.6	7.6	1824	14	1903	13	0.986	4.15134
AJ-21-28-34	5.155	0.36	0.3323	0.016	0.1045	0.11506	0.00083	0.44792	1845	6.2	1849	13	1880	13	0.942	1.6489362
AJ-21-28-35	5.142	0.74	0.3169	0.017	0.3969	0.12	0.0013	0.13621	1843	10	1774	15	1959	19	1.019	9.4435937
AJ-21-28-36	4.988	0.34	0.3238	0.015	0.38359	0.1157	0.0014	0.26762	1817	10	1808	17	1890	21	1.697	4.3386243
AJ-21-28-37	5.087	0.34	0.3306	0.016	0.51917	0.11552	0.00081	-0.0054909	1833.8	7	1841	14	1888	13	0.882	2.4894068

AJ-21-28-38	5.031	0.34	0.3249	0.015	0.35406	0.1167	0.0012	0.32723	1824	10	1813	20	1905	18	1.073	4.8293963
AJ-21-28-39	5.187	0.36	0.3244	0.016	0.04921	0.1171	0.0012	0.40837	1850.3	7.2	1811	10	1914	19	0.9909	5.3814002
AJ-21-28-40	5.025	0.33	0.3251	0.016	0.54211	0.11648	0.00059	0.11488	1824.1	5.6	1815	11	1902.4	9.1	0.972	4.5941968
AJ-21-34-01	5.459	0.37	0.3421	0.017	0.21709	0.11621	0.00051	0.84187	1893.8	3.9	1896.5	8.4	1897.9	7.8	0.711	0.0737657
AJ-21-34-02	5.501	0.37	0.3417	0.017	0.43023	0.11688	0.00094	0.23305	1900.3	6.8	1894	14	1908	14	1.106	0.7337526
AJ-21-34-03	5.356	0.38	0.3406	0.018	0.45511	0.1158	0.0011	0.39448	1877.5	7.4	1889	13	1895	17	0.708	0.3166227
AJ-21-34-04	5.115	0.36	0.3293	0.016	0.63773	0.11402	0.00091	0.018672	1839.4	8.2	1837	16	1863	14	0.726	1.3955985
AJ-21-34-06	5.45	0.37	0.3403	0.017	0.53291	0.11541	0.00049	0.22064	1892.7	4.5	1888.7	9.6	1886.4	7.6	0.994	-0.1219254
AJ-21-34-07	5.437	0.37	0.3407	0.017	0.60896	0.11567	0.00045	0.28769	1890.3	4.8	1889.6	8.2	1889.7	7	0.862	0.0052918
AJ-21-34-08	5.403	0.37	0.3392	0.017	0.2622	0.11589	0.0007	0.36321	1885.7	5.7	1883	12	1893	11	1.0132	0.528262
AJ-21-34-10	5.38	0.37	0.3392	0.017	0.32693	0.11494	0.00069	0.24389	1881.7	5.4	1882.9	7	1877	11	0.78	-0.3143314
AJ-21-34-11	5.342	0.37	0.3381	0.017	0.4846	0.11624	0.00099	0.187	1875.2	9	1880	17	1898	15	0.681	0.9483667
AJ-21-34-12	5.426	0.37	0.3398	0.017	0.35675	0.1157	0.00075	0.38359	1889.9	4.8	1886	10	1890	12	0.828	0.2116402
AJ-21-34-13	5.406	0.37	0.339	0.017	0.6318	0.11558	0.00048	0.35046	1886.3	5	1881.9	6.7	1888.3	7.5	1.172	0.3389292
AJ-21-34-14	5.299	0.37	0.336	0.017	0.50304	0.11534	0.00078	0.09543	1869.3	7.2	1867.1	9	1888	12	1.104	1.1069915
AJ-21-34-15	5.52	0.38	0.3438	0.017	0.06639	0.1165	0.0012	0.35912	1905.2	8.1	1905	12	1901	19	1.0726	-0.2104156
AJ-21-34-16	5.2	0.35	0.3288	0.016	0.24014	0.1183	0.0028	0.25977	1852	18	1842	26	1930	42	1.649	4.5595855
AJ-21-34-17	5.392	0.39	0.3405	0.018	0.57774	0.11539	0.00081	0.19727	1883.3	8.3	1889	12	1888	13	1.346	-0.0529661
AJ-21-34-18	5.553	0.37	0.3445	0.017	0.47873	0.1166	0.0012	0.1163	1909.2	9.9	1908	15	1905	19	0.783	-0.1574803

AJ-21-34-19	5.487	0.38	0.3429	0.017	0.37163	0.11565	0.00043	0.20913	1898.4	3.8	1900.5	5.5	1889.5	6.6	1.1971	-0.5821646
AJ-21-34-20	5.63	0.41	0.3452	0.017	-0.093241	0.1185	0.002	0.26549	1918	17	1912	12	1930	29	0.7018	0.9326425
AJ-21-34-21	5.418	0.37	0.3404	0.017	0.3275	0.1162	0.0013	0.23869	1887.2	8.6	1888	16	1899	19	0.759	0.5792522
AJ-21-34-22	5.652	0.4	0.347	0.018	0.6547	0.11711	0.00081	0.17199	1923.3	7.2	1920	11	1912	13	1.0376	-0.41841
AJ-21-34-23	5.594	0.38	0.3461	0.017	0.1991	0.11663	0.00063	0.36061	1914.8	4.5	1915.9	6.3	1905.7	9.7	0.945	-0.5352364
AJ-21-34-24	5.569	0.38	0.344	0.017	0.40539	0.11656	0.00067	0.2294	1911.8	5.5	1905.9	8.1	1905	10	0.8308	-0.0472441
AJ-21-34-25	5.394	0.37	0.3386	0.017	0.36661	0.11584	0.00074	0.30479	1883.5	6.1	1880	11	1893	12	0.6759	0.6867406
AJ-21-34-26	5.474	0.38	0.3416	0.017	0.4483	0.11705	0.00087	0.14363	1896.3	6.5	1894	12	1911	13	1.495	0.8895866
AJ-21-34-27	5.489	0.37	0.3422	0.017	0.2322	0.1161	0.0011	0.37886	1898.4	8.3	1897	15	1895	17	0.691	-0.1055409
AJ-21-34-28	5.54	0.38	0.3439	0.017	0.22019	0.11664	0.0004	0.32044	1906.7	4.1	1905.3	7.5	1905.2	6.2	0.954	-0.0052488
AJ-21-34-29	5.57	0.38	0.3444	0.017	0.37448	0.11786	0.00092	0.23755	1911	7.3	1908	13	1923	14	0.709	0.7800312
AJ-21-34-30	5.715	0.39	0.3495	0.018	0.40405	0.116	0.0011	0.31394	1933.2	8.6	1932.2	9.4	1898	16	1.065	-1.8018967
AJ-21-34-31	5.536	0.38	0.3433	0.017	0.38376	0.11677	0.00089	0.28085	1905.7	7.1	1904	14	1906	14	0.7467	0.1049318
AJ-21-34-32	5.628	0.39	0.3474	0.017	0.32246	0.11623	0.00058	0.28317	1920.1	4.8	1922.2	5.9	1900	9	0.8688	-1.1684211
AJ-21-34-33	5.414	0.37	0.3403	0.017	0.46952	0.11465	0.00069	0.2657	1886.7	5.6	1888	14	1875	11	0.6041	-0.6933333
AJ-21-34-34	5.491	0.4	0.3421	0.017	-0.12413	0.1168	0.0012	0.54829	1900	6.7	1899	12	1906	18	0.8829	0.3672613
AJ-21-34-35	6.18	0.43	0.3454	0.018	0.35399	0.1276	0.0022	-0.11795	2000	15	1912	11	2060	30	0.9287	7.184466
AJ-21-34-36	5.578	0.39	0.3429	0.017	0.30249	0.11733	0.00083	0.18602	1912	7.2	1900.3	9.8	1916	13	0.6637	0.8194154
AJ-21-34-37	5.515	0.39	0.345	0.018	0.27941	0.11479	0.00077	0.26924	1902.6	5.7	1910.8	9.3	1876	12	0.8695	-1.8550107

AJ-21-34-38	5.594	0.38	0.3452	0.017	0.50124	0.118	0.001	0.13755	1914.7	9.6	1911	18	1925	16	0.965	0.7272727
AJ-21-34-39	5.498	0.37	0.3425	0.017	0.38138	0.11583	0.00058	0.29924	1900.2	4.5	1899	11	1892.4	8.9	1.0026	-0.3487635
AJ-21-34-40	5.207	0.38	0.3331	0.017	0.052054	0.1149	0.0013	0.40708	1853.5	8.9	1853	13	1877	20	0.6818	1.2786361
AJ-21-04-1	5.25	0.37	0.3355	0.017	0.18664	0.1156	0.0012	0.32224	1862	9.2	1864.9	8.2	1891	18	0.9627	1.3802221
AJ-21-04-2	5.356	0.37	0.3382	0.017	0.098524	0.11604	0.00078	0.30665	1877.3	5.2	1878.5	5.7	1897	12	1.2167	0.975224
AJ-21-04-3	5.285	0.37	0.3348	0.017	0.50328	0.11533	0.00065	0.11612	1866.1	5.3	1861.5	7.4	1884	10	0.8454	1.1942675
AJ-21-04-4	5.33	0.37	0.3366	0.017	0.32878	0.11567	0.00085	0.2008	1873.2	6.6	1870	10	1889	13	1.2679	1.0058232
AJ-21-04-5	5.282	0.37	0.3351	0.017	0.40724	0.11552	0.00064	0.24612	1865.6	4.9	1862.8	8	1887.9	9.9	0.751	1.3295196
AJ-21-04-6	5.252	0.37	0.3346	0.017	0.31447	0.11407	0.00078	0.37592	1860.7	5.9	1860.6	7.7	1864	12	0.7612	0.1824034
AJ-21-04-7	5.242	0.36	0.3347	0.017	0.51866	0.11405	0.00086	0.028959	1859.4	7.8	1860.8	7	1864	13	1.0252	0.1716738
AJ-21-04-8	5.287	0.36	0.3358	0.017	0.57518	0.11574	0.0008	0.013512	1868	7.3	1866	13	1890	12	1.2828	1.2698413
AJ-21-04-9	5.377	0.37	0.3381	0.017	0.2654	0.11622	0.00082	0.29211	1880.8	6.3	1877	11	1898	13	0.8368	1.1064278
AJ-21-04-10	5.268	0.36	0.3347	0.017	0.4558	0.11513	0.00068	0.26474	1863.3	4.9	1860.7	8.9	1886	10	0.998	1.3414634
AJ-21-04-11	5.291	0.36	0.336	0.017	0.38553	0.11515	0.00064	0.21884	1867.4	5	1867.4	7.1	1884	10	0.7537	0.881104
AJ-21-04-12	5.242	0.36	0.3332	0.017	0.18641	0.115	0.0011	0.39518	1858.9	7.9	1853.6	8.7	1878	18	0.7283	1.2992545
AJ-21-04-14	5.363	0.37	0.3379	0.017	0.26307	0.1164	0.0012	0.26261	1879.3	8.1	1876	12	1899	19	1.218	1.2111638
AJ-21-04-15	5.338	0.37	0.3376	0.017	0.2359	0.11647	0.00088	0.17398	1876.3	6.6	1875	10	1902	14	1.189	1.4195584
AJ-21-04-16	5.354	0.37	0.3373	0.017	0.37772	0.1169	0.00098	0.13358	1877.1	6.9	1873	12	1910	15	0.6849	1.9371728
AJ-21-04-17	5.368	0.36	0.3391	0.017	0.34855	0.11599	0.00088	0.27508	1879.5	5.6	1882	12	1896	13	0.8554	0.7383966

AJ-21-04-18	5.3	0.36	0.3352	0.017	0.38045	0.11515	0.0007	0.20369	1869	5.2	1863.5	9.7	1884	11	1.16	1.0881104
AJ-21-04-19	5.231	0.36	0.3336	0.017	0.44892	0.11447	0.00067	0.20852	1857.4	5.4	1855.7	9.7	1874	10	1.02	0.9765208
AJ-21-04-20	5.379	0.37	0.3379	0.017	0.32009	0.11611	0.00066	0.25068	1881.6	5	1876.2	7.2	1897	10	0.979	1.0964681
AJ-21-04-21	5.369	0.37	0.3396	0.017	0.31181	0.11529	0.00075	0.20898	1879.9	5.6	1884.3	7.8	1884	12	1.1951	-0.0159236
AJ-21-04-22	5.429	0.37	0.3408	0.017	0.32694	0.11508	0.0009	0.29311	1888.9	7.3	1890.2	8.7	1881	14	1.1175	-0.4891015
AJ-21-04-23	5.345	0.37	0.3369	0.017	0.36778	0.11541	0.00069	0.19917	1877.1	5	1872.2	7.4	1887	11	0.8312	0.7843137
AJ-21-04-24	5.36	0.37	0.3385	0.017	0.40902	0.11492	0.00066	0.27705	1878.9	5.2	1879.1	8.8	1878	11	1.4242	-0.0585729
AJ-21-04-25	5.363	0.37	0.3388	0.017	0.35298	0.11546	0.0007	0.30269	1879	4.8	1881.2	8.6	1889	11	0.7908	0.4129169
AJ-21-04-26	5.376	0.37	0.3382	0.017	0.61155	0.11634	0.00075	0.064639	1880.6	6.8	1878	14	1900	12	0.804	1.1578947
AJ-21-04-27	5.346	0.37	0.3371	0.017	0.5182	0.11561	0.00046	0.1938	1876.4	3.9	1873.1	7	1889.3	7.3	0.6402	0.8574604
AJ-21-04-28	5.365	0.37	0.3396	0.017	0.34088	0.11506	0.00043	0.27919	1879.1	3.2	1884.7	5.8	1880.8	6.7	0.6982	-0.2073586
AJ-21-04-29	5.333	0.36	0.3374	0.017	0.20121	0.1161	0.00085	0.36211	1873.9	6.1	1874	12	1898	13	0.8103	1.2644889
AJ-21-04-30	5.337	0.37	0.3368	0.017	0.54894	0.11624	0.00081	0.084906	1874.4	6.5	1871	13	1900	13	0.8176	1.5263158
AJ-21-04-31	5.388	0.37	0.3387	0.017	0.36227	0.11601	0.00091	0.17561	1882.4	7.1	1880	12	1894	14	0.7515	0.7391763
AJ-21-04-32	5.289	0.36	0.335	0.017	0.19614	0.11456	0.00088	0.32896	1866.8	5.6	1862.3	9.3	1871	14	0.7399	0.464992
AJ-21-04-33	5.414	0.37	0.3385	0.017	0.34046	0.11682	0.00083	0.19961	1886.7	5.8	1879	11	1907	13	0.7891	1.4682748
AJ-21-04-34	5.455	0.38	0.3415	0.017	0.47376	0.11637	0.00079	0.19872	1893.4	6	1893.6	9.5	1903	12	0.877	0.4939569
AJ-21-04-35	5.437	0.37	0.341	0.017	0.36901	0.11548	0.00069	0.29424	1890.3	4.9	1891.4	8.7	1887	11	0.7627	-0.2331744
AJ-21-04-36	5.337	0.37	0.3367	0.017	0.39455	0.1155	0.00077	0.23145	1874.4	6.2	1871	12	1887	12	1.2127	0.8479067

AJ-21-04-37	5.398	0.37	0.3389	0.017	0.45998	0.11571	0.00051	0.29559	1884.3	3.7	1881.3	7.5	1890.9	8	0.9399	0.5076947
AJ-21-04-38	5.365	0.37	0.3374	0.017	0.45397	0.11547	0.00066	0.13211	1879.3	5.3	1874.6	8.1	1887	10	1.01	0.6571277
AJ-21-04-39	5.378	0.37	0.3385	0.017	0.52563	0.11533	0.00045	0.26408	1881.1	3.5	1879.5	7.3	1885.7	7	0.8966	0.3287904
AJ-21-23-1	5.037	0.35	0.3271	0.016	0.1386	0.11928	0.0009	0.38664	1825.4	6.4	1824	15	1945	13	0.744	6.2210797
AJ-21-23-2	5.076	0.35	0.3294	0.016	0.5709	0.1157	0.00069	0.13883	1831.9	7.1	1835	12	1890	11	0.998	2.9100529
AJ-21-23-3	5.186	0.35	0.3327	0.016	0.15189	0.116	0.0011	0.36419	1850	7.5	1851	14	1894	17	0.9294	2.2703273
AJ-21-23-4	5.243	0.36	0.3333	0.016	0.40872	0.11702	0.00073	0.25456	1860.3	6.6	1854	12	1912	11	0.816	3.0334728
AJ-21-23-5	3.616	0.25	0.2386	0.012	0.82184	0.1115	0.00057	0.29127	1553.5	6.8	1379	12	1823.5	9.3	0.9049	24.3762
AJ-21-23-6	1.95	0.11	0.1346	0.006	0.9835	0.10643	0.00067	-0.38263	1095	20	814	21	1739	11	1.856	53.191489
AJ-21-23-8	5.105	0.35	0.3302	0.016	0.55143	0.11601	0.00069	0.23108	1836.8	6.4	1839	14	1895	11	0.7132	2.9551451
AJ-21-23-9	5.092	0.36	0.3305	0.016	0.3229	0.11541	0.00088	0.12951	1834.4	6.7	1841	12	1885	14	1.22	2.3342175
AJ-21-23-10	3.797	0.25	0.2475	0.012	0.59705	0.11421	0.00046	-0.03333	1592.6	4.9	1425.6	7.1	1867.2	7.3	0.5006	23.650386
AJ-21-23-11	5.274	0.36	0.3345	0.017	0.30548	0.11564	0.00095	0.19606	1864.1	7.3	1859.9	8.6	1888	15	1.352	1.4883475
AJ-21-23-12	5.184	0.35	0.3324	0.016	0.35872	0.11624	0.00085	0.2215	1850.8	6.3	1850	12	1898	13	0.949	2.5289779
AJ-21-23-13	5.187	0.36	0.332	0.016	0.5408	0.11544	0.00044	0.1895	1850.5	3.3	1847.8	8.6	1886.5	6.8	1.0557	2.051418
AJ-21-23-14	5.28	0.38	0.3346	0.017	0.76162	0.11673	0.00076	-0.07264	1866	12	1860	12	1906	12	0.799	2.4134313
AJ-21-23-15	5.253	0.36	0.3351	0.017	0.22237	0.11475	0.00064	0.2798	1861.3	5.2	1863.7	6.6	1877	10	1.4248	0.7085775
AJ-21-23-16	5.352	0.36	0.3387	0.017	0.12587	0.11749	0.00091	0.5905	1877.8	5.9	1880	12	1917	14	0.882	1.9300991
AJ-21-23-17	5.197	0.36	0.3324	0.016	0.045205	0.1165	0.0011	0.50003	1851.7	7.3	1850	12	1903	17	0.8623	2.7850762

AJ-21-23-20	5.216	0.36	0.3326	0.017	0.52777	0.11511	0.00088	0.13745	1854.9	7.5	1850.7	9.4	1884	14	1.054	1.7675159
AJ-21-23-21	5.266	0.36	0.3345	0.017	0.55193	0.11675	0.00067	0.029031	1863.1	5.8	1860	11	1906	10	0.883	2.4134313
AJ-21-23-22	5.237	0.36	0.3341	0.017	0.60248	0.11528	0.00035	0.24594	1858.4	3.7	1858	7.7	1883.8	5.5	1.206	1.3695721
AJ-21-23-23	5.203	0.36	0.334	0.016	0.4557	0.11573	0.00075	0.039744	1853.6	6.1	1858	11	1891	12	0.9197	1.7451084
AJ-21-23-24	5.162	0.35	0.3324	0.016	0.32983	0.11501	0.00068	0.18702	1846.1	5.2	1850	9.7	1881	10	1.097	1.6480595
AJ-21-23-25	5.304	0.37	0.3363	0.017	0.65241	0.11631	0.00056	0.057307	1869.4	5.6	1869	10	1899.9	8.7	0.5418	1.6264014
AJ-21-23-26	5.295	0.36	0.3367	0.016	0.18301	0.1171	0.0015	0.32038	1867.5	9	1870	14	1911	22	1.395	2.1454736
AJ-21-23-27	5.33	0.36	0.3375	0.017	0.68358	0.11694	0.00069	-0.11719	1873.3	6.1	1874	14	1909	11	2.658	1.8334206
AJ-21-23-28	5.243	0.36	0.3348	0.016	0.35572	0.1152	0.0008	0.15759	1859.3	6.8	1861	12	1882	13	0.8169	1.1158342
AJ-21-23-29	5.223	0.36	0.3341	0.017	0.39874	0.11465	0.00065	0.22116	1856.9	4.9	1859	7.6	1874	10	1.3334	0.8004269
AJ-21-23-31	5.165	0.36	0.3327	0.017	0.31994	0.11438	0.0006	0.17806	1847.3	4.8	1851.4	8.9	1872.1	9.4	1.411	1.1057102
AJ-21-23-32	5.235	0.36	0.3346	0.016	0.18551	0.11576	0.00082	0.27916	1858	5.3	1861	11	1891	13	1.4655	1.5864622
AJ-21-23-33	5.283	0.36	0.3344	0.017	0.32366	0.11556	0.00058	0.27705	1866.2	4.4	1859.4	7.1	1888.4	8.9	1.1431	1.5356916
AJ-21-23-34	5.296	0.37	0.3359	0.017	0.47562	0.1176	0.0016	0.16342	1871	15	1867	19	1919	25	0.924	2.7097447
AJ-21-23-35	5.229	0.36	0.3347	0.017	0.48751	0.11548	0.00059	0.20687	1857.2	5.3	1861	13	1887	9.2	1.343	1.3778484
AJ-21-23-36	5.29	0.37	0.3365	0.017	0.32371	0.11623	0.00057	0.36261	1867	5	1870	10	1898.5	8.8	0.7656	1.5011851
AJ-21-23-37	5.259	0.36	0.3341	0.017	0.15577	0.1154	0.00053	0.43385	1862.9	3.6	1858.3	6.7	1886.7	8.2	0.8408	1.5052738
AJ-21-23-38	5.361	0.37	0.3387	0.017	0.34586	0.11592	0.00058	0.31182	1878.7	4.4	1880.1	6.6	1893.3	9	1.5055	0.6971954
AJ-21-23-39	5.207	0.36	0.3322	0.017	0.47789	0.11478	0.00038	0.30023	1853.5	3.2	1849	6.4	1875.9	6	0.656	1.4339784

AJ-21-23-40	5.26	0.36	0.3352	0.017	0.50814	0.11553	0.00054	0.16801	1862.8	4.3	1863.5	9.4	1887.7	8.4	0.8993	1.2819834
AJ-21-29-1	5.002	0.34	0.3137	0.015	0.2565	0.11652	0.00074	0.22263	1819.4	5.7	1758.7	8.7	1903	11	0.6562	7.5827641
AJ-21-29-2	5.139	0.35	0.3299	0.016	0.54845	0.117	0.0011	0.18619	1842	10	1838	20	1910	17	2.777	3.7696335
AJ-21-29-3	5.145	0.34	0.3308	0.016	0.58796	0.11523	0.00078	0.11359	1843.3	6.1	1842	14	1885	12	0.6289	2.2811671
AJ-21-29-4	5.004	0.36	0.3208	0.016	0.67646	0.1187	0.0011	-0.21737	1820	12	1794	15	1937	17	0.873	7.3825503
AJ-21-29-5	5.015	0.34	0.3266	0.016	0.59677	0.11529	0.00063	0.035345	1821.7	6.4	1825	16	1884.1	9.8	0.3826	3.1367762
AJ-21-29-6	4.263	0.3	0.2633	0.013	0.02479	0.1195	0.002	0.42437	1684	13	1506	12	1943	29	0.779	22.490993
AJ-21-29-7	4.931	0.34	0.3236	0.015	0.26811	0.11411	0.00094	0.22539	1807.2	8.2	1807	14	1865	15	0.6951	3.1099196
AJ-21-29-8	5.125	0.35	0.3308	0.016	0.37846	0.11572	0.00092	0.30115	1841	7.9	1842	18	1890	14	2.202	2.5396825
AJ-21-29-9	5.104	0.35	0.331	0.016	0.31248	0.11673	0.00099	0.27518	1836.5	8.2	1843	16	1906	15	0.6379	3.3053515
AJ-21-29-10	5.06	0.35	0.328	0.016	0.45871	0.11546	0.00063	0.45893	1829.2	5.5	1828	17	1886.6	9.8	0.5462	3.1061168
AJ-21-29-11	5.065	0.35	0.3285	0.016	-0.012164	0.1153	0.0013	0.55365	1831.4	6	1834	15	1883	20	0.4915	2.6022305
AJ-21-29- 12	5.114	0.35	0.3297	0.016	0.0099023	0.1171	0.0013	0.3393	1838.1	7.3	1837	13	1914	19	0.655	4.0229885
AJ-21-29-13	5.072	0.34	0.3282	0.016	-0.097391	0.117	0.0014	0.35353	1831.1	9.7	1830	15	1909	21	0.6624	4.1382923
AJ-21-29-14	5.05	0.34	0.3284	0.016	0.44806	0.11576	0.00075	0.12815	1827.6	6.4	1830	15	1896	10	0.4606	3.4810127
AJ-21-29-15	5.081	0.35	0.3287	0.016	0.28779	0.11467	0.00055	0.20167	1832.7	5	1834	11	1874.4	8.6	0.5092	2.1553564
AJ-21-29-16	5.028	0.35	0.3279	0.016	0.33461	0.1148	0.0012	0.12721	1825.3	9.2	1828	15	1876	19	0.6659	2.5586354
AJ-21-29-17	5.075	0.35	0.3286	0.016	0.072597	0.115	0.0012	0.3416	1832.5	7.4	1831	14	1878	19	1.0559	2.5026624
AJ-21-29-18	5.16	0.36	0.3324	0.016	0.20639	0.11619	0.00091	0.2463	1845.6	7.6	1850	14	1897	14	0.8195	2.4775962

AJ-21-29-19	5.391	0.37	0.3388	0.017	0.57185	0.11691	0.00041	0.31255	1883.4	4.4	1880.6	8.9	1909	6.3	0.3502	1.4876899
AJ-21-29-20	5.382	0.36	0.3128	0.016	0.46165	0.1261	0.0017	-0.19789	1880	14	1754.5	9.3	2040	24	0.538	13.995098
AJ-21-29-21	5.399	0.36	0.3384	0.017	0.61022	0.1155	0.0012	0.14401	1883.9	9.7	1879	14	1886	18	1.43	0.3711559
AJ-21-29-22	5.22	0.35	0.3339	0.016	0.47216	0.11702	0.00078	0.22363	1855.6	6.3	1857	12	1911	12	0.923	2.8257457
AJ-21-29-23	5.358	0.36	0.3377	0.017	0.85725	0.11546	0.00051	0.0099254	1878.8	6.9	1875	14	1886.4	7.9	0.5461	0.6043257
AJ-21-29-24	5.61	0.37	0.3467	0.017	0.55527	0.1183	0.0013	0.20177	1917	11	1919	16	1932	19	0.678	0.6728778
AJ-21-29-25	5.22	0.34	0.3301	0.016	0.93321	0.11635	0.00087	0.88244	1855.7	6.5	1839	18	1900	14	0.366	3.2105263
AJ-21-29-26	5.29	0.36	0.3349	0.017	0.53052	0.1163	0.0014	0.06801	1866	11	1862	14	1897	22	1.064	1.8450185
AJ-21-29-27	5.115	0.35	0.3304	0.016	0.46328	0.11425	0.00066	0.21253	1839.2	5.5	1840	10	1868	10	0.6326	1.4989293
AJ-21-29-28	4.835	0.35	0.296	0.015	0.37926	0.12046	0.00092	0.12859	1791.2	7.7	1671.5	7.3	1965	14	0.6533	14.936387
AJ-21-29-29	5.299	0.36	0.3353	0.016	0.60875	0.11617	0.00076	0.26888	1868.5	6.6	1863.9	9.8	1897	12	0.407	1.7448603
AJ-21-29-30	5.563	0.4	0.3293	0.017	0.26094	0.12362	0.00098	0.09867	1909.3	9.2	1835.1	6.9	2010	14	0.5344	8.7014925
AJ-21-29-31	5.264	0.38	0.336	0.018	0.52605	0.116	0.001	0.39661	1862.7	7.1	1867	20	1894	16	0.729	1.4255544
AJ-21-29-32	5.087	0.36	0.3303	0.016	0.4127	0.11526	0.00059	0.16561	1834.7	5.6	1840	10	1883.6	9.2	0.6687	2.3147165
AJ-21-29-34	5.255	0.36	0.3337	0.016	0.089626	0.1158	0.0024	0.65483	1861	13	1856	19	1891	36	0.343	1.8508726
AJ-21-29-35	5.226	0.36	0.3329	0.016	0.32644	0.11535	0.00049	0.25544	1856.9	3.8	1852.9	6.1	1885.3	7.6	0.7249	1.7185594
AJ-21-29-36	5.106	0.35	0.3291	0.016	0.43343	0.1166	0.00091	0.12448	1836.7	7.8	1834	12	1904	14	0.647	3.6764706
AJ-21-29-37	3.494	0.25	0.153	0.016	-0.49776	0.51	0.14	0.99699	1526	14	897	84	3180	430	1.402	71.792453
AJ-21-29-38	5.18	0.35	0.3313	0.016	0.42128	0.1167	0.00079	0.17223	1850	6.6	1845	10	1908	12	0.3861	3.3018868

AJ-21-29-39	5.319	0.37	0.3371	0.017	0.61043	0.11562	0.00049	0.30309	1871.8	4.7	1872.8	7	1889.1	7.6	0.27	0.8628447
AJ-21-29-40	1.051	0.074	0.07161	0.0037	0.88346	0.1077	0.00066	-0.13326	728.6	8.4	445.8	5.4	1761	11	1.735	74.684838
Ples_1	0.3707	0.026	0.05361	0.0025	0.15969	0.0531	0.0011	0.31403	320.2	4.8	336.7	2.8	331	48	9.02	-5.1530294
Ples_2	0.376	0.026	0.05287	0.0025	0.35937	0.05334	0.00065	-0.052627	324	4	332.1	3.2	345	29	10.116	-2.5
Ples_3	0.3741	0.026	0.05168	0.0026	0.26655	0.05315	0.00044	0.16704	322.6	2.3	324.8	1.7	336	19	10.236	-0.6819591
Ples_4	0.3781	0.026	0.05186	0.0026	0.25775	0.05365	0.0005	0.14359	325.5	2.6	325.9	1.7	351	21	10.135	-0.1228879
Ples_5	0.391	0.027	0.05332	0.0027	0.28921	0.05392	0.0005	0.12573	334.9	2.6	334.9	1.8	368	21	9.778	0
Ples_6	0.3921	0.027	0.05324	0.0027	0.36526	0.05371	0.00042	0.035652	335.8	2.3	334.4	1.5	358	18	9.354	0.4169148
Ples_7	0.3903	0.027	0.05237	0.0026	0.33251	0.05432	0.00041	0.11265	334.5	2.2	329	1.5	383	17	9.958	1.6442451
Ples_8	0.4011	0.028	0.05416	0.0027	0.078429	0.05386	0.00045	0.31196	342.5	2.4	340	1.3	366	19	8.397	0.729927
Ples_9	0.4001	0.028	0.05393	0.0027	0.22822	0.05354	0.00042	0.24694	341.8	2.2	338.6	1.7	351	18	9.822	0.93622
Ples_10	0.4043	0.028	0.05336	0.0027	0.13714	0.05439	0.00047	0.22374	344.9	2.5	335.1	1.4	385	19	9.529	2.8414033
Tem2_1	0.473	0.032	0.06329	0.0028	0.34083	0.0543	0.0013	-0.057073	393	11	395.6	4.6	398	64	2.195	-0.6615776
Tem2_2	0.474	0.032	0.06325	0.0029	0.68774	0.0555	0.0015	-0.53699	394	11	395.4	4.7	426	60	2.171	-0.3553299
Tem2_3	0.4811	0.032	0.06468	0.003	-0.28371	0.0554	0.0014	0.58253	398.6	6.5	404	4.9	421	57	2.102	-1.3547416
Tem2_4	0.477	0.033	0.06561	0.0031	0.14759	0.0549	0.0012	0.15893	395.8	7.3	409.7	5	401	49	1.91	-3.5118747
Tem2_5	0.4703	0.033	0.06276	0.0031	0.10495	0.05491	0.00069	0.28228	391.5	4	392.4	2.4	404	29	2.206	-0.2298851
Tem2_6	0.4807	0.034	0.06423	0.0032	0.036551	0.05505	0.00081	0.24219	398.6	4.5	401.3	2.2	417	32	2.484	-0.6773708

Appendix J: CL-BSE images for the U-Pb analyses.

AJ-21-04-1/2

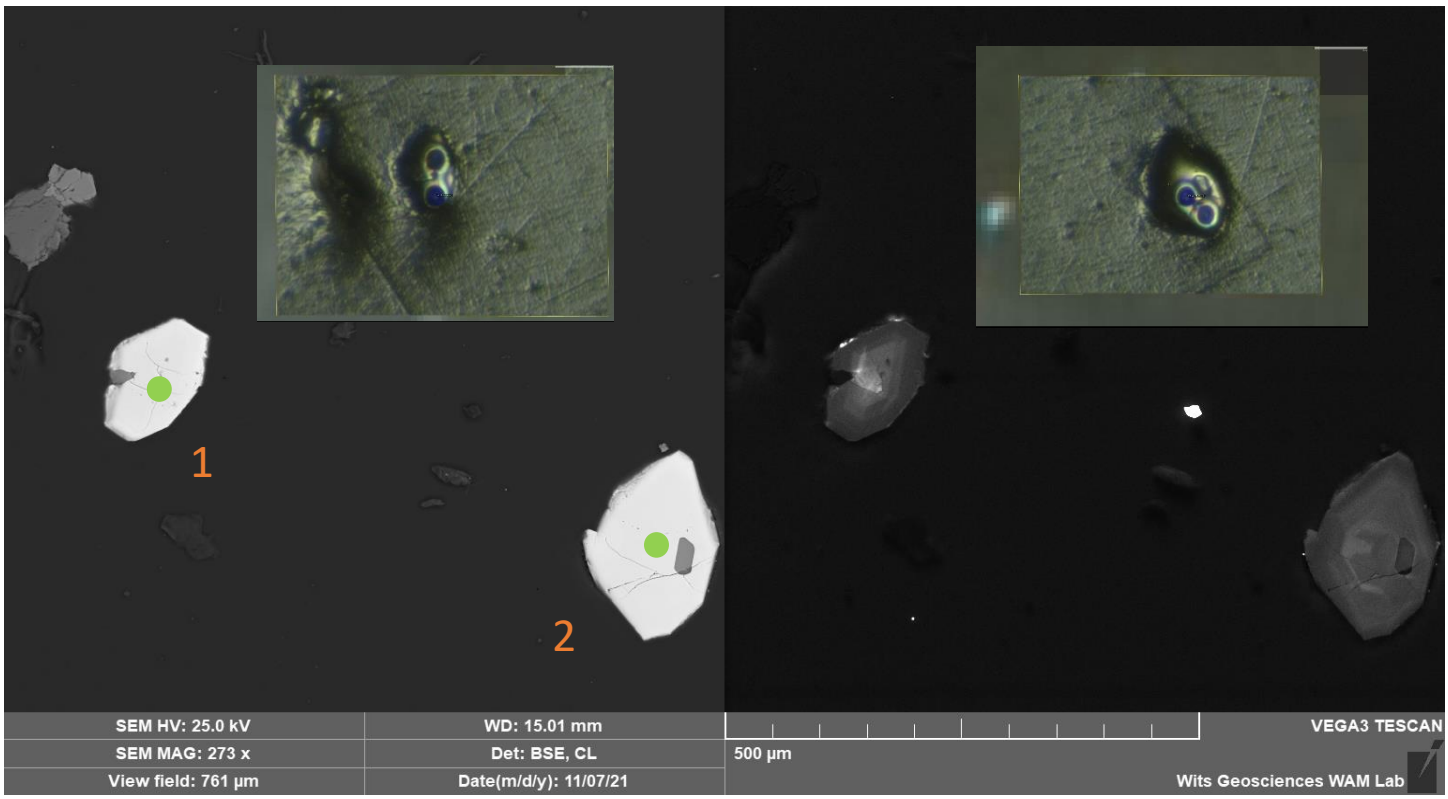

AJ-21-04-3

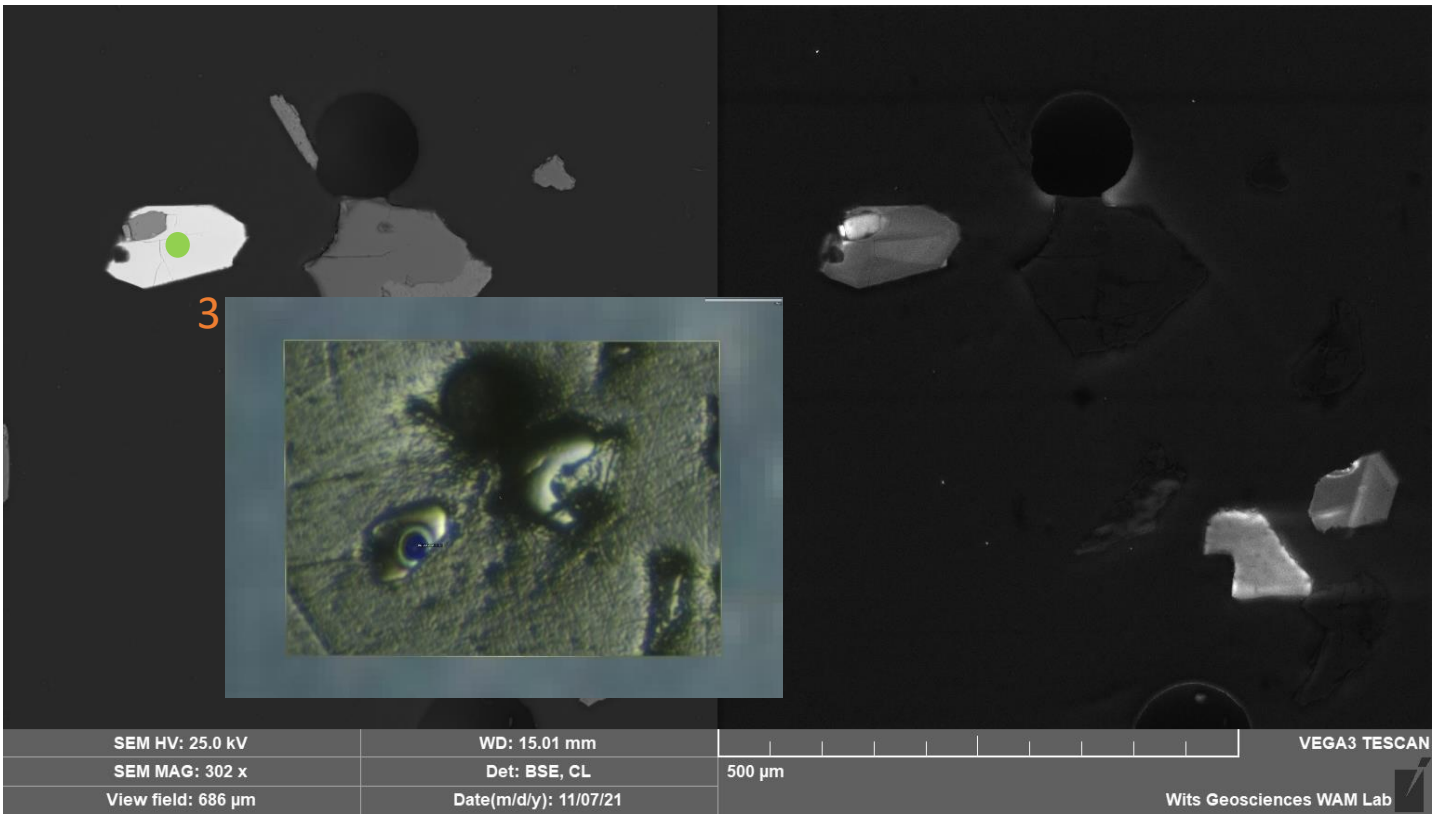

AJ-21-04-4

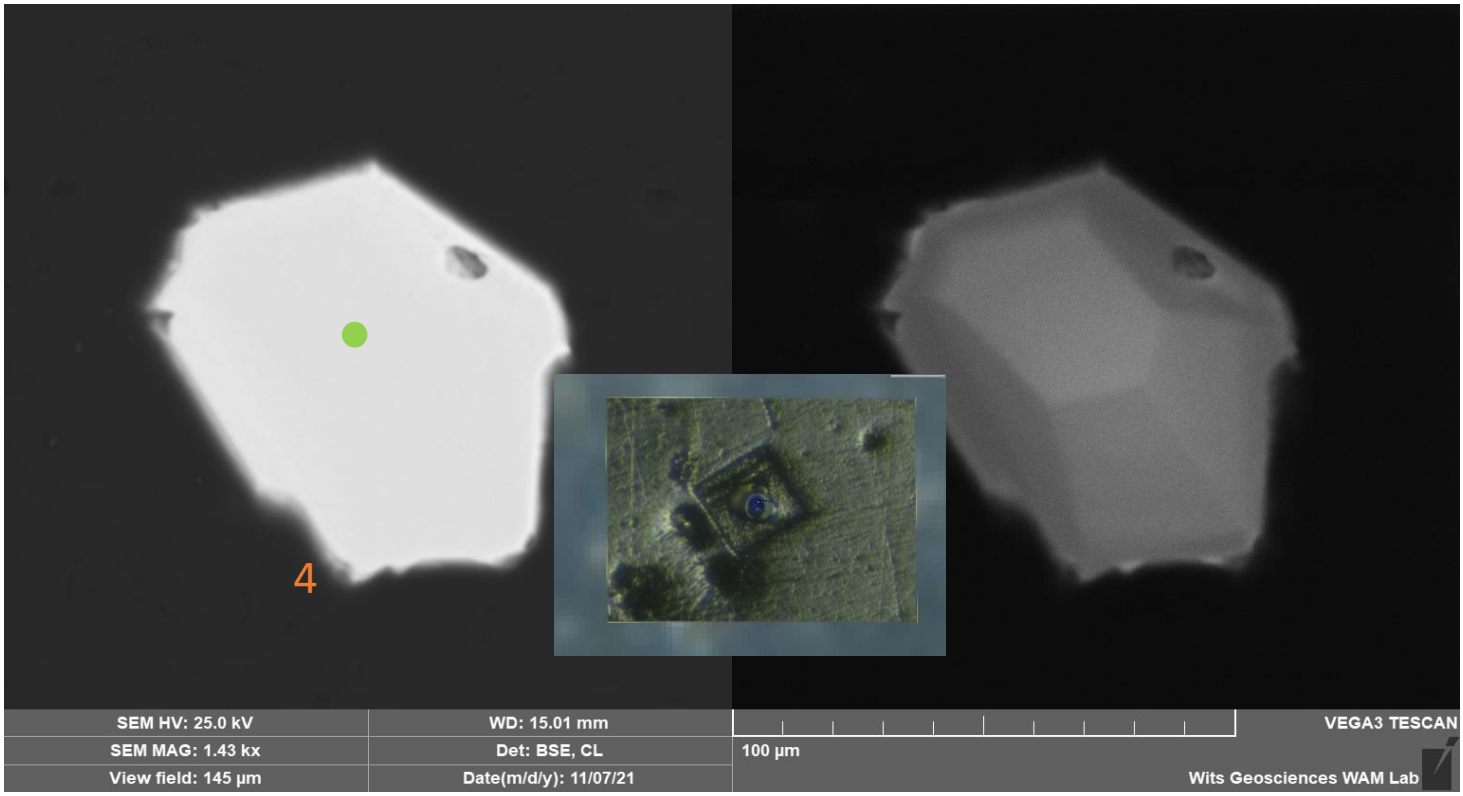

AJ-21-04-5/6

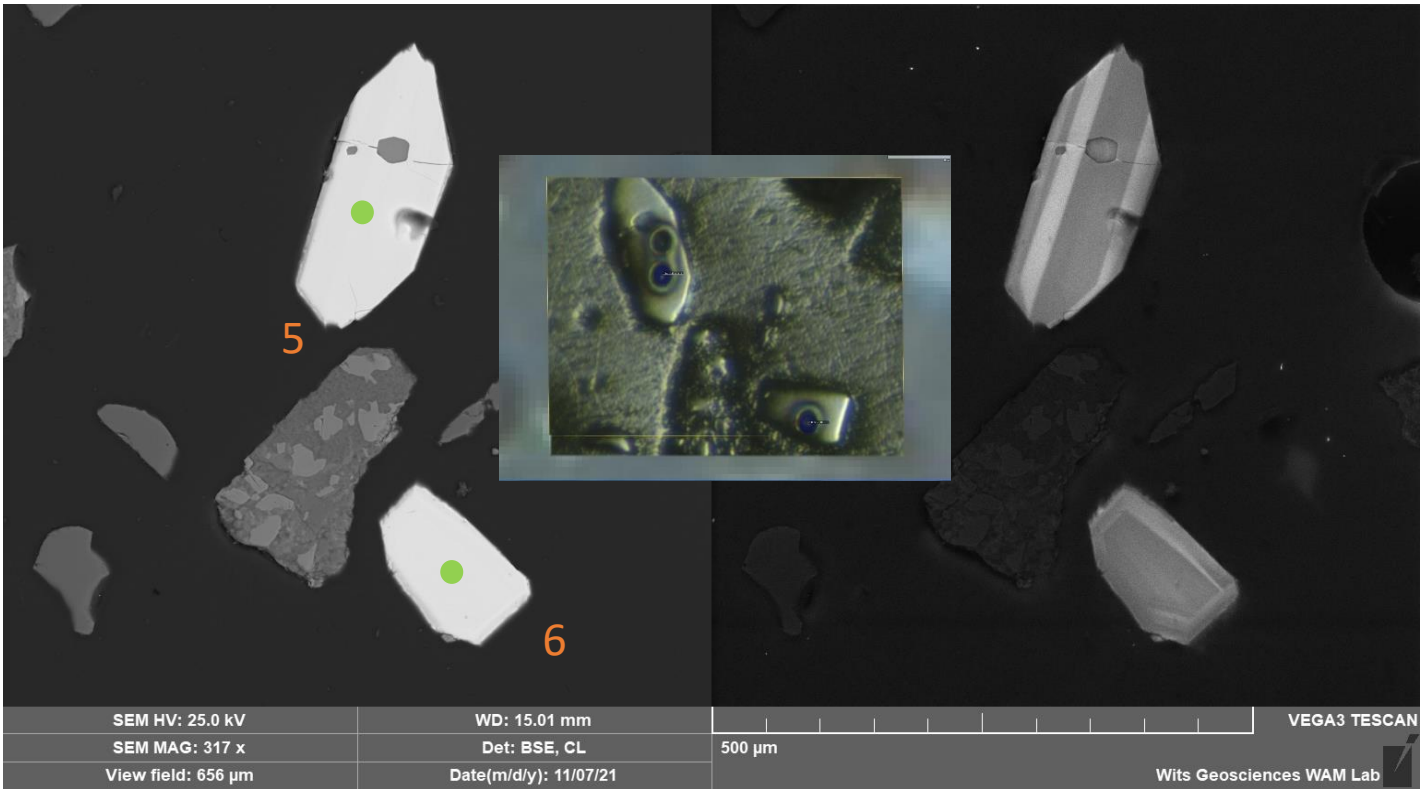

AJ-21-04-7/9/10

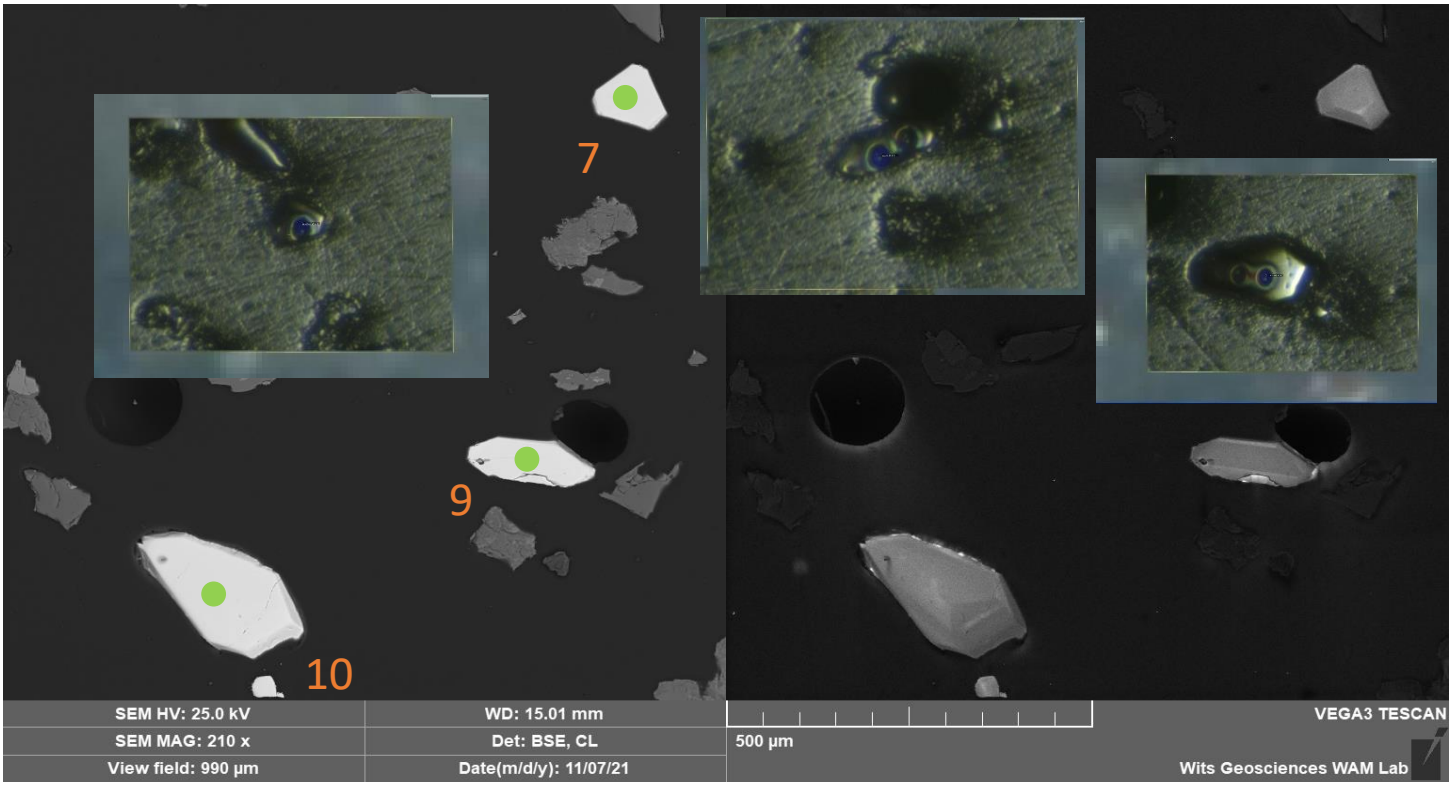

AJ-21-04-8/11

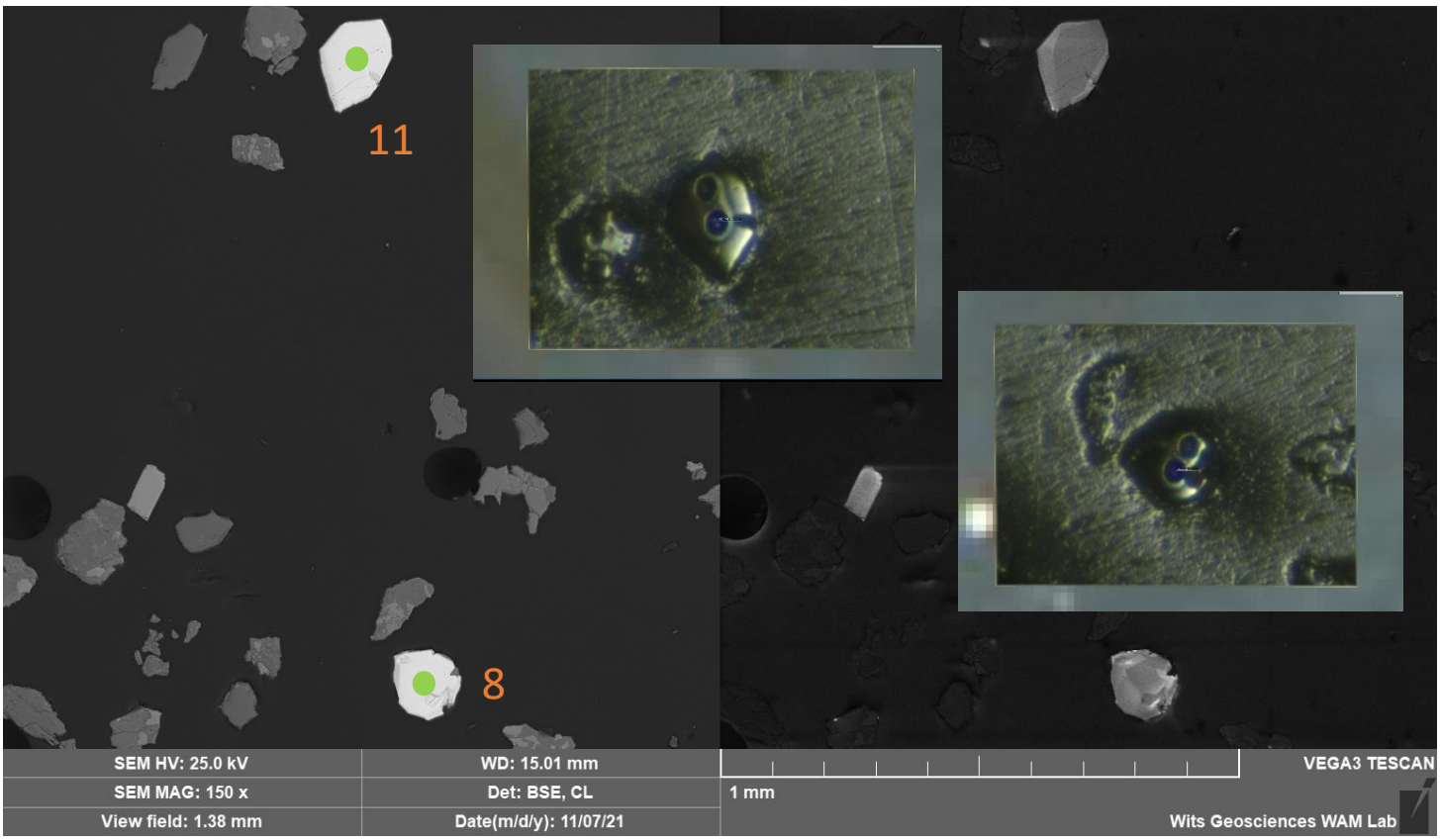

AJ-21-04-12

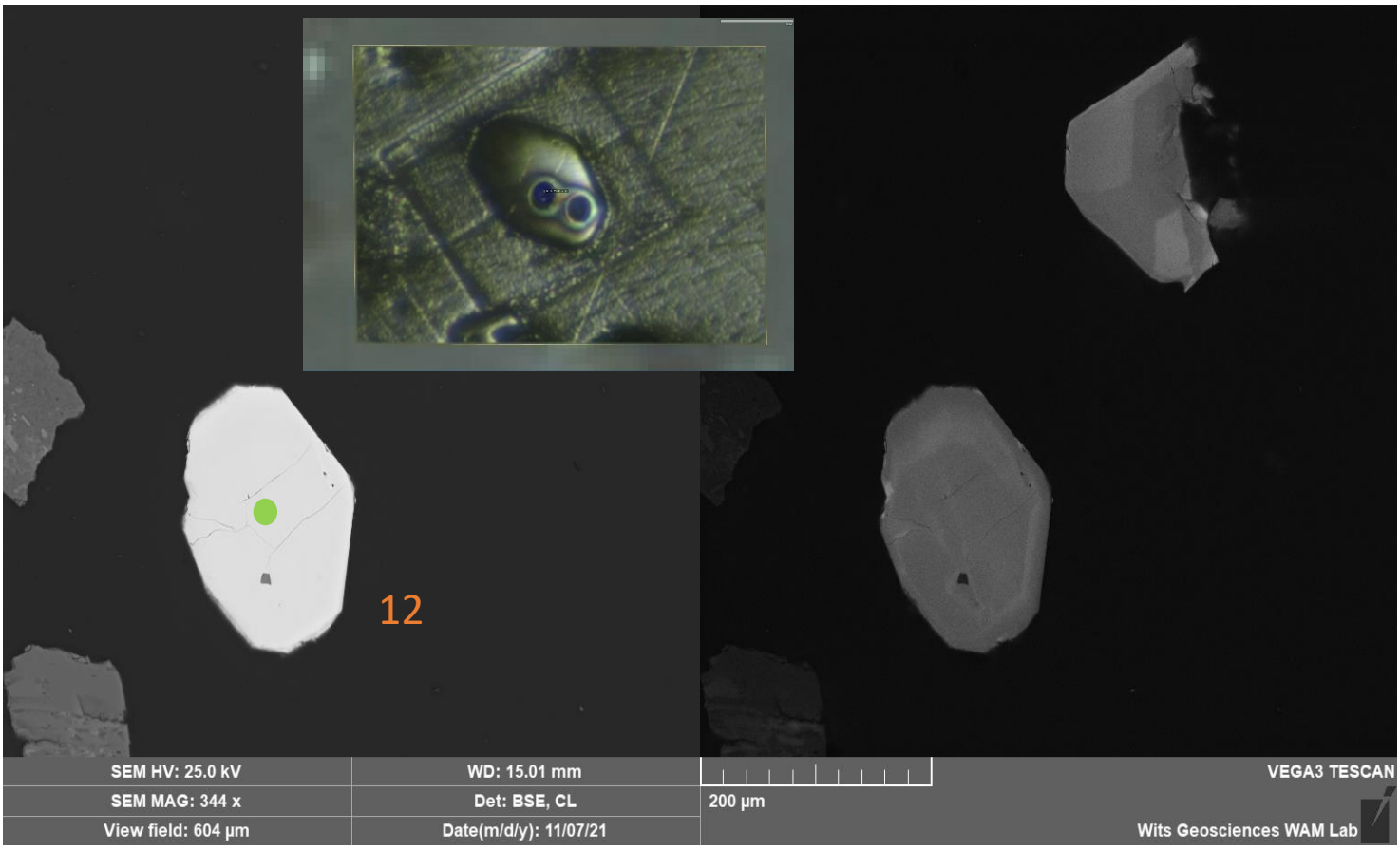

AJ-21-04-13

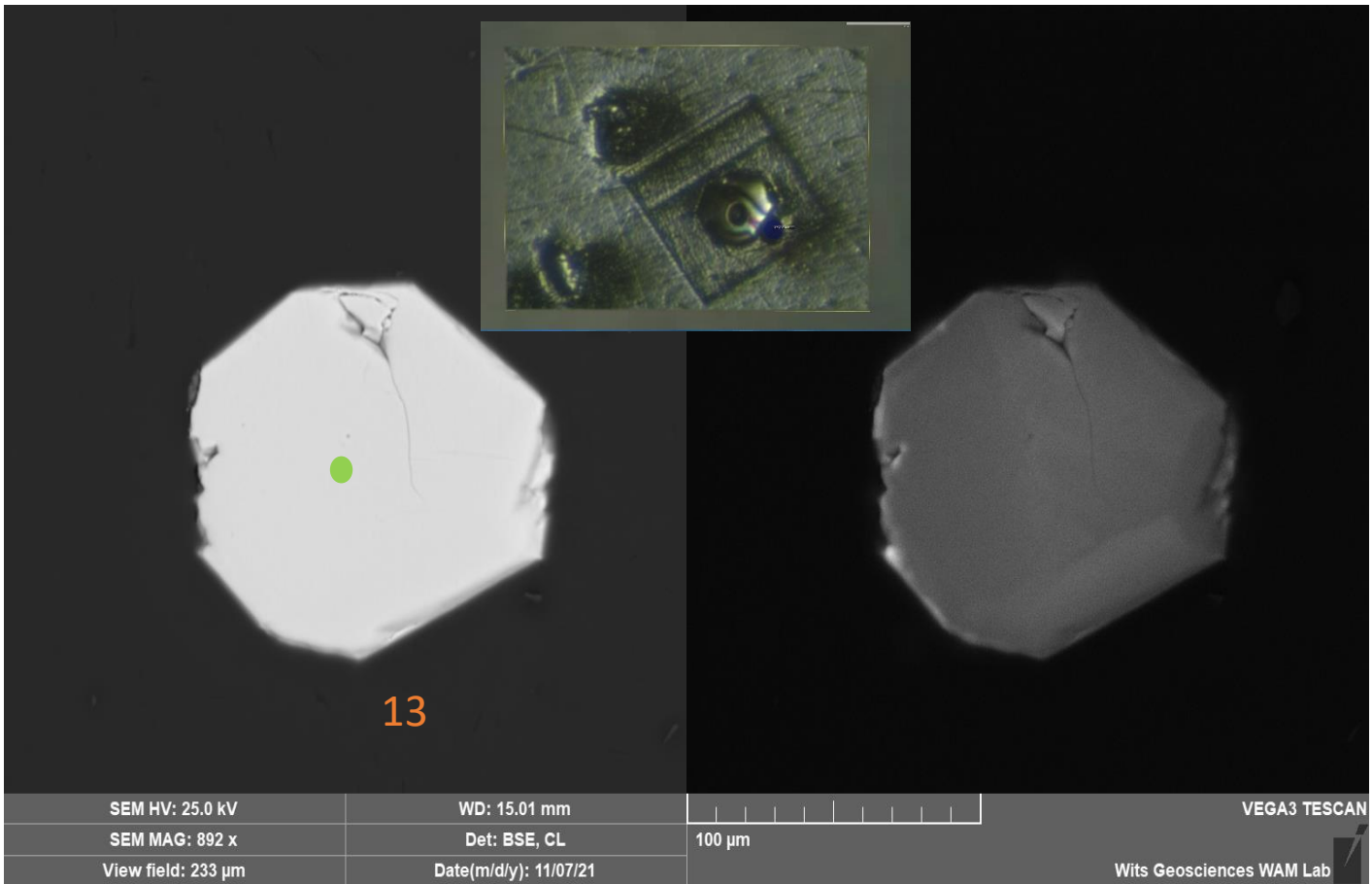

AJ-21-04-14

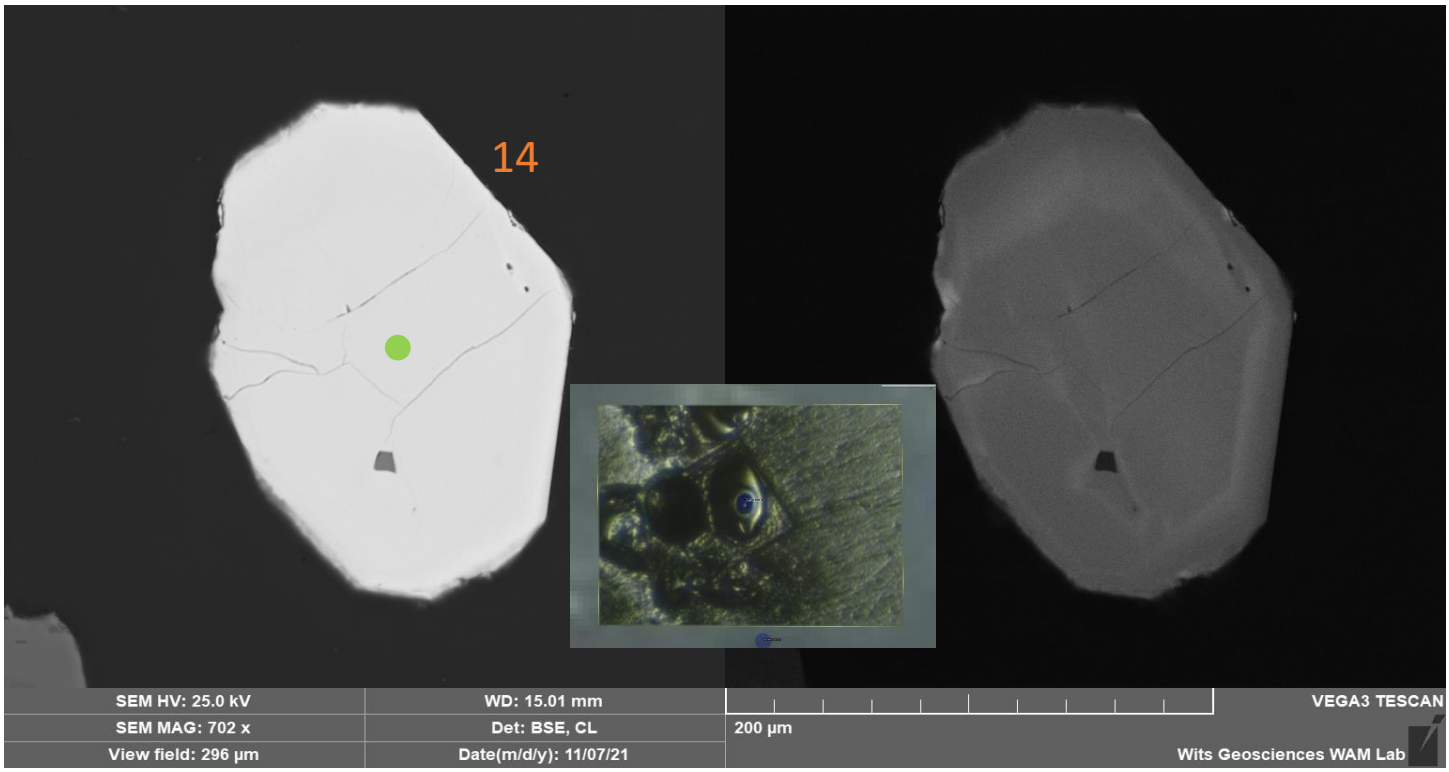

AJ-21-04-15

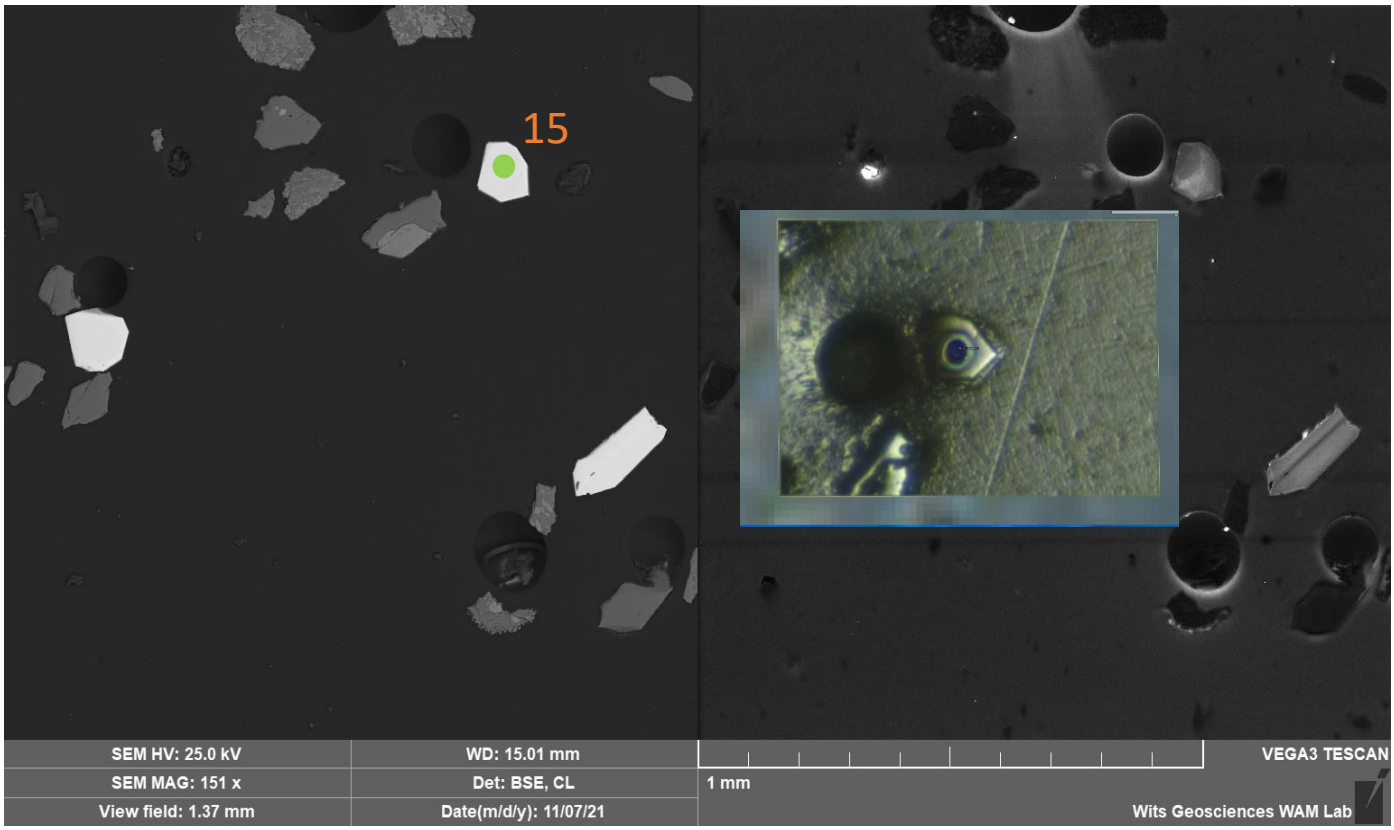

AJ-21-04-16

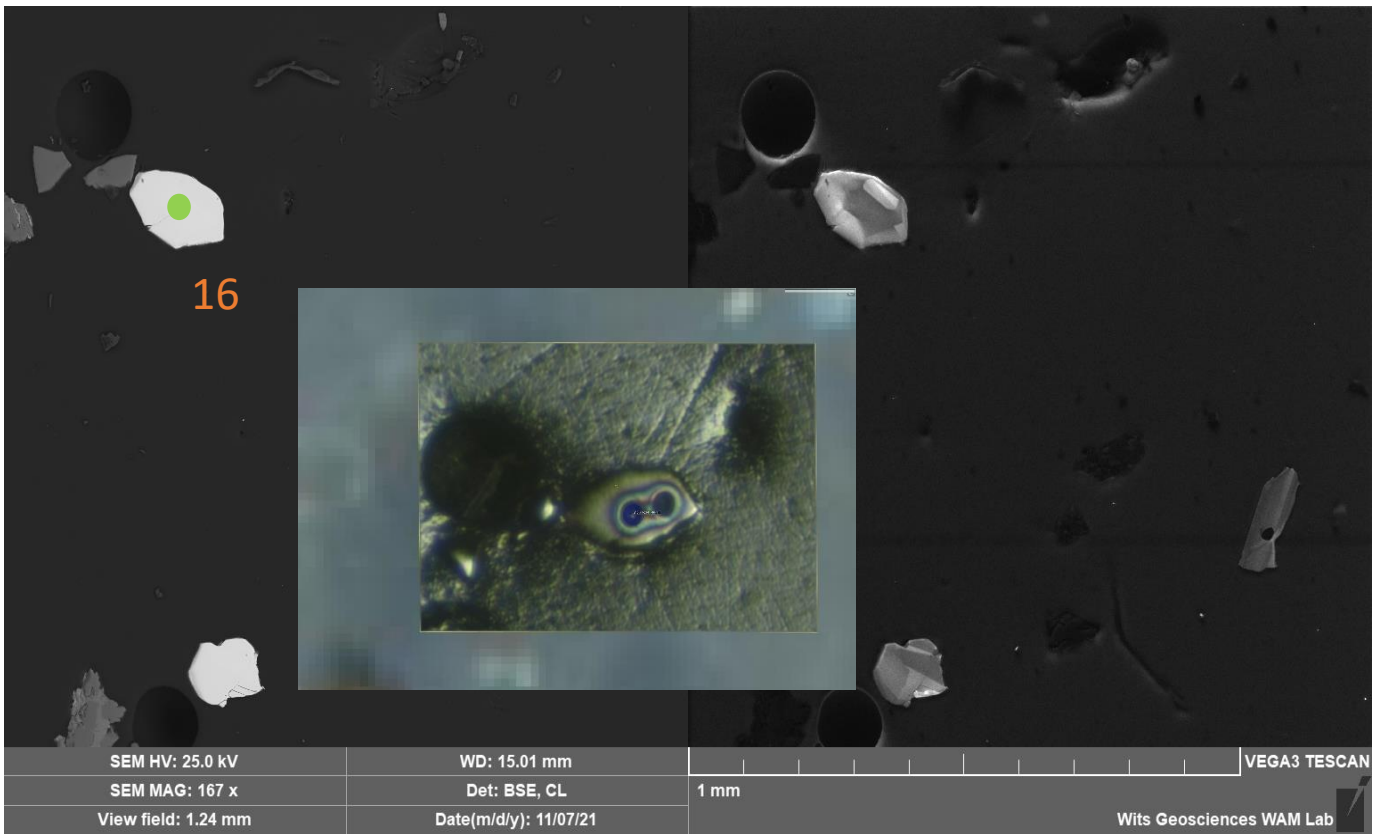

AJ-21-04-17

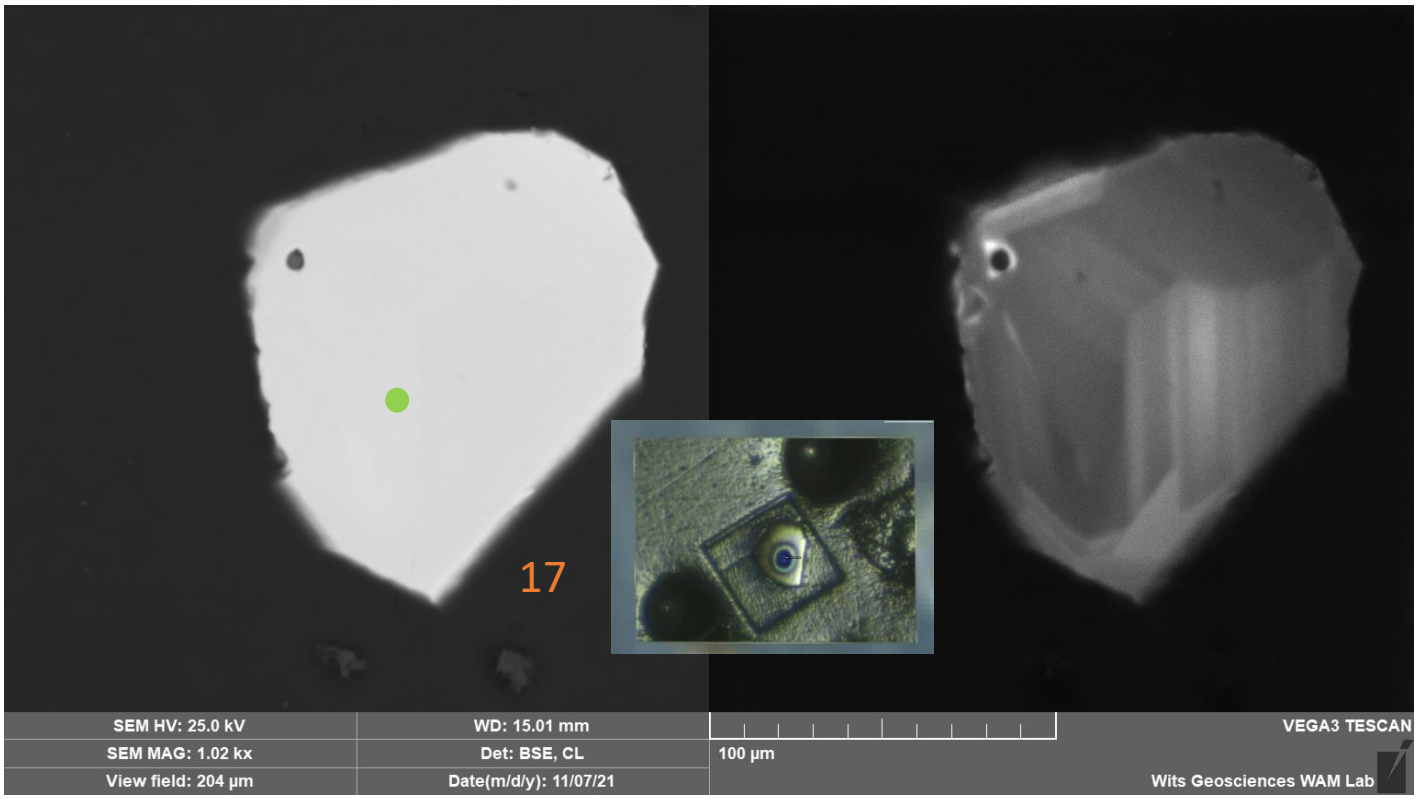

AJ-21-04-18

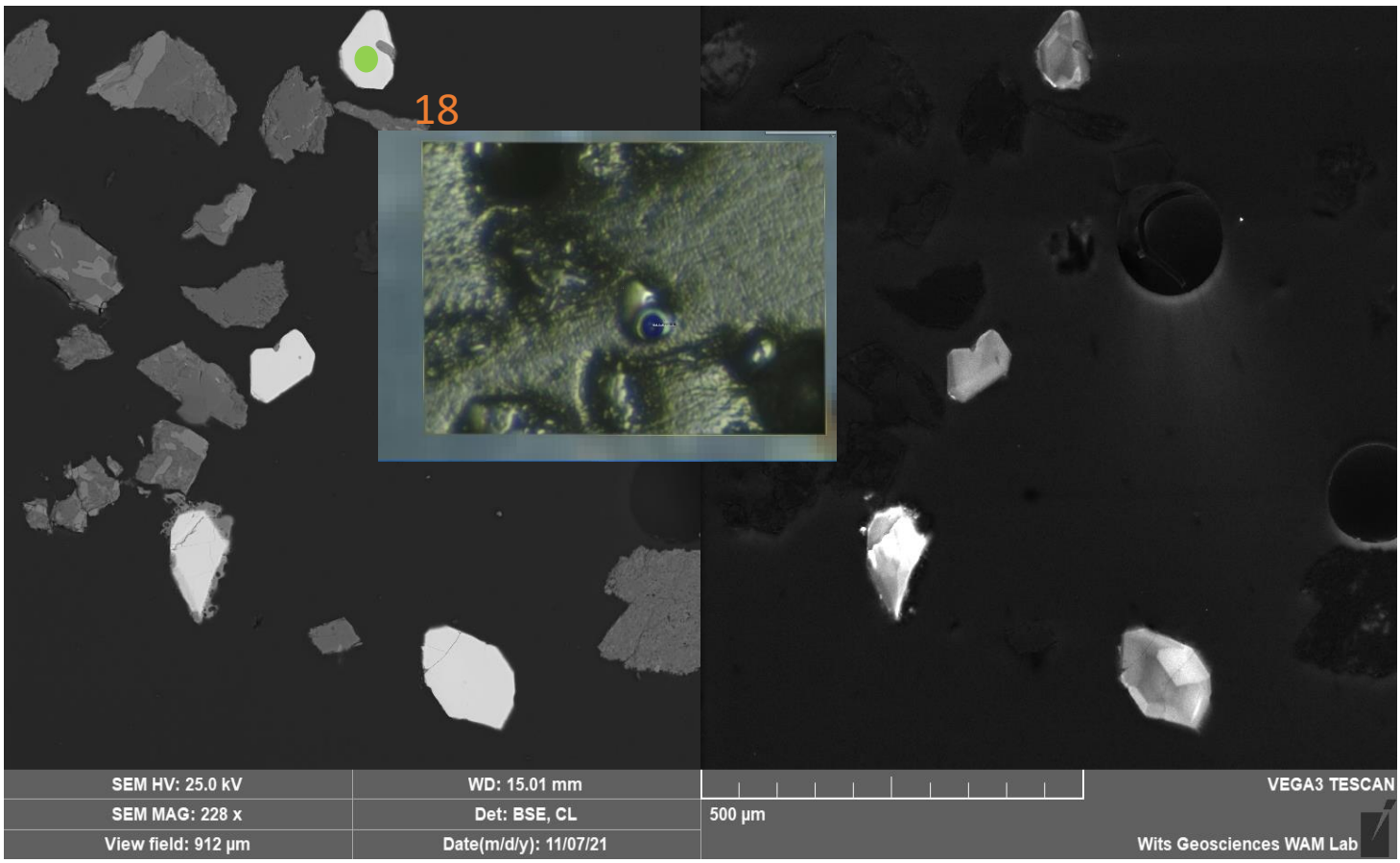

AJ-21-04-19

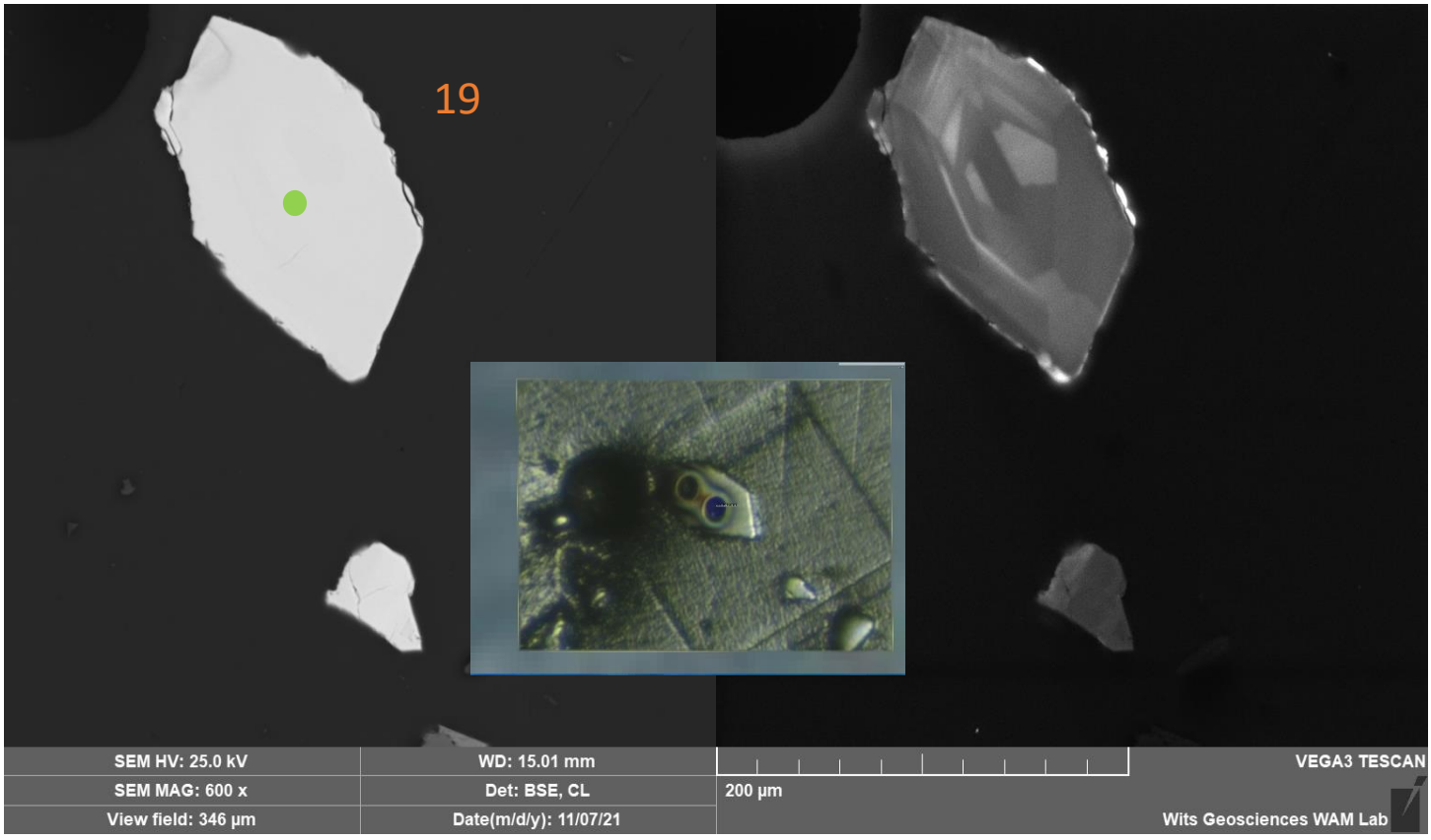

AJ-21-04-20

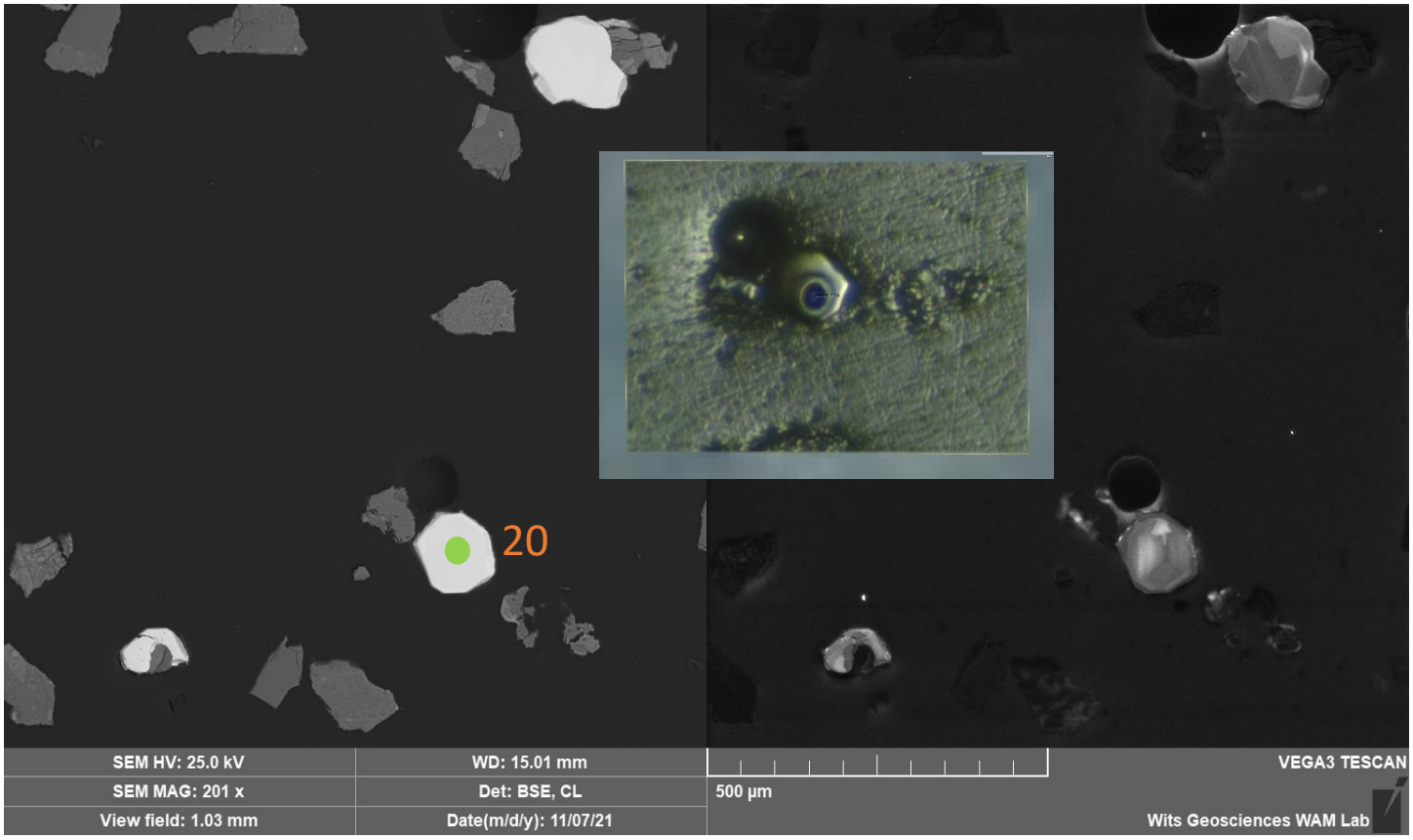

AJ-21-04-21/22

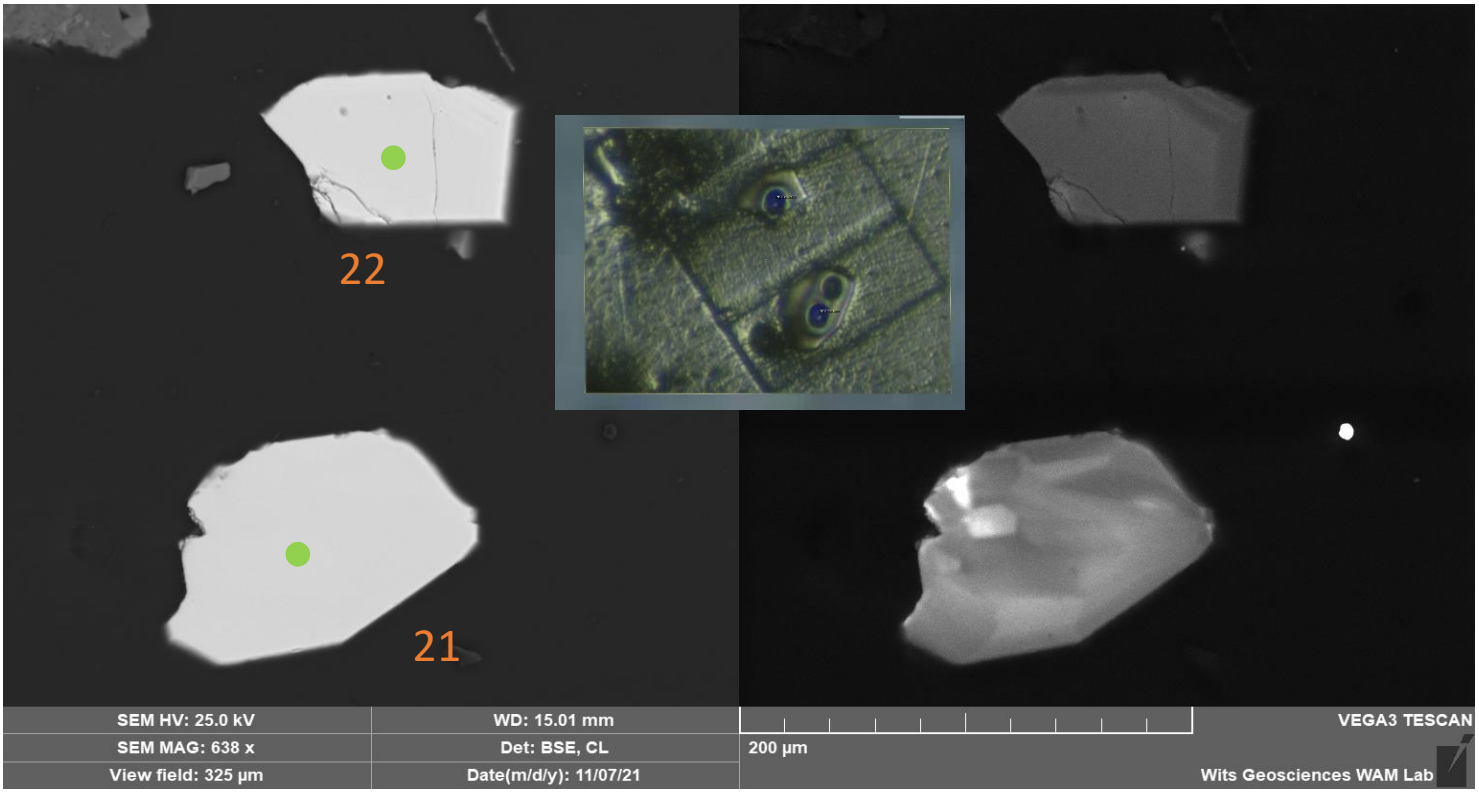

AJ-21-04-23/24

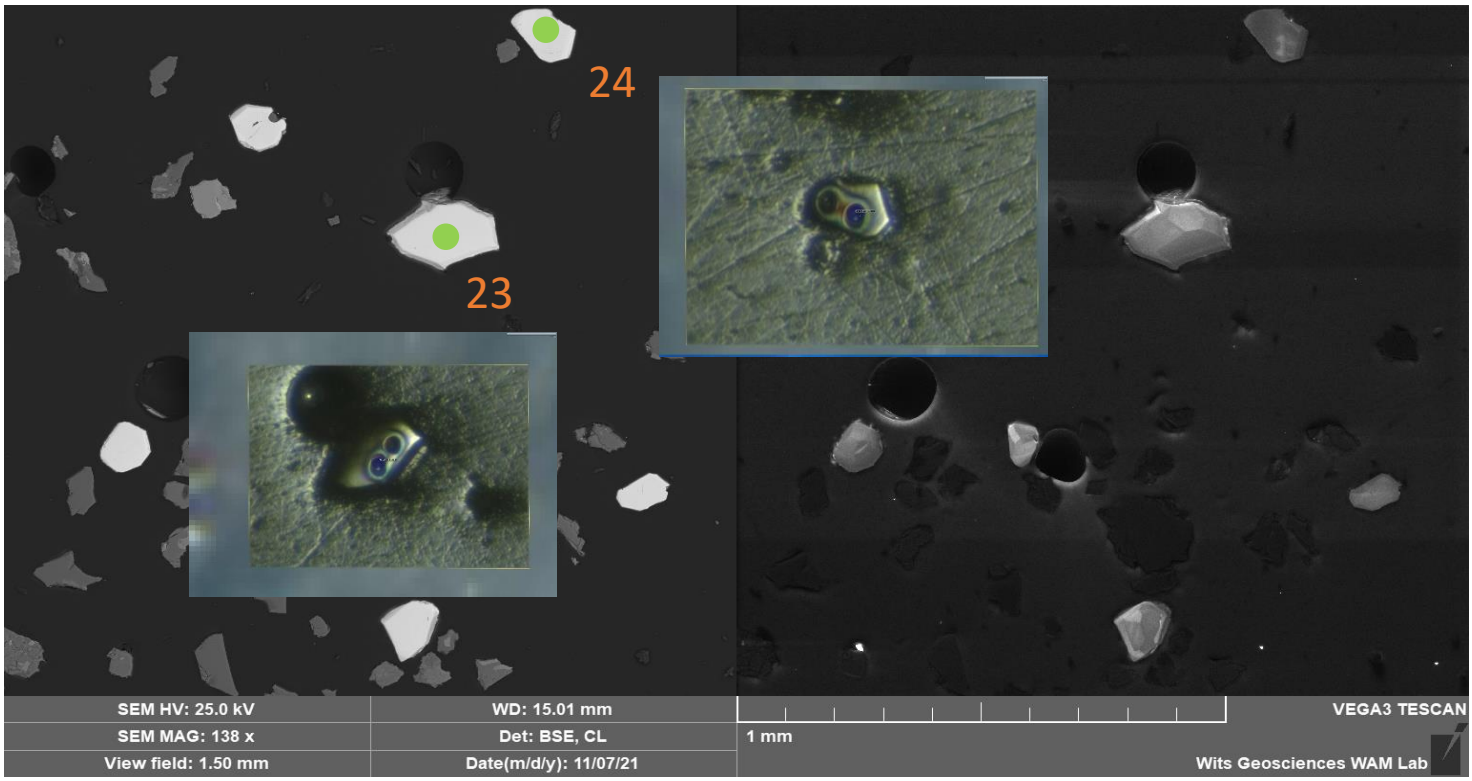

AJ-21-04-25

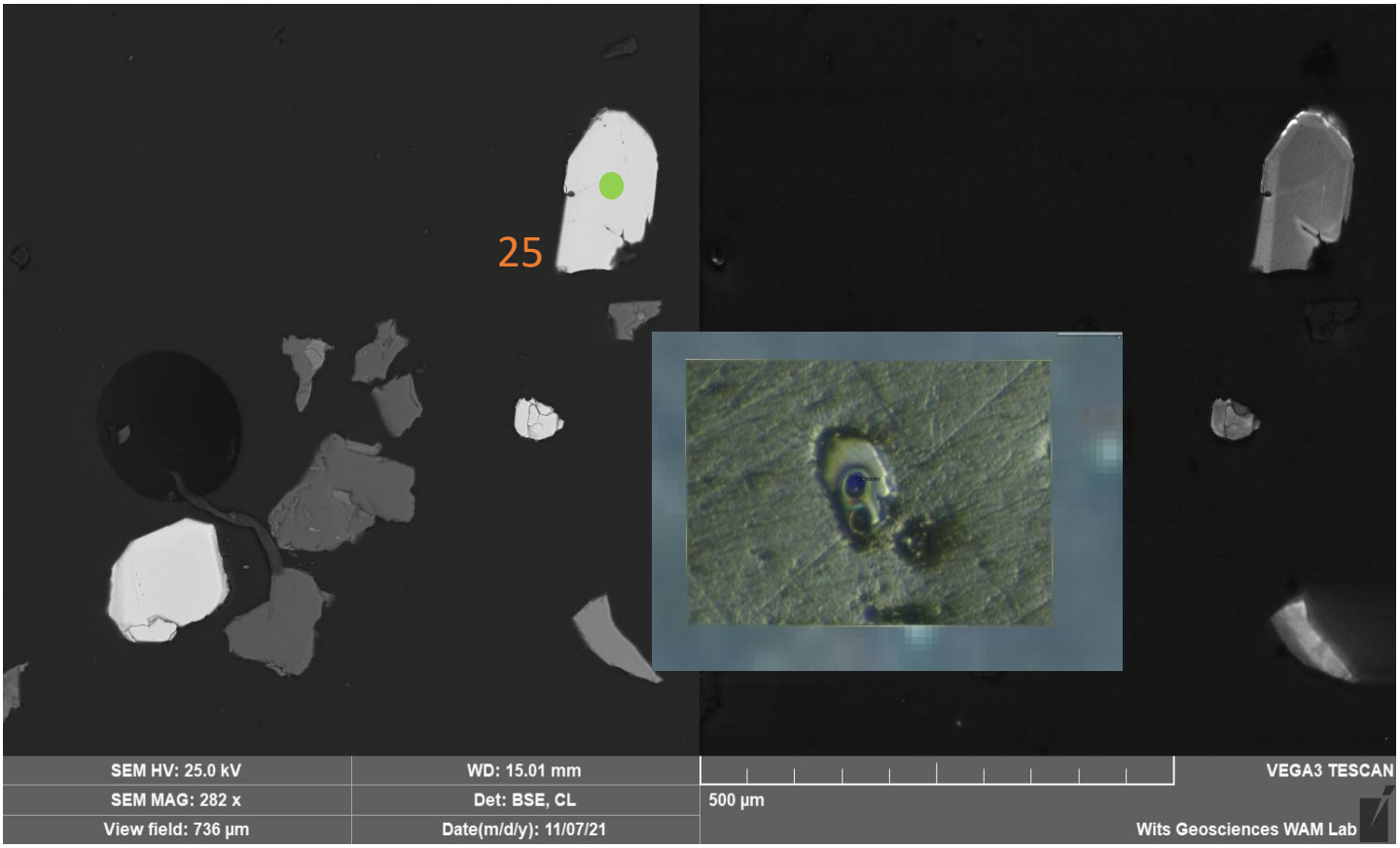

AJ-21-04-26

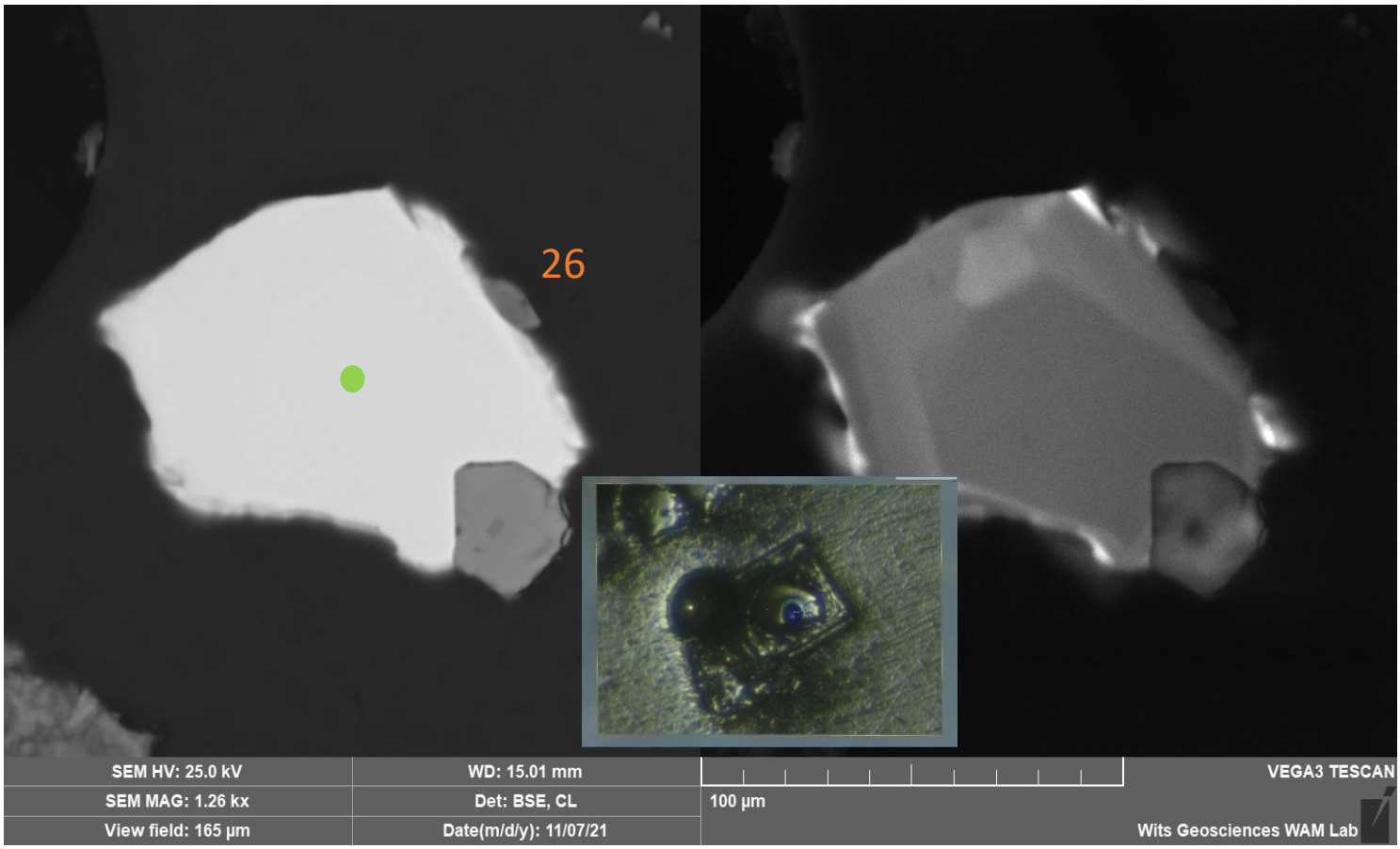

AJ-21-04-27

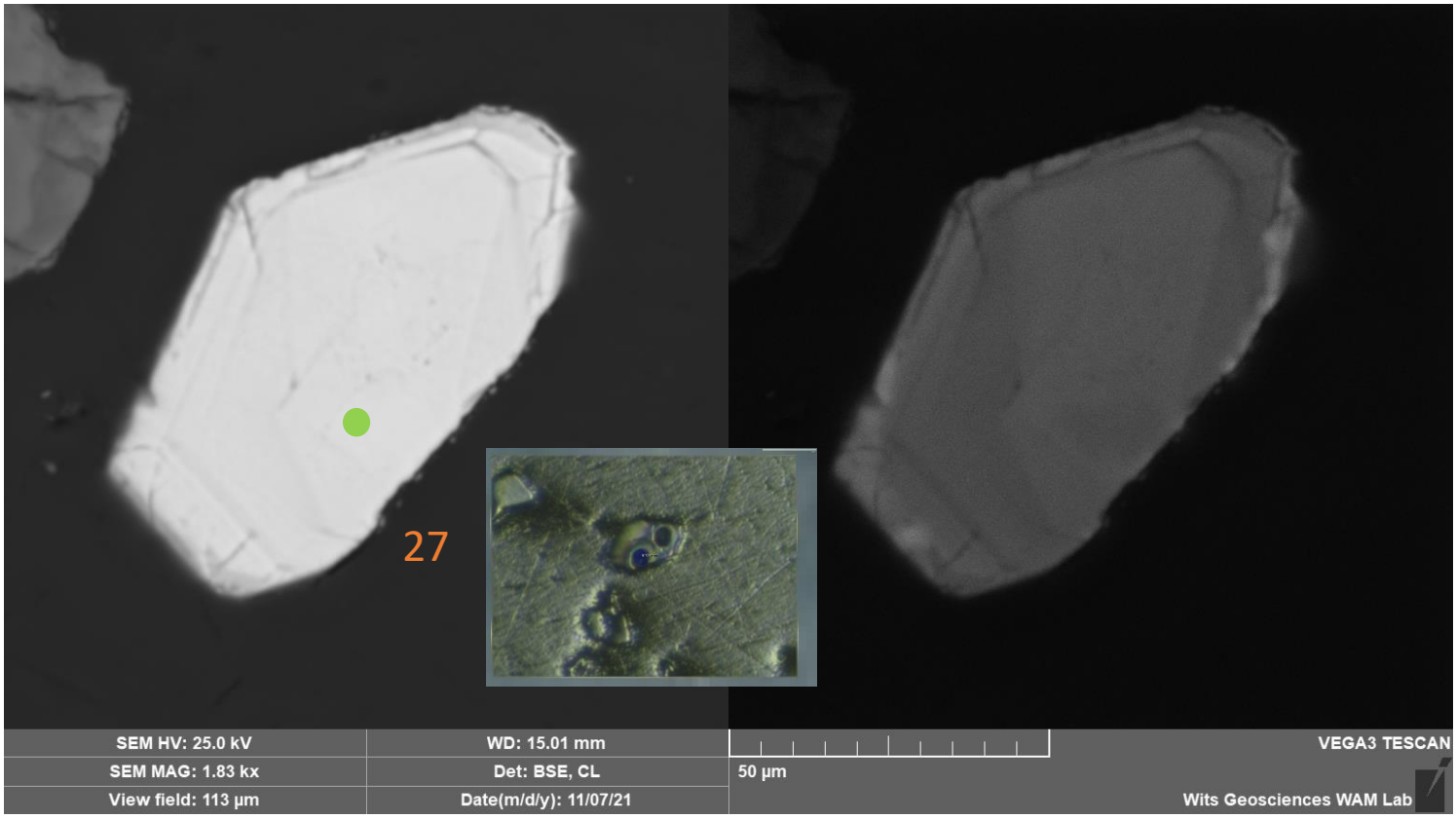

AJ-21-04-28

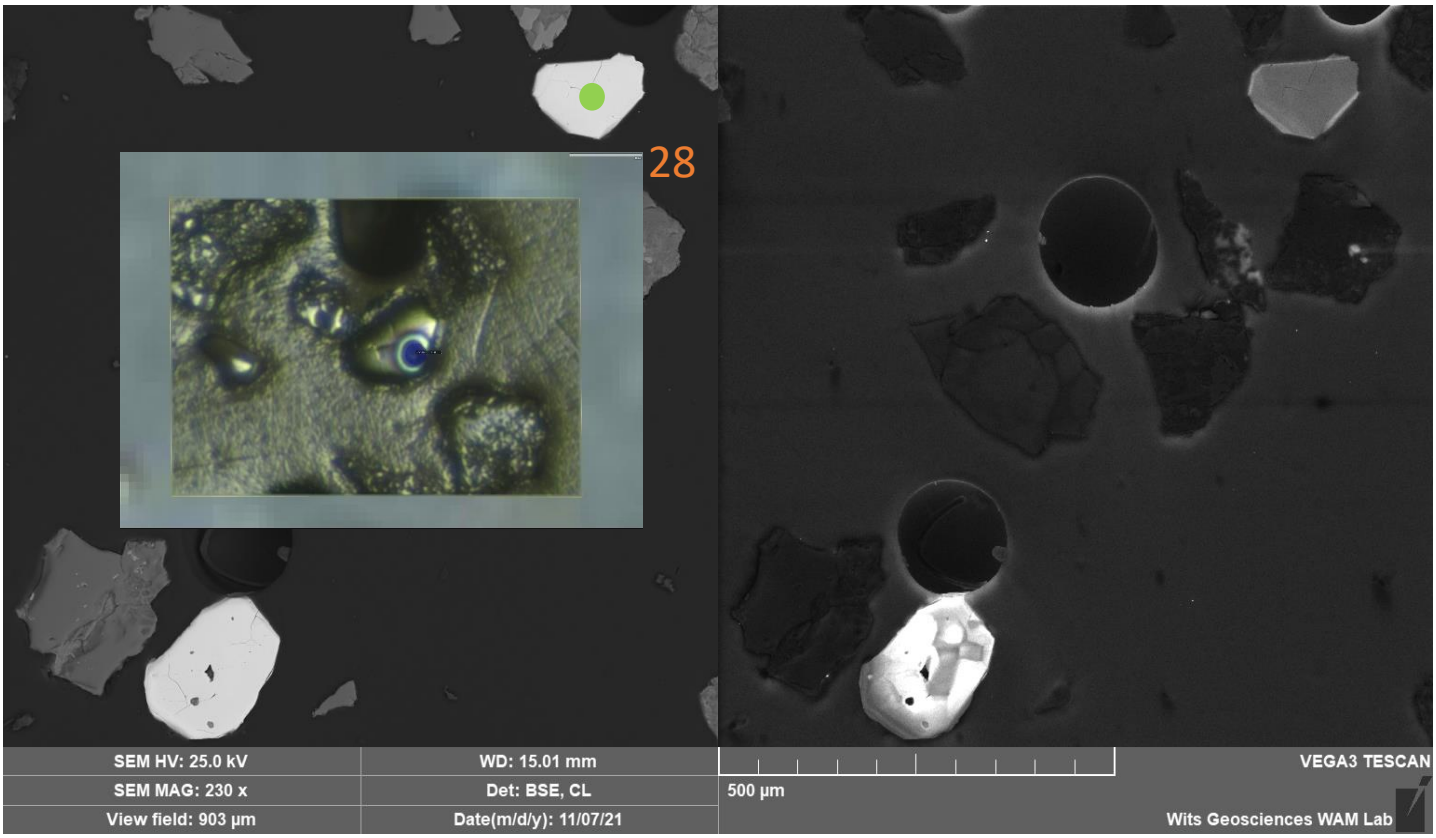

AJ-21-04-29

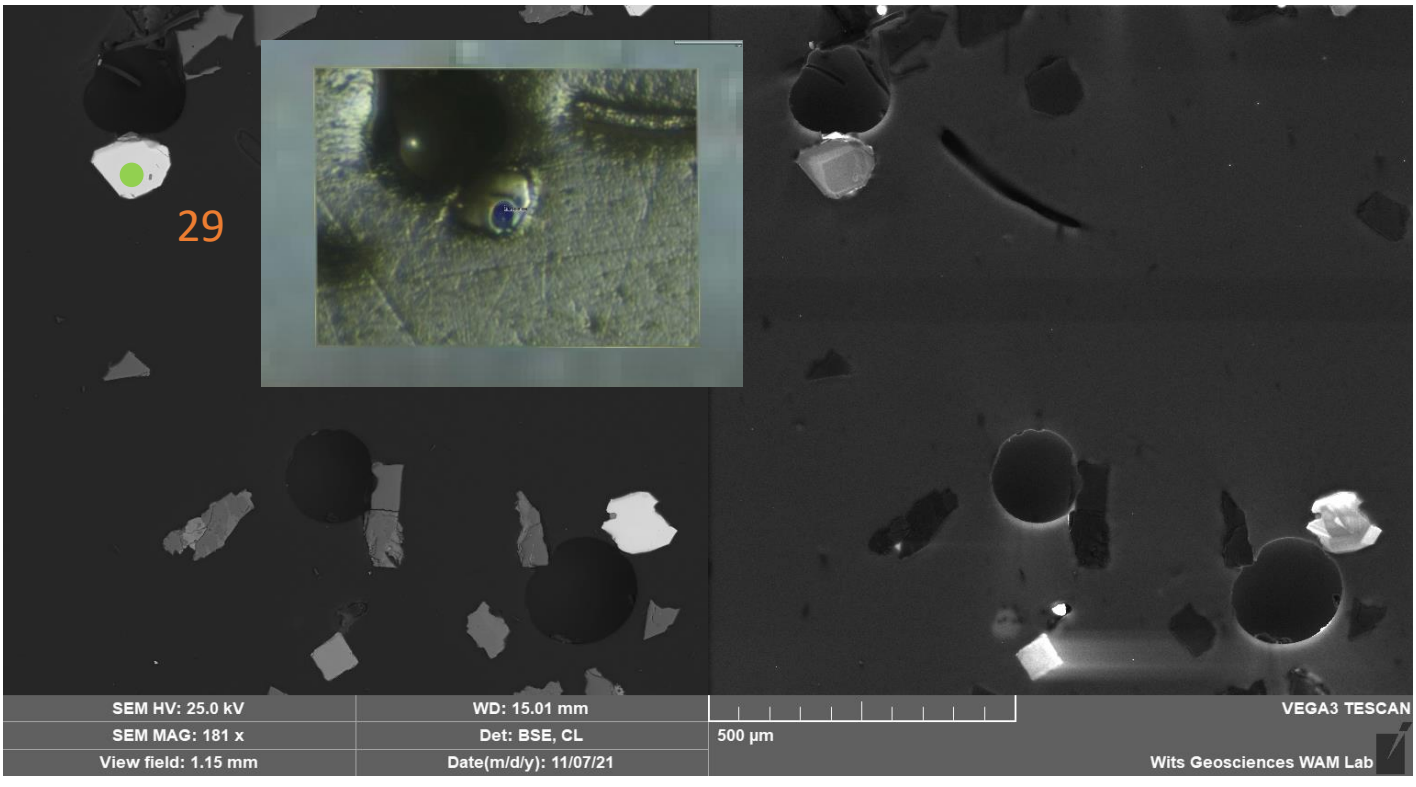

AJ-21-04-30

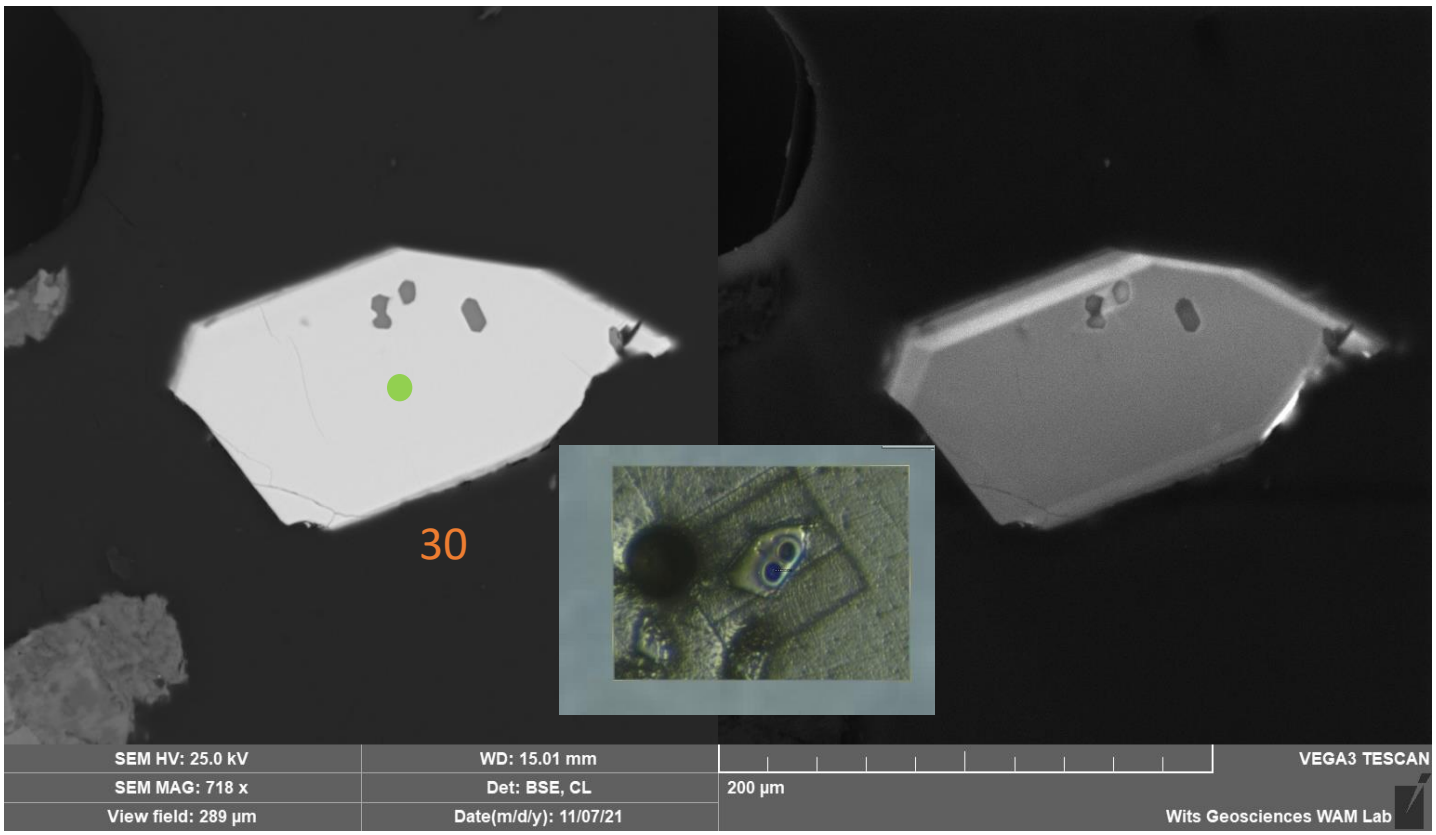

AJ-21-04-31

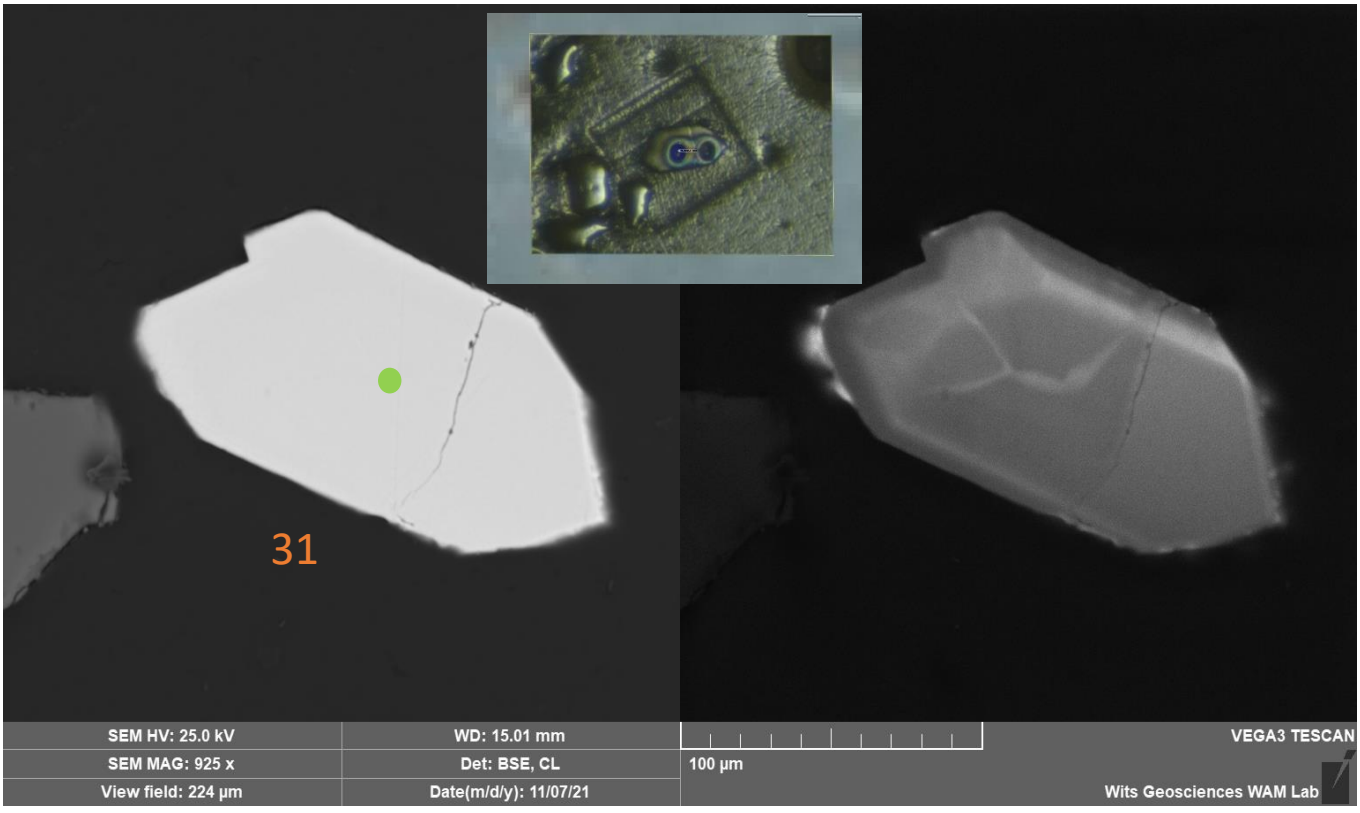

AJ-21-04-32

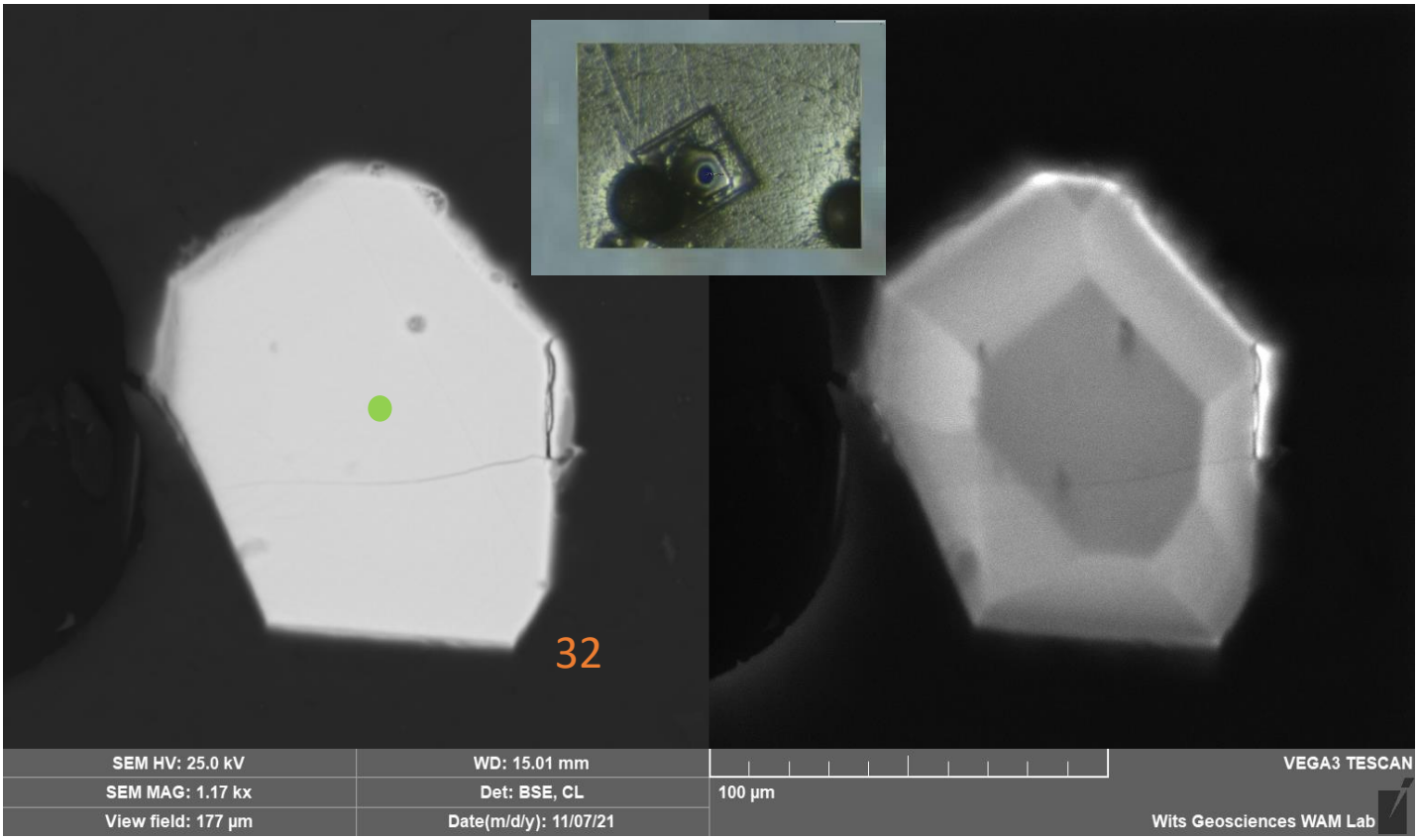

AJ-21-04-33/34

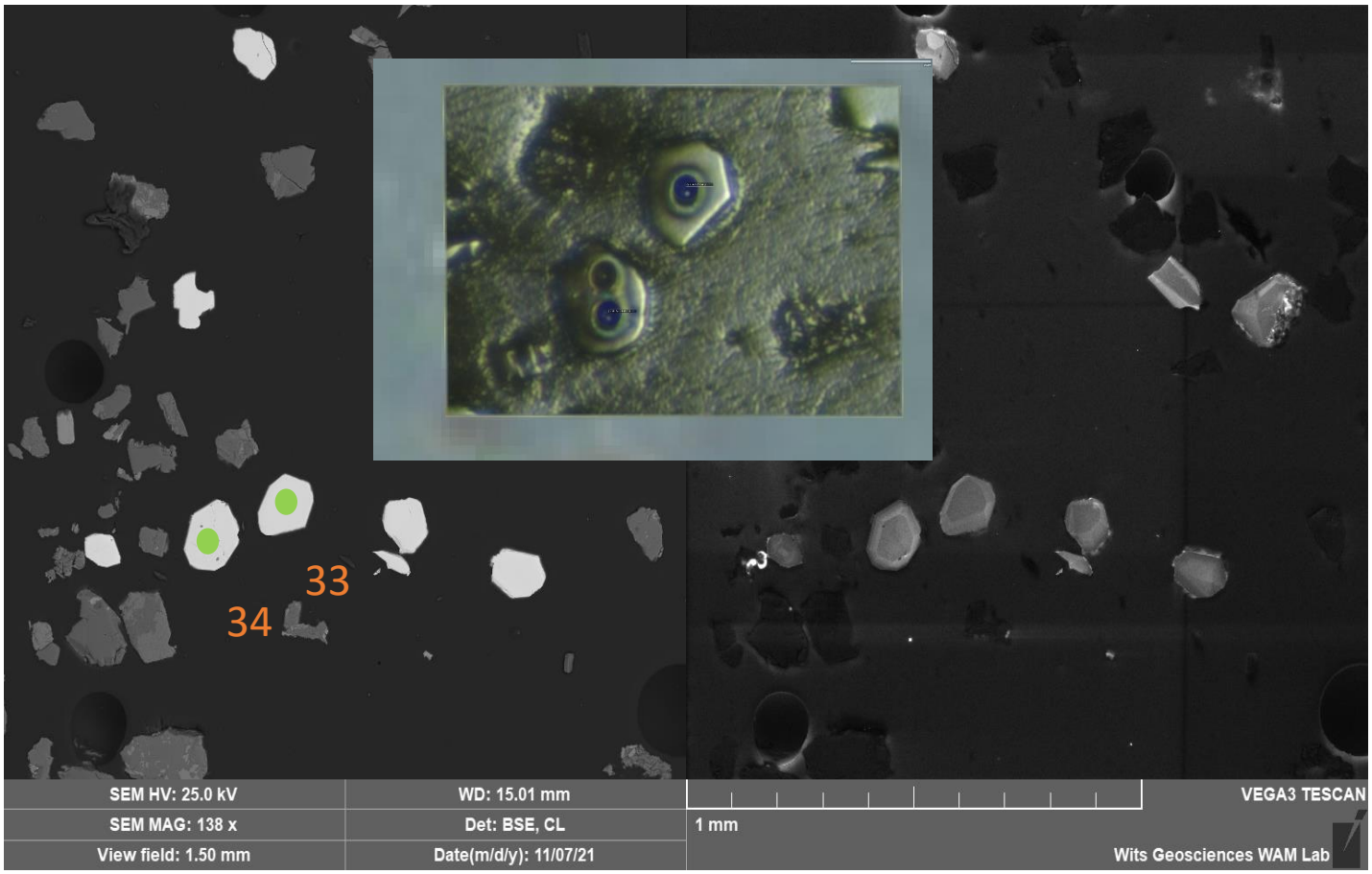

AJ-21-04-35

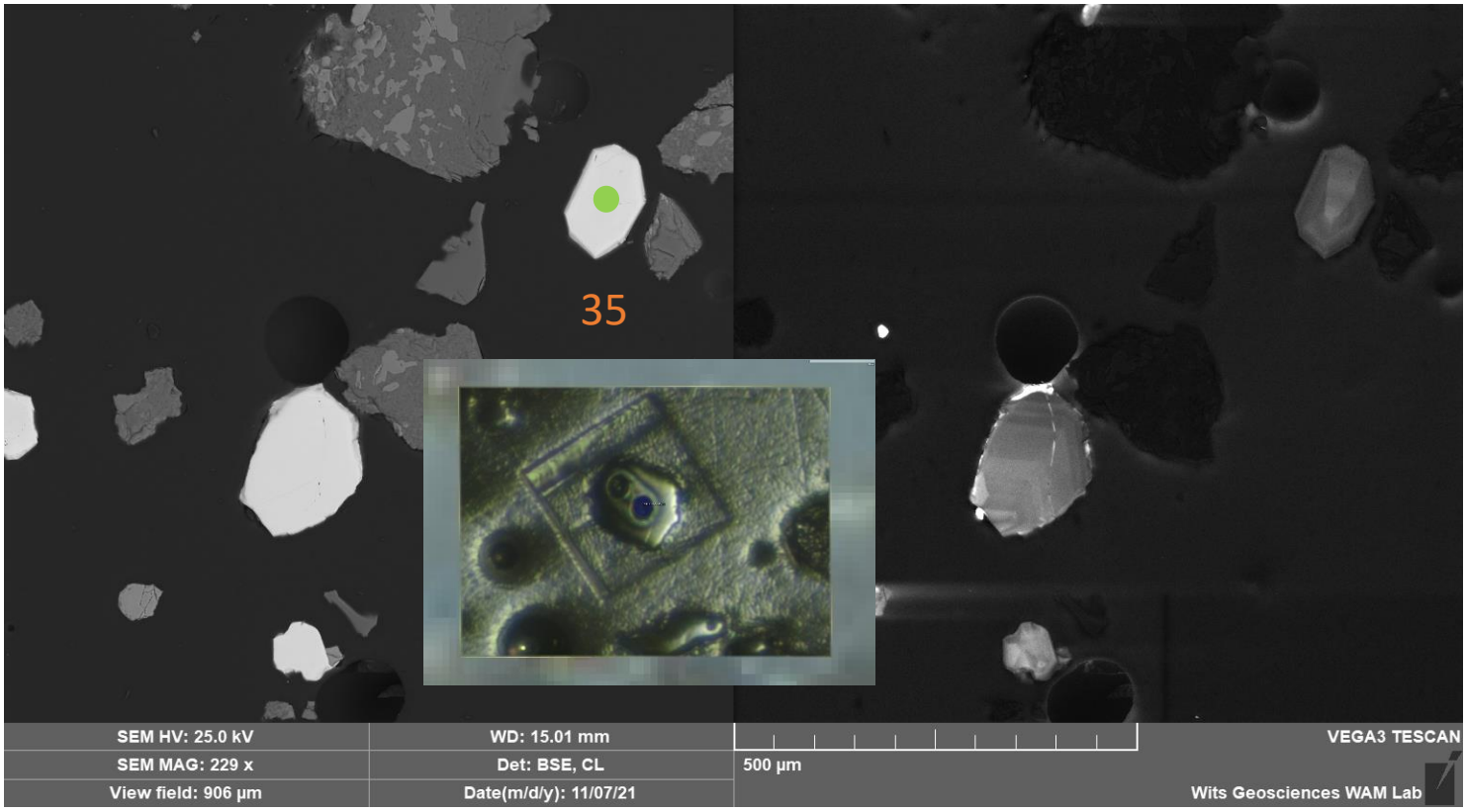

AJ-21-04-36

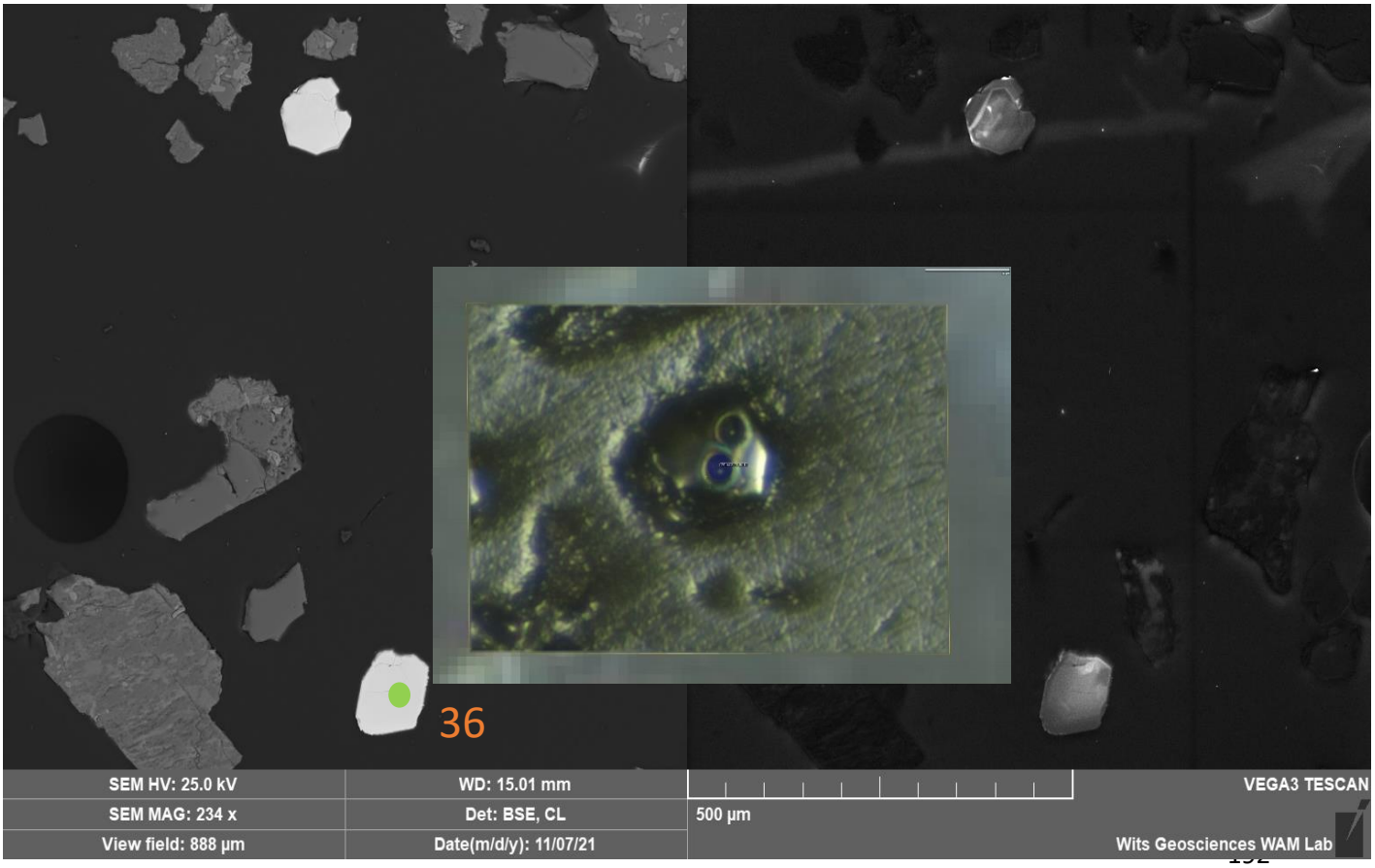

AJ-21-04-37

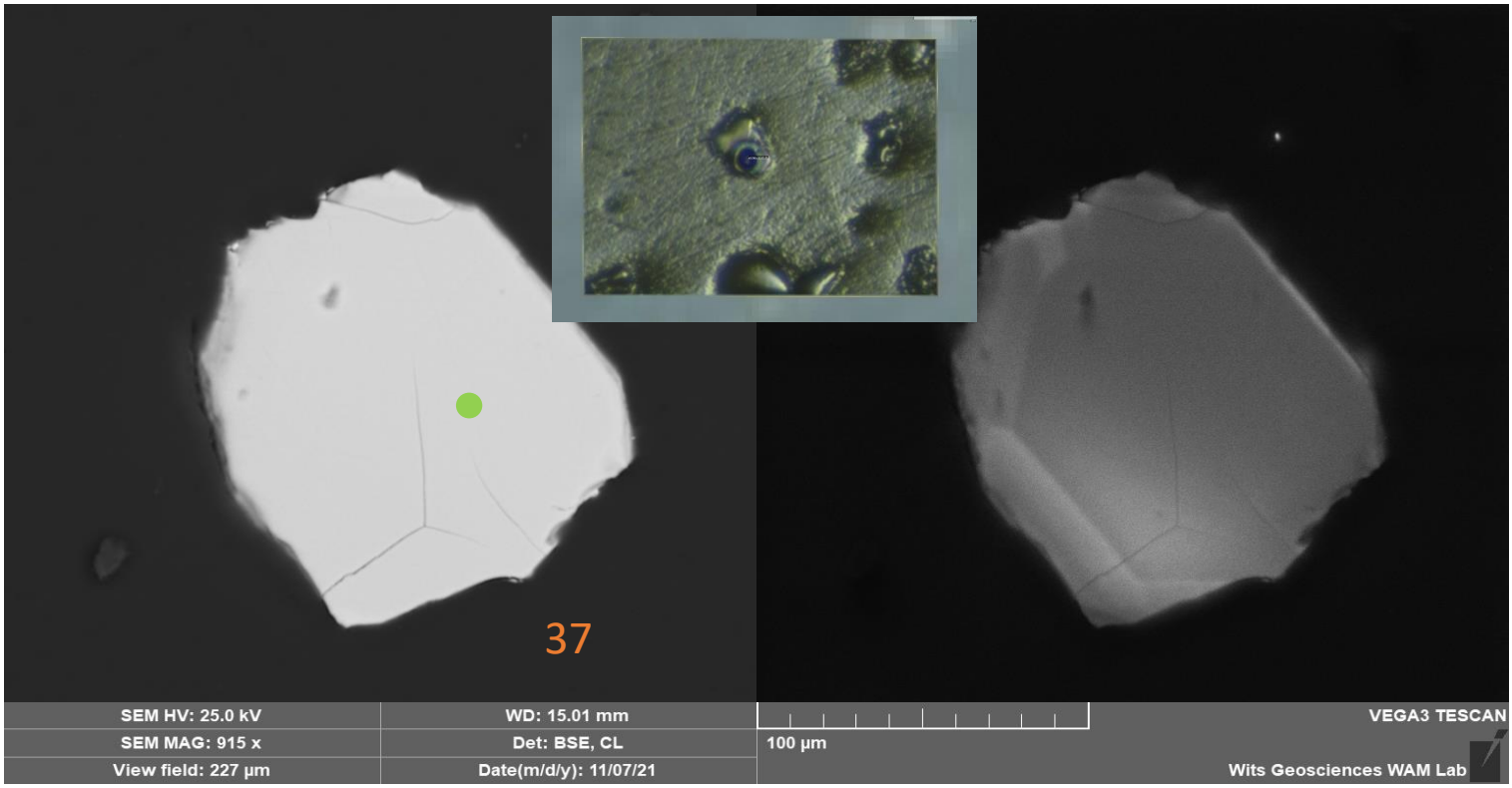

AJ-21-04-38

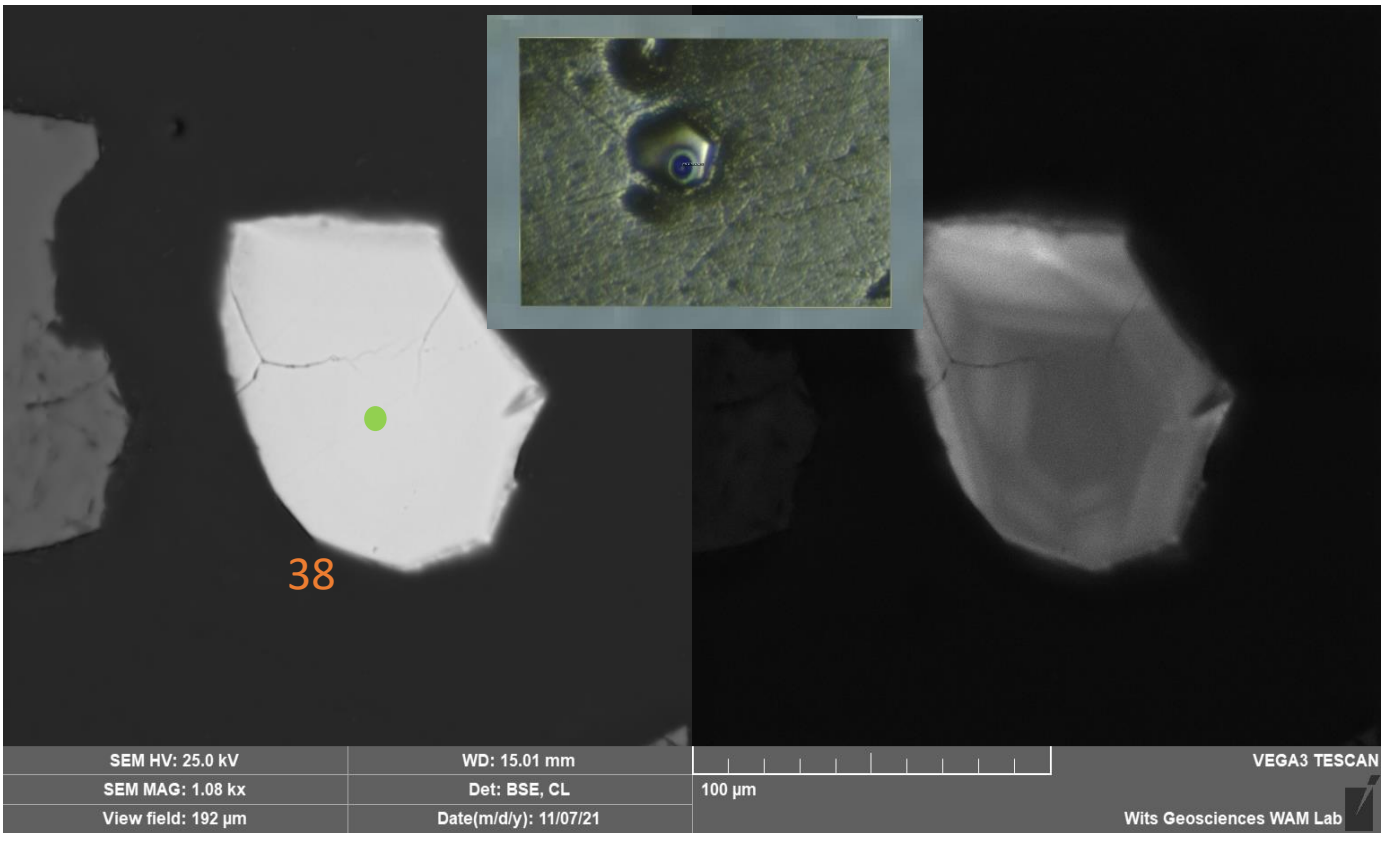

AJ-21-23-1

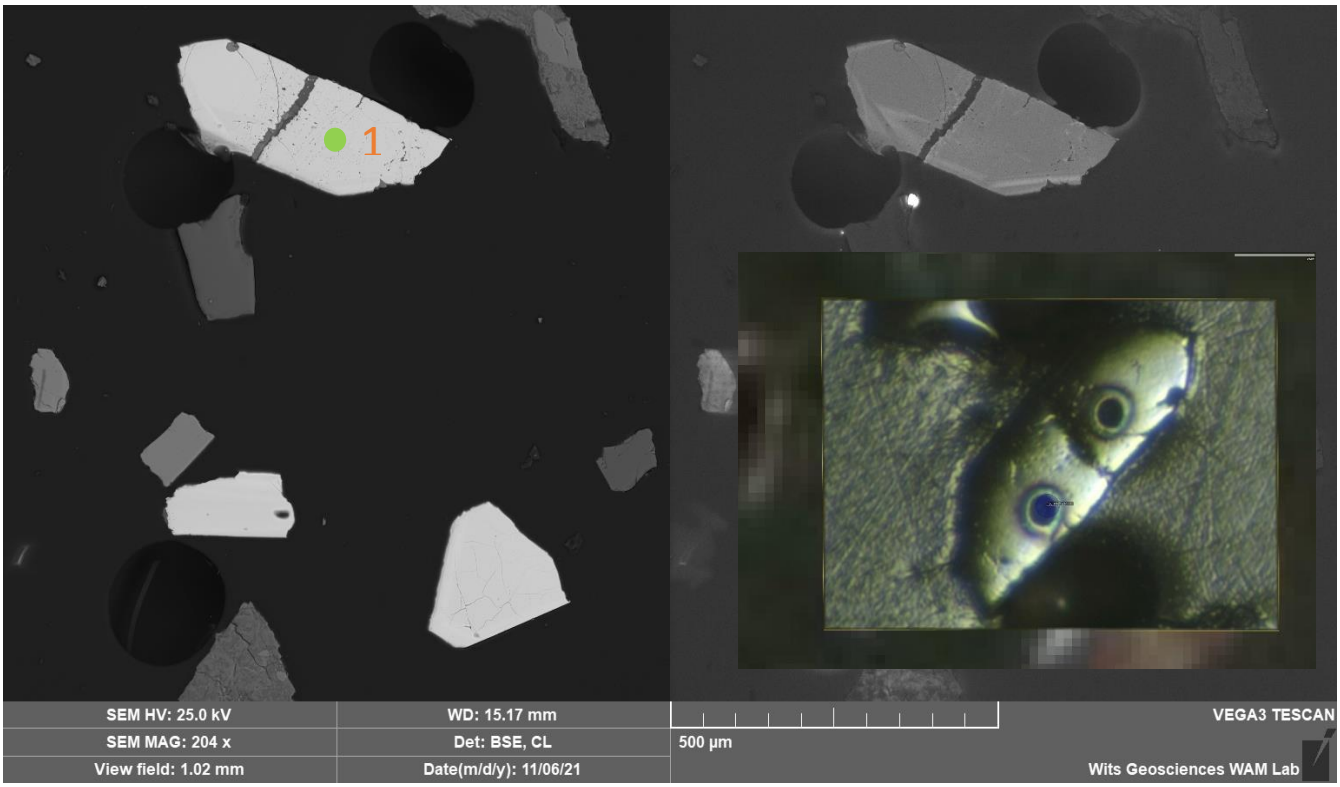

AJ-21-23-2

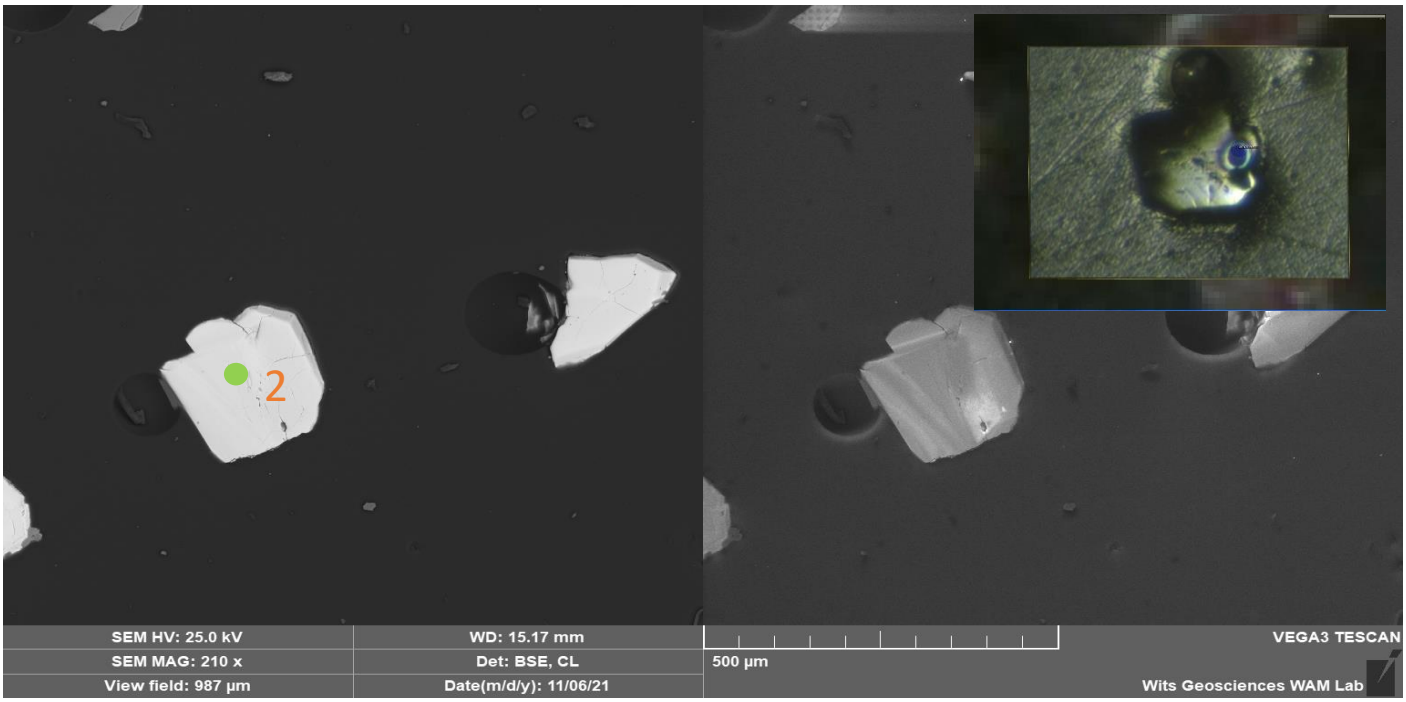

AJ-21-23-3

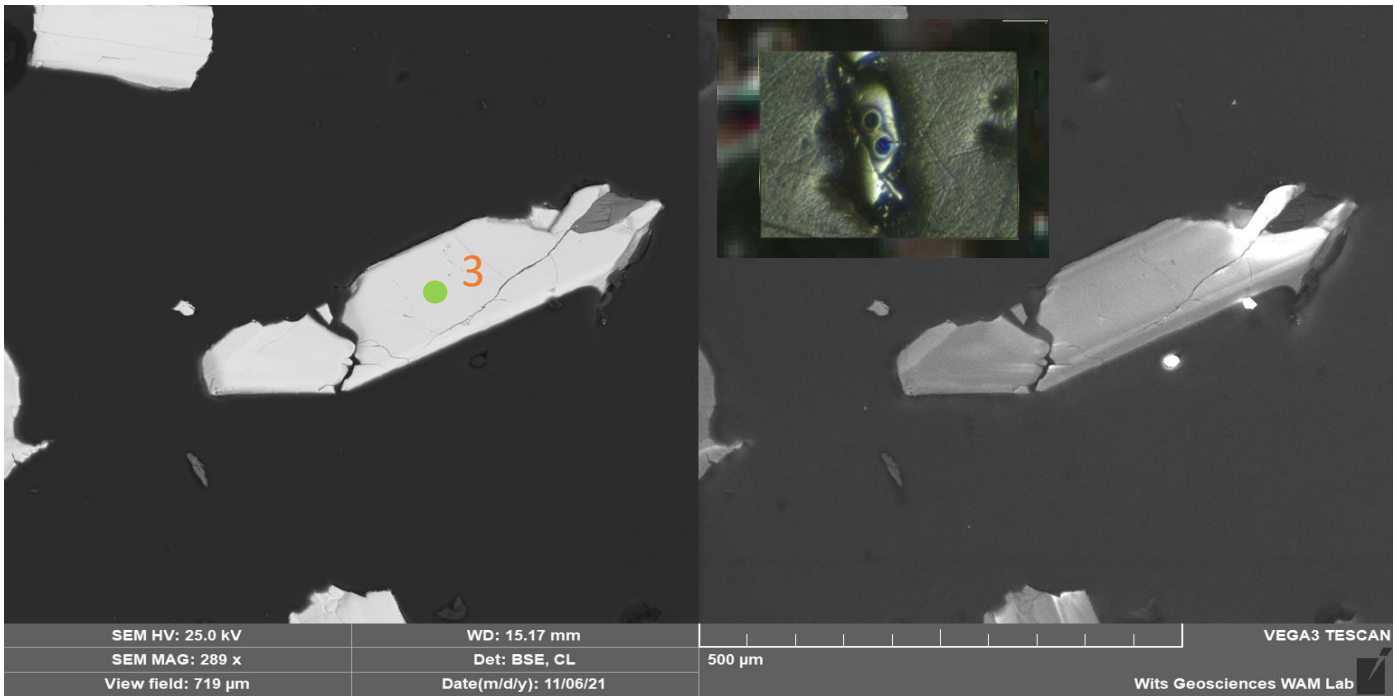

AJ-21-23-4/5

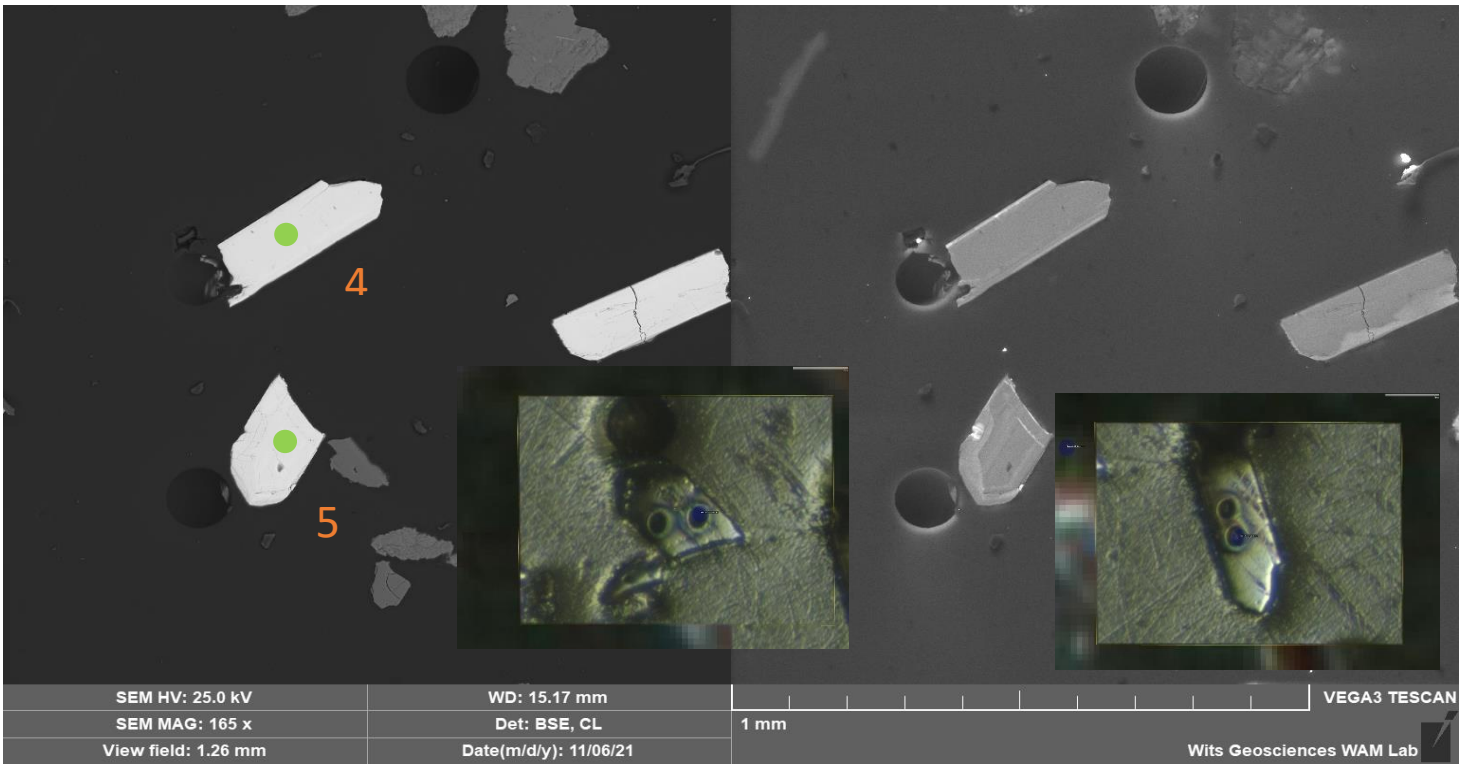

AJ-21-23-6/7

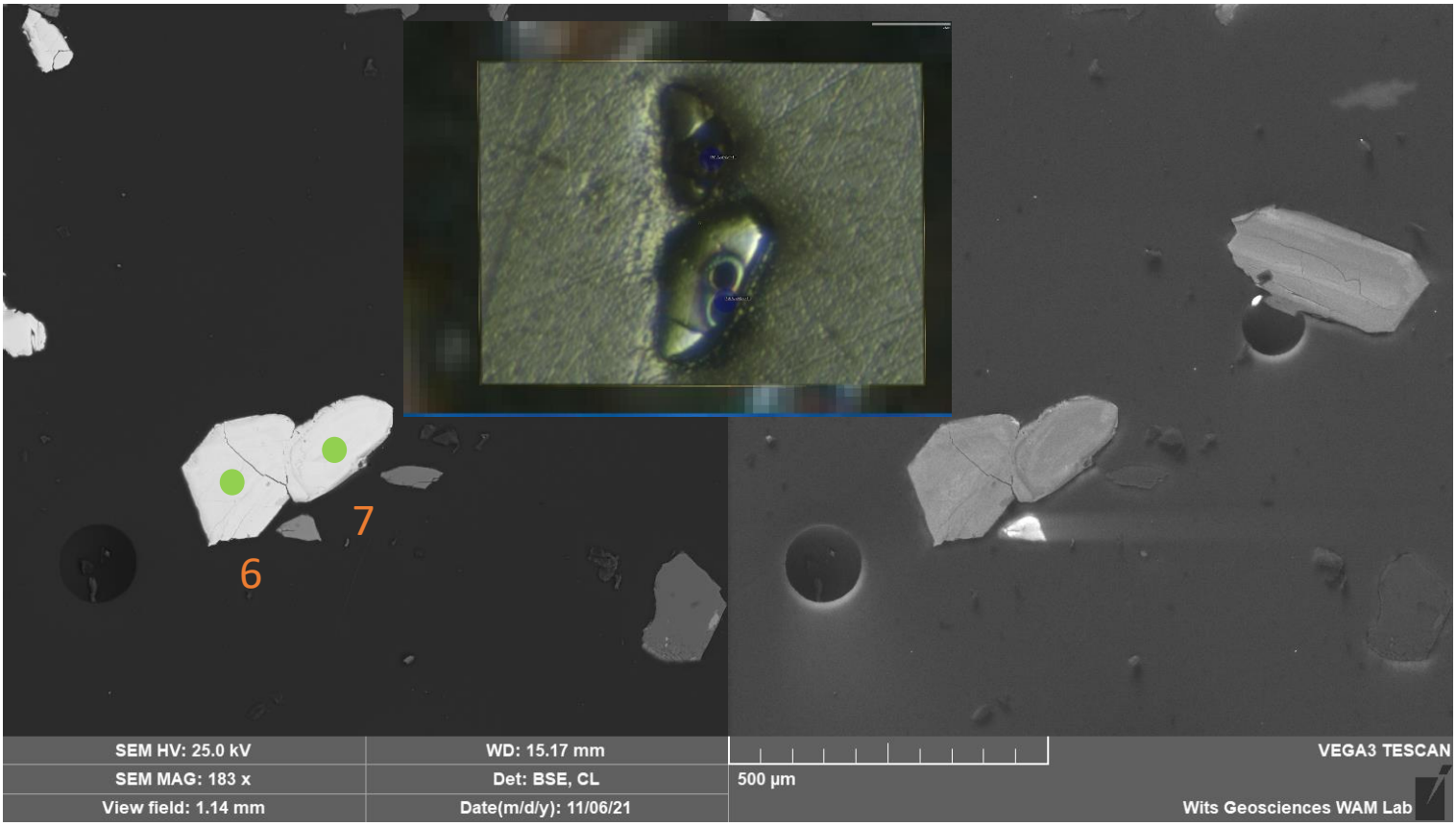

AJ-21-23-8/9

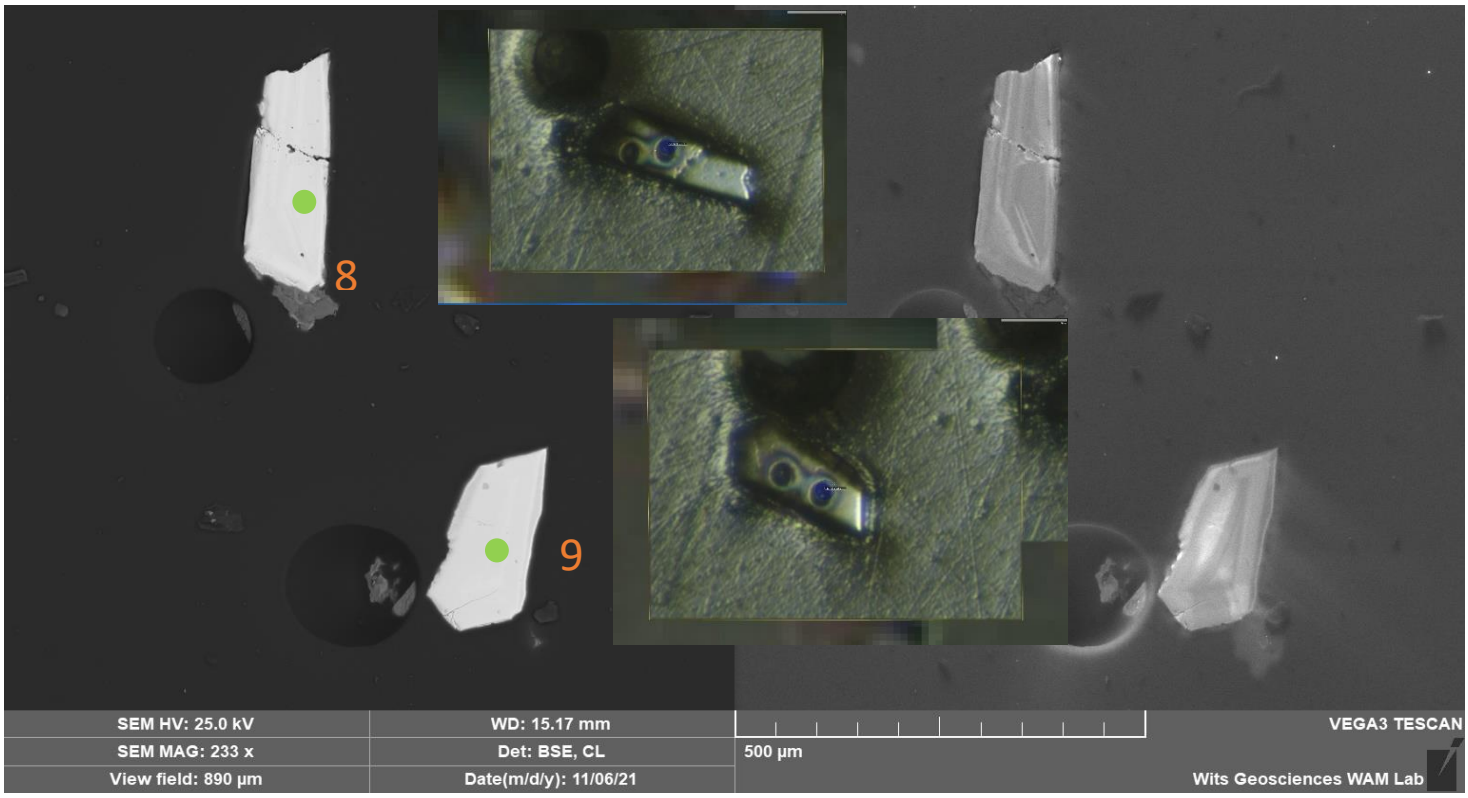

AJ-21-23-10

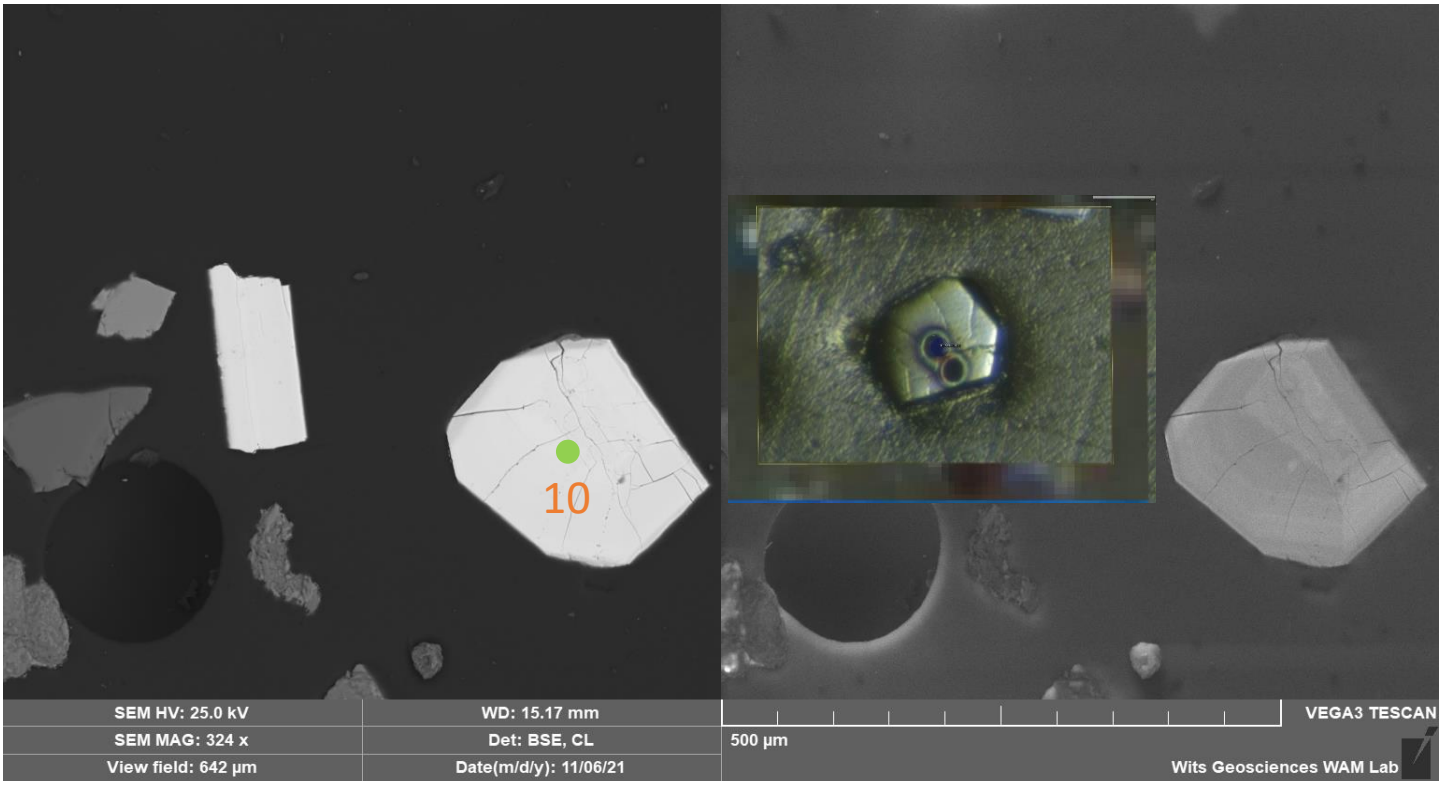

AJ-21-23-11

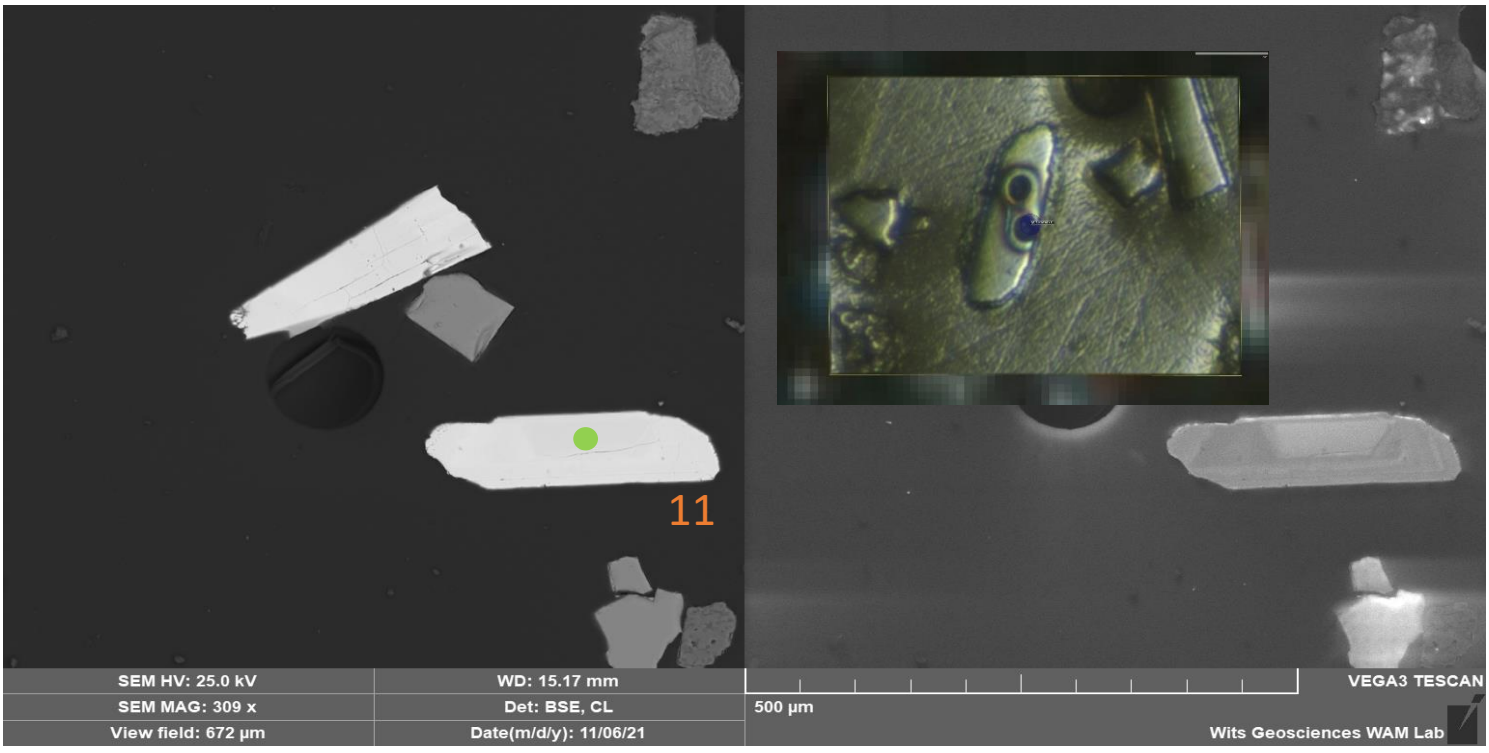

AJ-21-23-12

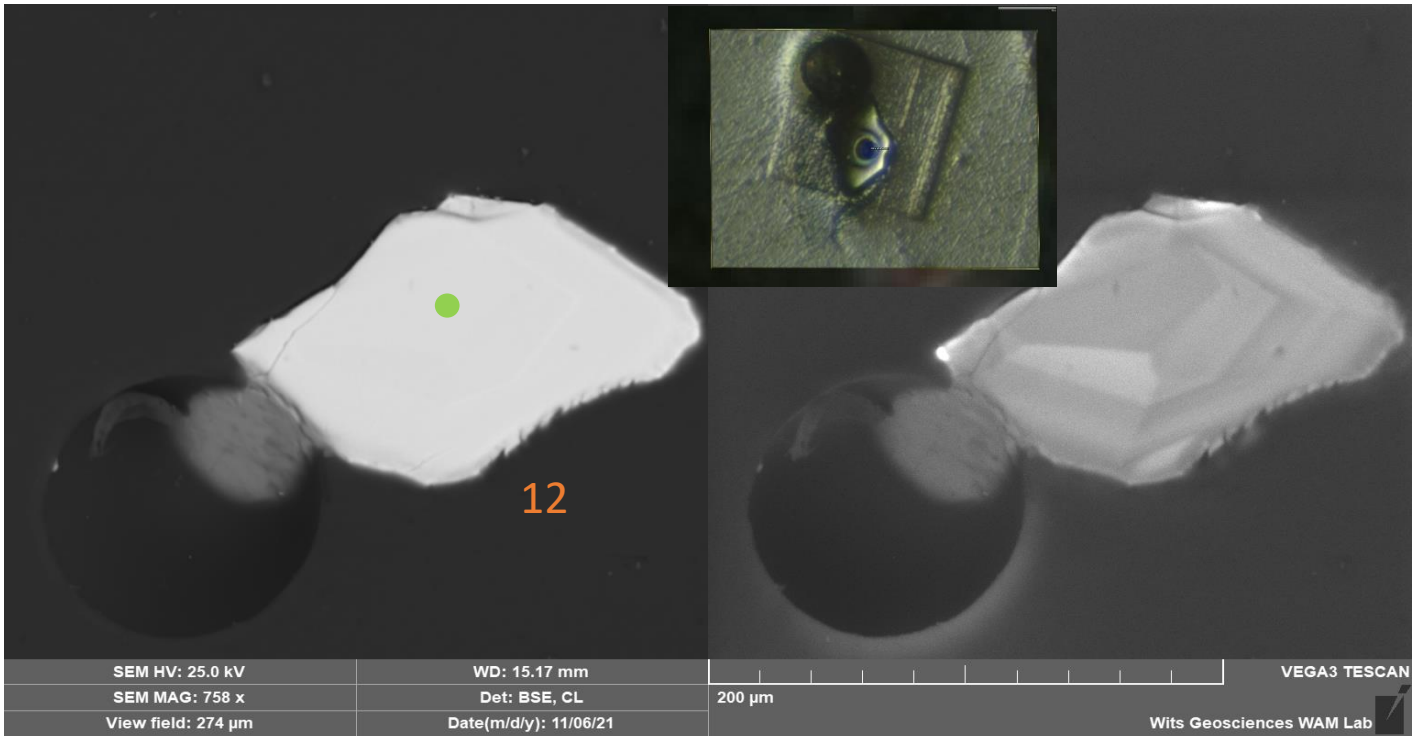

AJ-21-23-13

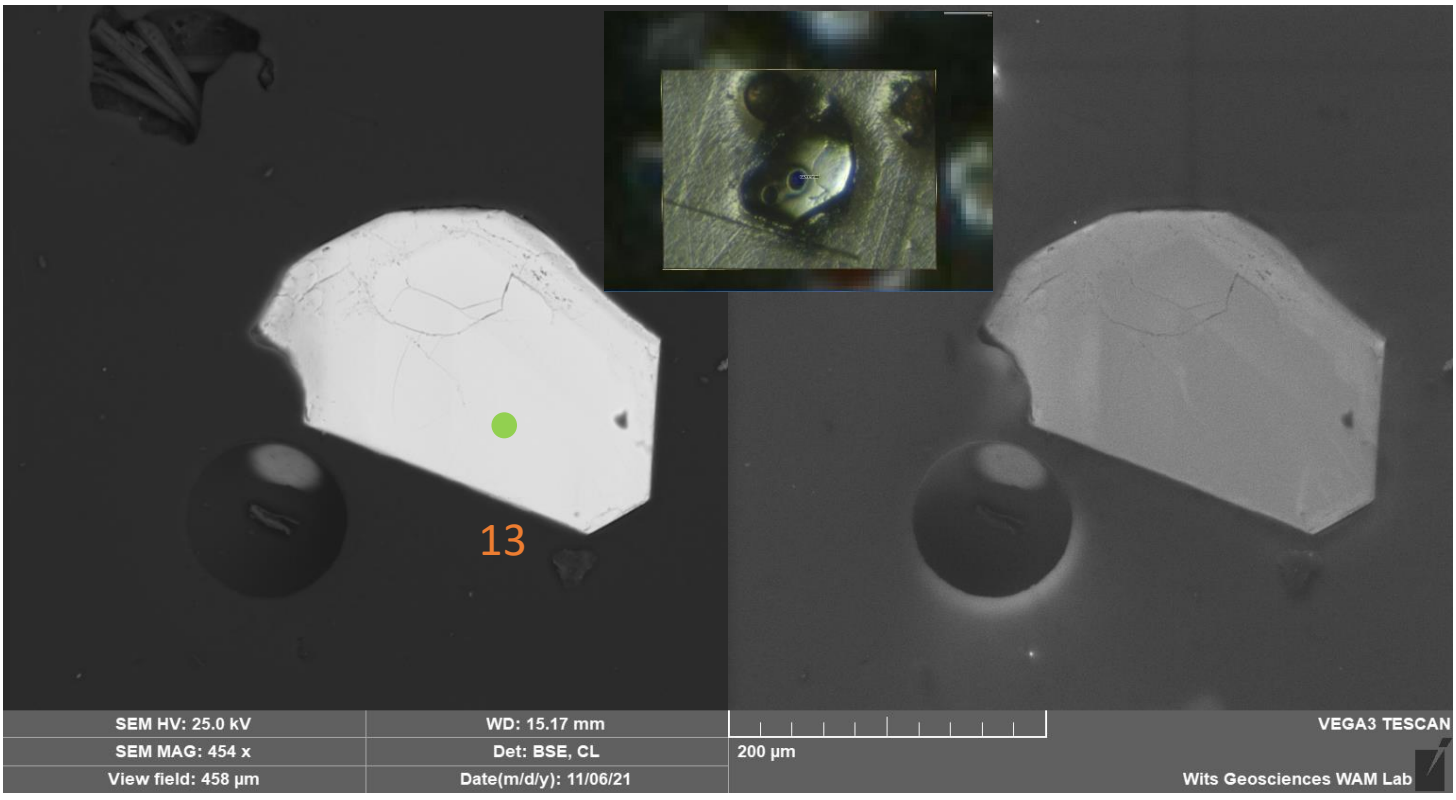

AJ-21-23-14/15

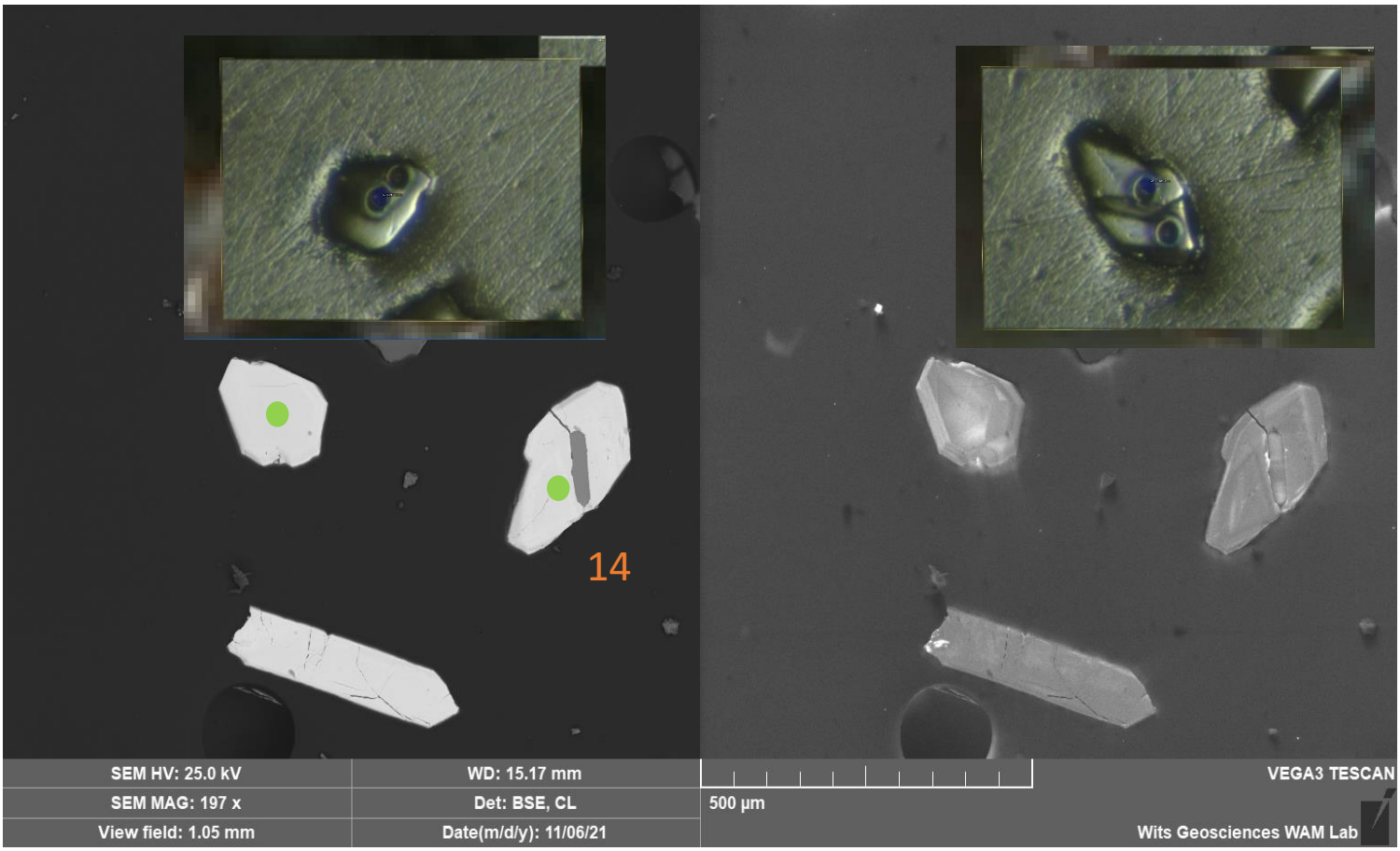

AJ-21-23-16

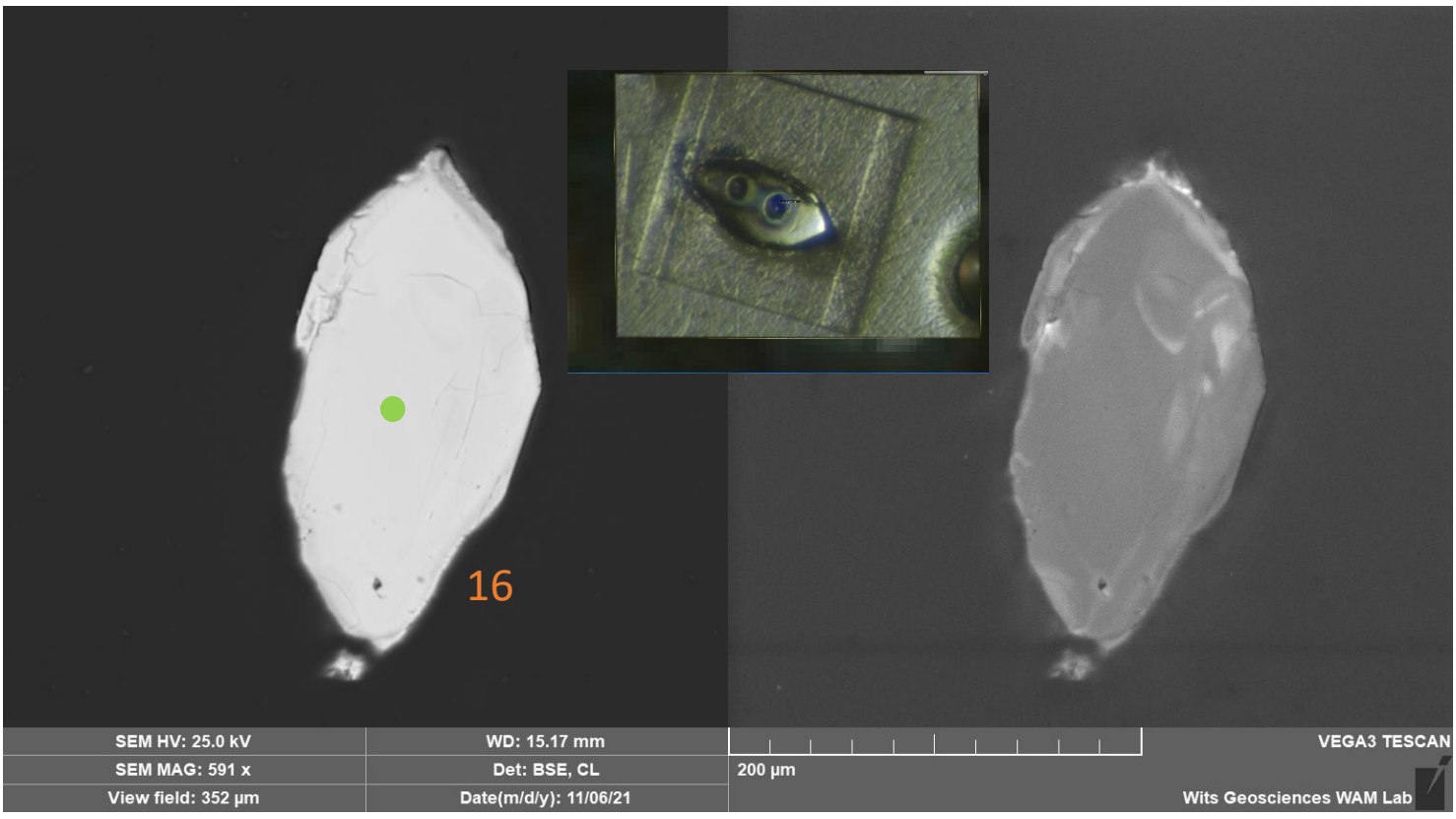

AJ-21-23-17

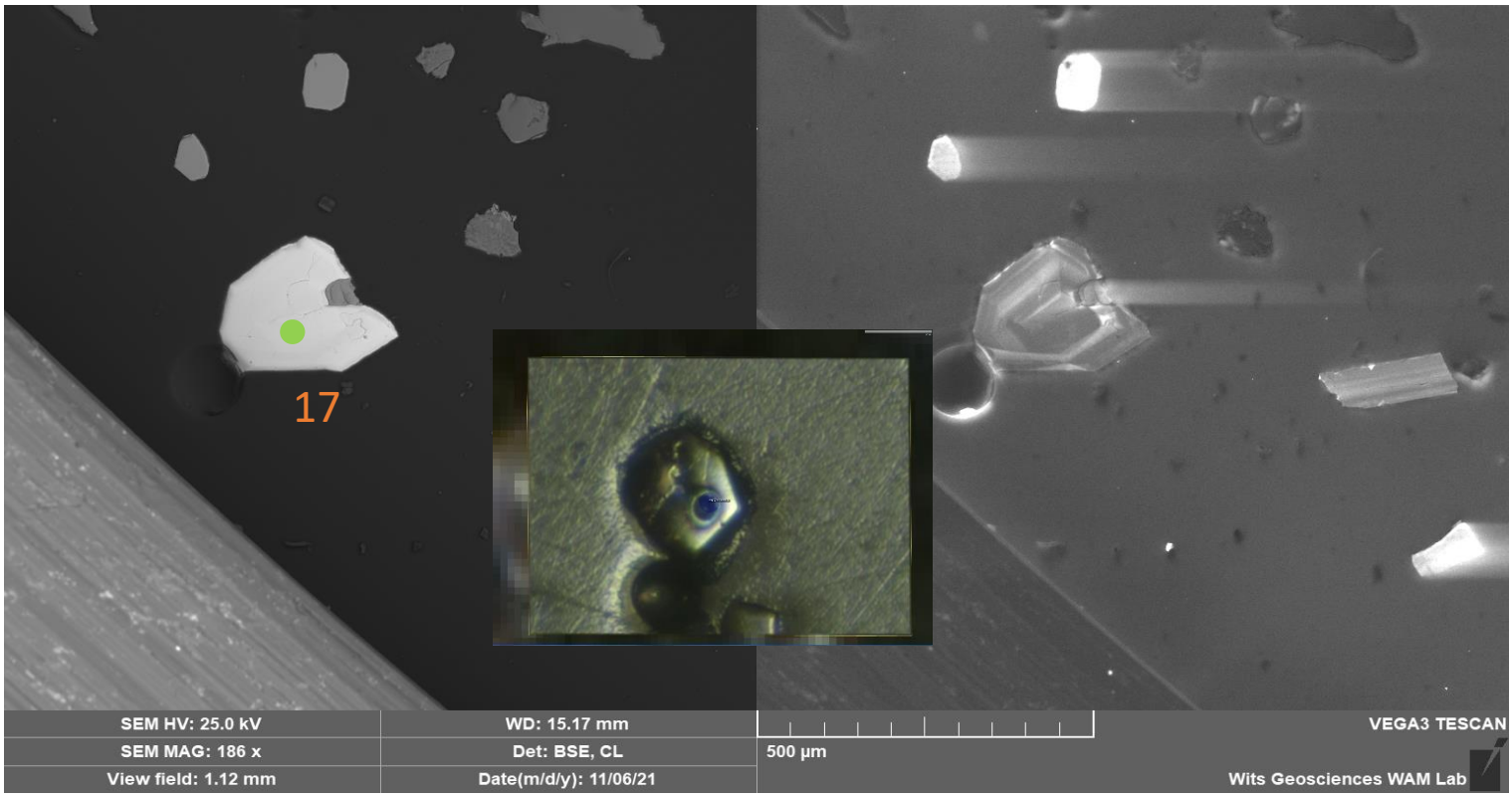

AJ-21-23-18/19

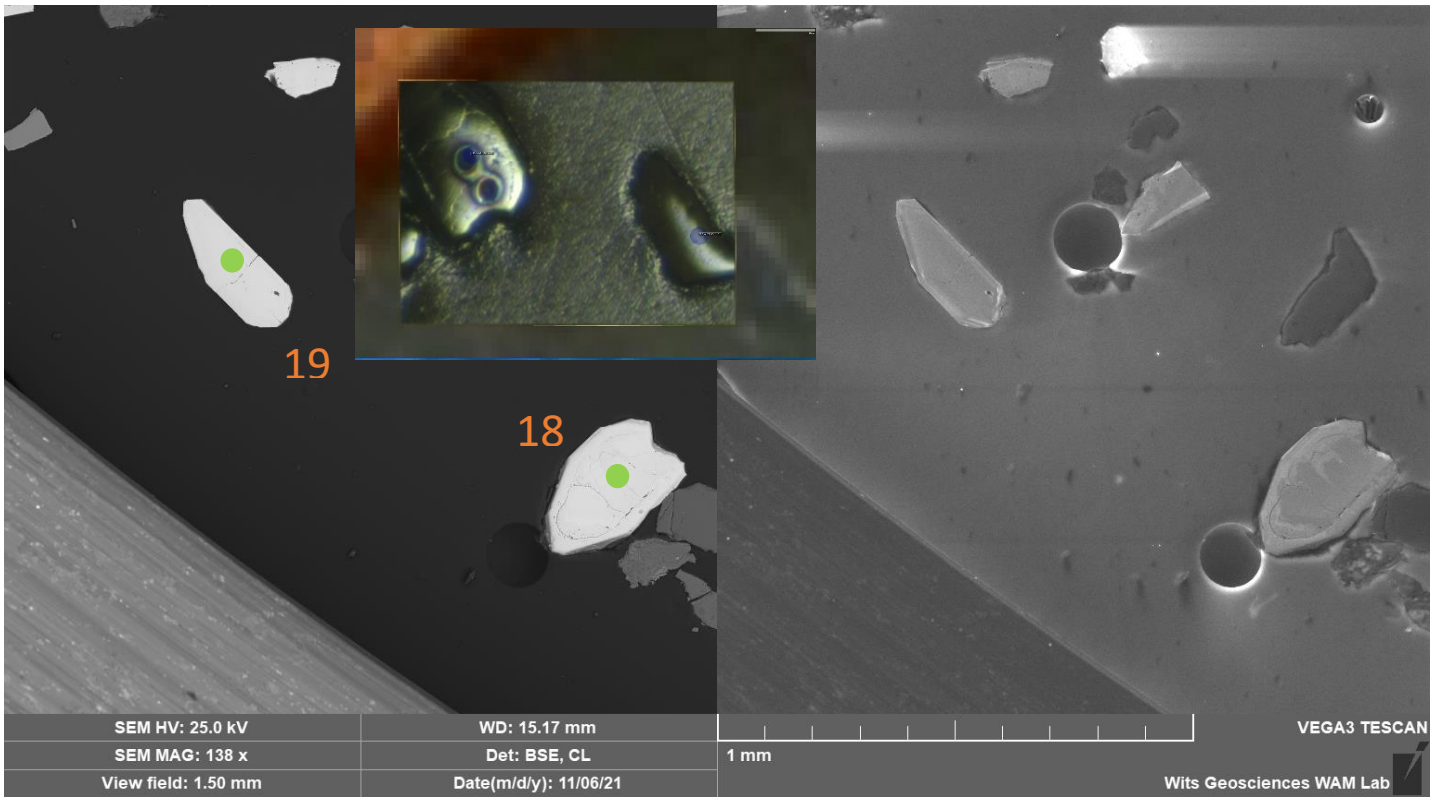

AJ-21-23-20

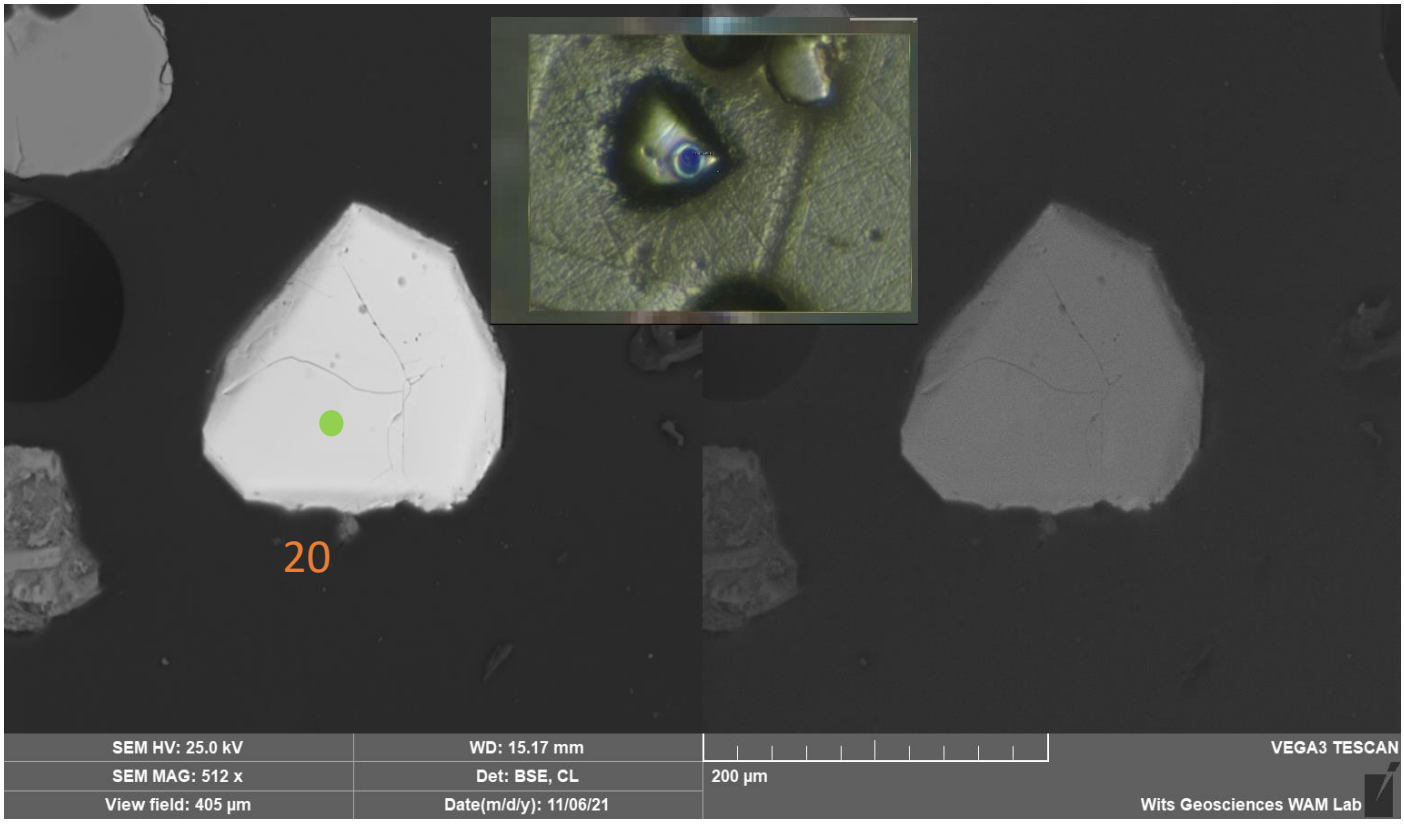

AJ-21-23-21/22

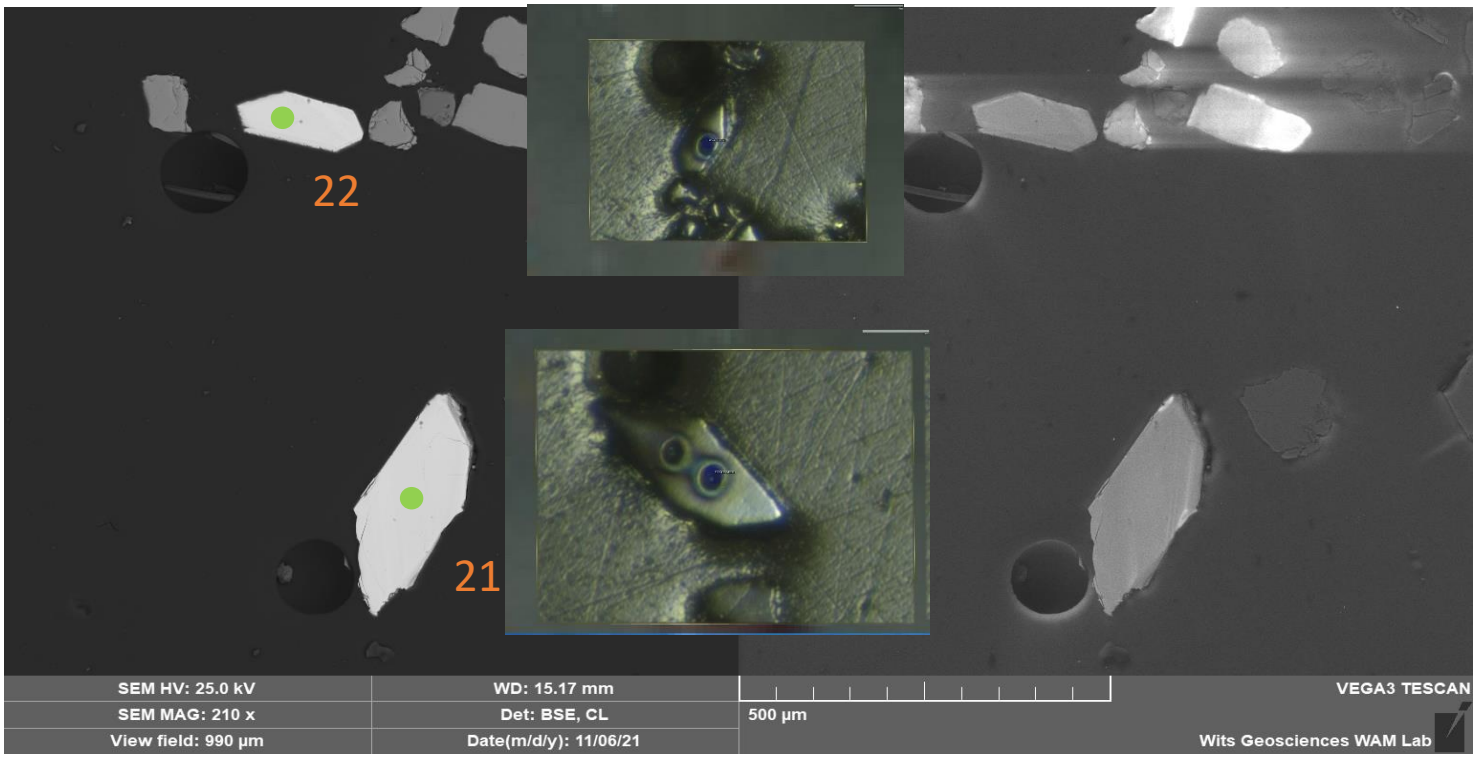

AJ-21-23-23/24/25

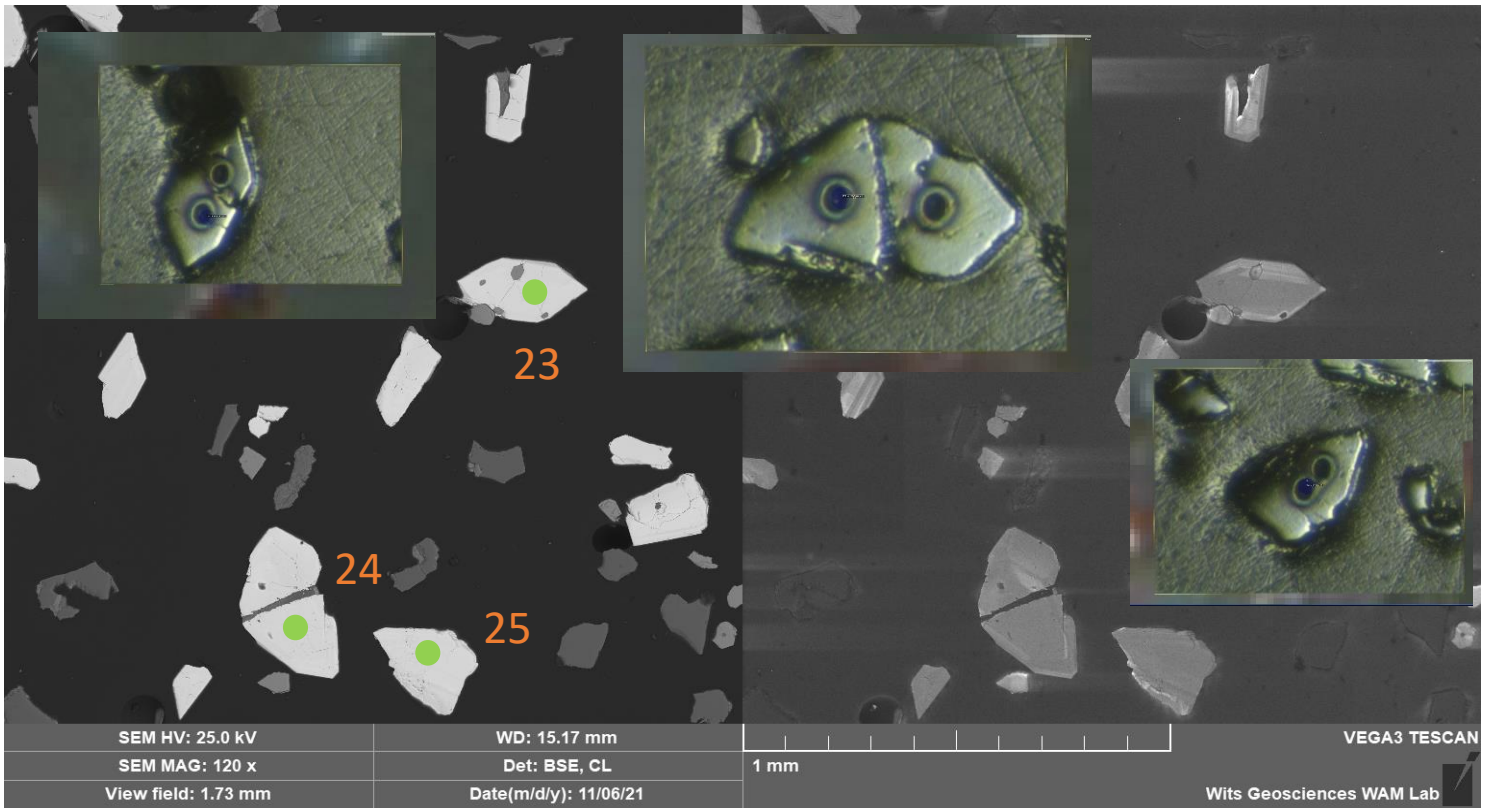

AJ-21-23-26

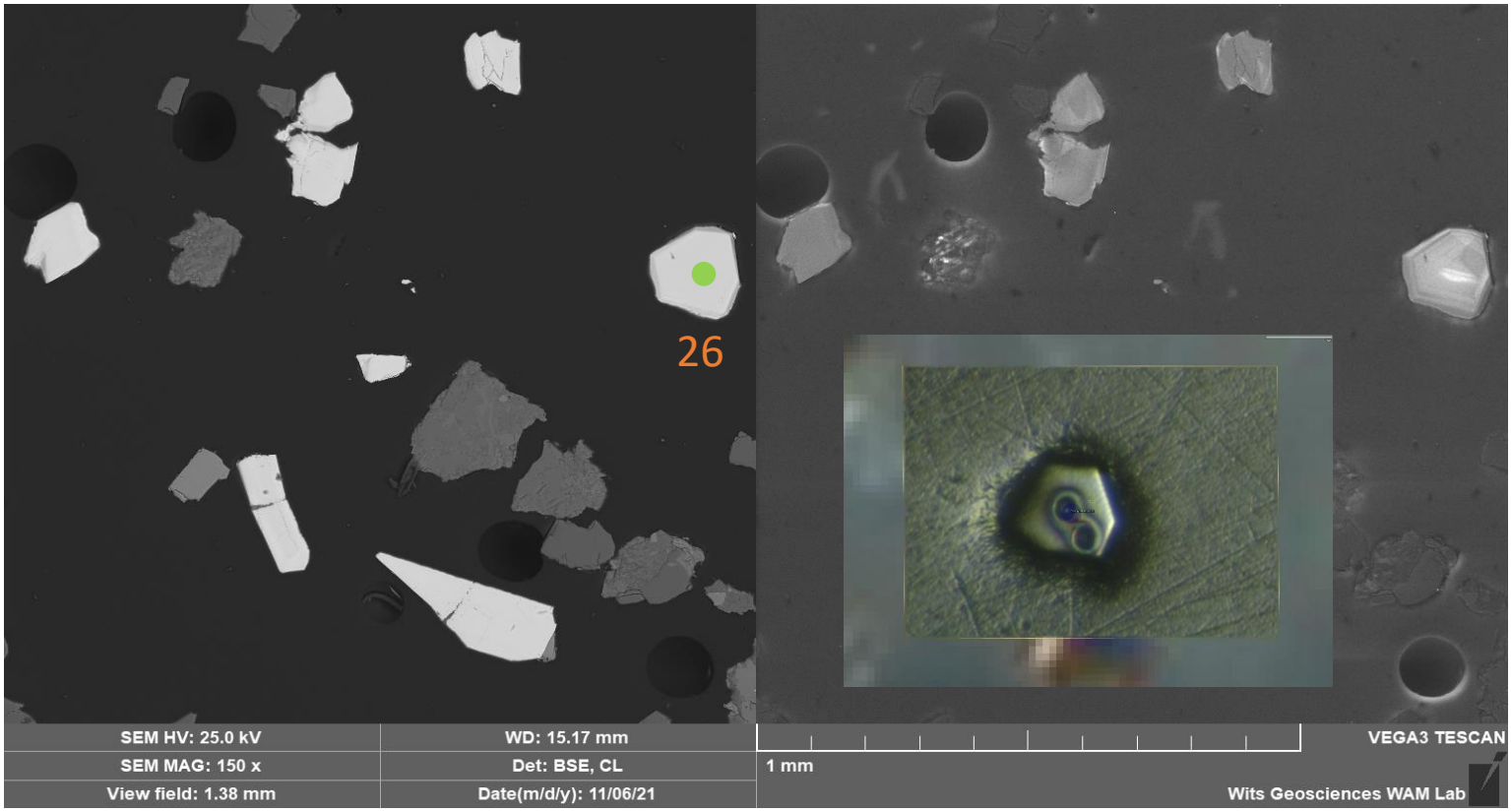

AJ-21-23-27/28

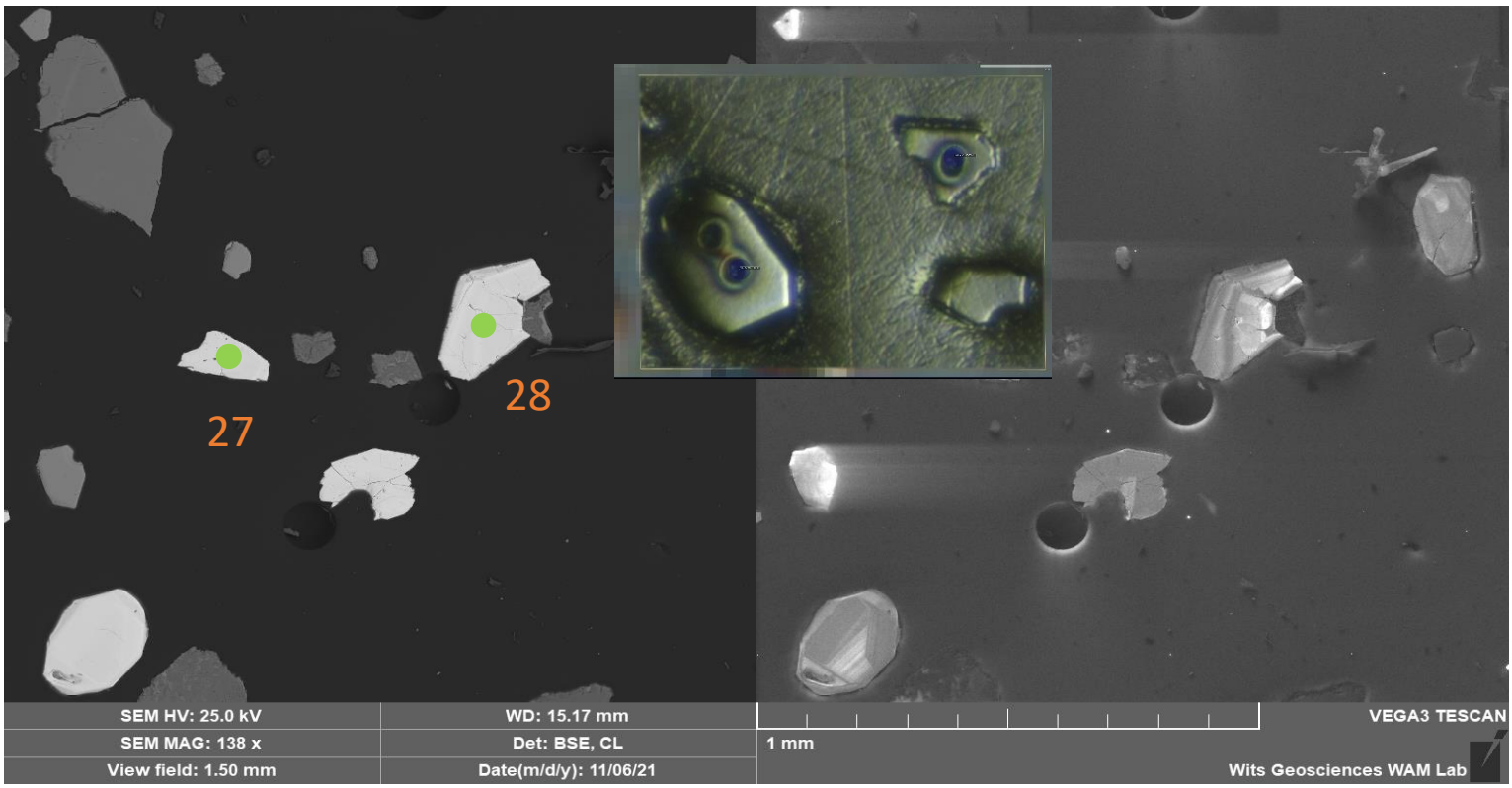

AJ-21-23-29

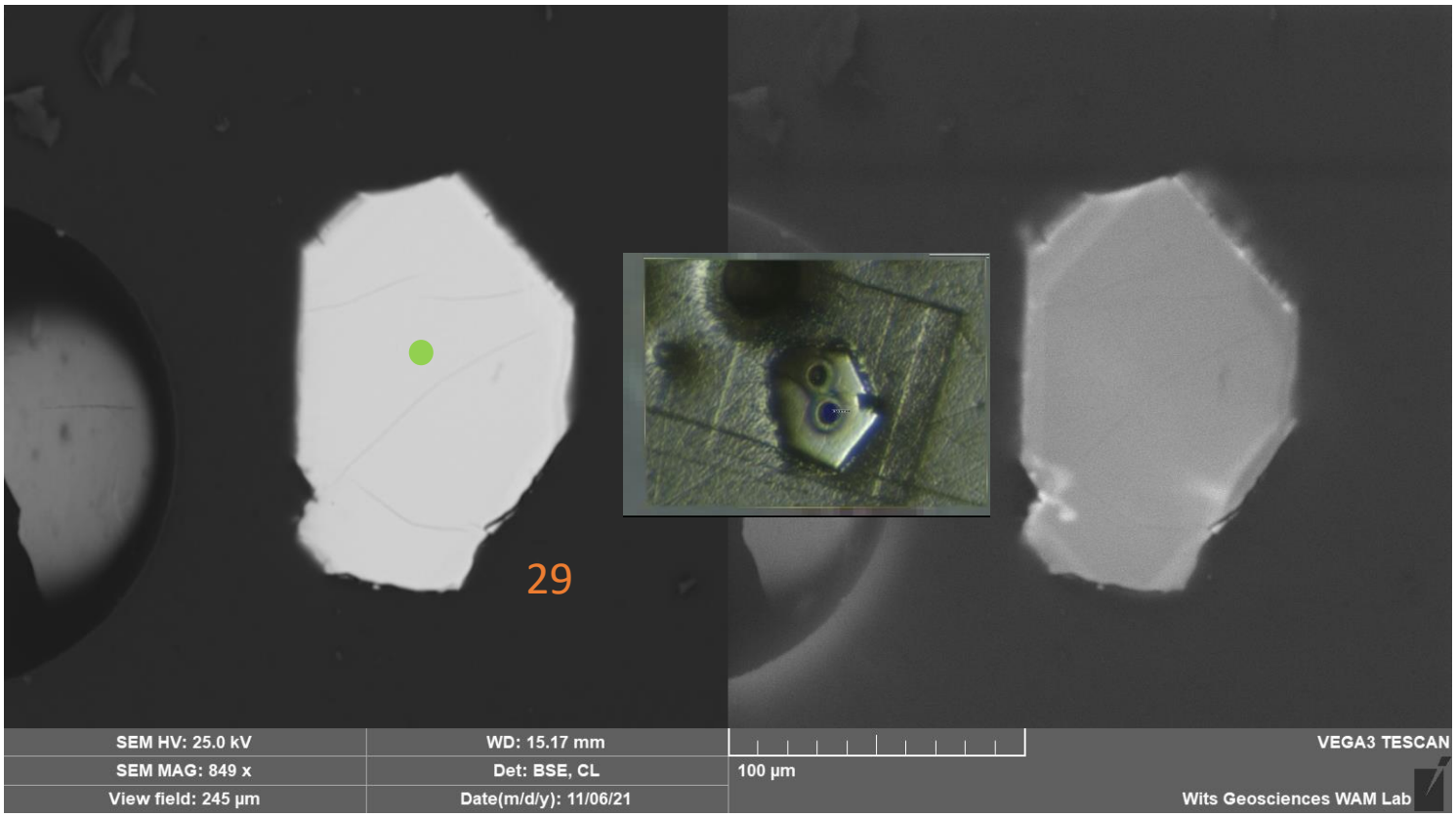

AJ-21-23-30

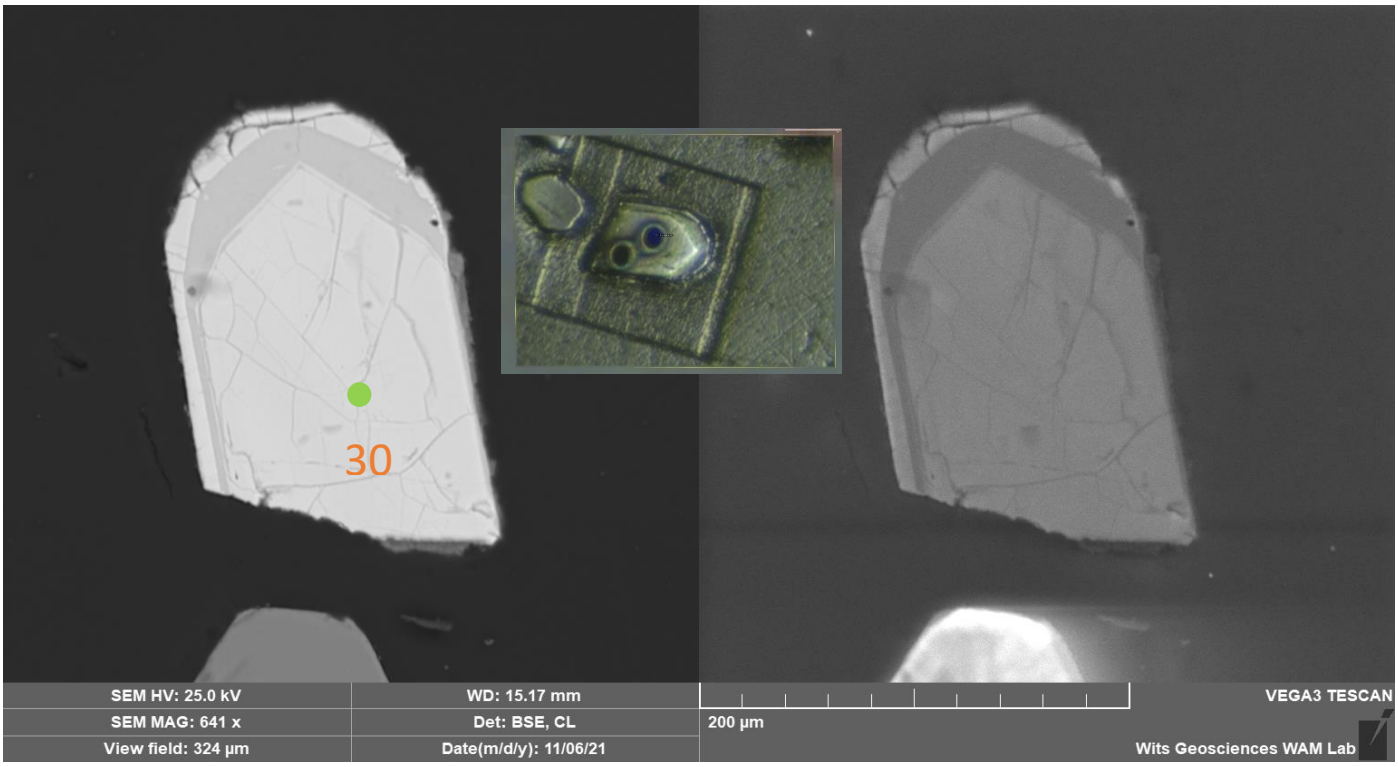

AJ-21-23-31

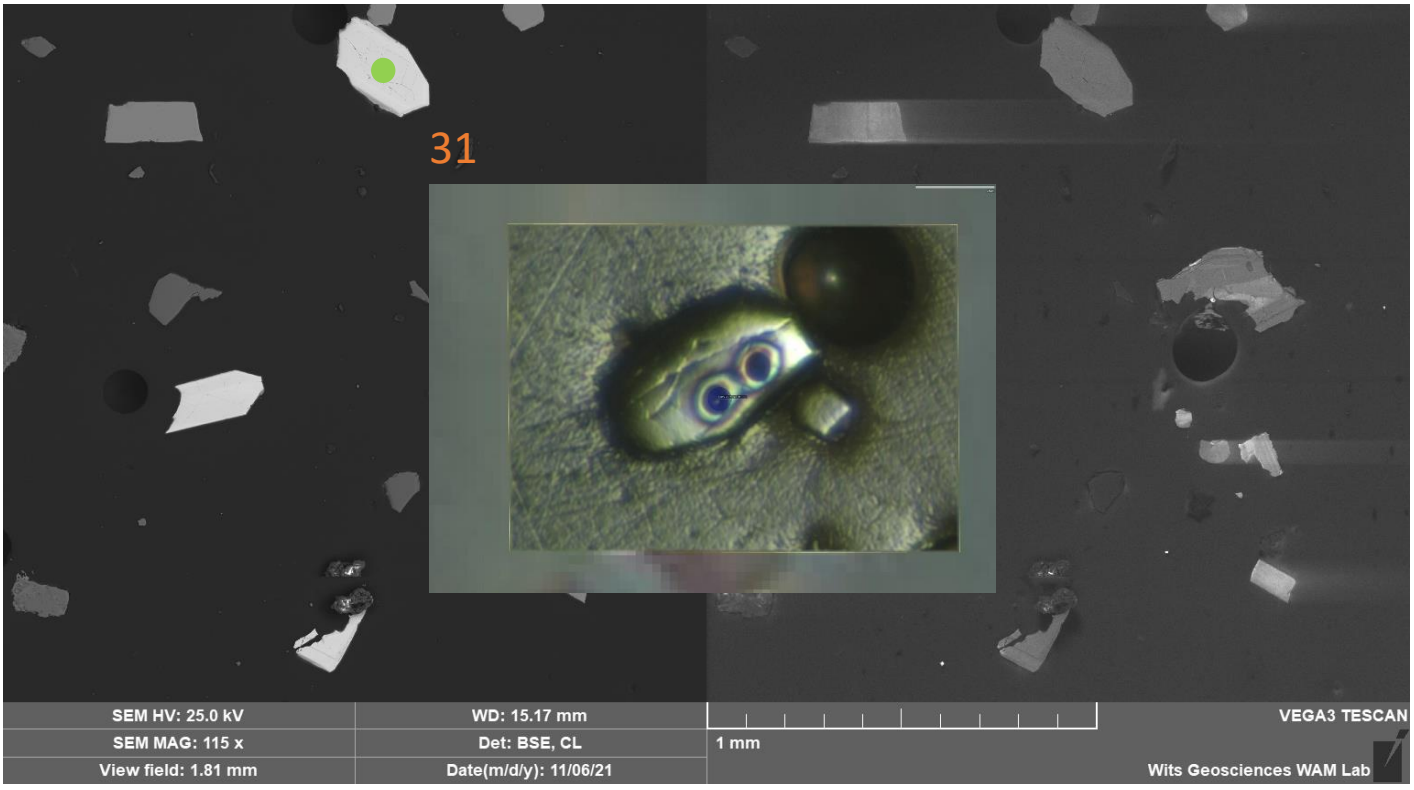

AJ-21-23-32

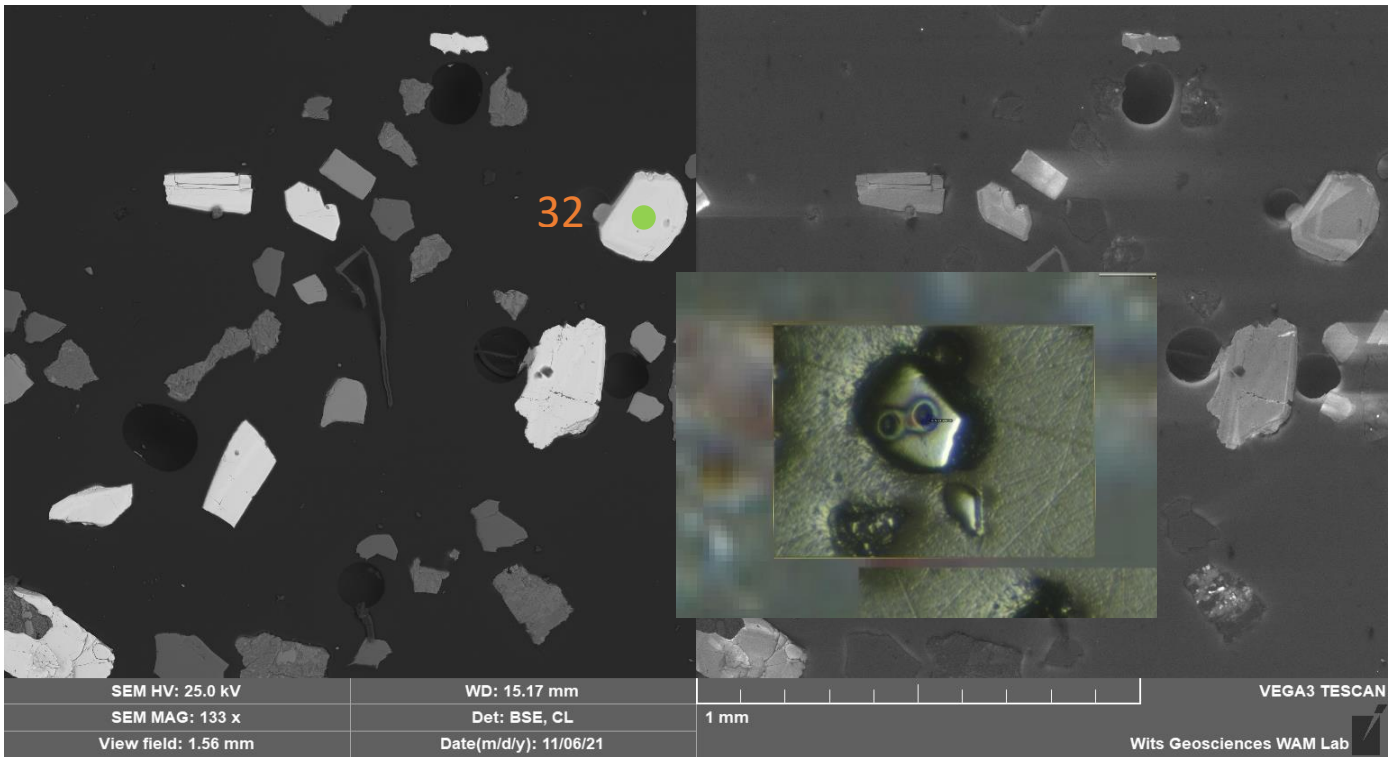

AJ-21-23-33

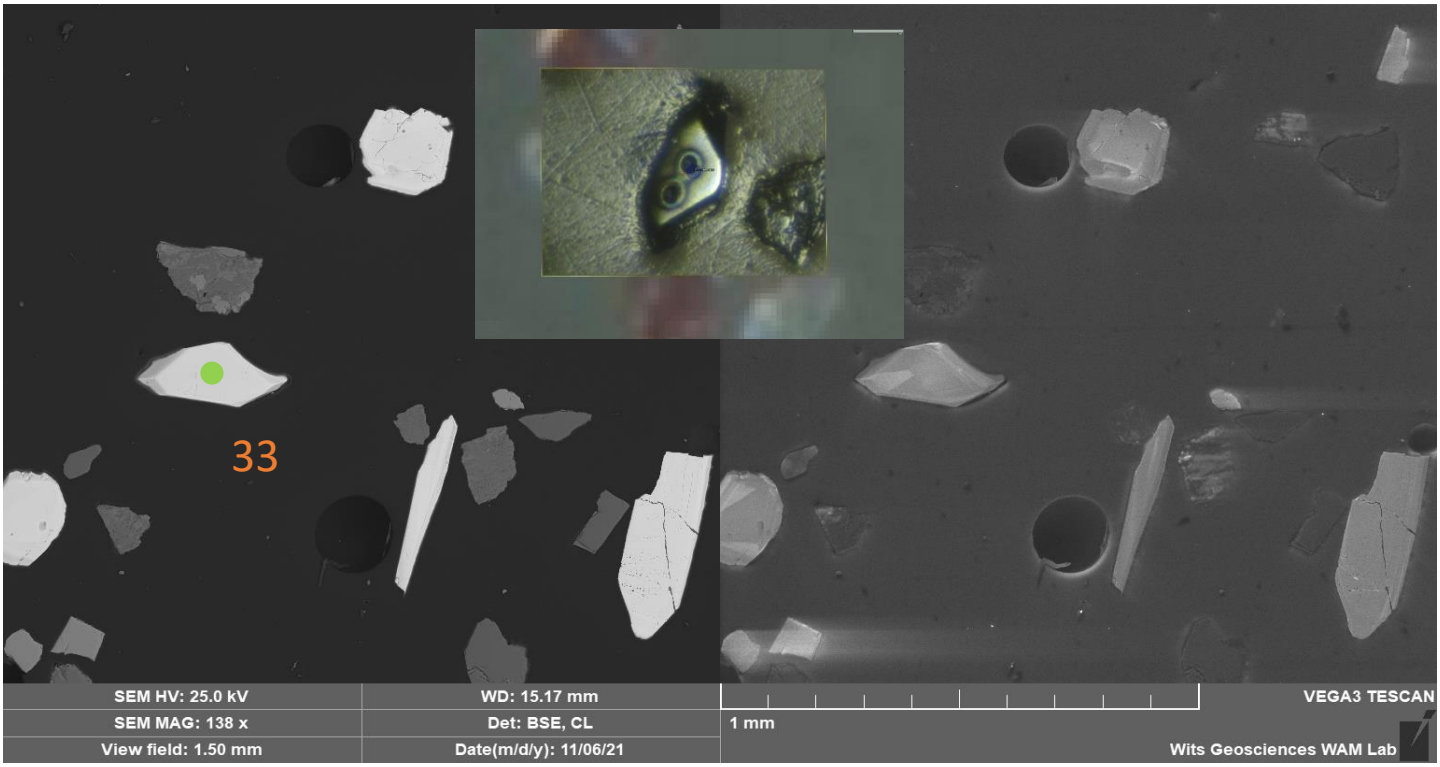

AJ-21-23-34/35

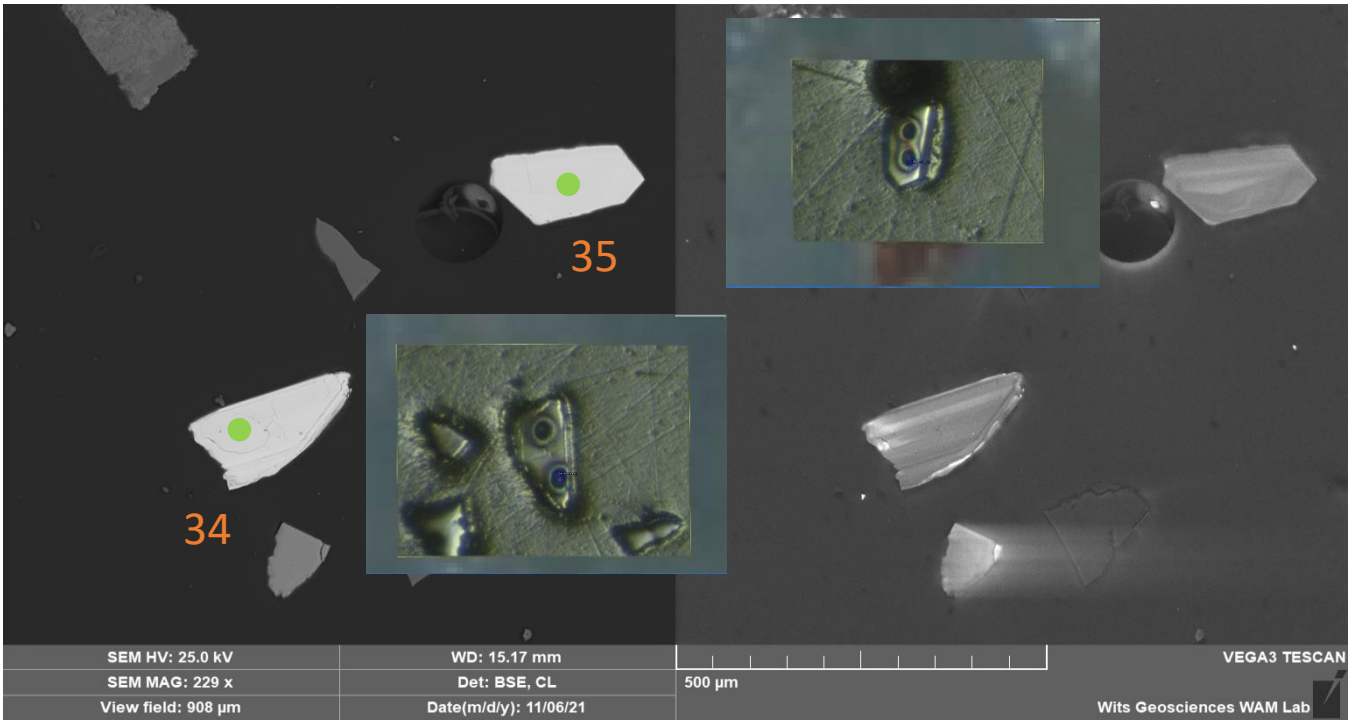

AJ-21-23-36

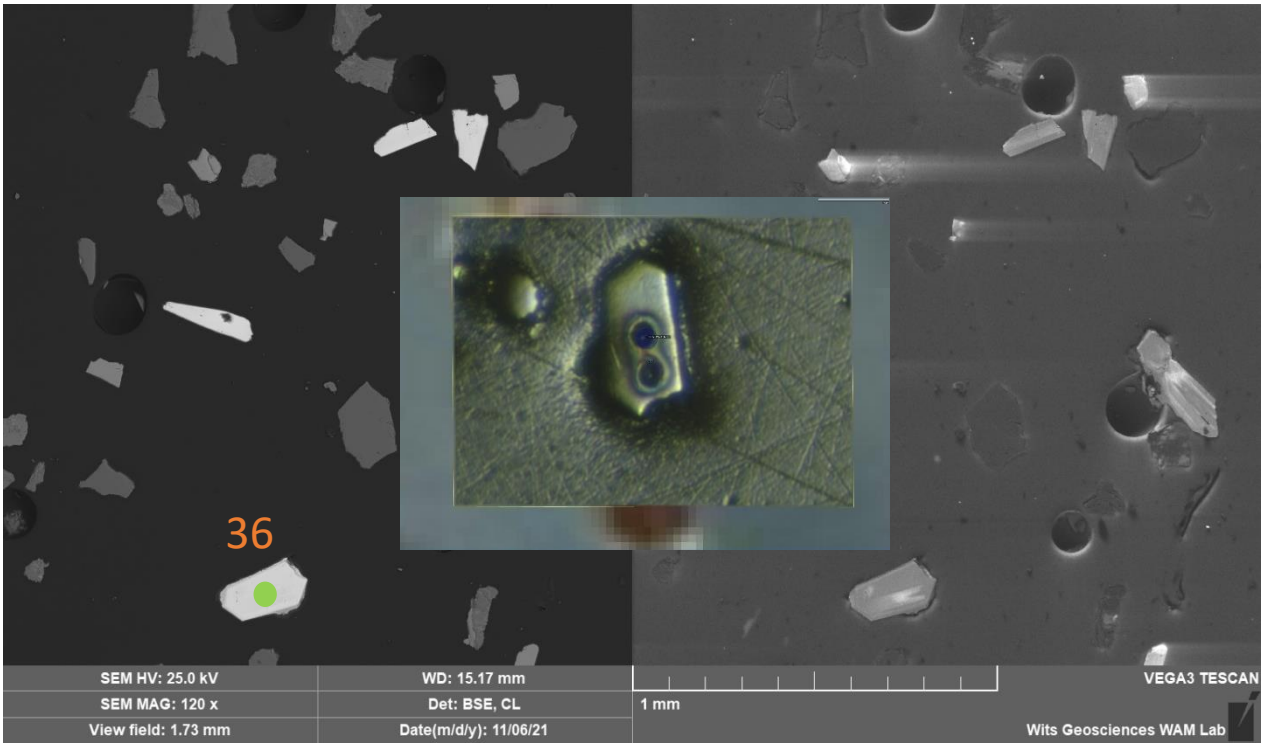

AJ-21-23-37/38

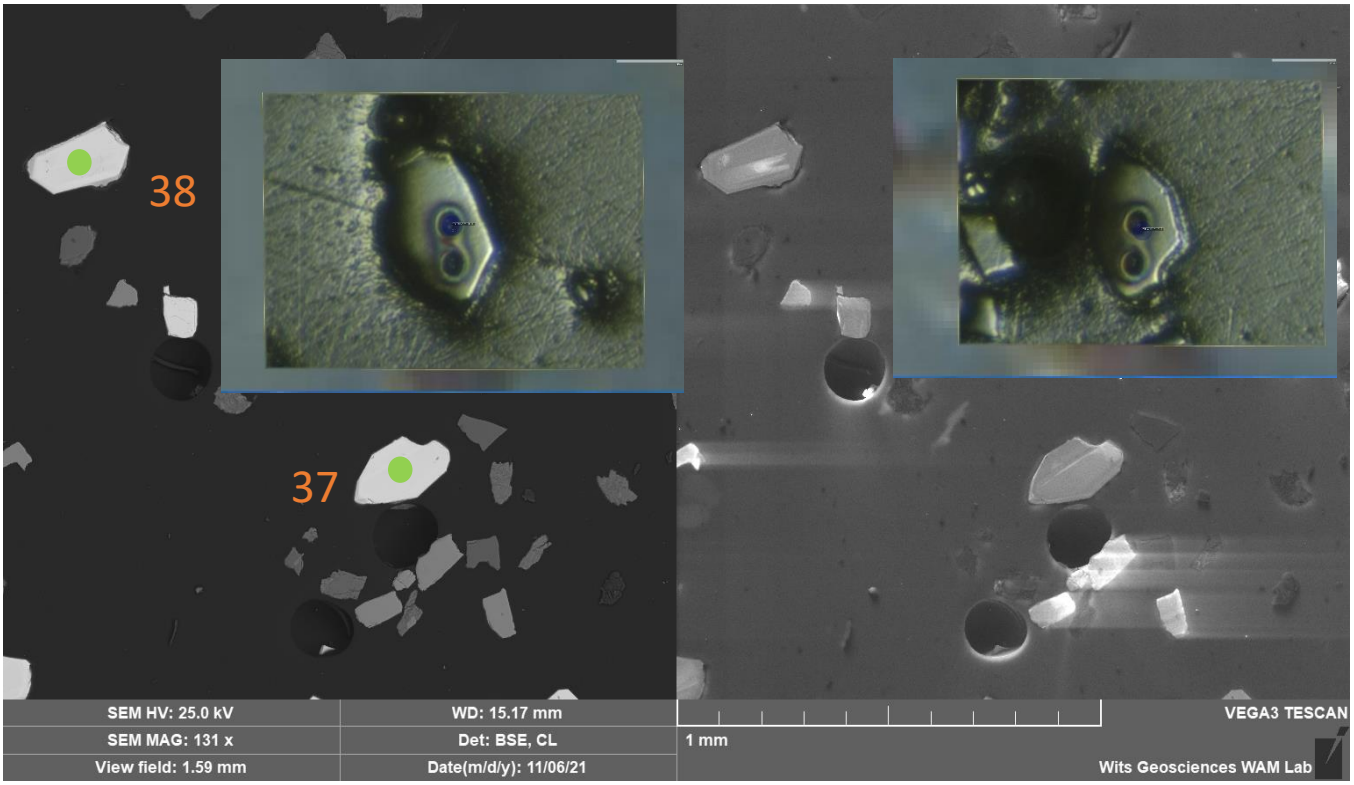

AJ-21-23-39

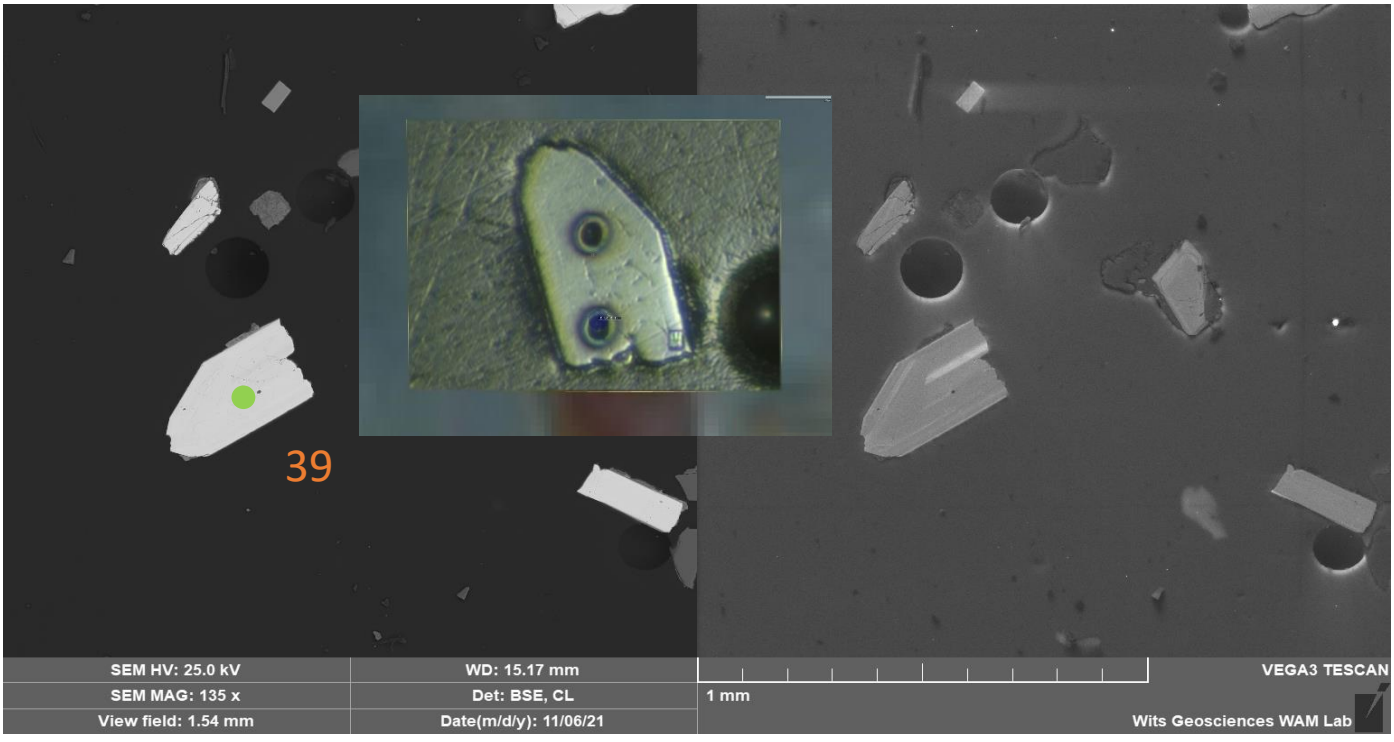

AJ-21-23-40

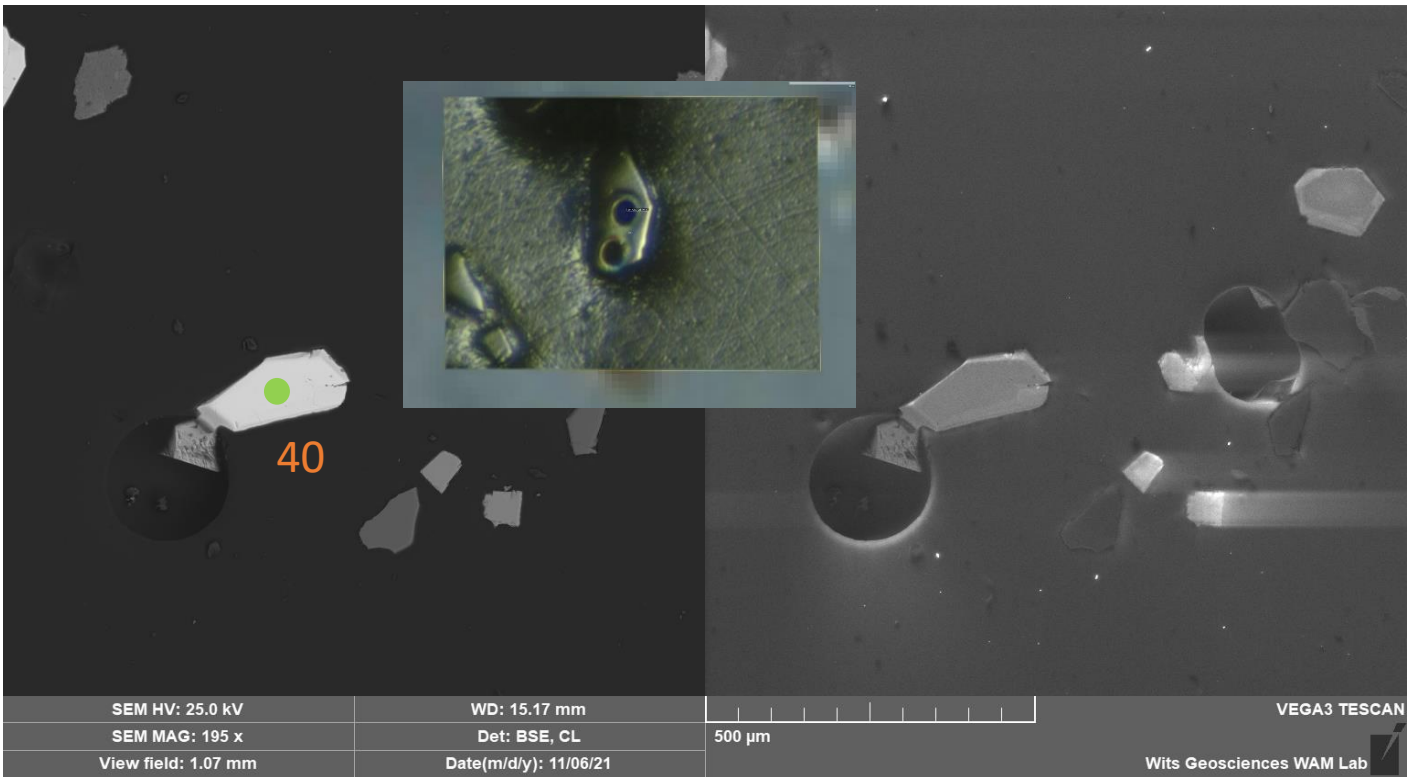
40
SEM HV: 25.0 kV
WD: 15.17 mm
VEGA3 TESCAN
SEM MAG: 195 x
Det: BSE, CL
500 µm
View field: 1.07 mm
Date(m/d/y): 11/06/21
Wits Geosciences WAM Lab

AJ-21-29-1/2

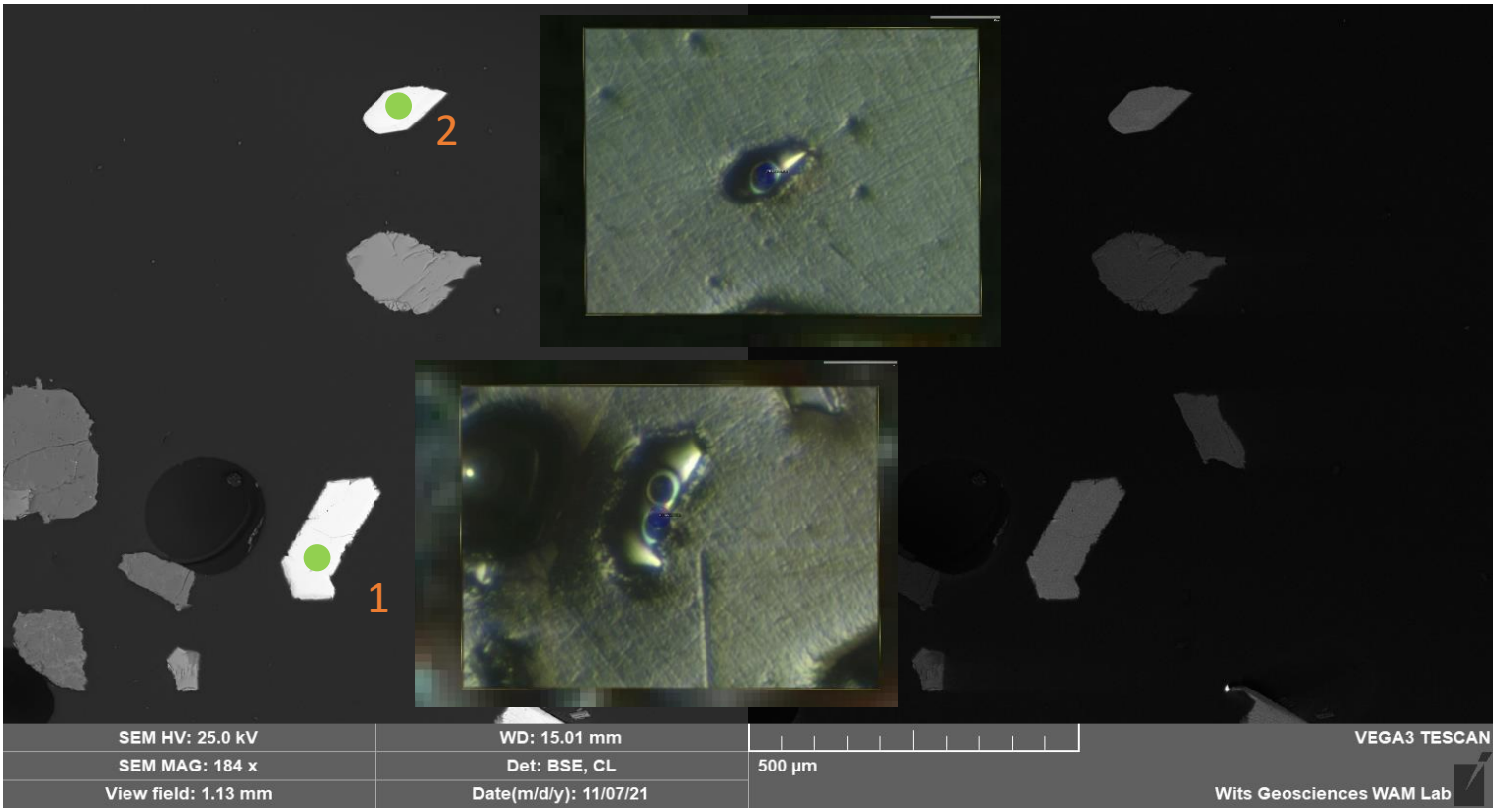

AJ-21-29-3

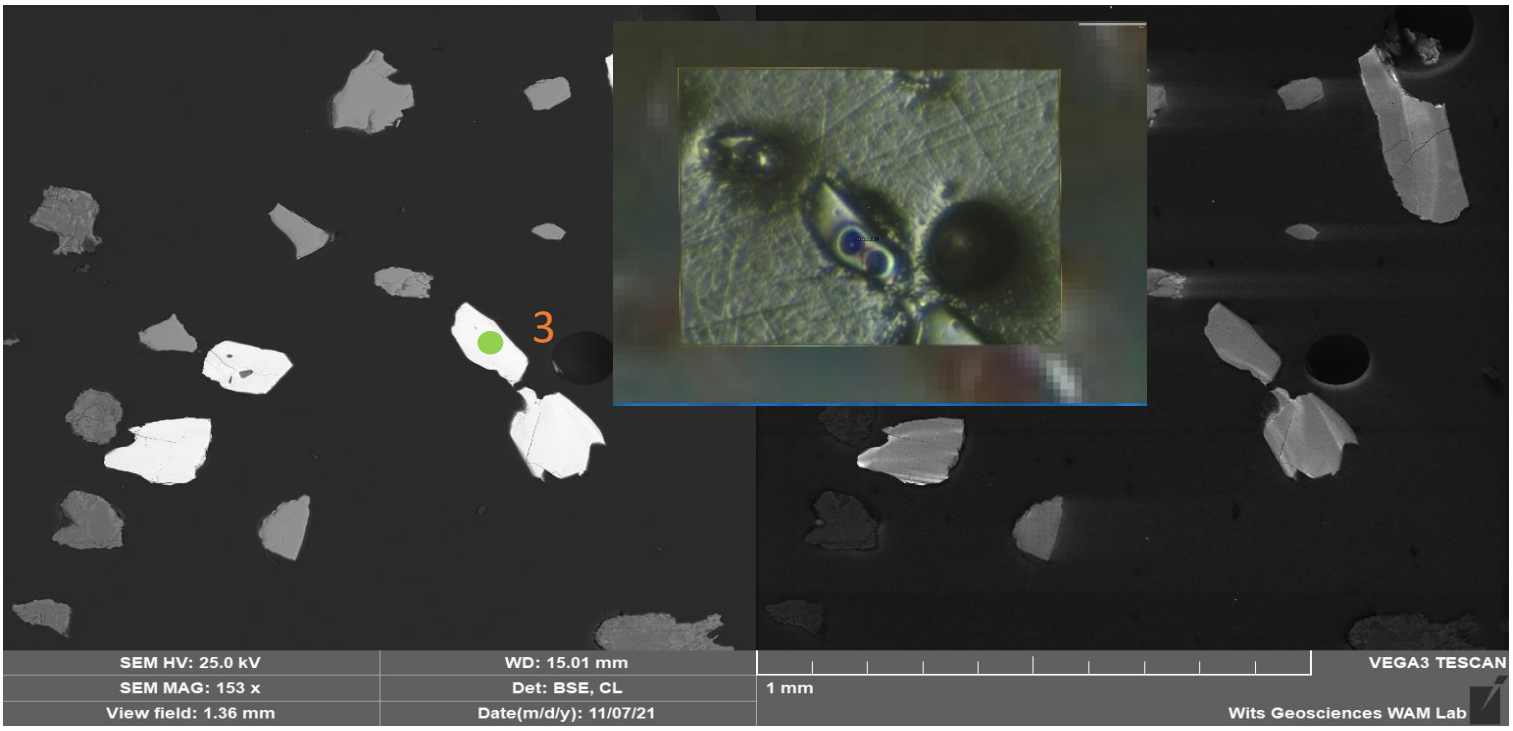

AJ-21-29-4

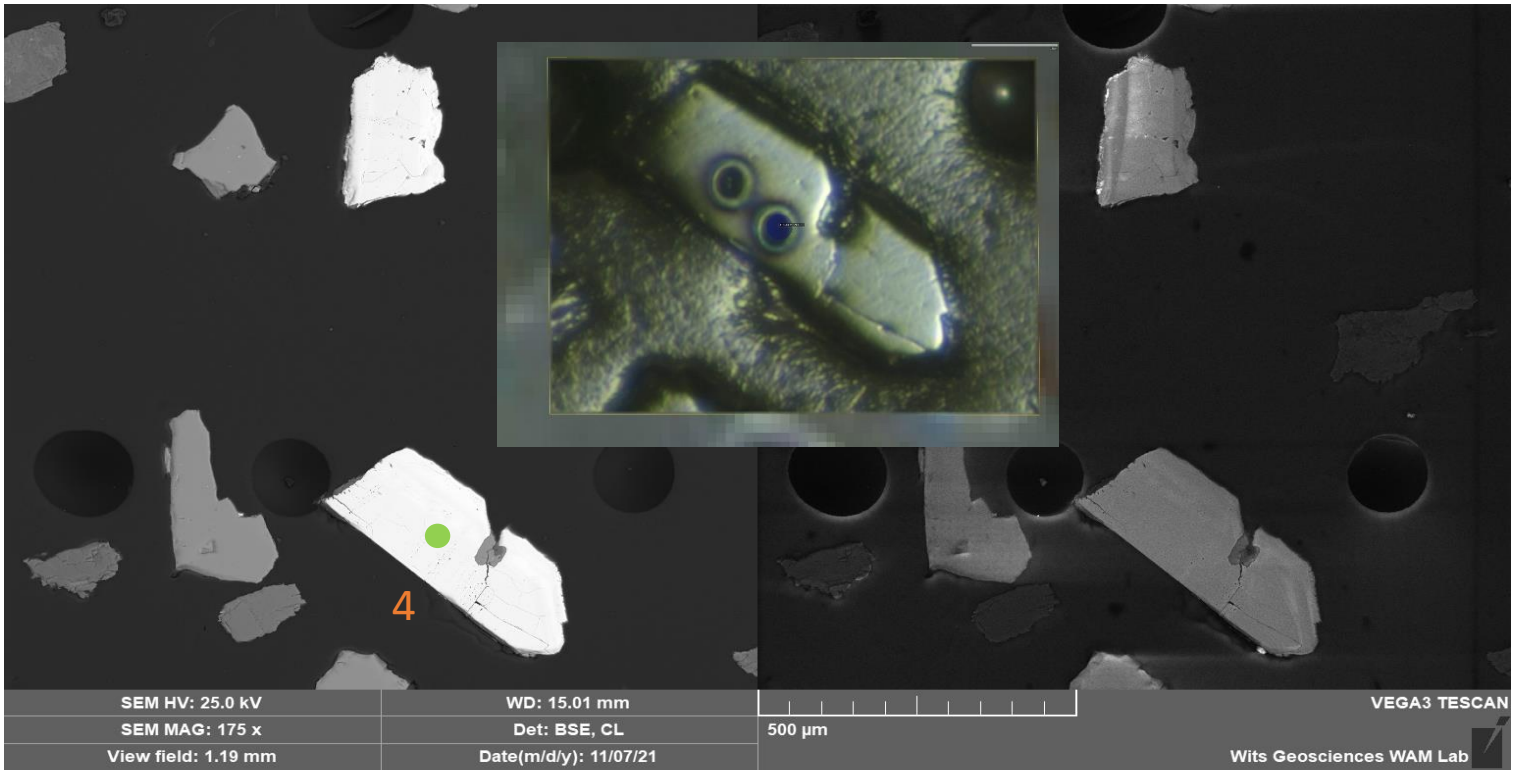

AJ-21-29-5/6

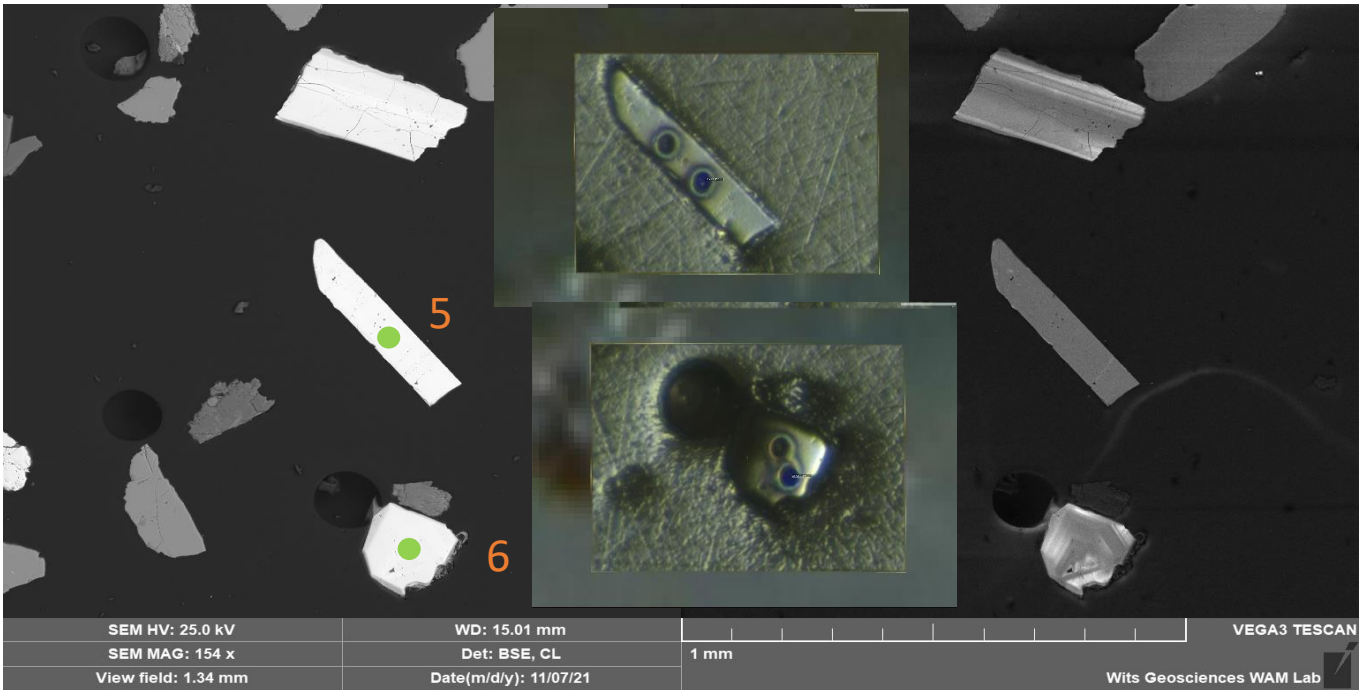

AJ-21-29-7/8

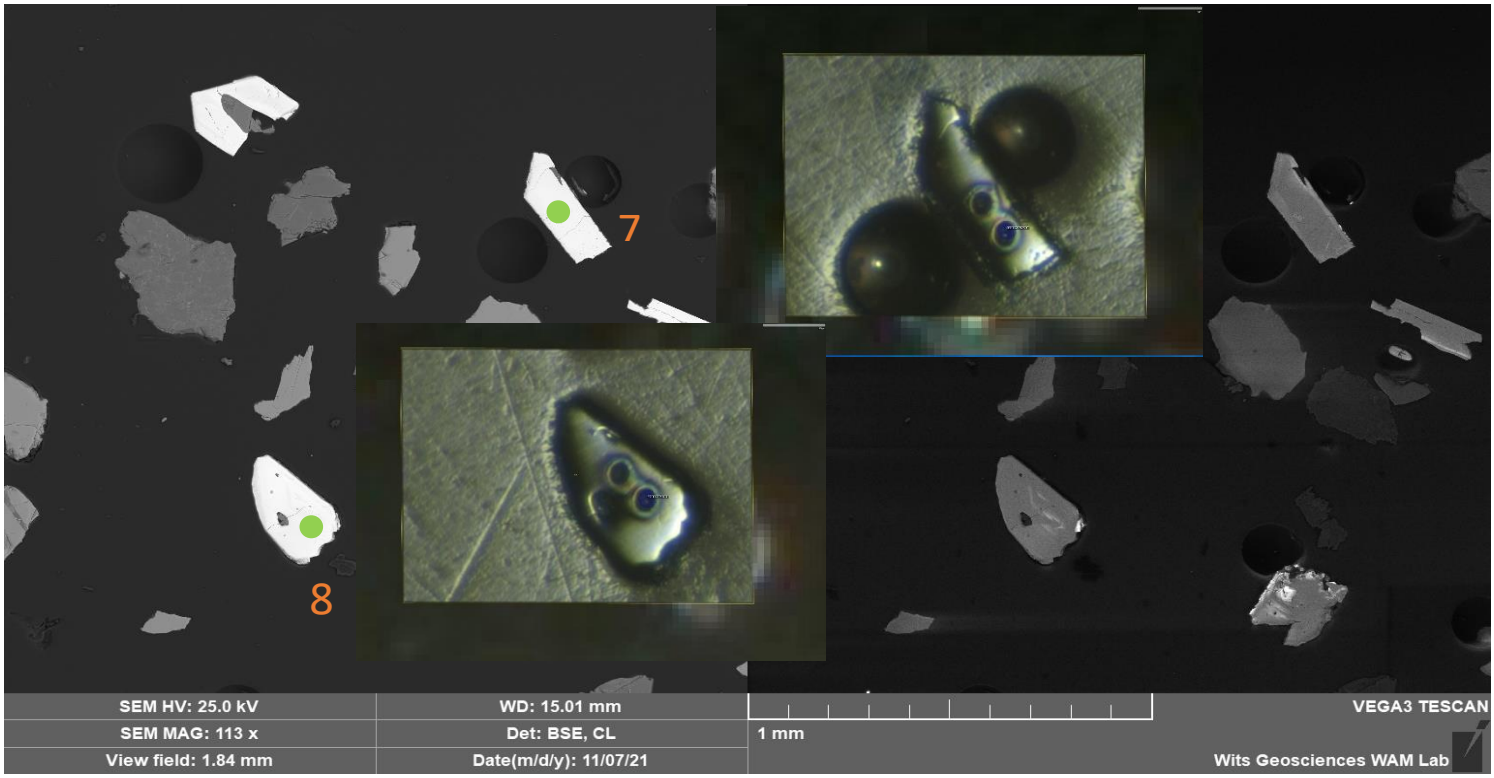

AJ-21-29-9/10

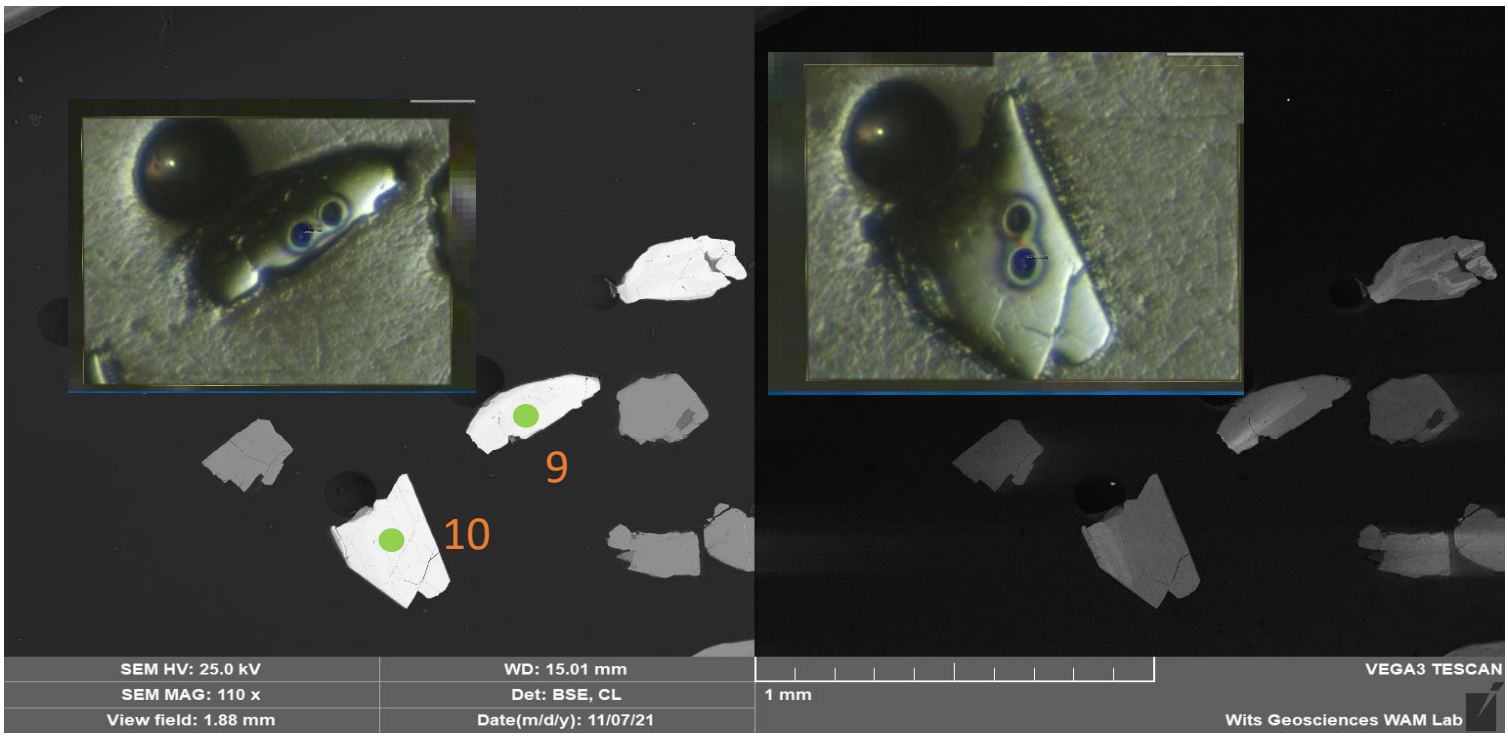

AJ-21-29-11

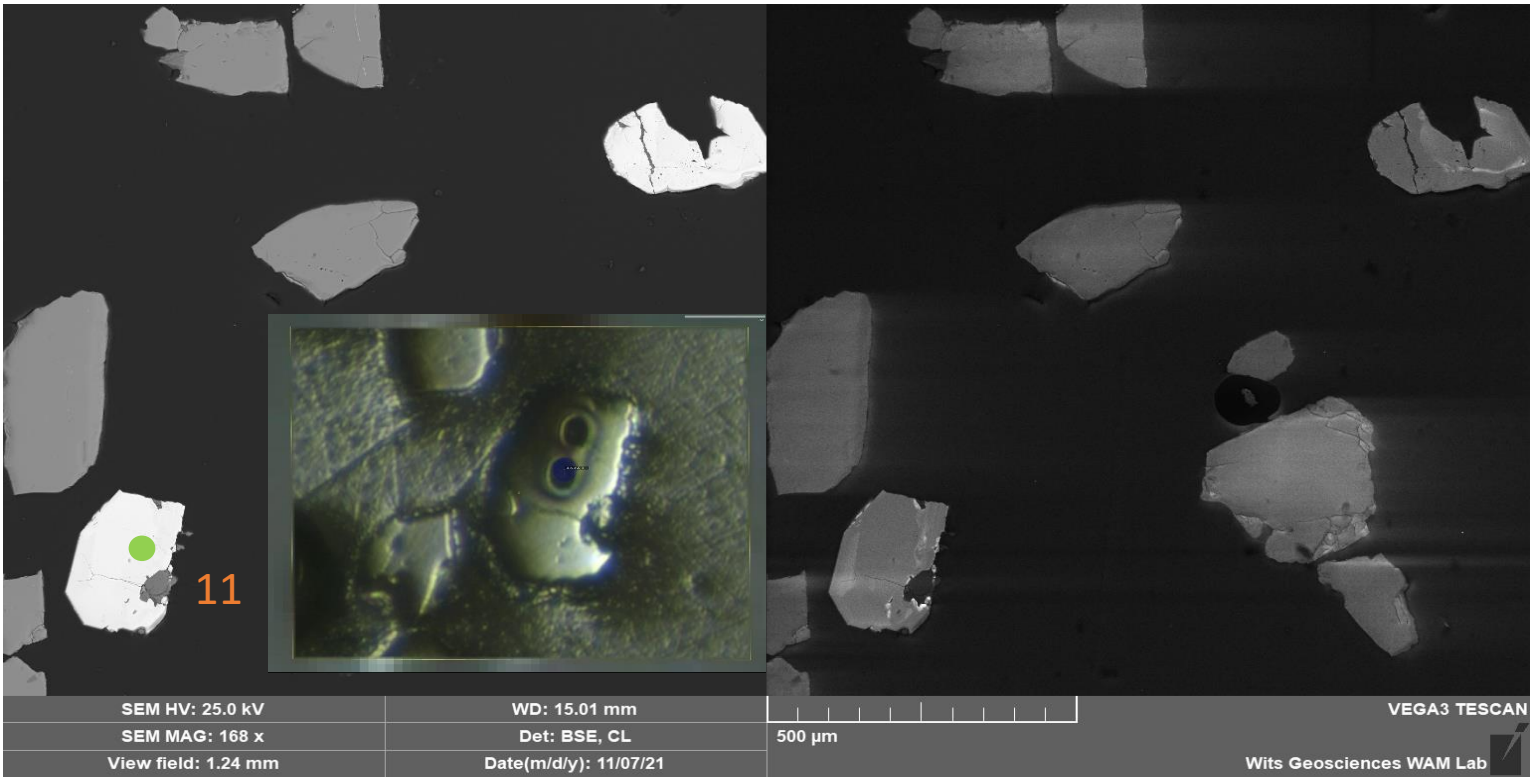

AJ-21-29-12

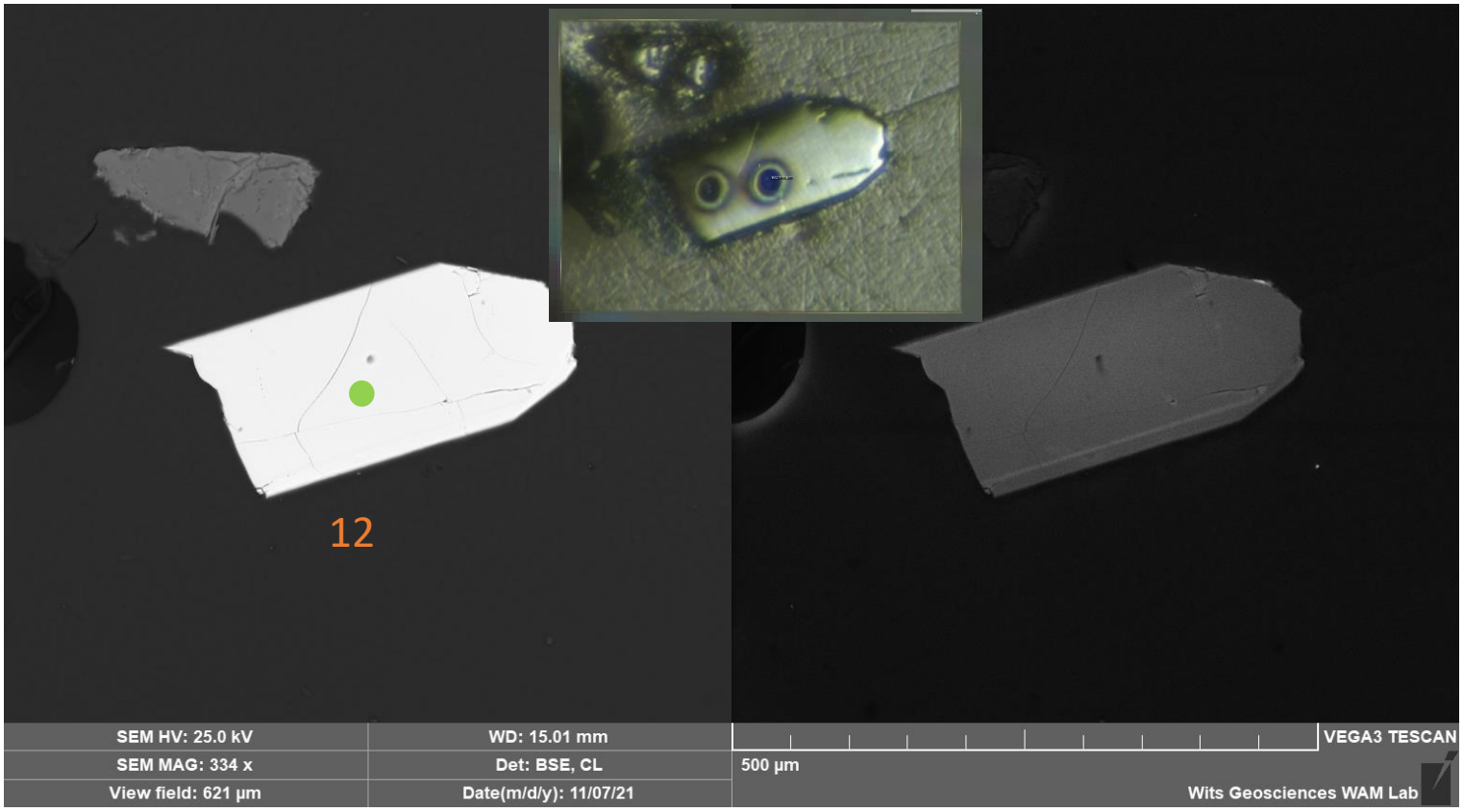

AJ-21-29-14

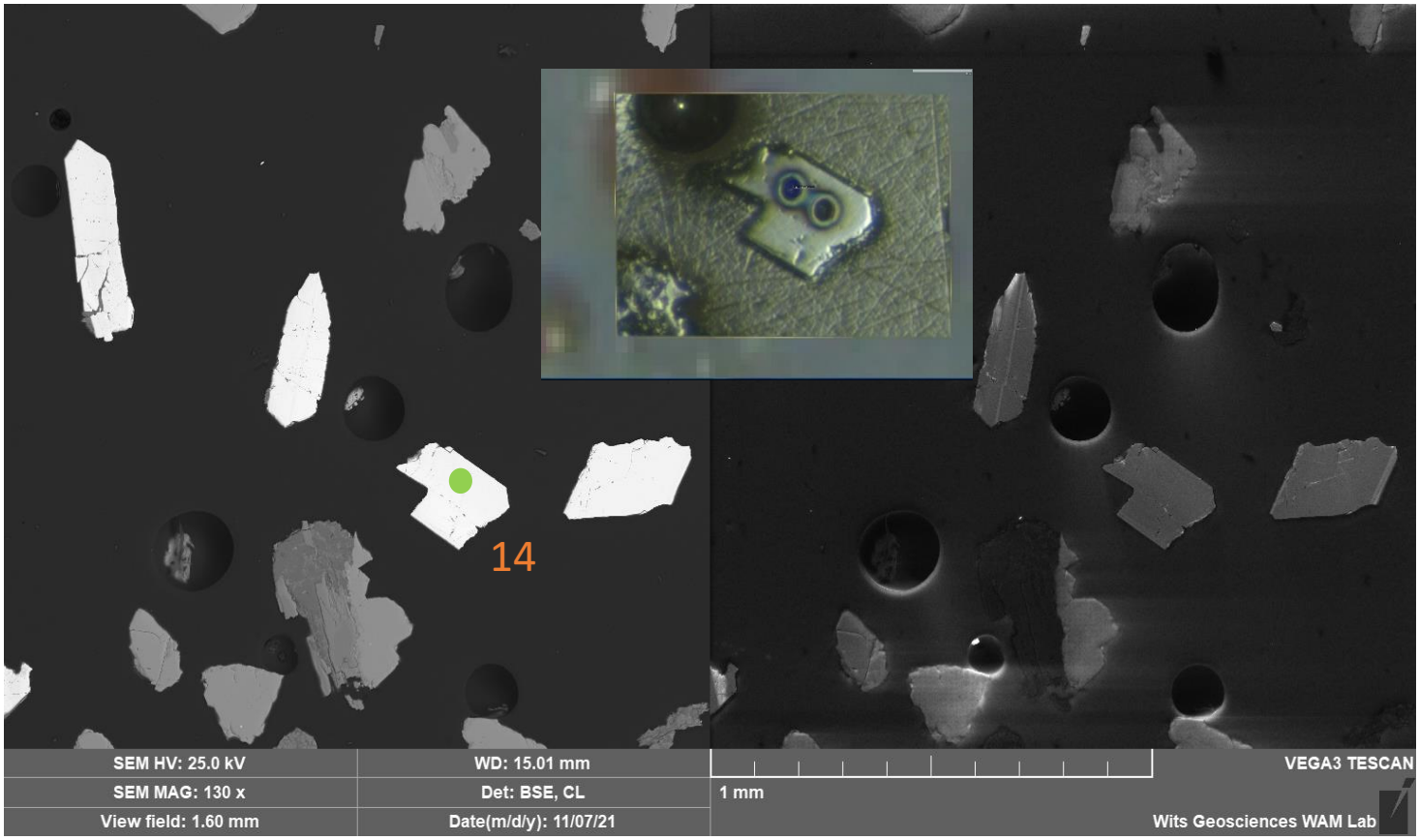

AJ-21-29-15

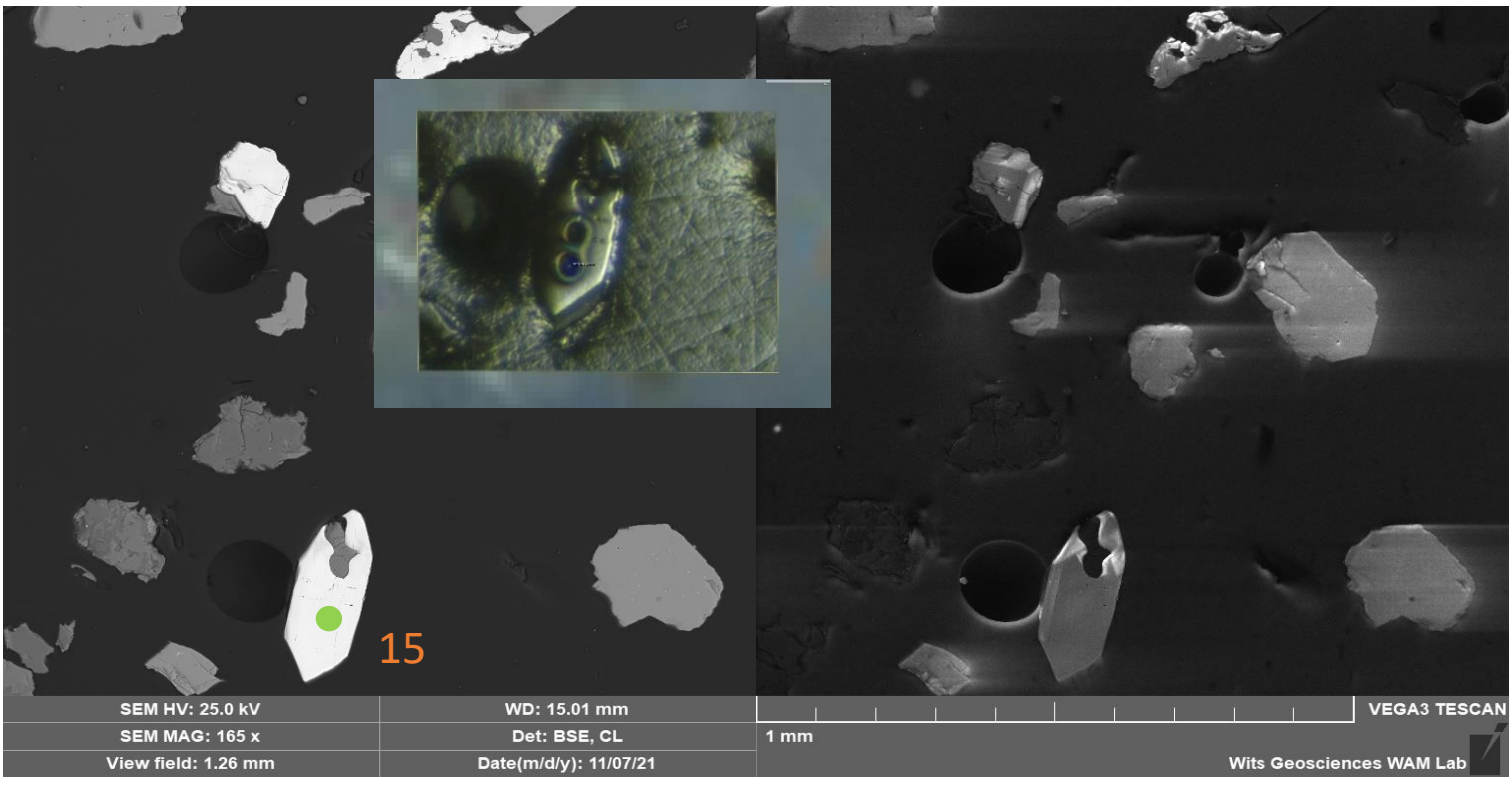

AJ-21-29-16

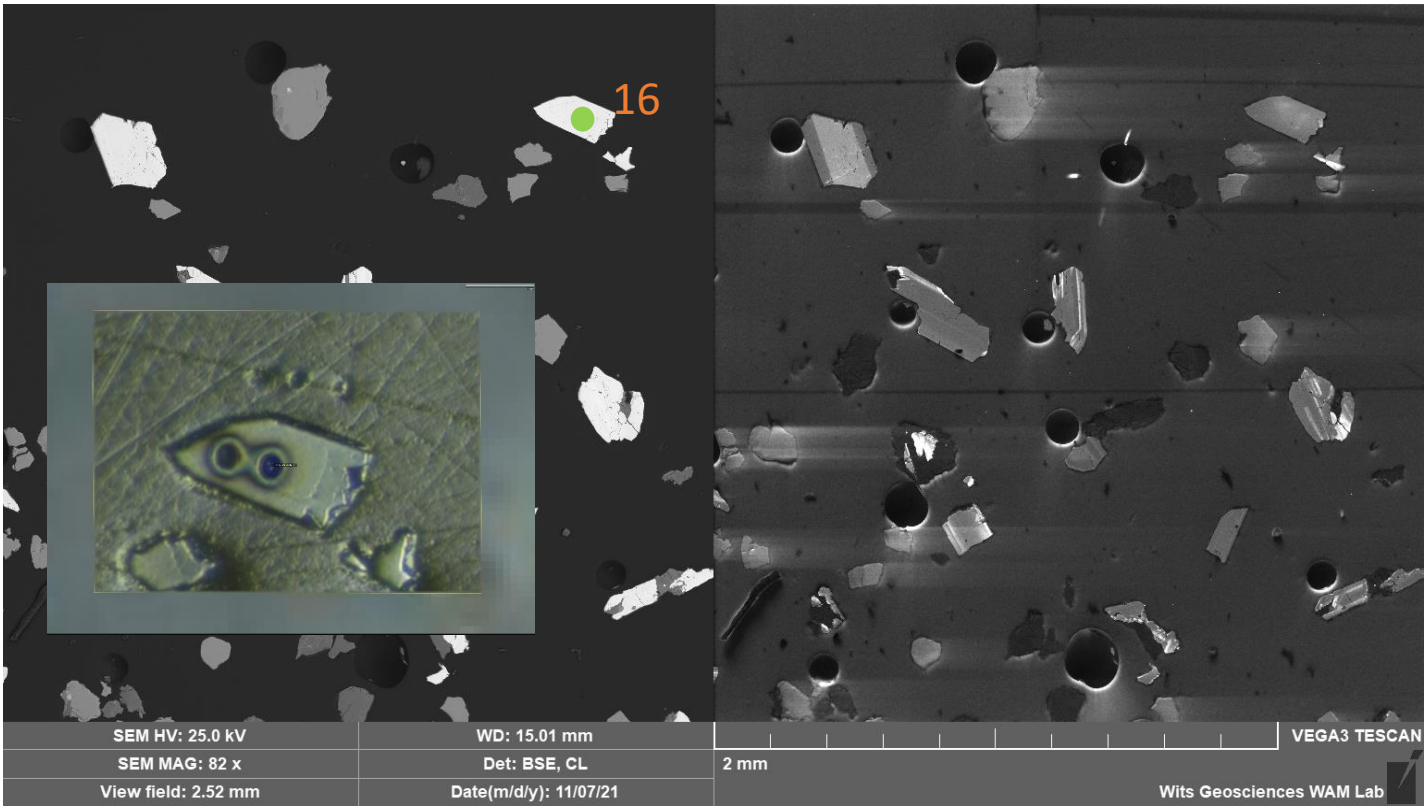

AJ-21-29-17

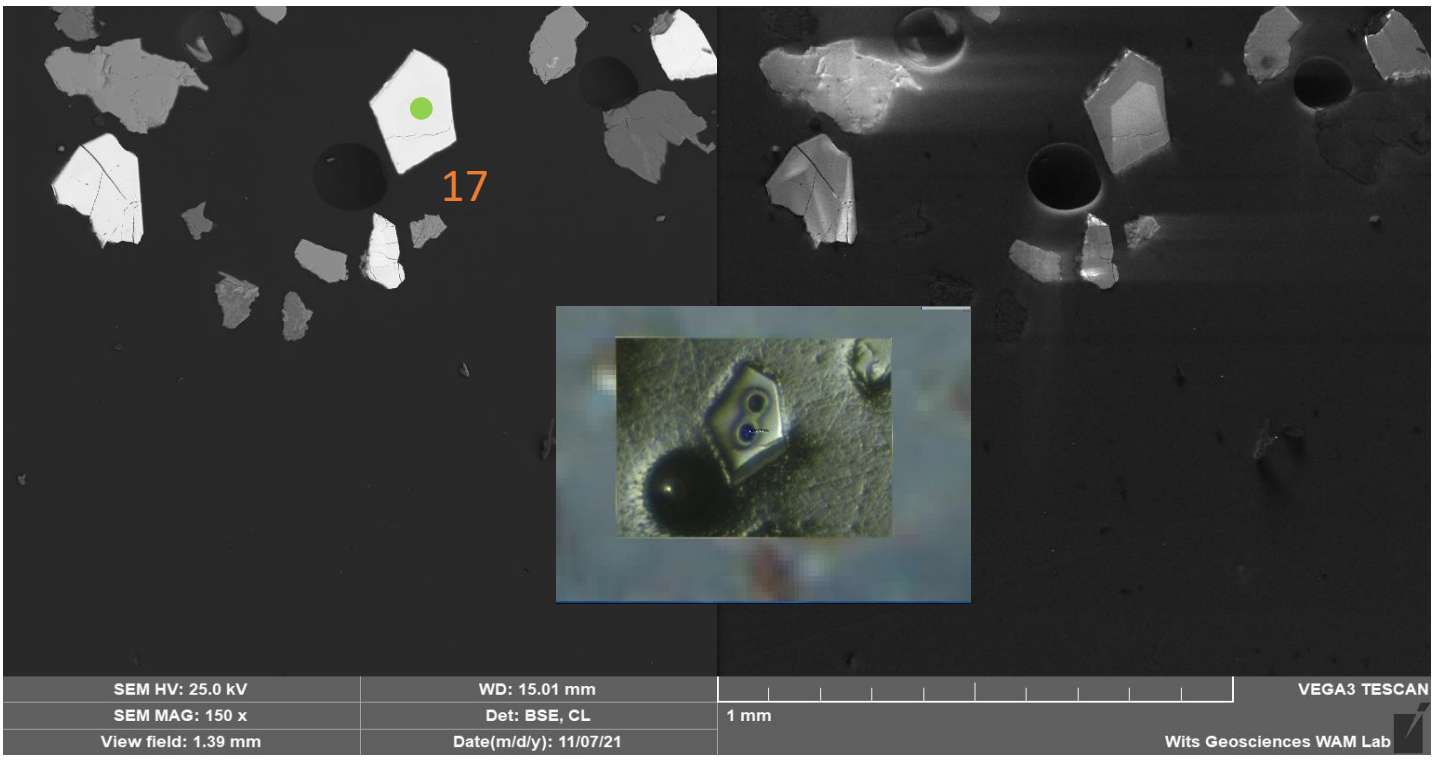

AJ-21-29-18

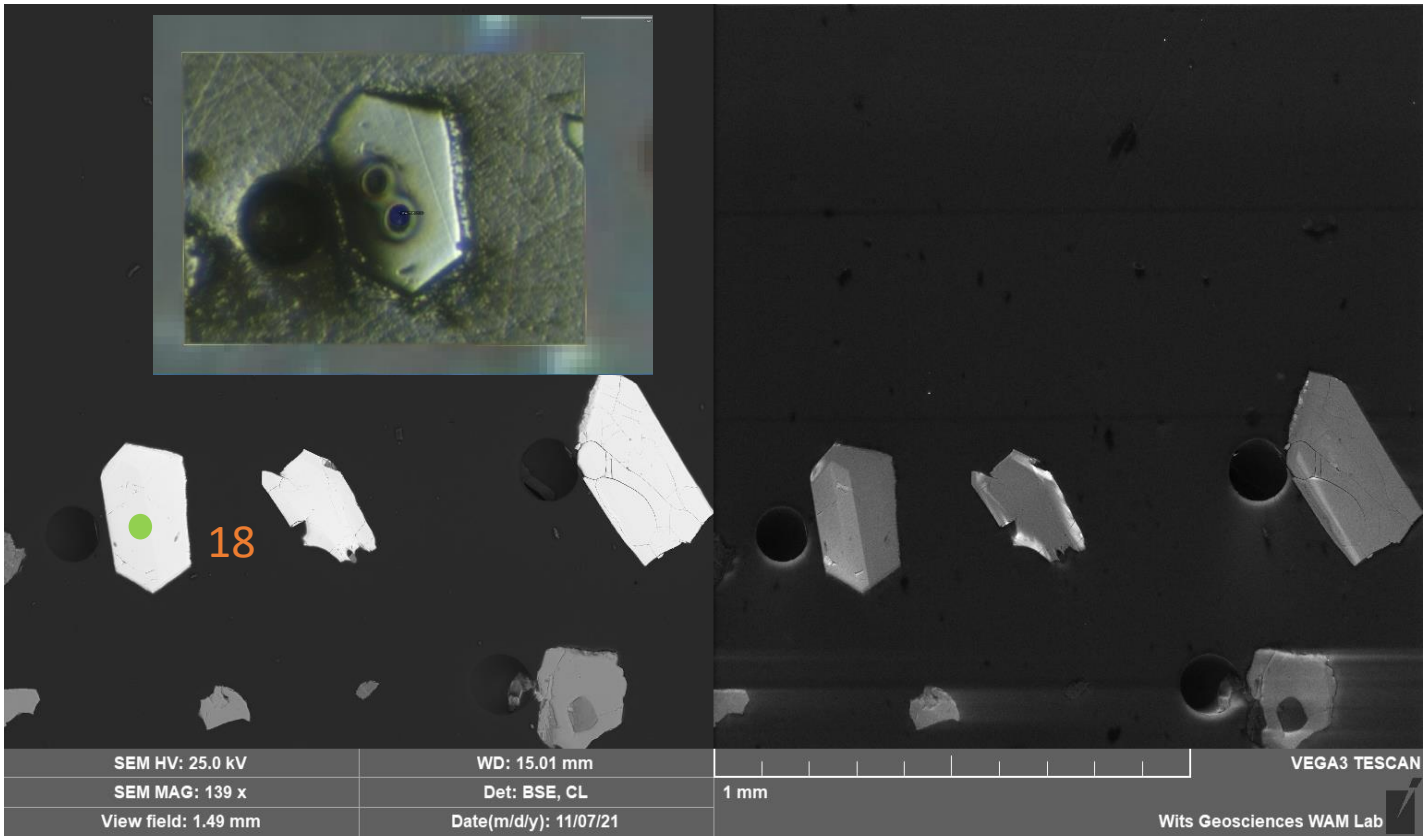

AJ-21-29-19/20

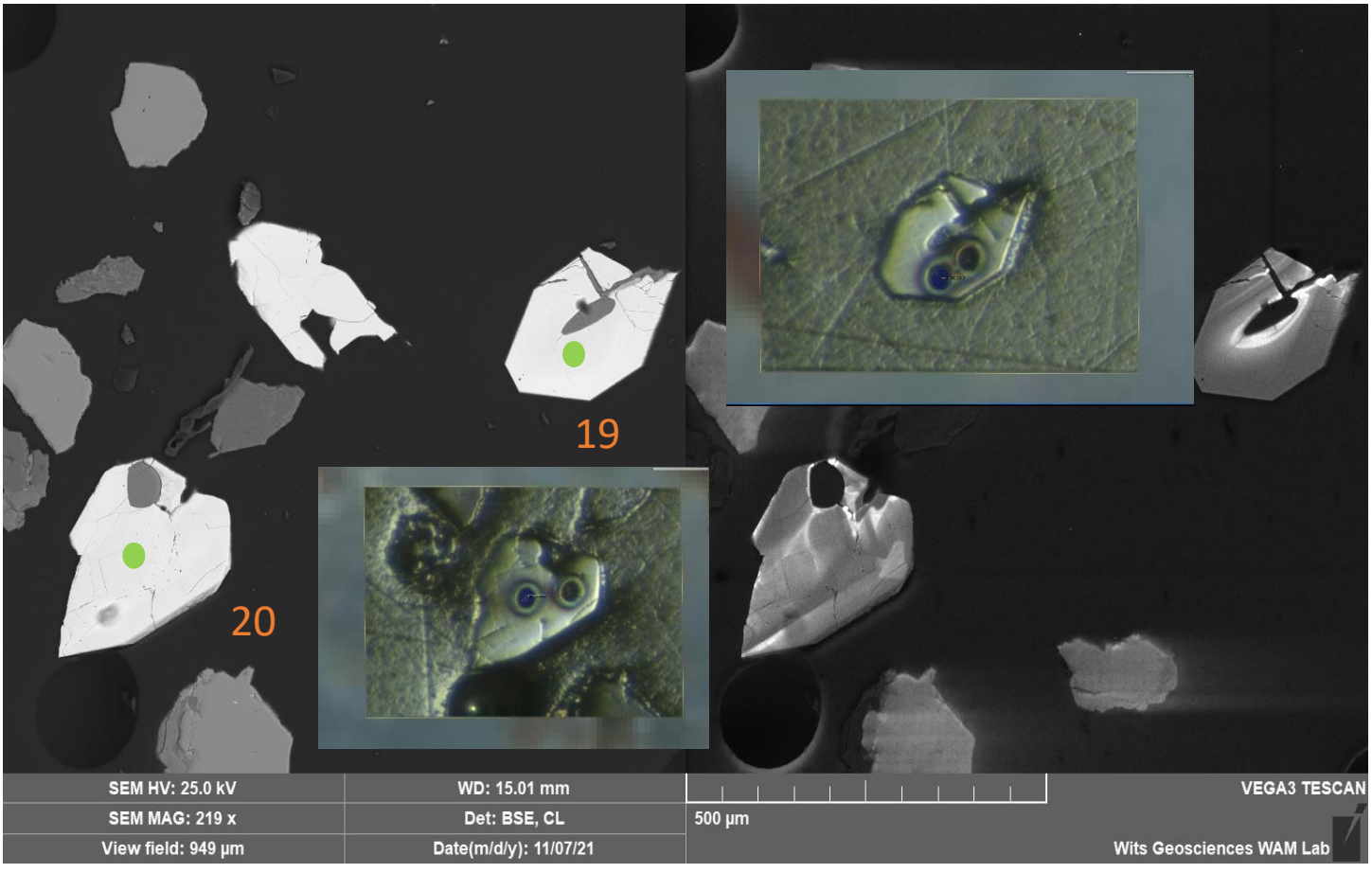

AJ-21-29-21

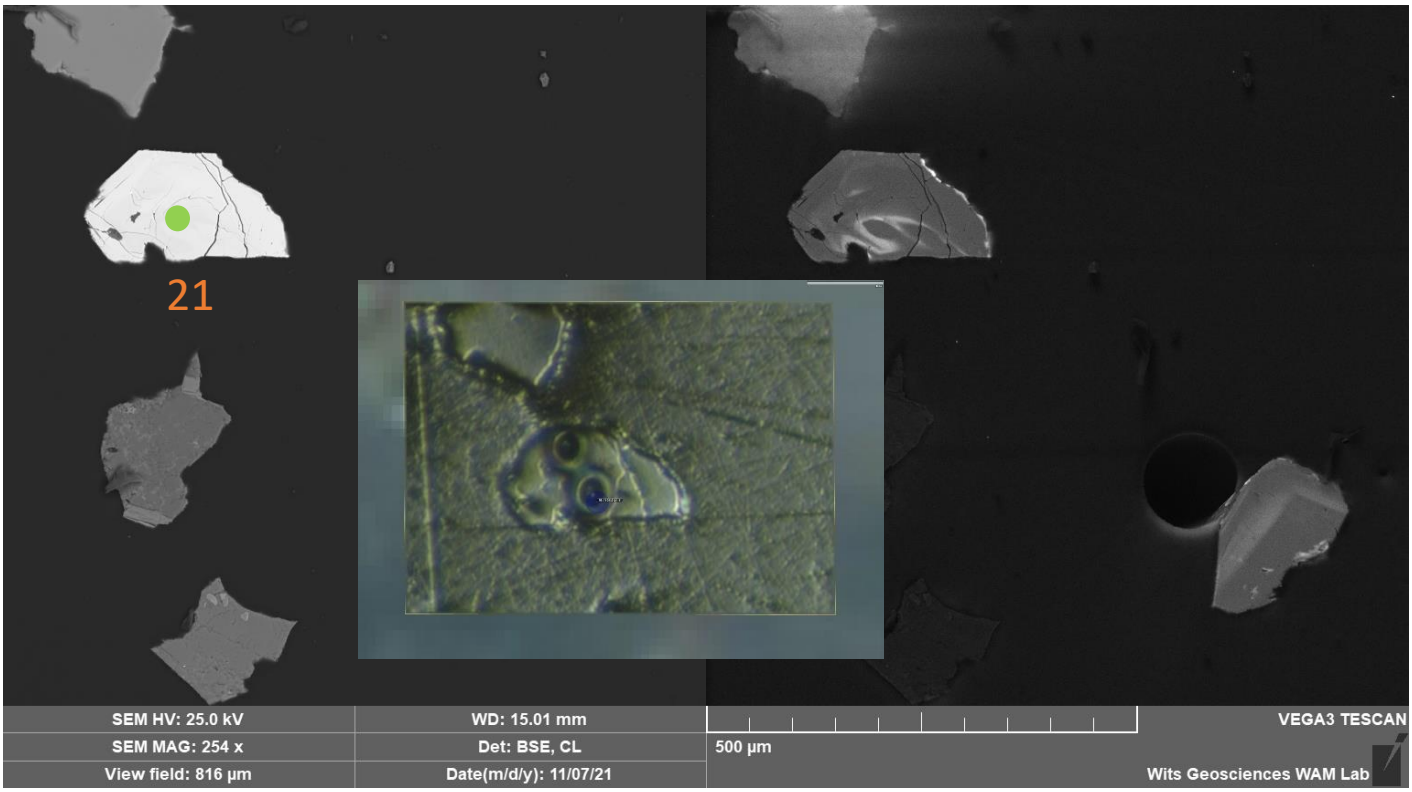

AJ-21-29-22

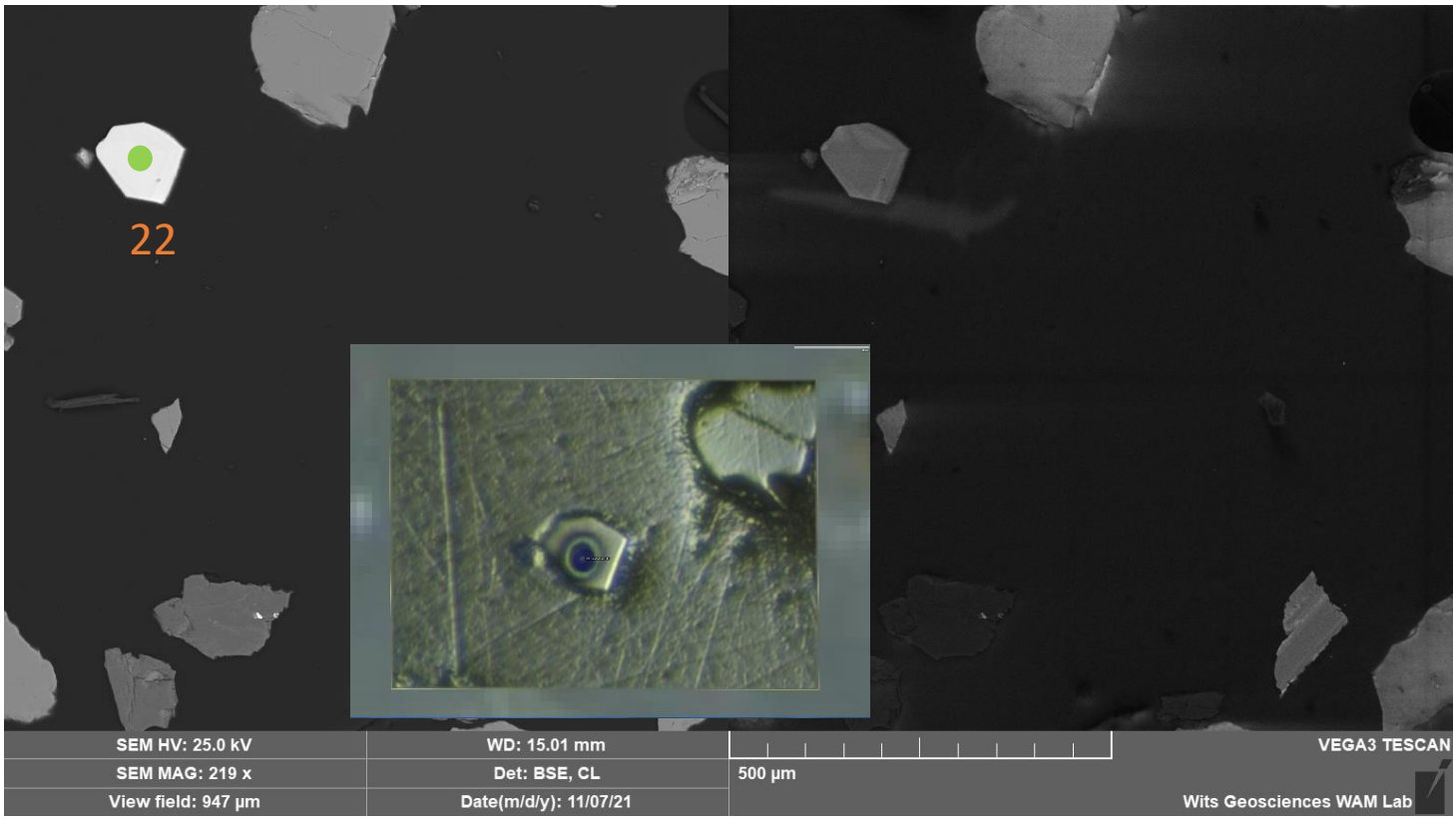

AJ-21-29-23/24/25

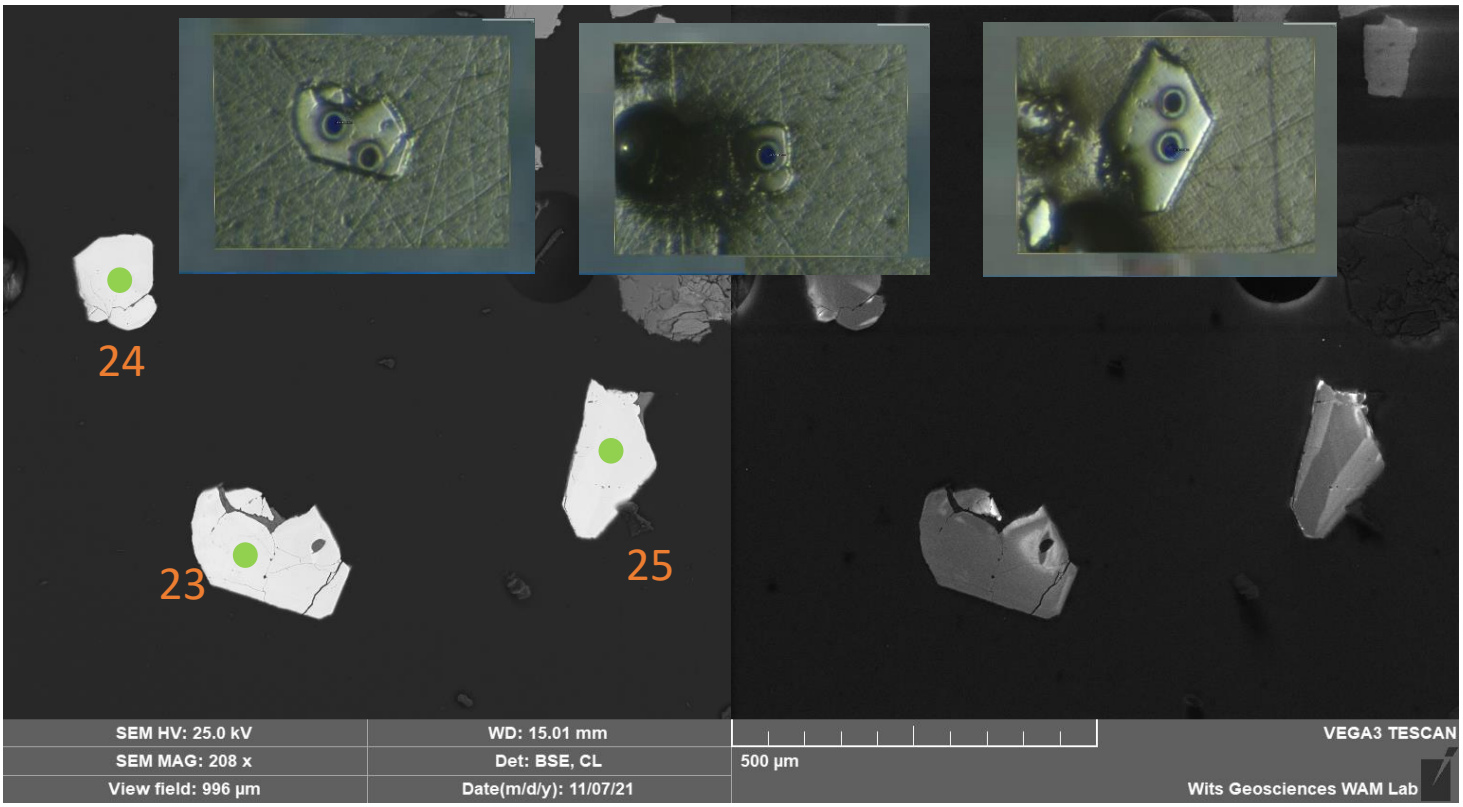

AJ-21-29-26

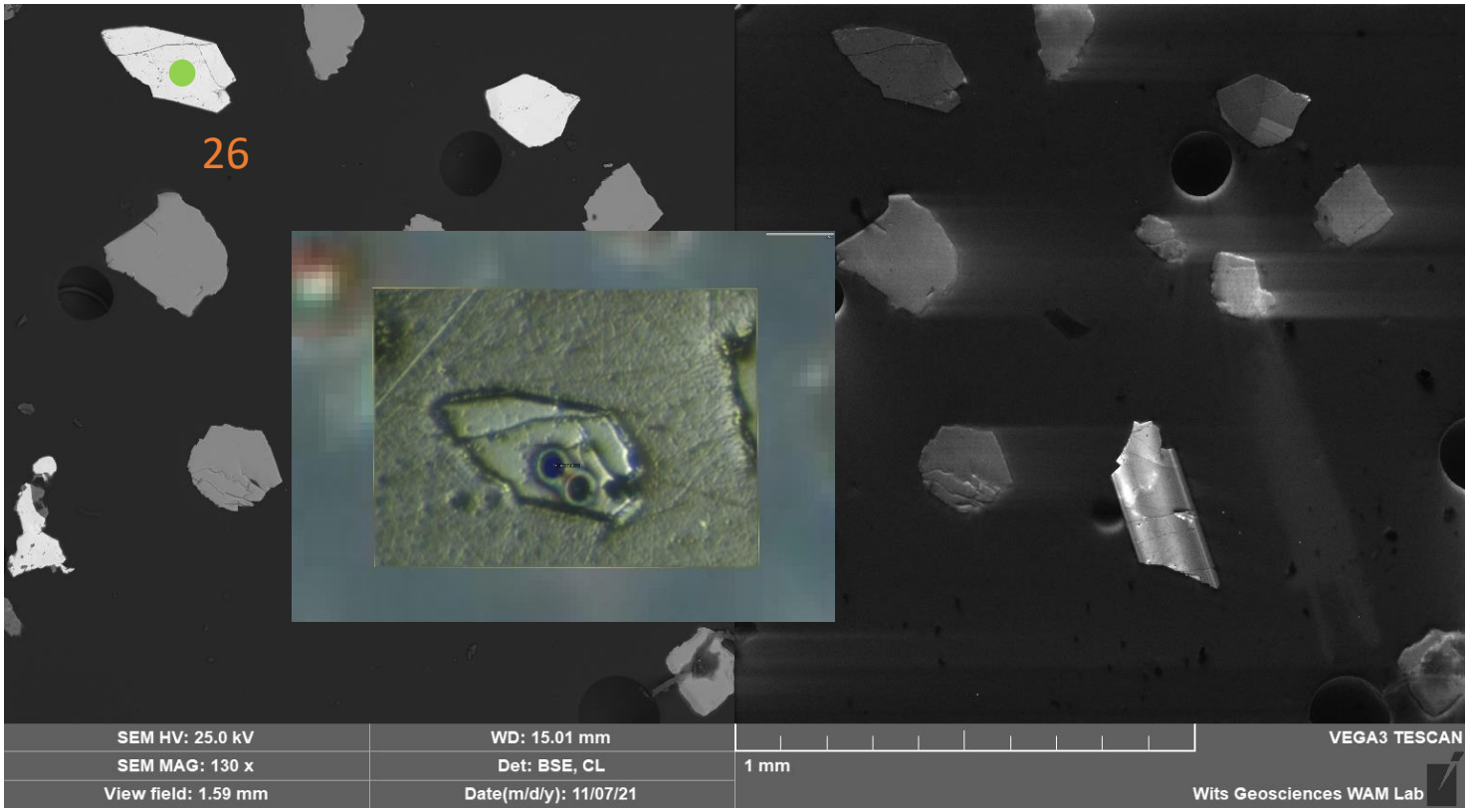

AJ-21-29-27

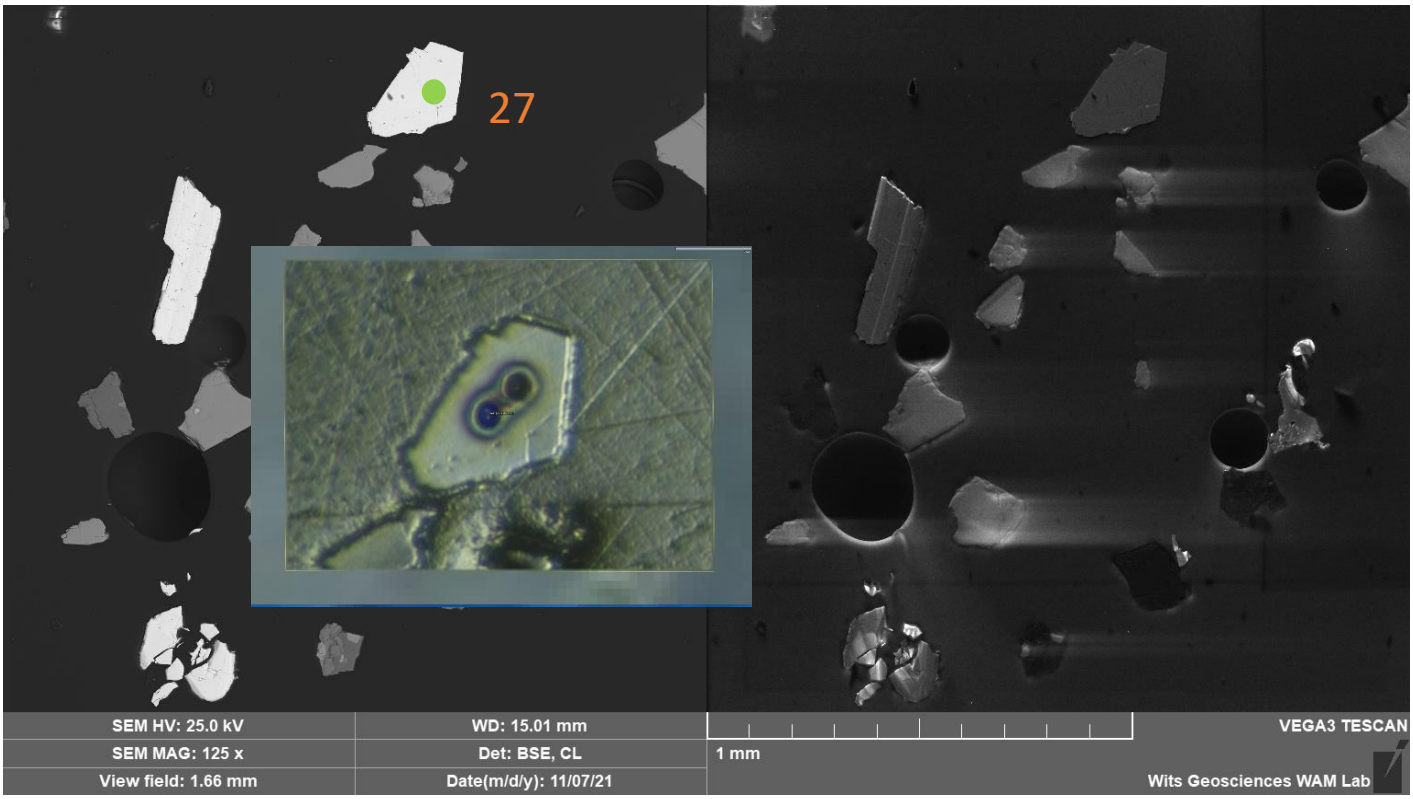

AJ-21-29-28

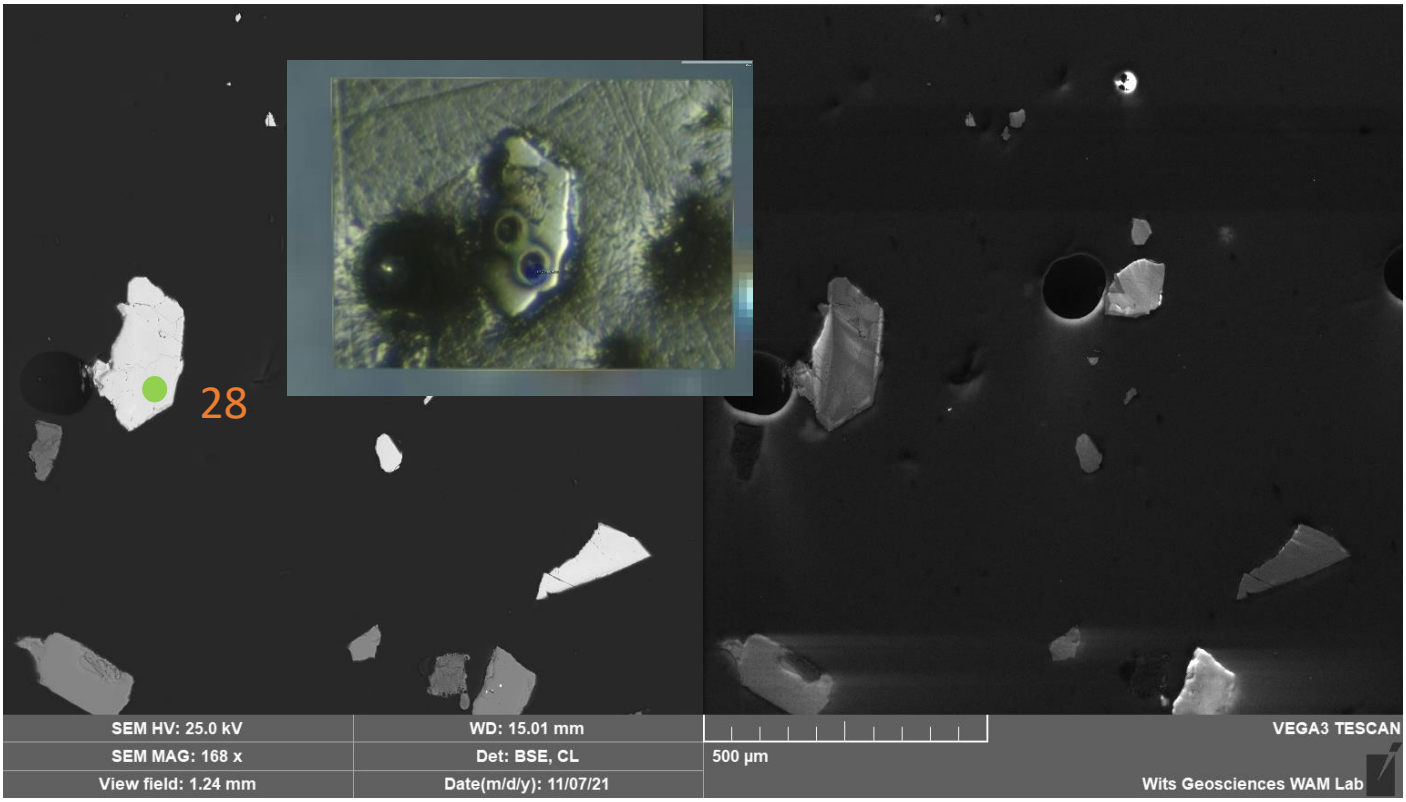

AJ-21-29-29/30/31/32

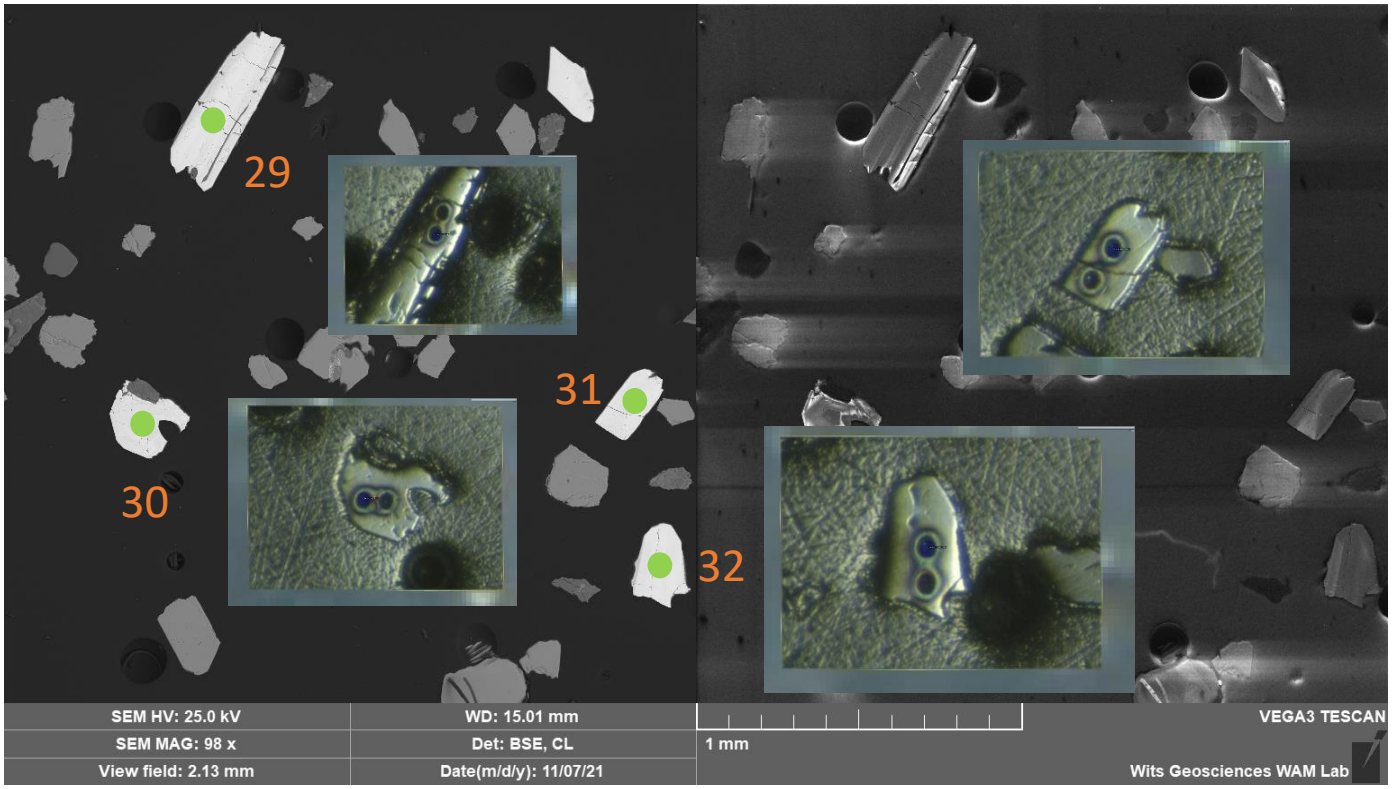

AJ-21-29-34/35/36

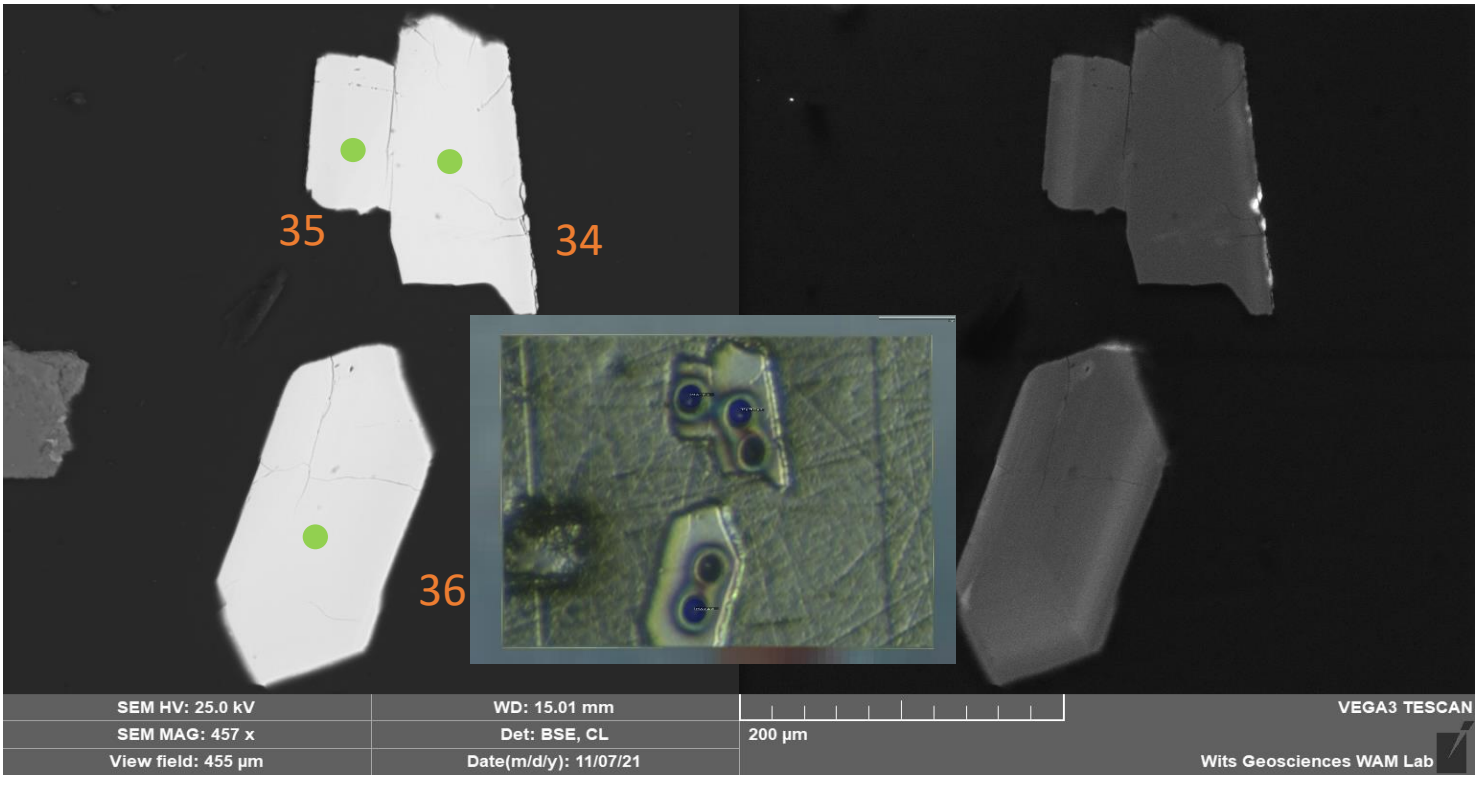

AJ-21-29-37/38

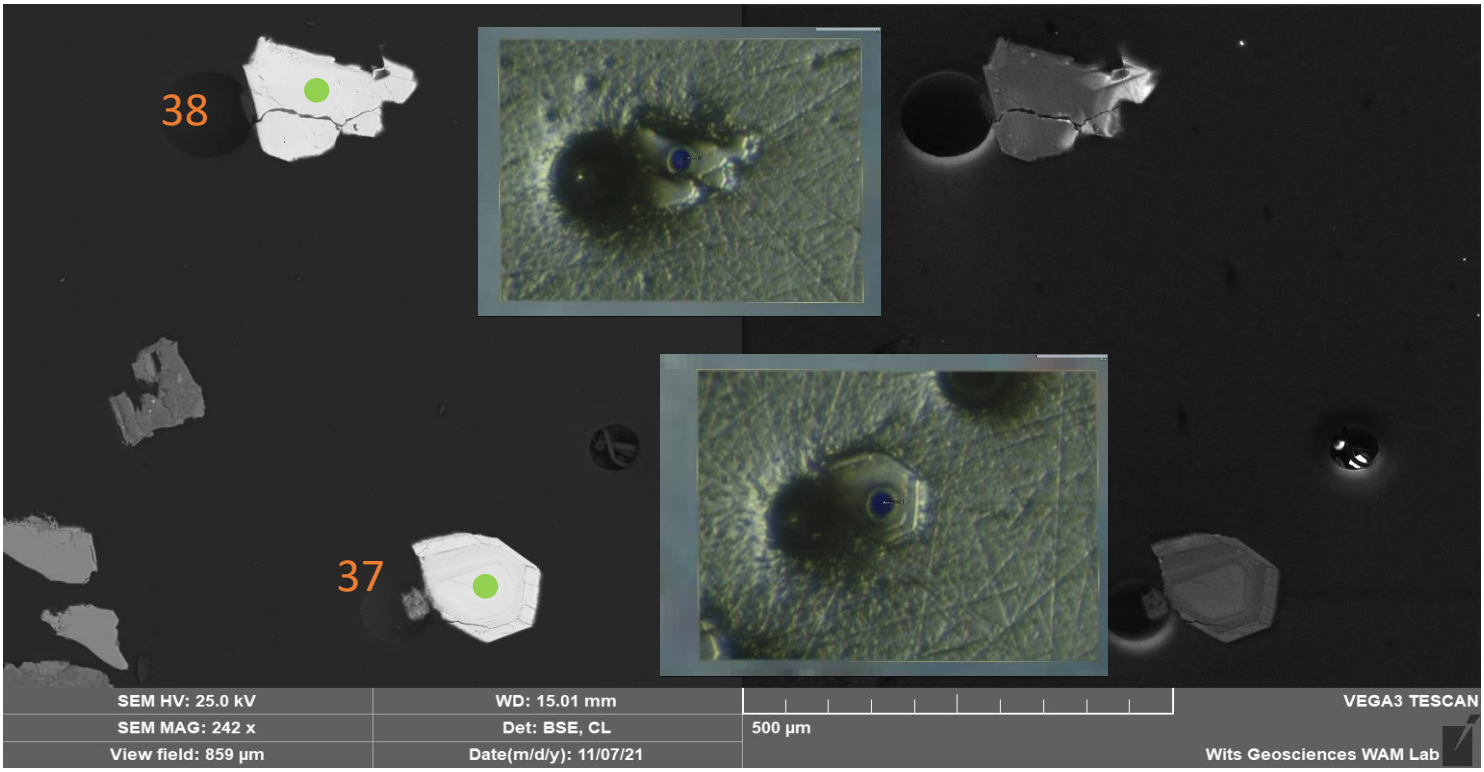

AJ-21-29-39/40

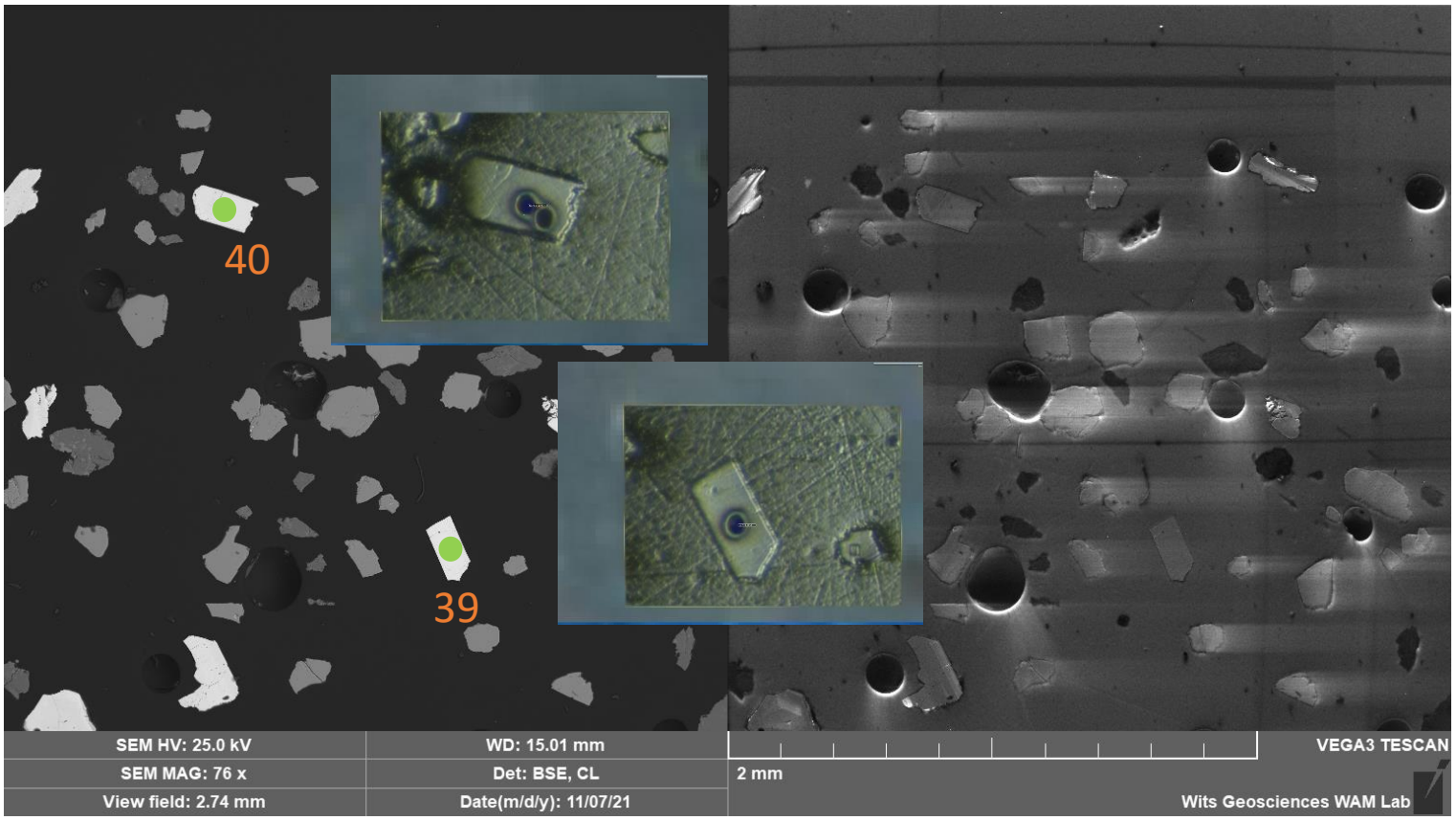

AJ-21-29-41

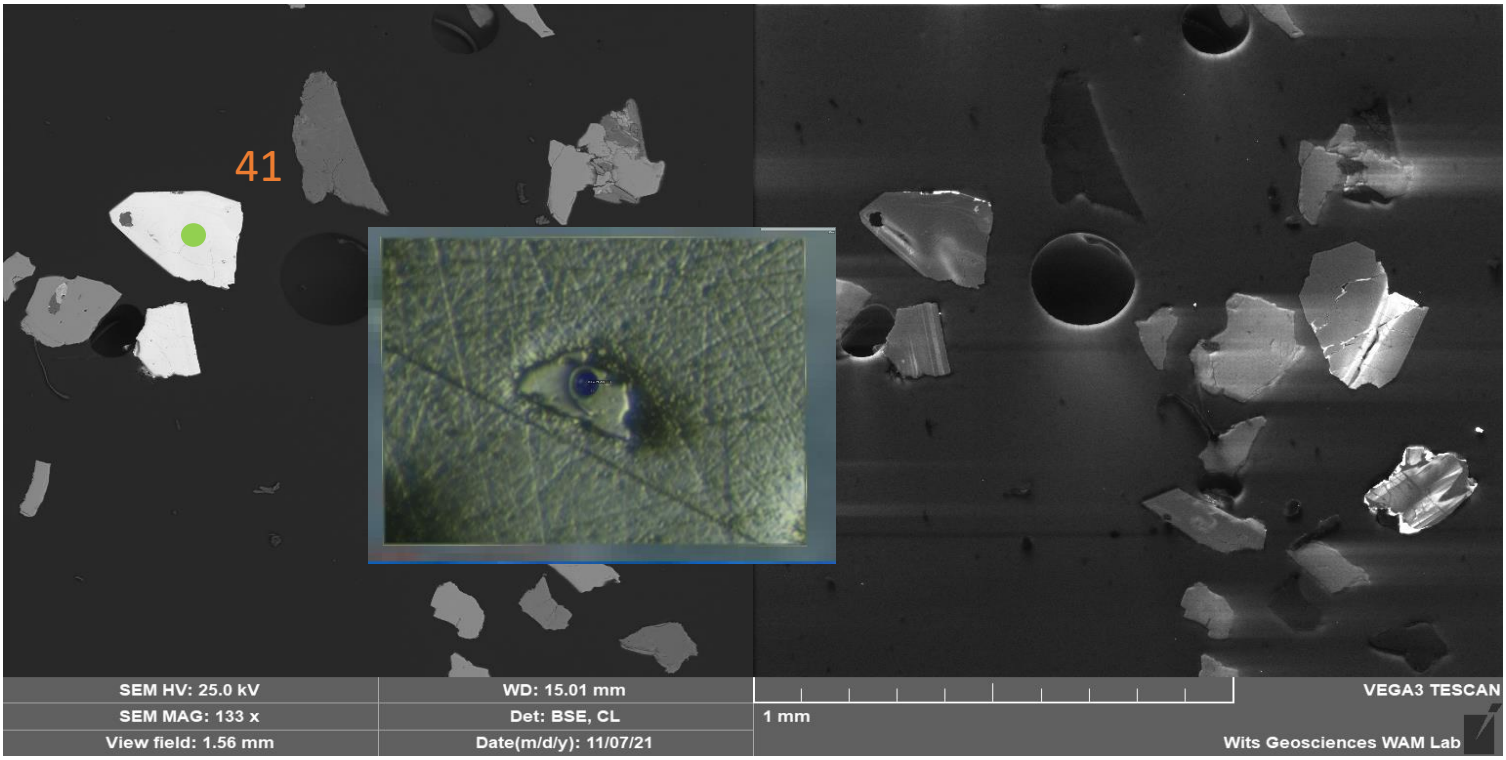
41
SEM HV: 25.0 kV
WD: 15.01 mm
VEGA3 TESCAN
SEM MAG: 133 x
Det: BSE, CL
1 mm
View field: 1.56 mm
Date(m/d/y): 11/07/21
Wits Geosciences WAM Lab

Appendix K: Whole rock and in-situ (on chalcopyrite grains) Cu and Fe isotope analyses conducted in this study.

Sample material	Rock type/sulphide type-texture	Sample #	δ^{56}Fe (‰)	SD	δ^{65}Cu (‰)	SD
Rio-Mayo lower crustal cumulate	Garnet-rich plagioclase bearing olivine hornblende pyroxenite	CA 14	0.230790139	0.07	0.864519561	0.07
Rio-Mayo lower crustal cumulate	Garnet-rich olivine hornblende pyroxenite	CA 15	-0.00647553	0.07	-0.937330751	0.07
Rio-Mayo lower crustal cumulate	Garnet-rich hornblende pyroxenite	CA 16	0.112358455	0.07	1.842012028	0.07
Rio-Mayo lower crustal cumulate	Garnet-rich hornblende pyroxenite	CA 17	0.127850193	0.07	0.08454902	0.07
Rio-Mayo lower crustal cumulate	Tonalite gneiss	CA 18	0.243282842	0.07	0.343078897	0.07
Rio-Mayo lower crustal cumulate	Tonalite gneiss	CA 24	0.304005057	0.07	0.238483085	0.07
Rio-Mayo lower crustal cumulate	Garnet clinopyroxenite	CA 25	0.16096696	0.07	0.389654	0.07
Rio-Mayo lower crustal cumulate	Garnet-rich plagioclase bearing olivine hornblende pyroxenite	CA 26	0.191064956	0.07	0.064007463	0.07
Rio-Mayo lower crustal cumulate	Quartz-rich granitoid gneiss	CA 27	0.151540583	0.07	STDS WERE POOR	0.07
Rio-Mayo lower crustal cumulate	Garnet-rich plagioclase bearing olivine hornblende pyroxenite	CA 28	0.227838187	0.07	1.250967552	0.07
Orange River Group	Sheared porphyritic andesite	AJ 13	0.318567799	0.07	0.254646572	0.07
Orange River Group	Rhyolite	AJ 14	0.259285604	0.07	0.7723295	0.07
Orange River Group	Mafic tuff	AJ 15	0.336455003	0.07	1.345806167	0.07
Orange River Group	Phenocrystic rhyolite	AJ 17	0.339035287	0.07	0.510820897	0.07
Orange River Group	Porphyritic andesite	AJ 38	0.252562608	0.07	0.25853417	0.07
Vioolsdrif Intrusive Suite	Leucogranite	AJ 2	0.094413007	0.07	0.24479065	0.07
Vioolsdrif Intrusive Suite	Adamellite	AJ 18	0.178550847	0.07	0.001010027	0.07
Vioolsdrif Intrusive Suite	Granodiorite	AJ 28	0.239862079	0.07	0.19876338	0.07
Vioolsdrif Intrusive Suite	Diorite	AJ 36	0.197613519	0.07	0.218952266	0.07
Vioolsdrif Intrusive Suite	Quartz-feldspar porphyry granodiorite	AJ 37	0.29393357	0.07	0.458163	0.07
Vioolsdrif Intrusive Suite	Quartz-feldspar porphyry granodiorite	AJ 9	-2.25	0.07	0.16	0.07

Kokerboom Intrusion	Clinopyroxenite	AJ 30	-0.073984201	0.07	-0.127718504	0.07
Kokerboom Intrusion	Gabbro	AJ 4	0.0096702	0.07	-0.144333922	0.07
Kokerboom Intrusion	Gabbro	AJ 23	0.154138279	0.07	-0.052279841	0.07
Sulphide	Disseminated chalcopyrite	AJ-21-39B 1	0.023611514	0.07	0.059418523	0.07
Sulphide	Disseminated chalcopyrite	AJ-21-09A	0.062771733	0.07	0.205155248	0.07
Sulphide	Massive chalcopyrite	AJ-21-39A 1	0.026694408	0.07	0.058070699	0.07
Sulphide	EDM vein chalcopyrite	AJ-21-39C	-0.108251583	0.07	-0.078752534	0.07
Sulphide	EDM vein chalcopyrite	AJ-21-41B 1	-0.010515858	0.07	-0.003001782	0.07
Sulphide	Vein-like chalcopyrite	AJ-21-39B 2	-0.080493112	0.07	0.112075124	0.07

high Cr content, not usable data

Standard	$\delta^{65}Cu$ (NIST 976)	$\delta^{66}Zn$ (lyon)
1643a 1	0.13	-0.03
1643a 2	0.08	-0.02
1643a 3	0.08	-0.02
BVHO- 2	0.12	0.02
2702	0.42	0.21
2702	0.38	0.19

Appendix L: Statistical analyses on the $\delta^{56}Fe$ isotope data

Table 1: Statistical analyses conducted on the $\delta^{56}Fe$ isotope data for the Kokerboom Intrusion, Orange River Group, Rio-Mayo lower crustal cumulates and Vioolsdrif Intrusive Suite.

	Count	Mean	Std	Min	25%	50%	75%	Max
Rio-Mayo lower crustal cumulates	10	0.1743	0.0865	-0.0065	0.1338	0.1760	0.2301	0.3040
Orange River Group	5	0.3012	0.0422	0.2526	0.2593	0.3186	0.3365	0.3390
Vioolsdrif Intrusive Suite	5	0.2009	0.0742	0.0944	0.1786	0.1976	0.2399	0.2939
Kokerboom Intrusion	3	0.0299	0.1154	-0.0740	-0.0322	-0.0097	0.0819	0.1541

From the statistical analyses in the table above, it is evident that the Kokerboom Intrusion has a lower $\delta^{56}Fe$ average (mean) compared to the Orange River Group and Vioolsdrif Intrusive Suite. This patten observed is also applicable to the lower, middle and upper quartiles for the Kokerboom Intrusion, Orange River Group and Vioolsdrif Intrusive Suite.

Appendix M: EPMA analyses conducted in this study.

Analysis #	Sample	Mineral	Na_2O	F	MgO	CaO	TiO_2	Cr_2O_3	Fe_2O_3	ZnO	SiO_2	Al_2O_3	Cl	K_2O	Total
1	AJ-21-36 A	Hornblende altered to biotite	0.130678	0.126665	12.883960	0.028637	1.590544	0.000015	18.466870	0.000012	40.769560	14.194390	0.015244	12.053770	100.558900
2	AJ-21-36 A	Hornblende altered to biotite	0.178273	0.143839	12.278970	0.000014	1.497097	0.003942	18.047400	0.000012	40.870210	13.888270	0.011570	12.014860	99.152660
3	AJ-21-36 A	Hornblende altered to biotite	0.150745	0.081547	12.252430	0.011556	1.438064	0.000015	17.289840	0.031613	39.426930	13.697770	0.000010	11.864310	96.484120
4	AJ-21-36 A	Hornblende altered to biotite	0.158818	0.142582	12.227230	0.022183	1.500593	0.028599	17.774470	0.000012	41.792520	14.050460	0.010399	12.099070	100.025900
5	AJ-21-36 A	Hornblende altered to biotite	0.135707	0.015585	11.567300	0.111641	1.444786	0.006028	17.027110	0.001115	39.978290	13.127460	0.005785	11.598830	95.215840
6	AJ-21-36 A	Hornblende altered to biotite	0.162014	0.041311	11.677160	0.019912	1.421983	0.003839	17.962200	0.046161	41.263730	14.167120	0.008188	12.396580	99.471240
7	AJ-21-36 A	Hornblende altered to biotite	0.129359	0.066268	11.778400	0.611250	1.987099	0.000015	17.833530	0.055482	41.561540	13.830410	0.018376	11.560780	99.671550
8	AJ-21-36 A	Hornblende altered to biotite	0.151980	0.008245	11.844990	0.141673	1.465469	0.001276	17.753720	0.014165	41.581120	14.008100	0.006640	11.818450	99.019470
9	AJ-21-36 A	Hornblende altered to biotite	0.131573	0.138338	12.178330	0.022618	1.471889	0.030788	18.103700	0.000012	43.028420	14.263340	0.030530	12.253100	101.914300
10	AJ-21-36 A	Hornblende altered to biotite	0.122911	0.042307	12.340710	0.032278	1.377266	0.037957	17.041720	0.018138	40.823060	14.094950	0.000010	12.191660	98.426240
11	AJ-21-36 A	Hornblende altered to biotite	0.131259	0.108300	12.041970	0.043666	1.441344	0.021970	17.310680	0.082488	40.282170	13.943220	0.007243	11.518400	97.184600
12	AJ-21-36 A	Hornblende altered to biotite	0.120519	0.114815	11.764460	0.033193	1.393781	0.035511	16.483060	0.008198	40.042400	14.060360	0.000010	11.936840	96.226970
13	AJ-21-36 A	Hornblende altered to biotite	0.140331	0.064986	11.677450	0.091275	1.513347	0.013928	17.649870	0.044599	36.331050	13.303620	0.006596	10.977600	92.003980

14	AJ-21-36 A	Hornblende altered to biotite	0.161944	0.146922	11.695840	0.002583	1.563997	0.047073	17.584870	0.098992	36.535570	13.284320	0.002037	11.379270	92.795660
15	AJ-21-36 A	Hornblende altered to biotite	0.050261	0.090960	11.754660	0.077230	1.415483	0.049101	17.519990	0.076740	34.681910	12.829880	0.006221	10.463360	89.263330
16	AJ-21-36 A	Hornblende altered to biotite	0.043217	0.058001	12.043550	0.117372	1.376376	0.041102	17.497920	0.032103	41.801170	13.699630	0.019576	11.062860	98.076170
17	AJ-21-36 A	Hornblende altered to biotite	0.178160	0.190695	12.011320	0.014333	1.495630	0.033412	17.980260	0.010696	42.236980	14.033310	0.007710	12.249240	100.706800
18	AJ-21-36 A	Hornblende altered to biotite	0.124838	0.203360	11.719180	0.000014	1.381525	0.015153	18.021960	0.054930	41.125170	13.936610	0.002022	12.012550	98.844380
19	AJ-21-36 A	Hornblende altered to biotite	0.139054	0.184674	12.040340	0.000014	1.420713	0.023396	16.986630	0.030014	40.276650	13.766010	0.003113	12.343400	97.446220
20	AJ-21-36 A	Hornblende altered to biotite	0.134673	0.113249	11.715670	0.019293	1.438916	0.000015	17.014100	0.000012	39.660500	13.713890	0.000010	11.352200	95.374120
21	AJ-21-36 A	Hornblende altered to biotite	0.114295	0.050061	12.333080	0.006347	1.501310	0.010358	17.941650	0.020371	40.541420	13.984400	0.010367	11.848230	98.630960
22	AJ-21-36 A	Hornblende altered to biotite	0.154235	0.174395	11.815240	0.072945	1.360970	0.045111	17.258970	0.033393	40.684410	13.857650	0.000010	11.342780	97.044880
23	AJ-21-36 A	Hornblende altered to biotite	0.089840	0.139680	12.088400	0.066343	1.413823	0.005099	17.357530	0.012967	40.223540	13.948050	0.000510	11.799720	97.366390
24	AJ-21-36 A	Hornblende altered to biotite	0.172920	0.049938	12.016850	0.029173	1.439062	0.041241	16.918110	0.005956	39.787490	13.705580	0.000010	11.801620	96.243270
25	AJ-21-36 A	Hornblende altered to biotite	0.174706	0.241363	12.368740	0.064881	1.450322	0.033626	17.592620	0.063400	41.049300	14.442060	0.005176	11.787450	99.537060
26	AJ-21-36 A	Hornblende altered to biotite	0.215320	0.181398	11.970670	0.115939	1.461522	0.037076	17.231350	0.037826	40.857520	14.012310	0.011762	11.653230	97.987340
27	AJ-21-36 A	Hornblende altered to biotite	0.136207	0.118432	11.518240	1.602769	1.355636	0.043022	16.909500	0.000012	40.895820	13.966950	0.002604	10.728740	97.494230
28	AJ-21-36 A	Hornblende altered to biotite	0.147555	0.089896	11.300970	0.038109	1.556904	0.000015	16.517260	0.003538	34.068780	12.520820	0.000010	10.487120	86.986510
29	AJ-21-36 A	Hornblende altered to biotite	0.146524	0.211455	11.390240	0.032760	1.541929	0.021632	17.554170	0.023618	33.894380	12.513000	0.002551	10.602210	88.152050

30	AJ-21-36 A	Hornblende altered to biotite	0.122119	0.105178	11.272440	0.010029	1.689022	0.016393	17.090910	0.026884	34.023020	12.565540	0.000010	10.694550	87.854480
31	AJ-21-36 B	Hornblende altered to biotite	0.130336	0.000010	11.593210	0.007186	1.339811	0.000015	17.542480	0.000012	40.773330	13.699910	0.002499	12.116200	97.442990
31	AJ-21-36 B	Hornblende altered to biotite	0.176623	0.179783	11.091650	0.816511	2.296119	0.016292	16.890840	0.027741	41.223940	13.336220	0.016479	11.564690	97.839710
33	AJ-21-36 B	Hornblende altered to biotite	0.136578	0.155014	11.749420	0.004695	1.533109	0.006315	18.038410	0.000012	42.799850	14.013390	0.011621	12.237280	100.877400
34	AJ-21-36 B	Hornblende altered to biotite	0.136354	0.024462	11.919180	0.012251	1.446002	0.010159	17.385340	0.042352	36.144930	12.859180	0.004575	11.265210	91.526000
35	AJ-21-36 B	Hornblende altered to biotite	0.148264	0.081640	11.673970	0.006628	1.385108	0.000015	17.535020	0.064310	40.996400	13.852460	0.012135	12.222100	98.256970
36	AJ-21-36 B	Hornblende altered to biotite	0.159180	0.129596	11.593420	0.064171	1.538814	0.020017	16.714570	0.015026	41.857400	13.975620	0.000010	11.516360	97.881880
37	AJ-21-36 B	Hornblende altered to biotite	0.122430	0.191075	12.099090	0.005428	1.326356	0.039844	17.431120	0.081921	43.036090	14.088770	0.005649	12.558310	101.246700
38	AJ-21-36 B	Hornblende altered to biotite	0.134765	0.186464	11.957110	0.000014	1.379014	0.000015	17.256630	0.047516	42.425460	14.023990	0.007018	12.370850	99.997650
39	AJ-21-36 B	Hornblende altered to biotite	0.136979	0.182007	11.664210	0.000014	1.223619	0.035510	17.170690	0.000012	42.393890	14.129100	0.010276	12.369340	99.512470
40	AJ-21-36 B	Hornblende altered to biotite	0.187844	0.048940	11.828470	0.054429	1.483858	0.000015	17.479640	0.052542	40.918230	14.052340	0.023730	12.134660	98.514670
41	AJ-21-36 B	Hornblende altered to biotite	0.234273	0.221905	11.139790	0.038226	1.485144	0.012245	16.577300	0.000012	42.516480	13.698360	0.028400	11.548800	97.694500
42	AJ-21-36 B	Hornblende altered to biotite	0.126914	0.120100	12.121770	0.038312	1.440428	0.007440	16.993600	0.027509	40.859090	14.098710	0.000010	11.611580	97.721280
43	AJ-21-36 B	Hornblende altered to biotite	0.112730	0.112188	11.869020	1.058571	1.311699	0.009959	17.079550	0.008071	37.633910	13.046370	0.005488	9.998134	92.490580
44	AJ-21-36 B	Hornblende altered to biotite	0.158845	0.050423	12.057290	0.033089	1.498617	0.067835	17.829390	0.018113	39.267810	13.669830	0.020362	11.723300	96.654550
45	AJ-21-36 B	Hornblende altered to biotite	0.172868	0.150350	11.926860	0.016057	1.512300	0.032491	18.472430	0.000012	39.316300	13.489400	0.018218	11.816100	97.157840

46	AJ-21-36 B	Hornblende altered to biotite	0.084827	0.034026	11.683350	0.040070	1.612182	0.000015	16.855050	0.074739	34.793760	12.933170	0.000010	11.110690	89.452760
47	AJ-21-36 B	Hornblende altered to biotite	0.090783	0.150520	11.589540	0.816577	2.392362	0.033590	16.699010	0.025079	33.814830	12.413930	0.004635	10.488790	88.759080
48	AJ-21-36 B	Hornblende altered to biotite	0.075809	0.059544	12.233880	0.085293	1.333079	0.009306	17.634840	0.093689	35.902520	13.465090	0.012261	10.910580	92.071660
49	AJ-21-36 B	Hornblende altered to biotite	0.138019	0.192745	12.194380	0.048454	1.441017	0.000015	17.143220	0.047967	40.749540	14.010640	0.008812	12.229650	98.473090
50	AJ-21-36 B	Hornblende altered to biotite	0.118507	0.243734	12.387110	0.000014	1.404942	0.000015	17.423850	0.054213	41.142170	14.440220	0.000010	12.520770	99.989700
51	AJ-21-36 B	Hornblende altered to biotite	0.106175	0.225268	12.104210	0.000014	1.433890	0.000015	16.133060	0.000012	40.806690	14.091780	0.006169	12.210950	97.380990
52	AJ-21-36 B	Hornblende altered to biotite	0.175212	0.200609	11.917290	0.050669	1.463762	0.000015	18.130920	0.050631	38.851250	14.025670	0.018234	11.969590	97.100410
53	AJ-21-36 B	Hornblende altered to biotite	0.135693	0.120909	11.739700	0.007841	1.523998	0.028817	17.690870	0.011599	38.364690	13.637740	0.005013	11.691700	95.199810
54	AJ-21-36 B	Hornblende altered to biotite	0.169044	0.133570	12.202090	0.026785	1.495643	0.000015	17.759940	0.025236	38.804620	13.532650	0.014543	11.770710	96.170520
55	AJ-21-36 B	Hornblende altered to biotite	0.165865	0.174276	12.224630	0.031764	1.456701	0.032026	16.183010	0.049625	41.708040	13.999170	0.000010	12.256240	98.544670
56	AJ-21-36 B	Hornblende altered to biotite	0.132678	0.173239	12.517870	0.026960	1.356975	0.012073	17.663940	0.019831	43.552960	14.479250	0.009653	12.483740	102.631700
57	AJ-21-36 B	Hornblende altered to biotite	0.122516	0.254397	11.946670	0.043234	1.377264	0.005251	17.481730	0.000012	43.029850	14.350410	0.014695	12.285140	101.160600
58	AJ-21-36 B	Hornblende altered to biotite	0.165466	0.076442	11.876950	0.000014	1.576578	0.011878	17.642890	0.025649	37.252960	13.455570	0.008438	11.958920	94.277780
59	AJ-21-36 B	Hornblende altered to biotite	0.161488	0.086951	11.098890	0.000014	1.473087	0.008608	16.851930	0.000012	35.972010	12.950920	0.000010	10.953260	89.772640
60	AJ-21-36 B	Hornblende altered to biotite	0.100534	0.213863	11.647720	0.003239	1.434942	0.000015	17.568250	0.007090	39.562410	13.559660	0.000010	11.796540	96.173820
61	AJ-21-36 B	Hornblende altered to biotite	0.170661	0.094264	11.925710	0.000014	1.511131	0.000015	17.721750	0.000012	38.646020	13.905100	0.007988	11.899510	96.084450

62	AJ-21-36 B	Hornblende altered to biotite	0.144466	0.200408	11.941840	0.000014	1.543519	0.033665	17.567910	0.022744	39.877650	13.845880	0.010861	12.279780	97.708840
63	AJ-21-36 B	Hornblende altered to biotite	0.171154	0.144517	11.992350	0.000014	1.383825	0.047516	17.858550	0.034190	40.541720	14.352720	0.005280	12.141110	98.879310
64	AJ-21-36 B	Hornblende altered to biotite	0.135106	0.110591	12.418470	0.000014	1.508208	0.040846	17.200720	0.012176	40.190810	13.869180	0.012104	12.175070	97.913860
65	AJ-21-36 B	Hornblende altered to biotite	0.128038	0.135016	12.237940	0.032556	1.402541	0.013106	17.577700	0.000012	40.665360	14.086250	0.004199	11.570960	98.094450
66	AJ-21-36 B	Hornblende altered to biotite	0.153173	0.097948	11.819340	0.010050	1.444889	0.005060	17.307210	0.003510	40.332480	13.550010	0.011636	11.883350	96.895870
67	AJ-21-36 B	Hornblende altered to biotite	0.133611	0.067334	12.643610	0.038918	1.351091	0.039254	17.129390	0.000012	38.572750	13.881160	0.010995	11.484690	95.617680
68	AJ-21-36 B	Hornblende altered to biotite	0.141279	0.098407	11.852620	0.019799	1.457981	0.005091	17.319440	0.031786	38.509200	13.822610	0.008648	11.895010	95.412380
69	AJ-21-36 B	Hornblende altered to biotite	0.105015	0.235940	11.517970	0.427539	1.845922	0.019544	16.745060	0.066182	37.317340	13.380260	0.001558	11.690210	93.633560
70	AJ-21-32	Hornblende altered to biotite	0.059099	0.217660	11.374320	0.037618	1.388278	0.000015	17.449580	0.008939	38.223580	13.189060	0.118689	12.110300	94.406220
71	AJ-21-32	Hornblende altered to biotite	0.070762	0.109822	11.813700	0.499694	2.041103	0.023410	17.655770	0.004800	41.056720	13.850640	0.101538	12.538870	99.969990
72	AJ-21-32	Hornblende altered to biotite	0.075664	0.053157	12.205400	0.064665	1.718300	0.028797	18.412940	0.039300	41.522820	14.630870	0.116139	12.631380	101.711100
73	AJ-21-32	Hornblende altered to biotite	0.091469	0.207972	11.747230	0.035686	1.588142	0.016817	18.208780	0.000012	38.524870	13.492530	0.108058	12.164200	96.364560
74	AJ-21-32	Hornblende altered to biotite	0.097403	0.147541	11.987010	0.137142	1.823182	0.006726	18.300040	0.013685	39.848630	13.851110	0.101532	12.400990	98.885500
75	AJ-21-32	Hornblende altered to biotite	0.091765	0.034247	11.698150	0.010560	1.532002	0.000015	17.923600	0.040532	39.083980	13.569590	0.099205	12.300440	96.585750
76	AJ-21-32	Hornblende altered to biotite	0.093940	0.110003	12.005380	0.000014	1.560585	0.000015	17.689990	0.002420	41.639190	13.964370	0.118693	12.544760	99.962820
77	AJ-21-32	Hornblende altered to biotite	0.122539	0.017019	12.035010	0.002218	1.564485	0.028892	17.594410	0.040020	43.029400	14.178900	0.116938	12.647480	101.584000

78	AJ-21-32	Hornblende altered to biotite	0.115387	0.155659	11.892640	0.000014	1.473816	0.010696	17.774510	0.028398	43.300400	14.552830	0.136111	12.875040	102.537900
79	AJ-21-32	Hornblende altered to biotite	0.106917	0.000010	11.679550	0.000014	1.622885	0.046456	17.280150	0.028613	39.214650	14.147140	0.108139	12.345380	96.781630
80	AJ-21-32	Hornblende altered to biotite	0.076368	0.075049	11.688370	0.280709	1.850928	0.011599	17.908860	0.059542	40.080430	13.538560	0.109005	12.383390	98.252310
81	AJ-21-32	Hornblende altered to biotite	0.096298	0.083673	11.573940	0.061415	1.642773	0.033633	17.210330	0.009561	39.570790	13.856410	0.097064	12.158350	96.607500
82	AJ-21-32	Hornblende altered to biotite	0.127373	0.094322	11.929710	0.000014	1.693755	0.035896	18.286350	0.000012	40.380310	13.641270	0.092980	12.380240	98.820270
83	AJ-21-32	Hornblende altered to biotite	0.096991	0.186781	11.730550	0.014725	1.424251	0.025054	17.793370	0.054876	39.811950	13.495780	0.095878	12.387870	97.319390
84	AJ-21-32	Hornblende altered to biotite	0.107316	0.016876	11.920030	0.006199	1.517927	0.026172	18.346530	0.004842	40.325560	14.159610	0.100924	12.589940	99.282270
85	AJ-21-32	Hornblende altered to biotite	0.098358	0.041882	11.376450	0.010746	1.473347	0.000015	17.398160	0.077914	39.968480	13.801740	0.121214	12.256520	96.800430
86	AJ-21-32	Hornblende altered to biotite	0.100423	0.042105	11.758910	0.000014	1.593703	0.023449	17.698280	0.000012	41.055560	13.610300	0.110340	12.281440	98.433720
87	AJ-21-32	Hornblende altered to biotite	0.134520	0.128818	12.140350	0.000014	1.683019	0.000015	18.411580	0.003688	42.074390	14.403900	0.107803	12.878380	102.151200
88	AJ-21-32	Hornblende altered to biotite	0.113267	0.137954	12.035750	0.000014	1.596047	0.000015	18.361000	0.077979	40.656290	14.143080	0.096794	12.593800	99.996250
89	AJ-21-32	Hornblende altered to biotite	0.085525	0.000010	11.800670	0.751583	2.221833	0.000015	17.353940	0.018283	40.057290	13.863760	0.111522	12.129210	98.599880
90	AJ-21-32	Hornblende altered to biotite	0.063602	0.252825	11.915100	0.000014	1.627367	0.085181	18.790840	0.042514	40.950780	14.276430	0.139275	13.041410	101.407200
91	AJ-21-32	Hornblende altered to biotite	0.080829	0.000010	11.519290	0.010672	1.545229	0.048671	17.490670	0.000012	40.255340	14.481700	0.102929	12.440930	98.187480
92	AJ-21-32	Hornblende altered to biotite	0.109411	0.112762	12.101630	0.000014	1.636597	0.000015	17.630350	0.033501	40.353400	14.301640	0.127537	12.681720	99.267310
93	AJ-21-32	Hornblende altered to biotite	0.092884	0.156612	11.882140	0.015474	1.427854	0.053870	17.135670	0.000012	40.279680	14.353230	0.110156	12.485670	98.233560

94	AJ-21-32	Hornblende altered to biotite	0.092661	0.154617	11.491460	0.000014	1.546494	0.000015	17.801690	0.045576	40.164440	13.948170	0.084650	12.149290	97.672730
95	AJ-21-32	Hornblende altered to biotite	0.124160	0.102135	11.726180	0.000014	1.532551	0.000015	18.169570	0.000012	39.574620	13.578110	0.110860	12.380530	97.526440
96	AJ-21-32	Hornblende altered to biotite	0.100817	0.056041	11.343880	0.000014	1.507899	0.042162	17.263220	0.089422	38.526730	13.405610	0.108950	12.068400	94.717350
97	AJ-21-32	Hornblende altered to biotite	0.109326	0.151970	11.666720	0.000014	1.689501	0.010448	17.754090	0.022924	40.570790	13.804280	0.102115	12.727560	98.820860
98	AJ-21-32	Hornblende altered to biotite	0.098199	0.067202	11.944840	0.000014	1.615916	0.001300	17.433060	0.000012	40.060110	14.078520	0.112427	12.786180	98.337240
99	AJ-21-32	Hornblende altered to biotite	0.082614	0.075092	11.788070	0.000014	1.630008	0.000015	17.230330	0.033350	39.775000	13.611910	0.109030	12.597340	97.169260
100	AJ-21-32	Hornblende altered to biotite	0.107911	0.124669	11.339640	0.000014	1.601685	0.019316	17.088270	0.032134	38.342310	13.696950	0.123368	12.037990	94.798240
101	AJ-21-32	Hornblende altered to biotite	0.090639	0.138781	11.883050	0.018402	1.620977	0.000015	17.800350	0.044708	40.319670	14.058850	0.116933	12.585080	98.850290
102	AJ-21-32	Hornblende altered to biotite	0.099580	0.059903	11.863870	0.000014	1.482947	0.009279	17.520700	0.000012	39.766320	13.880710	0.105814	12.523770	97.511940
103	AJ-21-32	Hornblende altered to biotite	0.128170	0.142320	11.919090	0.000014	1.603763	0.000015	17.977390	0.015551	42.413460	13.913200	0.114248	12.734150	101.172800
104	AJ-21-32	Hornblende altered to biotite	0.099706	0.000010	11.775920	0.000014	1.542708	0.022527	18.295020	0.026956	42.087320	14.227090	0.126593	12.587270	100.936000
105	AJ-21-32	Hornblende altered to biotite	0.067832	0.126612	12.006520	0.014382	1.402560	0.000015	18.214780	0.091950	42.709390	14.144660	0.116680	12.582100	101.677700
106	AJ-21-32	Hornblende altered to biotite	0.105831	0.205799	11.773890	0.007386	1.605560	0.000015	17.416070	0.018350	42.073570	14.359190	0.118938	12.750970	100.631000
107	AJ-21-32	Hornblende altered to biotite	0.115809	0.000010	11.847840	0.000014	1.716183	0.018469	17.764730	0.000012	42.425030	14.136630	0.099000	12.699450	101.020300
108	AJ-21-32	Hornblende altered to biotite	0.093219	0.235063	11.667040	0.000227	1.558966	0.024245	17.890440	0.000012	42.349530	14.157250	0.130128	12.767420	101.038900
109	AJ-21-32	Hornblende altered to biotite	0.096339	0.167562	11.475010	0.005706	1.673555	0.003894	17.909070	0.022800	40.356190	13.656480	0.119234	12.373830	98.075020

110	AJ-21-32	Hornblende altered to biotite	0.115975	0.043119	11.782490	0.000014	1.536442	0.032091	18.639650	0.033407	41.387930	14.097030	0.122999	12.534480	100.535900
111	AJ-21-32	Hornblende altered to biotite	0.098655	0.000010	11.340090	0.014318	1.496563	0.000015	17.617160	0.000012	39.989140	14.035720	0.106661	12.541190	97.426090
112	AJ-21-32	Hornblende altered to biotite	0.105554	0.173342	10.829560	1.856286	3.692409	0.005263	16.937360	0.041150	38.526420	12.957130	0.120888	11.380800	96.792410
113	AJ-21-32	Hornblende altered to biotite	0.090787	0.065293	11.105450	0.632587	2.243315	0.012602	18.591690	0.020986	38.026680	12.765370	0.121704	11.824530	95.720500
114	AJ-21-32	Hornblende altered to biotite	0.089440	0.123834	11.687930	0.000014	1.558926	0.002563	17.882760	0.000012	38.663210	13.455630	0.115141	12.366080	96.106350
115	AJ-21-321	Hornblende altered to biotite	0.083045	0.181755	11.198400	0.000014	1.647517	0.003874	16.973860	0.017898	42.608410	15.612390	0.000010	13.513550	102.148500
116	AJ-21-322	Hornblende altered to biotite	0.067037	0.332198	10.895170	0.000014	1.464015	0.005208	16.863460	0.049351	41.490820	15.451950	0.000010	13.295900	100.242000
117	AJ-21-323	Hornblende altered to biotite	0.072855	0.311490	11.047790	0.000014	1.461079	0.031161	16.342970	0.051310	41.401920	15.591900	0.005957	13.236190	99.828490
118	AJ-21-324	Hornblende altered to biotite	0.078757	0.180853	10.745290	0.000014	1.346352	0.005174	15.852000	0.000012	35.489990	14.345910	0.011371	12.585210	90.915290
119	AJ-21-325	Hornblende altered to biotite	0.082673	0.262343	10.550070	0.000014	1.497750	0.000015	16.021580	0.000012	36.643030	14.569050	0.009565	12.561850	92.482110
120	AJ-21-326	Hornblende altered to biotite	0.042291	0.253833	11.215220	0.006077	1.269741	0.027561	16.242020	0.052255	37.350070	15.019240	0.003856	12.905410	94.682560
121	AJ-21-327	Hornblende altered to biotite	0.090107	0.273488	10.389460	0.000014	1.395613	0.040314	16.743760	0.000012	40.650990	15.155730	0.000010	12.695660	97.739060
122	AJ-21-328	Hornblende altered to biotite	0.075372	0.223603	10.526580	0.000014	1.504439	0.000015	16.802740	0.025211	41.162700	15.327510	0.009355	12.854310	98.787790
123	AJ-21-329	Hornblende altered to biotite	0.058709	0.183085	10.785190	0.009725	1.354654	0.006832	16.443230	0.059368	40.508610	15.104420	0.004373	12.995720	97.839420
124	AJ-21-3210	Hornblende altered to biotite	0.073260	0.228139	10.714100	0.000224	1.426227	0.000015	16.540010	0.052623	41.064980	15.180090	0.000010	12.983720	98.596180
125	AJ-21-3211	Hornblende altered to biotite	0.036809	0.275404	10.822420	0.024184	1.523099	0.000015	16.469420	0.000012	41.232230	15.168410	0.005393	12.769800	98.667400

126	AJ-21-32 12	Hornblende altered to biotite	0.049946	0.112038	10.517070	0.005025	1.398041	0.000015	16.405340	0.036163	41.253480	15.445100	0.009182	12.661480	98.190470
127	AJ-21-32 13	Hornblende altered to biotite	0.064577	0.211481	10.420690	0.000014	1.182233	0.003980	15.847030	0.046613	39.835570	14.843490	0.014874	12.360210	95.081700
128	AJ-21-32 14	Hornblende altered to biotite	0.074753	0.271624	10.641260	0.009035	1.309062	0.009328	16.554880	0.008630	40.429850	14.783800	0.007471	12.695740	97.041630
129	AJ-21-32 15	Hornblende altered to biotite	0.084934	0.111895	10.626090	0.003422	1.373041	0.035018	16.163310	0.031129	40.009690	14.961900	0.000010	12.671560	96.370090
130	AJ-21-32 16	Hornblende altered to biotite	0.051523	0.159883	10.635670	0.001565	1.301537	0.021102	16.695380	0.031715	41.343360	15.450880	0.000010	12.936280	98.925910
131	AJ-21-32 17	Hornblende altered to biotite	0.079713	0.231728	10.155700	0.000228	1.491807	0.022841	16.312280	0.028582	40.706630	14.915750	0.000010	12.395030	96.629300
132	AJ-21-32 18	Hornblende altered to biotite	0.056372	0.181605	10.601100	0.001376	1.369926	0.012187	16.346460	0.000012	40.769940	15.069390	0.002711	12.656320	97.387940
133	AJ-21-32 19	Hornblende altered to biotite	0.050817	0.173277	10.678100	0.000014	1.438885	0.000015	15.985250	0.005004	41.296900	14.980660	0.000010	12.673480	97.538380
134	AJ-21-32 20	Hornblende altered to biotite	0.049120	0.181425	10.414580	0.000014	1.450757	0.000015	16.156890	0.004994	41.174060	14.994890	0.002163	12.582520	97.315780
135	AJ-21-32 21	Hornblende altered to biotite	0.008973	0.275361	10.571620	0.000014	1.443624	0.038846	15.854140	0.000012	41.623760	15.254210	0.011097	12.730370	98.164350
136	AJ-21-32 22	Hornblende altered to biotite	0.086721	0.062353	10.673870	0.049658	1.660535	0.015294	16.365510	0.000012	40.991250	15.129360	0.000010	12.770600	98.106640
137	AJ-21-32 23	Hornblende altered to biotite	0.058050	0.350022	10.660300	0.002555	1.490501	0.012344	16.496930	0.011412	40.809800	15.105270	0.003841	12.906050	98.162090
138	AJ-21-32 24	Hornblende altered to biotite	0.046430	0.267940	10.809820	0.000014	1.620542	0.000015	16.890680	0.033561	41.773270	15.304510	0.015076	13.436160	100.532900
139	AJ-21-32 25	Hornblende altered to biotite	0.084430	0.330592	10.509380	0.000014	1.671708	0.007951	16.173270	0.073464	40.945350	14.976580	0.003180	12.753170	97.823970
140	AJ-21-32 26	Hornblende altered to biotite	0.090485	0.207151	10.452840	0.001827	1.621375	0.018880	16.458280	0.036148	41.093130	15.006650	0.002698	12.819350	98.148640
141	AJ-21-32 27	Hornblende altered to biotite	0.082869	0.093586	10.247570	0.010343	1.592514	0.045156	16.052090	0.030683	40.180560	15.104970	0.006375	12.571530	96.297520

142	AJ-21-32 28	Hornblende altered to biotite	0.066250	0.423629	11.097450	0.000014	1.379609	0.000015	16.129010	0.007671	41.100120	15.577270	0.003320	12.905890	98.981190
143	AJ-21-32 29	Hornblende altered to biotite	0.082985	0.288157	10.884470	0.000014	1.424652	0.000015	16.192610	0.057271	41.294650	15.760240	0.003943	13.071590	99.368610
144	AJ-21-32 30	Hornblende altered to biotite	0.094360	0.094384	10.576120	0.000014	1.417246	0.000015	15.709260	0.023509	40.580940	15.320520	0.003750	12.671520	96.837760
145	AJ-21-32 31	Hornblende altered to biotite	0.091777	0.292953	10.765070	0.000014	1.272843	0.014857	16.369450	0.093621	42.031090	16.099000	0.003785	12.917790	100.210800
146	AJ-21-32 32	Hornblende altered to biotite	0.088243	0.377181	10.620760	0.000014	1.368209	0.036297	16.261660	0.000012	40.696610	15.228090	0.000010	12.719830	97.676250
147	AJ-21-32 33	Hornblende altered to biotite	0.025110	0.247377	11.045200	0.007043	1.217534	0.001386	16.164910	0.008970	40.856090	15.718500	0.002220	12.698290	98.251030
148	AJ-21-32 34	Hornblende altered to biotite	0.049586	0.124059	11.068430	0.020448	1.414341	0.000015	16.764830	0.038479	41.635620	15.515160	0.000555	13.090870	100.009800
149	AJ-21-32 35	Hornblende altered to biotite	0.045360	0.174737	11.203380	0.009275	1.363004	0.057478	16.910260	0.000012	41.672170	15.817120	0.003286	13.252240	100.800700
150	AJ-21-32 36	Hornblende altered to biotite	0.056386	0.079092	11.161520	0.050227	1.263908	0.001379	16.631560	0.063849	41.848430	15.765110	0.009970	12.046660	99.248960